



THE UNIVERSITY
of ADELAIDE

**Designing Two-Dimensional Nanomaterials for Electrocatalytic
Clean Energy Conversion**

By Huanyu Jin

School of Chemical Engineering and Advanced Materials
Faculty of Engineering, Computer and Mathematical Science

A thesis submitted for the degree of Doctor of Philosophy

The University of Adelaide

June 2020

Table of Contents

Abstract	1
Declaration	5
Acknowledgments	7
Chapter 1: Introduction	9
1.1 Significance of the Project	9
1.2 Research Objectives	10
1.3 Thesis Outline	11
1.4 References	12
Chapter 2: Literature Review	15
2.1 Introduction and Significance	15
2.2 Emerging Two-Dimensional Nanomaterials for Electrocatalysis.....	15
Chapter 3: Constructing Tunable Dual Active Sites on Two-Dimensional C₃N₄@MoN Hybrid for Electrocatalytic Hydrogen Evolution	91
3.1 Introduction and Significance	91
3.2 Constructing Tunable Dual Active Sites on Two-Dimensional C ₃ N ₄ @MoN Hybrid for Electrocatalytic Hydrogen Evolution	92
Chapter 4: Single-Crystal Nitrogen-Rich Two-Dimensional Mo₅N₆ Nanosheets for Efficient and Stable Seawater Splitting	113
4.1 Introduction and Significance	113
4.2 Single-Crystal Nitrogen-Rich Two-Dimensional Mo ₅ N ₆ Nanosheets for Efficient and Stable Seawater Splitting.....	114
Chapter 5: Heteroatom-Doped Transition Metal Electrocatalysts for Hydrogen Evolution Reaction	137
5.1 Introduction and Significance	137
5.2 Heteroatom-Doped Transition Metal Electrocatalysts for Hydrogen Evolution Reaction.....	138
Chapter 6: Nitrogen Vacancies on 2D Layered W₂N₃: A Stable and Efficient Active Site for Nitrogen Reduction Reaction	169
6.1 Introduction and Significance	169
6.2 Nitrogen Vacancies on 2D Layered W ₂ N ₃ : A Stable and Efficient Active Site for Nitrogen Reduction Reaction	170

Chapter 7: Molten Salt-Directed Catalytic Synthesis of 2D Layered Transition Metal Nitrides for Efficient Hydrogen Evolution	207
7.1 Introduction and Significance	207
7.2 Molten Salt-Directed Catalytic Synthesis of 2D Layered Transition Metal Nitrides for Efficient Hydrogen Evolution.....	208
Chapter 8: Conclusions and Perspectives.....	253
8.1 Conclusions	253
8.2 Perspectives.....	255
Appendix: Publications during PhD Candidature	258

Abstract

The development of efficient and clean energy conversion technologies is a key issue for the sustainability of energy technologies. Hydrogen is one of the best fuels for clean energy systems as its combustion product is only water. Therefore, the development of cost-effective energy conversion technologies for hydrogen generation is significant. Electrocatalytic water splitting using renewable energy is one of the best ways to obtain high-purity hydrogen and the process emits no carbon dioxide. Electrocatalytic reactions occur on the surface of electrode materials. Consequently, understanding and tuning the surface properties of electrode materials is a key aspect in the design and preparation of efficient electrocatalysts. Compared to other nanomaterials, such as nanowires or nanoparticles, the most important two features of two-dimensional (2D) nanomaterials for electrocatalysis are their tunable and uniformly exposed lattice plane and unique electronic state. This Thesis aims to synthesize and optimize novel 2D nanomaterials for the study of hydrogen-related electrocatalytic reactions. Our target reactions include the hydrogen evolution reaction (HER) and the nitrogen reduction reaction (NRR), which have great potential in hydrogen-related clean energy conversion systems.

The first two chapters provide a systematic review of the development of 2D nanomaterials for electrocatalysis. The unique advances of 2D electrocatalysts are discussed based on different compositions and functions followed by specific design principles. Following this, various 2D electrocatalysts for a series of electrocatalytic processes involved in the water cycle, carbon cycle, and nitrogen cycle are discussed from their fundamental conception to their functional application. A significant emphasis is placed on various engineering strategies for 2D nanomaterials and their influence on intrinsic material performance, such as electronic properties and adsorption energetics.

The first part of this Thesis focuses on the understanding of alkaline HER mechanism using 2D electrocatalyst as the platform. So far, the mechanistic understandings of

alkaline HER are inapplicable to highly active nanostructured catalysts in practice. This is because most of nanostructured catalysts have complicated active sites, which cannot be identified carefully using theoretical calculations. Compared to other nanomaterials, 2D nanomaterials have uniformly exposed lattice plane which is considered as the ideal platform for the investigation of electrocatalytic reactions. Consequently, various 2D electrocatalysts with tunable active sites were synthesized and studied *via* advanced experimental measurements and theoretical calculations. First, a hybrid material of 2D $C_3N_4@MoN$ was prepared using an interface engineering strategy. The intimate interaction of both inert C_3N_4 and MoN surfaces induced a highly active interface with tunable dual-active sites for alkaline HER. The enhanced activity originates from the synergy between the optimized hydrogen adsorption energy on the g- C_3N_4 sites and enhanced hydroxyl adsorption energy on the MoN sites. Second, atomically thin nitrogen-rich nanosheets, Mo_5N_6 , were synthesized using a Ni-induced growth method. The 2D Mo_5N_6 nanosheets exhibit high HER activity and stability in natural seawater, which were superior to other TMNs and even the Pt benchmark. The superior performance of the nitrogen-rich Mo_5N_6 nanosheets originates from their Pt-like electronic structure and the high valence state of Mo atoms. Thirdly, a multi-faceted heteroatom-doping method (nitrogen, sulfur, and phosphorus) was applied to tune the electronic structure and HER activity of non-noble metals (Ni and Co) 2D layer directly and continuously without changing their chemical composition. The dopant-induced charge redistribution in the Ni metal 2D layer significantly influences its catalytic performance for the HER in alkaline media. The principle that bridges the dopant effect with the resultant HER activity is visualized with a volcano relationship.

The second part of the thesis focuses on the exploration and synthesis of new 2D layered transition metal nitrides (TMNs) for hydrogen-related energy conversion. Firstly, the 2D layered W_2N_3 nanosheets with nitrogen vacancies was successfully obtained for the NRR. In this work, a new 2D layered W_2N_3 nanosheet was synthesized and the nitrogen vacancies demonstrate activity for electrochemical NRR. A series of ex-situ synchrotron based characterizations show that the nitrogen vacancies in the 2D W_2N_3 nanosheets

are stable due to the high valence state of the tungsten atoms and 2D confinement effect. Density function theory calculations suggest that the nitrogen vacancies provide an electron-deficient environment which facilitate nitrogen adsorption and lower the thermodynamic limiting potential of the NRR. Secondly, alkali molten salts were employed as the catalyst to explore and synthesize a new family of 2D layered TMNs under atmospheric pressure. The resultant 2D layered TMNs show superior performance for the HER with small overpotentials of 129 mV and 122 mV at a current density of 10 mA cm⁻² in 0.5 M H₂SO₄ and 1 M KOH, respectively. This level of performance surpasses most of the 2D layered electrocatalysts reported in the literature. They also exhibit excellent oxidation resistance and film-forming properties for practical applications.

At last, the challenges and perspectives of 2D nanomaterials for electrocatalysis were discussed. The novel 2D nanomaterials demonstrate great potential for energy-relevant electrocatalytic processes such as HER and NRR. By rationally modifying the surface property and electronic structure at atomic level, the 2D nanomaterials can be extended to more research areas. Moreover, insightfully unveiling the reaction mechanisms of electrocatalysis can lay a solid foundation for designing more efficient 2D electrocatalysts.

Declaration

I certify that this work contains no material which has been accepted for the award of any other degree or diploma in my name, in any university or other tertiary institution and, to the best of my knowledge and belief, contains no material previously published or written by another person, except where due reference has been made in the text. In addition, I certify that no part of this work will, in the future, be used in a submission in my name, for any other degree or diploma in any university or other tertiary institution without the prior approval of the University of Adelaide and where applicable, any partner institution responsible for the joint-award of this degree.

I acknowledge that copyright of published works contained within this thesis resides with the copyright holder(s) of those works.

I also give permission for the digital version of my thesis to be made available on the web, via the University's digital research repository, the Library Search and also through web search engines, unless permission has been granted by the University to restrict access for a period of time.

I acknowledge the support I have received for my research through the provision of an Australian Government Research Training Program Scholarship.

Name of Candidate: Huanyu Jin

Signature: 

Date: 22/June/2020

Acknowledgments

This thesis would not have come to fruition without the support and help from my supervisors, friends, and families. Here, I would like to express my gratitude to them all.

First and foremost, I would like to thank my principal supervisor Prof. Shizhang Qiao for offering me professional suggestions and continuous support for my research. Under his wonderful supervision, I learned how to do the research in the right way with a positive attitude. More importantly, he also enlightens me throughout my PhD research with his enthusiasm, fortitude, and sagacity. I could not get these achievements without his generous encouragement and support. I sincerely appreciate my co-supervisor Dr. Yao Zheng, for his insightful suggestions and continuous encouragement.

I am also grateful to the members in the Qiao's group who give me many supports during my PhD study. I express my thanks to Dr. Yan Jiao, Dr. Lei Zhang, Dr. Chunxian Guo, Dr. Cheng Tang, Dr. Dongliang Chao, Dr. Bo You, Dr. Jingjing Duan, Dr. Anthony Vasileff, Dr. Dongdong Zhu, Dr. Jinlong Liu, Dr. Ke Zhang, Dr. Fangxi Xie, Dr. Xuesi Wang, Dr. Chao Ye, Xin Liu, Laiquan Li, Yongqiang Zhao, Yang Shi, Jieqiong Shan, Chaochen Xu, Xialong Zhou, Xing Zhi, Xin Xu, Huan Li, and Dazhi Yao for their generous help and inspiring discussions.

It is a great pleasure to express my heartfelt appreciation to those who assisted me in materials characterizations and data analysis: Dr. Ashley Slattery, Dr Sarah Gilbert, and Mr. Ken Neubauer, from Adelaide Microscopy for their technical supports; Dr. Qinfen Gu, Dr. Justin Kimpton, of PD beamline team, Dr. Bruce Cowie, Dr. Anton Tadich, of soft X-ray spectroscopy team of Australian Synchrotron, and Prof. Li Song, Dr. Shuangming Chen from University of Science and Technology of China for the synchrotron-based spectroscopy; Prof. Hua Zhang, Dr. Bo Chen from City University of Hong Kong, Prof. Mietek Jaroniec from Kent State University for data analysis and paper writing. I have benefited greatly from their generous help and passionate discussions.

Special thanks go to Michelle Fitton, Sue Earle, Jason Peak and Analytical Services Coordinator Dr. Qihong Hu from School of Chemical Engineering and Advanced Materials for their administrative and technical helps.

I would also like to acknowledge the Australian Government, The University of Adelaide, and Australia Research Council for their financial support; Adelaide Microscopy, and Australian Synchrotron, ANSTO for their technical support.

Finally, I would express my deepest gratitude to my family, my parents Zhengri and Jin and Huimin for their forever love and support. Without their unconditional trust and support, I could not have completed my PhD research. It would be a great pleasure to dedicate this thesis to my family. And also, my sincere gratitude goes to my dear friends in China and Australia for their support.

Chapter 1: Introduction

1.1 Significance of the Project

The Australian government has determined energy to be a priority area of research, and one important focus identified in this research area is the development of efficient, cost-effective, and reliable energy conversion and storage technologies.¹ Hydrogen is considered to be one of the best fuels for future clean energy systems as its combustion product is only water.²⁻⁴ Therefore, the research of cost-effective technologies for hydrogen generation is significant.⁵ Currently, several sources can produce hydrogen, such as coal, natural gas, biomass, or water. In these sources, directly converting water into hydrogen and oxygen through electrocatalysis is the best way as it produces no greenhouse emissions.⁶

Electrocatalysis is a process which facilitates and accelerates a chemical reaction on the surface of electrode materials.⁷ Accordingly, the performance of electrocatalysts is dependent on the properties of the electrode material, such as surface area, conductivity, catalytic activity and cycling stability.⁸

For many years, water electrolysis has demonstrated the feasibility of efficient hydrogen generation and conversion. In this process, the dominant reactions are the hydrogen evolution reaction (HER) and the oxygen evolution reaction (OER).⁹ The benchmarks for the HER are Pt supported on carbon and RuO₂/IrO₂, respectively.⁹ However, the large-scale commercialization of effective catalysts for energy conversion technologies is hindered by the high price of these noble metals.² Consequently, finding new and cost-effective electrode materials is imperative for reducing the price of current electrocatalysts.

A key factor in developing efficient electrocatalysts is understanding their activity origin.¹⁰ As electrocatalysis proceeds at the surface of a catalyst, understanding the surface properties of electrocatalysts enables rational modification of the material.¹¹ Compared to other nanomaterials, such as nanowires or nanoparticles, the most important two features of 2D nanomaterials for electrocatalysis are their tunable and

uniformly exposed lattice plane and unique electronic state.¹⁰ In particular, nitrogen doped graphene (N-graphene) can act as a metal-free catalyst for the electrocatalytic ORR in fuel cells which could dramatically reduce cost and promote their scalable application.⁶ Besides favorable catalytic performance, 2D nanomaterials have significantly high specific surface area and robust mechanical properties, resulting in an ideal and programmable platform for practical applications. However, most pristine 2D nanomaterials have very low catalytic performance.² As a result, various optimizing protocols have been developed to prepare efficient 2D electrocatalysts, including heteroatom doping, defect engineering, edge engineering, strain engineering, and interfacial structure engineering etc.² As these methods modify the physical, electronic, chemical, and surface properties of 2D nanomaterials (e.g. intermediate adsorption free energy, charge transfer kinetics, and reaction kinetics, etc.), inherent changes to their performance can be realized.

With recent significant advances in surface characterization technologies, various advanced imaging and spectroscopic characterization methods can be applied, such as transmission electron microscopy (TEM), scanning probe microscopy (SPM), and synchrotron-based X-ray absorption spectroscopy (XAS), to probe the active sites of these materials and reveal the reaction mechanism. At the same time, with the considerable improvement in computing power, density functional theory (DFT) calculations can offer a precise description of the electronic structure of solid catalysts. Consequently, for a certain electrocatalytic process, one can optimize the chemisorption energies of reaction intermediates by tailoring the catalyst's intrinsic electronic structure to achieve a favorable surface reaction rate. Therefore, the goal of this Thesis is to study the mechanisms of different reactions on 2D nanomaterial surfaces and designing new 2D electrocatalysts based on our discovery. The reactions of interest are the alkaline HER and the nitrogen reduction reaction (NRR), which have great potential for energy and environmental sustainability.

1.2 Research Objectives

The major goals of this Thesis are to design novel 2D nanomaterials and their

derivatives for electrocatalysis and investigate their reaction mechanisms for energy-related electrocatalytic processes such as the HER and NRR. In particular, the objectives of this thesis are:

- *To understand* the HER mechanism in alkaline media using 2D $C_3N_4@MoN$ nanosheets as a platform.
- *To synthesize* nitrogen rich Mo_5N_6 nanosheets for electrocatalytic seawater splitting using simple methods.
- *To design* heteroatom doped transition metal electrocatalysts for alkaline hydrogen evolution.
- *To investigate* the nitrogen vacancies on 2D layered W_2N_3 for the NRR.
- *To explore* a new family of 2D layered materials for hydrogen evolution using a molten salt directed method.
- *To investigate* the advantages of 2D nanomaterials for advanced energy conversion technologies.

1.3 Thesis Outline

This thesis is presented in the form of journal publications. It contains research results on the design of novel 2D nanomaterials for electrocatalytic energy conversion reactions. Recent progresses and challenges of 2D electrocatalysts for electrocatalysis were reviewed followed by discussion of the applications of novel 2D nanomaterials in electrocatalysis. Specifically, the chapters in the Thesis are presented in the following sequence:

- **Chapter 1** introduces the significance of this project and outlines the research objectives and key contributions to the field of 2D nanomaterials and electrocatalysis.
- **Chapter 2** reviews the recent progresses and challenges of 2D electrocatalysts for electrocatalysis.
- **Chapter 3** presents 2D $C_3N_4@MoN$ hybrid nanosheets with tuneable dual-active sites for efficient electrocatalytic hydrogen evolution
- **Chapter 4** investigates 2D nitrogen rich Mo_5N_6 nanosheets for enhanced seawater splitting.

- **Chapter 5** presents heteroatom doped transition metal nanoparticles for alkaline hydrogen evolution.
- **Chapter 6** studies the nitrogen vacancies on 2D layered W_2N_3 for the nitrogen reduction reaction.
- **Chapter 7** develops a catalytic molten salt method for the facile synthesis of 2D layered transition metal nitrides for hydrogen evolution.
- **Chapter 8** presents the conclusion and perspectives for further work on the design, application, and mechanisms of novel 2D nanomaterials for electrocatalysis.

1.4 References

1. Ryan, D.; Merrick, R. Finkel on the future: Australia to renew its energy policy and recharge investment with a clean energy target. *Australian Environmental Law Digest* **2017**, *4*, 7.
2. Zheng, Y.; Jiao, Y.; Zhu, Y.; Li, L. H.; Han, Y.; Chen, Y.; Du, A.; Jaroniec, M.; Qiao, S. Z. Hydrogen evolution by a metal-free electrocatalyst. *Nat. Commun.* **2014**, *5*, 3783.
3. Chu, S.; Majumdar, A. Opportunities and challenges for a sustainable energy future. *Nature* **2012**, *488*, 294-303.
4. Stamenkovic, V. R.; Strmcnik, D.; Lopes, P. P.; Markovic, N. M. Energy and fuels from electrochemical interfaces. *Nat. Mater.* **2016**, *16*, 57-69.
5. Turner, J. A. Sustainable hydrogen production. *Science* **2004**, *305*, 972-974.
6. Duan, J.; Chen, S.; Jaroniec, M.; Qiao, S. Z. Heteroatom-doped graphene-based materials for energy-relevant electrocatalytic processes. *ACS Catal.* **2015**, *5*, 5207-5234.
7. Zheng, Y.; Jiao, Y.; Chen, J.; Liu, J.; Liang, J.; Du, A.; Zhang, W.; Zhu, Z.; Smith, S. C.; Jaroniec, M.; Lu, G. Q.; Qiao, S. Z. Nanoporous graphitic- C_3N_4 @carbon metal-free electrocatalysts for highly efficient oxygen reduction. *J. Am. Chem. Soc.* **2011**, *133*, 20116-20119.
8. Zhu, Y. P.; Guo, C.; Zheng, Y.; Qiao, S. Z. Surface and interface engineering of noble-metal-free electrocatalysts for efficient energy conversion processes. *Acc. Chem. Res.* **2017**, *50*, 915-923.

9. Markovic, N. M. Electrocatalysis: Interfacing electrochemistry. *Nat. Mater.* **2013**, *12*, 101-102.
10. Jiao, Y.; Zheng, Y.; Davey, K.; Qiao, S.-Z. Activity origin and catalyst design principles for electrocatalytic hydrogen evolution on heteroatom-doped graphene. *Nat. Energy* **2016**, *1*, 16130.
11. Kibsgaard, J.; Chen, Z.; Reinecke, B. N.; Jaramillo, T. F. Engineering the surface structure of MoS₂ to preferentially expose active edge sites for electrocatalysis. *Nat. Mater.* **2012**, *11*, 963-969.

Chapter 2: Literature Review

2.1 Introduction and Significance

This Chapter reviews the recent advances in two-dimensional (2D) materials for electrocatalytic processes such as the hydrogen evolution reaction (HER), oxygen reduction reaction (ORR), and oxygen evolution reaction (OER). The global demand for energy has increased rapidly. Consequently, many advanced technologies for clean and sustainable energy conversion have become the subjects of extensive studies. Recently, 2D materials have displayed great potential in electrocatalysis due to their unique physical, chemical, and electronic properties. Their low-cost and high performance demonstrate their potential as next generation electrocatalysts as replacements for conventional precious metal catalysts. At the same time, there are tremendous opportunities in advancing electrochemical surface science at the atomic level by merging theoretical and experimental methodologies, which has led to many breakthroughs in the research and development of advanced 2D electrocatalysts.

This Chapter presents a comprehensive summary of recent advances in the electrocatalytic application of 2D materials through the merger of fundamental science with practical technologies. A special emphasis is placed on the development of design principles and determining working mechanisms. Various 2D material-based electrocatalysts are reviewed for applications such as fuel cells, water splitting, and CO₂ conversion, etc. Furthermore, various engineering strategies for 2D materials and their influence on the intrinsic material activities are discussed at length.

2.2 Emerging Two-Dimensional Nanomaterials for Electrocatalysis

This Chapter is included as it appears as a journal paper published by **Huanyu Jin**, Chunxian Guo, Xin Liu, Jinlong Liu, Anthony Vasileff, Yan Jiao, Yao Zheng, Shi-Zhang Qiao, Emerging Two-Dimensional Nanomaterials for Electrocatalysis. *Chem. Rev.* 2018, 118, 6337–6408.

Statement of Authorship

Title of Paper	Emerging Two-Dimensional Nanomaterials for Electrocatalysis
Publication Status	<input checked="" type="checkbox"/> Published <input type="checkbox"/> Accepted for Publication <input type="checkbox"/> Submitted for Publication <input type="checkbox"/> Unpublished and Unsubmitted work written in manuscript style
Publication Details	Huanyu Jin, Chunxian Guo, Xin Liu, Jinlong Liu, Anthony Vasileff, Yan Jiao, Yao Zheng,* Shi-Zhang Qiao* Emerging Two-Dimensional Nanomaterials for Electrocatalysis. Chem. Rev. 2018, 118, 6337–6408.

Principal Author

Name of Principal Author (Candidate)	Huanyu Jin		
Contribution to the Paper	Project design and manuscript drafting.		
Overall percentage (%)	70		
Certification:	This paper reports on original research I conducted during the period of my Higher Degree by Research candidature and is not subject to any obligations or contractual agreements with a third party that would constrain its inclusion in this thesis. I am the primary author of this paper.		
Signature	_____	Date	22/June/2020

Co-Author Contributions

By signing the Statement of Authorship, each author certifies that:

- the candidate's stated contribution to the publication is accurate (as detailed above);
- permission is granted for the candidate to include the publication in the thesis; and
- the sum of all co-author contributions is equal to 100% less the candidate's stated contribution.

Name of Co-Author	Chunxian Guo		
Contribution to the Paper	Discussion and revision of manuscript.		
Signature	_____	Date	22/June/2020

Name of Co-Author	Xin Liu		
Contribution to the Paper	Discussion and revision of manuscript.		
Signature	_____	Date	22/June/2020

Name of Co-Author	Jinlong Liu		
Contribution to the Paper	Discussion and revision of manuscript.		
Signature		Date	22/June/2020

Name of Co-Author	Anthony Vasileff		
Contribution to the Paper	Manuscript revision.		
Signature		Date	22/June/2020

Name of Co-Author	Yan Jiao		
Contribution to the Paper	Manuscript revision.		
Signature		Date	22/June/2020

Name of Co-Author	Yao Zheng		
Contribution to the Paper	Supervision of the work, discussion of this manuscript and manuscript evaluation.		
Signature		Date	22/June/2020

Name of Co-Author	Shi-Zhang Qiao		
Contribution to the Paper	Supervision of the work, discussion of this manuscript and manuscript evaluation.		
Signature		Date	22/June/2020

Please cut and paste additional co-author panels here as required.

Emerging Two-Dimensional Nanomaterials for Electrocatalysis

Huanyu Jin, Chunxian Guo, Xin Liu, Jinlong Liu, Anthony Vasileff, Yan Jiao,^{1b} Yao Zheng,^{*1b} and Shi-Zhang Qiao^{*1b}

School of Chemical Engineering, The University of Adelaide, Adelaide, SA 5005, Australia

ABSTRACT: Over the past few decades, the design and development of advanced electrocatalysts for efficient energy conversion technologies have been subjects of extensive study. With the discovery of graphene, two-dimensional (2D) nanomaterials have emerged as some of the most promising candidates for heterogeneous electrocatalysts due to their unique physical, chemical, and electronic properties. Here, we review 2D-nanomaterial-based electrocatalysts for selected electrocatalytic processes. We first discuss the unique advances in 2D electrocatalysts based on different compositions and functions followed by specific design principles. Following this overview, we discuss various 2D electrocatalysts for electrocatalytic processes involved in the water cycle, carbon cycle, and nitrogen cycle from their fundamental conception to their functional application. We place a significant emphasis on different engineering strategies for 2D nanomaterials and the influence these strategies have on intrinsic material performance, such as electronic properties and adsorption energetics. Finally, we feature the opportunities and challenges ahead for 2D nanomaterials as efficient electrocatalysts. By considering theoretical calculations, surface characterization, and electrochemical tests, we describe the fundamental relationships between electronic structure, adsorption energy, and apparent activity for a wide variety of 2D electrocatalysts with the goal of providing a better understanding of these emerging nanomaterials at the atomic level.



CONTENTS

1. Introduction	6338		
2. Categories of 2D Electrocatalysts	6340		
2.1. Metal-Free 2D Nanomaterials	6341		
2.1.1. Graphene	6341		
2.1.2. Graphyne	6342		
2.1.3. Graphitic Carbon Nitride	6342		
2.1.4. Hexagonal Boron Nitride	6342		
2.1.5. Black Phosphorus	6343		
2.2. Metal Chalcogenides	6344		
2.2.1. Transition-Metal Dichalcogenides	6344		
2.2.2. Non-layered Metal Chalcogenides	6344		
2.3. Transition-Metal Oxides and Hydroxides	6344		
2.3.1. Transition Metal Oxides	6344		
2.3.2. Layered Transition Metal Hydroxides	6345		
2.4. MXenes and Non-layered Transition-Metal Carbides and Nitrides	6345		
2.5. Transition Metals	6346		
2.6. Metal–Organic Frameworks and Covalent–Organic Frameworks	6346		
3. Engineering Protocols for Catalyst Design	6347		
3.1. Heteroatom Doping	6347		
3.1.1. Non-Metal-Atom Doping	6348		
3.1.2. Metal-Atom Doping	6348		
3.2. Defect Engineering	6350		
3.3. Lateral Size and Thickness Regulation	6350		
3.4. Strain and Phase Engineering	6351		
3.5. Interface Engineering	6351		
4. Advanced Approaches for Determining Active Sites and Detecting Intermediates on 2D Electrocatalysts	6353		
4.1. Microscopy	6353		
4.2. X-ray Absorption Spectroscopy	6354		
5. Catalysts Design and Development Protocols	6354		
5.1. Design Principles of Electrocatalysts through Multidisciplinary Approaches	6354		
5.2. Combination of Experiments and Theoretical Computations	6355		
6. 2D Nanomaterials for Oxygen Reduction Reaction Applications	6355		
6.1. Fundamental Principles of the ORR	6355		
6.1.1. Reaction Mechanism	6355		
6.1.2. Reaction Kinetics	6356		
6.1.3. Measurement Criteria	6357		
6.2. Doped Graphene	6358		
6.2.1. Nitrogen-Doped Graphene	6358		
6.2.2. ORR Mechanism on Nitrogen-Doped Graphene	6359		
6.2.3. Other Heteroatom-Doped Graphene	6359		
6.2.4. Dual-Doped Graphene	6361		
6.3. Graphene Derivatives	6361		
6.3.1. Graphene Quantum Dots and Graphene Nanoribbons	6361		

Special Issue: 2D Materials Chemistry

Received: November 15, 2017

Published: March 19, 2018

6.3.2. Defective Graphene	6362	11. Conclusions and Outlook	6391
6.4. Graphitic Carbon Nitride	6363	Author Information	6392
6.5. Challenges for 2D Nanomaterials as Acidic ORR Catalysts	6364	Corresponding Authors	6392
7. 2D Nanomaterials for Oxygen Evolution Reaction Applications	6364	ORCID	6392
7.1. Fundamental Principles of the OER	6364	Notes	6392
7.1.1. Reaction Kinetics	6364	Biographies	6392
7.1.2. Reaction Mechanism	6365	Acknowledgments	6392
7.1.3. Measurement Criteria	6365	References	6392
7.2. Transition-Metal-Based Electrocatalysts	6365		
7.2.1. Transition-Metal Oxides	6365		
7.2.2. Layered Transition-Metal Hydroxides and Double Hydroxides	6368		
7.2.3. Transition-Metal Dichalcogenides	6368		
7.2.4. Other Metal-Based Materials	6370		
7.3. Metal–Organic Framework-Based Electrocatalysts	6370		
7.4. Metal-Free Electrocatalysts	6371		
7.5. OER/ORR Bifunctional Electrocatalysts	6372		
7.6. Challenges for 2D Nanomaterials as Acidic OER Catalysts	6372		
8. 2D Nanomaterials for Hydrogen Evolution Reaction Applications	6372		
8.1. Fundamental Principles of the HER	6372		
8.1.1. Reaction Mechanism	6372		
8.1.2. Activity Descriptor	6373		
8.1.3. Free-Energy Diagram	6373		
8.2. Graphene-Based Electrocatalysts	6373		
8.2.1. Heteroatom-Doped Graphene	6373		
8.2.2. Single-Atom Catalyst Supported by Graphene Derivatives	6374		
8.3. Transition-Metal Dichalcogenides	6375		
8.3.1. Origin of Catalytic Activity	6375		
8.3.2. Nanostructure Engineering	6375		
8.3.3. Heteroatom Doping at the Edge/Basal Plane	6376		
8.3.4. Defect Engineering	6379		
8.3.5. Interface and Strain Engineering	6379		
8.3.6. Phase Engineering	6380		
8.4. Challenges for 2D Nanomaterials as Alkaline HER Catalysts	6381		
9. 2D Nanomaterials for Electrochemical CO ₂ Reduction Applications	6382		
9.1. Fundamental Principles of Electrochemical CO ₂ Reduction	6382		
9.1.1. Reaction Mechanism	6382		
9.1.2. Measurement Criteria	6383		
9.2. Transition Metals	6383		
9.3. Transition-Metal Oxides	6384		
9.4. Transition-Metal Dichalcogenides	6385		
9.5. Carbon-Based 2D Nanomaterials	6385		
9.6. Other 2D Nanomaterials	6387		
9.7. Challenges for 2D Nanomaterials as Electrochemical CO ₂ Reduction Catalysts	6387		
10. 2D Nanomaterials for Other Reactions and Beyond	6387		
10.1. Nitrogen Cycle	6387		
10.1.1. Urea Oxidation	6387		
10.1.2. Nitrogen Reduction Reaction	6388		
10.2. Oxidation of Carbon Fuels	6390		
10.2.1. Oxidation of Methanol	6390		
10.2.2. Oxidation of Formic Acid	6391		

1. INTRODUCTION

With increasing concern regarding climate change, pollution, and energy security related to the decreasing availability of fossil fuels, the search for clean and renewable energy sources has become one of the greatest challenges for the sustainable development of society.^{1–3} Core to this development is the need for advanced energy conversion systems such as water electrolysis, fuel cells, and metal–air batteries. However, a profound understanding of the fundamental principles, concepts, and knowledge of electrocatalysis is required for realizing these next-generation energy devices.^{4–8} Heterogeneous electrocatalysis is a process that can accelerate electrochemical reactions on the surface of electrode materials.^{4,9} Generally, for energy-related applications in electrocatalysis, there are two main energy cycles: the water cycle and the carbon cycle. As shown in [Figure 1](#), central to the water cycle is a series of hydrogen- and oxygen-related electrocatalytic processes. The oxygen reduction reaction (ORR) and hydrogen oxidation reaction (HOR) occur on the cathode and anode of a hydrogen–oxygen fuel cell, respectively ([Figure 1a](#)). For electrolytic cells, the hydrogen evolution reaction (HER) and oxygen evolution reaction (OER) occur at the cathode and the anode, producing gaseous hydrogen and oxygen molecules, respectively ([Figure 1a](#)).^{4,10} The ideal technological loop for the water cycle consists of water splitting through the HER and OER for fuel generation, followed by power generation through the ORR and HOR in fuel cells.¹¹ Development of this technology has been driven by the growing hydrogen economy, which has pushed the electrocatalytic water cycle to a prominent area of research.¹² In the past two decades, significant research has reported the development of high-performing electrocatalysts for the water cycle. Generally, the kinetics of the two-electron transfer processes in the half-cell HER and HOR processes is simple ([Figure 1b](#)).^{9,10} However, the sluggish kinetics of the multi-electron transfer OER and ORR processes limit the performance of corresponding energy devices ([Figure 1b](#)).^{10,13} Conventionally, catalysts for these reactions are based on precious metals such as Pt, Ir, and Ru, which can deliver satisfactory reaction rates.¹⁴ However, these precious-metal catalysts suffer from poor stability, and their cost greatly prohibits their large-scale application.^{1,8,15,16} Thus, the development of high-performance and low-cost alternatives to these precious metals has become a significant endeavor in clean energy research.^{7,17}

Due to increasing emissions of CO₂ in our industrial world, anthropogenic climate change is an ever growing issue.^{16,18,19} An ideal solution to this problem is the capture and direct use of CO₂ as a chemical feedstock.^{18,20,21} Compared to biochemical or photochemical approaches,²² reducing CO₂ electrochemically is suitable for this application because it offers high efficiency and product specificity and can be operated at ambient conditions ([Figure 2a,b](#)).^{16,23} However, the electrochemical CO₂ reduction reaction (ECR), which is central to the carbon cycle, is challenged with reducing the extremely stable CO₂ molecule.

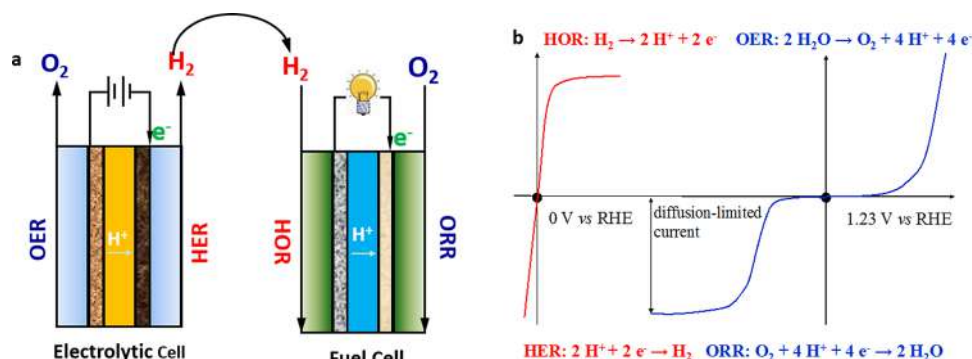


Figure 1. (a) Schematic representation of the electrolytic cell and the fuel cell. (b) Typical polarization curves for the hydrogen-involving (red curves) and oxygen-involving reactions (blue curves), respectively. The curves are not drawn to scale. Reproduced with permission from ref 10. Copyright 2015 Royal Society of Chemistry.

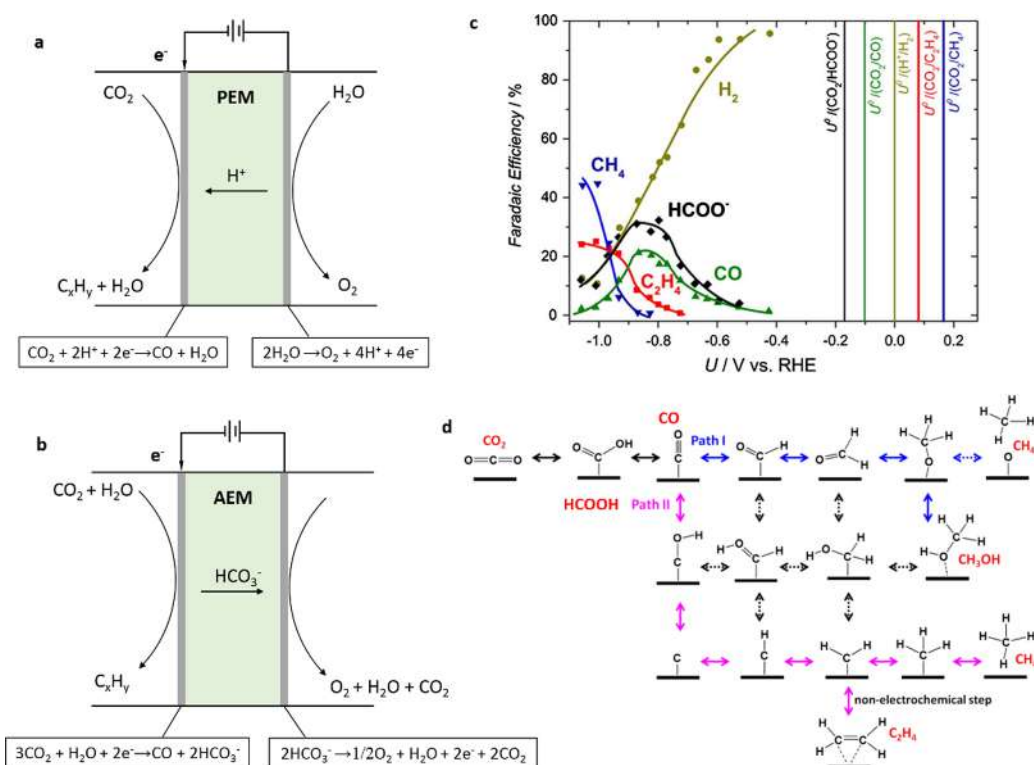


Figure 2. (a,b) Schematic configurations of an ECR electrolysis cells composed of (a) a proton exchange membrane (PEM) and (b) an anion exchange membrane (AEM). (c) Product distribution expressed as Faradaic yield as a function of potential on a polycrystalline Cu electrode. The vertical lines represent the reversible potentials for various products. Reproduced with permission from ref 31. Copyright 2016 Elsevier. (d) Proposed ECR reaction pathways to different products on Cu (111). Reproduced with permission from ref 32. Copyright 2013. John Wiley & Sons, Inc.

This results in a large kinetic barrier.^{22,24} Another challenge the ECR faced with is the controllable selectivity of products. In principle, the ECR is a proton-coupled multi-step reaction involving multi-electron reaction pathways to carbon monoxide (CO), formate (HCOO^-), methanol (CH_3OH), methane (CH_4), ethylene (C_2H_4), etc.^{25–29} Using the widely studied Cu electrode as an example (Figure 2c,d), selectivity toward a particular reduction product fundamentally depends on the adsorption energetics of a series of key reaction intermediates and kinetic reaction barriers governed by the nature of the electrocatalyst surface and applied potential.^{30–32} Hence, understanding the relationship between a catalyst's physical and electronic structures with the reaction mechanism is key to controlling its products selectivity.

Both the water cycle and carbon cycle are applied in various clean energy devices. For example, the ORR is the core reaction for fuel cells and metal–air batteries.^{7,14,33} The HER and OER are the core reactions of water electrolysis cells that supply ultrahigh-purity hydrogen as fuel for proton exchange membrane fuel cells (PEMFCs).^{34,35} In the carbon cycle, direct methanol/ethanol fuel cells play important roles for future energy systems which could overcome both the storage and infrastructure challenges of hydrogen.³⁶ However, common among all these technologies is the requirement for high-performing electrocatalysts. In general, a good electrocatalyst features high activity, high surface area, good electrical conductivity, and long-term stability.⁹ The activity of an electrode strongly depends on the physicochemical properties of the electrocatalyst surface and the electrode–electrolyte interaction.^{4,37,38} To achieve high catalytic

activity, electrocatalysts need to be effective at lowering the energy barriers of electrocatalytic reactions and promoting the rate of surface electron charge transfer.^{38,39} Accordingly, the development of well-defined surfaces and structures is a valued approach to promote electrochemical processes. Moreover, a high electrode surface area and electrical conductivity can be achieved by structuring conductive supports/substrates at the nanoscale.⁴⁰ The durability of a catalyst determines the operating life of the electrocatalytic cell which is very important for practical applications. For example, in the ORR process, Pt-based catalysts have low tolerance to byproducts such as methanol/CO, resulting in a limited operating life. This is also further stimulus to pursue high-performance catalysts outside of precious metals.^{8,10} Therefore, the development of next generation electrocatalysts with enhanced activity, selectivity, efficiency, and stability is an ongoing challenge in energy conversion/storage research.

Since graphene was first reported in 2004, 2D materials have emerged in various research fields.^{41–45} Recently, the exploration of new 2D nanomaterials has prompted the development of 2D electrocatalysts.⁴⁶ Other than graphene, many new types of 2D nanomaterials and their derivatives have been applied in electrocatalysis.^{47–49} Compared to other nanomaterials, such as nanowires or nanoparticles, the two most important features of 2D nanomaterials for electrocatalysis are their tunable and uniformly exposed lattice plane and unique electronic state.^{5,50,51} Consequently, 2D metal-free materials such as nitrogen doped graphene (N-graphene) have been developed to a point where they begin to rival conventional catalysts. Application of N-graphene ORR electrocatalysts in fuel cells could provide significant cost reduction and facilitate scaling of the technology.⁵² Another example is 2D molybdenum disulfide (MoS₂), which is a promising active material for the HER as its hydrogen adsorption Gibbs free energy (ΔG_{H^*}) is only 0.08 eV, which is even lower than that of benchmark Pt ($\Delta G_{H^*} \approx 0.09$ eV).^{53,54} Besides favorable catalytic performance, 2D nanomaterials have significantly high specific surface areas and robust mechanical properties, making them ideal and programmable platforms for practical applications.⁴³ For instance, most 2D nanomaterials are easily fabricated into freestanding flexible films with uniform thickness.^{55–61} Compared to powder-type catalysts, freestanding electrodes are much more suitable for actual utilization as they can prevent catalyst agglomeration and exfoliation from supports, which is beneficial for activity retention.⁹

However, most pristine 2D nanomaterials have very low catalytic performance. For example, graphene has poor HER performance as its hydrogen adsorption ability is very weak.⁴⁸ Therefore, various optimization protocols have been developed to prepare efficient electrocatalysts based on graphene and other 2D materials.^{62–67} Summarized in Figure 3, these optimization protocols modify the physical, electronic, chemical, and surface properties of 2D nanomaterials (e.g., intermediate adsorption free energy, charge-transfer kinetics, reaction kinetics, etc.) which directly alter their inherent performance.^{15,48,68–70} As a result, these protocols hold great potential for the design high-performance electrocatalysts. To better understand the effects of these modifications, recent advances in surface characterization technologies allow for the direct study of active sites to reveal the reaction mechanisms. Various advanced imaging and spectroscopic characterization methods can be used such as transmission electron microscopy (TEM), scanning probe microscopy (SPM), and synchrotron-based X-ray absorption

spectroscopy (XAS).^{71–74} Further, owing to the considerable improvements in computing power, density functional theory (DFT) calculations can offer a precise description of the electronic structure of solid catalysts. The famous “d-band center” theory, developed by Nørskov et al., describes the relationship of a catalyst’s physical band structure with its chemical surface adsorption behavior.⁷⁵ Consequently, for a certain electrocatalytic process, one can optimize the chemisorption energies of reaction intermediates by tailoring the catalyst’s intrinsic electronic structure to achieve a favorable surface reaction rate. At this stage, the combination of quantum computational chemistry, surface electrochemistry, and materials science has significantly accelerated the development of 2D nanomaterials for high-performance electrocatalysis in energy conversion/storage applications. Accordingly, 2D nanomaterials are currently one of the hottest research fields.^{5,8,76,77} Many excellent reviews exist in the literature regarding either the molecular design and synthesis of 2D nanomaterials,^{65,78–80} or nanostructured materials for advanced electrocatalysis.^{1,4,8,10,34,81–83} In this timely Review, we aim to offer a comprehensive overview of 2D nanomaterials for various electrocatalytic applications, mainly for the water and carbon cycles, providing the complete picture on 2D electrocatalysts.

We begin by giving a brief introduction encompassing all the electrocatalysts based on 2D nanomaterials and their derivatives. Both material physicochemical properties and their potential in electrocatalytic applications are discussed. In the following sections, we describe the design principles and synthesis protocols for 2D electrocatalysts, followed by an insightful overview of the advanced techniques and analysis methods utilized for probing catalytic activity origins. Then, we provide a summary of 2D electrocatalysts employed for the major electrocatalytic processes (ORR, HER, OER, ECR, etc.) from their fundamental conception to functional application. This is achieved by a comprehensive review of the development of 2D electrocatalysts based on an understanding of the reaction mechanisms, catalytic activity trends, and materials design. Additionally, we describe the relationship between 2D nanomaterials and electrocatalytic performance by bridging the fundamental DFT calculations with electrochemical experiments to provide tutorial-level guidance. Especially highlighted is the significance of merging computational quantum chemistry, surface electrochemistry, materials chemistry, and nanotechnology for electrocatalysis through a range of examples covering various 2D metals, metal compounds, and non-metallic materials. Finally, we provide some insight into the current progress of 2D electrocatalysts along with the remaining challenges and future directions for this emerging field.

2. CATEGORIES OF 2D ELECTROCATALYSTS

For electrocatalytic applications, 2D nanomaterials have a more uniformly exposed crystal lattice compared to other nanomaterials, such as nanoporous materials, nanowires, or nanotubes, and achieve a higher concentration of exposed electrocatalytically active sites under a certain electrocatalyst mass loading. Also, the simple and ordered molecular framework of 2D nanomaterials makes the identification of active sites easier from both theoretical and experimental perspectives. Another motive to study and develop 2D electrocatalysts is that they are typically inexpensive which makes them ideal replacements for precious-metal-based electrocatalysts.

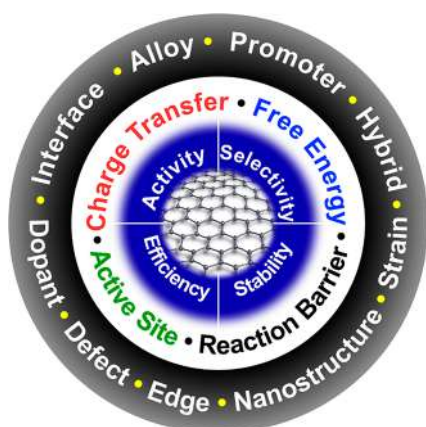


Figure 3. Typical strategies for engineering 2D nanomaterials and their roles for enhancing electrocatalytic performance.

2.1. Metal-Free 2D Nanomaterials

As early as 2009, Dai et al. discovered that nitrogen-doped carbon nanotubes (N-CNT) were promising alternatives to Pt for ORR applications.^{8,52,84} Since then, tremendous progress has been made in the development of 2D metal-free materials for effective catalysis in various electrocatalytic processes. These materials include: graphene-based materials (Figure 4a), graphdiyne (Figure 4b) graphitic carbon nitride (g-C₃N₄) (Figure 4c), hexagonal boron nitride (h-BN) (Figure 4d), and black phosphorus (BP) (Figure 4e).^{48,73,85,86}

2.1.1. Graphene. Since its discovery in 2004 by Geim and Novoselov using their famous Scotch tape method, graphene has become a leading research interest in various fields such as electronics, biomedical engineering, and electrocatalysis.⁴² Graphene is a one-atom-thick 2D carbon crystal in which sp²-bonded carbon atoms are packed in a hexagonal lattice resembling a honeycomb (Figure 4a). Being the most basic of carbon structures, it is considered the fundamental building

block for other dimensional carbon materials, including 0D fullerenes, 1D CNTs, and 3D bulk graphite or other carbon architectures.⁴⁴ The cause of such interest in graphene is due to its many unique properties, such as high theoretical surface area (2630 m² g⁻¹),⁸⁷ high modulus of elasticity (1.0 TPa),⁸⁸ and good thermal (5000 W m⁻¹ K⁻¹),⁸⁹ and electrical conductivities (10⁶ S cm⁻¹).⁴³ For electrocatalytic applications, graphene presents both challenges and opportunities. Given the delocalized π bonding network of graphene, adsorption of reaction intermediates is generally very endothermic, resulting in low intrinsic activity.⁷³ Therefore, the basal plane of pristine graphene is normally considered inert for electrocatalytic processes. However, its large specific surface area and good electrical conductivity make it very attractive as a platform for electrocatalytic applications. Furthermore, the electronic and surface properties of graphene can be easily tuned by defect engineering, heteroatom doping, and heterostructure construction.

It is well known that the electronic states at the edges and defects of graphene differ from the basal plane, and are significantly more active for electrocatalysis.¹⁵ For instance, Deng et al. found that the edges of graphene are the active sites for the ORR process using DFT calculations.⁹⁰ Other than edge effects, heteroatom doping by replacing sp² carbon atoms with sulfur, nitrogen, phosphorus, boron, etc. is also an effective way to activate graphene for electrocatalysis, which will be discussed in sections 6.2 and 8.2.1. For example, Qu et al. reported N-graphene as a metal-free ORR catalyst with a performance that was comparable to benchmark Pt but immune to CO deactivation.⁶² Since then, heteroatom-doped graphene has shown great potential for the ORR and HER applications. Jiao et al. investigated the HER on a series of non-metal heteroatom-doped graphene by mutually corroborating electrochemical reaction rate measurements with theoretically computed adsorption energetics of key reaction intermediates.⁷³ This work is one of the first to propose a strategy for atomic design of

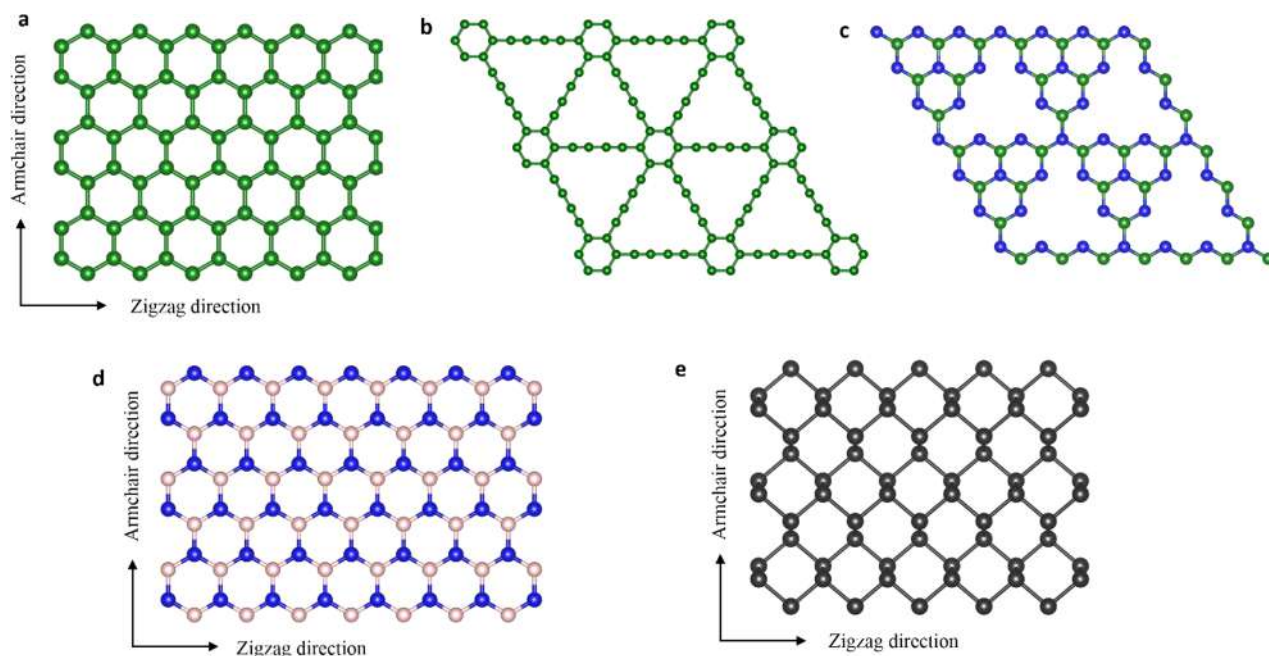


Figure 4. Schematic molecular configurations of (a) graphene; (b) graphdiyne; (c) graphitic carbon nitride; (d) hexagonal boron nitride; (e) black phosphorus.

efficient graphene-based electrocatalysts for broader electrocatalytic processes. Interestingly, graphene is also an ideal platform for anchoring and supporting single-atom catalysts.^{66,91,92} Sun et al. found that N-graphene can be used as a matrix for Pt single-atom and cluster catalysts.⁶⁶ The as-prepared catalyst had superior performance for the HER compared to commercial 40% Pt/C catalysts. Spectroscopic and DFT analyses indicated that the partially unoccupied density of states (DOS) of the Pt 5d orbitals on the N-graphene were responsible for its excellent performance. Apart from water cycle reactions, graphene-based catalysts have also exhibited high electrocatalytic activity in the carbon cycle reactions, which will be discussed in detail in section 9.5.^{16,93} In one example, N-graphene demonstrated significant ECR efficiency toward formate generation.⁹⁴ To explain this enhancement in ECR activity, DFT calculations suggest that the existence of N-atoms in the graphene framework lowered the free energy barrier to adsorption of intermediates which resulted in more favorable binding of *COOH.⁹⁵

2.1.2. Graphyne. Graphyne is another allotrope of carbon that is a one-atom-thick planar sheet of sp and sp²-bonded carbon atoms arranged in a crystal lattice.⁹⁶ Comprised of benzene rings (sp²-like carbon atoms) and acetylenic (sp-like carbon atoms) linkers, graphynes were named after their relationship to graphite and acetylenic components.⁹⁸ They are differentiated as graphyne, graphdiyne (Figure 4b), graphtriyne, etc. based on the number of acetylenic groups between two adjacent benzene rings.^{97,98} The synthesis of 2D graphdiyne is mainly based on bottom-up methods such as chemical vapor deposition (CVD) and gas/liquid or liquid/liquid processes using hexaethynylbenzene as a precursor monomer.^{99,100} Different from graphene, graphyne is a semiconductor with a direct band gap.¹⁰¹ Furthermore, it has been predicted that some graphyne allotropes without hexagonal symmetry and with two self-doped non-equivalent distorted Dirac cones might possess electronic properties superior to those of graphene. Consequently, graphyne may have superior performance in some specific electrocatalytic processes.

As shown by Liu et al., N-doped graphdiyne can act as a metal-free electrocatalyst for the ORR.¹⁰² The as-prepared catalyst exhibited good electrocatalytic performance, even comparable to commercial Pt/C. DFT calculations indicated that N-doping causes a high positive charge localized on the C-atoms adjacent to the N-atoms, thereby attracting electrons more readily and facilitating the ORR. Moreover, reported by Zhang et al., multi-heteroatom co-doping of graphdiyne has shown to further improve the ORR performance of this material.¹⁰³ They synthesized a series dual-heteroatom doped graphdiyne (N, S, B, F) which all showed enhanced ORR performance compared to single-doped samples but N and F co-doped graphdiyne exhibited the best performance.¹⁰³ DFT calculations indicated that when F and N are simultaneously incorporated into the graphdiyne matrix to form dual-doping sites, those C-atoms neighboring these sites are activated through a large positive charge density. This charge density is induced locally over the C-atoms which increases electrocatalytic activity. Other than the ORR, graphdiyne also has also shown excellent performance for the HER. For example, graphdiyne-coated Cu nanowires exhibited efficient HER performance in acidic media with an overpotential of 79 mV at a current density of 10 mA cm⁻² and a Tafel slope of 69 mV dec⁻¹.¹⁰⁴ Similarly, graphdiyne supported Co nanoparticles in N-doped carbon layers also exhibited high HER activity.¹⁰⁵ It should be noted that some studies have found

that graphdiyne has potential performance for the CO oxidation reaction.¹⁰⁶

2.1.3. Graphitic Carbon Nitride. Carbon nitride is one of the first artificial polymers reported in the scientific literature.^{107,108} Graphitic carbon nitride (g-C₃N₄) is a 2D crystal with a van der Waals layered structure, and is considered to be the most stable allotrope of all the various carbon nitride materials.¹⁰⁷ Analogous to graphene, the crystal structure of g-C₃N₄ can be described as a hexagonal carbon framework with N-substituted carbon through the sp² hybridization of carbon and nitrogen atoms.¹¹ Two structural isomers of g-C₃N₄ exist and are synthesized using different precursors and condensation methods. The first one is constructed by condensed triazine (1,3,5-triazine, C₃N₃) units with a periodic array of single carbon atom vacancies.¹⁰⁹ The second one is composed of condensed heptazine (1,3,4,6,7,9,9b-heptaazaphenalene, C₆N₇) subunits connected through planar tertiary amino groups, and has larger periodic vacancies in the lattice (Figure 4c).¹¹⁰ Generally, various nitrogen-rich precursors, such as urea,¹¹¹ thiourea,¹¹² melamine,¹¹³ cyanamide,¹¹⁴ and Dicyandiamide,¹¹⁵ can be used for synthesizing g-C₃N₄ via thermal treatment. Like graphene, 2D g-C₃N₄ nanosheets can be obtained from the exfoliation of bulk g-C₃N₄ materials. Corresponding techniques include ultrasonication-assisted liquid exfoliation, liquid ammonia-assisted lithiation, post-thermal oxidation etching, and thermal delamination combined with sonication.^{116–121} To date, heptazine-based g-C₃N₄ has been used as either an active material, support material, or as a metal atom coordinator in various electrocatalytic applications like the ORR, OER, HER, and ECR.^{48,122}

Due to its band gap (~2.7 eV), the semiconducting properties of g-C₃N₄ make it very suitable for photocatalytic processes.^{11,123} However, the degree of condensation of g-C₃N₄ directly affects its electronic structure and band gap which in turn affects its activity.^{124,125} In this regard, bulk g-C₃N₄ suffers from low activity. On the other hand, 2D g-C₃N₄ nanosheets have exhibited desirable activity due to the abundant structural defects and surface terminations that play key roles in catalytic activation. Other than band gap, the nitrogen-rich carbon framework of g-C₃N₄ is another important feature for electrocatalysis. Normally, nitrogen doping can enhance the electron-donor properties of graphene and other carbon networks, resulting in an improvement to interactions between carbon and intermediates during electrocatalytic processes (which will be discussed in section 6.2.2). Therefore, two basic design principles are typically employed for synthesizing g-C₃N₄-based electrocatalysts. These are (1) optimization of material conductivity and (2) appropriate tuning of active sites. To optimize conductivity, g-C₃N₄ has been composited with conductive carbon materials. For example, g-C₃N₄ was incorporated into a mesoporous carbon framework and showed significantly enhanced ORR activity compared to pristine g-C₃N₄.¹²⁶ Active sites can be tuned in various ways but the intention is to favorably modify the adsorption energy of target intermediates. In one example, a g-C₃N₄ and N-graphene composite achieved HER performance comparable to that of metallic catalysts.⁴⁸ Combined atomic imaging, spectroscopic analysis, and DFT calculations revealed that the interfacial structure of the composite optimized the electronic state and ΔG_{H*} which facilitated electron/charge transfer and enhanced catalytic activity.⁴⁸

2.1.4. Hexagonal Boron Nitride. Hexagonal boron nitride (h-BN) is another analogue of graphite and is also known as “white graphene”.¹²⁷ Bulk h-BN has a layered structure with lattice constants of 2.50 Å and interlayer distances of 3.33 Å

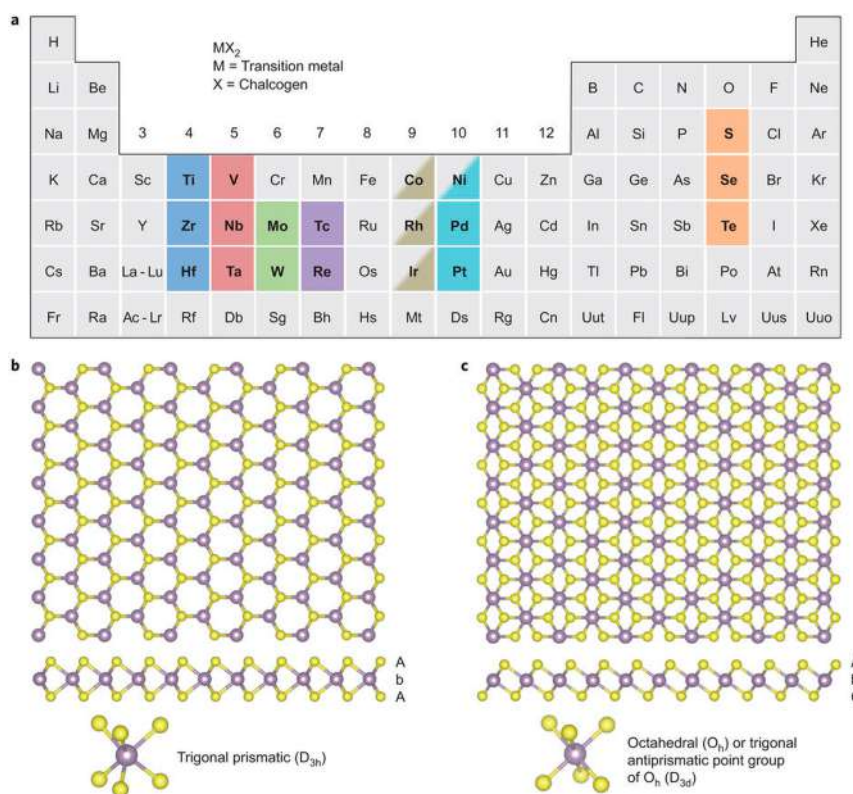


Figure 5. (a) Distribution of about 40 different layered TMD compounds in the periodic table. The transition metals and the three chalcogen elements that predominantly crystallize in those layered structures are highlighted. (b,c) Schematic view of single-layer TMD with trigonal prismatic (2H) and octahedral (1T) coordination. Reproduced with permission from ref 65. Copyright 2013 Nature Publishing Group.

(Figure 4d).¹²⁸ Differing from graphene, h-BN is an insulator with a thickness dependent band gap. In electronic and optical devices, h-BN nanosheets have been used as dielectric substrates for graphene and MoS₂-based heterostructures.^{129,130} However, pristine h-BN displays barely no performance for electrocatalysis, limited by its poor conductivity and poor catalytic activity. Therefore, various experiments using physical or chemical methods have been conducted to activate h-BN. Uosaki et al. found that the electronic properties of h-BN can be tuned through coupling with Au nanoparticles.¹³¹ The resultant composite exhibited increased ORR activity which originated from the effective activation of adsorbed O₂ and improved selectivity for the 2e⁻ reduction pathway from O₂ to H₂O₂. Like for other 2D nanomaterials, heteroatom doping is also an ideal method for activating the catalytic activity of h-BN. Through DFT computations, Li et al. explored the possibility of utilizing heteroatom-doped h-BN sheets as ORR electrocatalysts by examining their O₂ adsorption ability and subsequent ORR pathways.¹³² Predicted from their calculations, carbon doped h-BN showed promise as an ORR catalyst because it could facilitate the ORR with a lower energy barrier compared to Pt-based catalysts in acidic media. Uosaki et al. also demonstrated that h-BN can modify the activity of Au for the HER, whereby its activity was improved by the existence of sites energetically favorable for hydrogen adsorption.¹³³ Carbon doped h-BN sheets have also been used as sustainable and stable visible-light photocatalysts for CO₂ reduction.¹³⁴ Therefore, these materials also have potential in ECR applications when appropriate engineering strategies are utilized (e.g., optimization of electrical conductivity).

2.1.5. Black Phosphorus. Black phosphorus (BP) has a 100 year long history as its bulk form was first synthesized in 1914.¹³⁵ BP is a layered semiconductor with an orthorhombic crystal structure; one phosphorus atom is covalently bonded with another three to form a puckered honeycomb structure in a single layer (Figure 4e).¹³⁶ The three bonds take up all three valence electrons of phosphorus, resulting in a band gap of ~2 eV which can be tuned by controlling its thickness.^{137,138} So far, BP has been widely studied in electronic and optical devices.^{137,139} However, only a few works have been reported about its applications in electrocatalysis, which may be due to its low-stability under electrocatalytic conditions and poor electrical conductivity.

Recently, it was found that various forms of bulk BP (such as thin films and particles) have electrocatalytic activities for the OER process comparable to commercial RuO₂-based catalysts.⁸⁶ However, bulk BP has a low density of active sites which likely limits its electrocatalytic performance. Compared to its bulk form, 2D BP nanosheets synthesized by liquid exfoliation techniques possess increased exposed active sites and surface area.⁸⁵ Therefore, the intrinsic benefits of this ultrathin lamellar structure can promote the development of BP for efficient electrocatalysis. As predicted, few-layered BP showed improved OER performance compared to the bulk form, achieving an onset-potential of 1.45 V vs RHE (reversible hydrogen electrode) and Tafel slope of 88 mV dec⁻¹ in alkaline conditions.⁸⁵ BP also exhibits synergistic effects for the HER when assembled into heterostructures with other materials. For example, Luo et al. synthesized a 0D–2D Ni₂P and BP heterostructure which had a superior HER performance in acidic media compared to commercial Ni₂P.¹⁴⁰ The outstanding

electrocatalytic performance of this hybrid was attributed to the high surface area of the BP and tuned charge carrier concentration between the Ni₂P and BP interface.

2.2. Metal Chalcogenides

Metal chalcogenides are the largest class of materials for electrocatalysis due to their intriguing structural and electronic properties and have been applied for the ORR, OER (discussed in section 7.2.3), HER (discussed in section 8.3), and ECR (discussed in section 9.4).¹⁴¹ In their 2D form, metal chalcogenides can be divided into layered transition-metal dichalcogenides (TMDs) and non-layered metal chalcogenides (NMCs),^{43,45} in which the development of 2D TMD-based electrocatalysts has the greatest potential for realizing low-cost and high-performing electrocatalysts for clean energy conversion applications.

2.2.1. Transition-Metal Dichalcogenides. As shown in Figure 5a, layered TMDs can be described with the general chemical formula MX₂ (M is a transition-metal element and X is a chalcogen such as S or Se).^{46,51} Bulk TMDs consist of monolayers stacked by van der Waals forces whereas the general crystal structure of a TMD monolayer can be described as a sandwich structure where one layer of transition metal is situated between two layers of chalcogen (i.e., X-M-X). A unique feature of 2D TMDs is their multicrystal structures. For example, 2H (hexagonal), 1T (trigonal), and 3R (rhombohedral) are the three common crystal structures of MoS₂ which are dependent on the different coordination models between Mo and S-atoms and the stacking order between layers.¹⁴² The band gaps of bulk and monolayer MoS₂ are also different due to the strong changes in electronic structure.^{65,143,144} The different crystal types and band gaps among the various TMDs lead to different surface properties and hence varied catalytic activities.

To date, there are two main synthesis methods for 2D TMDs. These are the top-down liquid exfoliation method and the bottom-up growth method.^{43,55,145} For example, CVD can grow TMD nanosheets with very high quality and large lateral size. However, the yield is insufficient for energy storage and electrocatalytic applications. The liquid exfoliation method is widely used in producing high-quality 2D TMD suspensions via direct sonication techniques. However, the nanosheets in the resultant dispersion are generally highly polydisperse, which is not ideal for practical applications. To fully exfoliate TMDs, studies have found that lithium-ion intercalation using *n*-butyl lithium and hexane is one of the best methods.¹⁴⁶ The degree of lithiation can also tune the crystal phase of the TMDs from the semiconducting 2H (trigonal prismatic) to the metallic 1T (octahedral) phase (Figure 5b,c).⁶⁵ In the case of WS₂, transformation from the 2H to 1T phase after the exfoliation process caused the structure to become highly distorted with a high proportion of zigzag-like strain in the lattice.¹⁴⁷ DFT calculations suggest that the tensile strain in the exfoliated WS₂ nanosheets could enhance the DOS near the Fermi level which favorably influences ΔG_{H^*} and significantly enhances the HER performance.

For electrocatalytic applications, the X sites at the layer edges, rather than the sites within the basal plane, have been identified as the catalytically active sites by both DFT calculations and experiments.^{53,54} Inspired by this finding, various methods have been developed to expose more active edge sites (such as lateral size control, nanostructuring, defect engineering, etc.) and further improve the electrocatalytic performance of TMDs.^{148–150} Additionally, either the M or X sites located in

the basal plane can be activated using heteroatom doping.¹⁵¹ Experiments and DFT calculations indicate that metallic atom (Fe, Co, Ni) and non-metallic atom (B, N, O) doping are both effective for improving the HER activity of TMDs.^{74,151} TMDs also have great potential in ECR applications.^{152,153} For example, Asadi et al. identified that the edge sites of MoS₂ to be active for the ECR due to the high density of *d* electrons in Mo-terminated edges and its low work function.¹⁵⁴ They also found a trend between work function and ECR performance for various nanostructured TMDs in ionic liquid media.¹⁵⁵ According to calculations, the work functions of TMDs show the following trend: MoS₂ > WS₂ > MoSe₂ > WSe₂, which is consistent with experimentally measured ECR activities.

2.2.2. Non-layered Metal Chalcogenides. NMCs are a class of metal chalcogenides with 3D crystal structures. The general formula of a NMC is MX_a (*a* = 1, 2), where M represents a metal such as Cd, Co, Ni, Sn, Zn, etc. and X represents a chalcogen (S, Se, and Te).⁴³ It is still a great challenge to synthesize 2D NMC nanosheets through traditional methods (e.g., liquid exfoliation or micromechanical cleavage) due to the difficulty of breaking the in-plane bonds (e.g., covalent, metallic, and ionic bonding) and the lack of an intrinsic anisotropic growth driving force. To overcome this, new methods have been developed, such as oriented-attachment growth, 2D-templated synthesis, lamellar intermediate-assisted exfoliation, ultrathin 2D precursors-based topotactic conversion, and selective extraction-assisted exfoliation.^{45,156–159} Toward electrocatalysis, 2D NMCs have demonstrated excellent electrocatalytic performance because of their unique physical and chemical properties. For example, 2D CoSe₂ nanosheets exhibited HER and OER performances that were superior to its bulk form.^{45,156} It was also found that subtle lattice distortion induced by Mn-atom doping in this material can further improve its HER performance.¹⁶⁰ 2D NMCs with double metal cations (e.g., Fe-NiS₂) have also demonstrated improved HER performance due to the increased density and accessibility of catalytic active sites.¹⁶¹ For the ECR, Sun et al. synthesized Mo–Bi bimetallic chalcogenide nanosheets which showed highly selective CO₂ reduction to methanol.¹⁶² The Faradaic efficiency toward methanol production reached 71.2% with a current density of 12.1 mA cm⁻², which is significantly higher than others reported in the literature.

2.3. Transition-Metal Oxides and Hydroxides

Transition-metal oxides (TMOs) and hydroxides (TMHs) have been employed for almost all electrocatalytic processes mentioned already.⁴⁵ However, most pristine TMOs and TMHs exhibit unsatisfactory performance compared to benchmark electrocatalysts due to their low activity and poor conductivity. Many recent studies have shown that the electrocatalytic activity of TMOs and TMHs can be improved by reducing their thickness. Thus, 2D TMOs and TMHs have become promising candidate electrocatalysts for OER (discussed in section 7.2.1) and ECR (discussed in section 9.3) applications.

2.3.1. Transition Metal Oxides. 2D TMOs present great potential in electrocatalysis due to their low cost, high stability, and tunable activity. Two main classes of 2D TMOs exist: layered TMOs and non-layered TMOs. The layered class consists of metal trioxides (e.g., MoO₃, TaO₃, and WO₃) which have a layered structure like graphene and can be transformed into 2D nanosheets by typical exfoliation methods such as liquid exfoliation.^{55,163–165} Non-layered TMOs typically have 3D crystal structures which cannot be easily synthesized via top-down approaches as they contain strong chemical bonds between

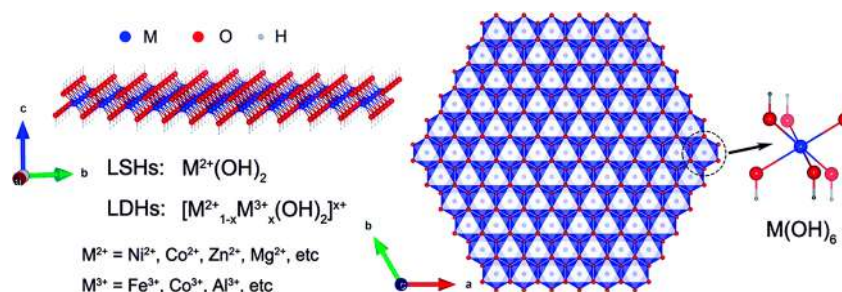


Figure 6. Illustration of a brucite or brucite-like single layer in layered metal hydroxides, including LSHs and LDHs. Reproduced with permission from ref 169. Copyright 2016 Royal Society of Chemistry.

the different crystal layers. Accordingly, methods including ultrathin 2D precursor-based topotactic conversion strategies and salt-template methods have been developed to synthesize these non-layered 2D nanomaterials.^{45,166} For example, Xiao et al. developed a general method to synthesize a range of 2D TMO nanosheets (MoO_3 , WO_3 , MoO_2 , MnO) using salt crystals as a template. The lateral growth of TMOs on the salt surfaces is guided by the salt crystal geometry and promoted by lattice matching. Any growth perpendicular to the salt surface is limited by precursor depletion. The result is the formation of TMO nanosheets with nanometer thickness and is even a suitable method for materials with non-layered crystal structures.¹⁶⁶

To date, many studies have demonstrated that 2D TMOs are active for various electrocatalytic reactions in the water and carbon cycles. Most 2D TMOs can be used as electrocatalysts directly without further modification. However, 2D TMOs are significantly limited by their weak electron transfer abilities. Therefore, optimizing their electrical conductivity is an ideal way to improve their catalytic performance. For example, plasma-engraved 2D Co_3O_4 nanosheets exhibited efficient OER performance due to their highly exposed surface area, enhanced electrical conductivity, and vacancy introduced active sites.¹⁶⁷ Furthermore, the catalytic performance of 2D TMOs can be improved using defect engineering. For example, 2D CeO_2 nanosheets with surface-confined pits showed a faster reaction rate for CO oxidation than its bulk form.¹⁶⁸

2.3.2. Layered Transition Metal Hydroxides. Layered transition-metal hydroxides (LMHs), including layered single metal hydroxides (LSHs) and layered double hydroxides (LDHs), are a group of layered materials which have metal-hydroxyl host layers with or without intercalated anions (Figure 6).¹⁶⁹ Due to the increased interest in graphene, studies have found that many materials with 2D confinement have unique properties that are different from their bulk forms. In particular, LDHs comprise positively charged brucite-like layers and an interlayer region containing charge-balancing anions and solvation molecules. The incorporated anions and various metal cations also lead to large interlayer spacing and unique redox characteristics. All of these properties result in the notable electrochemical performance of LDHs.^{170,171} As a result of their combined physiochemical properties and ultrathin nanostructure, 2D LMHs have been widely investigated as one of the most promising candidates for electrocatalytic applications.^{172,173}

Currently, various 2D LMHs have been synthesized and most of them exhibit efficient electrocatalytic performance. For example, Song et al. reported that 2D single-layer LDHs have superior OER performance in alkaline media compared to bulk LDHs.¹⁷⁴ This improved OER performance was attributed to the greater active site density and improved electrical conductivity of

the 2D LDHs. Furthermore, an electrode which integrated ultrathin $Ni(OH)_2$ with a Pt substrate demonstrated a synergistic effect which greatly promoted the alkaline HER.¹⁷⁵ In this hybrid system, it was found that $Ni(OH)_2$ expedited water adsorption and dissociation while the Pt surface subsequently facilitated hydrogen recombination and desorption.¹⁷⁶ For the carbon cycle, very few studies exist regarding LMH-based electrocatalysts. However, evidence has shown that LDHs demonstrate photocatalytic activity for CO_2 conversion which creates opportunities for its application in the ECR process.¹⁷⁷

2.4. MXenes and Non-layered Transition-Metal Carbides and Nitrides

In 2011, a new category of 2D nanomaterials named MXene was discovered.^{178,179} The first MXene studied was $Ti_3C_2T_x$, which was synthesized by selectively etching the Al-atoms from its MAX phase.¹⁷⁹ To date, over 70 different MXene type carbides and nitrides have been confirmed through experimental synthesis or theoretical prediction.¹⁷⁹ The general chemical composition of MXene is $M_nA_nX_n$, where M represents an early transition metal, A is a group IIIA or IVA element primarily, X is C and/or N, and $n = 1, 2, \text{ or } 3$.¹⁸⁰ MXene-type materials are very suitable for electrocatalysis because they possess metallic conductivity and are hydrophilic. However, despite these advantages, MXenes were limited by the fact that many highly active metal nitrides (such as cobalt, nickel, and iron) were not present in the MAX list. Accordingly, alternative synthetic methods were developed in order to extend the category of 2D transition-metal carbides/nitrides.¹⁸¹ For example, Xu et al. developed a CVD method to synthesize large lateral size and high-quality non-layered 2D transition-metal carbides like $\alpha-Mo_2C$, WC, and TaC ultrathin nanosheets.¹⁸² Xiao et al. also developed a facile and scalable method using salt as a template to synthesize a series of non-layered 2D transition-metal nitrides.¹⁸³

Pristine MXenes like $Ti_3C_2T_x$ have low catalytic activity and are therefore hardly used directly as electrocatalysts. Ma et al. assembled a freestanding film using exfoliated g- C_3N_4 and $Ti_3C_2T_x$ as the active materials which showed OER performance comparable to commercial IrO_2 -based catalysts.⁶⁹ Other hybridization methods have also been introduced to produce high-performance MXene-based catalysts such as 2D cobalt 1,4-benzenedicarboxylate/MXene composites and $CdS/MXene$.^{184,185} Alternatively, non-layered 2D transition-metal nitrides possess inherent electrical conductivity and hydrophilicity which affords them many advantages for electrocatalytic applications. As a result, they have been directly applied as efficient electrocatalysts without any modification.^{186,187}

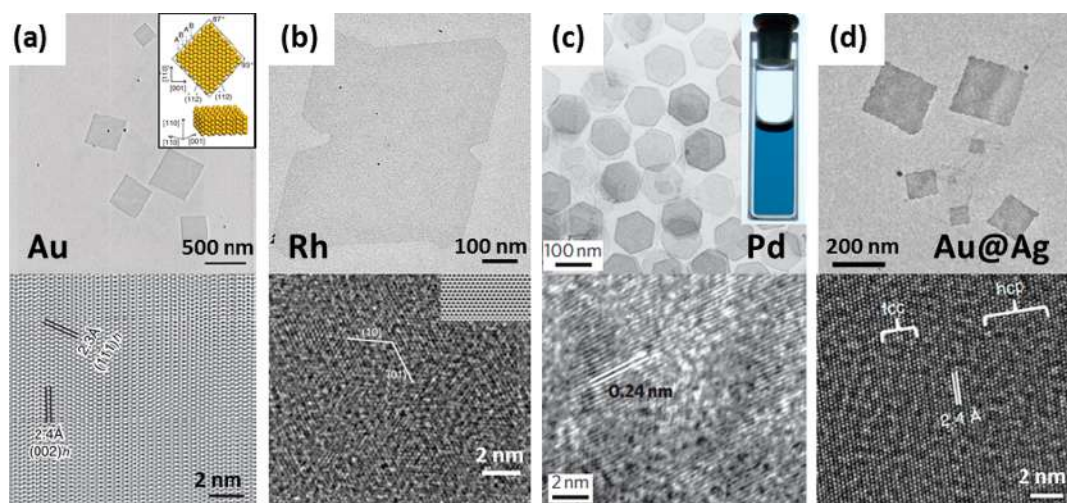


Figure 7. TEM (top) and HRTEM (bottom) images of (a) Au, (b) Rh, (c) Pd, and (d) Au@Ag nanosheets. Reproduced with permission: (a) From ref 192. Copyright 2011 Nature Publishing Group. (b) From ref 190. Copyright 2014 Nature Publishing Group. (c) From ref 193. Copyright 2011 Nature Publishing Group. (d) From ref 194. Copyright 2015 Nature Publishing Group, respectively.

2.5. Transition Metals

Transition metals are a class of materials with a long history in electrocatalysis, and for decades, fundamental studies for electrocatalysis were all based on metals and metal alloys.^{4,38,188,189} To date, the precious metal Pt is still the benchmark electrocatalyst for the HER and ORR processes.¹⁸⁴ Since the discovery of CNTs and graphene, the role of dimensionality in determining the intrinsic properties and functions of nanomaterials has been widely accepted.¹⁸⁸ Similar to other 2D nanomaterials, metal nanoplates and nanosheets have shown some unique properties.^{188,190–192} Most synthetic methods for large-scale production of 2D metal nanosheets can be described as “bottom-up” methods (e.g., 2D template-assisted synthesis, seeded growth, hydrothermal, and solvothermal methods).^{45,188} For example, metal nanocrystals can be directed or confined to grow into a 2D nanosheet in the presence of 2D templates. As shown in Figure 7a, Au square sheets (AuSSs) with an unconventional *hcp* phase were synthesized via a 2D template-assisted method.¹⁹² Duan et al. synthesized single-layered Rh nanosheets using a simple solvothermal method (Figure 7b) which could also be used for fabricating similar structures for other metals.¹⁹⁰ However, the poly(vinylpyrrolidone) supports used for these single layered Rh nanosheets have a negative effect on their electrocatalytic application. Compared to this surfactant induced solvothermal method, the CO confined growth method is more appropriate for electrocatalyst fabrication as adsorbed CO can easily be removed. CO can also be used advantageously to direct the growth of metal nanocrystals. For example, CO is strongly adsorbed on low-index facets of Pd during the synthesis of freestanding Pd nanosheets (Figure 7c) which can then reduce Pd salts in a particular direction and produce particular phases.¹⁹³

The metal crystal phase is very important for electrocatalytic processes as metals are anisotropic. It was found that AuSSs can be transformed from *hcp* to *fcc* structures via surface ligand exchange or surface coating of a thin metal layer.^{188,194} For example, in the Ag coated Au nanosheet system, the surface coating can lead to two types of phase transformation based on the surfactant used. This can result in the formation of *fcc* Au@Ag core–shell square sheets with (100)_f orientation, and *hcp/fcc* mixed Au@Ag core–shell nanosheets with (110)_h/(101)_f orientation (Figure 7d). This method realizes the phase control

of 2D metal nanosheets which is important in regulating their catalytic properties for electrocatalysis. 2D metal nanosheets have exhibited enhanced catalytic performance over commercial catalysts due to their significantly larger surface area. For example, Huang et al. reported that Pd nanosheets have a larger electrochemically active surface area (ECSA) than commercial Pd-based catalysts for formic acid oxidation.¹⁹³ Saleem et al. also confirmed that Pt–Cu alloy nanosheets have better performance for ethanol oxidation compared to commercial Pt/C catalysts due to their large ECSA.¹⁹⁵

2.6. Metal–Organic Frameworks and Covalent–Organic Frameworks

Metal–organic frameworks (MOFs) are porous crystalline compounds consisting of metal ions or clusters coordinated to organic ligands forming bulk structures.^{196,197} Recently, MOFs have attracted significant interest in electrocatalysis due to their tailorable structures, high porosity, and large surface area.¹⁹⁸ More importantly, the crystal structures of MOFs can be varied from 3D structures to 2D layered structures.^{17,199,200} Compared to their bulk forms, 2D MOFs have highly accessible active sites for electrocatalysis. Like other 2D nanomaterials, 2D MOFs can also be synthesized via top-down (exfoliating bulk MOFs) and bottom up (directly synthesizing from metal ions and ligands) methods.^{184,201–203} In electrocatalysis, 2D MOFs have been applied in many electrocatalytic processes including the HER, OER, and ECR.^{201,204} For example, Zhao et al. synthesized NiCo bimetal–organic framework nanosheets from a mixed solution of Ni²⁺, Co²⁺, and benzenedicarboxylic acid (BDC) and applied them as OER electrocatalysts.²⁰¹ The excellent performance of this 2D MOF was attributed to its ultrathin thicknesses, high degree of exposed catalytic active sites, and distinct surface atomic bonding arrangements. Currently, most works on 2D MOF-based electrocatalysts are related to the water cycle reactions. As a pioneering work, Kornienko et al. demonstrated the possibility applying MOFs for the ECR which has created new opportunities for MOFs in energy-related applications.²⁰²

Another important application of MOFs is its use in the synthesis of metal single-atom catalysts (M-SACs). Metal single-atom catalysts demonstrate unique properties in a wide variety of heterogeneous catalysis and electrocatalytic processes as they represent maximum atom utilization efficiency.^{92,205} Very

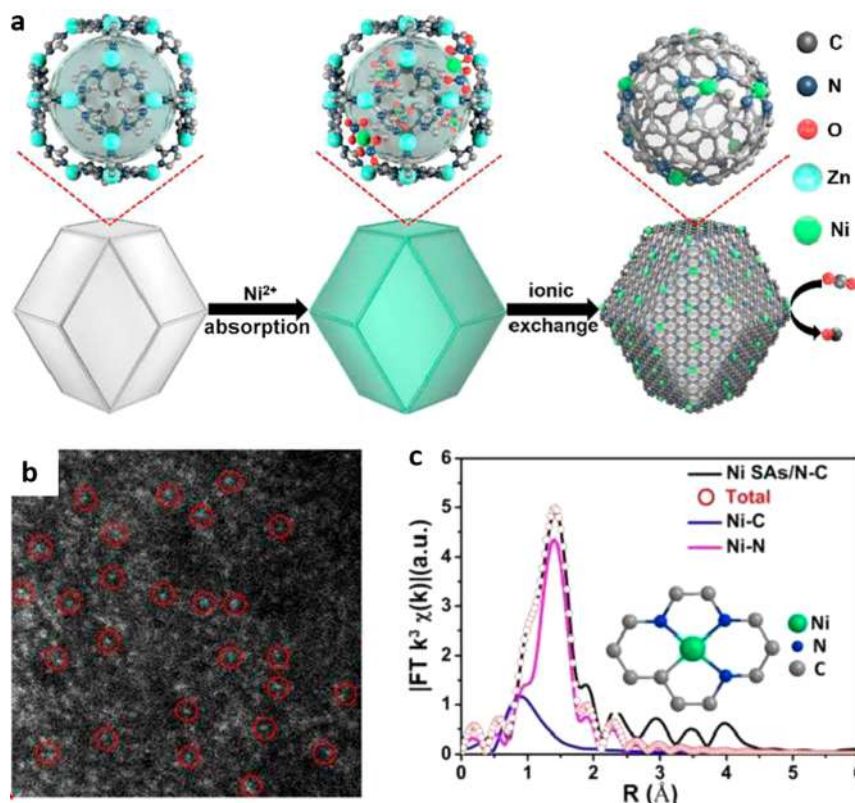


Figure 8. (a) Scheme of the formation of Ni single-atom electrocatalyst. (b) TEM image of Ni single atom. (c) EXAFS fitting curves for various electrocatalysts, inset shows the molecular Ni single atom bonded with nitrogen atoms. Reproduced with permission from ref 207. Copyright 2017 American Chemical Society.

recently, Li's group developed a general synthetic strategy for M-SACs by applying particular zeolitic imidazolate frameworks (ZIFs; a kind of MOF that are topologically isomorphic with zeolites) as precursors.^{205–207} The resultant M-SACs (M = Fe, Co, Ni) demonstrated excellent activities for energy-related electrocatalytic reactions (Figure 8a). The most important principle of this methodology is the utilization of low-boiling-point Zn (mp 420 °C, bp 907 °C) in ZIF-8 and Zn/Co bimetallic ZIF-67, which can be evaporated away at high temperature and leave abundant N-rich defects. As a result, aggregation of the isolated metal ions was avoided during pyrolysis due to strong N-coordination (Figure 8b). The precise molecular structures of these isolated metal atoms were identified by high-resolution imaging (Figure 8b) and X-ray absorption spectra (XAS; Figure 8c).

Similar to MOFs, covalent-organic frameworks (COFs) are organic solids with porous crystal structures in which the building blocks are made of light elements such as H, B, C, N, and O linked by strong covalent bonds.^{208,209} Discovered by Yaghi et al., COFs have emerged in various research fields such as gas storage, photoelectric applications, and electrocatalysis.^{210,211} Normally, 2D COFs are obtained from their bulk counterparts via top-down methods such as solvent assisted exfoliation, self-exfoliation, mechanical delamination, and sequential strategies.^{212–216} Also similar to MOFs, COFs have many advantages for electrocatalysis such as high surface area, regular pore size, tailorable structure, and predictable synthesis routes. Accordingly, 2D COFs have been applied in many electrocatalytic processes.^{217–219} For example, Lin et al. developed a catalyst of modular optimized COFs with building units of cobalt porphyrins linked by organic struts through imine bonds for

the electrochemical reduction of CO₂ to CO.²¹⁹ This COF-based catalyst exhibited high activity and selectivity compared to existing heterogeneous systems. Besides MOFs and COFs, 2D polymers are emerging as electrocatalysts for processes such as the HER and ORR.²²⁰ For instance, Dong et al. synthesized a 2D supramolecular polymer via the Langmuir–Blodgett method.²²¹ The large-area and ordered 2D nanosheets exhibited HER activity superior to that of recently reported CNT-supported molecular catalysts.

3. ENGINEERING PROTOCOLS FOR CATALYST DESIGN

As mentioned in previous sections, most pristine 2D nanomaterials are inert for electrocatalysis due to their low adsorption energy, limited number of active sites, and low conductivity.^{48,53,62} Therefore, preparation of high-performance 2D catalysts with favorable composition, thickness, defects, and surface properties is extremely important for their practical application. To this end, various methods such as heteroatom doping, defect engineering, interfacial structure engineering, etc. have been utilized to tailor the catalytic activity of 2D nanomaterials.^{48,62,222} In this section, we briefly summarize catalyst design protocols for a wide variety 2D catalysts. The advantages and limitations of each protocol are systematically discussed together with some featured examples of electrocatalytic applications.

3.1. Heteroatom Doping

Chemical doping with heteroatoms is an effective method for tailoring electronic properties, manipulating surface chemistry, and modifying the elemental composition of 2D nanomaterials. To date, heteroatom doping has demonstrated its ability to

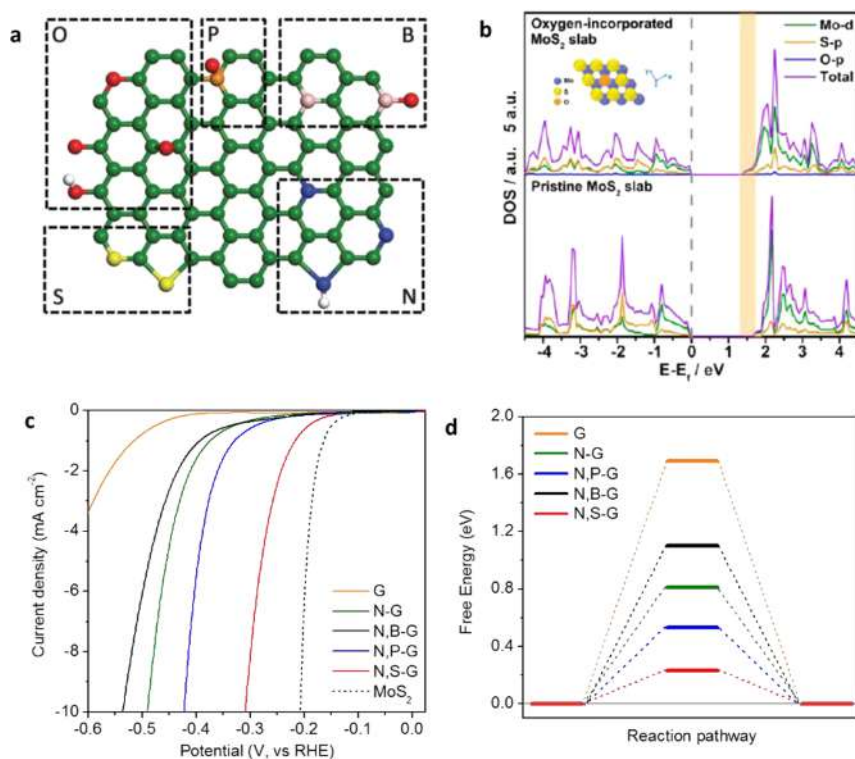


Figure 9. (a) Typical single-atomic configuration of different types of dopants at different doping sites in the graphene matrix. Reproduced with permission from ref 10. Copyright 2015 American Chemical Society. (b) Calculated DOS of the oxygen incorporated MoS₂ slab (top) and the pristine 2H-MoS₂ slab (bottom). Reproduced with permission from ref 149. Copyright 2013 American Chemical Society. (c,d) HER polarization curves and three-state free energy diagram for the pure, single- and dual-doped graphene models. Reproduced with permission from ref 73. Copyright 2016 Nature Publishing Group.

impart catalytic activity for various 2D nanomaterials such as graphene, MoS₂, g-C₃N₄, etc. It is generally divided into two categories: non-metal-atom doping and metal-atom doping. Non-metal-atom doping normally includes doping N-, B-, O-, S-, and P-atoms into the nanomaterial framework. For example, all of these elements have been successfully used to dope the carbon framework in graphene and CNTs. Metal-atom doping is mainly used for synthesizing single-atom catalysts on a support structure, such as Pt single atoms on graphene. Heteroatom doping is an efficient and controllable method that can tune 2D nanomaterials for particular electrocatalytic processes such as the ORR (discussed in section 6.2), OER (discussed in section 7.4), HER (discussed in sections 8.2.1 and 8.3.3), and ECR (discussed in section 9.5).

3.1.1. Non-Metal-Atom Doping. Doping graphene with nitrogen was one of the first strategies used to effectively tailor the electronic properties and chemical reactivity of graphene. Therefore, N-graphene is considered to be the pioneer of 2D electrocatalysts. Nitrogen is an effective heteroatom primarily due to its greater electronegativity compared to that of carbon and the conjugation between the nitrogen lone pair electrons and the graphene π -system.^{223,224} Inspired by this discovery, other heteroatoms such as O, B, S, and P have been used as graphene dopants (Figure 9a). These heteroatoms usually exist in the 2D matrix in the form of substitutional dopants at the edges or in the basal plane and can disrupt the pristine atom network, creating defect regions.^{149,225} These defect sites can serve as the active sites for electrocatalysis. Doping mode and total dopant content significantly affect the electrocatalytic performance of heteroatom-doped graphene, but can be carefully tuned by doping procedure and precursor choice.¹⁰ It should be noted that

different non-metal atoms can induce different types of active sites in the graphene matrix. For example, the active sites of N-graphene are generally considered to be the C-atoms adjacent to the N-dopants,²²³ whereas the active sites of B-graphene for the ORR are the B dopants.^{49,226} From this ability to tune electronic states and optimize adsorption energies, non-metal-atom doped 2D nanomaterials have shown catalytic performance for the ORR, OER, HER, and ECR.^{10,95,226,227} Other than doped graphene, non-metal-atom doping has been extended to other materials for various reactions.^{9,149} For example, Xie et al. demonstrated that oxygen incorporation can effectively regulate the electronic structure of MoS₂ and further improve its HER performance (Figure 9b).¹⁴⁹ Optimization of their catalyst was also achieved by being able to control the degree of structural disorder through oxygen doping, which demonstrates the ability to improve 2D nanomaterials through synergistic structural and electronic modulation. Beyond single element doping, double- or triple-doped 2D nanomaterials have shown significantly greater electrocatalytic activity than single-doped materials. As an example, multiple-atom-doped graphene nanosheets (N/B, N/S, N/P dopants) exhibited superior HER performance compared to their single doped counterparts (Figure 9c,d).⁷³ DFT calculations revealed that the origin of this enhancement is from synergistic intermolecular catalysis.

3.1.2. Metal-Atom Doping. The size of metal nanoparticles is a key factor in determining the performance of metal-based electrocatalysts. Theoretical and experimental studies have demonstrated that sub-nanometer-sized metal clusters can sometimes have better catalytic activity or selectivity than nanometer-sized counterparts.^{228–230} Inspired by these studies, single-atom catalysts were developed to utilize every metal atom

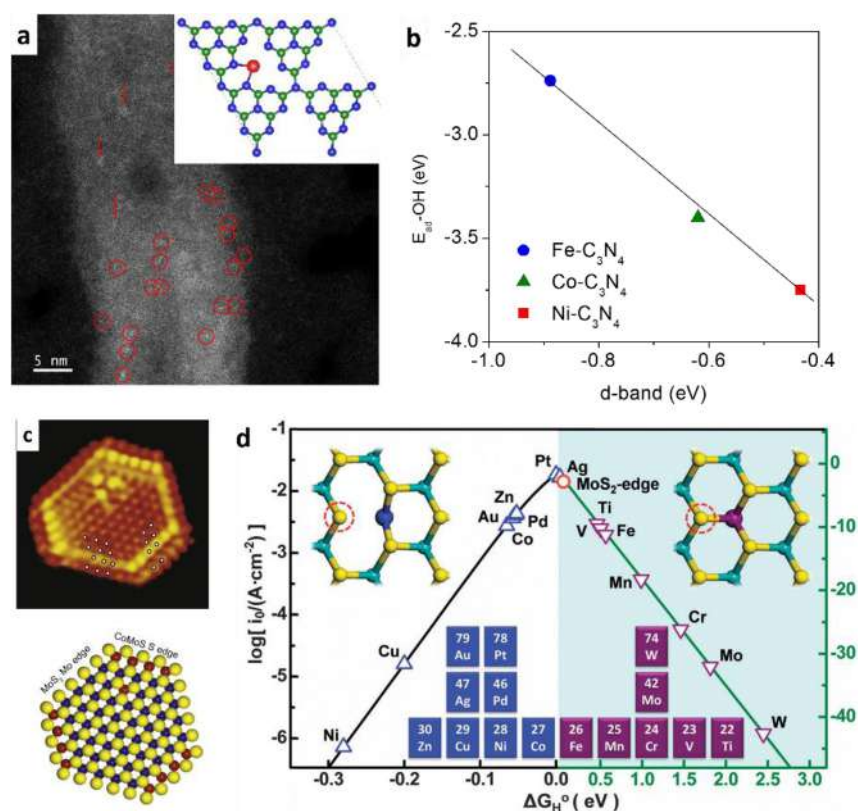


Figure 10. (a) HAADF-STEM images of Co-C₃N₄/CNT. Circles and arrows indicate single Co atoms and Co clusters, respectively. Inset shows the molecular model of the Co-C₃N₄ complex. (b) Dependence of OH* adsorption energy with the d-band position on various metal-g-C₃N₄ models. Reproduced with permission from ref 234. Copyright 2017 American Chemical Society. (c) Molecular model based on the DFT calculations (top) and atom-resolved STM image of a Co-Mo-S nanocluster (bottom). Reproduced with permission from ref 235. Copyright 2007 Elsevier. (d) A “volcano” plot displaying HER activity of various MoS₂ nanosheets doped with different single metal atoms. Reproduced with permission from ref 151. Copyright 2015 Royal Society of Chemistry.

in supported catalysts.^{92,222,231} Further, doping 2D nanomaterials with single metal atoms is an effective way to build active sites for various catalytic processes.²³² For instance, Lu et al. predicted the CO oxidation ability of Au-doped graphene catalysts with DFT calculations.²³³ The high catalytic activity of Au-doped graphene was attributed to the partially occupied *d* orbital localized in the vicinity of the Fermi level caused by the interactions between the Au-atom and graphene. Even through this model can be extended to other metal atoms, the low stability of the metal sites, owing to the weak bonding between the metal and the graphene matrix, presents a significant problem. As a result, an ideal 2D platform for single metal atoms should have strong coordination ability for effective anchoring. For example, Zheng et al. synthesized a new class of single-atom catalysts based on a series of transition-metal atoms doped in g-C₃N₄.²³⁴ The transition-metal atoms (such as Co) were anchored by two nitrogen atoms to form a Co-N₂ coordination moiety in the g-C₃N₄ matrix (Figure 10a). The as-prepared catalysts revealed excellent performance for bifunctional ORR and OER processes in alkaline media. DFT computations indicated that the catalytic ability of this new class of materials is the result of a modified d-band position which induces optimal adsorption energy of key reaction intermediates (Figure 10b).

Other than carbon-based electrocatalysts, metal-atom doping can also activate the inert basal plane of TMDs. It has been proven that the catalytic activity of 2D TMDs originates from the edge S sites.⁵³ Interestingly, experimental studies demonstrate that doping with transition-metal atoms (Fe, Co, or Ni) can tune

the electronic structure of TMDs and activate the in-plane S sites, increasing the total number of active sites for catalysis.^{236–239}

This promotion effect was theoretically investigated by projected DOS analysis showing that Co or Ni can weaken the bonding of S at the S-edges due to a decreased filling of antibonding states. Consequently, some coordinated unsaturated metal atoms are created which can interact with adsorbates.²³⁸ For example, Co incorporation at the S-edges of MoS₂ can reduce the ΔG_{H^*} from 0.2 to 0.1 eV. Scanning tunneling microscopy (STM) images of the chemically synthesized Co-Mo-S nanoparticles also showed that Co incorporation can change the shape of pristine triangular MoS₂ to a truncated hexagonal plane with both Mo and S-Co exposure (Figure 10c).²³⁵ This was found to result in an increased length of active edges. To extend this, DFT was used to screen the HER activity trend of MoS₂ doped with a range of transition metals.¹⁵¹ The results predict a volcano plot along the H adsorption free energy with an interesting trend caused by the metal dopant bonding configuration. It was found that when metal atoms substitute the Mo atoms in the MoS₂ matrix, some metals (V, Ti, Fe, Mn, Cr) prefer to remain in the Mo position to bond with six S atoms. For these metal dopants, H adsorption was endergonic. Other metals (Pt, Ag, Pd, Co, Ni) tend to shift toward one side and bond with only four S atoms, leaving the other two S-atoms unsaturated (Figure 10d). For these metal dopants, H adsorption was exergonic. These findings demonstrate the potential of metal-atom doping for enhanced catalytic ability of 2D nanomaterials and provides a rational strategy for activating inert 2D TMDs in energy-related catalytic processes.

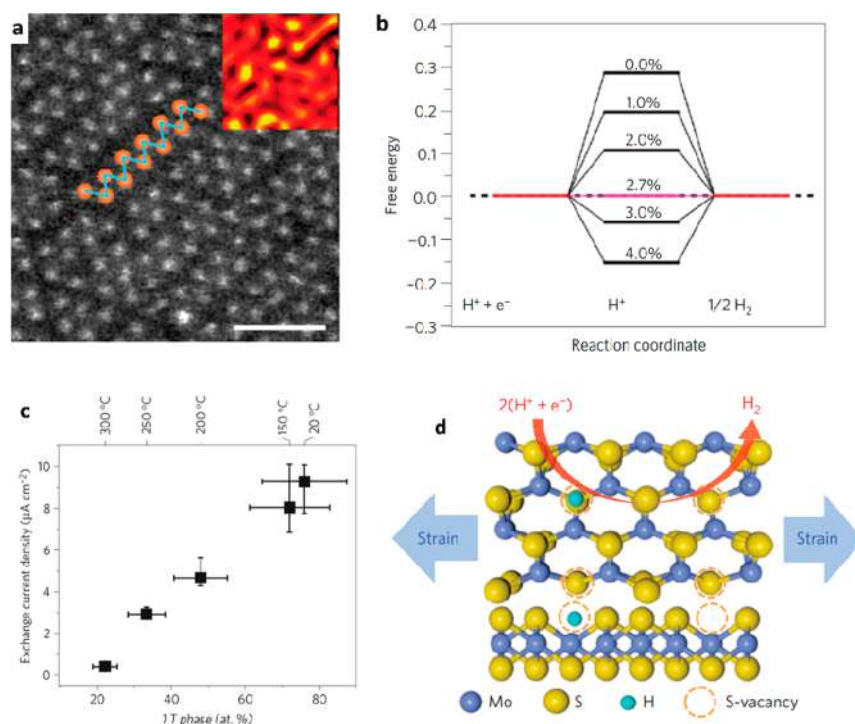


Figure 11. (a) High-resolution STEM image of an exfoliated WS₂ monolayer with 1T superlattice structures. The scale bar is 1 nm. The inset shows the strain tensor map where light (yellow) and dark (black) colors correspond to regions where the strain is in tension and compression, respectively. (b) The HER free energy pathways on WS₂ monolayers with different degrees of strain. (c) Catalytic activity as a function of the 1T phase concentration on a series of WS₂ electrocatalysts obtained by annealing in an inert atmosphere. Reproduced with permission from ref 147. Copyright 2013 Nature Publishing Group. (d) Schematic of the top (upper panel) and side (lower panel) views of MoS₂ with strained S-vacancies in the basal plane. Reproduced with permission from ref 250. Copyright 2016 Nature Publishing Group.

3.2. Defect Engineering

Defects present in 2D nanomaterials are commonly recognized as the active sites for electrocatalytic processes.⁹⁰ For example, the electronic state is strongly enhanced at the edges of graphene compared to in-plane sites.^{72,240} This has been supported by DFT calculations which have indicated that the zigzag edges of graphene are chemically active for the ORR and that these defects can be used as the active sites directly due to their unique electronic density of states.^{15,242–244} In addition, the band gaps of most 2D TMDs can be tuned through crystal strain which can be induced by defects at the edges or basal plane. As a result, defect engineering has been widely adopted for 2D nanomaterial preparation to increase their electrocatalytic activities.²⁴¹ However, controllable defect engineering methods are essential for the precise study of defects and their effect on reaction mechanisms. Jia et al. developed a defect-rich graphene by the removal of nitrogen dopants in N-graphene.²⁴² Very interestingly, the results indicated that the lower the nitrogen content, the higher the ORR activity, demonstrating the feasibility of defect engineering for graphene-based electrocatalysts. Exposing more defects or edges is also a promising protocol for developing high-performance TMD-based materials.²⁴⁵ For example, Liu et al. reported that vacancies formed in ultrathin CoSe₂ nanosheets can serve as the active sites for the OER.¹⁵⁶ These vacancies were formed through ultrasonic treatment, whereby ultrasonication with diethylenetriamine enabled the removal of Co-atoms from the CoSe₂ lattice. This resulted in the formation of many vacancies in the ultrathin nanosheets. A similar phenomenon was also observed for ultrathin nanosheets of Ni₃N, Co₃O₄, and BiVO₄.^{246–248}

3.3. Lateral Size and Thickness Regulation

Lateral size and thickness of 2D nanomaterials have great implications on their electrocatalytic properties for the following reasons.²⁴³ (1) By reducing the lateral size of 2D nanomaterials, more defects and/or edge sites will be exposed; (2) changing the thickness of 2D nanomaterials can modify their electronic structures, resulting in tunable catalytic performance; (3) when reducing the thickness to the atomic level, catalytic activity enhancement may result from in-plane defects generated by structural disordering; (4) single-layered 2D nanomaterials have the highest theoretical surface area giving them the highest theoretical specific density of active sites for catalytic processes. Specifically, Kibsgaard et al. demonstrated how morphological control of MoS₂ at the nanoscale can significantly impact the surface structure at the atomic scale and consequently enhance HER performance.²⁴⁹ More interestingly, when reducing thicknesses to sub-nanometer scales, the lattice distortion that occurs for many 2D nanomaterials introduces a large number of vacancies for catalytic activity. Another feature of thickness regulation is that 2D morphologies can expose the maximum possible area of a catalyst and create a larger ECSA. In this regard, Huang et al. developed freestanding Pd nanosheets for plasmonic and catalytic applications.¹⁹³ In the electrocatalytic oxidation of formic acid, the Pd nanosheets with a larger ECSA exhibited a higher current density than commercial Pd black. Following this, various strategies have been developed to maximize the ECSA of metal and metal alloy nanosheets (e.g., Rh, Pd–Cu, and Pt–Cu).^{47,190,195}

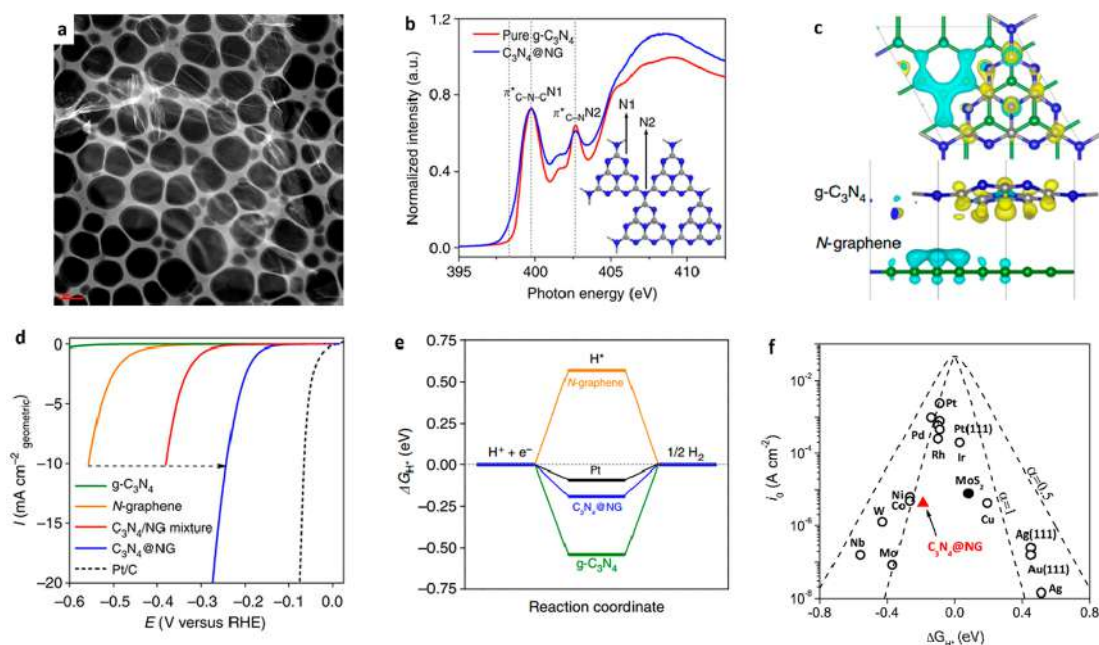


Figure 12. (a) HAADF-STEM image of $C_3N_4@NG$ nanosheet. (b) Nitrogen K-edge NEXAFS spectra of different catalysts. The scale bar is $1 \mu m$. Inset illustrating two types of nitrogen species in the $g-C_3N_4$ molecular network. (c) Interfacial electron transfer in $C_3N_4@NG$. Yellow and cyan iso-surface represents electron accumulation and electron depletion. (d) The HER polarization curves of various electrocatalysts in acidic media. (e) The calculated free-energy diagram of the HER at the equilibrium potential for three metal-free catalysts and Pt reference. (f) Volcano plots of i_0 as a function of the ΔG_{H^*} for newly developed $C_3N_4@NG$ and common metal-based catalysts. Reproduced with permission from ref 48. Copyright 2014 Nature Publishing Group.

3.4. Strain and Phase Engineering

Lattice strain alters the electronic state of a material and many studies have demonstrated the possibility of optimizing electrocatalytic performance with this strategy.^{142,250–253} Voiry et al. synthesized 1T WS_2 nanosheets with strained crystal lattices for the HER (Figure 11a).¹⁴⁷ It can be seen that a frequent occurrence of kinks in the zigzag chains leads to strong deformation and regions of high local strain with an overall isotropic strain of $\sim 3\%$. DFT computations indicated that an increase in tensile strain leads to an enhancement of the DOS near the Fermi level (Figure 11b). As a result, hydrogen adsorption becomes stronger. Experimentally, it was found that the HER characteristics are strongly linked to both the 1T phase concentration and the strain, as indicated by a gradual decrease in the HER j_0 with increasing 2H fraction and decreasing strain (Figure 11c). The above strategy can be further extended by integrating crystal strain with defect engineering. Li et al. reported that by combining vacancy and lattice strain, the HER activity of MoS_2 can be greatly improved.²⁵⁰ Their theoretical and experimental results showed that the S-vacancies provide new catalytic sites in the basal plane where gap states around the Fermi level allow hydrogen to bind directly to exposed Mo-atoms (Figure 11d). Hydrogen adsorption ability can be further manipulated by straining the surface with S-vacancies. Moreover, crystal strain can also change the phase of 2D nanomaterials. For example, MoS_2 demonstrated a phase transition from the semiconducting 2H phase to the metallic 1T phase through Li ion intercalation. The improved conductivity and altered band gap of 1T TMDs can significantly enhance their charge transfer kinetics to improve their HER performance.²⁵⁴ Experimental results indicate that Li ion intercalation not only increases the layer spacing (which modifies the band gap), but also reduces the oxidation state of Mo by changing the d-band filling.²⁵⁵

3.5. Interface Engineering

Interface engineering is another important protocol for designing high-performance electrocatalysts. As demonstrated by many experiments, interactions at the interface between two different materials will change their electronic states and chemical properties simultaneously, which has a great impact on their electrocatalytic performances.^{48,256,257} Interface engineering can be divided into two categories: heterostructure engineering and synergistic interaction, and they are always involved with each other. Heterostructure engineering usually involves complex chemical bonding between two different materials, whereas synergistic interaction is the physical contact of two materials with confined electron transport.⁴⁸ Interface engineering is an efficient way to synthesize high-performance electrocatalysts with unique physical/chemical properties. For example, Zheng et al. hybridized $g-C_3N_4$ with N-graphene *in situ* to form an ultrathin nanosheet (Figure 12a).⁴⁸ The XAS spectrum confirmed that there is a strong interfacial interaction between $g-C_3N_4$ and N-graphene layers by forming out-of-plane oriented C–N bonds (Figure 12b). These interlayer bonds can change a composite's electronic state and facilitate electron transport from the N-graphene to the $g-C_3N_4$ layer (Figure 12c). As a result, improved HER performance was achieved on the hybridized C_3N_4/NG sample compared to the physically mixed sample (Figure 12d). DFT computations indicated that this enhancement originates from the synergistic effect of chemical and electronic couplings, resulting in more favorable proton adsorption/reduction kinetics on the $C_3N_4@NG$ surface (Figure 12e). This activity trend also validated the predictive capability of the DFT model employed beyond metals. The most important finding of this study is that (similar to precious metals) rationally designed metal-free materials also have great potential for highly efficient electrocatalytic HER (Figure 12f). Similarly, Duan et al. synthesized a 3D free-standing hybrid film of $g-C_3N_4$ and N-graphene which

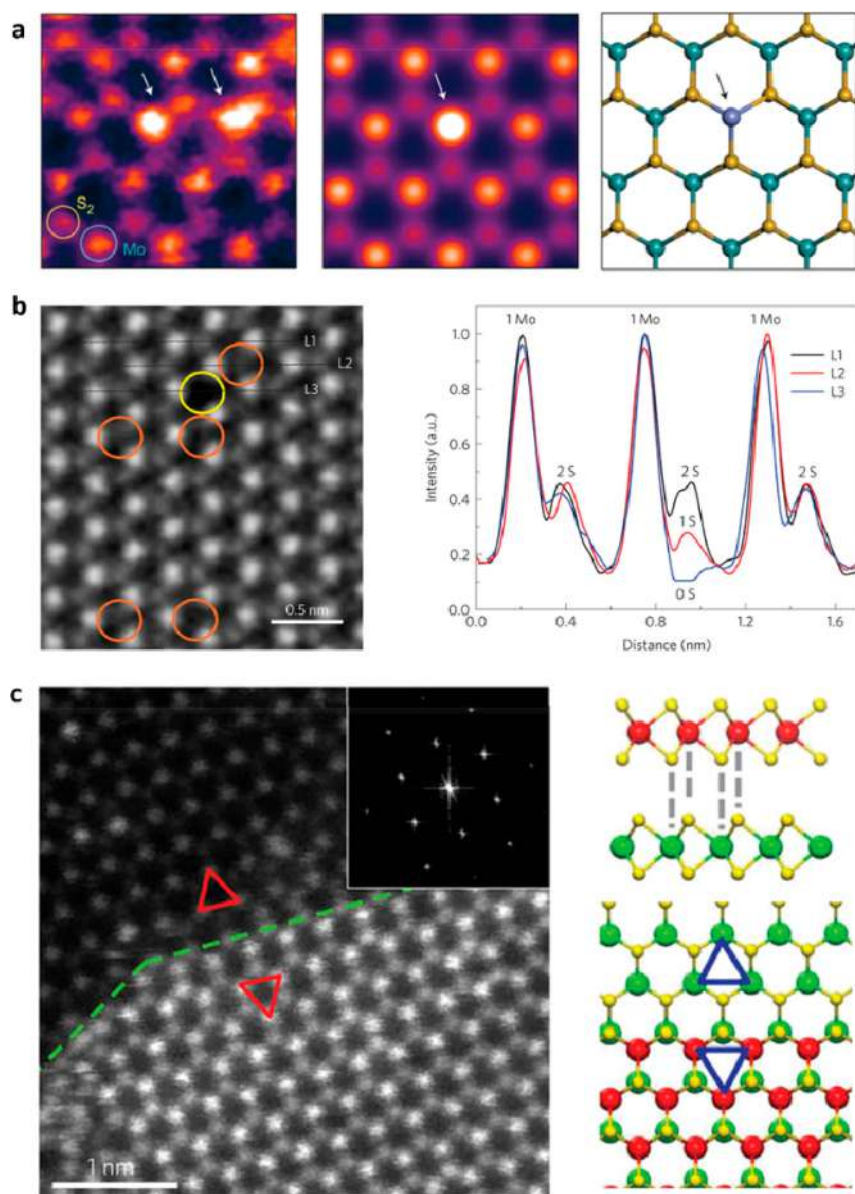


Figure 13. (a) HAADF-STEM image, simulated image, and corresponding molecular structure of a Co-doped MoS₂ monolayer (Co-atoms identified by arrows). Reproduced with permission from ref 266. Copyright 2017 Nature Publishing Group. (b) STEM image and corresponding intensity profiles of a single-layer CVD-grown MoS₂ nanosheet with a single sulfur vacancy (orange circles) and double sulfur vacancy (yellow circles). Reproduced with permission from ref 267. Copyright 2016 Nature Publishing Group. (c) HAADF-STEM image and schematic of the 2H stacking in the stacked WS₂/MoS₂ heterostructure. Reproduced with permission from ref 268. Copyright 2014 Nature Publishing Group.

showed comparable performance to the 2D heterostructured C₃N₄@NG hybrid.^{48,258} This method of forming 3D porous films can be extended to other 2D nanomaterials.^{227,255,259,260} The resultant performance of the film-like electrode is attributed to the following two reasons: (1) the 3D porous structure can maximize the exposed catalytic active sites, and (2) hierarchical intra- and interlayer pores generated in the films can increase its surface area and the rate of mass transport during electrocatalytic processes.

Other than metal-free materials, 2D TMDs can also form heterostructures. As an example, the MoS₂/CoSe₂ hybrid structure with a heterojunction-like interface showed enhanced catalytic performance compared to pure MoS₂ and CoSe₂ units.²⁶¹ Interestingly, the long-term stability of the MoS₂/CoSe₂ hybrid structure is also better than that of pure MoS₂, indicating the successful combination of the stability of MoS₂

with the high catalytic properties of CoSe₂. A similar phenomenon has also been observed for amorphous Co–Mo–S_x chalcogels.²⁶² It was found that although CoS_x materials are more active than MoS_x, they are less stable. Enhanced HER activity was achieved by hybridizing the more active CoS_x building blocks with the higher stability MoS_x units into a compact structure. The authors further suggested that the relationship between activity and stability of TMD materials is governed by a synergy between electronic effects (substrate–adsorbate binding energies) and morphological effects (number of defects).²⁶² Other hybrid systems such as reduced graphene oxide (rGO)/WS₂,²⁶³ MoS₂/Au,²⁶⁴ and rGO/MoS₂ have been designed using a similar principle.¹⁵⁰

Generally, design principles for constructing heterostructures for 2D electrocatalysts are governed by the following parameters: (1) both (or more) 2D nanomaterials should have similar crystal

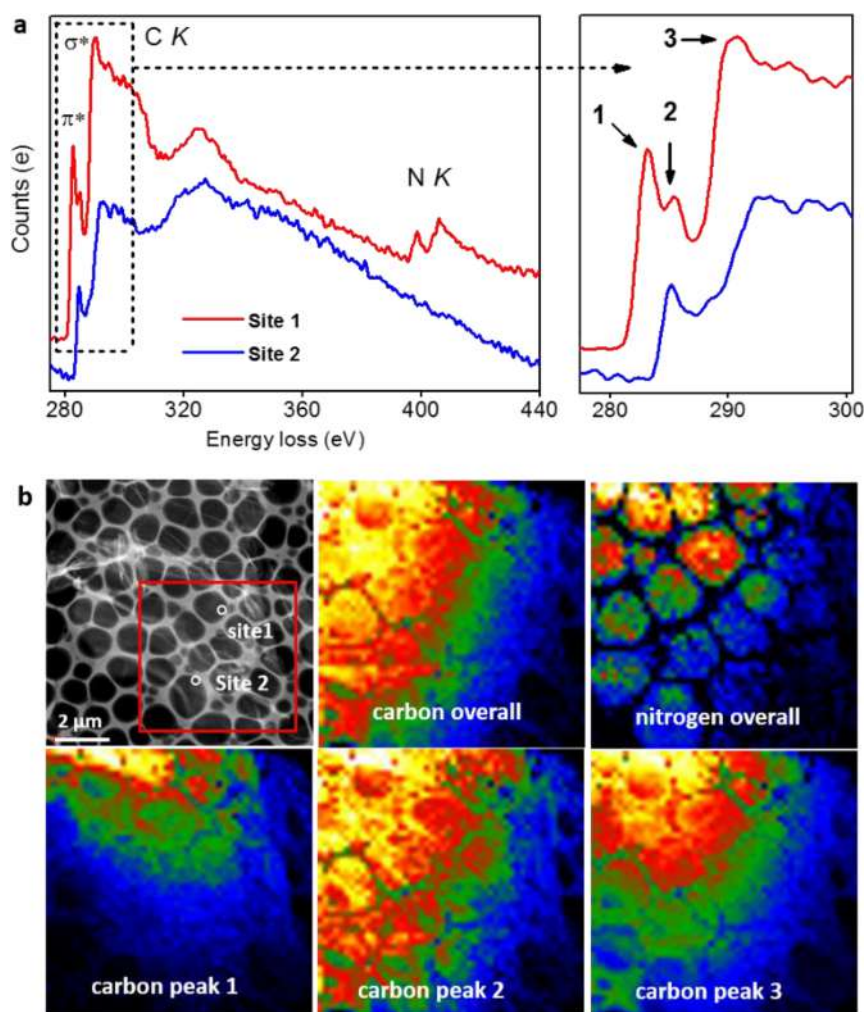


Figure 14. (a) EELS spectra of $C_3N_4@NG$ collected at two specific sites and (b) corresponding mappings of different species. Reproduced with permission from ref 48. Copyright 2014 Nature Publishing Group.

structures to facilitate the formation of heterostructures; (2) at least one 2D nanomaterial should have potential activity for the target electrocatalytic process; (3) the hybrids should have good conductivity for electron transport to reactive intermediates; (4) the properties of one material should compensate for the lack of properties of the other, such as intermediate absorption energy, low conductivity, and poor stability.

4. ADVANCED APPROACHES FOR DETERMINING ACTIVE SITES AND DETECTING INTERMEDIATES ON 2D ELECTROCATALYSTS

With the proliferation of nanotechnology, many advanced characterization and computational techniques have been developed for characterizing the morphology, defects, thicknesses, electronic states, and catalytic properties of nanomaterials.⁴³ In electrocatalysis, determining active sites is crucial for understanding the catalytic mechanism and is essential for developing new catalyst materials. In this section, we summarize the various advanced approaches for determining the active sites and reaction intermediates on 2D nanomaterials. These approaches are of particular importance for understanding the strong correlation between material characteristics and functional properties, as well as for guiding the rational design of 2D electrocatalysts with desired active sites for a specified application. Given that each technique has its own advantages

and limitations, combining different approaches is highly desirable for a full understanding of the catalytic mechanism and working principles of 2D electrocatalysts.

4.1. Microscopy

TEM provides the possibility to directly observe the size, crystallinity, exposed facets, and growth direction of nanomaterials, and is one of the most widely used techniques for determining the active sites of 2D electrocatalysts.²⁶⁵ Low-magnification imaging can be used to examine the morphology of nanosheets and the contact mode of hybrid 2D composites. The crystallinity, phase, crystal orientation, and exposed lattice plane of 2D nanomaterials can be explored by high-resolution TEM (HRTEM) images combined with selected area electron diffraction (SAED).⁴³ For example, the exposed lattice plane of crystalline nanosheets can be characterized by measuring the lattice distances from HRTEM images. However, it is difficult to verify the presence of defects, lattice distortion, or atom doping sites accurately in regular HRTEM. Luckily, the development of aberration-corrected scanning TEM (STEM) can resolve these problems. Unlike conventional TEM where electrons are transmitted to the sample in a raster, focused electrons in STEM mode are scanned over, similar to that of electrons in scanning electron microscopy (SEM). Further, images with atomic resolution can be obtained using high-angle annular dark-

field scanning transmission electron microscopy (HAADF-STEM) where the contrast of the atoms is directly proportional to the atomic number of the atoms. For example, Deng et al. demonstrated the utilization of HAADF-STEM to identify Pt single atoms in MoS₂ nanosheets.¹⁵¹ Due to their different elemental properties, Pt-atoms are much brighter than the other atoms present, causing an obvious contrast. The location of Pt-atoms in the MoS₂ nanosheet were clearly observed, and it could be concluded that the Pt-atoms replaced the Mo-atoms in the MoS₂ matrix. Not only limited to chemical identification, HAADF-STEM is also a compelling technique for characterizing single-layer TMD nanosheets with various heteroatom doping (Figure 13a), defects (Figure 13b), and heterostructures (Figure 13c).^{266–268}

Electron energy loss spectroscopy (EELS) and EELS mapping are important functions of HAADF-STEM which can identify different elements or single elements with different valence states.⁴⁸ As the energy loss peak intensity varies for different species, Zheng et al. conducted EELS measurements on C₃N₄@NG hybrid nanosheets to identify the distribution of g-C₃N₄ clusters on N-graphene sheets.⁴⁸ As shown in the EELS mappings presented in Figure 14b, the carbon species are distributed over the entire sheet, whereas the nitrogen species concentrate in specific regions, indicating that the g-C₃N₄ nanodomains are partially covered on the surface of N-graphene. More interestingly, the EELS mapping reveals that the defective carbon species (peak 1 in Figure 14a) are only present in the g-C₃N₄-containing regions but absent in the g-C₃N₄-free regions. In addition, an enhanced intensity of new sp³ carbon species (peak 3 in Figure 14a) was also observed in the g-C₃N₄-containing region only. These observations directly prove the generation of chemical bonds between the g-C₃N₄ and N-graphene during the coupling process.

4.2. X-ray Absorption Spectroscopy

XAS is a synchrotron-based characterization technique that can be divided into X-ray absorption near-edge structure (XANES), also known as near edge X-ray absorption fine structure (NEXAFS), and extended X-ray absorption fine structure (EXAFS).^{269–273} In the last 40 years, XAS spectroscopy has evolved into a powerful structural characterization tool and is widely used in many scientific fields, including physics, chemistry, biology, materials sciences, environmental sciences, etc.^{274–276} XAS has many advantages such as element-specificity, and sensitivity to short-range order (typically several Å) and chemical state. Therefore, it can provide quantitative structural information about materials at the atomic scale, such as the oxidation state, coordination number, bond length, and atomic species. As mentioned previously, in numerous cases, defects, crystal distortion, and dopants are commonly recognized as the active sites for electrocatalysis. Additionally, it is widely accepted that 2D electrocatalysts have many unique characteristics compared to their bulk counterparts, such as lower coordination number and strained crystal structures. However, it is difficult to detect most of these features using X-ray diffraction (XRD) or X-ray photoelectron spectroscopy (XPS) as their concentration in the material is extremely low.²⁷⁷ In this regard, *ex situ* XAS provides the possibility to detect these sites in an accurate way. For example, *ex situ* XAS has become the main method used to investigate novel single-atom catalysts. Other than *ex situ* techniques, *in situ* XAS provides a reliable way to measure the transformation process of a catalyst material, which can be utilized for formulating a comprehensive understanding of

electrocatalytic mechanisms. As shown in Figure 15, XANES characterization was used to detect the potential-dependent

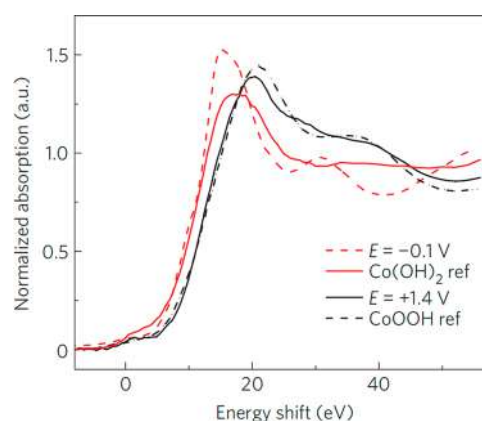


Figure 15. XANES spectra for the Co^{2+δ}O^δ(OH)_{2-δ} (0 < δ < 1.5) electrocatalyst under different potentials. Reproduced with permission from ref 176. Copyright 2012 Nature Publishing Group.

stoichiometry and structure of 3d M(Ni,Co,Fe,Mn) hydr(oxy)-oxide catalysts.¹⁷⁶ For example, at -0.1 V (HER potential region) the Co-atoms in Co(OH)₂ remain mostly in the Co²⁺ valence state in the form of Co(OH)₂. However, at 1.4 V (OER potential region) the valence state is closer to Co³⁺ resembling CoOOH. This *in situ* measurement clearly characterizes the transformation of the Co(OH)₂ electrocatalyst under different potentials, which is significant for evaluating the performance of electrocatalysts under real electrocatalytic conditions.

5. CATALYSTS DESIGN AND DEVELOPMENT PROTOCOLS

The ultimate challenge in the field of electrocatalysis is the ability to recognize and understand the relationships between reaction intermediate adsorbed states (microscopic property) and reaction kinetics (macroscopic property). From the many examples mentioned already, it can be seen that the apparent rate of an electrocatalytic reaction is strongly dependent on the extrinsic physical properties (morphology, crystalline, etc.) and intrinsic electronic structure (d-band position, work function, etc.) of an electrocatalyst, and always act together in determining the intermediate adsorption energetics, activation energies, and reaction energy barriers.^{278,279} Significant developments in DFT calculations and experimental nanotechnology, and especially their successful combination, have provided new insight into electrocatalytic processes at the atomic/molecular level.^{10,82} At present, there are tremendous opportunities in advancing surface electrochemistry by merging advanced materials preparation technologies, surface characterization techniques, and theoretical computation. Doing so is practically expedient for developing in-depth understandings of electrocatalyst design principles for a specific catalytic process.

5.1. Design Principles of Electrocatalysts through Multidisciplinary Approaches

In the past few years, there have been remarkable advances in a broad range of advanced ultrahigh-vacuum (UHV) characterization techniques involved in surface science studies, like XAS, XPS, and X-ray scattering (SXS). Further, the availability of high-quality 2D crystals provides ideal models for *in situ* structural probes like HAADF-STEM and STM to directly monitor intermediates on the surface or in the interface of catalysts.^{4,280}

Consequently, from collaboration between material scientists and electrochemists emerges in-depth understandings of the relationship between surface chemical properties of solid catalysts and their electrocatalytic activity.^{280,281} On the other hand, due to the remarkable developments in DFT mainly dealing with reaction thermodynamics and kinetic reaction barriers, one can establish the intimate relationship between electronic structure, adsorption energy, and apparent activity of a solid catalyst from the macroscopic to microscopic levels.⁷⁵ Therefore, one can use predictions regarding chemical composition and/or physical structure from theoretical models to engineer potential catalysts with desired performance (Figure 16).^{282–284} As a result, DFT has been extensively used for the

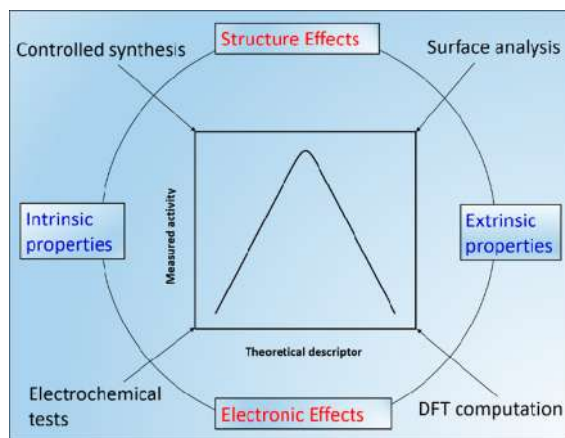


Figure 16. Design principles of electrocatalysts through multi-disciplinary approaches.

identification of active centers present on the catalyst surface, the evaluation and prediction of catalytic activity trends on a range of catalysts, and ultimately the design of better catalysts for specific electrochemical processes.^{1,285}

5.2. Combination of Experiments and Theoretical Computations

As a featured study, Jiao et al. applied DFT computation, precise structural characterization, and electrochemical experiments to determine the activity origins for the electrocatalytic ORR and HER on nonmetallic heteroatom-doped graphene materials.^{73,226} They first synthesized five doped graphene samples (i.e., B-, N-, O-, S-, P-doped) to cover virtually all experimentally available cases. A series of physicochemical characterizations were conducted to show that the properties like morphology, surface area, and defects were comparable between the different heteroatom-doped samples (Figure 17a). Subsequently, a series of surface characterizations like NEXAFS were conducted in order to identify the doping configurations in the different samples (Figure 17b). Accordingly, they carefully constructed a series of representative molecular models such that the computational outcomes could be compared with the experimental outcomes (Figure 17c). Based on these models, free energy diagrams for the ORR and HER were computed while the apparent electrocatalytic activities were experimentally measured on the synthesized samples (Figure 17d–g). By correlating the suitable theoretical and experimental descriptors (e.g., ΔG and i_0 , respectively), a volcano-shaped plot was constructed. These volcano plots demonstrate the inherent activity trend for these materials, and more importantly, predict the “best” performance an ideal electrocatalyst can achieve (Figure 17h,i). Fundamen-

tally, the volcano plot is related to the Sabatier principle,²⁸⁶ which states the optimal catalytic activity can be achieved on a catalyst surface with appropriate binding energies for reactive intermediates. In the event that the intermediates bind too weakly, surface activation and reaction become difficult. However, if they bind too strongly, they will occupy all available surface sites and “poison” the reactive surface. As can be seen from Figure 17h,i, all samples are located on the right branch of the volcano plot, indicating that the adsorption of key reaction intermediates is relatively weak (for both the ORR and HER). Therefore, it is apparent that if a catalyst can achieve a ΔG value closer to the volcano center (i.e., smaller value/stronger adsorption in this case of doped graphene), it will possess a greater i_0 value from both theoretical and experimental perspectives. By applying the molecular orbital concept, they then proposed a catalyst design principle to optimize graphene-based materials (closer to the volcano peak), which will be discussed in sections 6.2.3 and 8.2.1.

6. 2D NANOMATERIALS FOR OXYGEN REDUCTION REACTION APPLICATIONS

Oxygen electrocatalysis is one of the most studied topics in the fields of electrochemistry and catalysis because of its importance for electrochemical energy conversion applications. As the cathode reaction of PEMFCs, the ORR exhibits more sluggish kinetics compared to the anodic HOR. As a result, the activity of the ORR is recognized as kinetically limiting for overall device performance. Therefore, the selection of an effective and efficient ORR electrocatalyst is one of the key targets in fuel cell technology development. Fundamentally, the ORR process in aqueous solutions is highly irreversible and consists of multiple reaction steps involving oxygen-containing species such as O^* , OH^* , and OOH^* .^{287,288} The thermodynamic adsorption energetics of these intermediates and the kinetic energy barriers between two states govern the apparent ORR rate.²⁸⁹ From both mechanistic and practical perspectives, the most well studied ORR electrocatalysts are precious Pt metal and its alloys. Accordingly, there are many excellent reviews regarding the rational design and development of these kinds of electrocatalysts.^{38,81,290–292} To date, a wide range of 2D nanomaterials have shown promising ORR activity including graphene and its derivatives,⁸ ultrathin MOFs and their derivatives,²⁹³ TMOs and TMHs,²⁹⁴ etc. Here, we mainly focus on non-metallic graphene-based ORR electrocatalysts due to their uniform physical and chemical structures.

6.1. Fundamental Principles of the ORR

6.1.1. Reaction Mechanism. The ORR can proceed through a two-step $2e^-$ pathway with formation of H_2O_2 (in acidic medium) or HO_2^- (in alkaline medium) as the intermediate species, or by a more efficient $4e^-$ process directly to H_2O (in acidic medium) or OH^- (in alkaline medium).⁸ The selectivity toward the $2e^-$ or $4e^-$ pathway on an electrode catalyst primarily depends on the adsorption energetics of these intermediates and the reaction barriers on its surface. In fuel cell processes, the direct $4e^-$ pathway is preferred as it delivers a high current efficiency, while the $2e^-$ reduction pathway is used in industry for H_2O_2 production. At the molecular level, there are two possible mechanisms (i.e., dissociative and associative pathways) containing a series of elementary reactions proposed for the $4e^-$ pathway. Table 1 summarizes those in alkaline solution.^{295,296} The biggest difference between these two mechanisms is the intermediates involved (i.e., dissociative: O^* and OH^* ; associative: O^* , OOH^* , and OH^*), which alters the

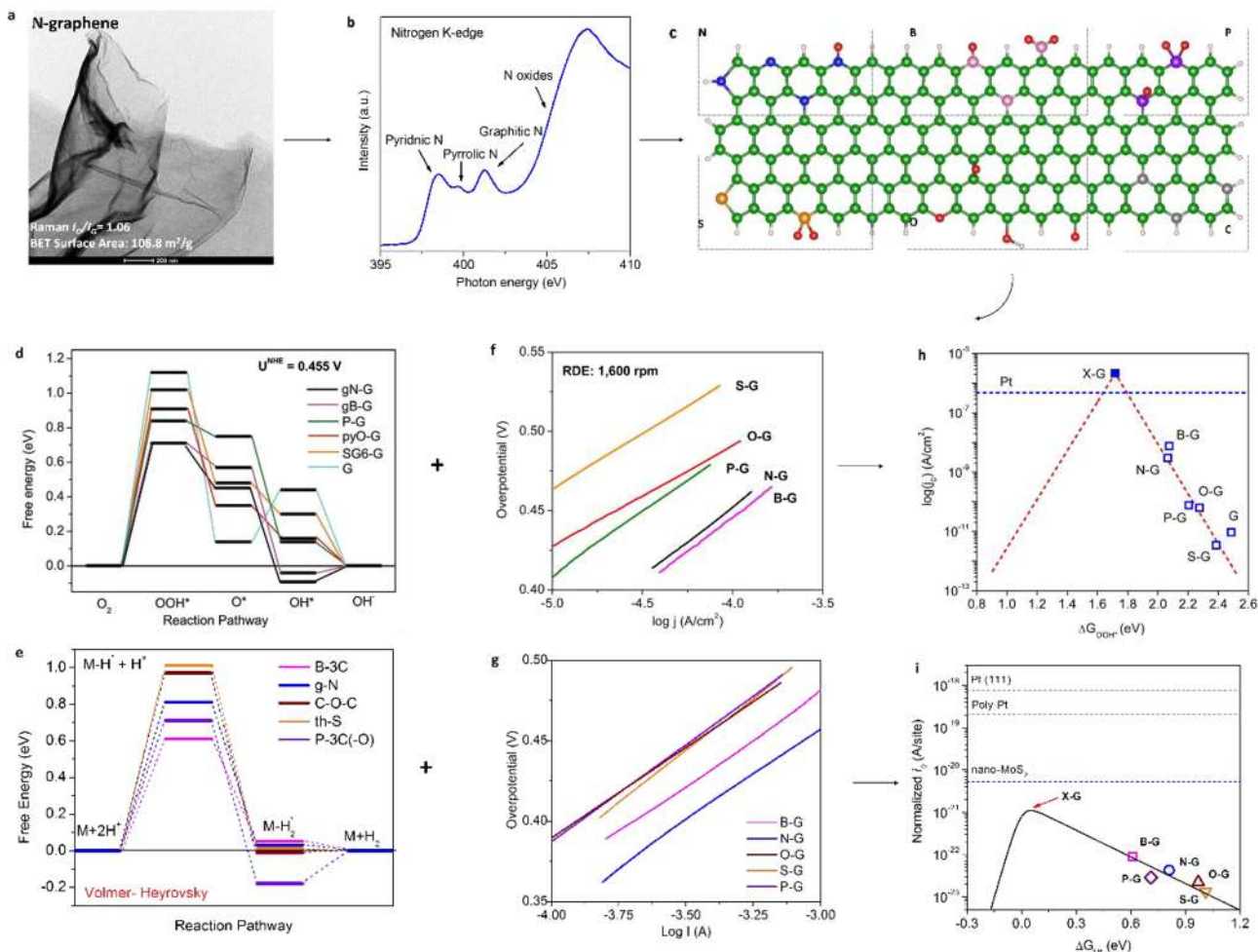


Figure 17. (a) TEM image of N-graphene as an example; the inset values represent the I_D/I_G ratios and the specific surface areas obtained from Raman spectra and nitrogen adsorption isotherms, respectively. The scale bar is 200 nm. (b) Nitrogen K-edge NEXAFS spectrum for N-graphene as an example. (c) Schematic summary of the heteroatom doping configurations. (d) ORR and (e) HER free energy diagrams of different models at the equilibrium potential. (f) ORR and (g) HER Tafel plots of different synthesized samples measured under corresponding conditions. (h) ORR and (i) HER volcano plots containing theoretically computed free energy ΔG for key intermediates (x -axis) and experimentally measured i_0 (y -axis) as descriptors. Panels (a), (d), (f), (h) are reproduced with permission from ref 226. Copyright 2014 American Chemical Society. Panels (b), (c), (e), (g), (i) are reproduced with permission from ref 73. Copyright 2016 Nature Publishing Group.

Table 1. Mechanisms of the ORR in Alkaline Conditions

mechanism	reactions
dissociative ($4e^-$)	$O_2 + 2^* \rightarrow 2O^*$ $2O^* + 2e^- + 2H_2O \rightarrow 2OH^* + 2OH^-$ $2OH^* + 2e^- \rightarrow 2OH^- + 2^*$
associative ($4e^-$)	$O_2 + ^* \rightarrow O_2^*$ $O_2^* + H_2O + e^- \rightarrow OOH^* + OH^-$ $OOH^* + e^- \rightarrow O^* + OH^-$ $O^* + H_2O + e^- \rightarrow OH^* + OH^-$ $OH^* + e^- \rightarrow OH^- + ^*$
associative ($2e^-$)	$O_2 + ^* \rightarrow O_2^*$ $O_2^* + H_2O + e^- \rightarrow OOH^* + OH^-$ $OOH^* + e^- \rightarrow OOH^- + ^*$

construction of the free energy pathway. It is found that the reaction progression through an associative or dissociative pathway mainly depends on the initial O_2 dissociation energy barrier.²⁹⁵ For example, DFT computational studies show that the dissociation barrier is very high on carbon surfaces, which is

unfavorable for a $4e^-$ dissociative pathway.²⁹⁷ Therefore, the experimentally measured electron transfer number on almost all carbon materials is always less than four and usually exactly two.^{298,299} In contrast, the ORR on metal surfaces (e.g., Pt) normally takes a dissociative pathway due to the strong initial O_2 adsorption. This theoretical result is also consistent with experimental evidence as Pt-based materials always exhibit selectivity for a $4e^-$ pathway. Another criterion is the adsorption energy of the OOH^* intermediate: a relatively strong OOH^* adsorption energy facilitates a $4e^-$ pathway, while a relatively weak OOH^* adsorption facilitates a $2e^-$ pathway.²²⁶

6.1.2. Reaction Kinetics. The kinetic current-overpotential relationship of the ORR that occurs on solid surfaces can be described by the classic Butler–Volmer equation. In real ORR conditions, the overpotential (η) is relatively large. Therefore, the backward reaction is negligible and the Butler–Volmer equation becomes

$$j_k = j_0 e^{n\alpha F\eta/RT} \quad (1)$$

where j_k is the kinetic ORR current density, j_0 is the exchange current density which represents the current density of the

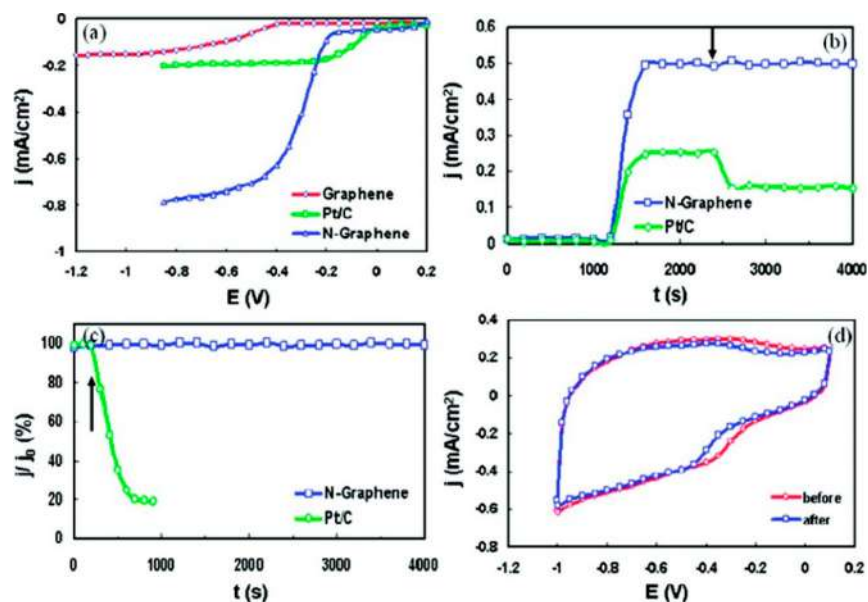


Figure 18. (a) RRDE voltammograms for the ORR for Graphene, N-graphene, and Pt/C electrocatalysts. (b,c) Chronoamperometric responses for N-graphene and Pt/C electrocatalysts (b) after adding 2% (w/w) methanol into the electrolytes (shown by the arrow) and (c) after adding 10% (v/v) CO into the electrolytes (shown by the arrow). (d) Cyclic voltammograms of N-graphene before and after a continuous potentiodynamic sweeping for 200 000 cycles. Reproduced with permission from ref 62. Copyright 2010 American Chemical Society.

forward reaction equal to that of the backward reaction at equilibrium, n is the number of electrons transferred in the rate-determining step (rds), α is the electron transfer coefficient (always 0.5–1 for the ORR), F is the Faraday constant, R is the gas constant, and T is the temperature in Kelvin. Based on eq 1, the plot of η vs $\log(j_k)$ gives a linear relationship with a slope of $2.303RT/\alpha nF$, also called the Tafel slope. Obviously, to obtain a high cathodic j_k at a certain value of η , j_0 should be large and/or the value of the Tafel slope should be small. Here, the value of j_0 is related to the adsorption energetics of a series of reaction intermediates according to the simple microkinetic model in electrochemistry developed by Nørskov et al.³⁰⁰

$$j_0 = nFk^0C_{\text{total}}[(1 - \theta)^{1-\alpha}\theta^\alpha] \quad (2)$$

where k^0 is the standard rate constant, C_{total} is the total number of active sites, and coverage of surface adsorbates θ is a quantity related to the highest free energy change of the whole reaction as

$$\theta = \frac{C_R}{C_{\text{total}}} = \frac{K}{1 + K} \quad (3)$$

where the equilibrium constant K is related with the free energy change (ΔG) for the rds as

$$K = \exp\left(-\frac{\Delta G}{k_B T}\right) \quad (4)$$

where k_B is the Boltzmann constant. For the ORR, usually two Tafel slopes are obtained, 60 and 120 mV/dec, respectively, depending on the electrode material used and the potential applied. The first value corresponds to a pseudo two-electron reaction being the rds of the whole reaction, whereas the latter one suggests the first-electron reduction of oxygen being the rds.^{288,301}

6.1.3. Measurement Criteria. The most frequently used techniques for evaluating the ORR activity of an electrocatalyst are steady-state polarizations on a rotating disk electrode (RDE) or a rotating ring-disk electrode (RRDE). Some apparent ORR

performance indicators, including onset potential, half-wave potential ($E_{1/2}$), and diffusion-limiting current density (j_L), can be obtained from a typical RDE polarization curve.²⁸⁸ These parameters serve as the standard criteria for different electrocatalysts under the same conditions. As the ORR potential window is far from the equilibrium potential, and the mechanism consists of multiple steps, j_0 should generally not be used as an indicator of catalytic activity for the ORR.²²⁶ The other important role of a RDE in the ORR is the calculation of the total electron transfer number (n_{KL}) by the Koutecky–Levich (KL) equation:

$$\frac{1}{j} = \frac{1}{j_K} + \frac{1}{j_L} = \frac{1}{B}\omega^{-1/2} + \frac{1}{j_K} \quad (5)$$

where j_K is assumed to be a constant at a certain potential. The j_L is proportional to the square root of the RDE angular velocity (ω). The reciprocal of proportionality coefficient (B) is

$$B = 0.62D^{2/3}\nu^{-1/6}\eta_{\text{KL}}FC^* \quad (6)$$

where D is the diffusion coefficient of the reactant, ν is the kinematic viscosity of the electrolyte, and C^* is the concentration of the reactant in the bulk electrolyte. Thus, n_{KL} can be deduced from the slope of the linear plot of $1/j$ vs $\omega^{-1/2}$. Another method (using RRDE) can also provide n_{RRDE} by directly measuring the amount of intermediates present (e.g., H_2O_2 or OOH^-) through

$$n_{\text{KL}} = 4 \times \frac{I_d}{I_d + \frac{I_r}{N_C}} \quad (7)$$

where the disk current (I_d) and ring current (I_r) can be directly measured, and N_C is the collection efficiency of the RRDE, defined as the fraction of product from the disk to the ring. In principle, n_{KL} and n_{RRDE} should be identical for one catalyst under the same overpotential. However, the calculated n_{KL} values were always slightly larger than the n_{RRDE} values under the same conditions for the most widely developed ORR electrocatalysts with various 3D nanostructures. More importantly, the KL plots

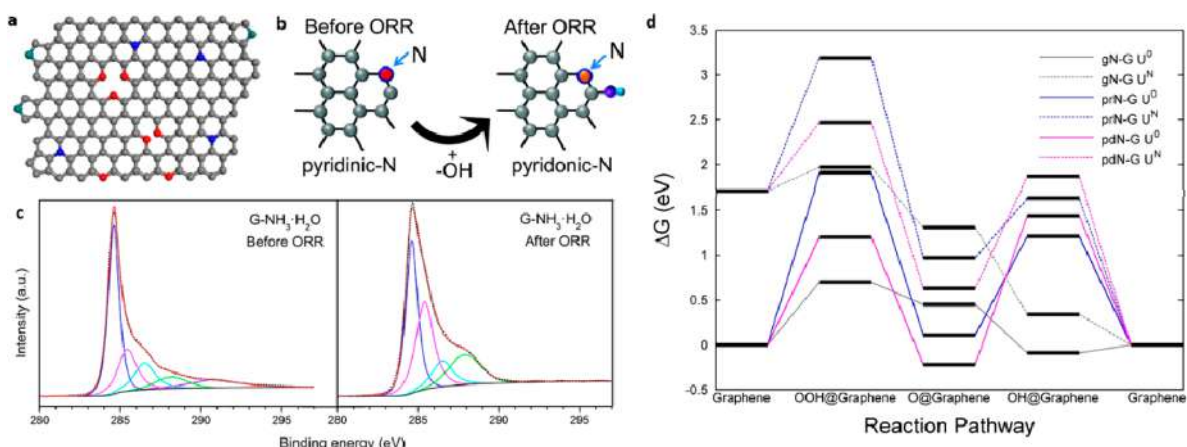


Figure 19. (a) Illustration of the structure of N-graphene with pyridinic-N (red balls), pyrrolic-N (cyan balls), and graphitic-N (blue balls) moieties. (b) Illustration of the formation of pyridonic-N by the attachment of OH to the carbon atom next to pyridinic-N. Reproduced with permission from ref 316. Copyright 2016 American Association for the Advancement of Science. (c) Carbon 1s XPS spectra of N-graphene before and after the ORR. Reproduced with permission from ref 317. Copyright 2014 American Chemical Society. (d) Calculated free energy diagram for N-graphene with different nitrogen moieties at the equilibrium potential (U^0) and at the experimentally observed onset potential (U^N). Reproduced with permission from ref 226. Copyright 2014 American Chemical Society.

were often not perfectly linear and the calculated n_{KL} values sometimes exceeded the theoretical limit (four), prompting re-evaluation of these studies by the material research community.³⁰² A study by Zhou et al. systematically investigated the inconsistencies between n_{KL} and n_{RRDE} and tried to develop a correct and accurate method for the determination of the electron transfer number during the ORR.³⁰² They found that the widely applied RRDE method with a Pt ring is not suitable for H_2O_2 collection in alkaline electrolytes because the oxidation of H_2O_2 on Pt is not a mass-transfer-limited process. As an alternative, a properly biased Au ring was found to be suitable for H_2O_2 collection and leads to relatively accurate n_{RRDE} values. Additionally, the n_{KL} value depends significantly on ω for all tested electrocatalysts, including 2D and 3D metallic/non-metallic electrodes across all potential regions. This means that the KL method, which requires n_{KL} to be constant at certain potentials, is not applicable for the ORR. They concluded that only the RRDE method with a properly biased Au ring and calibrated collection efficiency is correct for n_{RRDE} calculation from both theoretical and experimental viewpoints.

6.2. Doped Graphene

As mentioned above, pure graphene is inactive for electrocatalytic applications, due to the absence of free electrons for reaction. Doping graphene with other non-metallic heteroatoms is the most widely applied and most effective approaches for inducing intramolecular charge transfer in graphene frameworks and for enhancing electrocatalytic activity. Generally, the origin of this activity may be the unique electronic structure for reactant/intermediate adsorption and variable nanostructure which increases the number of exposed active sites.^{51,303–307}

6.2.1. Nitrogen-Doped Graphene. N-graphene is the most studied graphene-based electrocatalyst due to its simple synthesis process and relatively good electrocatalytic performance. Nitrogen is of similar atomic size to carbon, but is more electronegative. Therefore, doping with nitrogen can change the electron configuration of graphene while minimizing the lattice mismatch after doping. Being the earliest studied and the most important metal-free electrocatalyst for the ORR, N-graphene has demonstrated some unique characteristics compared to metal-based electrocatalysts.^{8,304} For example, the

first reported N-graphene ORR electrocatalyst was prepared by CVD and showed excellent $4e^-$ pathway ORR activity, even superior to Pt/C (Figure 18a).⁶² Compared with Pt metal, one of the most important features of non-metallic N-graphene is its tolerance to the fuel (e.g., methanol and CO) present in the anode chamber of fuel cells, which largely prevents the crossover effect (Figure 18b,c). Due to its stable chemical structure, N-graphene also exhibits good stability in alkaline conditions (Figure 18d).

At the atomic level, nitrogen doping can significantly enhance the ORR activity of graphene by changing the electronic character of the nearby carbon atoms and by creating defect structures to enable stronger oxygen adsorption.^{303,308} From both experimental and theoretical perspectives, the ORR activity of N-graphene is strongly dependent on the nitrogen doping sites and types. These are parameters which can be carefully controlled by doping procedures and precursor choice. Generally, there are two types of N-doping methods used to obtain N-graphene materials. The first one is referred to as structural or *in situ* doping, where the appropriate choice of nitrogen-containing precursors is critical to the successful incorporation of nitrogen atoms into the selected sites of the carbon matrix. The other general N-doping method employed is the post-synthesis treatment of as-prepared graphene, more specifically, graphene oxide (GO) or reduced GO (rGO) with a nitrogen-containing gas (N_2 , NH_3 , CH_3CN , etc.). However, some morphological defects and structural degradation can appear in the resultant materials due to the need for high-temperature treatment (900–1200 °C). In general, there are three nitrogen groups in N-graphene: pyridinic-N, pyrrolic-N, and graphitic-N. Pyridinic-N refers to nitrogen atoms at the edge of graphene planes, each of which is bonded to two carbon atoms and donates one p-electron to the aromatic π system; pyrrolic-N refers to nitrogen atoms that are bonded to two carbon atoms and contribute to the π system with two p-electrons; and graphitic-N refers to nitrogen atoms that are incorporated into the graphene framework and bonded to three carbon atoms.^{306,309} Generally, the *in situ* doping method at low-temperatures mainly forms pyridinic- and/or pyrrolic-N species, while high-temperature post-treatment doping methods nor-

mally form graphitic-N species in the carbon framework. The roles of the different nitrogen species toward ORR activity will be discussed at the end of this section.

CVD is a method widely used to synthesize high-quality N-graphene by mixing a carbon containing gas with either a nitrogen-containing gas (e.g., NH_3),^{62,310,311} or an organic liquid precursor (e.g., acetonitrile, pyridine).^{312,313} The types of nitrogen dopants formed can be varied by the type of N-precursor used. For example, graphitic-N in N-graphene can be achieved by using Cu as the catalyst and CH_4/NH_3 (1:1) as the precursors,³¹⁰ while pyridinic-N can be achieved by using $\text{C}_2\text{H}_4/\text{NH}_3$ as the precursors.³¹¹ The nitrogen content can be controlled at around 4–9 at.% by changing the flow rate and the ratio of carbon to nitrogen sources.^{310,311} For electrocatalytic applications, milligram-scale and powder-based samples are preferred. Therefore, post treatment of GO or graphite is the most widely applied method for producing N-graphene electrocatalysts. For example, annealing GO with solid or gaseous nitrogen containing precursors at high temperatures (>700 °C) can remove the oxygen-containing groups during pyrolysis, allowing nitrogen dopants to interact with the exposed active carbons in the framework. Due to the abundance of oxygen in GO, the nitrogen content in the resultant N-graphene are always high, and they form a wide variety of species. For example, a 10.1 at.% nitrogen dopant level was achieved by annealing a mixture of GO and melamine at 700 °C.³¹⁴ The choice of precursor can also be varied, e.g., NH_3 ,^{315–317} polyaniline/polypyrrole,^{318–320} and melamine.^{314,317} Normally, an increased pyrolysis temperature will result in a decrease in overall nitrogen dopant level and formation of mainly graphitic-N.

6.2.2. ORR Mechanism on Nitrogen-Doped Graphene.

The ORR mechanism on N-graphene has been extensively investigated from both experimental and theoretical perspectives. As with N-CNT, the ORR performance observed for N-graphene can be attributed to a charge-transfer effect associated with the nitrogen dopants.^{8,84} More specifically, DFT studies indicate that the doping-induced charge and/or spin redistributions of the active sites play an important role in the enhancement of ORR activity.²²⁵ However, there is still debate regarding identification of the active sites in N-graphene, mainly due to (1) the complexity of nitrogen functionality in N-graphene (Figure 19a); (2) the disconnect between ideal theoretical models and real electrocatalysts; (3) the difficulty of direct experimental observation of intermediate adsorption on active sites. For example, Sidik et al. proposed that graphitic-N far from the graphene sheet edges are active for the ORR,³²¹ while Huang et al. showed that only pyridinic-N can enhance O_2 adsorption for the ORR.³²² In a significant study by Lai et al., a range of N-graphene electrocatalysts were synthesized with different nitrogen dopant levels and species and characterized by electrochemical experiments.³¹⁸ It was found that the graphitic-N content determined the j_L of the ORR, while the pyridinic-N content improved the onset potential. Guo et al. experimentally confirmed the ORR active sites in N-carbon using highly oriented pyrolytic graphite catalysts with well-defined π conjugation and well-controlled nitrogen doping species.³¹⁶ They found that O_2 molecules are adsorbed as the initial step in the ORR pathway on pyridinic-N with Lewis basicity (Figure 19b).³¹⁶ This result agrees well with Xing et al.'s synchrotron-based spectroscopic studies.³¹⁷ Through a comparison of the C 1s and O 1s XPS spectra before and after ORR testing, they found that the number of C(aliphatic)–OH/C(aliphatic)–O–C–(aliphatic) species decreased while the number of C–

(aromatic)–OH species increased after the ORR test (Figure 19c). In the N 1s spectrum, there was a change in the pyridinic-N species after the ORR test, with the formation of pyridonic-N as shown in Figure 19b.

The ORR free energy pathway according to two different mechanisms on N-graphene with graphitic-N moieties has also been constructed by DFT.²⁹⁵ It was found that the dissociation barrier of O_2 is too high for the reaction to achieve a reasonable rate. Therefore, the associative mechanism is more energetically favored. Furthermore, it was proposed that the rds for $4e^-$ ORR on N-graphene in alkaline medium is the removal of adsorbed O from the surface. By studying the ORR pathway on three types of N-graphene, Ni et al. showed that the overall energy barrier to the ORR on pristine graphene is as high as 2.71 eV. Graphitic-N and Stone–Wales defect nitrogen, with dissociation barriers lower than 0.2 eV, decrease the energy barrier more effectively than pyridinic-N.³²³ Jiao et al. also constructed an ORR free energy diagram by calculating the thermodynamic energetics of a series of intermediates adsorbed on N-graphene with pyridinic-N, pyrrolic-N, and graphitic-N moieties (Figure 19d).²²⁶ It was found that the graphitic-N doped model showed the best ORR performance, having the smallest free energy difference among the three models, while pyrrolic-N showed the worst. Therefore, it is predicted that N-graphene with more graphitic-N dopants will possess a larger ORR j_0 (smaller value of ΔG_{OOH^*}) and larger j_k (smaller value of ΔG_{OH^*}).

6.2.3. Other Heteroatom-Doped Graphene. Besides nitrogen, other p-block elements (e.g., B, S, P) have been doped into the graphene matrix by physical or chemical approaches. Similar to nitrogen, the differing size and electronegativity of these heteroatoms to carbon can also induce electron modulation which changes the electronic properties of pristine graphene. These kinds of electrocatalysts can usually be prepared by annealing GO with the appropriate heteroatom containing precursor at high temperatures (>900 °C). Normally, the precursors for B, S, and P dopants are boron oxide or boric acid,^{324–326} solid phenyl disulfide, benzyl disulfide, or CS_2 gas flow,^{327–329} and triphenylphosphine,⁷⁰ respectively. The doping level of these materials is normally lower than that of N-graphene. It is known that doping graphene with heteroatoms of either higher or lower electronegativities than carbon ($\chi = 2.55$), such as N ($\chi = 3.04$), B ($\chi = 2.04$), and P ($\chi = 2.19$), can induce electrocatalytic ORR activity through intramolecular charge transfer in the graphene matrix.⁸ However, this theory cannot explain the enhanced ORR activity on S-graphene as the difference in electronegativity between carbon and sulfur ($\chi = 2.58$) is almost negligible. Based on DFT calculations, Zhang et al. analyzed spin density difference and found that the covalently bonded sulfur or sulfur oxide at the zigzag and armchair edges of graphene induces both charge and spin redistribution in S-graphene.^{330,331} Therefore, carbon atoms with either high spin densities and/or positive charge could act as the active sites for the ORR. This has also been supported by experimental results.

Although the macroscopic effects of heteroatom doping are well documented, a microscopic view of the activity trend has not been built. Jiao et al. presented a significant study which linked the experimental ORR performance descriptor (e.g., j_0 , onset potential, and j_k) on a range of heteroatom-doped graphene materials with the thermodynamic adsorption energies of a series of key reaction intermediates.²²⁶ Similar to the d-band center theory for metallic catalysts, they introduced a descriptor, E_{diff} , to quantitatively represent the valence orbital level. This descriptor is defined as the difference between the lowest valence orbital

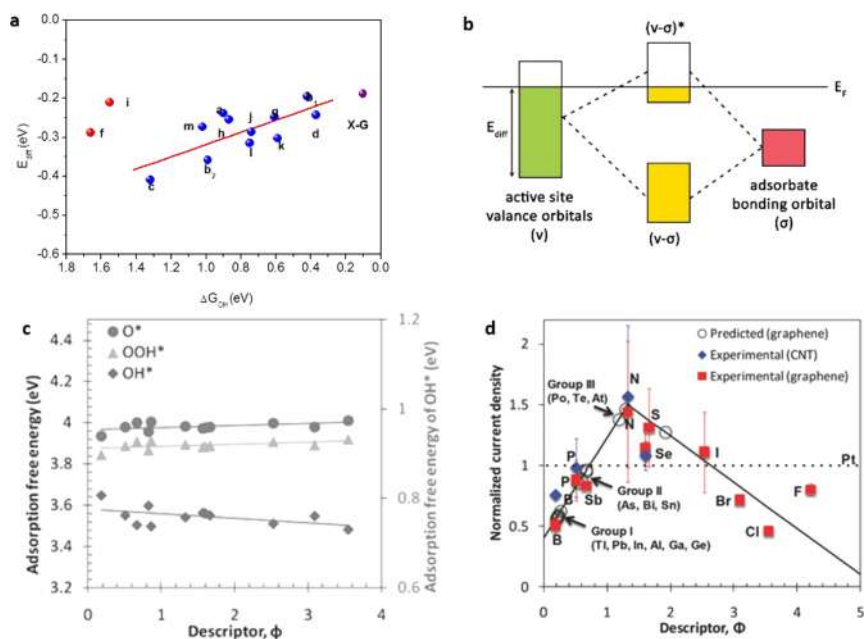


Figure 20. (a) Relationship between ΔG_{OH^*} and E_{diff} on various doped graphene models. (b) Scheme of orbital hybridization of the valence band from active sites with the adsorbates bonding orbital for doped graphene. Reproduced with permission from ref 226. Copyright 2014 American Chemical Society. (c) Adsorption free energy of OOH^* , OH^* , and O^* as a function of the descriptor Φ . (d) Volcano plots of measured ORR activity with the theoretical descriptor Φ . Reproduced with permission from ref 332. Copyright 2010 John Wiley & Sons, Inc.

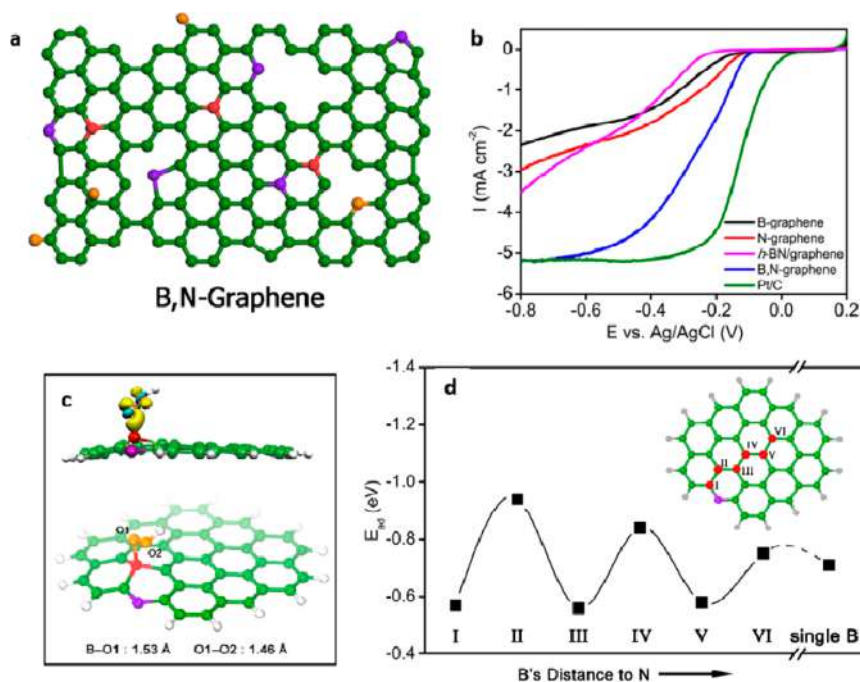


Figure 21. (a) Schematic structure of h-BN free B,N-graphene. (b) ORR polarization curves of various electrocatalysts in alkaline conditions. (c) Optimized adsorption configuration of OOH intermediate on B, N-graphene. (d) OOH adsorption energies (E_{ad}) on various B,N-graphene models with B active sites as a function of the distance to a pyridinic N-atom (sites I–VI as marked in inset). Reproduced with permission from ref 49. Copyright 2013 John Wiley & Sons, Inc.

energy of the active center and the highest valence orbital energy of the entire graphene cluster. As shown in Figure 20a, the adsorption free energies of OH^* showed a linear relationship against E_{diff} for a wide variety of graphene active sites. The underlying principle is that the valence band (v) of the active sites hybridizes with the bonding (σ) orbital of the adsorbed species to form bonding ($v-\sigma$) and antibonding ($v-\sigma$)^{*} states. For graphene

models, the ($v-\sigma$) state is full while the filling of the ($v-\sigma$)^{*} state depends on the valence orbital levels of the active atom on the graphene surface (Figure 20b). An increased filling of the antibonding ($v-\sigma$)^{*} state, induced by a lower valence band, could lead to destabilization of the graphene–adsorbate interaction and hence weaken the binding between them, and *vice versa*.²²⁶ As a result, a better graphene-based ORR catalyst should possess

active atoms with higher valence orbital energies to induce stronger adsorption of OOH^* and OH^* intermediates.²²⁶ Zhao et al. also developed a design principle for p-block element-doped graphene by correlating their activity trend with a dimensionless theoretical descriptor, Φ , which considered both the electronegativity and electron affinity of the heteroatom.³³² They found that the adsorption free energies of O^* , OH^* , and OOH^* are linearly proportional to Φ (Figure 20c), which also suggests that Φ is linearly correlated to E_{diff} . Electronegativity dominates when the descriptor is small ($\Phi < 0.5$), whereas electron affinity dominates for $\Phi > 2.5$. Both cases will result in a low ORR activity (Figure 20d). Through a comparison with experimental results, they predicted that the best dopant should possess both affinity and electronegativity slightly higher than carbon (ratio ≈ 1.2).

6.2.4. Dual-Doped Graphene. Double- and triple-doped graphene (e.g., B/N,^{49,333–335} S/N,^{336–340} P/N,^{70,341,342} or N/B/P,³⁴³ N/S/P³⁴⁴) have also been studied and show significantly enhanced ORR activity compared to their single-doped counterparts. DFT calculations reveal that the origin of this enhancement is the synergistic effect between the two or more different dopant elements. Although direct experimental observation of this synergy within the graphene matrix is difficult, theoretical analysis indicates that dual dopants can tailor the electron-donor properties of nearby carbon atoms to enhance intermediate adsorption.⁴⁹

The most widely studied dual dopant pair for carbon materials is B and N. As early as 2011, Wang et al. used a CVD method to synthesize vertically aligned CNTs containing both B- and N-atoms (BCN nanotubes) from melamine diborate as both the nitrogen and boron sources.³⁴⁵ Later, they extended this research to prepare BCN graphene by thermal annealing GO in the presence of boric acid and ammonia.³³⁴ Using DFT, they then investigated the band gap energy dependency on the doping level, spin density, and charge density in BCN-graphene systems with different B/N concentrations and moiety type.³³⁴ Xue et al. used CVD to prepare 3D N- and B-doped graphene foams on the surface of sacrificial nickel foam templates.³³⁵ Differing from single-doped graphene, the precursor(s) choice for dual-doped graphene needs to consider any possible side reactions between the precursors themselves. For example, even though the above two studies show the successful incorporation of B and N into the graphene framework, there was also a significant portion of non-conductive and inactive h-BN observed in the composites.

Zheng et al. developed a unique two-step procedure which prevents the formation of h-BN in the synthesis of B,N-graphene.⁴⁹ In the first step, GO is thermally treated in ammonia gas at an intermediate temperature (500 °C), to achieve partial reduction and nitrogen incorporation into the rGO. The product is then treated with boric acid at high temperature (900 °C) to incorporate boron dopants. By separating the doping steps, B and N was incorporated into the desired positions in the graphene matrix (Figure 21a). As a result, B,N-graphene (free of h-BN) showed significantly higher ORR activity compared to h-BN-graphene synthesized by the single-step method and single B- or N-doped graphene samples (Figure 21b). With the help of DFT computation, they found that in a B–C–N heteroring, N acts an electron-withdrawing group which indirectly activates B and thus makes B the active site (Figure 21c). More interestingly, the strength of the synergistic effect decreases gradually as the distance between B and pyridinic-N dopants increases (Figure 21d), indicating that the B dopant is a critical factor for this synergistic effect.

S,N-graphene can also be synthesized by thermally treating a single precursor (e.g., thiourea) or two precursors (e.g., melamine and benzyl disulfide) with GO at high temperature.^{336,338} In the S,N-graphene system, the resultant synergy can be explained by the following three factors.³⁰⁵ First, due to the electronic modifications provided by the dopant species, a larger number of carbon atoms are activated, creating an increased number of active sites. Second, a higher intrinsic ORR activity is achieved in S, N-graphene due to the increase in charge and spin densities of the atoms. For example, DFT calculations showed that the S,N co-modified graphene lattice had higher spin density on the C-atoms adjacent to the N-atoms, while the C-atoms bonded to S-atoms had a relatively smaller spin density.³³⁶ Third, the incorporation of S-dopants in the five-fold-coordinated thiophenic arrangement disrupts the lattice of graphene and increases the number of exposed edge sites that are electrocatalytically active. Consequently, S, N-graphene has shown the best electrocatalytic activity for both the ORR and HER among all dual-doped graphene materials.³⁴⁶

P has a similar electronic structure to N and is considered to be a good secondary atom to modify the properties of N-graphene. Consideration for P-doping is based on the following two points. First, similar to B, P also possesses a smaller electronegativity than C. Second, substituting a sp^2 C-atom with a larger size P-atom can disturb the geometry of the carbon lattice, and consequently modify the electronic structure of the graphene matrix. A modified CNT system was first used to investigate the ORR function of a P–N pair in a carbon framework.³⁴³ It was shown that P promoted the reduction of HO^{2-} within the overall potential range. Additionally, the P–N co-modification could generate more edges and wrinkled surfaces, which disturbed the uniform distribution of charge and spin densities in the pristine CNTs. Using a simple cooperative assembly, Tang et al. synthesized melamine–phytic acid supermolecular aggregates which were converted into P,N co-doped carbon foams with 3D structures.³⁴⁷ By substituting the nitrogen source from melamine to polyaniline, they prepared P,N-graphene nanosheets with mesopores, which demonstrated good electrocatalytic properties for both the ORR and OER in rechargeable Zn–air batteries.³⁴² DFT computations indicated that the P,N co-doping and graphene edge effects were essential for its bifunctional electrocatalytic activity.

6.3. Graphene Derivatives

Some dopant-free nanocarbon materials have also been shown to possess considerable ORR activity, and are even better than some heteroatom-doped carbons.^{243,342,347–349} This indicates that the intrinsic structural and edge defects may also modify the overall electronic structure of the graphene matrix and introduce active sites for the ORR. For example, Shen et al. found that the edge carbon atoms in the graphene matrix are highly charged and are more active than those in the basal plane.³⁵⁰ This has led to a variety of carbon structures abundant in edge sites, e.g., 0D graphene quantum dots (GQDs) and 1D graphene nanoribbons (GNRs), being extensively studied as effective ORR electrocatalysts.^{109,351,352}

6.3.1. Graphene Quantum Dots and Graphene Nanoribbons. Considered domains of the graphene matrix, both GQDs and GNRs can be synthesized by either “top-down” or “bottom-up” methods (Figure 22). The most popular top-down strategy for GQD synthesis is to cut GO using hydrothermal or solvothermal treatments. GQDs with diameters in the range of 5–13 nm and thicknesses of 1–2 nm have been produced in this

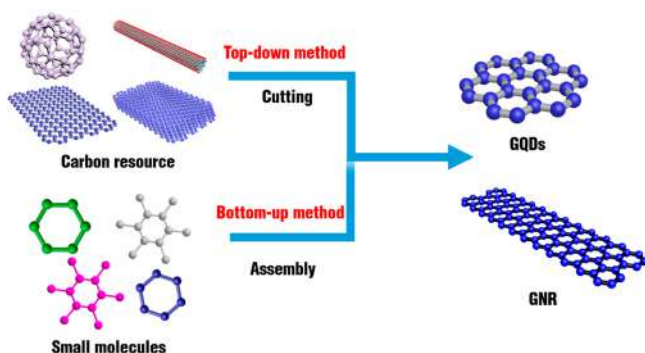


Figure 22. Schematic diagram of the top-down and bottom-up methods for synthesizing GQDs and GNRs. Reproduced with permission from ref 352. Copyright 2017 MDPI.

way.^{353,354} During the hydrothermal deoxidation process, linear defects in GO that are composed of fewer epoxy groups and more carbonyl groups may break up further by removing bridging O-atoms to form GQDs. Alternatively, the GQDs can be prepared through stepwise solution chemistry of alicyclic compounds.³⁵⁵ For example, large colloidal GQDs with uniform and tunable size were obtained by oxidative condensation reactions, in which the process of combining graphene moieties was achieved by the oxidation of polyphenylene dendritic precursors.⁹⁶ As a result, a series of GQDs that contained 132, 168, and 170 carbon atoms were obtained. GNRs can be thought of as narrow strips of graphene with widths much smaller than their length. One of the most popular methods for large-scale GNR production is by unzipping CNTs through selective

etching, chemical attack, nanoparticle cutting, and metal atom intercalation.^{356–358} On the other hand, a “bottom-up” approach based on organic precursors and CVD has been exploited to produce GNRs with precise control at the molecular level.³⁵⁹ GNRs can also be synthesized by a solution-based polymerization of pre-prepared molecular precursors followed by a cyclodehydrogenation method. Using this method, GNRs with atomically smooth armchair edges were produced with dimensions of 1 nm in width by >100 nm in length.³⁶⁰

Heteroatom doping is also an important strategy for enhancing the ORR performance of GQDs and GNRs.³⁵² In a pioneering work by Li et al., N-GQDs with promising ORR activity were prepared using an electrochemical approach.³⁶¹ Other heteroatom-doped GQDs and GQD/graphene hybrids have also been applied as ORR electrocatalysts.^{362–365} For these materials, DFT calculations showed that pyridinic-N dopants at the zigzag edges have the smallest overpotential in the dissociative mechanism while the OOH mechanism is blocked by weak OOH* adsorption.³⁶⁶ Kim et al. also found that edge doping in N-GNRs enhances the oxygen adsorption for the first electron transfer and also the selectivity toward the 4e⁻ reduction pathway.³⁶⁷ Additionally, in the GQD/GNR composite system, the numerous defects and efficient charge transfer at the GQD/GNR surfaces/interface contribute significantly to the overall ORR activity.³⁶⁸

6.3.2. Defective Graphene. Some extrinsic or intrinsic defects (sometimes energetically unfavorable) are introduced in the graphene matrix during the synthesis or post-treatment processes.³⁶⁹ Generally, these defects are considered to be beneficial for reactant adsorption. However, as the defects in

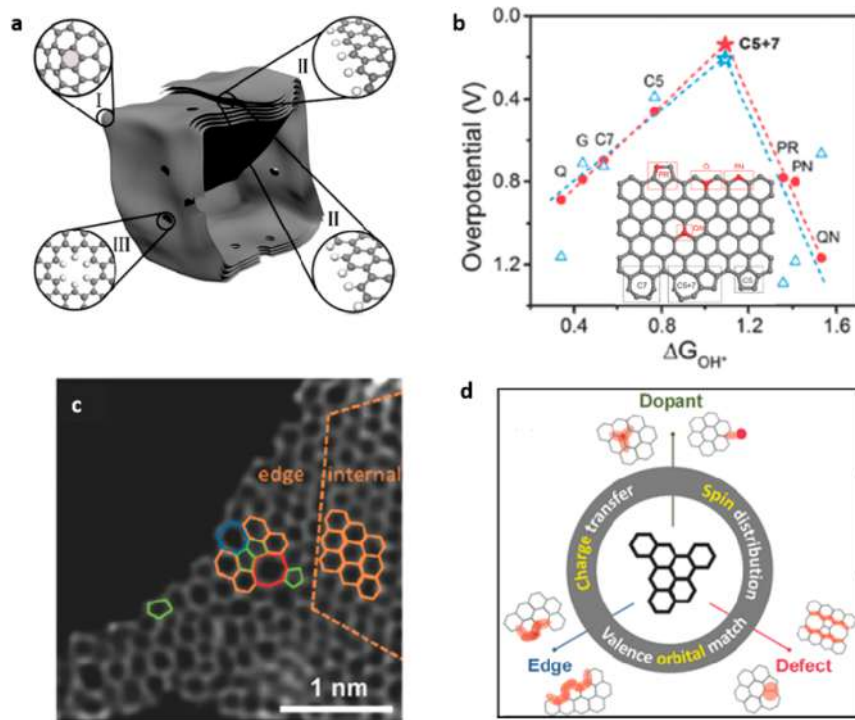


Figure 23. (a) Schematic structural features of the carbon nanocages. I, II, and III represent three typical defective locations such as a corner, broken fringe, and hole, respectively. Reproduced with permission from ref 348. Copyright 2015 American Chemical Society. (b) The proposed volcano plots of overpotential versus adsorption energy of OH* for different doped and defective graphene models shown in the inset. Reproduced with permission from ref 347. Copyright 2016 John Wiley & Sons, Inc. (c) HAADF-STEM image of N-graphene with various types of defects. Reproduced with permission from ref 242. Copyright 2016 John Wiley & Sons, Inc. (d) Schematic illustration of different active sites and underlying mechanism for nanocarbon catalysts. Reproduced with permission from ref 172. Copyright 2017 John Wiley & Sons, Inc.

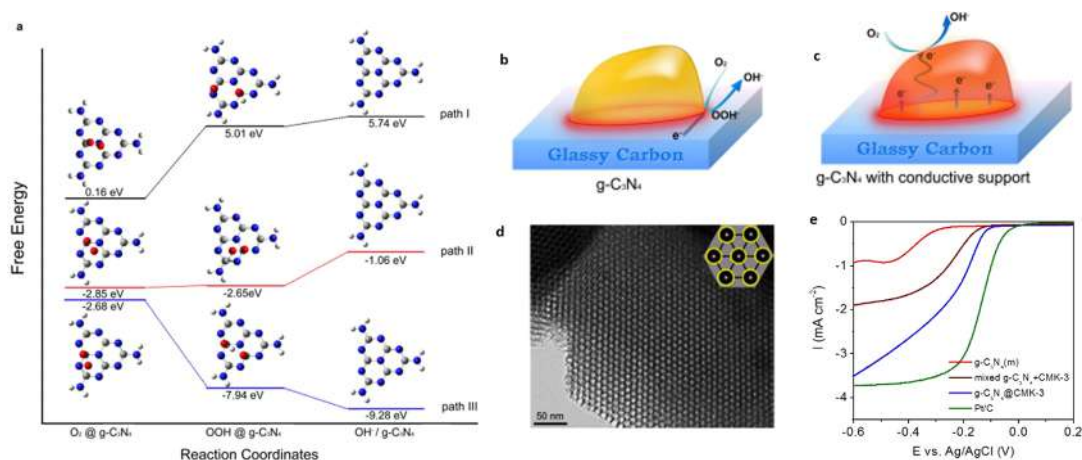


Figure 24. (a) ORR free energy diagram and optimized intermediates adsorption configurations on the g-C₃N₄ surface with 0 (path I), 2e⁻ (path II), and 4e⁻ (path III) participation. (b,c) Schemes of the ORR pathways on pristine g-C₃N₄ with 2e⁻ participation, and g-C₃N₄/conductive support composite with 4e⁻ participation, respectively. Red areas represent the active sites for the ORR. (d) Typical HRTEM image of ordered mesoporous C₃N₄@CMK-3 nanorods. Inset represents a schematic illustration of the structure (yellow, g-C₃N₄; black, carbon). (e) LSV of various electrocatalysts in 0.1 M KOH solution. Reproduced with permission from ref 126. Copyright 2011 American Chemical Society.

graphene are always concomitant with heteroatom doping and edge regions, the identification of the real active sites in these materials is always complicated, even in the best-known N-graphene systems.¹⁷² For ORR applications, the most extensively studied cases are in-plane topological defects (i.e., non-hexagonal rings such as pentagons and heptagons). By DFT computation, Zhang et al. found that the line-defect pentagon–pentagon–octagon chain can induce significant local charge/spin polarization at the graphene edge, at which the energy barriers to the 4e⁻ reduction pathway were comparable to benchmark Pt (111).³⁴² Experimentally, Jiang et al. found that even dopant-free carbon nanocages with abundant holes, edges, and positive topological disclinations showed enhanced ORR activity compared to doped counterparts (Figure 23a).³⁴⁸ A theoretical study by Tang et al. also showed that the N-dopant moieties have a higher ORR overpotential than pristine graphene with specific defects.³⁴⁷ As shown in Figure 23b, topological defects at the edge were shown to have a greater effect on overpotential than doping and edge effects.

Although these theoretical studies have revealed clearly the effectiveness of intrinsic defects in graphene materials for ORR electrocatalysis, it is still a big challenge to characterize and distinguish them experimentally. This may be due to the difficulty in preparing graphene with desired defects.

For example, Jia et al. introduced different types of topological defects into the graphene lattice via the removal of intentionally doped heteroatoms.²⁴² The aberration-corrected HRTEM image in Figure 23c directly shows various defects (pentagons, heptagons, and octagons) on the edge of the graphene sheet at the atomic scale. Besides the local electronic environment, the defects also modified the surface properties of the graphene, such as surface area and hydrophobicity. Unsurprisingly, the defective graphene showed an enhanced ORR activity compared to pristine and doped graphene samples. As mentioned above, controlling intrinsic defects is difficult because they always interrelate with heteroatom dopants and the edges of graphene.³⁴⁷ At the level of electron structure, all of them demonstrate to have effectively modified the charge/spin distribution in the carbon matrix and adsorption energies of the intermediates (Figure 23d).¹⁷² This leads to a similar activity origin. However, different configurations of dopants, edges, and

defects are thought to contribute distinctly to the modification of electron structure, and thereby induce distinctly different catalytic activities.¹⁷² Therefore, by considering all three features, it is rational to conclude that specific heteroatom-doping at defective edges is the most effective strategy for achieving optimal ORR activity on carbon electrocatalysts.¹⁷²

6.4. Graphitic Carbon Nitride

In principle, the high level of pyridine-like nitrogen in the heptazine heterorings of g-C₃N₄ can provide rich electron lone pairs and serve as the active sites for the ORR. However, its poor conductivity (band gap = 2.7 eV) hinders its application in electrocatalysis.¹¹ Based on the calculated ORR free energy pathway, the limited electron transfer ability of g-C₃N₄ causes an accumulation of OOH⁻ intermediates on the catalyst surface via an inefficient 2e⁻ reduction process (Figure 24a).¹²⁶ As shown in Figure 24b, the ORR active sites on pure g-C₃N₄ are limited to very narrow zones of the electrode–electrolyte–gas three-phase boundaries due to its poor electron transfer ability, resulting in poor ORR activity.³⁷⁰ Incorporating an electron-conductive material with g-C₃N₄ has shown to be an effective way of facilitating electron transfer on the surface and increasing the concentration of active sites. Predictably, the active sites on g-C₃N₄ with a conductive support can spread over the whole surface of the catalyst due to the increased electron transfer efficiency, which in turn facilitates the efficient 4e⁻ reduction process (Figure 24c). As proof-of-concept studies, various types of carbons, e.g. carbon black,³⁷⁰ mesoporous carbon,¹²⁶ macroporous carbon,³⁷¹ and 2D graphene sheets,^{372,373} have been incorporated with g-C₃N₄. All resultant nanocomposites showed enhanced ORR performance compared to g-C₃N₄. For example, Zheng et al. incorporated g-C₃N₄ into the channels of a highly ordered mesoporous carbon (CMK-3) following a nanocasting method (Figure 24d).¹²⁶ Indeed, the C₃N₄@CMK-3 hybrid exhibited a lower onset potential and higher ORR current density compared to the constituents and physically mixed samples (Figure 24e). The optimized ORR performance on C₃N₄@CMK-3 can be attributed to the participation of the CMK-3 mesoporous carbon framework, which serves as the support for g-C₃N₄ and facilitates electron accumulation on the surface of the g-C₃N₄ catalyst which enhances electron transfer efficiency during the ORR process.¹²⁶

Additionally, by applying silica microspheres as hard templates, Liang et al. reported macroporous g-C₃N₄/C composites with 3D ordered interconnected structures.³⁷¹ Due to the strong carbon skeleton, the macroporous g-C₃N₄/C metal free electrocatalyst showed excellent stability, which was better than commercial Pt/C in alkaline media.

6.5. Challenges for 2D Nanomaterials as Acidic ORR Catalysts

Most of the heteroatom-doped graphene, defective graphene, and graphene-based hybrid electrocatalysts mentioned were tested in alkaline media. With advanced nanomaterial fabrication techniques, they all showed very promising electrocatalytic activities which were comparable to precious Pt/C. However, fuel cells that operate with acidic electrolytes, particularly PEMFCs, are still far more commercially viable and are based on more mature infrastructure.³⁷⁴ To date, most of the carbon-based electrocatalysts reported for the acidic ORR are doped and functionalized CNTs,^{375–378} while graphene-based examples are limited.³⁷⁹ In our opinion, this may be due to iron impurities in the CNTs which can form iron–nitrogen/carbon complexes that are highly active toward the ORR in acidic conditions.³⁸⁰ For example, Li et al. showed that few-walled CNTs attached with nanoscale sheets of graphene (formed by the outer walls of partially unzipped CNTs) exhibited a high ORR activity in acidic conditions.³⁷⁶ A series of electrochemical tests and atomic imaging characterizations confirmed that the graphene sheets contained extremely small amounts of iron (originating from the CNTs growth seeds) and nitrogen impurities, which together facilitated the formation of catalytically active sites for the ORR.³⁷⁶ In terms of pure metal-free graphene, it is clear that N-graphene shows much closer ORR activity with Pt/C in alkaline media than in acidic media (Figure 25). This pH dependency associated with carbon-based materials for the ORR has attracted increased attention toward the development of new metal-free

catalysts due to their low cost and stability.⁸⁴ However, there is currently no explanation from either experimental or theoretical perspectives as to why carbon-based materials show comparable ORR performance to Pt in alkaline solutions, while very poor activity in acidic solutions.

Although this pH effect has long been known,³⁸¹ from a computational point of view, the ORR should follow the same pathway in alkaline and acidic media because the adsorption properties of the reaction intermediates are identical.³⁸² This, however, does not agree with the experimentally observed pH dependent ORR activity on carbon-based materials as shown in Figure 25. Based on current knowledge, we provide several possible explanations for this phenomenon. First, the ORR in alkaline and acidic solutions may not follow the same pathway. As mentioned previously, there are dissociative and associative pathways for the ORR.²⁹⁵ For the dissociative pathway, O₂ molecules dissociate on the surface into two oxygen atoms chemically bonded to different sites of the electrocatalyst, followed by the hydrogenation processes. This pathway is favorable when the kinetics of O₂ dissociation are fast, with an energy barrier comparable to or lower than 0.8 eV.²²⁶ When the dissociation barrier is high, and this process is kinetically prohibited, the associative pathway occurs. Therefore, for the same material, the ORR might follow different pathways with a different rds in alkaline and acidic solutions. Second, in an alkaline solution, OH[−] anions are adsorbed to the electrocatalyst surface, while in an acidic solution, H⁺ cations are adsorbed. These two adsorbates might change the Fermi energy level of the substrate, and therefore affect the adsorption of reaction intermediates which leads to a change in the overall reaction thermodynamics.^{383,384} Specifically on graphene surfaces, single functional groups (e.g., hydroxyl) can induce electronic bound states which can strongly perturb the electronic charge density of the surface and generate different adsorption configurations.³⁸⁵ Third, the ions solvated in the solution, i.e., Cl[−], SO₄^{2−} in acidic solutions and Na⁺, K⁺ in alkaline solutions, can also influence the ORR pathway by affecting the oxygen dissociation barrier and the adsorption strength of reaction intermediates.^{384,386} Fourth, the physicochemical properties of the synthesized samples, including the nanostructure and the hydrophilicity, should also be considered when comparing activities in different testing conditions because these two factors could affect mass transport to the reaction surface.

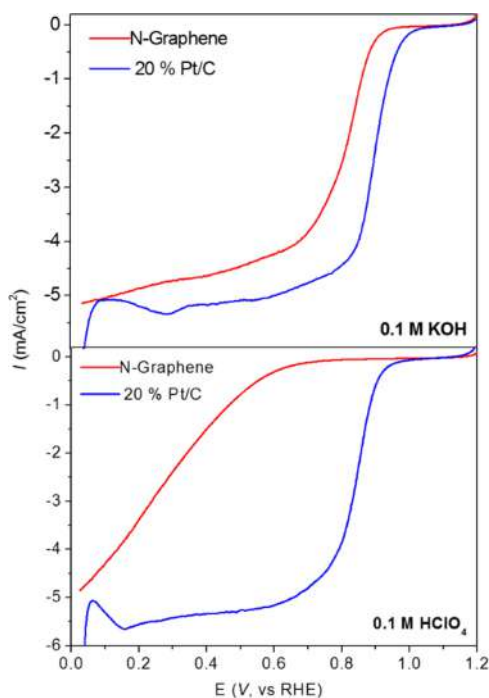


Figure 25. Comparison of ORR polarization curves on N-graphene and Pt/C electrocatalysts in alkaline and acidic media (measured by the authors themselves).

7. 2D NANOMATERIALS FOR OXYGEN EVOLUTION REACTION APPLICATIONS

The OER is a 4e[−] transfer process and is the reverse reaction of the ORR. Many studies have demonstrated that various 2D nanostructured electrocatalysts can efficiently catalyze the OER and significant development has been achieved in recent years. In this section, we first discuss the fundamental principles of the OER process and then summarize recently reported 2D nanomaterials developed for OER electrocatalysts.

7.1. Fundamental Principles of the OER

7.1.1. Reaction Kinetics. Like the ORR, η , j_0 , and Tafel slope are the parameters generally used for evaluating the reaction kinetics of an OER electrocatalyst, and are crucial for gaining insightful information into the OER mechanism.^{10,387} Specifically for the OER, η_{10} is a common comparison for performance and is defined as the overpotential required to produce a catalytic current density of 10 mA cm^{−2} (j_{10}). The magnitude of j_0 reflects the intrinsic charge transfer rate between an OER electrocatalyst

and the reactant/intermediates. Although a high η is always required to achieve a high magnitude of OER current density, a small increase in η which results in a large increase in OER catalytic current is highly desirable. Therefore, Tafel slope is a very important parameter in evaluating the relationship between j and η of an OER electrocatalyst. A smaller Tafel slope indicates that j can increase faster with a smaller change in η (i.e., faster reaction rate constant), implying good electrocatalytic kinetics. In addition, the value of the Tafel slope provides insightful information toward the OER mechanism, especially for elucidating the rds.

7.1.2. Reaction Mechanism. The OER can operate in either acidic ($2\text{H}_2\text{O} \rightarrow \text{O}_2 + 4\text{H}^+ + 4\text{e}^-$) or alkaline ($4\text{OH}^- \rightarrow \text{O}_2 + 2\text{H}_2\text{O} + 4\text{e}^-$) conditions as shown in Figure 26.^{51,388} The

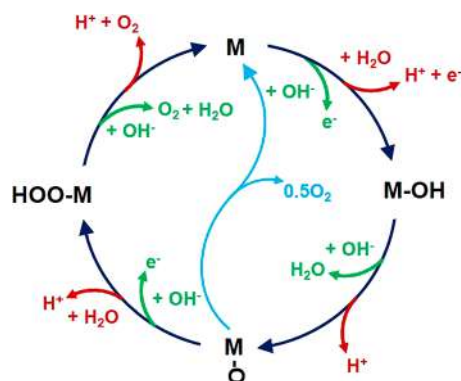
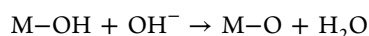
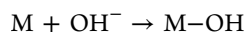
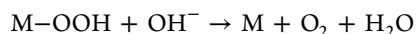
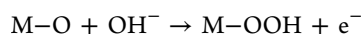


Figure 26. OER mechanism for alkaline (red route) and acidic (green route) conditions. The black line indicates that the OER involves the formation of a peroxide (M–OH) intermediate, while the light blue line indicates the direct reaction of two adjacent oxo (M–O) intermediates to produce oxygen.

following possible mechanisms for the OER in alkaline conditions have been proposed (M indicates an electrocatalyst surface):



followed by either



Like the ORR, the same intermediates (OH^* , OOH^* and O^*) exist in the proposed OER mechanisms for both acidic and alkaline conditions. As shown in Figure 26, the OER can proceed either by a direct combination of two O^* to produce O_2 (light blue route), or by the formation of the OOH^* intermediate (black route). Although possibly involving both routes, a common factor for overall OER catalytic ability is the bonding interactions with intermediates (e.g., M–OH, M–O, and M–OOH). The OER is also a multi-electron reaction that consists of a series of consecutive reaction steps, which can be either electron transfer steps or chemical steps, such as association or dissociation reactions.^{389,390} The OER mechanism on a particular electrocatalyst can be obtained by the measured Tafel slope, which is related to the electron transfer coefficient (α). A smaller Tafel slope suggests that the rds occurs at a later step in the OER pathway, indicating efficient OER kinetics.

7.1.3. Measurement Criteria. To better evaluate and compare the catalytic activity of OER electrocatalysts, some important measurement criteria have been established. The most commonly used criteria used are the total electrode activity (e.g., η and j), Tafel slope, turnover frequency (TOF), Faradaic efficiency (FE), and long-term operating stability. The total electrode activity, Tafel slope, and j_0 can be directly measured by recording OER polarization curves and derived Tafel plots. TOF is defined as the number of reactants that a catalyst can convert to a desired product per catalytic site per unit of time, exhibiting the intrinsic catalytic activity of an active catalytic site. The TOF value can be calculated by eq 8:

$$\text{TOF} = \frac{jA}{4nF} \quad (8)$$

where A is the area of the working electrode, and n is the number of moles of the active materials which can be calculated using the ECSA of the material. Although not all of the surface atoms in a material are catalytically active or equally accessible, TOF is still relevant and useful for comparing similar catalyst materials. FE reflects the utilization efficiency of electrons involved in the OER, and can be obtained by calculating the ratio of the experimentally produced O_2 detected with an oxygen sensor, to the theoretical maximum that can be produced calculated from the total charge passed. Long-term operating stability is also an important parameter for evaluating an OER electrocatalyst that normally operates under highly oxidizing environments. Two methods are always used to evaluate the operating stability of an OER electrocatalyst. The first one is by comparing the cyclic voltammetry (CV) or linear sweep voltammetry (LSV) scans after several thousand (e.g., >5000 cycles) cycles or scans. The second one is to measure the current variation with time (i.e., the $i-t$ response) under a constant potential/voltage in the OER region, or to measure the potential/voltage variation with time (i.e., the $V-t$ response) under a fixed j (e.g., 10 mA cm^{-2}).

7.2. Transition-Metal-Based Electrocatalysts

Transition-metal-based materials including TMOs, TMHs and their derivatives, such as chalcogenides and nitrides, are the subject of intense research for OER electrocatalysts.^{83,248,391} These materials are relatively inexpensive and it is relatively easy to tailor their structures, morphologies, and physicochemical properties. To date, Co/Ni/Fe/Mo/V/Zr-based materials have been explored for the OER, and some of them have exhibited promising catalytic performance.^{392,393} In this section, we summarize recent advances in the design, fabrication, and applications of 2D transition-metal-based OER electrocatalysts, focusing on the first-row transition-metal (Co, Ni, Fe)-based materials as summarized in Table 2.

7.2.1. Transition-Metal Oxides. First-row TMOs (denoted MO_x), such as CoO_x , NiO_x , and FeO_x , have been widely studied as electrocatalysts for the OER.^{176,410} Their OER catalytic activities appear to be related to the $\text{OH}-\text{M}^{2+\delta}$ bond strength ($0 \leq \delta \leq 1.5$), which increases along the following order: $\text{Ni} < \text{Co} < \text{Fe}$. This order, however, is opposite to that of their activities ($\text{NiO}_x > \text{CoO}_x > \text{FeO}_x$).⁴¹¹ The OER catalytic activity of MO_x materials can be improved by fabrication into desired nanostructures. Additionally, the M–O bond strength in MO_x materials can be tuned by alloying with other metallic elements. Based on these findings, 2D MO_x materials that possess high specific surface area, short paths for charge/mass transport, and rich surface reactive sites have been designed for OER electrocatalysts.³⁹⁵

Table 2. Comparison of the Electrocatalytic Activity of Some Recently Reported OER Electrocatalysts

catalyst	electrolyte	η at 10 mA cm ⁻² (V) ^a	Tafel slope (mV/dec)	TOF (s ⁻¹) ^b
porous Co ₃ O ₄ ³⁹⁴	1 M KOH	~0.42	25	N.A.
NiO stabilized by TiO ₂ ³⁹⁵	1 M KOH	0.32	52	0.07 (0.50 V)
porous FeNi oxide ³⁹⁶	1 M KOH	0.21	32	N.A.
γ -CoOOH ³⁰¹	1 M KOH	0.30	38	0.09 (0.34 V)
exfoliated FeNi LDH ¹⁷⁴	1 M KOH	0.30	40	0.05 (0.3 V)
CoMn LDH ³⁹⁷	1 M KOH	0.29	43	1.05 (0.35 V)
Ni _{0.75} V _{0.25} LDH ³⁹⁸	1 M KOH	0.32	50	0.54 (0.35 V)
CoNiFe hydroxide ³⁹⁹	1 M KOH	0.21 (Ni foam)	42	N.A.
O–Ni–Fe–S ⁴⁰⁰	1 M KOH	0.26 at 20 mA cm ⁻² (Ti plate)	39	0.76 (0.30 V)
CoSe ₂ ¹⁵⁶	0.1 M KOH	0.32	44	0.33 (0.50 V)
Ni ^{II} –Se ⁴⁰¹	1 M KOH	0.33	80	N.A.
NiCo ₂ Se ₄ ⁴⁰²	1 M KOH	0.45	53	N.A.
Co _{0.4} Fe _{0.6} Se ₂ ⁴⁰³	1 M KOH	0.22 (Ni foam)	41	N.A.
Co ₃ S ₄ ⁴⁰⁴	1 M KOH	0.35	107	N.A.
Ni _x Co _{3-x} S ₄ -decorated Ni ₃ S ₂ ³⁹¹	1 M KOH	0.14 (Ni foam)	48	N.A.
Ni ₃ N ²⁴⁶	1 M KOH	0.35 at 52.3 mA/cm ²	45	N.A.
Co–Mn carbonate hydroxide ⁴⁰⁵	0.1 M KOH	0.29 at 30 mA/cm ² (Ni foam)	N.A.	N.A.
Fe-doped (Ni ₂ P) ⁴⁰⁶	1 M KOH	0.27 (Ni foam)	96	N.A.
ternary NiCoP ⁴⁰⁷	1 M KOH	0.31 at 50 mA/cm ² (Ni foam)	N.A.	N.A.
cobalt borate/graphene ⁴⁰⁸	1 M KOH	0.29 V	53	N.A.
NiCo bimetal MOF ²⁰¹	1 M KOH	0.25; 0.189 (Cu foam)	42	0.86 (0.30 V)
NiFe-MOF array ²⁰⁴	0.1 M KOH	0.24 (Ni foam)	34	3.8 (0.40 V)
Ti ₃ C ₂ T _x –CoBDC ¹⁸⁴	0.1 M KOH	0.41	48.2	N.A.
N,S-graphene ⁴⁰⁹	0.1 M KOH	0.33	71	N.A.
g-C ₃ N ₄ /Ti ₃ C ₂ ⁶⁹	0.1 M KOH	0.42 (free-standing)	74.6	N.A.

^aThe values were obtained for electrocatalysts loaded on glassy carbon working electrodes. Working electrodes fabricated with other substrates are indicated by parentheses. ^bThe values in the brackets are the operating overpotential.

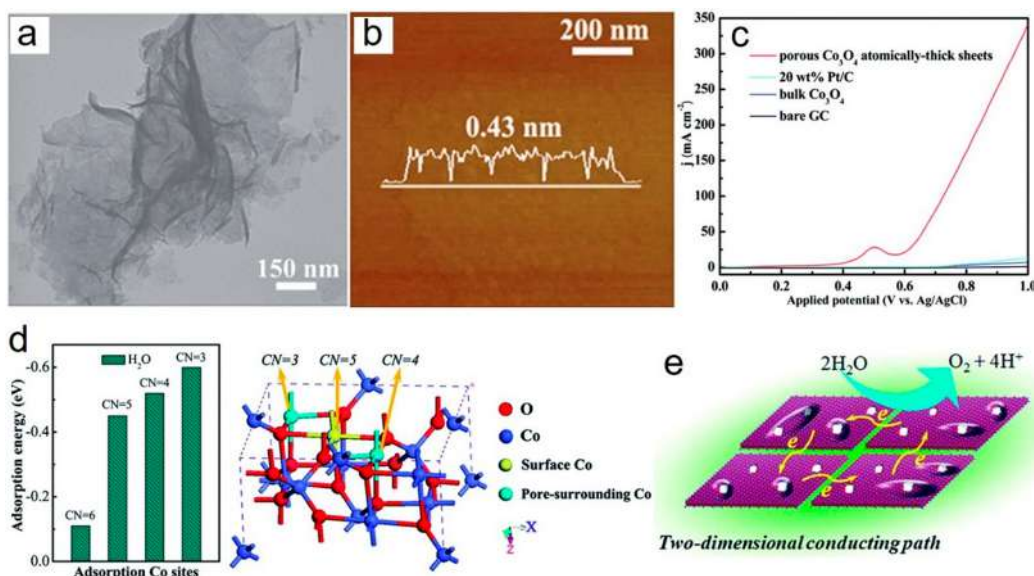


Figure 27. (a) TEM and (b) AFM images of porous Co₃O₄ nanosheets. (c) OER Polarization curves of different electrodes in alkaline conditions. (d) Calculated adsorption energy for water molecules on Co³⁺ sites with different coordination numbers and crystal structure. (e) Advantages of using the porous Co₃O₄ nanosheets as OER electrocatalysts. Reproduced with permission from ref 394. Copyright 2014 Royal Society of Chemistry.

Co₃O₄ is a spinel oxide that contains Co²⁺ in tetrahedral sites and Co³⁺ in octahedral sites.⁴¹² Ultrathin porous Co₃O₄ nanosheets have been synthesized from atomically thick CoO sheets which undergo a fast annealing process in air.³⁹⁴ The resultant nanosheets had a porous structure, a lateral size of around a micrometer, and an average thickness of around 0.43 nm (Figure 27a,b). For the OER, it achieved a catalytic current density of up to 341.7 mA cm⁻² at 1.0 V vs Ag/AgCl, which is

roughly 50 times larger than that of its bulk counterpart (Figure 27c). DFT calculations revealed that this enhanced catalytic activity is the result of low-coordinated surface Co³⁺-atoms which are more favorable for adsorbing H₂O reactants (Figure 27d). More significantly, the 2D nanostructure provides an extremely large surface area for intimate interfacial contact between the electrode and electrolyte and facilitates interfacial charge transfer. Therefore, a greater number of coordinated-unsaturated surface

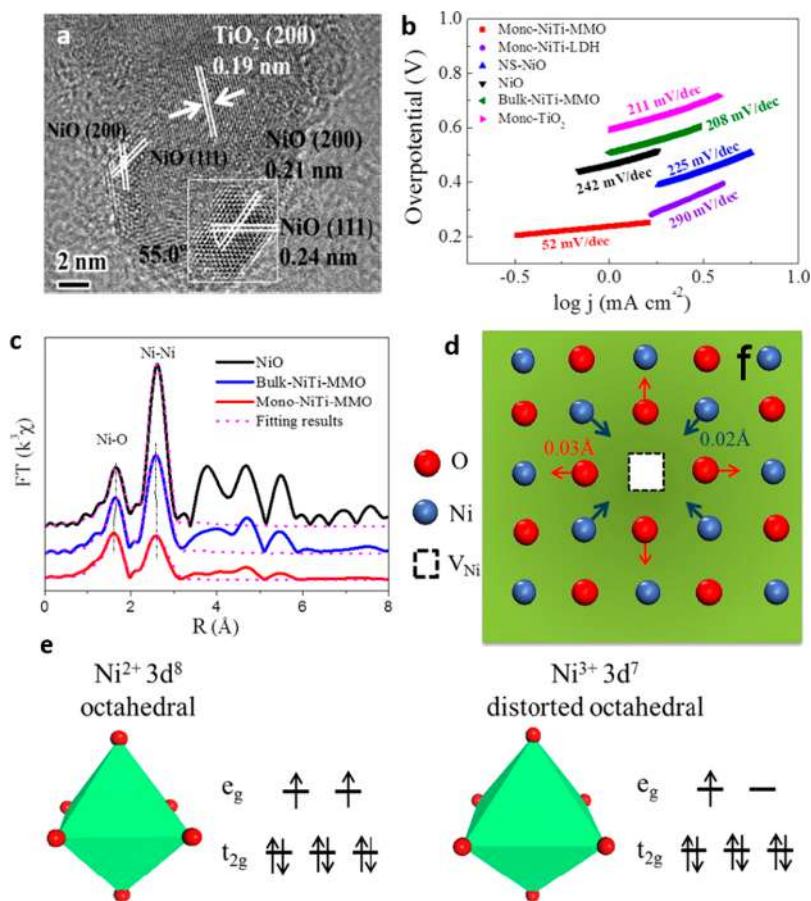


Figure 28. (a) TEM images of NiTi-MMO nanosheets. (b) Tafel plots of different materials in 1.0 M KOH. (c) Ni K-edge XANES spectra for different catalysts. (d) Schematic view of the Ni- and O-atoms relaxation around V_{Ni} in NiTi-MMO. (e) Schematic of the electronic configuration of Ni cations in NiO_6 of bulk NiO and V_{Ni} doped NiO. Reproduced with permission from ref 395. Copyright 2016 American Chemical Society.

atoms can provide more active sites to expedite the OER (Figure 27e).

Due to the increased covalency of their M–O bonds, 3d transition-metal oxide electrocatalysts are ideal candidates for the OER as the e_g orbital occupancy approaches unity for surface cations like Ni^{3+} ($t_{2g}^6 e_g^1$).^{413,414} Bulk NiO with a $t_{2g}^6 e_g^2$ electronic configuration does not have favorable OER activity. However, 2D NiO structures with abundant surface defects can significantly alter the electronic structure of Ni^{2+} centers, leading to the desired Ni^{3+} sites with $t_{2g}^6 e_g^1$ electronic configurations.^{250,415} In a recent work, ultrathin NiO nanosheets stabilized by TiO_2 (NiTi-MMO) were synthesized by calcination of monolayer thick NiTi-LDH nanosheets.³⁹⁵ The size of the resultant NiTi-MMO hybrid structures were around 20 nm and contained ultrafine NiO nanosheets (1 nm thickness by 4 nm lateral size; Figure 28a). In this system, the NiO nanosheets were highly dispersed on the TiO_2 . This reduced aggregation of the NiO nanosheets and, more importantly, altered their geometric/electronic structure. EXAFS spectra showed that the Ni–O octahedral bond distance is around 2.05 Å, smaller than that observed for both NiO and bulk-NiTi-MMO (2.08 Å; Figure 28c). This indicates more structural distortion for Ni centers in the NiTi-MMO nanosheets, where the six nearest O-atoms move away from the Ni vacancy (V_{Ni}) by 0.03 Å (Figure 28d). Meanwhile, the neighboring Ni-atoms move slightly closer to V_{Ni} , leading to an increased average Ni–Ni distance. As shown in Figure 28e, compared with the $t_{2g}^6 e_g^2$ electronic configuration of Ni^{2+} in bulk NiO, Ni^{3+} active sites in distorted NiO nanosheets

possess a near-unity occupancy of the e_g orbital ($t_{2g}^6 e_g^1$). This is desirable for improving OER activity. As a result, the NiTi-MMO required $\eta = 0.32$ V to reach j_{10} , which was much smaller than that of pure NiO and bulk-NiTi-MMO electrocatalysts (Figure 28b). Additionally, the NiTi-MMO also showed a much higher TOF (0.068 s^{-1}) at $\eta = 0.50$ V, which is approximately 14 and 24 times higher than the corresponding values for NiO (0.005 s^{-1}) and bulk-NiTi-MMO (0.003 s^{-1}), respectively.³⁹⁵

Some reports indicate that doping with certain elements can tailor the electronic structures of 2D MO_x materials and enhanced OER activity. For example, the OER catalytic performances of a series of NiO_x , CoO_x , FeO_x , $\text{Ni}_y\text{Co}_{1-y}\text{O}_x$, and $\text{Ni}_{0.9}\text{Fe}_{0.1}\text{O}_x$ were investigated, of which $\text{Ni}_{0.9}\text{Fe}_{0.1}\text{O}_x$ was found to be the most active.⁴¹⁰ Other studies also found that the introduction of Fe into NiO materials can increase the oxidation ability of NiO and significantly improve their OER catalytic activity.^{416,417} It was also found that the formation of a NiO/ NiFe_2O_4 hybridized phase at low Fe concentrations can change the Fe coordination shells and enhance OER activity.⁴¹⁸ In a recent study, porous NiFe oxide nanosheets were synthesized via a controlled transformation from LDH precursors.³⁹⁶ Due to their high specific surface area, abundant active sites, small charge transfer resistance, and optimum intermediates adsorption energy, the NiFe oxide nanosheets exhibited a high OER performance with an η_{10} of 213 mV. Additionally, some complicated MO_x materials, such as perovskite-like $\text{Ba}_{0.5}\text{Sr}_{0.5}\text{Co}_{0.8}\text{Fe}_{0.2}\text{O}_{3-\delta}$, have exhibited promising OER performance with high intrinsic activities.⁴¹⁹ A design principle has been

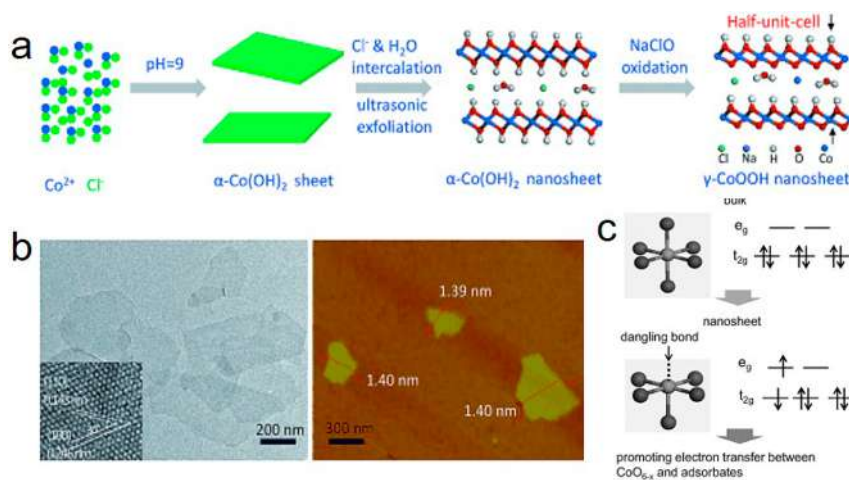


Figure 29. (a) Fabrication route for the γ -CoOOH nanosheets. (b) TEM and AFM images of the γ -CoOOH nanosheets. (c) Calculated adsorption energy of the γ -CoOOH nanosheets and bulk γ -CoOOH. Reproduced with permission from ref 301. Copyright 2015 John Wiley & Sons, Inc.

established to link the intrinsic OER activity of perovskites with 3d electron occupancy to an e_g orbital symmetry of the surface transition-metal cations.⁴¹³

7.2.2. Layered Transition-Metal Hydroxides and Double Hydroxides. A two-step soft chemistry route called an “atomic-scale phase transformation process” was used to fabricate γ -CoOOH LDH nanosheets from layered α -Co(OH)₂ sheets considering their similar spatial structures but different inter-slab spacings (Figure 29a).³⁰¹ The ultrathin γ -CoOOH nanosheets had a size of several hundred nanometers and thickness of about 1.4 nm (Figure 29b). As an OER electrocatalyst, the γ -CoOOH nanosheets showed an onset potential of 1.47 V vs RHE, which was superior to that of the bulk sample (1.53 V vs RHE). The mass activity of the γ -CoOOH nanosheets was 66.6 A g⁻¹ at $\eta = 0.3$ V, which was around 20 times higher than that of the bulk sample and 2 times higher than that of the state-of-the-art IrO₂ electrocatalyst. It was found that the increased hole states in the t_{2g} orbital of CoO_{6-x} can enhance the electrophilicity of O* and facilitate adsorption of the hydroxy group on the catalytically active sites to form OOH* (Figure 29c). Moreover, because the σ -bonding e_g orbital has a stronger ability to overlap with adsorbates (compared to the π -bonding t_{2g} orbital), it can promote electron transfer between the surface cation (CoO_{6-x}) and OOH* intermediates. This beneficial for improving performance as it can act as the active site for effective water adsorption and decreases the barrier to the OER.

A series of ultrathin single-layer LDH nanosheets were successfully synthesized from the exfoliation of bulk LDHs. The single-layer nanosheets exhibited significantly higher OER catalytic activity compared to their bulk phases owing to their increased number of active sites and improved electronic conductivity.¹⁷⁴ For example, a NiFe-based LDH required an η_{10} of 0.30 V and achieved a TOF of 0.05 s⁻¹, which is superior to that of benchmark IrO₂ electrocatalysts.¹⁷⁴ In another work, ultrathin Co–Mn LDH nanoplates were synthesized by a simple one-pot co-precipitation method, in which Mn³⁺ ions replaced Co²⁺ sites in β -Co(OH)₂.³⁹⁷ The resultant product was 50–100 nm in diameter and had an average thickness of \sim 3.6 nm. As an OER electrocatalyst, it showed a much higher intrinsic OER activity than Co and Mn oxides, Co–Co and Ni–Co LDHs, and IrO₂ counterparts. Interestingly, it was found that the OER performance of the Co–Mn LDH was improved after an anodic conditioning process. This was likely due to the leaching of Mn

ions which resulted in the formation of thin amorphous regions with abundant uncoordinated Co ions possessing high OER activity.³⁹⁷ Monolayers of Ni–V LDH with thicknesses of around 0.9 nm were prepared by incorporating V into Ni(OH)₂ by a simple one-step hydrothermal strategy.³⁹⁸ After compositional optimization, the Ni_{0.75}V_{0.25}-LDH exhibited significant OER activity with a small Tafel slope of 50 mV dec⁻¹ and a low η_{10} of 318 mV. Mechanistic studies showed that the doping of V into Ni(OH)₂ caused a decrease in free energies of key OER intermediates. Ultrathin trimetal (Fe, Ni, and Co) LDH nanosheets with controlled Co-doping were prepared by a hydrothermal method using Ni–Fe LDH nanosheets.³⁹⁹ It was found that the OER activities of the trimetal LDHs increased due to the increased surface areas and number of active Co sites. In this system, the electron structure of the nanosheets could be modulated to reduce reaction activation energy. The optimized Fe–Ni₈–Co₂-LDH displayed an outstanding OER activity with an η_{10} of 210 mV, superior to most previously reported OER electrocatalysts.³⁹⁹

Coupling LDHs with conducting materials, such as carbon nanomaterials, has shown to be a promising way of overcoming their inherently poor electrical conductivities. Recent development in the rational integration of LDHs with nanocarbon materials has been comprehensively summarized in a recent review.⁴²⁰ More importantly, the combination of coupling the LDHs with carbon supports and defect engineering can induce synergistic effects for greatly improved OER performance.³⁸⁵ Despite extensive studies into LDHs and their derived materials, their OER catalytic mechanisms have not yet been clearly identified. Additionally, extensive efforts have been devoted to modulating the electrocatalytic activity of these materials via metal cation choice in the LDH precursors. However, engineering of anion chemistry to control their electrochemical performances has not been extensively explored despite its high potential in modifying the activity of these electrocatalysts.

7.2.3. Transition-Metal Dichalcogenides. TMDs are attracting much attention as promising non-precious-metal catalysts in many energy-related applications (mainly for the HER which is discussed in section 8.3).⁴²¹ Compared to metal oxides/hydroxides, reports of 2D TMDs as OER electrocatalysts are limited (as summarized in Table 2). Specifically, amorphous-like oxygen-incorporated Ni–Fe–S ultrathin nanosheets (O-NFS) were fabricated through the calcination of Ni–Fe–S

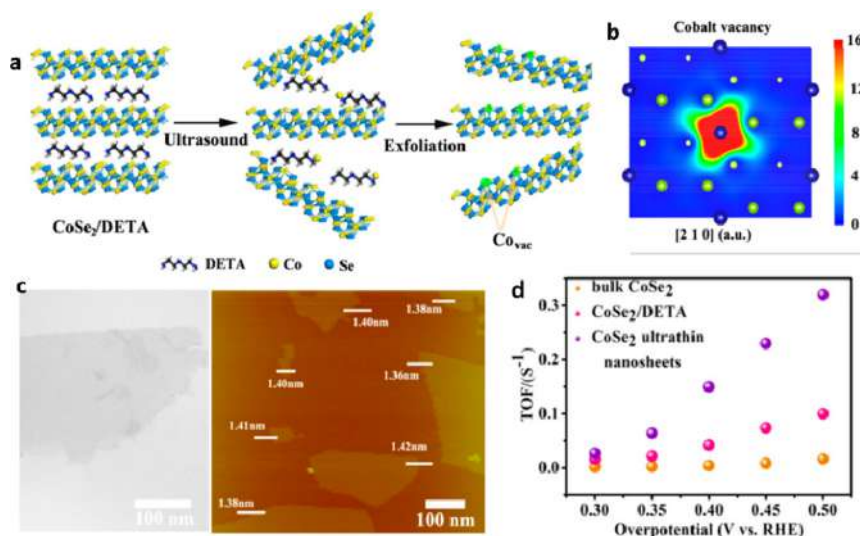


Figure 30. (a) Schematic illustration of the formation of V_{Co} vacancies in CoSe_2 nanosheets. (b) The trapped positrons of cobalt vacancies. (c) TEM and AFM images of CoSe_2 nanosheets. (d) TOFs with respect to Co-atoms of various electrocatalysts at different overpotentials. Reproduced with permission from ref 156. Copyright 2014 American Chemical Society.

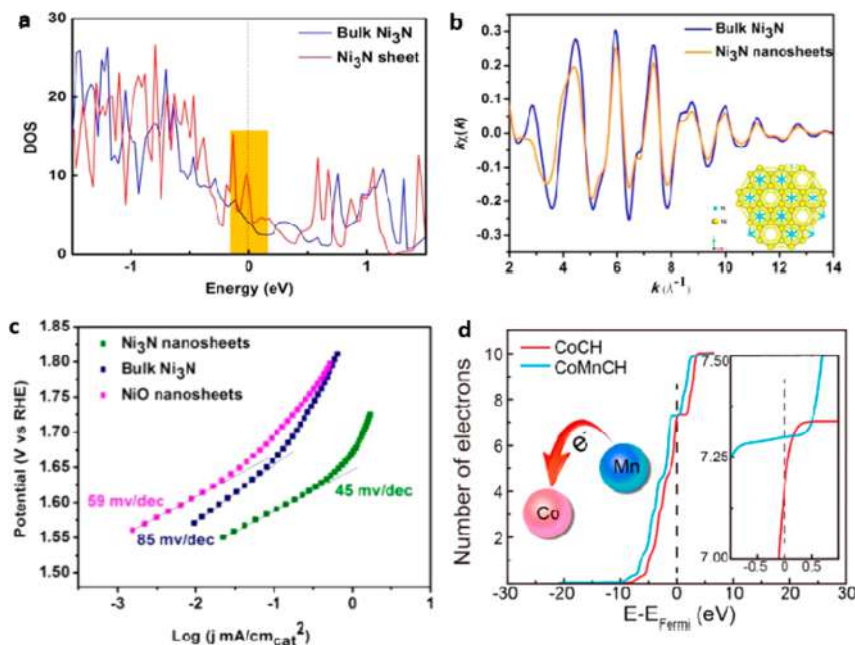


Figure 31. (a) Calculated DOS for bulk and nanosheets Ni_3N . (b) Ni K-edge EXAFS of Ni_3N ; inset shows the geometrical structure of Ni_3N . (c) Tafel plots of various electrocatalysts. Reproduced with permission from ref 246. Copyright 2015 American Chemical Society. (d) Number of electrons in the 3d orbital per Co-atom in CoCH and CoMnCH . Reproduced with permission from ref 405. Copyright 2017 American Chemical Society.

nanosheets in air, followed by an electrochemical tuning method to modify their electronic structure.⁴⁰⁰ As an OER electrocatalyst, the O-NFS exhibited a $\eta = 259$ mV at $j = 20$ mA cm^{-2} , which is much smaller than that of RuO_2 (370 mV). Notably, it can achieve a large j of up to 500 mA cm^{-2} under $\eta = 300$ mV as well as a 100% Faradaic efficiency. The origins of this highly significant OER activity is believed to be attributed to (1) the self-supported open architecture that affords more active sites, and efficient charge and mass transport; and (2) the synergistic regulation of electronic structure and catalytically active areas. Cubic CoSe_2 is also a promising candidate for high OER performance because it has a $t_{2g}^6 e_g^1$ electronic configuration near the optimal e_g filling, and a metallic behavior from the large local DOS across its Fermi level. Accordingly, atomically thick CoSe_2

nanosheets were fabricated by exfoliating CoSe_2 -based inorganic–organic lamellar nanohybrids (Figure 30a,c).¹⁵⁶ The resultant material effectively catalyzed the OER with an η_{10} of 0.32 V and a TOF of 0.33 s $^{-1}$ at $\eta = 0.5$ V (Figure 30d). Local atomic arrangements and electronic structure characterizations showed that the formation of V_{Co} vacancies in the 2D plane likely contribute to its significant OER catalytic activity (Figure 30b). In another work, single-unit-cell thick CoSe_2 nanosheets fabricated by a thermal exfoliation approach displayed a Tafel slope of 64 mV dec^{-1} and an onset overpotential of 270 mV.⁴²² Additionally, a series of 2H- MoS_2 , 1T- MoS_2 , 2H-TaS $_2$, and 1T-TaS $_2$ were fabricated, in which 1T- MoS_2 showed the best activity with an η_{10} of 420 mV in acidic conditions.⁴²³ Due to their better stabilities over metal oxides/hydroxides in acidic media, further

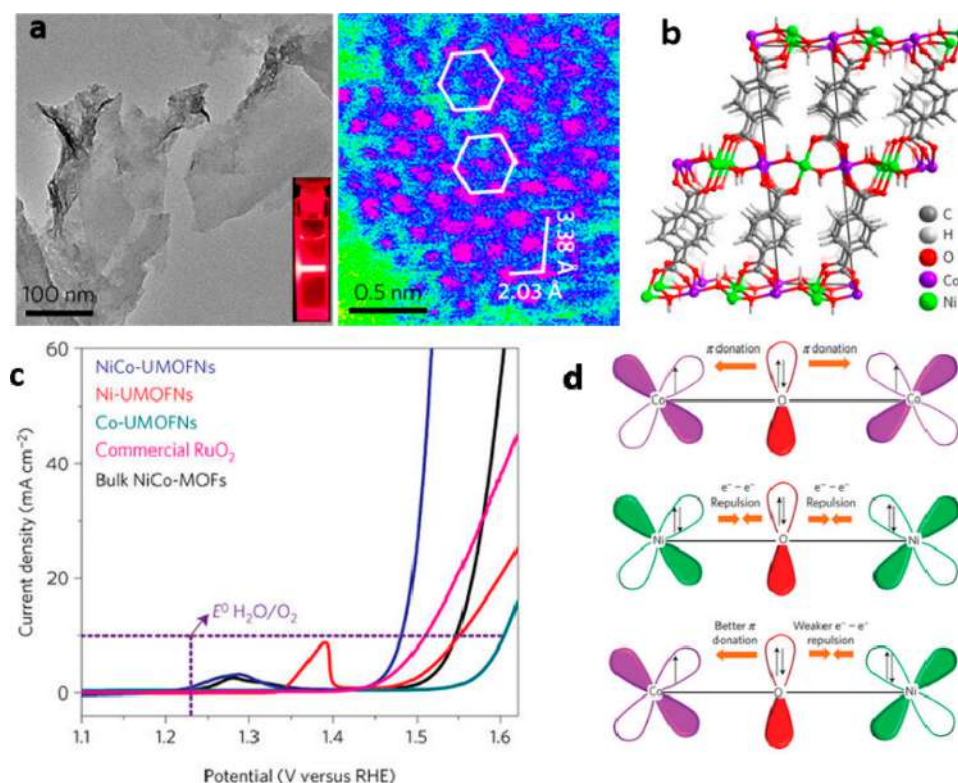


Figure 32. (a) TEM and HAADF-STEM images of NiCo-UMOFNs. (b) Crystal structure of NiCo-UMOFNs. (c) Polarization curves of NiCo-UMOFNs and control samples. (d) Schematic representation of the electronic coupling between Co and Ni in NiCo-UMOFNs. Reproduced with permission from ref 201. Copyright 2016 Nature Publishing Group.

improvements to 2D TMDs should be made by enhancing their electrical conductivities and active site densities.

7.2.4. Other Metal-Based Materials. Several types of other transition-metal compounds such as nitrides, carbonate hydroxides, phosphides, and borates (summarized in Table 2) have also attracted considerable interest for the OER due to their unique physicochemical properties.^{405,406,424–428} In a recent work, well-defined Ni₃N nanosheets were prepared by annealing metal precursors in ammonia gas.²⁴⁶ DFT calculations showed that these nanosheets were different from their bulk counterparts, being intrinsically metallic and having significantly improved carrier concentration as a result of dimensional confinement (Figure 31a).²⁴⁶ Benefiting from an atomically disordered structure (Figure 31b), the Ni₃N nanosheets exhibited a much higher OER activity compared to bulk Ni₃N and NiO nanosheets (Figure 31c). In another work, FeNi₃N nanosheets synthesized by redox-etching and thermal annealing exhibited a high OER activity with an η_{10} of 202 mV and a Tafel slope of 40 mV dec⁻¹.⁴²⁵ Metal carbonate hydroxides have also been investigated and applied as OER electrocatalysts. For example, Co–Mn carbonate hydroxide (CoMnCH) nanosheet arrays, with controlled morphology and composition, were produced by doping Mn into Co carbonate hydroxide (CoCH).⁴⁰⁵ Mn doping not only modulated the nanosheet morphology to significantly increase the ECSA, but also tuned the electronic structure of Co centers for effective enhancement of intrinsic catalytic activity (Figure 31d). As a result, the optimized CoMnCH exhibited high OER catalytic activity, requiring only $\eta = 294$ mV to produce 30 mA cm⁻², and was able to deliver a large and stable current density of 1000 mA cm⁻² at $\eta = 462$ mV. CoMnCH also demonstrated bifunctional ability as an electrocatalyst for both

the OER and HER in a two-electrode electrolyzer operating at a cell voltage of 1.68 V at j_{10} .

Although there are many new reports on the high performance of transition-metal sulfides, selenides, nitrides, phosphides, etc. in OER electrocatalyst applications, there are concerns regarding their compositional stabilities under OER conditions.^{395,429} Many of these materials have demonstrated stable OER electrocatalytic performance for hours or even longer without apparent performance decay. However, from the perspective of solid-state chemistry, it is known that metal sulfides are thermodynamically less stable than metal oxides under corrosive and oxidizing environments, with metal nitrides and phosphides being even less stable again. Therefore, especially under high overpotentials, it is very likely that metal sulfides, selenides, nitrides, and phosphides are oxidized to their corresponding metal oxides/hydroxides under OER operation and form a core–shell structure. This concern is even greater for 2D nanomaterials with ultrathin structures. Therefore, it is of great importance to carry out surface-sensitive structural characterization analysis before and after OER tests to identify the true catalytically active species. We believe that more should be done in this regard because it is crucial knowledge for designing highly efficient OER electrocatalysts under real reaction conditions.

7.3. Metal–Organic Framework-Based Electrocatalysts

Designing MOFs into 2D nanostructures is an effective strategy for fabricating high-performing electrocatalysts because of the following resultant characteristics: (1) their nanometer thickness allows rapid mass transport and electron transfer; (2) a significantly high percentage of coordinatively unsaturated metal sites are exposed, allowing high catalytic activity; and (3) their easily identifiable and tunable surface atomic structures and

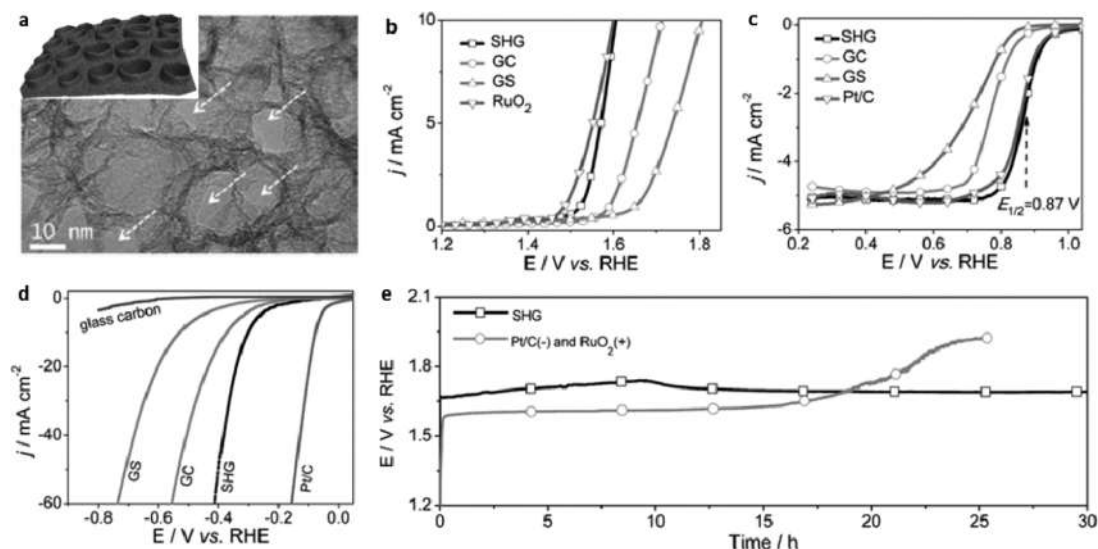


Figure 33. (a) TEM image of SHG with corresponding schematic model (inset). (b–d) OER, ORR, and HER polarization curves of various electrocatalysts in corresponding test conditions. (e) Chronopotentiometric curves of water electrolysis for SHG as both cathode/anode and Pt/C(cathode)/RuO₂(anode) under a constant current density of 10 mA cm⁻² in 1.0 M KOH. Reproduced with permission from ref 409. Copyright 2017 John Wiley & Sons, Inc.

bonding arrangements.^{430,431} Ultrathin 2D NiCo bimetallic MOF nanosheets (NiCo-UMOFNs) have been synthesized from a mixed solution of metal salts and benzenedicarboxylic acid under sonication.²⁰¹ The product displayed a well-defined sheet structure with a thickness of around 3.09 nm (Figure 32a), corresponding to four metal coordination layers or three coordination structural layers (Figure 32b). The NiCo-UMOFNs on planar glassy-carbon electrodes required an η_{10} of 250 mV (Figure 32c). This decreased to 189 mV when the nanosheets were loaded on copper foam. Based on experimental measurements and DFT calculations, it was proposed that the surface atoms in the NiCo-UMOFNs are coordinatively unsaturated and are the active centers for reactant/intermediate adsorption. Additionally, the electronic coupling between Ni and Co metals in the MOFs is likely crucial for its high OER performance (Figure 32d). In another work, ultrathin 2D NiFe-MOF nanosheet arrays were fabricated on different substrates through a dissolution–crystallization mechanism.²⁰⁴ The arrays demonstrated promising OER performance with an η_{10} of 0.24 V and a TOF of 3.8 s⁻¹ at $\eta = 0.40$ V. It was proposed that their high OER performance originates from their unique physicochemical properties and hierarchical porosity.²⁰⁴

Most MOF materials have relatively poor electrical conductivity resulting from their inherent molecular configuration. Thus, combining 2D MOFs with other 2D conductive materials to construct hybrid materials with well-defined interfacial structures should improve their conductivity and enhance their OER performance. Very recently, a MXene-MOF hybrid material composed of cobalt 1,4-benzenedicarboxylate on the surface of MXene Ti₃C₂T_x nanosheets (Ti₃C₂T_x-CoBDC) was prepared via an interdiffusion reaction strategy.¹⁸⁴ The hybrid achieved an η_{10} of 1.64 V vs RHE, which is better than its constituent components (CoBDC and Ti₃C₂T_x) and even IrO₂. Additionally, given their structural tunability and chemical versatility, 2D MOFs can also be combined with other functional 2D nanomaterials, such as heteroatom-doped graphene and black phosphorus, for further synergistic enhancement to OER performance.

7.4. Metal-Free Electrocatalysts

Metal-free electrocatalysts that can reduce the cost and increase the efficiency of energy conversion systems have been recently reported in many studies.^{342,432} Very recently, graphene- and g-C₃N₄-based nanosheets were applied as OER electrocatalysts.¹⁷² Similar to the ORR, it was found that spin redistribution induced by heteroatom-doping in the graphene matrix can impart high OER catalytic activities.^{423,433} For example, N,S-co-doped 2D graphitic nanosheets (SHG) with a unique hierarchical structure, were fabricated by a salt-assisted carbonization process.⁴⁰⁹ The 2D graphitic sheets contained stereoscopic holes (ranging from 5 to 20 nm in diameter) which could provide numerous accessible active sites and rich mesoporosity for effective electron and electrolyte transport (Figure 33a). As a result, the SHG electrode showed a lower η and a smaller Tafel slope than that of the control samples without a 2D structure or without co-dopants, and even the state-of-the-art RuO₂ electrode (Figure 33b). In SHG materials, the co-doping of N and S is important for activity by providing low resistance to electron or ion transport and by facilitating the electrochemical process. Of note is that the SHG electrode is an effective trifunctional electrocatalyst, being active for the HER and ORR processes also (Figure 33c,d). Remarkably, a water electrolysis cell composed of SHG as both cathode and anode showed comparable activity, but better stability, to a cell using state-of-the-art precious-metal electrodes (Figure 33e).

As mentioned previously, g-C₃N₄ has a much higher N content than N-carbon materials, and its 2D layered structure is stable and tunable.⁴³⁴ These unique characteristics make g-C₃N₄ a potential candidate for efficient OER electrocatalysts. As with the ORR, the combination of g-C₃N₄ with conductive materials can eliminate its inherent semiconductivity and achieve high catalytic activity. Based on this strategy, a hybrid film composed of overlapping g-C₃N₄ and Ti₃C₂T_x nanosheets was designed and fabricated by sonication-assisted exfoliation and vacuum suction.⁶⁹ The resultant hybrid film was flexible and was a few centimeters in size with a thickness of 8–10 μ m. In this hybrid, the oriented assembly of g-C₃N₄ and Ti₃C₂T_x nanosheets imparted many large interlayer pores ranging from tens to

hundreds of nanometers. Moreover, the hybrid film had a well-defined interface between the $g\text{-C}_3\text{N}_4$ and $\text{Ti}_3\text{C}_2\text{T}_x$ components. Through a combination of NEXAFS and XPS analysis, it was found that the interfacial Ti–N_x interaction was highly active for the OER. Another conductive film with porous structure and high nitrogen content was fabricated through the self-assembly of $g\text{-C}_3\text{N}_4$ nanosheets and CNTs through π – π stacking and electrostatic interactions.⁴³⁵ This hybrid offered efficient mass and charge transfer in its porous nanostructure, and exhibited higher OER catalytic activity than Ir-based electrocatalysts.

7.5. OER/ORR Bifunctional Electrocatalysts

For practical applications, zinc (Zn)–air batteries are attracting increased attention due to their low cost and inherent safety. Furthermore, rechargeable Zn–air batteries can be easily fabricated into flexible designs with high energy density and are environmentally friendly.⁶ However, the biggest challenge for flexible rechargeable Zn–air batteries is the development of biocompatible and high-efficiency bifunctional OER/ORR electrocatalysts.^{8,52,342} Therefore, electrode flexibility and multifunctionality are the new design criteria for practical applications of electrocatalysts. Theoretically, the design principles for OER/ORR bifunctional electrocatalysts should be focused on the balance of OH* adsorption free energy (ΔG_{OH^*}). In this regard, Zheng et al. developed a dual volcano plot for evaluating the performance of oxygen electrode electrocatalysts.²³⁴ This model indicates that for a material with OH* adsorption within the top zone of the dual volcano plot, it is neither the best ORR nor OER catalyst, but shows the best bifunctional performance for reversible OER/ORR.

7.6. Challenges for 2D Nanomaterials as Acidic OER Catalysts

OER electrocatalysts operating in alkaline conditions can be applied in alkaline electrolyzers and metal–air batteries, and have become a well-matured technology for commercial production of hydrogen fuel (up to the megawatt range).⁴³⁶ However, alkaline electrolyzers still face three major problems: low partial load range, limited current density, and limited to low operating pressures.⁴³⁷ On the other hand, PEM water electrolyzers using polymer electrolyte membranes (e.g., Nafion) can provide high proton conductivity, low gas crossover, compact system design, high current density, and high-pressure operation.^{285,438} Moreover, PEM water electrolyzers can also be integrated with PEMFC systems for integrated energy conversion/storage devices. However, one major challenge for PEM water electrolyzers is that the operating conditions require the use of robust materials which can resist harsh acidic environments (e.g., pH \sim 2) and sustain high applied overvoltages (\sim 2 V).^{439,440} To date, only a few scarce and expensive noble catalysts (Ir and Ru) show acceptable OER catalytic activity in such acidic environments.^{441,442} However, Ir- and Ru-based materials also degrade during OER operation because of oxidation and dissolution into the acidic electrolyte.

Recently, the stabilities of some noble metal-based OER electrocatalysts in acidic electrolytes have been improved by alloying and *in situ* leaching strategies. For example, a new synthetic strategy, utilizing the surface segregation method, was used to tune the near-surface composition of Ru and Ir elements.⁴⁴³ This method could balance the near-surface Ir and Ru composition in such a way that the stability of the surface atoms was enhanced during OER operation without compromising activity. After treating a $\text{Ru}_{0.5}\text{Ir}_{0.5}$ alloy with this surface segregation method, the surface composition of Ir increased to

approximately 75 at.%, while the concentration profile of Ir monotonically decreased until the bulk atomic composition was reached. Consequently, the treated sample exhibited four times higher stability than the best Ru–Ir OER electrocatalysts, while still maintaining the same activity. Similarly, in a recent work, an $\text{IrO}_x/\text{SrIrO}_3$ catalyst was formed *in situ* during electrochemical testing by Sr leaching from thin films of SrIrO_3 .⁴⁴⁴ In an acidic electrolyte, the catalyst achieved an η_{10} of 0.27 V and DFT calculations suggest that highly active IrO_3 or anatase IrO_2 surface layers were formed during the Sr leaching process. It is predicted that alloy surface segregation and *in situ* leaching strategies can be utilized to prepare unique 2D noble alloy materials for stable OER electrocatalysts in acidic electrolytes. Apart from Sr, other possible elements such as Ti and Mo can also be used to tailor the electronic structure or spin states of 2D noble metal-based nanosheets.

8. 2D NANOMATERIALS FOR HYDROGEN EVOLUTION REACTION APPLICATIONS

In recent decades, the HER has served as the bridge between fundamental surface electrocatalysis and emerging materials chemistry. At the same time, water electrolysis is one of the oldest electrochemical processes and is still employed for producing high-purity hydrogen fuel. As a result, designing high-performance HER electrocatalysts is critical for the development of clean energy at both fundamental and utilization levels. The intriguing structural and electronic properties of 2D nanomaterials provide new opportunities for exploring reaction mechanisms, especially for alkaline HER. As a result, many new studies have explored various 2D structured electrocatalysts that can efficiently catalyze the HER in both acidic and alkaline media.^{445,446} In the following sections, we summarize recent progress on the application of 2D nanomaterials for the HER. ΔG_{H^*} and band structure are two crucial factors for HER activity that are discussed in various systems throughout these sections. For brevity, we focus on typical 2D metal-free graphene-based and metallic TMDs materials which demonstrate the combination of DFT computations and experimental observations for revealing the nature of the HER.

8.1. Fundamental Principles of the HER

8.1.1. Reaction Mechanism. Although diatomic hydrogen is the only reaction product, the HER is a multi-step reaction consisting of adsorption, reduction, and desorption processes. The overall reaction and elementary steps of the HER in acidic and alkaline media are listed in Table 3.⁴⁴⁷ The “Volmer step” refers to the adsorption of hydrogen from either a hydronium ion (in acidic conditions) or dissociated water molecule (in alkaline

Table 3. HER Mechanism in Acid and Alkaline Conditions^a

	acid	alkaline	Tafel slope
overall	$* + 2\text{H}^+ + 2\text{e}^- \rightarrow \text{H}_2$	$* + 2\text{H}_2\text{O} + 2\text{e}^- \rightarrow \text{H}_2 + 2\text{OH}^-$	–
Volmer	$* + \text{H}^+ + \text{e}^- \rightarrow \text{H}^*$	$* + \text{H}_2\text{O} + \text{e}^- \rightarrow \text{H}^* + \text{OH}^-$	$b = \frac{2.3RT}{\alpha F} \approx 120 \text{ mV dec}^{-1}$
Heyrovsky	$* + \text{H}^+ + \text{e}^- + \text{H}^* \rightarrow \text{H}_2 + *$	$* + \text{H}_2\text{O} + \text{e}^- + \text{H}^* \rightarrow \text{H}_2 + \text{OH}^- + *$	$b = \frac{2.3RT}{(1+\alpha)F} \approx 40 \text{ mV dec}^{-1}$
Tafel	$2\text{H}^* \rightarrow \text{H}_2 + 2*$	$2\text{H}^* \rightarrow \text{H}_2 + 2*$	$b = \frac{2.3RT}{2F} \approx 30 \text{ mV dec}^{-1}$

^aWhere * denotes an active site on the surface of an electrocatalyst.

conditions).⁴⁴⁸ The adsorbed hydrogen (H^*) is then combined to form molecular hydrogen via either a Heyrovsky or Tafel step. Under real electrocatalytic conditions, these pathways are strongly dependent on the inherent chemical and electronic properties of the electrode surface. As with heterogeneous catalysis, rate measurement is crucial for both evaluating the performance of HER electrocatalysts and providing insightful knowledge about the HER reaction mechanism, especially for determining the rds of the overall reaction. For example, the calculated Tafel slopes from LSV polarization curves for each step in the reaction pathway are shown in Table 3.

8.1.2. Activity Descriptor. Although experimental rate measurements can provide direct evaluation of HER performance, developing new electrocatalysts requires design principles to guide proof-of-concept studies. Luckily, the past decades have witnessed the success of a descriptor-based method with a basis in DFT computations. This method is useful for understanding the activity trends of various HER catalysts, including precious metals and alloys, transition metals and their compounds, and even metal-free materials.⁸² It was found that the overall reaction kinetics of the HER on a range of surfaces is largely determined by the theoretical activity descriptor ΔG_{H^*} .^{449–451} If hydrogen adsorption is too weak ($\Delta G_{H^*} > 0$), the Volmer step will be limited, and if hydrogen adsorption is too strong ($\Delta G_{H^*} < 0$), the desorption step (via either the Heyrovsky or Tafel step) will limit the rate. Both will likely result in a poor apparent HER activity. As a result, by correlating the experimentally measured activity (e.g., j_0), and the computed ΔG_{H^*} , a volcano shaped plot can be derived based on the microkinetic model (Figure 34).^{449,450} This

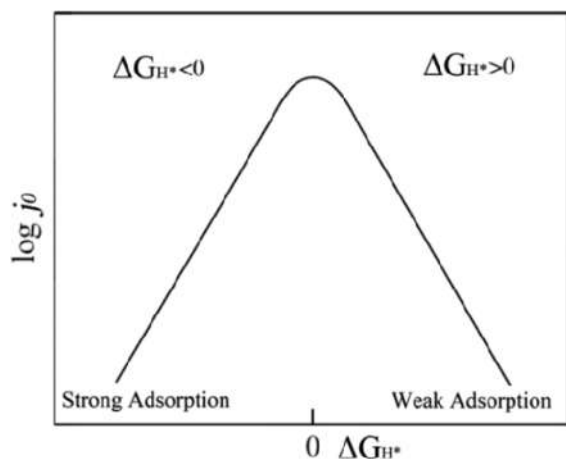


Figure 34. Schematic representation of a HER volcano plot. Reproduced with permission from ref 82. Copyright 2015 John Wiley & Sons, Inc.

relationship is quite useful because it demonstrates the trend of HER activities for a series of electrocatalysts and can prescribe parameters for the ideal HER catalyst. In Figure 34, the ideal catalyst at the peak of the volcano plot would have a ΔG_{H^*} of 0 eV while delivering the largest j_0 possible.

Although calculated ΔG_{H^*} can successfully serve as the sole descriptor for the HER in acidic solutions, its validity remains to be determined in alkaline solutions and there is still debate among the experimentalists. For example, Strmcnik et al. proposed that the hydrogen source for the HER in alkaline solutions is generated by the water dissociation process prior to the reduction step.^{175,176,448,452,453} In addition to H^* , the energetics of OH^* species also have to be taken into account

since the dissociation process is kinetically slow. On the other hand, Sheng et al. presented a series of studies on nanostructured precious-metal surfaces to show that the hydrogen binding energy (HBE) could still be the sole descriptor for HER kinetics over the full range of pH conditions. They suggested that the pH dependent behavior of HER activity is a consequence of the pH dependence of the HBE.^{454–456} However, Ledezma-Yanez et al. found that there were no clear differences in the underpotential deposited hydrogen (upd) region of the CV curves on single crystal Pt (111) surfaces obtained in acid and alkaline media.⁴⁵⁷ Therefore, they concluded that the significant pH dependence of HER activity on Pt (111) surfaces cannot be attributed to the small shift of HBE (if any) under different pH conditions. Although recent advances in nanotechnology have led to the development of many high-performing electrocatalysts for alkaline HER, the inherent causes underlying its sluggish kinetics are still debatable. Further, the nature of the HER active sites in alkaline conditions is still not fully understood. Given the complexity of alkaline HER, we mainly focus on the acidic HER in the next sections unless specifically noted.

8.1.3. Free-Energy Diagram. The free-energy diagram, containing both the thermodynamic adsorption free energies of each intermediate and the kinetic barrier between each elementary step, can present the possible extra information that cannot be taken into account by ΔG_{H^*} . For example, the overall reaction rate largely relates to the reaction barrier between two intermediate states of the rds. Therefore, we emphasize here that the combination of thermodynamic and kinetic analyses is of great importance for theoretically evaluating the performance of a HER catalyst, especially in alkaline media where there is a sluggish water dissociation step involved.⁴⁴⁸ The standard free energy (ΔG) can be calculated using eq 9.

$$\Delta G = \Delta E + \Delta ZPE - T\Delta S \quad (9)$$

where the ground-state energy ΔE can be obtained by first-principles calculations, and the change of zero point energy, ΔZPE , and entropy, $T\Delta S$, can be calculated from frequency calculations. However, some factors regarding the actual electrochemical conditions need to be taken into account. These are the electrode potential, the solution pH, solvation effects, and electric double layer effects.⁴⁵⁸ A shift can be applied to the states (initial, final, or intermediate states) involving electrons by $-ne\eta$, where n is the number of electrons, e is the electron, and η is the applied potential.³⁰⁰ Adding layers of water molecules can simulate the environment near the catalyst surface,⁴⁵⁹ and the effect of pH can be taken into account by adding protons into the water layers. Under this scheme, the energy barriers between two thermodynamically stable states can be determined by calculating the kinetic barriers for some selected unit cell sizes.⁴⁵⁹

8.2. Graphene-Based Electrocatalysts

In this section, we first introduce the mechanistic studies which use a combination of DFT calculations and experimental measurements to explore the origins of HER activity on graphene-based materials. We then summarize recent progress in the design of graphene-based HER catalysts which focuses on chemical composition control to improve performance.

8.2.1. Heteroatom-Doped Graphene. The basal plane of pure graphene is considered to be inert for the HER with a relatively large (positive) ΔG_{H^*} (1.85 eV).⁷⁰ This means that hydrogen adsorption is difficult and inhibits the HER, which agrees with experimental observations. Similar to the ORR,

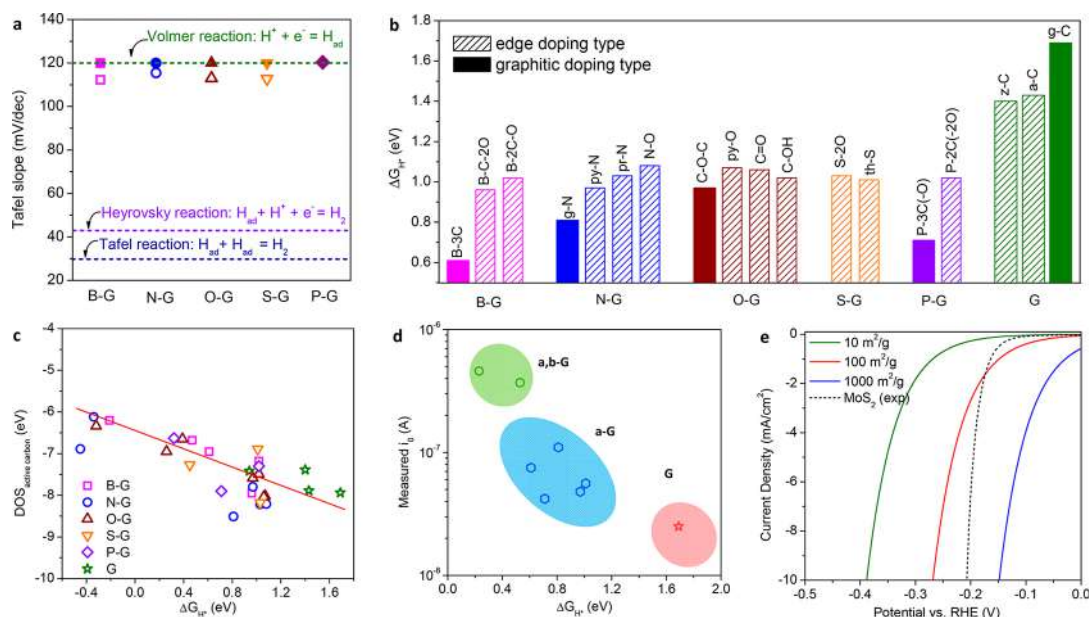


Figure 35. (a) Tafel slopes obtained from theoretical computation (hollow symbols) and experimental measurements (solid symbols) on various graphene models/samples. (b) Computed lowest ΔG_{H^*} for different models. (c) Relationship between ΔG_{H^*} and the highest peak position of DOS for the active carbon; the red line presented as a guide. (d) Volcano trend that includes pure (G), single-doped (a-G) and dual-doped (a,b-G) graphene samples. (e) Calculated HER polarization curves of graphene-based materials with different surface areas ($i_0 = 1.10 \times 10^{-21}$ A/site, doping level = 5%, mass loading = 40 μg). Reproduced with permission from ref 73. Copyright 2016 Nature Publishing Group.

doping one or more elements with different electronegativity into the carbon matrix of graphene can result in the redistribution of charge/spin in the graphene which improves its HER performance.^{70,73,225,336} Among various single heteroatom doped graphene materials, B-graphene shows the best specific HER activity. However, it is still fairly poor compared to metallic MoS₂ and Pt-based catalysts as shown in Figure 17i.⁷³ In addition, the Tafel slopes for all doped graphene samples that have been investigated are close to 120 mV dec⁻¹. This indicates that the Volmer step is the rds due to their weak hydrogen adsorption abilities, which is supported by DFT results (Figure 35a). Theoretical calculations show that although heteroatom doping can substantially increase the hydrogen adsorption strength of graphene, the ΔG_{H^*} values of all cases are still positive, indicating that adsorption is thermodynamically unfavorable (Figure 35b). Therefore, the positions of all samples are located toward the bottom of the right branch of the volcano plot (Figure 17i). To climb to the top of volcano plot through further optimizing ΔG_{H^*} , an underlying principle was clarified by Jiao et al. based on the molecular orbital theory.⁷³ They examined the DOS of the active centers for all models and found that the highest peak position of the DOS for the active carbon shows the best linear relation with ΔG_{H^*} (Figure 35c). Therefore, because the hydrogen adsorption strength on the investigated graphene models is normally weak, a peak on the DOS of the active carbon closer to the Fermi level is required to achieve a stronger H* adsorption and consequently a lower value of ΔG_{H^*} . According to this theoretical prediction, a dual doping strategy was developed to further optimize ΔG_{H^*} of graphene-based materials. For example, N,S-, N,P-, and N,B-graphene were chemically synthesized by annealing GO with selected precursors.^{70,73,460–462} As predicted, it was found that dual doped samples showed enhanced HER activities compared to single doped samples (except N,B-graphene), which agreed well with the DFT calculated ΔG_{H^*} values (Figure 35d). It is known that the apparent activity for a solid catalyst is governed by both

intrinsic activity of each active site, and extrinsic physiochemical properties related to exposing these active sites. Specifically for doped materials, the number of active sites depends on the doping level, and the accessible number of active sites is determined by the specific surface area. In principle, by tuning these two parameters, the HER performances of graphene-based materials can be improved.⁷³ For example, assuming that a sample possesses a doping level of 5%, if its specific surface area could be improved to 1000 m² g⁻¹, then the overall performance of an optimal graphene material ($\Delta G_{H^*} = 0$ eV) would be better than that of MoS₂ from the point of view of overpotential (Figure 35e). This design principle was validated by other studies. For example, Ito et al. reported that a N,S codoped nanoporous graphene with ultrahigh specific surface area (1320 m² g⁻¹) achieved an η_{10} of only 280 mV, which is comparable to the benchmarked 2D MoS₂ material.⁴⁶³

8.2.2. Single-Atom Catalyst Supported by Graphene Derivatives. Graphene, with its large specific surface area (high catalyst loading), good stability (tolerance to harsh operating conditions), and high electrical conductivity (facilitated electron transfer), is considered to be an ideal support for single-atom catalysts. Atomically dispersing metal catalytic centers on graphene, especially earth-abundant elements, could be a promising approach for producing alternative HER catalysts to precious Pt metal. Cheng et al. reported a practical synthesis method to produce isolated single Pt-atoms and clusters on N-graphene using an atomic layer deposition technique.⁶⁶ The nitrogen dopants could enhance the interaction between Pt and the carbon matrix, thus reducing atomic diffusion and agglomeration. The as-prepared single-Pt-atom catalyst exhibited a significantly enhanced mass activity that was 37.4 times greater than state-of-the-art Pt/C catalysts. DFT calculations confirmed that the excellent kinetics on this single-atom catalyst was attributed to its small activation barriers. Besides precious metals, atomic cobalt on N-graphene (Co-NG) was obtained by a simple thermal treatment of GO and small

amounts of cobalt salts in a gaseous NH_3 atmosphere.²³² The overpotential needed to deliver 10 mA cm^{-2} cathodic current density was determined to be $\sim 147 \text{ mV}$, much smaller than that for N-graphene only and cobalt supported on un-doped graphene. Therefore, the active sites in Co-NG are associated with the Co and N coordination. It was also found that a higher N doping level results in higher HER activity, suggesting that N plays a critical role in forming the catalytically active sites. Qiu et al. developed single-atom Ni catalysts anchored to nanoporous graphene via a CVD method followed by chemical exfoliation.⁴⁶¹ The as-prepared single-atom Ni catalysts displayed excellent HER activity in acidic solution with an onset potential of $\sim 50 \text{ mV}$. DFT calculations indicated that this material has a small ΔG_{H^*} of 0.1 eV , which originates from the sp-d orbital charge transfer between the Ni dopants and the surrounding carbon atoms.

8.3. Transition-Metal Dichalcogenides

To date, TMDs are the biggest and most intensively studied group of 2D HER electrocatalysts. MoS_2 is the most common TMD example, and in the next sections, we briefly introduce several methods (e.g., heteroatom doping, defect engineering, interaction engineering, phase transition engineering, etc.) that have been used to tune its ΔG_{H^*} and band structure for enhanced activity. We do not include all newly developed TMDs or similar 2D nanomaterials (e.g., FeS_2 ,¹⁵⁹ Fe-NiS ,¹⁶¹ Mo_2C ,⁴⁶⁴ H-TaS_2 , H-NbS_2 ,⁴⁶⁵ etc.), but instead focus on those TMDs whose HER mechanisms have been relatively well explored.

8.3.1. Origin of Catalytic Activity. As early as 2005, Hinnemann et al. found that the Mo ($\bar{1}010$) edge of MoS_2 possesses a ΔG_{H^*} of approximately 0.08 eV at 50% hydrogen coverage, which is very close to the optimum value of 0 eV (Figure 36a).⁵⁴ Later, it was confirmed experimentally that the MoS_2 edges are active for the HER by Jaramillo et al.⁵³ By measuring the area and perimeter length of MoS_2 on Au(111) by STM, they found that the reaction rate scaled with perimeter length rather than area (Figure 36b). This is clear evidence that the edge sites and not the basal plane sites are the active sites in MoS_2 . After the identification of the active sites for MoS_2 materials, a wide variety of chemical and/or physical strategies were developed to expose and/or extend their active edge sites.

8.3.2. Nanostructure Engineering. The earliest and the most common strategy for modifying the HER performance of MoS_2 electrocatalysts is to enlarge its specific surface area by fabricating different nanostructures such as mesostructures,²⁴⁹ nanowires,⁴⁶⁶ creating nanoporosity,^{467,468} nanosheets,⁴⁶⁹ nanoparticles, etc.^{470,471} This approach normally does not alter the electronic properties of pristine MoS_2 but can physically increase the number or fraction of electrocatalytically active sites per unit geometric area of the electrode to enhance its apparent cathodic current density. For example, Kibsgaard et al. synthesized contiguous thin films of a highly ordered double-gyroid (DG) MoS_2 bicontinuous network, which enable the surface structure to preferentially expose active edge sites (Figure 37a).²⁴⁹ The HER current density measurements showed a clear trend that the apparent activity increased with the thickness of the sample due to the enhancement of ECSA. However, the activity trend in terms of TOF was reversed; i.e., the thinner films achieved a higher TOF than the thicker ones (Figure 37b). This was due to the semiconducting nature of 2H- MoS_2 which contributed significantly to internal resistance (Figure 37c). This indicates that a balance between the exposure of more active sites, the

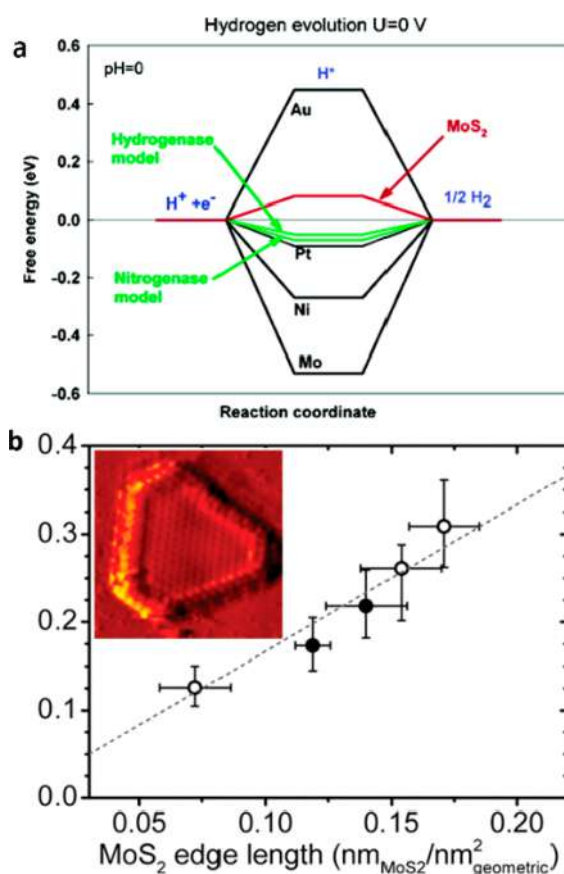


Figure 36. (a) Calculated HER free energy diagram on MoS_2 and different metals. Reproduced with permission from ref 54. Copyright 2005 American Chemical Society. (b) Relationship of j_0 with MoS_2 nanoplatelet edge length measured from STM image as shown in the inset. Reproduced with permission from ref 53. Copyright 2007 American Association for the Advancement of Science.

crystallinity, and the conductivity of TMDs should be considered when optimizing their HER activities.

Chen et al. synthesized vertically oriented core-shell nanowires with a MoO_3 core of $\sim 20\text{--}50 \text{ nm}$ and a MoS_2 shell of $\sim 2\text{--}5 \text{ nm}$.⁴⁶⁶ The MoO_3 core provided a high aspect ratio foundation that facilitated charge transport, while the conformal MoS_2 shell provided excellent catalytic activity and protection against corrosion in strong acids. As a result, the resultant product had enhanced HER activity and excellent stability. Benck et al. reported a scalable wet chemical method for the synthesis of nanostructured amorphous MoS_3 .⁴⁷² When applied for the HER, the MoS_3 material achieved an η_{10} of $\sim 200 \text{ mV}$. A series of spectroscopic studies showed that the *in situ* created MoS_2 domains may contribute to its high electrochemical activity. Kong et al. first developed MoS_2 and MoSe_2 thin films with vertically aligned layers to provide maximum exposure of edges on the film surface.⁴⁷³ Using a similar growth process, Wang et al. demonstrated that vertical layer orientation could be realized on curved and rough surfaces such as nanowires and microfibers.⁴⁷⁴ Apart from maintaining perpendicular orientation of the layers, such structures can increase the surface areas of TMDs to contribute more active sites. As a result, both these materials showed much higher HER activity compared to their bulk counterparts. Yu et al. found that the HER activity of MoS_2 decreases by a factor of ~ 4.47 for every additional layer added in the controlled growth of atomically thin MoS_2 films.¹⁴⁸ They

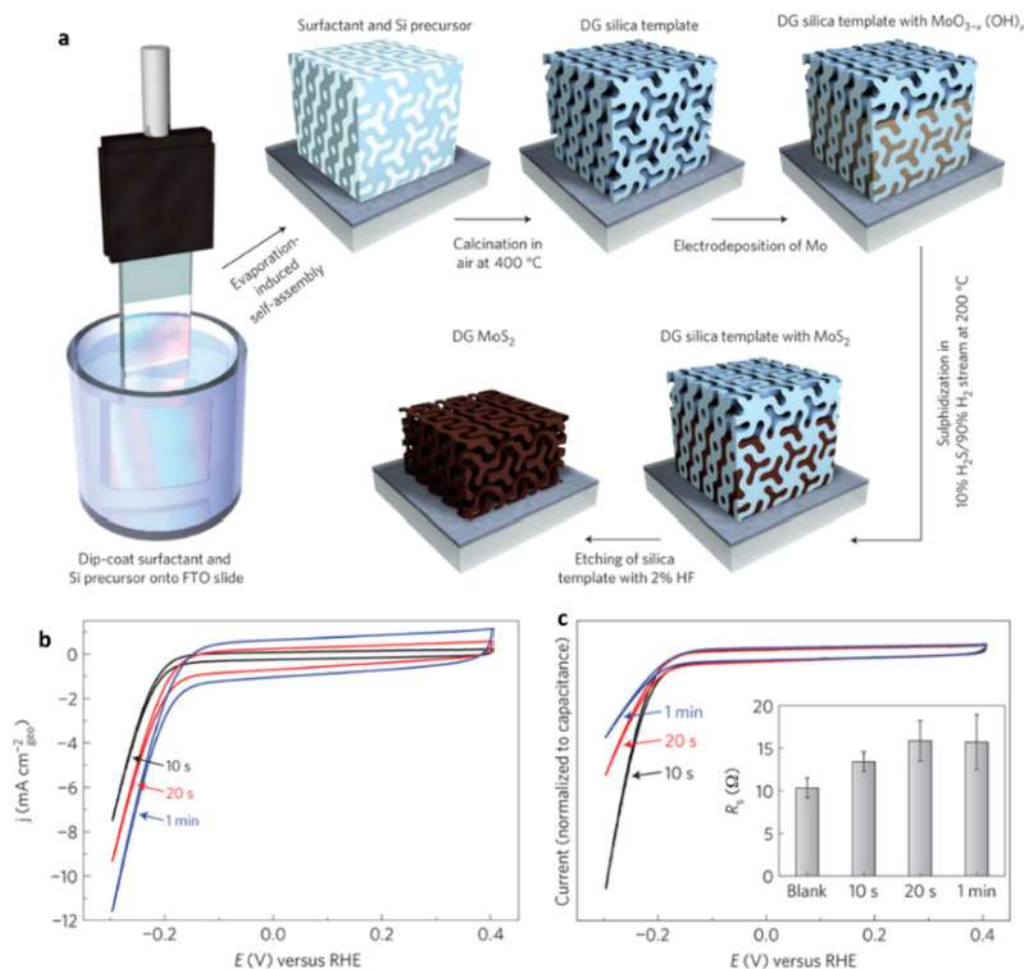


Figure 37. (a) Synthesis procedure and structural model for mesoporous MoS₂ with a DG morphology. (b) Comparison of the apparent activities on different samples. (c) Comparison of the activities normalized to the capacitance of different samples. Reproduced with permission from ref 249. Copyright 2012 Nature Publishing Group.

held the view that this layer-dependent electrocatalysis could be correlated to the hopping of electrons in the vertical direction of MoS₂ layers over an interlayer potential barrier. Therefore, as found by Kibsgaard et al.,²⁴⁹ electrical conductivity is an essential issue that should be considered when engineering the morphology of MoS₂. In the next sections, we discuss other strategies that extend the active sites of MoS₂ and, more importantly, modify its electronic properties to achieve better intrinsic performance.

8.3.3. Heteroatom Doping at the Edge/Basal Plane. As with graphene, doping heteroatoms at the edge or in the basal plane of TMDs can modify their electronic structures and consequently increase the number of active sites. Therefore, the identification of heteroatom doping sites in TMDs is crucial for revealing the effect that doping has on HER activity. Using STM imaging, Kibsgaard et al. found that first-row transition metals, like Fe, Co, Ni, and Cu, could be doped into the S-edges of MoS₂ nanoclusters and change both the geometric parameters and the intrinsic activity of MoS₂.⁴⁷⁵ Further, Bonde et al. employed DFT calculations to reveal the effect of Co doping in MoS₂ edges for HER activity.²³⁹ The results showed that for pristine MoS₂ nanoparticles, $\Delta G_{\text{H}^*} = 0.08$ and 0.18 eV for Mo- and S-edges, respectively. Incorporating Co dopants at the S-edge decreased ΔG_{H^*} to 0.10 eV, while no change was observed for the Mo-edge. Therefore, the presence of cobalt can activate the S-edges which

can then contribute to the active sites. Similar results were found for Co doped WS₂, where ΔG_{H^*} decreased from 0.22 to 0.07 eV on the S-edge after Co doping.²³⁹ Experimental measurements agreed well with the theoretical analysis, and the following HER activity trend was formulated: WS₂ < MoS₂ = Co-MoS₂ < Co-WS₂. Apart from MoS₂, Merki et al. prepared transition-metal-doped ternary metal sulfide films, M-MoS₃ (M = Mn, Fe, Co, Ni, Cu, Zn), using electrochemical methods.⁴⁷⁶ The experimental results showed that the Mn-, Cu-, and Zn-MoS₃ materials had similar or only slightly higher catalytic activity compared to pristine MoS₃, while the Fe-, Co-, and Ni-MoS₃ materials were significantly more active. However, the origin of the promotional effects of Fe, Co, and Ni is unclear from an experimental perspective.⁴⁷⁶ The reason for this is that the incorporation of Fe, Co, or Ni also results in obvious changes to the morphology of MoS₃ by increasing its surface area, which could also contribute to the enhancement of HER activity. Therefore, it seems that this promotional effect on intrinsic activity cannot be solely attributed to doping. Based on the above example, a well-defined model system with desired doping sites, identical morphology, and similar surface area to the resultant catalysts was needed to verify the transition-metal doping effect on the HER activity of TMDs. In this respect, Wang et al. prepared a series of vertically standing, edge-terminated MoS₂ nanofilms to ensure that the transition-metal dopant (Co, Fe, Ni, Cu) was restricted to the

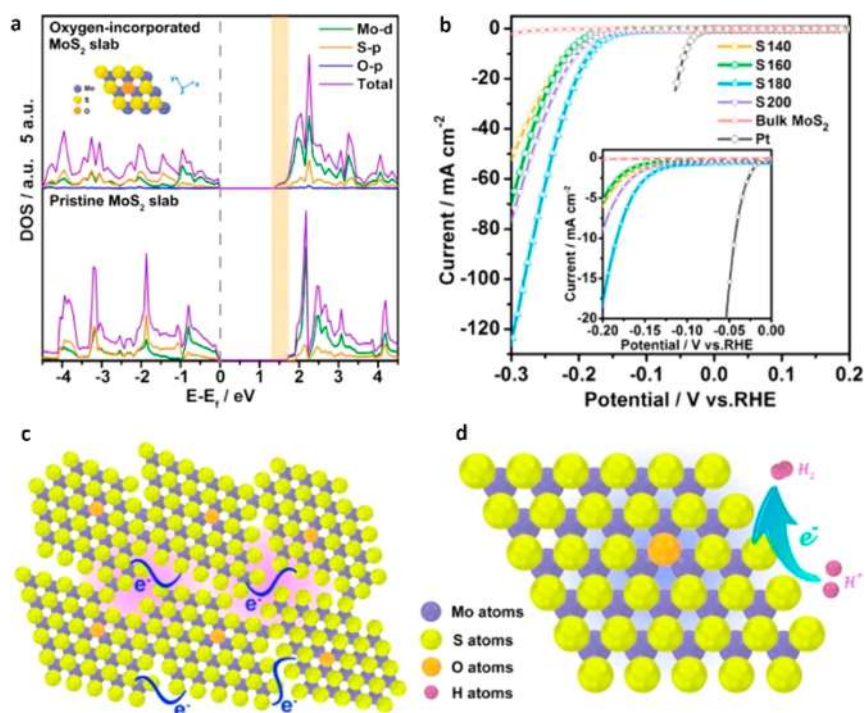


Figure 38. (a) Calculated DOS of the O-MoS₂ (top) and the pristine 2H-MoS₂ slabs (bottom). (b) HER polarization curves of various electrocatalysts. (c) Schematic representation of the disordered structure in O-MoS₂ ultrathin nanosheets. (d) Constructed model of an individual O-MoS₂ nanodomain and illustration of the HER process at the active sites. Reproduced with permission from ref 149. Copyright 2013 American Chemical Society.

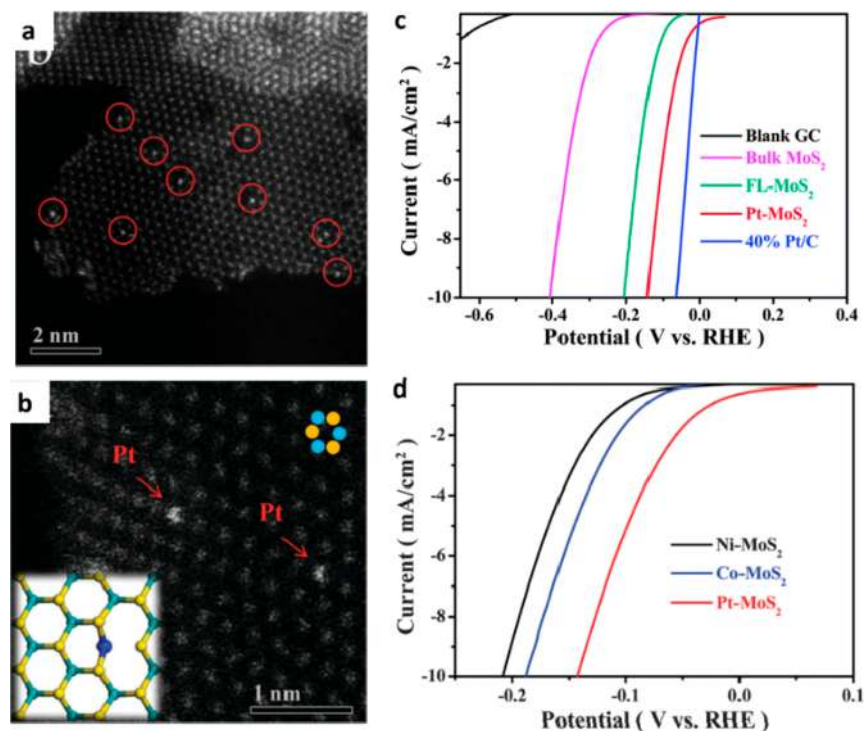


Figure 39. (a) HAADF-STEM images of Pt-MoS₂ showing single Pt-atoms (marked with red circles) uniformly dispersed in the 2D MoS₂ plane. (b) Magnified HAADF-STEM images of Pt-MoS₂ showing a honeycomb arrangement of MoS₂, and the single Pt-atoms occupying the exact positions of the Mo-atoms. (c) HER polarization curves of various MoS₂-based electrocatalysts. (d) HER polarization curves of various metal doped MoS₂ electrocatalysts. Reproduced with permission from ref 151. Copyright 2015 Royal Society of Chemistry.

edges with a fixed morphology.⁴⁷⁷ Electrochemical tests showed that the transition-metal-doped MoS₂ nanofilms had an at least 2-fold increase in j_0 . A follow up DFT study showed that the Mo-edges were un-doped in all samples, therefore indicating the

enhancement in activity should only be attributed to the modification of ΔG_{H^*} at the metal-doped S-edges.

In-plane doping of MoS₂ is also a promising way of improving its HER activity, since the basal plane is considered to be inert for

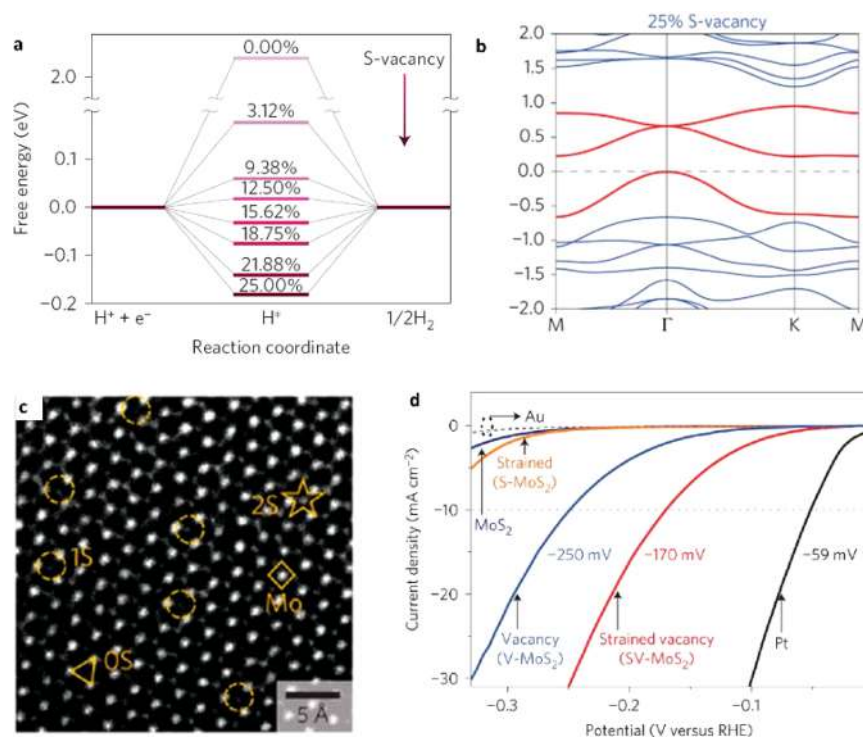


Figure 40. (a) Free energy versus the reaction coordinate of the HER for an S-vacancy range of 0–25%. (b) Band structure of monolayer 2H-MoS₂ with 25% S-vacancies. (c) HRTEM image of a 4 × 4 nm² MoS₂ monolayer with about 43 S-vacancies (~11.3% S-vacancy). (d) HER polarization curves of various electrocatalysts. Reproduced with permission from ref 250. Copyright 2016 Nature Publishing Group.

the HER. Differing from edge doping which can tune ΔG_{H^*} at the edge sites, in-plane doping can both activate the MoS₂ basal plane and narrow the band gap for enhanced catalytic activity. To date, both metal (e.g., V,⁴⁷⁸ Pt¹⁵¹) and non-metal (e.g., O,¹⁴⁹ S⁴⁷⁹) dopants have been incorporated into MoS₂ to tune its in-plane conductivity and intrinsic activity. For example, Xie et al. found that oxygen incorporation could effectively regulate the electronic structure of pristine MoS₂.¹⁴⁹ DFT calculations revealed that the DOS of the oxygen-incorporated MoS₂ (O-MoS₂) slab had a much narrower bandgap (1.30 eV) than the pristine 2H-MoS₂ slab (1.75 eV), indicating that oxygen incorporation could lead to more charge carriers and higher intrinsic conductivity (Figure 38a). As a result, the best O-MoS₂ sample had a remarkable j_0 of 12.6 $\mu\text{A cm}^{-2}$, which is almost 40 times larger than that of bulk MoS₂ (Figure 38b). The authors attributed this high HER activity to the synergistic structural and electronic modulations caused by oxygen incorporation. Particularly, (1) the disordered structure offers large amounts of unsaturated S-edges as active sites for hydrogen adsorption (Figure 38c); (2) the moderate degree of disorder provides quasi-periodic arrangement of nanodomains, leading to fast interdomain electron transport (Figure 38c); (3) the oxygen incorporation in MoS₂ enhances the intrinsic conductivity of these nanodomains and facilitates charge transfer (Figure 38d).

Given that theoretical calculations have shown that MoSe₂ edges may be more active than that of MoS₂,⁴⁸⁰ Xu et al. synthesized MoSe₂ nanosheets with S doping, which possessed a narrower bandgap (1.65 eV) compared to pristine MoSe₂ nanosheets (1.75 eV).⁴⁷⁹ Electrochemical tests showed that S-doped MoSe₂ exhibited a smaller onset overpotential and Tafel slope than pristine MoSe₂ nanosheets, due to the more active sites exposed by the small nanodomains and the enhanced charge transfer kinetics. Besides non-metallic-atom doping, Sun et al.

developed a novel intralayer vanadium doping strategy to produce semi-metallic V-MoS₂ ultrathin nanosheets with less than five atomic layers.⁴⁷⁸ Compared to pure MoS₂, V-MoS₂ had enhanced catalytic activity with smaller onset overpotential and Tafel slope. The authors attributed the enhancement of activity to the improved electrical conductivity caused by vanadium doping, which was further verified by combining DFT calculations and a series of experimental resistivity measurements. Deng et al. demonstrated that the HER activity of in-plane S-atoms of MoS₂ can also be tuned by single-metal-atom doping.¹⁵¹ Using a one-pot chemical reaction, they prepared single Pt-atom-doped few-layer MoS₂ nanosheets (Pt-MoS₂). In this system, Pt atoms were uniformly dispersed in the 2D MoS₂ plane, and one Pt-atom exactly occupied the position of one Mo-atom (Figure 39a,b). With computational techniques they confirmed that this direct replacement of in-plane Mo-atoms with Pt-atoms is the most stable configuration. Experimentally, Pt-MoS₂ showed enhanced activity compared to MoS₂, evidenced by its smaller overpotential of ~60 mV at a current density of 10 mA cm⁻² (Figure 39c). Through DFT calculations, the authors revealed that single-Pt-atom doping could activate the in-plane S-atoms for the HER with an ideal ΔG_{H^*} value, which likely accounts for its enhanced HER activity. The authors also screened MoS₂ materials with in-plane doping of more single-metal atoms using DFT. Due to the doping configuration differences of various dopants, a volcano plot was formed in which on the left side the dopant metal atoms tend to bind with four S-atoms, while on the right side, the dopant metal atoms prefer to bind with six S-atoms (Figure 10d). Experimentally, the trend of HER activity in these doping cases was Pt > Co > Ni (Figure 39d), which was in a good agreement with the calculated volcano plot.

Partially replacing S or Mo in MoS₂ with other atoms can also continuously tune their compositions and band gaps, and provides the possibility to modify the HBE and improve HER performance.^{109,481–483} The most widely studied example of partial S replacement is with Se substitution. For example, Kiran et al. prepared few-layered MoS_{2(1-x)Se_{2x}} via a high-temperature solid-state reaction, which showed enhanced HER activity compared to single units of MoS₂ and MoSe₂.⁴⁸² Gong et al. also developed a low-temperature solution-based method to synthesize MoS_{2(1-x)Se_{2x}} nanoflakes with tunable chemical compositions.⁴⁸³ It was found that when the S and Se content were equal, the as-prepared sample displayed the best HER performance due to having the most optimal band gap and ΔG_{H^*} . Yang et al. used a CVD method to prepare large area monolayers of MoS_{2(1-x)Se_{2x}} alloys with tunable band gaps that showed enhanced HER performance compared to pristine MoS₂ and MoSe₂.⁴⁸⁴ Alternatively, replacing Mo-atoms with W to form an alloyed phase heterostructure is also an effective way to improve HER performance.⁴⁸⁵ Very recently, Yang et al. developed novel Mo_{1-x}W_xS₂ nanosheets with a mixed 1T/2H structure.⁴⁸⁶ By alloying WS₂ and MoS₂ to tune the composition and phase, the composite nanosheets exhibited an enhanced HER performance. This enhancement originates the introduction of more active sites through the alloying method.

8.3.4. Defect Engineering. Intentionally introducing defects in the basal plane of TMDs can tune their band structures and result in the cracking of the basal planes to generate edges. Xie et al. reported a scalable process to engineer defects into MoS₂ surfaces and expose active edge sites.²⁴⁵ HRTEM images confirmed that there was slight rotation in the orientation of individual (100) planes, which indicated a relatively disordered atomic arrangement on the basal surface. This disordered atomic arrangement caused the cracking of the basal planes and thus resulted in the formation of additional edges. For example, the estimation of active sites revealed that the defect-rich MoS₂ nanosheets possessed a much higher density of active sites than defect-free nanosheets and bulk MoS₂. As a result, an enhanced HER activity was observed on the defect-rich sample. Similarly, Ye et al. introduced cracks and triangular holes in monolayer MoS₂ by treating pristine MoS₂ in O₂ plasma or H₂ annealing, respectively.⁴⁸⁷ By comparing the HER activities for a series of samples, it was also found that the current density increased linearly with the density of exposed edges, consistent with a previous study.⁵³

DFT calculations indicated that ΔG_{H^*} on defective MoS₂ decreased with an increased concentration of S-vacancies, and reaches the optimal value when the concentration of S-vacancies is between 12 and 16% (Figure 40a).²⁵⁰ Evidence shows that when S-vacancies are introduced, new bands appeared in the gap near the Fermi level and are responsible for hydrogen adsorption on the S-vacancies (Figure 40b). Additionally, the more S-vacancies, the closer the bands moved to the Fermi level, which explains the gradual strengthening of H binding on S-vacancy sites as shown in Figure 40a. A proof-of-concept study was carried out which introduced S-vacancies in monolayer 2H-MoS₂ nanosheets using Ar plasma treatment (Figure 40c).²⁵⁰ Electrochemical experiment results confirmed that monolayer 2H-MoS₂ with S-vacancies had better performance compared to pristine monolayer 2H-MoS₂ from both apparent and intrinsic activity perspectives (Figure 40d). This is a good validation of the DFT prediction. More recently, Tsai et al. developed a novel route (inspired by the generation of oxygen vacancies in metal oxides under cathodic current) toward generating S-vacancies on the

MoS₂ basal plane (V-MoS₂) using an electrochemical desulfurization process.⁴⁸⁸ Specifically, under a certain negative potential, sulfur atoms in the basal plane would be hydrogenated and then removed as H₂S gas to form S-vacancies. DFT calculation showed that the formation of S-vacancies in the basal plane are thermodynamically favorable at a sufficiently negative potential and the concentration of S-vacancies could be varied by changing the applied voltage. Similar to Li et al.,²⁵⁰ the ΔG_{H^*} in these V-MoS₂ models increased with the concentration of S-vacancies and reached the optimal value (0 eV) at a concentration between 12.5 and 15.62%. Electrochemical results showed that the synthesized V-MoS₂ samples had a better HER activity (e.g., larger TOF) than pristine MoS₂, and was comparable to the previously reported defective MoS₂ with S-vacancies in the same concentration range.

8.3.5. Interface and Strain Engineering. When hybridizing 2D MoS₂ with support structures (e.g., graphene and metal single crystals), the hydrogen binding on Mo-edges can be weakened.⁴⁸⁹ Therefore, interfacial engineering through hybridization could be used to tune the hydrogen binding on MoS₂ edges. In addition, it was found that the top layer of MoS₂ has a similar hydrogen binding to unsupported MoS₂, suggesting that the support effect is short-range. Electronic structure analysis revealed that the downshift in p states of S-atoms at the MoS₂ edge and the s state of the adsorbed H-atom resulted in greater filling of antibonding states and a weaker hydrogen binding.⁴⁸⁹

Guided by this prediction, a wide variety of MoS₂-based hybrids were prepared and generally showed enhanced HER activities compared to pristine MoS₂. Support materials can range from conventional 2D graphene to 3D metal foams. For example, Li et al. first reported a MoS₂/rGO hybrid that exhibited superior HER activity with a small Tafel slope of only 41 mV dec⁻¹.¹⁵⁰ In this system, the GO sheets provided a platform for the nucleation and subsequent selective growth of MoS₂, where there were interactions between functional groups on the GO sheets and Mo precursors in a suitable solvent environment. Similarly, Yang et al. reported the synthesis of WS₂/r-GO nanosheets using a one-pot hydrothermal treatment.²⁶³ The authors attributed the better performance of WS₂/rGO nanosheets (in comparison to pristine WS₂) to the formation of an interconnected conducting rGO network that likely facilitates rapid electron transfer from the electrode to the catalyst. Chang et al. reported that MoS_x supported on Ni foams and protected by graphene sheets also displayed a promising HER activity with a small Tafel slope of 42.8 mV dec⁻¹.⁴⁹⁰ The enhanced catalyst loading and highly conductive 3D graphene/Ni foam structure led to significant HER activity.

The support can further facilitate the HER performance of TMDs by the strain effect.^{147,201,491,492} Tan et al. developed a CVD method to prepare continuous monolayer MoS₂ films grown on a 3D nanoporous gold (NPG).⁴⁹¹ STEM images revealed that there were significant lattice distortions with few under-coordinated surface steps and lattice defects on the monolayer MoS₂, which may be due to the significant out-of-plane lattice strain of MoS₂ on the curved regions of the NPG. Although the density of edge sites on the continuous monolayer MoS₂ film was significantly less than typical nanostructured MoS₂ materials, the onset overpotential of the monolayer MoS₂@NPG film was still smaller than previously reported defective MoS₂ materials.^{245,487} DFT calculations indicated that the band gap of monolayer MoS₂ could be tuned by out-of-plane lattice bending induced by the NPG substrate. Moreover, this strain decreased ΔG_{H^*} to ~0.2 eV when the S–Mo–S bond

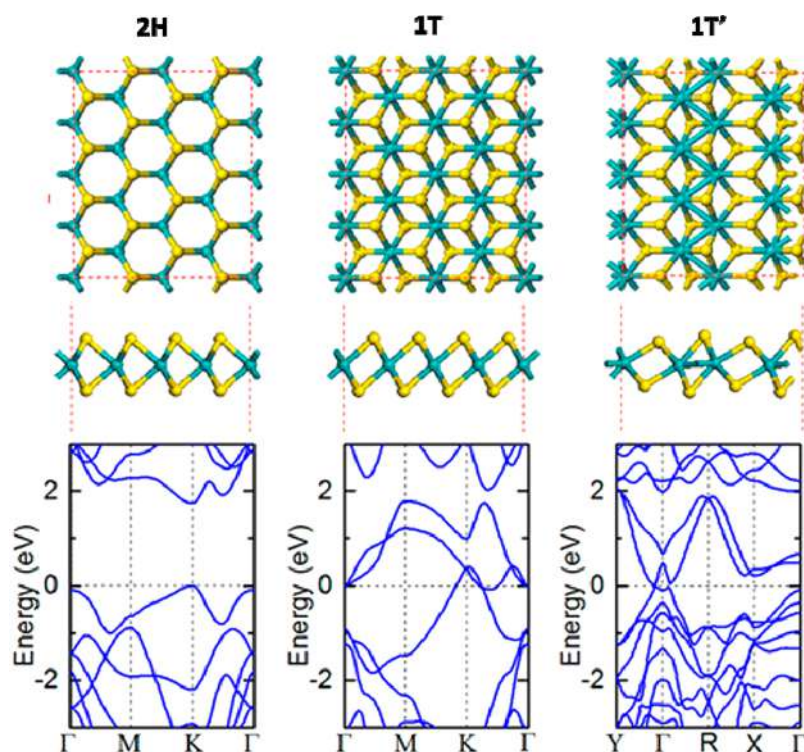


Figure 41. Top view and side view of 2H, 1T, and 1T' $4 \times 4 \times 1$ MoS₂ and their band structures. Reproduced with permission from ref 494. Copyright 2015 American Chemical Society.

angle was larger than 155° . Interestingly, Voiry et al. found that strain provided no improvement to the catalytic activity of 2H-WS₂.¹⁴⁷ For example, even with strain as high as 4%, ΔG_{H^*} remained close to ~ 2 eV on 2H-WS₂. However, they found that it significantly affects 1T-WS₂ as ΔG_{H^*} was close to zero when strain was varied between 2.0 and 3.0% on the 1T-WS₂ basal plane. They show that this was due to an enhancement of the DOS near the Fermi level. However, compressive strain did not have a significant influence on the DOS compared to tensile strain. Additionally, Li et al. systematically explored the influence of strain on the HER for 2H-MoS₂ with and without S-vacancies.²⁵⁰ DFT calculations revealed that in the absence of S-vacancies, elastic strain alone is insufficient to activate the basal plane of 2H-MoS₂, even with large applied strains of 8%. However, the optimal condition could be achieved under multiple combinations of S-vacancy concentrations and strain magnitudes. This offered flexibility for simultaneously tuning the activity and density of S-vacancy sites on the basal plane of 2H-MoS₂.

8.3.6. Phase Engineering. Phase engineering TMDs (i.e., from 2H to 1T or disordered 1T') can activate their basal planes, significantly change their band gaps, and enhance their charge transfer kinetics, simultaneously improving their HER performances.^{493,494} Gao et al. showed computationally that the band gap of semiconducting 2H- and metallic 1T'-MoS₂ is 1.74 and 0.006 eV, respectively (Figure 41), indicating that the phase transition from the 2H phase to the 1T or 1T' phase would largely improve the charge transfer ability of MoS₂.⁴⁹⁴ The overall reaction kinetics on 1T-MoS₂ were also explored by DFT calculations. Tsai et al. and Tang et al. both showed that the Volmer–Heyrovsky mechanism was favored over the Volmer–Tafel mechanism, and the Heyrovsky step is the limiting step for the HER on 1T-MoS₂, consistent with the experimentally observed Tafel slope of about 40 mV dec^{-1} .^{495,496} While identifying the

active sites, the authors found that the Mo edges of 1T'-MoS₂ had comparable HER activity with that of the 2H phase. However, the 1T' phase showed more favorable charge transfer kinetics than the 2H phase, therefore demonstrating a superior HER activity. More generally, Putungan et al. investigated HER activity on the basal plane of 1T'-MX₂ (M = Mo, W; X = S, Se, Te) nanosheets. Consistent with Gao et al., they also found that monolayer 1T'-MX₂ materials had more favorable H* adsorption and better stability compared to the 1T counterparts.^{494,497} Band structure analysis showed that 1T'-MX₂ were either metals or small gap semiconductors (0.10–0.15 eV), which was beneficial for the HER. More interestingly, the basal plane of 1T'-MX₂ could also be further activated by a longer M-X bond length induced by local tensile strain. For example, sulfides showed more optimized ΔG_{H^*} compared to selenides and tellurides.⁴⁹⁷ Correspondingly, the ΔG_{H^*} could be further tuned by the application of tensile strain due to increased states near the Fermi level.

From an experimental perspective, Lukowski et al. first reported the significant HER performance of metallic 1T-MoS₂ nanosheets chemically exfoliated via a lithium intercalation from 2H-MoS₂.⁴⁹⁸ Electron transfer from intercalated Li caused the transition from the 2H to the 1T phase, which destabilized the original trigonal prismatic 2H-MoS₂ structure and favored the octahedrally coordinated Mo-atoms. Electrochemical tests showed a significant HER activity on 1T-MoS₂ nanosheets with a small Tafel slope of 43 mV dec^{-1} , which was also consistent with DFT predictions.^{495,496} Although the efficient exfoliation of MoS₂ nanoflowers resulted in an increased density of active edge sites, the authors held the view that the phase transition into the metallic 1T polymorph is even more important for enhancing catalytic activity. More recently, Yin et al. developed a liquid-ammonia-assisted lithiation strategy to synthesize mesoporous 1T-MoS₂ nanosheets with abundant

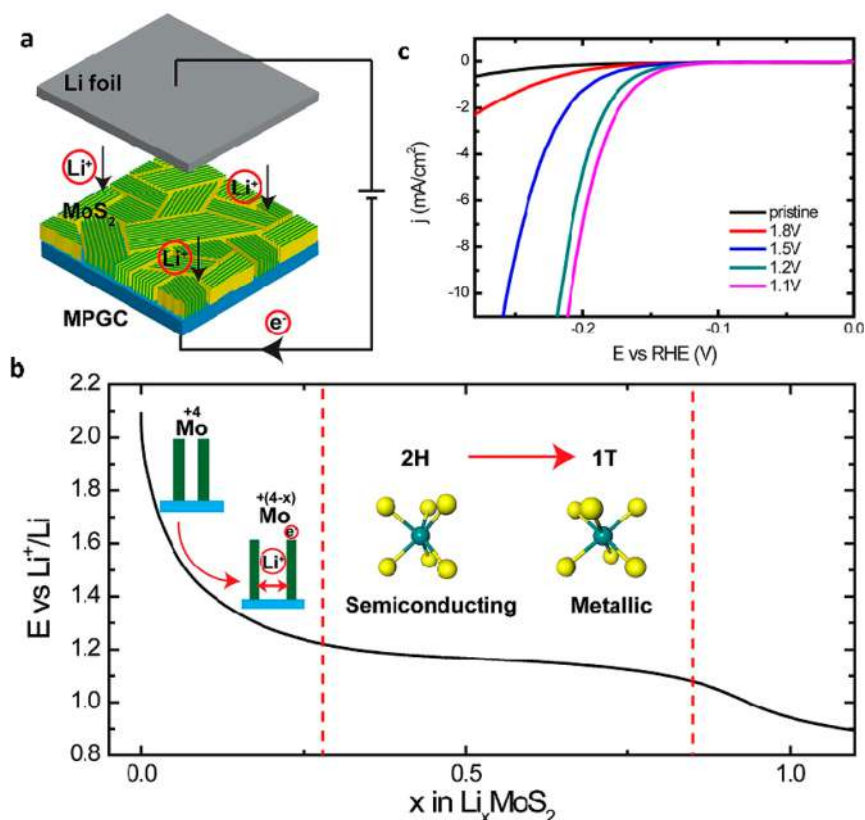


Figure 42. (a) Schematic of the battery testing system with a cathode of MoS₂ nanofilms and an anode of Li foil. (b) Galvanostatic discharge curve representing the lithiation process. The voltage monotonically drops to 1.2 V vs Li⁺/Li, after which the system undergoes a 2H to 1T MoS₂ phase transition. (c) HER polarization curves of MoS₂ samples synthesized under different potentials. Reproduced with permission from ref 255. Copyright 2013 National Academy of Sciences.

edge sites and a large concentration of S-vacancies.⁴⁹⁹ Voiry et al. also used lithium borohydride as the lithium intercalant to exfoliate bulk MoS₂ powder into single layered nanosheets.²⁵⁴ Very interestingly, it was found that the active sites on chemically exfoliated nanosheets were mainly located in the basal plane and the contribution of the metallic edges to the overall HER was relatively small.

Beyond MoS₂, 1T-WS₂ nanosheets which exhibited extraordinary catalytic activity, have been synthesized with the help of a microwave-assisted exfoliation process.^{498,500} Voiry et al. also reported the synthesis of chemically exfoliated WS₂ nanosheets from WS₂ powders via the lithium intercalation method.¹⁴⁷ The exfoliated WS₂ nanosheets consisted predominantly of the 1T structure, in which distortion and strain developed during Li intercalation. MoSe₂ nanosheets composed of up to 55% of the 1T phase were synthesized by a simple hydrothermal technique.⁵⁰¹ Ambrosi et al. systematically compared the effect of 2H to 1T transition on four TMD materials (MoS₂, MoSe₂, WS₂, and WSe₂).⁵⁰² It was found that the different catalytic properties could be linked to the efficiency of the 2H-1T transition of the materials upon intercalation. For example, WS₂ and MoSe₂ were converted more efficiently from the 2H to the 1T phase compared to MoS₂ and WSe₂, and achieved better HER activities as a result. It should be noted that Voiry et al. found that the electron injection effect, induced by coupling MoS₂ with a substrate, can significantly improve the HER activity of the 2H basal planes of monolayer MoS₂ nanosheets to be comparable to the metallic 1T phase.²⁶⁷ This work shows that the HER kinetics on TMDs are dependent on both the conductivity of the

electrocatalysts themselves and the contact resistance between the catalysts and substrates.

Besides chemical exfoliation, Wang et al. used an electrochemical method to drive the intercalation of Li⁺ ions under different potentials (Figure 42a).²⁵⁵ This method enabled the continuous tuning of the transition from the 2H to 1T phase and the oxidation state of Mo in vertically aligned MoS₂ nanosheets. This could be helpful for a systematic investigation to correlate the gradual tuning of electronic structures with HER activity. For example, it was found that deeper Li discharge processes increased the spacing of MoS₂ layers, and resulted in lower oxidation states of Mo, leading to the 2H to 1T phase transition at 1.1 V vs Li⁺/Li (Figure 42b). Unsurprisingly, samples which used lower voltages for Li intercalation had improved HER activities (Figure 42c). It is believed that the lower oxidation states of Mo and increased 1T phase accounted for the HER enhancement of the nanosheets.

8.4. Challenges for 2D Nanomaterials as Alkaline HER Catalysts

As discussed above, the HER performance on a range of TMDs can be significantly enhanced with the help of various strategies used to increase active site exposure and intrinsic conductivity. Although great progress has been achieved toward the application of TMDs for the HER, there are still some unresolved questions. First, most electrochemical experimentalists hold the view that the most active phase in MoS₂ is the 1T phase,^{498,499,502} while some theorists believed that the 1T' phase is more stable compared to the 1T phase due to the local strain.^{494,497,503} This ambiguity hinders the further improvement of HER activity via

widely applied phase engineering.⁵⁰⁴ Second, there are few works focused on systematically investigating the contribution of several factors like defects, strain, S-vacancy, and phase transition.^{147,250,493,505} As with graphene-based materials for the ORR (Figure 23d), these features always act cumulatively and contribute to fundamentally changing the electronic structure of MoS₂ and consequently its apparent HER activity (Figure 43).

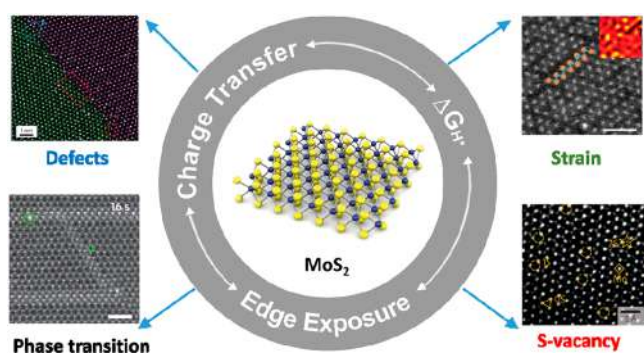


Figure 43. Scheme of the HER activity origin on different types of MoS₂-based catalysts. The scale bars for “Strain” and “Phase transition” TEM images are both 1 nm. The TEM images (clockwise, starting from the defects image) are reproduced with permission from ref 505, copyright 2013 Nature Publishing Group; ref 147, copyright 2013 Nature Publishing Group; ref 250, copyright 2013 Nature Publishing Group; and ref 493, copyright 2014 Nature Publishing Group, respectively.

For example, Yin et al. quantified the S-vacancies, phase, and edges of model mesoporous 1T-MoS₂ nanosheets to their HER activity.⁴⁹⁹ However, more effort is required for controllable design and synthesis of TMDs to elucidate the contribution of each factor individually to intrinsic activity. Third, similar to nanostructure engineering strategies, a balance between the exposure of more active sites, defects, and vacancies with the crystallinity of TMDs should be considered for obtaining desired ΔG_{H^*} and charge transfer kinetics. Fourthly, the activity and stability of catalysts should be considered simultaneously over a range of electrolyte pH. For example, Staszak-Jirkovský et al. clarified that the activity and stability of metal chalcogenides can be balanced to an appropriate level by tuning their composition.²⁶² By combining CoS_x (high activity) with MoS_x (high stability) into an amorphous composite, they designed a low-cost and pH-universal alternative to noble metal catalysts for the HER. In addition, compared with the numerous works on 2D nanomaterials for acidic HER discussed in the previous sections, there are few studies which explore the application of 2D nanomaterials for alkaline HER.^{506–508} Even though electrolyzers operating with alkaline anion exchange membranes can provide a mild environment which non-precious-metal electrocatalysts can tolerate, the HER rate in alkaline solutions is ~ 2 – 3 orders of magnitude lower than in acidic solutions.^{448,509–511} Additionally, although the acidic HER is well documented,⁴⁵¹ the mechanistic knowledge for the alkaline HER is yet to be settled.⁵¹² We hope that the intriguing structural and electronic properties of 2D nanomaterials, as well as various methods used to control their morphology and electronic structures, can provide a new platform for exploring the inconclusive alkaline HER mechanism.

9. 2D NANOMATERIALS FOR ELECTROCHEMICAL CO₂ REDUCTION APPLICATIONS

Due to the increasing depletion of fossil fuels and continued emission of CO₂, utilizing the ECR coupled with renewable energy sources (e.g., sunlight, wind, etc.) for fuel and chemical production offers a highly desirable solution to future energy sustainability and security.^{21,22,513} Although the ECR is viable from a thermodynamics perspective,²⁵ the CO₂ molecule is extremely stable, making the reaction kinetically sluggish. Therefore, efficient electrocatalysts are needed to promote the ECR.⁵¹³ Over the last few decades, extensive efforts have been devoted to the development of highly efficient catalysts for CO₂ electrolysis.⁵¹⁴ Traditional bulk metals are generally classified into three groups according to their binding strength of various intermediates and final products. Sn, Hg, Pb, and In (group I) comprise the group of formate producing metals; Au, Ag, Zn, and Pd (group II) comprise the group of CO producing metals; and Cu (group III) is capable of producing hydrocarbons and alcohols.^{514,515} Despite their activity for the ECR, bulk metals possess very limited active sites and are subject to deactivation through poisoning by impurities or some strongly bound intermediates.⁵¹⁶ In this regard, various nanostructured materials have emerged as advanced ECR catalysts in recent years.^{250,355,517–524} 2D nanomaterials, especially atomically thin nanosheets, are favorable for exposing abundant unsaturated surface atoms, thus providing a large number of active sites.^{20,248,525,526} In this section, we mainly introduce recent 2D nanomaterials, including transition metals, TMOs, TMDs, and carbon-based materials, which have been fabricated into highly efficient catalysts for the ECR.

9.1. Fundamental Principles of Electrochemical CO₂ Reduction

9.1.1. Reaction Mechanism. The ECR includes three major steps similar to other electrocatalytic processes: (1) the chemical adsorption of CO₂ molecules on the active sites of a cathode catalyst; (2) electron transfer and/or proton migration to cleave C–O bonds and/or form C–H bonds; (3) configuration rearrangement of products followed by desorption from the electrode surface and release to the electrolyte.⁵²⁷ However, the second step of the ECR is a complex process, because it is a proton-coupled multi-step reaction involving two-, four-, six-, eight-, 12-, 14-, or 18-electron reaction pathways to different products (Table 4).^{25–29} From an energy point of view, it is preferable for the ECR to proceed through proton-coupled

Table 4. Standard Redox Potentials of CO₂ Reduction to Different Products

electron transfer	reaction	E ⁰ (V vs SHE)
e ⁻	CO ₂ + e ⁻ → CO ₂ ^{•-}	-1.9
2e ⁻	CO ₂ + 2H ⁺ + 2e ⁻ → CO + H ₂ O	-0.53
	CO ₂ + 2H ⁺ + 2e ⁻ → HCOOH	-0.61
	2CO ₂ + 2H ⁺ + 2e ⁻ → H ₂ C ₂ O ₄	-0.913
4e ⁻	CO ₂ + 4H ⁺ + 4e ⁻ → HCHO + H ₂ O	-0.48
6e ⁻	CO ₂ + 6H ⁺ + 6e ⁻ → CH ₃ OH + H ₂ O	-0.38
8e ⁻	CO ₂ + 8H ⁺ + 8e ⁻ → CH ₄ + 2H ₂ O	-0.24
12e ⁻	2CO ₂ + 12H ⁺ + 12e ⁻ → C ₂ H ₄ + 4H ₂ O	-0.349
	2CO ₂ + 12H ⁺ + 12e ⁻ → C ₂ H ₅ OH + 3H ₂ O	-0.329
14e ⁻	2CO ₂ + 14H ⁺ + 14e ⁻ → C ₂ H ₆ + 4H ₂ O	-0.27
18e ⁻	3CO ₂ + 18H ⁺ + 18e ⁻ → C ₃ H ₇ OH + H ₂ O	-0.31

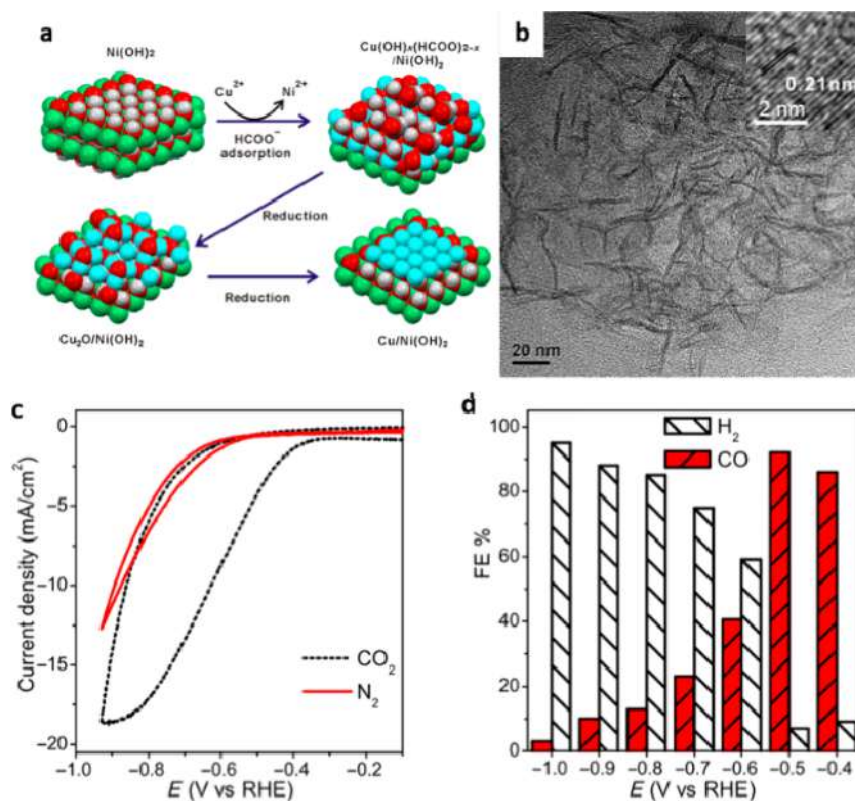


Figure 44. (a) Synthesis mechanism of Cu/Ni(OH)₂ nanosheets. (b) TEM image of the hybrid Cu/Ni(OH)₂ nanosheets. (c) CV curves of Cu/Ni(OH)₂ nanosheets in N₂-saturated and CO₂-saturated 0.5 M NaHCO₃. (d) FEs of CO and H₂ at different potentials. Reproduced with permission from ref 525. Copyright 2017 American Association for the Advancement of Science.

multi-electron transfer. However, the actual detailed reaction pathways strongly depend on many factors as discussed below.

9.1.2. Measurement Criteria. According to the Nernst equation, the ECR is more thermodynamically favorable for those reaction pathways with more positive standard redox potentials E^0 . However, the actual ECR kinetics rely on many factors, such as the electrocatalyst, electrolyte, temperature, and pressure, regardless of the position of thermodynamic equilibrium. The electrocatalyst especially has a critical role in determining the ECR mechanism and kinetics. For example, bulk transition metals are divided into three groups according to their ability of binding certain reaction intermediates. In addition to composition, a large number of studies suggest that catalyst size, morphology, crystal structure, and chemical state also have a significant impact on reaction kinetics.^{524,528–530} The electrolyte is also another important factor affecting ECR kinetics. In most cases, aqueous solutions containing inorganic salts (e.g., NaHCO₃ and KHCO₃) are employed as the electrolyte, and thus the HER ($E^0 = -0.42$ V vs SHE) becomes an undesired competing reaction.⁵²⁸ Although nonaqueous organic electrolytes can effectively suppress the competing HER and improve the solubility of CO₂, their relatively low viscosity is unfavorable for electrolyte diffusion, and their high cost and potential toxicity limit their practical application.^{26,531,532} Temperature and pressure also affect ECR kinetics by affecting the solubility of CO₂ in the electrolyte. In general, low temperature and high CO₂ partial pressure are beneficial for increasing the solubility of CO₂.^{26,533} To some extent, higher CO₂ concentrations yield larger reaction rates,⁵³⁴ but extra energy is needed to create these conditions. As a result, the majority of ECR studies have been

conducted in CO₂-saturated aqueous electrolyte at ambient conditions.

Besides onset potential, η , and j , two extra parameters (i.e., Faradaic efficiency and energy efficiency) are critical and essential for evaluating the performance of ECR electrocatalysts due to the various products formed in this process. The Faradaic efficiency of a certain product can be calculated by the following equation:

$$FE = \frac{\alpha nF}{Q} \quad (10)$$

where α is the number of electrons transferred in the pathway to a particular product, n is the number of moles produced of a particular product, and Q is the total charge passed throughout the electrolysis process. The energy efficiency under a certain η is estimated as

$$EE = \frac{E^0}{E^0 + \eta} \times FE \quad (11)$$

9.2. Transition Metals

It is well-known that the catalytic performance of a specific catalyst is closely related to its morphology.⁵³⁵ However, few studies have focused on this for ECR electrocatalysts. Recently, Kim et al. demonstrated the significance of nanostructured morphologies for developing high-performance ECR catalysts using three shape-controlled Bi nanostructures (i.e., nanodot, nanoflake, and dendrite).⁵³⁶ Even with the same chemical composition, the Bi nanostructures showed different efficiencies and selectivities for the ECR. Remarkably, the Bi nanoflakes achieved a HCOO⁻ Faradaic efficiency (FE_{HCOO^-}) of 79.5% at

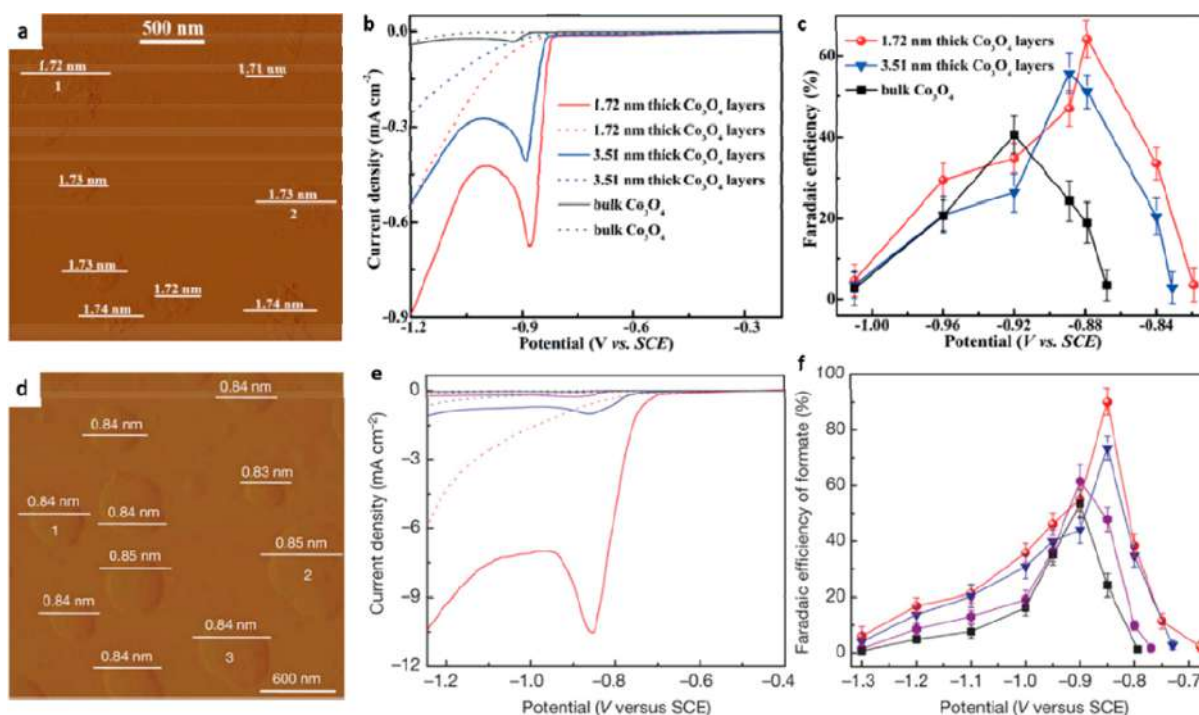


Figure 45. (a) AFM image of Co_3O_4 atomic layers with average thickness of 1.72 nm. (b) LSV curves of various electrocatalysts in CO_2 saturated (solid line) and N_2 saturated (dashed line) 0.1 M KHCO_3 aqueous solution. (c) FEs of formate for various electrocatalysts under different applied potentials after 4 h. Reproduced with permission from ref 248. Copyright 2016 John Wiley & Sons, Inc. (d) AFM image of 4-atom-thick layers of partially oxidized Co. (e) LSV curves of various electrocatalysts in CO_2 saturated (solid line) and N_2 saturated (dashed line) 0.1 M Na_2SO_4 aqueous solution. (f) FEs of formate for various electrocatalysts under different applied potentials after 4 h. Reproduced with permission from ref 20. Copyright 2016 Nature Publishing Group.

-0.4 V vs RHE, while no formate was detected for the nanodots or nanodendrites at the same potential. A simulation of the electric field distribution indicated that the 2D nanostructure with higher edge and corner site ratios caused stronger local electric fields at low overpotentials. It is believed that these stronger localized fields facilitated the ECR and improved the activity and selectivity of the Bi nanoflakes. Notably, the simulation suggested that the thinner the Bi nanoflakes, the stronger the electric field formed on the edge and corner sites. The identification of this morphological effect may provide a good foundation for establishing rational design strategies for high-performing ECR electrocatalysts.

Very recently, ultrathin $\text{Cu}/\text{Ni}(\text{OH})_2$ nanosheets, comprised of atomically thick Cu nanosheets on the surface of $\text{Ni}(\text{OH})_2$ nanosheets, were fabricated by Dai et al. and exhibited fascinating ECR properties.⁵²⁵ The nanosheets were prepared via a typical solvothermal method in DMF containing Ni^{2+} , Cu^{2+} , and HCOO^- (Figure 44a). Specifically, $\text{Ni}(\text{OH})_2$ nanosheets were first formed, and then ion-exchange between Ni^{2+} and Cu^{2+} preferentially occurred on the surface due to the smaller solubility product constant of $\text{Cu}(\text{OH})_2$ compared to $\text{Ni}(\text{OH})_2$. Meanwhile, HCOO^- was adsorbed on the newly formed $\text{Cu}(\text{OH})_2$, which was later found to be essential in stabilizing the resultant Cu nanosheets. As the reaction progressed, the deposited Cu precursor was gradually reduced into Cu nanosheets (Figure 44b). Electrochemical investigation indicated that the $\text{Cu}/\text{Ni}(\text{OH})_2$ nanosheets were highly selective in reducing CO_2 to CO at low η , and achieved a maximum FE_{CO} of 92% at -0.5 V (Figure 44c,d). In the same study, atomically thick Cu nanosheets obtained by etching the underlying $\text{Ni}(\text{OH})_2$ also achieved a high FE_{CO} of up to 89%, which demonstrates the high

intrinsic ECR activity of ultrathin Cu nanosheets. The $\text{Cu}/\text{Ni}(\text{OH})_2$ nanosheets were also found to be stable, benefiting from the stabilization of the metallic Cu by adsorbed formate, and performed for 22 h of continuous operation without noticeable performance decay. Therefore, reducing the thickness of 2D transition-metal nanosheets and protecting their surfaces with capping molecules provides new strategies for constructing efficient and durable ECR electrocatalysts.

9.3. Transition-Metal Oxides

Ever since the discovery of oxide-derived metals as a novel class of ECR electrocatalysts by Chen et al.,⁵¹⁷ TMOs have stimulated great research interest for ECR applications.^{18,38,537,538} The work done by Gao et al. was particularly pioneering and focused on enhancing the electrocatalytic activity and selectivity of 2D TMOs by reducing their thickness to atomically thin layers (Figure 45a–c).²⁴⁸ When the thickness of 2D TMOs is reduced to below 2 nm, the majority of the transition-metal atoms are exposed on the surface. Since these atoms are lower in coordination number compared with interior atoms, they can serve as the active sites for efficient CO_2 adsorption. Additionally, DFT calculations predicted that the atomic thickness also ensured a high electrical conductivity. As a prototype, 1.72 nm thick Co_3O_4 layers exhibited an ECR current density of 0.68 mA cm^{-2} at -0.88 V vs SCE, which is 1.5 and 20 times greater than those of 3.51 nm thick Co_3O_4 layers and bulk Co_3O_4 samples, respectively (Figure 45b). Additionally, a maximum $\text{FE}_{\text{HCOO}^-}$ of 64.3% was achieved at -0.88 V vs SCE for 1.72 nm thick Co_3O_4 layers, while 3.51 nm thick Co_3O_4 layers and bulk Co_3O_4 samples only achieved 51.2% and 18.5%, respectively (Figure 45c). ECSA investigations and adsorption isotherms demonstrated that the ultrathin Co_3O_4 layers could contribute a high fraction of low-

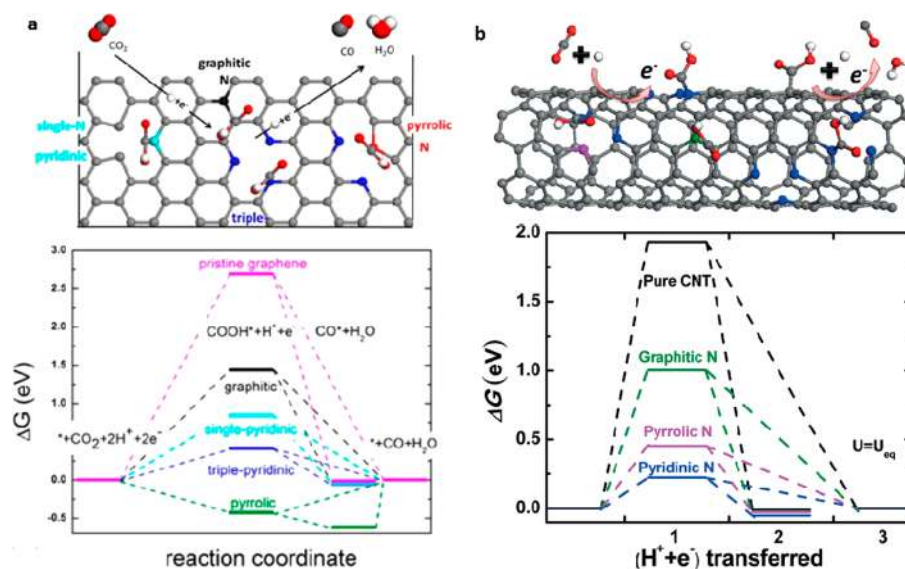


Figure 46. Schematic illustration of CO formation (top) and free-energy diagram at the equilibrium potential of CO₂ reduction (bottom) on different N defects for (a) N-graphene and (b) N-CNT. Panel (a) was reproduced with permission from ref 95. Copyright 2016 American Chemical Society. Panel (b) was reproduced with permission from ref 541. Copyright 2015 John Wiley & Sons, Inc.

coordinated surface atoms as active sites, leading to improved intrinsic ECR activity. Gao et al. later expanded these findings and used a solvothermal approach to prepare even thinner samples of oxidized Co layers with a thickness of only a few atoms (Figure 45d).²⁰ Unsurprisingly, these thinner 2D Co-based nanosheets were able to expose more abundant unsaturated surface atoms for further improved ECR activity. For example, 4-atom-thick layers of partially oxidized Co afforded a current density of up to 10.59 mA cm⁻² at an η of 0.24 V, greatly outperforming 4-atom-thick layers of Co, partially oxidized bulk Co, and bulk Co (Figure 45e). Also, at this overpotential, the FE_{HCOO-} on 4-atom-thick layers of partially oxidized Co reached 90.1% and was retained throughout a 40 h stability test (Figure 45f). The ECSA-corrected Tafel plots revealed that the 4-atom-thick layers of partially oxidized Co showed more favorable kinetics for the ECR. From comparison between the layers of partially oxidized Co and the layers of Co, it was found that atomic Co₃O₄ has much higher intrinsic activity and selectivity than atomic Co toward CO₂ reduction to formate. In addition, Gao et al. introduced oxygen vacancies (V_o) into Co₃O₄ single-unit-cell layers (average 0.84 nm thickness) and studied the correlation between the level of V_o and ECR performance.⁵²⁶ At -0.87 V vs SCE, V_o-rich Co₃O₄ single-unit-cell layers achieved a current density of 2.7 mA cm⁻² and a maximum FE_{HCOO-} of 87.6%, whereas V_o-poor samples afforded about 1.35 mA cm⁻² and a FE_{HCOO-} of 67.3%. This unambiguously demonstrated the significant role of V_o in improving ECR activity. DFT calculations proved that the presence of V_o allowed for the stabilization of the radical formate anion intermediate as the rate-limiting activation barrier was reduced from 0.51 to 0.40 eV. Hence, defect engineering on 2D TMO atomic platforms provides another effective strategy for improving ECR electrocatalysts.

9.4. Transition-Metal Dichalcogenides

Nanostructured TMDs, such as MoS₂ nanosheets and WSe₂ nanoflakes,^{154,155} have also shown attractive properties for the ECR. For example, Asadi et al. found that MoS₂ exhibited significant ECR performance in an ionic liquid (EMIM-BF₄).¹⁵⁴ In this system, the catalyst required an overpotential of only 54 mV to produce CO, and achieved a FE_{CO} of 98% at -0.76 V vs

RHE. Both theoretical and experimental results revealed that ECR activity of this material was related to its edge Mo-atoms with metallic character, high d-electron density, and relatively low work function. Following this work, they investigated other TMDs including MoS₂, WS₂, MoSe₂, and WSe₂ nanoflakes for the ECR in EMIM-BF₄ aqueous electrolyte. Out of those TMDs, the W-terminated WSe₂ exhibited the best ECR performance. Specifically, at small a small η of 54 mV, the WSe₂ nanoflakes achieved an ECR current density of 18.95 mA cm⁻², a FE_{CO} of 24%, and a TOF of 0.28 s⁻¹. In addition to its highly active edge W-atoms and robust structure, the superior ECR properties of WSe₂ were assigned in part to its significantly small charge transfer resistance.

To better study the ECR properties of TMDs, extensive theoretical studies have been carried out on MoS₂ models.^{539,540} For instance, Chan et al. proposed a method for breaking scaling relationships by creating different sites (e.g., atomic doping) for binding key reaction intermediates.⁵³⁹ For example, they indicated that doping the S edge of MoS₂ with Ni enabled the selective binding of COOH* and CHO* for improved CO selectivity.⁵³⁹ DFT studies revealed that breaking the scaling relationships was realized through binding key intermediates on different active sites.⁵⁴⁰ For example, CO* species were bound on the doped Ni site, while COOH*, CHO* and COH* species were bound on the S sites.⁵⁴⁰ Importantly, this principle may provide some direction for future ECR catalyst design and may be extended to other heterogeneous electrocatalysts. Sun et al. provided experimental evidence for such synergetic catalysis using a Mo-Bi bimetallic chalcogenide system as a highly efficient ECR catalyst.¹⁶² Here, Bi promotes the conversion of CO₂ into CO and Mo facilitates the hydrogenation of CO. As a result, the Mo-Bi bimetallic chalcogenide produced methanol with a FE_{CH₃OH} of 71.2% at -0.7 V vs SHE.¹⁶²

9.5. Carbon-Based 2D Nanomaterials

Carbon-based 2D nanomaterials, represented by N-graphene,^{93,95} and g-C₃N₄,⁵⁴² are another group of important ECR electrocatalysts. For the ECR, the N-species in the carbon framework are considered to be the origins of catalytic activity.^{17,543-545} For example, Wu et al. prepared a series of

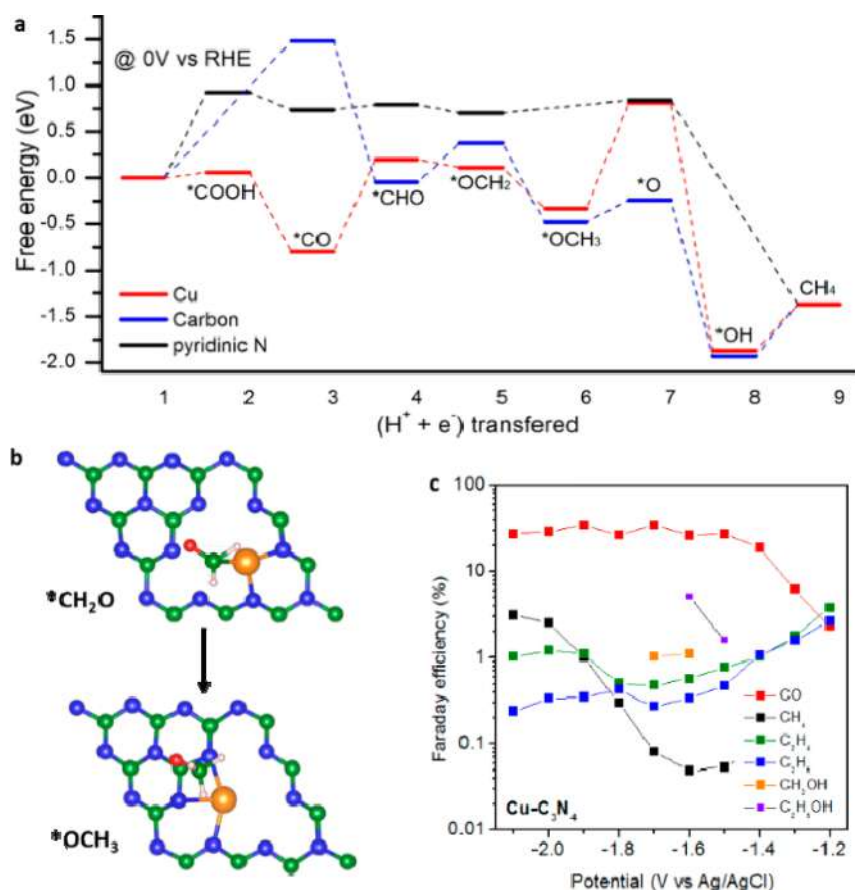


Figure 47. (a) Free energy diagram of CO₂ reduction to CH₄ on different sites of Cu–C₃N₄. (b) Migration of the active center from Cu to carbon. (c) Measured Faradaic efficiencies of various products on Cu–C₃N₄ electrodes under different overpotentials. Reproduced with permission from ref 548. Copyright 2015 American Chemical Society.

N-graphene with different N content by a CVD method under different temperatures.⁹⁵ Among them, N-graphene-800, with the highest N content, achieved a FE_{CO} of ~85% at an η of -0.47 V. A correlation of experimental and computational results confirmed that pyridinic-N in the graphene matrix is the most active site toward CO₂ reduction to CO (Figure 46a), which has also been validated in other N-carbon systems such as N-CNTs (Figure 46b).^{541,545–547} On N-doped carbon materials, the ECR pathways is typically limited to 2e⁻ reduction products (CO and formate). Wang et al. reported the selective reduction of CO₂ to formate on N-graphene synthesized using specific nitrogen sources.⁹⁴ For example, N-graphene derived from thiourea, polypyrrole, polyaniline, and dicyandiamide precursors showed no or very little activity for the ECR. However, when melamine was used as the N precursor, the N-graphene achieved a FE_{HCOO⁻} of 73% at -0.84 V vs RHE. Similar to other N-carbon materials, its excellent ECR activity and selectivity were attributed to the unique pyridinic-N species in its carbon framework. Additionally, Srekanth et al. reported that B-graphene is also active for formate generation, exhibiting a FE_{HCOO⁻} of 66% at -1.4 V vs SCE.⁹³ However, an in-depth understanding of the role of heteroatoms in the ECR mechanism is still unclear as it remains a significant challenge to precisely control the content and configurations of doped elements.

As a typical 2D nanomaterial, g-C₃N₄ in principle possesses at least two properties distinct from other N-carbon substrates.⁵⁴⁸ First, the abundant pyridinic-N species in its framework show strong affinity for CO₂ under electrocatalytic conditions.^{549,550}

Second, carbon species in g-C₃N₄ show high oxophilicity for the adsorption of oxygen-bound reaction intermediates (e.g., *OCHO, *OCH₂, *OCH₃, *OH, and *O) during the ECR, which can help steer the pathway toward high-e⁻ reduction products.¹²⁶ For example, Lu et al. prepared g-C₃N₄/MWCNTs for the ECR, in which g-C₃N₄ was covalently attached to MWCNTs via C–N bonds.⁵⁴² The hybrid exhibited considerable activity toward the ECR with a FE_{CO} of 60% at -0.75 V vs RHE. For individual g-C₃N₄ and MWCNTs samples, no obvious ECR activity was observed under the same conditions, suggesting that the origin of the ECR activity is from the covalent C–N bonds. Another important role of g-C₃N₄ for electrocatalytic reactions is its ability to coordinate a variety of transition-metal atoms into its vacancies due to its unique molecular framework.²³⁴ Very interestingly, Jiao et al. studied g-C₃N₄ molecular scaffolds to coordinate Cu (Cu–C₃N₄) and found that the hybrid possesses intramolecular synergistic catalysis with dual active centers for hydrocarbon/alcohol production.⁵⁴⁸ Systematic DFT computations indicated that the origin of this observed behavior derives from the strong binding of carbon-bound reaction intermediates to Cu (e.g., *COOH, *CO, *CHO), while the carbon in g-C₃N₄ shows stronger binding to oxygen-bound reaction intermediates (e.g., *OCH₂, *OCH₃, *O, and *OH) (Figure 47a,b). In this dual active center system, the overall reaction barriers for CO₂ reduction to hydrocarbon/alcohol products were significantly smaller than those on either Cu or C/N in g-C₃N₄ (Figure 47a,b). Experimental measurements showed that under the same potential, Cu–C₃N₄ produced a wider variety of high-e⁻

reduction products and at higher FE compared to Cu–N/C control samples. The Cu–C₃N₄ samples also demonstrated the ability to generate C2 species like C₂H₅OH, C₂H₄, and C₂H₆ (Figure 47c), which also supported the DFT findings.

9.6. Other 2D Nanomaterials

Many other 2D nanomaterials have also demonstrated promising ECR performance. For example, Bi₂O₂CO₃ (BOC) nanosheets showed a maximum FE_{HCOO⁻} of 83% at an η of 0.59 V.⁵⁵¹ Compared to metallic Bi (reduced from BOC) which exhibited a FE_{HCOO⁻} of 90% at an η of 0.99 V, the overpotential of CO₂ reduction to formate on BOC was dramatically lowered. It is likely that the carbonate in the BOC acted as the ECR intermediate through a regenerative cycle and was beneficial for reducing the overpotential to formate production. In addition, metal-doped nitrogenated carbon (M–N–C),⁵⁵² metal-porphyrin-like structures incorporated into graphene layers,⁵⁵³ and some 2D nanocomposites (e.g., rGO-PEI-MoS_x¹⁰⁷ and Cu/MoS₂⁵²⁵) have also been investigated as prospective ECR electrocatalysts. 2D COFs have been applied for the ECR due to their excellent charge carrier mobility originating from π conjugation and π – π stacking. Additionally, as they consist of porphyrins connected by strong covalent bonds, their structures are also very tunable through precursor choice. For example, Lin et al. designed and synthesized Co-COFs with precisely tuned spatial arrangements.²¹⁹ With enlarged pore volume, COF-367-Co demonstrated a maximum FE_{CO} of 90% and TOF of 290,000 h⁻¹ at an η of –0.67 V vs RHE. This was 26 times higher than that of the molecular cobalt complex. More importantly, COF-367-Co displayed outstanding durability over 24 h due to the strong covalent bonding and reticular geometry of its structure.

Parallel to intensive experimental studies in this field, theoretical calculations open up new opportunities to screen novel catalysts for the ECR.^{526,554} For example, Li et al. recently reported MXenes as prospective ECR catalysts using well-resolved DFT calculations.⁵⁵⁴ Their theoretical results indicated that MXenes from the group IV to VI series are capable of capturing CO₂ and reducing it into hydrocarbon fuels. Cr₃C₂ and Mo₃C₂ MXenes especially were predicted to be the most promising ECR candidates toward selective CO₂ conversion to CH₄. Of particular interest is that OCHO• and HOCO• radical intermediate species are predicted to form in the early hydrogenation steps through spontaneous reactions. This provides a more insightful understanding of the ECR mechanisms on these materials. Hopefully, these theoretical predictions will encourage the experimental testing of MXene, especially Cr₃C₂ and Mo₃C₂, for ECR electrocatalysis.

9.7. Challenges for 2D Nanomaterials as Electrochemical CO₂ Reduction Catalysts

Although 2D nanomaterials have experienced considerable progress as ECR catalysts, this research field is still in its infancy. First, from the experimental perspective, the current ECR mechanisms are primarily hypothesized without direct intermediate detection. This may be due to the much more complicated sub-reactions of the ECR compared to the ORR, OER, and HER. To develop improved ECR catalysts, it is necessary to obtain clear theoretical insights into detailed ECR mechanisms for more rational materials design. This is especially needed for tuning ECR efficiency and selectivity, which are highly potential and material dependent. In addition, stability is another issue for ultrathin 2D nanomaterials, as the majority of ECR candidates display activity decay within 100 h of operation.

Lastly, the poor selectivity of these materials leads to the generation of various gas and liquid products. Therefore, significant work must be undertaken to improve the selectivity of 2D nanomaterials for the efficient production of one distinct product.

10. 2D NANOMATERIALS FOR OTHER REACTIONS AND BEYOND

Other than reactions in the water and carbon cycles that can be efficiently catalyzed by 2D nanomaterials, there are a multitude of other emerging energy conversion reactions such as the nitrogen reduction reaction (NRR), the urea oxidation reaction (UOR), the methanol oxidation reaction (MOR), and the formic acid oxidation reaction (FAOR). Compared to oxygen electrode and hydrogen electrode reactions, the nature of electrocatalysis and corresponding electrocatalysts for these reactions is relatively less explored.¹ However, several of them are of particular importance for safe and high-efficiency energy conversion systems. For example, liquid fuels such as methanol and formic acid can be applied in the anode of PEMFCs to produce electricity.^{555,556} These liquid fuels have largely expanded the energy resources for fuel cells as they can be easily derived from biomass.⁵⁵⁷ Furthermore, direct-methanol/formic acid fuel cells (DMFCs/ DFAFSs) are much safer than hydrogen-based fuel cells due to their safer transportation. Therefore, developing high-performance electrocatalysts for the electrochemical oxidation of these fuels is highly desirable. On the other hand, the nitrogen cycle is becoming increasingly important in the modern energy cycle as ammonia (NH₃) is a safer energy carrier compared to hydrogen.^{558,559} As a result, electrocatalytic NRR and UOR are becoming ever more important in electrocatalysis research. To date, various 2D electrocatalysts have displayed significant performance for these advanced reactions. In this section, we summarize the application of 2D nanomaterials based on the fundamental considerations required for these important electrocatalytic processes.

10.1. Nitrogen Cycle

Beyond the carbon cycle and water cycle, the nitrogen cycle is the next most important energy cycle in nature.^{1,560,561} Organic and inorganic compounds of nitrogen feature prominently in many biological, environmental, and industrial processes. In the natural nitrogen cycle, atmospheric nitrogen is primarily converted into inorganic bio-available compounds through enzymatic reactions.⁵⁶² Among these compounds, NH₃ is one of the most important chemicals to society. In industry, the main route to NH₃ is through the Haber–Bosch process. Considering the huge energy consumption of this process and the great potential for NH₃ use in future energy systems, electrocatalytic NRR is becoming increasingly important in realizing low-cost artificial nitrogen fixation. In this section, we summarize recent 2D electrocatalysts for the UOR and NRR, which are two energy-related processes in the nitrogen cycle.

10.1.1. Urea Oxidation. Urea (CO(NH₂)₂) is a promising hydrogen storage material because of its high energy density (16.9 MJ L⁻¹), low cost, chemical stability, and low toxicity along with the fact that it is easily stored and transported. Meanwhile, urea fuel cells that utilize the UOR (CO(NH₂)₂ + 6OH⁻ → N₂ + 5H₂O + CO₂ + 6e⁻) and ORR at the anode and cathode, respectively, would be an efficient method of generating power from fertilizer urea, urine, and wastewater.⁵⁶³ Urea is also a promising chemical for hydrogen generation in electrolyzer cells. During the electrochemical UOR in alkaline media, N₂ and CO₂

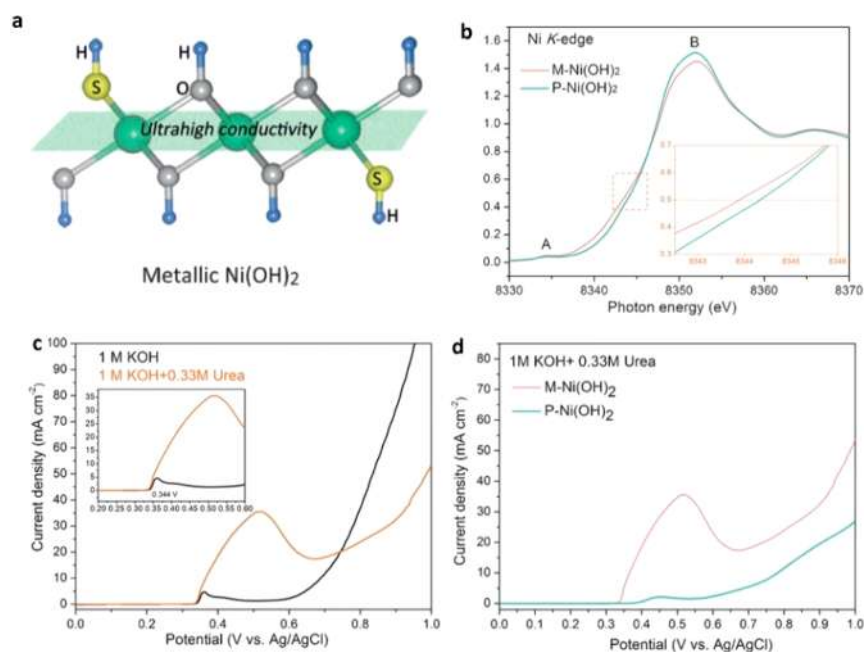


Figure 48. (a) Schematic illustration of the sulfur incorporation into $\text{Ni}(\text{OH})_2$. (b) Ni K -edge XANES of two different $\text{Ni}(\text{OH})_2$ nanosheets. (c) LSVs of M- $\text{Ni}(\text{OH})_2$ under different conditions. (d) LSVs of two different $\text{Ni}(\text{OH})_2$ nanosheets. Reproduced with permission from ref 568. Copyright 2016 John Wiley & Sons, Inc.

gases are generated from the anode, while water is reduced at the cathode producing valuable hydrogen gas via the HER.⁵⁶⁴ The equilibrium potential of the electrochemical UOR is 0.37 V vs RHE, which is much lower than the equilibrium potential of the OER (1.23 V vs RHE).⁵⁶⁵ As a result, the UOR is in principle a more efficient process for producing hydrogen via “water splitting”. However, the UOR requires high-performing electrocatalysts due to its sluggish kinetics and complicated gas evolution steps. Usually, noble metal-based catalysts, such as Pt, Rh, and Pd, are required to catalyze the UOR at adequate reaction rates. However, the high cost of these catalysts hinders their large-scale application.

To date, various 2D nanomaterials (such as TMOs, TMHs, and MOFs) with different sizes, thicknesses, conductivities, and active site oxidation states have been developed for electrochemical UOR.^{76,77,565–569} Similar to other 2D electrocatalysts, defects in these materials are commonly regarded as the active sites for the UOR. As a result, thickness and lateral size are very important factors for tuning their UOR activities.^{77,567} Chen et al. demonstrated that small-sized MnO_2 nanosheets had a higher UOR activity compared to large-sized MnO_2 nanosheets.⁷⁷ Specifically, small size MnO_2 nanosheets (50 to 200 nm) demonstrated excellent UOR performance, requiring a potential of 1.33 V vs RHE to produce a current density of 10 mA cm^{-2} , which was significantly better than the large size nanosheets (500 nm to several micrometers). This work demonstrated that rich defects, thickness, and exposed edges are important factors for designing UOR electrocatalysts. Additionally, most 2D nanomaterials developed for the UOR have been transition-metal oxides/hydroxides, which suffer from low electrical conductivity. Considering the UOR is a six-electron transfer process with sluggish reaction kinetics, tuning the conductivity of 2D nanomaterials is important for developing high-performance UOR electrocatalysts. In this regard, Zhu et al. used S doping to engineer the electronic structure $\text{Ni}(\text{OH})_2$ nanosheets to produce nanosheets with metallic character (M- $\text{Ni}(\text{OH})_2$;

Figure 48a).⁵⁶⁸ XANES results showed an increased electron concentration in M- $\text{Ni}(\text{OH})_2$ compared to pristine $\text{Ni}(\text{OH})_2$ (P- $\text{Ni}(\text{OH})_2$), resulting in an enhanced conductivity (Figure 48b). Electrochemical tests showed that the high valence state NiOOH species were the real active sites for the UOR (Figure 48c). As expected, metallic M- $\text{Ni}(\text{OH})_2$ nanosheets with sulfur incorporation had a higher UOR activity and stability than P- $\text{Ni}(\text{OH})_2$ (Figure 48d). This work elucidates the significance of conductivity in improving the catalytic performance of 2D nanomaterials for the UOR. It is well-known that the high oxidation state of transition-metal species can facilitate oxidation reactions like the OER.^{83,570,571} Inspired by this concept, Zhu et al. investigated UOR performance on 2D Ni-based MOF (Ni-MOF) nanosheets with a high nickel oxidation state.⁷⁶ It was found that the organic ligands of benzenedicarboxylic acid could act as electron acceptors which cause electron redistribution from Ni to O and a higher oxidation state of Ni cations in the Ni-MOF. As a result, the Ni-MOF exhibited significant UOR performance, requiring a potential of 1.36 V vs RHE to produce a current density of 10 mA cm^{-2} , which is better than that of $\text{Ni}(\text{OH})_2$ nanosheets and commercial Pt/C catalysts. This work shows that the high oxidation state of active sites can also facilitate the UOR process, and may be extended to other 2D electrocatalysts.

10.1.2. Nitrogen Reduction Reaction. As an energy carrier, NH_3 is one of the most important chemicals in the electrocatalytic nitrogen cycle.^{562,572,573} NH_3 is also becoming an important carbon-free energy storage intermediate and widely used in producing various chemicals.^{574,575} The Haber–Bosch process, which uses Fe- or Ru-based catalysts to synthesize NH_3 using gaseous N_2 and H_2 at high temperatures and pressures, is the main method for industrial NH_3 production.^{561,576} This process consumes $\sim 1\%$ of the world’s annual energy, 3–5% of the world’s annual natural gas production, and releases large quantities of CO_2 into the atmosphere.⁵⁶¹ Alternative processes for NH_3 production, such as biological N_2 fixation and

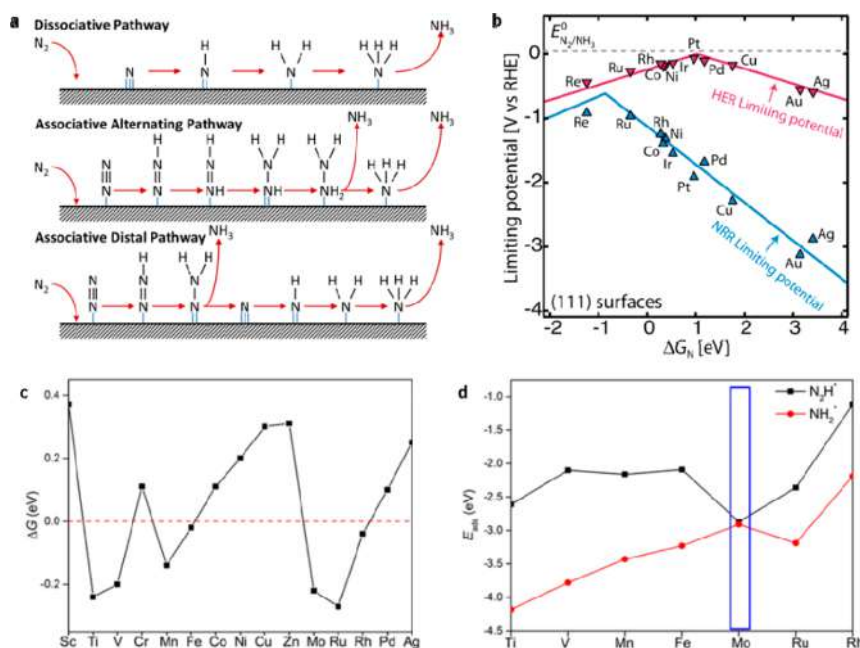


Figure 49. (a) Schemes of the NRR via different pathways. Reproduced with permission from ref 579. Copyright 2017 Elsevier. (b) Volcano plot for the NRR on a range of metals, with that of HER overlaid for comparison. Reproduced with permission from ref 1. Copyright 2017 American Association for the Advancement of Science. (c) Calculated Gibbs free energies of N₂ molecule adsorption and (d) N₂H* and NH₂* species on various single transition-metal atoms supported by defective BN nanosheets. Reproduced with permission from ref 580. Copyright 2017 American Chemical Society.

geochemical processes, suffer from relatively slow reaction rates and poor control.⁵⁷⁷

Proton-assisted electrocatalytic NRR ($\text{N}_2 + 6\text{H}^+ + 6\text{e}^- \rightarrow 2\text{NH}_3$) at ambient conditions offers relatively high efficiency for NH₃ production.^{558,561,578–581} More importantly, the NRR system can be easily integrated with renewable solar and wind energy into an environmentally benign process for NH₃ production.^{559,578} However, due to the high energy required to break the strong triple bond (N≡N bond energy of 940.95 kJ/mol) into elemental nitrogen,^{553,573} this promising approach generally suffers from relatively low catalytic activity and undesired byproducts like N₂H₄ and N₂H₂, which are toxic and reduce selectivity toward NH₃.^{582,583} Like the ORR, NRR mechanisms can also be categorized into dissociative and associative mechanisms (Figure 49a).^{561,579} Specifically, in the dissociative mechanism, the triple bond of the nitrogen molecule is broken before any addition of hydrogen occurs, leaving two adsorbed N-atoms on the catalyst surface. While in the associative mechanism, the two N-atoms remain bound to each other and the triple bond is cleaved while each N undergoes hydrogenation. The hydrogenation process in the associative mechanism can also occur through two ways (Figure 49a). In the associative alternating pathway, single hydrogenation occurs in turn on the two N-atoms on the catalyst surface, and the second NH₃ molecule is released following release of the first one. In the associative distal pathway, hydrogenation occurs preferentially on the N-atom farthest away from the catalyst surface, leading to the release of the distal NH₃ molecule first. The hydrogenation process of the other bound N then proceeds to produce the second NH₃ molecule.

Like other electrocatalytic processes, a volcano plot of different transition-metal surfaces has been constructed through DFT calculations for the NRR (Figure 49b).⁵⁸⁴ According to this framework, the design principle for NRR catalysts is to balance the adsorption energy of N₂ with the protonation energy of NH₂* to form NH₂* or the removal of NH₂* as NH₃. Meanwhile,

competition from the HER needs to be avoided.¹ Catalysts near the top of the volcano plot, metals such as Ru, Rh, and Re, bind N₂ neither too strongly nor too weakly. However, the large theoretical overpotentials of these metals still limits their performance. Further DFT studies suggest that transition-metal nitrides, such as VN and ZrN, are very suitable for the NRR with high activity at low onset potentials.^{1,585} Overall, the following criteria should be considered for NRR electrocatalyst design: (1) the catalyst should facilitate the chemisorption of N₂ molecules for sufficient activation of its inert N≡N triple bond and (2) the catalyst should selectively stabilize N₂H* and (3) destabilize NH₂* species to reduce the overpotential required.^{580,584} Following these criteria, Zhao et al. reported DFT calculations for single transition-metal atoms anchored on defective h-BN monolayers for the NRR.⁵⁸⁰ The screening process showed the ΔG values of N₂ adsorption on anchored Sc, Cr, Co, Ni, Cu, Zn, Pd, and Ag were positive. This suggests that these anchored transition-metal atoms are not appropriate for NRR electrocatalysts due to their poor ability to activate N₂ (Figure 49c). Ti, V, Mn, Fe, Mo, Ru, and Rh were found to have negative adsorption energies. Therefore, these metals are identified as candidates that should be considered further for the NRR. Although having a negative N₂ adsorption energy, Rh-atoms are excluded from this list due to its very weak stabilization of N₂H* species (Figure 49d). Similarly, Ti-, V-, Mn-, and Ru-atoms are also not eligible due to their relatively strong interaction with NH₂* (Figure 49d). From this screening, Mo-atoms on defective BN nanosheets were found to be the best electrocatalyst for the NRR, satisfying all three screening criteria.

It is worth noting that current studies on the NRR mainly rely on theoretical calculations. Therefore, 2D nanomaterials for the NRR is a relatively new research field with limited examples. Of those explored, Li et al. developed a 2D hybrid composite of amorphous Au nanoparticles, CeO₂, and rGO for the NRR.⁵⁸⁶ The noble metal content of the resultant catalyst was low (1.31 wt% Au) and the existence of CeO_x promoted the formation of

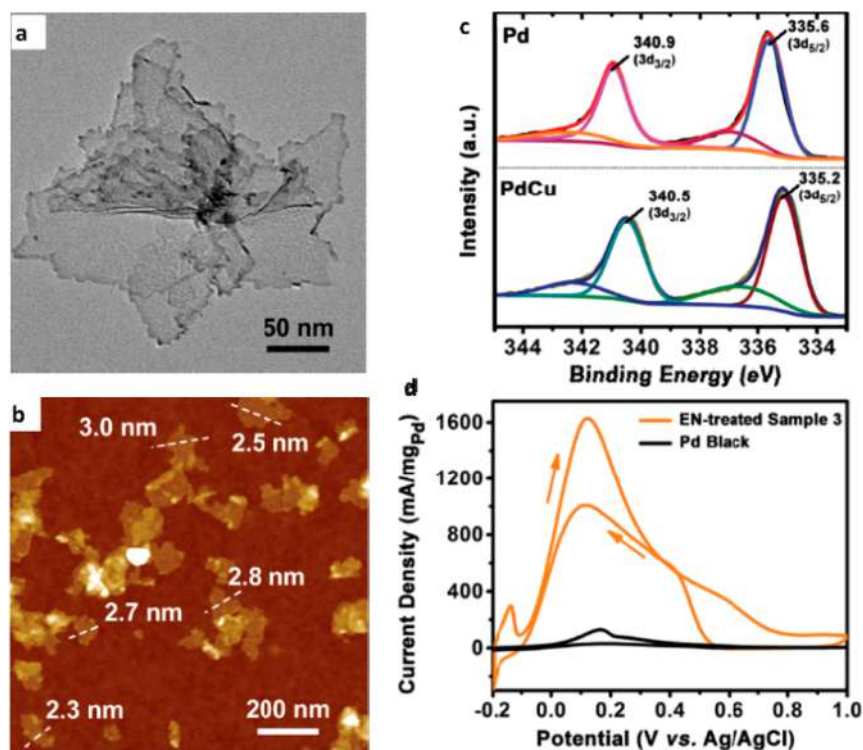


Figure 50. (a,b) TEM and AFM image of ultrathin PdCu alloy nanosheets. (c) XPS analyses of Pd 3d in pure Pd and PdCu nanosheets. (d) CV curves of treated PdCu nanosheets and Pd black. Reproduced with permission from ref 47. Copyright 2017 John Wiley & Sons, Inc.

amorphous/low-crystalline Au nanoparticles. At a potential of -0.2 V vs RHE, the NH_3 generation rate and Faradaic efficiency on this catalyst was $8.3 \mu\text{g h}^{-1} \text{mg}^{-1}$ and 10.1%, respectively. Further, no hydrazine was detected. This significant catalytic performance is even comparable to the yields and efficiencies under high temperatures and/or pressures.^{577,587,588} For the photocatalytic NRR, Zhao et al. demonstrated that LDH nanosheets could be used directly as photocatalysts for artificial dinitrogen fixation under ambient conditions. The oxygen vacancies of the LDH nanosheets enhanced the adsorption and activation of N_2 and H_2O , which contributed to their excellent photocatalytic NRR activity.^{589,590} Additionally, 2D BiOBr nanosheets also exhibited high photocatalytic NRR performance as a result of oxygen vacancies on their exposed surfaces.⁵⁶⁰ Inspired by these works, it may also be beneficial to control the O vacancies in 2D electrocatalysts for improving NRR electrocatalysts.

10.2. Oxidation of Carbon Fuels

Apart from the electrode materials, commercialization of H_2 -fed PEMFC technology is limited by the high cost of hydrogen containment, the potential dangers in the transport of hydrogen, and its low gas-phase energy density, despite many years of intense research.⁵⁹¹ Consequently, new fuel cells using liquid fuels (e.g., formic acid and methanol) are obtaining increased interest. Furthermore, when combined with the ECR using renewable wind or solar energy to produce carbon-based fuels, a sustainable energy cycle can be realized, which is very important for the balance of greenhouse gases.⁵⁹² In this section, we summarize the development of various 2D nanomaterials for the MOR and FAOR processes.

10.2.1. Oxidation of Methanol. Using the same basic cell construction as PEMFCs, DMFCs can convert methanol directly into electricity via the MOR ($\text{CH}_3\text{OH} + \text{H}_2\text{O} - 6\text{e}^- \rightarrow 6\text{H}^+ +$

CO_2) at the anode and the ORR at the cathode.^{592,593} Previously, the commercialization of DMFCs was hindered by two factors: significant cost associated with precious-metal electrocatalysts (e.g., Pt) and stability of the anode operation.^{589,594,595} For example, Pt is an ideal candidate for the MOR. However, it is very expensive and has low tolerance to some reaction intermediates such as CO, leading to the loss of electrocatalytic activity within a few hundred seconds of operation.^{589,595} A conventional method used to solve this problem is by utilizing alloys of Pt and oxophilic metals.^{589,595} For instance, in the most successful and widely studied Pt–Ru binary system, Ru assists the dissociative adsorption of water molecules to form OH species on its surface, which then promote the oxidation of CO molecules on neighboring Pt sites and thereby facilitate the regeneration of active sites. Therefore, two design principles for MOR electrocatalysts have typically been employed: (1) balancing the activity of Pt with the OH adsorption energy of co-catalysts; (2) controlling the distribution and morphology of noble metal nanostructures on advanced support materials.

Graphene is a candidate with great potential for the MOR due to its high surface area, superior conductivity and excellent stability.⁵⁹⁶ Zhang et al. reported a N-doped carbon nanotube and graphene hybrid nanostructure (NCNT-GHN) as a carbon platform on which PtRu nanoparticles (2–4 nm in size) were well-dispersed.⁵⁹⁷ Due to the large electron affinity of nitrogen, stronger anchoring and uniform dispersion of the noble metal nanoparticles was achieved through the activation of nitrogen-neighboring carbon atoms in the NCNT-GHN support.⁵⁹⁸ As a result, PtRu/NCNT-GHN showed a much higher oxidation peak current density compared to commercial PtRu/C and Pt/C catalysts with the same mass loading. Besides Ru, Huang et al. developed a Pt/Ni(OH)₂/rGO ternary hybrid based on the optimal interaction between Ni(OH)₂ and *OH species.^{589,595} In this system, Ni(OH)₂ facilitated the oxidative removal of CO

from the Pt active sites and rGO provided high electrical conductivity needed for fast electrocatalysis. As expected, Pt/Ni(OH)₂/rGO exhibited a MOR peak current density of 1236 mA mg⁻¹_{Pt}, which is better than commercial Pt/C catalysts. Additionally, Pt/Ni(OH)₂/rGO also had good stability due to the optimal interaction of Ni(OH)₂ with OH species. Very interestingly, the oxidative removal process of CO on Pt/Ni(OH)₂/rGO followed the Langmuir–Hinshelwood adsorption mechanism with faster kinetics and not the Eley–Rideal adsorption mechanism which is usually observed.

10.2.2. Oxidation of Formic Acid. Compared to DMFCs, DFAFCs which utilize the FAOR ($\text{HCOOH} \rightarrow \text{CO}_2 + 2\text{H}^+ + 2\text{e}^-$) as the anode reaction are advantageous due to their use of low-toxicity reactants, higher kinetic activity, and low crossover effect through the PEM.⁵⁹¹ Accordingly, the development of active electrocatalysts for the FAOR is becoming an active area of research. Recently, some studies demonstrated that ultrathin 2D nanomaterials, especially 2D metals, exhibited excellent performance for the FAOR due to their quantum size and surface effects.^{47,193,195,599} Huang et al. developed freestanding 2D Pd nanosheets for the FAOR which showed an activity enhancement of 2.5 times compared to Pd black catalysts.¹⁹³ This work demonstrated that highly exposed surface area is the most important advantage of 2D electrocatalysts for the FAOR. Another promising design strategy for FAOR electrocatalysts is the preparation of 2D metal alloys to enhance activity and stability, and to reduce the use of precious metals. For example, Yang et al. developed ultrathin PdCu alloy nanosheets with an average thickness of 2.8 ± 0.3 nm (Figure 50a,b).⁴⁷ The atomic ratio of Cu and Pd could be tuned from ~ 0.14 to ~ 0.56 by controlling the precursor molar ratio. It should be noted that the metal alloy had a different electronic structure from the parent metals, owing to the smaller electronegativity of Cu. (Figure 50c).⁵⁹⁵ The sample with a Cu/Pd ratio of 0.37 ± 0.01 had the largest ECSA of 137.6 ± 13.6 m² g⁻¹ and a high mass activity of 1628.3 ± 41.4 mA mg⁻¹. The electrocatalytic performance of these PdCu nanosheets was much higher than that of commercial Pd black (Figure 50d), due to their ultrathin morphology, unique electronic structure, and synergistic effect between Pd and Cu.

11. CONCLUSIONS AND OUTLOOK

Advanced energy conversion systems, such as fuel cells and (photo)electrocatalytic water splitting, represent the next generation of power and fuel production processes. Toward commercialization of these technologies, a series of high-performance electrocatalysts are required with fast reaction kinetics and high yields. Therefore, profound insights into the fundamental principles, concepts, and knowledge behind electrocatalysis are imperative for the molecular design of these electrocatalysts. For typical water cycle processes like the ORR and OER, the main bottleneck is their sluggish kinetics. Meanwhile, current commercial precious-metal-based electrocatalysts for these processes suffer from high cost and inadequate stability. For the carbon cycle, the ability to tune catalyst selectivity for a specific ECR product is the central issue. In the past decade, the development 2D nanomaterials and their application in electrocatalysis have revolutionized the unique role of these materials for next-generation clean energy systems. We have summarized recent progress in emerging 2D nanomaterials for a wide variety of energy-related types of electrocatalysis. Aspects such as catalyst design principles, advanced approaches in determining active sites and intermediates, and various engineering strategies have been highlighted through numerous

examples. Electrocatalytic applications of various 2D nanomaterials including metals, metal compounds, and non-metallic materials for the water cycle and carbon cycle have been reviewed systematically. Among these examples, the significance of merging computational quantum chemistry and experimental nanotechnology for 2D electrocatalyst design and fabrication has been especially highlighted.

With development beyond heteroatom-doped graphene, a wide range of new 2D electrocatalysts have shown great potential for breaking through the current bottlenecks in various electrocatalytic processes. As a result, suitable materials for specific applications can be utilized. Taking graphene-based electrocatalysts as an example, the ORR performance of these metal-free 2D electrocatalysts has increased significantly within the past 10 years through logical iterative approaches. The variability of chemical components and physical structures (and especially their integration) in graphene-based electrocatalysts has shown their significance in ORR applications. Furthermore, the combination of computational and experimental methods has led to a significantly more advanced understanding of the reaction mechanisms on graphene-based electrocatalysts for the ORR and HER, and have led to the development of rational design principles for advanced electrocatalysts. Inspired by this concept, more varied 2D nanomaterials such as TMDs, LDHs, and MXenes can be designed, fabricated, and engineered with significantly improved performance.

Although many opportunities exist for 2D electrocatalysts, this field is also faced with many challenges. First, the current production yield, quality, and quantity of 2D nanomaterials are still inadequate for industrial and commercial requirements. Consequently, the optimization of current synthesis methods is highly needed. Second, although there has been significant progress in the development of high-performance 2D electrocatalysts, a fundamental basis for their activity origins in many electrocatalytic processes is still required. For example, one of the biggest obstacles facing the alkaline HER is its inconclusive activity descriptor. This is partially due to the limitation of current computing power and the complexity of currently available candidates with a wide variety of physicochemical properties. Third, current characterization of 2D electrocatalysts is usually based on *ex situ* methods. However, one of the most important factors in electrocatalysis is the reaction intermediates, which cannot be probed using these methods, leading to a poor understanding of the working mechanism. Fourth, 2D electrocatalysts at present cannot satisfy current requirements, as many electrocatalytic processes, such as the ECR and NRR, lack examples of efficient 2D electrocatalysts. However, this provides significant opportunity for development in these fields. Consequently, new 2D electrocatalysts with suitable compositions and functionalities are highly needed. Fifth, advanced synthetic methods should be developed to realize precise control of the physical and chemical properties for modeling 2D nanomaterials, such as size, thickness, edges, doping sites, and defects. These model catalysts can therefore bridge the gap between molecular configurations in theoretical calculations and the actual samples used in experiments. With the development of materials science and chemistry, we believe that any kind of 2D nanomaterial can be prepared (using proper experimental conditions) as single or few atomic layers if its growth can be confined to two dimensions.

Although research on 2D electrocatalysts is only about 10 years old, great progress and many exciting achievements have been made. We believe that in the near future, 2D electrocatalysts

can make a significant contribution in both fundamental studies and practical applications in clean energy systems. First, the development of new types of 2D nanomaterials is very promising because they can be tailored to target specific electrocatalytic processes. For example, developing 2D electrocatalysts with appropriate thermodynamic adsorption energies and kinetic reaction barriers is essential to enhance the activity and selectivity for ECR electrocatalysts. Second, to fully utilize the unique properties of different 2D nanomaterials, hybridization is a promising strategy for specific applications. Further, hybridization of 2D nanomaterials can also generate new properties and functionalities. Last, further efforts are needed to elucidate many details of the working mechanisms, as they currently remain poorly understood. Looking forward, a combination of theoretical computation and experimental electrochemical measurements, with the help of advanced spectroscopic characterizations, is very likely the best way to design and develop new electrocatalysts. It is of paramount importance to fill the gap between theory and experiments for 2D electrocatalysts, which requires close collaboration among material scientists, computational chemists, and electrochemists.

AUTHOR INFORMATION

Corresponding Authors

*E-mail: yao.zheng01@adelaide.edu.au (Y. Zheng).

*E-mail: s.qiao@adelaide.edu.au (S. Z. Qiao).

ORCID

Yan Jiao: 0000-0003-1329-4290

Yao Zheng: 0000-0002-2411-8041

Shi-Zhang Qiao: 0000-0002-4568-8422

Notes

The authors declare no competing financial interest.

Biographies

Huanyu Jin received his B.S. in Optical Information Science and Technology from Huazhong University of Science and Technology (China) in 2013, and then completed his M.Phil. in Applied Physics from The Hong Kong Polytechnic University in 2015. Currently, he is a Ph.D. candidate in Chemical Engineering under the supervision of Prof. Shi-Zhang Qiao at The University of Adelaide. His research interest focuses on the development of novel nanomaterials for energy related applications.

Chunxian Guo received his Bachelor and Ph.D. degrees from Nanyang Technological University (Singapore) in 2007 and 2011, respectively. He is currently working as a DECRA research fellow with Prof. Shi-Zhang Qiao at The University of Adelaide. His research focuses on the design and fabrication of efficient and stable electrocatalysts through surface atomic engineering of low-dimensional materials.

Xin Liu received his B.E. and M.E. degrees in Thermal Engineering at the Harbin Institute of Technology (China) in 2014 and 2016, respectively. He is currently a Ph.D. student under the supervision of Prof. Shi-Zhang Qiao in the School of Chemical Engineering at The University of Adelaide. His current research focuses on revealing the electronic structure origin of electrocatalytic activity in some key electrocatalysis processes like hydrogen evolution and N₂ reduction reactions.

Jinlong Liu received his B.E. and M.E. degrees in Applied Chemistry from Central South University in 2011 and 2014, respectively. He is currently a Ph.D. candidate in Chemical Engineering under the supervision of Prof. Shi-Zhang Qiao at The University of Adelaide.

His current research is focused on the design and synthesis of functional materials for energy storage and catalysis.

Anthony Vasileff received his B.E. in chemical engineering at The University of Adelaide in 2014. He is currently a Ph.D. student under the supervision of Prof. Shi-Zhang Qiao at The University of Adelaide and is working on developing new nanostructured carbon and metal alloy materials for efficient CO₂ reduction electrocatalysts.

Yan Jiao received her Ph.D. in 2012 from the University of Queensland. She is currently a University of Adelaide fellow working with Prof. Shi-Zhang Qiao. Her current research area is computational electrochemistry, which involves investigating the nature and origin of electrocatalytic activity on nanostructured materials, and developing novel catalysts for clean energy conversion reactions using Density Functional Theory computations.

Yao Zheng received his Ph.D. degree in Chemical Engineering from the University of Queensland in 2014. Currently he is a DECRA research fellow working with Prof. Shi-Zhang Qiao in The University of Adelaide. His research focuses on fundamental studies of some key electrocatalysis processes such as oxygen reduction, hydrogen evolution, and CO₂ reduction reactions.

Shi-Zhang Qiao is currently a Chair Professor and Australian Laureate Fellow at the School of Chemical Engineering of The University of Adelaide, Australia. His research expertise is in nanomaterials for electrocatalysis, photocatalysis, and energy storage and conversion technologies. Prof. Qiao is a Thomson Reuters/Clarivate Analytics Highly Cited Researcher (Chemistry, Materials Science).

ACKNOWLEDGMENTS

The authors gratefully acknowledge financial support from the Australian Research Council (ARC) through the Discovery Project and Linkage Project programs (DP160104866, DP170104464, LP160100927, DE160101163, and FL170100154).

REFERENCES

- (1) Seh, Z. W.; Kibsgaard, J.; Dickens, C. F.; Chorkendorff, I.; Nørskov, J. K.; Jaramillo, T. F. Combining Theory and Experiment in Electrocatalysis: Insights into Materials Design. *Science* **2017**, *355*, eaad4998.
- (2) Simon, P.; Gogotsi, Y.; Dunn, B. Where Do Batteries End and Supercapacitors Begin? *Science* **2014**, *343*, 1210–1211.
- (3) Chu, S.; Majumdar, A. Opportunities and Challenges for a Sustainable Energy Future. *Nature* **2012**, *488*, 294–303.
- (4) Stamenkovic, V. R.; Strmcnik, D.; Lopes, P. P.; Markovic, N. M. Energy and Fuels from Electrochemical Interfaces. *Nat. Mater.* **2017**, *16*, 57–69.
- (5) Sun, Y.; Gao, S.; Lei, F.; Xie, Y. Atomically-Thin Two-Dimensional Sheets for Understanding Active Sites in Catalysis. *Chem. Soc. Rev.* **2015**, *44*, 623–636.
- (6) Wang, Z. L.; Xu, D.; Xu, J. J.; Zhang, X. B. Oxygen Electrocatalysts in Metal-Air Batteries: From Aqueous to Nonaqueous Electrolytes. *Chem. Soc. Rev.* **2014**, *43*, 7746–7786.
- (7) Gasteiger, H. A.; Marković, N. M. Just a Dream—or Future Reality? *Science* **2009**, *324*, 48–49.
- (8) Dai, L.; Xue, Y.; Qu, L.; Choi, H. J.; Baek, J. B. Metal-Free Catalysts for Oxygen Reduction Reaction. *Chem. Rev.* **2015**, *115*, 4823–4892.
- (9) Duan, J.; Chen, S.; Jaroniec, M.; Qiao, S. Z. Heteroatom-Doped Graphene-Based Materials for Energy-Relevant Electrocatalytic Processes. *ACS Catal.* **2015**, *5*, 5207–5234.
- (10) Jiao, Y.; Zheng, Y.; Jaroniec, M.; Qiao, S. Z. Design of Electrocatalysts for Oxygen- and Hydrogen-Involving Energy Conversion Reactions. *Chem. Soc. Rev.* **2015**, *44*, 2060–2086.

- (11) Zheng, Y.; Liu, J.; Liang, J.; Jaroniec, M.; Qiao, S. Z. Graphitic Carbon Nitride Materials: Controllable Synthesis and Applications in Fuel Cells and Photocatalysis. *Energy Environ. Sci.* **2012**, *5*, 6717–6731.
- (12) Turner, J. A. Sustainable Hydrogen Production. *Science* **2004**, *305*, 972–974.
- (13) Yin, Q.; Tan, J. M.; Besson, C.; Geletii, Y. V.; Musaev, D. G.; Kuznetsov, A. E.; Luo, Z.; Hardcastle, K. I.; Hill, C. L. A Fast Soluble Carbon-Free Molecular Water Oxidation Catalyst Based on Abundant Metals. *Science* **2010**, *328*, 342–345.
- (14) Gasteiger, H. A.; Kocha, S. S.; Sompalli, B.; Wagner, F. T. Activity Benchmarks and Requirements for Pt, Pt-Alloy, and Non-Pt Oxygen Reduction Catalysts for Pemfcs. *Appl. Catal., B* **2005**, *56*, 9–35.
- (15) Deng, D.; Novoselov, K. S.; Fu, Q.; Zheng, N.; Tian, Z.; Bao, X. Catalysis with Two-Dimensional Materials and Their Heterostructures. *Nat. Nanotechnol.* **2016**, *11*, 218–230.
- (16) Vasileff, A.; Zheng, Y.; Qiao, S. Z. Carbon Solving Carbon's Problems: Recent Progress of Nanostructured Carbon-Based Catalysts for the Electrochemical Reduction of CO₂. *Adv. Energy Mater.* **2017**, *7*, 1700759.
- (17) Liu, J.; Zhu, D.; Guo, C.; Vasileff, A.; Qiao, S.-Z. Design Strategies toward Advanced MOF-Derived Electrocatalysts for Energy-Conversion Reactions. *Adv. Energy Mater.* **2017**, *7*, 1700518.
- (18) Zhu, D. D.; Liu, J. L.; Qiao, S. Z. Recent Advances in Inorganic Heterogeneous Electrocatalysts for Reduction of Carbon Dioxide. *Adv. Mater.* **2016**, *28*, 3423–3452.
- (19) Larcher, D.; Tarascon, J. M. Towards Greener and More Sustainable Batteries for Electrical Energy Storage. *Nat. Chem.* **2015**, *7*, 19–29.
- (20) Gao, S.; Lin, Y.; Jiao, X.; Sun, Y.; Luo, Q.; Zhang, W.; Li, D.; Yang, J.; Xie, Y. Partially Oxidized Atomic Cobalt Layers for Carbon Dioxide Electroreduction to Liquid Fuel. *Nature* **2016**, *529*, 68–71.
- (21) Aresta, M.; Dibenedetto, A.; Angelini, A. Catalysis for the Valorization of Exhaust Carbon: From CO₂ to Chemicals, Materials, and Fuels. Technological Use of CO₂. *Chem. Rev.* **2014**, *114*, 1709–1742.
- (22) Kondratenko, E. V.; Mul, G.; Baltrusaitis, J.; Larrazabal, G. O.; Perez-Ramirez, J. Status and Perspectives of CO₂ Conversion into Fuels and Chemicals by Catalytic, Photocatalytic and Electrocatalytic Processes. *Energy Environ. Sci.* **2013**, *6*, 3112–3135.
- (23) Qiao, J.; Liu, Y.; Hong, F.; Zhang, J. A Review of Catalysts for the Electroreduction of Carbon Dioxide to Produce Low-Carbon Fuels. *Chem. Soc. Rev.* **2014**, *43*, 631–675.
- (24) Chai, G.-L.; Guo, Z.-X. Highly Effective Sites and Selectivity of Nitrogen-Doped Graphene/CNT Catalysts for CO₂ Electrochemical Reduction. *Chem. Sci.* **2016**, *7*, 1268–1275.
- (25) Lim, R. J.; Xie, M.; Sk, M. A.; Lee, J.-M.; Fisher, A.; Wang, X.; Lim, K. H. A Review on the Electrochemical Reduction of CO₂ in Fuel Cells, Metal Electrodes and Molecular Catalysts. *Catal. Today* **2014**, *233*, 169–180.
- (26) Sun, Z.; Ma, T.; Tao, H.; Fan, Q.; Han, B. Fundamentals and Challenges of Electrochemical CO₂ Reduction Using Two-Dimensional Materials. *Chem.* **2017**, *3*, 560–587.
- (27) Benson, E. E.; Kubiak, C. P.; Sathrum, A. J.; Smieja, J. M. Electrocatalytic and Homogeneous Approaches to Conversion of CO₂ to Liquid Fuels. *Chem. Soc. Rev.* **2009**, *38*, 89–99.
- (28) Schneider, J.; Jia, H.; Muckerman, J. T.; Fujita, E. Thermodynamics and Kinetics of CO₂, CO, and H⁺ Binding to the Metal Centre of CO₂ reduction catalysts. *Chem. Soc. Rev.* **2012**, *41*, 2036–2051.
- (29) Kortlever, R.; Shen, J.; Schouten, K. J. P.; Calle-Vallejo, F.; Koper, M. T. M. Catalysts and Reaction Pathways for the Electrochemical Reduction of Carbon Dioxide. *J. Phys. Chem. Lett.* **2015**, *6*, 4073–4082.
- (30) Peterson, A. A.; Abild-Pedersen, F.; Studt, F.; Rossmeisl, J.; Nørskov, J. K. How Copper Catalyzes the Electroreduction of Carbon Dioxide into Hydrocarbon Fuels. *Energy Environ. Sci.* **2010**, *3*, 1311–1315.
- (31) Jovanov, Z. P.; Hansen, H. A.; Varela, A. S.; Malacrida, P.; Peterson, A. A.; Nørskov, J. K.; Stephens, I. E. L.; Chorkendorff, I. Opportunities and Challenges in the Electrocatalysis of CO₂ and CO Reduction Using Bifunctional Surfaces: A Theoretical and Experimental Study of Au–Cd Alloys. *J. Catal.* **2016**, *343*, 215–231.
- (32) Nie, X.; Esopi, M. R.; Janik, M. J.; Asthagiri, A. Selectivity of CO₂ Reduction on Copper Electrodes: The Role of the Kinetics of Elementary Steps. *Angew. Chem., Int. Ed.* **2013**, *52*, 2459–2462.
- (33) Zhu, Y. P.; Guo, C.; Zheng, Y.; Qiao, S. Z. Surface and Interface Engineering of Noble-Metal-Free Electrocatalysts for Efficient Energy Conversion Processes. *Acc. Chem. Res.* **2017**, *50*, 915–923.
- (34) Walter, M. G.; Warren, E. L.; McKone, J. R.; Boettcher, S. W.; Mi, Q.; Santori, E. A.; Lewis, N. S. Solar Water Splitting Cells. *Chem. Rev.* **2010**, *110*, 6446–6473.
- (35) Nocera, D. G. The Artificial Leaf. *Acc. Chem. Res.* **2012**, *45*, 767–776.
- (36) Kamarudin, S. K.; Achmad, F.; Daud, W. R. W. Overview on the Application of Direct Methanol Fuel Cell (Dmfc) for Portable Electronic Devices. *Int. J. Hydrogen Energy* **2009**, *34*, 6902–6916.
- (37) Markovic, N. M. Electrocatalysis: Interfacing Electrochemistry. *Nat. Mater.* **2013**, *12*, 101–102.
- (38) Kang, Y.; Yang, P.; Markovic, N. M.; Stamenkovic, V. R. Shaping Electrocatalysis through Tailored Nanomaterials. *Nano Today* **2016**, *11*, 587–600.
- (39) Somorjai, G. A. Modern Surface Science and Surface Technologies: An Introduction. *Chem. Rev.* **1996**, *96*, 1223–1236.
- (40) Zheng, Y.; Jiao, Y.; Qiao, S. Z. Engineering of Carbon-Based Electrocatalysts for Emerging Energy Conversion: From Fundamental to Functionality. *Adv. Mater.* **2015**, *27*, 5372–5378.
- (41) Zhang, H. Ultrathin Two-Dimensional Nanomaterials. *ACS Nano* **2015**, *9*, 9451–9469.
- (42) Novoselov, K. S.; Geim, A. K.; Morozov, S. V.; Jiang, D.; Zhang, Y.; Dubonos, S. V.; Grigorieva, I. V.; Firsov, A. A. Electric Field Effect in Atomically Thin Carbon Films. *Science* **2004**, *306*, 666–669.
- (43) Tan, C.; Cao, X.; Wu, X. J.; He, Q.; Yang, J.; Zhang, X.; Chen, J.; Zhao, W.; Han, S.; Nam, G. H.; et al. Recent Advances in Ultrathin Two-Dimensional Nanomaterials. *Chem. Rev.* **2017**, *117*, 6225–6331.
- (44) Geim, A. K.; Novoselov, K. S. The Rise of Graphene. *Nat. Mater.* **2007**, *6*, 183–191.
- (45) Yang, W.; Zhang, X.; Xie, Y. Advances and Challenges in Chemistry of Two-Dimensional Nanosheets. *Nano Today* **2016**, *11*, 793–816.
- (46) Tan, C.; Lai, Z.; Zhang, H. Ultrathin Two-Dimensional Multinary Layered Metal Chalcogenide Nanomaterials. *Adv. Mater.* **2017**, *29*, 1701392.
- (47) Yang, N.; Zhang, Z.; Chen, B.; Huang, Y.; Chen, J.; Lai, Z.; Chen, Y.; Sindoro, M.; Wang, A. L.; Cheng, H.; et al. Synthesis of Ultrathin PdCu Alloy Nanosheets Used as a Highly Efficient Electrocatalyst for Formic Acid Oxidation. *Adv. Mater.* **2017**, *29*, 1700769.
- (48) Zheng, Y.; Jiao, Y.; Zhu, Y.; Li, L. H.; Han, Y.; Chen, Y.; Du, A.; Jaroniec, M.; Qiao, S. Z. Hydrogen Evolution by a Metal-Free Electrocatalyst. *Nat. Commun.* **2014**, *5*, 3783.
- (49) Zheng, Y.; Jiao, Y.; Ge, L.; Jaroniec, M.; Qiao, S. Z. Two-Step Boron and Nitrogen Doping in Graphene for Enhanced Synergistic Catalysis. *Angew. Chem.* **2013**, *125*, 3192–3198.
- (50) Fan, Z.; Luo, Z.; Huang, X.; Li, B.; Chen, Y.; Wang, J.; Hu, Y.; Zhang, H. Synthesis of 4H/fcc Noble Multimetallic Nanoribbons for Electrocatalytic Hydrogen Evolution Reaction. *J. Am. Chem. Soc.* **2016**, *138*, 1414–1419.
- (51) Tao, H.; Gao, Y.; Talreja, N.; Guo, F.; Texter, J.; Yan, C.; Sun, Z. Two-Dimensional Nanosheets for Electrocatalysis in Energy Generation and Conversion. *J. Mater. Chem. A* **2017**, *5*, 7257–7284.
- (52) Liu, X.; Dai, L. Carbon-Based Metal-Free Catalysts. *Nat. Rev. Mater.* **2016**, *1*, 16064.
- (53) Jaramillo, T. F.; Jørgensen, K. P.; Bonde, J.; Nielsen, J. H.; Horch, S.; Chorkendorff, I. Identification of Active Edge Sites for Electrochemical H₂ Evolution from MoS₂ Nanocatalysts. *Science* **2007**, *317*, 100–102.
- (54) Hinnemann, B.; Moses, P. G.; Bonde, J.; Jørgensen, K. P.; Nielsen, J. H.; Horch, S.; Chorkendorff, I.; Nørskov, J. K. Biomimetic Hydrogen Evolution: MoS₂ Nanoparticles as Catalyst for Hydrogen Evolution. *J. Am. Chem. Soc.* **2005**, *127*, 5308–5309.

- (55) Nicolosi, V.; Chhowalla, M.; Kanatzidis, M. G.; Strano, M. S.; Coleman, J. N. Liquid Exfoliation of Layered Materials. *Science* **2013**, *340*, 1226419.
- (56) Helander, M. G. Solution-Processible Electrodes. *Science* **2012**, *336*, 302–303.
- (57) Coleman, J. N.; Lotya, M.; O'Neill, A.; Bergin, S. D.; King, P. J.; Khan, U.; Young, K.; Gaucher, A.; De, S.; Smith, R. J.; et al. Two-Dimensional Nanosheets Produced by Liquid Exfoliation of Layered Materials. *Science* **2011**, *331*, 568–571.
- (58) Ghidui, M.; Lukatskaya, M. R.; Zhao, M. Q.; Gogotsi, Y.; Barsoum, M. W. Conductive Two-Dimensional Titanium Carbide 'Clay' with High Volumetric Capacitance. *Nature* **2014**, *516*, 78–81.
- (59) Acerce, M.; Voiry, D.; Chhowalla, M. Metallic 1T Phase MoS₂ Nanosheets as Supercapacitor Electrode Materials. *Nat. Nanotechnol.* **2015**, *10*, 313–318.
- (60) Torrisi, F.; Coleman, J. N. Electrifying Inks with 2D Materials. *Nat. Nanotechnol.* **2014**, *9*, 738–739.
- (61) Gao, W.; Singh, N.; Song, L.; Liu, Z.; Reddy, A. L. M.; Ci, L.; Vajtai, R.; Zhang, Q.; Wei, B.; Ajayan, P. M. Direct Laser Writing of Micro-Supercapacitors on Hydrated Graphite Oxide Films. *Nat. Nanotechnol.* **2011**, *6*, 496–500.
- (62) Qu, L.; Liu, Y.; Baek, J.-B.; Dai, L. Nitrogen-Doped Graphene as Efficient Metal-Free Electrocatalyst for Oxygen Reduction in Fuel Cells. *ACS Nano* **2010**, *4*, 1321–1326.
- (63) Deng, J.; Ren, P.; Deng, D.; Bao, X. Enhanced Electron Penetration through an Ultrathin Graphene Layer for Highly Efficient Catalysis of the Hydrogen Evolution Reaction. *Angew. Chem., Int. Ed.* **2015**, *54*, 2100–2104.
- (64) Zheng, Y.; Jiao, Y.; Zhu, Y.; Li, L. H.; Han, Y.; Chen, Y.; Jaroniec, M.; Qiao, S. Z. High Electrocatalytic Hydrogen Evolution Activity of an Anomalous Ruthenium Catalyst. *J. Am. Chem. Soc.* **2016**, *138*, 16174–16181.
- (65) Chhowalla, M.; Shin, H. S.; Eda, G.; Li, L. J.; Loh, K. P.; Zhang, H. The Chemistry of Two-Dimensional Layered Transition Metal Dichalcogenide Nanosheets. *Nat. Chem.* **2013**, *5*, 263–275.
- (66) Cheng, N.; Stambula, S.; Wang, D.; Banis, M. N.; Liu, J.; Riese, A.; Xiao, B.; Li, R.; Sham, T. K.; Liu, L. M.; et al. Platinum Single-Atom and Cluster Catalysis of the Hydrogen Evolution Reaction. *Nat. Commun.* **2016**, *7*, 13638.
- (67) Mahmood, J.; Li, F.; Jung, S. M.; Okyay, M. S.; Ahmad, I.; Kim, S. J.; Park, N.; Jeong, H. Y.; Baek, J. B. An Efficient and pH-Universal Ruthenium-Based Catalyst for the Hydrogen Evolution Reaction. *Nat. Nanotechnol.* **2017**, *12*, 441–446.
- (68) Fan, L.; Liu, P. F.; Yan, X.; Gu, L.; Yang, Z. Z.; Yang, H. G.; Qiu, S.; Yao, X. Atomically Isolated Nickel Species Anchored on Graphitized Carbon for Efficient Hydrogen Evolution Electrocatalysis. *Nat. Commun.* **2016**, *7*, 10667.
- (69) Ma, T. Y.; Cao, J. L.; Jaroniec, M.; Qiao, S. Z. Interacting Carbon Nitride and Titanium Carbide Nanosheets for Highperformance Oxygen Evolution. *Angew. Chem., Int. Ed.* **2016**, *55*, 1138–1142.
- (70) Zheng, Y.; Jiao, Y.; Li, L. H.; Xing, T.; Chen, Y.; Jaroniec, M.; Qiao, S. Z. Toward Design of Synergistically Active Carbon-Based Catalysts for Electrocatalytic Hydrogen Evolution. *ACS Nano* **2014**, *8*, 5290–5296.
- (71) Xu, K.; Cao, P.; Heath, J. R. Graphene Visualizes the First Water Adlayers on Mica at Ambient Conditions. *Science* **2010**, *329*, 1188–1191.
- (72) Girit, Ç. Ö.; Meyer, J. C.; Erni, R.; Rossell, M. D.; Kisielowski, C.; Yang, L.; Park, C.-H.; Crommie, M. F.; Cohen, M. L.; Louie, S. G.; et al. Graphene at the Edge: Stability and Dynamics. *Science* **2009**, *323*, 1705–1708.
- (73) Jiao, Y.; Zheng, Y.; Davey, K.; Qiao, S.-Z. Activity Origin and Catalyst Design Principles for Electrocatalytic Hydrogen Evolution on Heteroatom-Doped graphene. *Nat. Energy* **2016**, *1*, 16130.
- (74) Deng, J.; Li, H.; Wang, S.; Ding, D.; Chen, M.; Liu, C.; Tian, Z.; Novoselov, K. S.; Ma, C.; Deng, D.; et al. Multiscale Structural and Electronic Control of Molybdenum Disulfide Foam for Highly Efficient Hydrogen Production. *Nat. Commun.* **2017**, *8*, 14430.
- (75) Nørskov, J. K.; Bligaard, T.; Rossmeisl, J.; Christensen, C. H. Towards the Computational Design of Solid Catalysts. *Nat. Chem.* **2009**, *1*, 37–46.
- (76) Zhu, D.; Guo, C. X.; Liu, J.; Wang, L.; Du, Y.; Qiao, S. Two-Dimensional Metal-Organic Frameworks with High Oxidation State for Efficient Electrocatalytic Urea Oxidation. *Chem. Commun.* **2017**, *53*, 10906–10909.
- (77) Chen, S.; Duan, J.; Vasileff, A.; Qiao, S. Z. Size Fractionation of Two-Dimensional Sub-Nanometer Thin Manganese Dioxide Crystals Towards Superior Urea Electrocatalytic Conversion. *Angew. Chem., Int. Ed.* **2016**, *55*, 3804–3808.
- (78) Jariwala, D.; Marks, T. J.; Hersam, M. C. Mixed-Dimensional Van Der Waals Heterostructures. *Nat. Mater.* **2017**, *16*, 170–181.
- (79) Butler, S. Z.; Hollen, S. M.; Cao, L.; Cui, Y.; Gupta, J. A.; Gutiérrez, H. R.; Heinz, T. F.; Hong, S. S.; Huang, J.; Ismach, A. F.; et al. Progress, Challenges, and Opportunities in Two-Dimensional Materials Beyond Graphene. *ACS Nano* **2013**, *7*, 2898–2926.
- (80) Bhimanapati, G. R.; Lin, Z.; Meunier, V.; Jung, Y.; Cha, J.; Das, S.; Xiao, D.; Son, Y.; Strano, M. S.; Cooper, V. R.; et al. Recent Advances in Two-Dimensional Materials Beyond Graphene. *ACS Nano* **2015**, *9*, 11509–11539.
- (81) Shao, M.; Chang, Q.; Dodelet, J.-P.; Chenitz, R. Recent Advances in Electrocatalysts for Oxygen Reduction Reaction. *Chem. Rev.* **2016**, *116*, 3594–3657.
- (82) Zheng, Y.; Jiao, Y.; Jaroniec, M.; Qiao, S. Z. Advancing the Electrochemistry of the Hydrogen-Evolution Reaction through Combining Experiment and Theory. *Angew. Chem., Int. Ed.* **2015**, *54*, 52–65.
- (83) Suen, N.-T.; Hung, S.-F.; Quan, Q.; Zhang, N.; Xu, Y.-J.; Chen, H. M. Electrocatalysis for the Oxygen Evolution Reaction: Recent Development and Future Perspectives. *Chem. Soc. Rev.* **2017**, *46*, 337–365.
- (84) Gong, K.; Du, F.; Xia, Z.; Durstock, M.; Dai, L. Nitrogen-Doped Carbon Nanotube Arrays with High Electrocatalytic Activity for Oxygen Reduction. *Science* **2009**, *323*, 760–764.
- (85) Ren, X.; Zhou, J.; Qi, X.; Liu, Y.; Huang, Z.; Li, Z.; Ge, Y.; Dhanabalan, S. C.; Ponraj, J. S.; Wang, S.; et al. Few-Layer Black Phosphorus Nanosheets as Electrocatalysts for Highly Efficient Oxygen Evolution Reaction. *Adv. Energy Mater.* **2017**, *7*, 1700396.
- (86) Jiang, Q.; Xu, L.; Chen, N.; Zhang, H.; Dai, L.; Wang, S. Facile Synthesis of Black Phosphorus: An Efficient Electrocatalyst for the Oxygen Evolving Reaction. *Angew. Chem.* **2016**, *128*, 14053–14057.
- (87) Stoller, M. D.; Park, S.; Zhu, Y.; An, J.; Ruoff, R. S. Graphene-Based Ultracapacitors. *Nano Lett.* **2008**, *8*, 3498–3502.
- (88) Lee, C.; Wei, X.; Kysar, J. W.; Hone, J. Measurement of the Elastic Properties and Intrinsic Strength of Monolayer Graphene. *Science* **2008**, *321*, 385–388.
- (89) Balandin, A. A.; Ghosh, S.; Bao, W.; Calizo, I.; Teweldebrhan, D.; Miao, F.; Lau, C. N. Superior Thermal Conductivity of Single-Layer Graphene. *Nano Lett.* **2008**, *8*, 902–907.
- (90) Deng, D.; Yu, L.; Pan, X.; Wang, S.; Chen, X.; Hu, P.; Sun, L.; Bao, X. Size Effect of Graphene on Electrocatalytic Activation of Oxygen. *Chem. Commun.* **2011**, *47*, 10016–10018.
- (91) Sun, S.; Zhang, G.; Gauquelin, N.; Chen, N.; Zhou, J.; Yang, S.; Chen, W.; Meng, X.; Geng, D.; Banis, M. N.; et al. Single-Atom Catalysis Using Pt/Graphene Achieved through Atomic Layer Deposition. *Sci. Rep.* **2013**, *3*, 1775.
- (92) Yang, X.-F.; Wang, A.; Qiao, B.; Li, J.; Liu, J.; Zhang, T. Single-Atom Catalysts: A New Frontier in Heterogeneous Catalysis. *Acc. Chem. Res.* **2013**, *46*, 1740–1748.
- (93) Sreekanth, N.; Nazrulla, M. A.; Vineesh, T. V.; Sailaja, K.; Phani, K. L. Metal-Free Boron-Doped Graphene for Selective Electroreduction of Carbon Dioxide to Formic Acid/Formate. *Chem. Commun.* **2015**, *51*, 16061–16064.
- (94) Wang, H.; Chen, Y.; Hou, X.; Ma, C.; Tan, T. Nitrogen-Doped Graphenes as Efficient Electrocatalysts for the Selective Reduction of Carbon Dioxide to Formate in Aqueous Solution. *Green Chem.* **2016**, *18*, 3250–3256.

- (95) Wu, J.; Liu, M.; Sharma, P. P.; Yadav, R. M.; Ma, L.; Yang, Y.; Zou, X.; Zhou, X.-D.; Vajtai, R.; Yakobson, B. I.; et al. Incorporation of Nitrogen Defects for Efficient Reduction of CO₂ Via Two-Electron Pathway on Three-Dimensional Graphene Foam. *Nano Lett.* **2016**, *16*, 466–470.
- (96) Li, G.; Li, Y.; Liu, H.; Guo, Y.; Li, Y.; Zhu, D. Architecture of Graphdiyne Nanoscale Films. *Chem. Commun.* **2010**, *46*, 3256–3258.
- (97) Malko, D.; Neiss, C.; Görling, A. Two-Dimensional Materials with Dirac Cones: Graphynes Containing Heteroatoms. *Phys. Rev. B: Condens. Matter Mater. Phys.* **2012**, *86*, 045443.
- (98) Baughman, R. H.; Eckhardt, H.; Kertesz, M. Structure-Property Predictions for New Planar Forms of Carbon: Layered Phases Containing sp² and sp Atoms. *J. Chem. Phys.* **1987**, *87*, 6687–6699.
- (99) Liu, R.; Gao, X.; Zhou, J.; Xu, H.; Li, Z.; Zhang, S.; Xie, Z.; Zhang, J.; Liu, Z. Chemical Vapor Deposition Growth of Linked Carbon Monolayers with Acetylenic Scaffoldings on Silver Foil. *Adv. Mater.* **2017**, *29*, 1604665.
- (100) Matsuoka, R.; Sakamoto, R.; Hoshiko, K.; Sasaki, S.; Masunaga, H.; Nagashio, K.; Nishihara, H. Crystalline Graphdiyne Nanosheets Produced at a Gas/Liquid or Liquid/Liquid Interface. *J. Am. Chem. Soc.* **2017**, *139*, 3145–3152.
- (101) Hybertsen, M. S.; Louie, S. G. Electron Correlation in Semiconductors and Insulators: Band Gaps and Quasiparticle Energies. *Phys. Rev. B: Condens. Matter Mater. Phys.* **1986**, *34*, 5390–5413.
- (102) Liu, R.; Liu, H.; Li, Y.; Yi, Y.; Shang, X.; Zhang, S.; Yu, X.; Zhang, S.; Cao, H.; Zhang, G. Nitrogen-Doped Graphdiyne as a Metal-Free Catalyst for High-Performance Oxygen Reduction Reactions. *Nanoscale* **2014**, *6*, 11336–11343.
- (103) Zhang, S.; Cai, Y.; He, H.; Zhang, Y.; Liu, R.; Cao, H.; Wang, M.; Liu, J.; Zhang, G.; Li, Y.; et al. Heteroatom Doped Graphdiyne as Efficient Metal-Free Electrocatalyst for Oxygen Reduction Reaction in Alkaline Medium. *J. Mater. Chem. A* **2016**, *4*, 4738–4744.
- (104) Xue, Y.; Guo, Y.; Yi, Y.; Li, Y.; Liu, H.; Li, D.; Yang, W.; Li, Y. Self-Catalyzed Growth of Cu@Graphdiyne Core-Shell Nanowires Array for High Efficient Hydrogen Evolution Cathode. *Nano Energy* **2016**, *30*, 858–866.
- (105) Xue, Y.; Li, J.; Xue, Z.; Li, Y.; Liu, H.; Li, D.; Yang, W.; Li, Y. Extraordinarily Durable Graphdiyne-Supported Electrocatalyst with High Activity for Hydrogen Production at All Values of pH. *ACS Appl. Mater. Interfaces* **2016**, *8*, 31083–31091.
- (106) Wu, P.; Du, P.; Zhang, H.; Cai, C. Graphdiyne as a Metal-Free Catalyst for Low-Temperature CO Oxidation. *Phys. Chem. Chem. Phys.* **2014**, *16*, 5640–5648.
- (107) Ong, W.-J.; Tan, L.-L.; Ng, Y. H.; Yong, S.-T.; Chai, S.-P. Graphitic Carbon Nitride (G-C₃N₄)-Based Photocatalysts for Artificial Photosynthesis and Environmental Remediation: Are We a Step Closer to Achieving Sustainability? *Chem. Rev.* **2016**, *116*, 7159–7329.
- (108) Liebig, J. V. About Some Nitrogen Compounds. *Ann. Pharm.* **1834**, *10*, 10.
- (109) Zhao, Y.; Zhang, J.; Qu, L. Graphitic Carbon Nitride/Graphene Hybrids as New Active Materials for Energy Conversion and Storage. *ChemNanoMat* **2015**, *1*, 298–318.
- (110) Zambon, A.; Mouesca, J. M.; Gheorghiu, C.; Bayle, P. A.; Pecaut, J.; Claeys-Bruno, M.; Gambarelli, S.; Dubois, L. S-Heptazine Oligomers: Promising Structural Models for Graphitic Carbon Nitride. *Chem. Sci.* **2016**, *7*, 945–950.
- (111) Liu, J.; Li, W.; Duan, L.; Li, X.; Ji, L.; Geng, Z.; Huang, K.; Lu, L.; Zhou, L.; Liu, Z.; et al. A Graphene-Like Oxygenated Carbon Nitride Material for Improved Cycle-Life Lithium/Sulfur Batteries. *Nano Lett.* **2015**, *15*, 5137–5142.
- (112) Zhang, G.; Zhang, J.; Zhang, M.; Wang, X. Polycondensation of Thiourea into Carbon Nitride Semiconductors as Visible Light Photocatalysts. *J. Mater. Chem.* **2012**, *22*, 8083–8091.
- (113) Bian, J.; Li, Q.; Huang, C.; Li, J.; Guo, Y.; Zaw, M.; Zhang, R.-Q. Thermal Vapor Condensation of Uniform Graphitic Carbon Nitride Films with Remarkable Photocurrent Density for Photoelectrochemical Applications. *Nano Energy* **2015**, *15*, 353–361.
- (114) Shiraiishi, Y.; Kofuji, Y.; Sakamoto, H.; Tanaka, S.; Ichikawa, S.; Hirai, T. Effects of Surface Defects on Photocatalytic H₂O₂ Production by Mesoporous Graphitic Carbon Nitride under Visible Light Irradiation. *ACS Catal.* **2015**, *5*, 3058–3066.
- (115) Ma, T. Y.; Tang, Y.; Dai, S.; Qiao, S. Z. Proton-Functionalized Two-Dimensional Graphitic Carbon Nitride Nanosheet: An Excellent Metal-/Label-Free Biosensing Platform. *Small* **2014**, *10*, 2382–2389.
- (116) Kessler, F. K.; Zheng, Y.; Schwarz, D.; Merschjann, C.; Schnick, W.; Wang, X.; Bojdy, M. J. Functional Carbon Nitride Materials — Design Strategies for Electrochemical Devices. *Nat. Rev. Mater.* **2017**, *2*, 17030.
- (117) Niu, P.; Zhang, L.; Liu, G.; Cheng, H.-M. Graphene-Like Carbon Nitride Nanosheets for Improved Photocatalytic Activities. *Adv. Funct. Mater.* **2012**, *22*, 4763–4770.
- (118) Wang, W.; Yu, J. C.; Shen, Z.; Chan, D. K. L.; Gu, T. g-C₃N₄ Quantum Dots: Direct Synthesis, Upconversion Properties and Photocatalytic Application. *Chem. Commun.* **2014**, *50*, 10148–10150.
- (119) Yang, S.; Gong, Y.; Zhang, J.; Zhan, L.; Ma, L.; Fang, Z.; Vajtai, R.; Wang, X.; Ajayan, P. M. Exfoliated Graphitic Carbon Nitride Nanosheets as Efficient Catalysts for Hydrogen Evolution under Visible Light. *Adv. Mater.* **2013**, *25*, 2452–2456.
- (120) Han, Q.; Wang, B.; Gao, J.; Cheng, Z.; Zhao, Y.; Zhang, Z.; Qu, L. Atomically Thin Mesoporous Nanomesh of Graphitic C₃N₄ for High-Efficiency Photocatalytic Hydrogen Evolution. *ACS Nano* **2016**, *10*, 2745–2751.
- (121) Ma, L.; Fan, H.; Wang, J.; Zhao, Y.; Tian, H.; Dong, G. Water-Assisted Ions in Situ Intercalation for Porous Polymeric Graphitic Carbon Nitride Nanosheets with Superior Photocatalytic Hydrogen Evolution Performance. *Appl. Catal., B* **2016**, *190*, 93–102.
- (122) Ma, T. Y.; Ran, J.; Dai, S.; Jaroniec, M.; Qiao, S. Z. Phosphorus-Doped Graphitic Carbon Nitrides Grown in Situ on Carbon-Fiber Paper: Flexible and Reversible Oxygen Electrodes. *Angew. Chem., Int. Ed.* **2015**, *54*, 4646–4650.
- (123) Su, F.; Mathew, S. C.; Lipner, G.; Fu, X.; Antonietti, M.; Blechert, S.; Wang, X. mpg-C₃N₄-Catalyzed Selective Oxidation of Alcohols Using O₂ and Visible Light. *J. Am. Chem. Soc.* **2010**, *132*, 16299–16301.
- (124) Lau, V. W.-h.; Mesch, M. B.; Duppel, V.; Blum, V.; Senker, J.; Lotsch, B. V. Low-Molecular-Weight Carbon Nitrides for Solar Hydrogen Evolution. *J. Am. Chem. Soc.* **2015**, *137*, 1064–1072.
- (125) Hong, Z.; Shen, B.; Chen, Y.; Lin, B.; Gao, B. Enhancement of Photocatalytic H₂ Evolution over Nitrogen-Deficient Graphitic Carbon Nitride. *J. Mater. Chem. A* **2013**, *1*, 11754–11761.
- (126) Zheng, Y.; Jiao, Y.; Chen, J.; Liu, J.; Liang, J.; Du, A.; Zhang, W.; Zhu, Z.; Smith, S. C.; Jaroniec, M.; et al. Nanoporous Graphitic-C₃N₄@Carbon Metal-Free Electrocatalysts for Highly Efficient Oxygen Reduction. *J. Am. Chem. Soc.* **2011**, *133*, 20116–20119.
- (127) Li, L. H.; Chen, Y. Atomically Thin Boron Nitride: Unique Properties and Applications. *Adv. Funct. Mater.* **2016**, *26*, 2594–2608.
- (128) Geick, R.; Perry, C. H.; Rupprecht, G. Normal Modes in Hexagonal Boron Nitride. *Phys. Rev.* **1966**, *146*, 543–547.
- (129) Levendorf, M. P.; Kim, C.-J.; Brown, L.; Huang, P. Y.; Havener, R. W.; Muller, D. A.; Park, J. Graphene and Boron Nitride Lateral Heterostructures for Atomically Thin Circuitry. *Nature* **2012**, *488*, 627–632.
- (130) Lee, G.-H.; Yu, Y.-J.; Cui, X.; Petrone, N.; Lee, C.-H.; Choi, M. S.; Lee, D.-Y.; Lee, C.; Yoo, W. J.; Watanabe, K.; et al. Flexible and Transparent MoS₂ Field-Effect Transistors on Hexagonal Boron Nitride-Graphene Heterostructures. *ACS Nano* **2013**, *7*, 7931–7936.
- (131) Uosaki, K.; Elumalai, G.; Noguchi, H.; Masuda, T.; Lyalin, A.; Nakayama, A.; Taketsugu, T. Boron Nitride Nanosheet on Gold as an Electrocatalyst for Oxygen Reduction Reaction: Theoretical Suggestion and Experimental Proof. *J. Am. Chem. Soc.* **2014**, *136*, 6542–6545.
- (132) Li, F.; Shu, H.; Liu, X.; Shi, Z.; Liang, P.; Chen, X. Electrocatalytic Activity and Design Principles of Heteroatom-Doped Graphene Catalysts for Oxygen-Reduction Reaction. *J. Phys. Chem. C* **2017**, *121*, 14434–14442.
- (133) Uosaki, K.; Elumalai, G.; Dinh, H. C.; Lyalin, A.; Taketsugu, T.; Noguchi, H. Highly Efficient Electrochemical Hydrogen Evolution Reaction at Insulating Boron Nitride Nanosheet on Inert Gold Substrate. *Sci. Rep.* **2016**, *6*, 32217.

- (134) Huang, C.; Chen, C.; Zhang, M.; Lin, L.; Ye, X.; Lin, S.; Antonietti, M.; Wang, X. Carbon-Doped BN Nanosheets for Metal-Free Photoredox Catalysis. *Nat. Commun.* **2015**, *6*, 7698.
- (135) Bridgman, P. Two New Modifications of Phosphorus. *J. Am. Chem. Soc.* **1914**, *36*, 1344–1363.
- (136) Zhang, X.; Xie, H.; Liu, Z.; Tan, C.; Luo, Z.; Li, H.; Lin, J.; Sun, L.; Chen, W.; Xu, Z.; et al. Black Phosphorus Quantum Dots. *Angew. Chem.* **2015**, *127*, 3724–3728.
- (137) Li, L.; Yu, Y.; Ye, G. J.; Ge, Q.; Ou, X.; Wu, H.; Feng, D.; Chen, X. H.; Zhang, Y. Black Phosphorus Field-Effect Transistors. *Nat. Nanotechnol.* **2014**, *9*, 372–377.
- (138) Ling, X.; Wang, H.; Huang, S.; Xia, F.; Dresselhaus, M. S. The Renaissance of Black Phosphorus. *Proc. Natl. Acad. Sci. U. S. A.* **2015**, *112*, 4523–4530.
- (139) Lei, W.; Liu, G.; Zhang, J.; Liu, M. Black Phosphorus Nanostructures: Recent Advances in Hybridization, Doping and Functionalization. *Chem. Soc. Rev.* **2017**, *46*, 3492–3509.
- (140) Luo, Z.-Z.; Zhang, Y.; Zhang, C.; Tan, H. T.; Li, Z.; Abutaha, A.; Wu, X.-L.; Xiong, Q.; Khor, K. A.; Hippalgaonkar, K.; et al. Multifunctional 0D–2D Ni₂P Nanocrystals–Black Phosphorus Heterostructure. *Adv. Energy Mater.* **2017**, *7*, 1601285.
- (141) Faber, M. S.; Jin, S. Earth-Abundant Inorganic Electrocatalysts and Their Nanostructures for Energy Conversion Applications. *Energy Environ. Sci.* **2014**, *7*, 3519–3542.
- (142) Voiry, D.; Mohite, A.; Chhowalla, M. Phase Engineering of Transition Metal Dichalcogenides. *Chem. Soc. Rev.* **2015**, *44*, 2702–2712.
- (143) Splendiani, A.; Sun, L.; Zhang, Y.; Li, T.; Kim, J.; Chim, C.-Y.; Galli, G.; Wang, F. Emerging Photoluminescence in Monolayer MoS₂. *Nano Lett.* **2010**, *10*, 1271–1275.
- (144) Xiao, D.; Liu, G.-B.; Feng, W.; Xu, X.; Yao, W. Coupled Spin and Valley Physics in Monolayers of MoS₂ and Other Group-VI Dichalcogenides. *Phys. Rev. Lett.* **2012**, *108*, 196802.
- (145) Bonaccorso, F.; Bartolotta, A.; Coleman, J. N.; Backes, C. 2D-Crystal-Based Functional Inks. *Adv. Mater.* **2016**, *28*, 6136–6166.
- (146) Joensen, P.; Frindt, R. F.; Morrison, S. R. Single-Layer MoS₂. *Mater. Res. Bull.* **1986**, *21*, 457–461.
- (147) Voiry, D.; Yamaguchi, H.; Li, J.; Silva, R.; Alves, D. C. B.; Fujita, T.; Chen, M.; Asefa, T.; Shenoy, V. B.; Eda, G.; et al. Enhanced Catalytic Activity in Strained Chemically Exfoliated WS₂ Nanosheets for Hydrogen Evolution. *Nat. Mater.* **2013**, *12*, 850–855.
- (148) Yu, Y.; Huang, S.-Y.; Li, Y.; Steinmann, S. N.; Yang, W.; Cao, L. Layer-Dependent Electrocatalysis of MoS₂ for Hydrogen Evolution. *Nano Lett.* **2014**, *14*, 553–558.
- (149) Xie, J.; Zhang, J.; Li, S.; Grote, F.; Zhang, X.; Zhang, H.; Wang, R.; Lei, Y.; Pan, B.; Xie, Y. Controllable Disorder Engineering in Oxygen-Incorporated MoS₂ Ultrathin Nanosheets for Efficient Hydrogen Evolution. *J. Am. Chem. Soc.* **2013**, *135*, 17881–17888.
- (150) Li, Y.; Wang, H.; Xie, L.; Liang, Y.; Hong, G.; Dai, H. MoS₂ Nanoparticles Grown on Graphene: An Advanced Catalyst for the Hydrogen Evolution Reaction. *J. Am. Chem. Soc.* **2011**, *133*, 7296–7299.
- (151) Deng, J.; Li, H.; Xiao, J.; Tu, Y.; Deng, D.; Yang, H.; Tian, H.; Li, J.; Ren, P.; Bao, X. Triggering the Electrocatalytic Hydrogen Evolution Activity of the Inert Two-Dimensional MoS₂ Surface Via Single-Atom Metal Doping. *Energy Environ. Sci.* **2015**, *8*, 1594–1601.
- (152) Yeston, J. An Edgy Way to Transform Carbon Dioxide. *Science* **2014**, *345*, 1132.
- (153) Liu, X.; Xiao, J.; Peng, H.; Hong, X.; Chan, K.; Nørskov, J. K. Understanding Trends in Electrochemical Carbon Dioxide Reduction Rates. *Nat. Commun.* **2017**, *8*, 15438.
- (154) Asadi, M.; Kumar, B.; Behranginia, A.; Rosen, B. A.; Baskin, A.; Repnin, N.; Pisasale, D.; Phillips, P.; Zhu, W.; Haasch, R.; et al. Robust Carbon Dioxide Reduction on Molybdenum Disulfide Edges. *Nat. Commun.* **2014**, *5*, 4470.
- (155) Asadi, M.; Kim, K.; Liu, C.; Addepalli, A. V.; Abbasi, P.; Yasaei, P.; Phillips, P.; Behranginia, A.; Cerrato, J. M.; Haasch, R.; et al. Nanostructured Transition Metal Dichalcogenide Electrocatalysts for CO₂ Reduction in Ionic Liquid. *Science* **2016**, *353*, 467–470.
- (156) Liu, Y.; Cheng, H.; Lyu, M.; Fan, S.; Liu, Q.; Zhang, W.; Zhi, Y.; Wang, C.; Xiao, C.; Wei, S.; et al. Low Overpotential in Vacancy-Rich Ultrathin CoSe₂ Nanosheets for Water Oxidation. *J. Am. Chem. Soc.* **2014**, *136*, 15670–15675.
- (157) Wang, F.; Seo, J. H.; Luo, G.; Starr, M. B.; Li, Z.; Geng, D.; Yin, X.; Wang, S.; Fraser, D. G.; Morgan, D.; et al. Nanometre-Thick Single-Crystalline Nanosheets Grown at the Water-Air Interface. *Nat. Commun.* **2016**, *7*, 10444.
- (158) Sun, Y.; Sun, Z.; Gao, S.; Cheng, H.; Liu, Q.; Piao, J.; Yao, T.; Wu, C.; Hu, S.; Wei, S.; et al. Fabrication of Flexible and Freestanding Zinc Chalcogenide Single Layers. *Nat. Commun.* **2012**, *3*, 1057.
- (159) Jasion, D.; Barforoush, J. M.; Qiao, Q.; Zhu, Y.; Ren, S.; Leonard, K. C. Low-Dimensional Hyperthin FeS₂ Nanostructures for Efficient and Stable Hydrogen Evolution Electrocatalysis. *ACS Catal.* **2015**, *5*, 6653–6657.
- (160) Liu, Y.; Hua, X.; Xiao, C.; Zhou, T.; Huang, P.; Guo, Z.; Pan, B.; Xie, Y. Heterogeneous Spin States in Ultrathin Nanosheets Induce Subtle Lattice Distortion to Trigger Efficient Hydrogen Evolution. *J. Am. Chem. Soc.* **2016**, *138*, 5087–5092.
- (161) Long, X.; Li, G.; Wang, Z.; Zhu, H.; Zhang, T.; Xiao, S.; Guo, W.; Yang, S. Metallic Iron–Nickel Sulfide Ultrathin Nanosheets as a Highly Active Electrocatalyst for Hydrogen Evolution Reaction in Acidic Media. *J. Am. Chem. Soc.* **2015**, *137*, 11900–11903.
- (162) Sun, X.; Zhu, Q.; Kang, X.; Liu, H.; Qian, Q.; Zhang, Z.; Han, B. Molybdenum–Bismuth Bimetallic Chalcogenide Nanosheets for Highly Efficient Electrocatalytic Reduction of Carbon Dioxide to Methanol. *Angew. Chem., Int. Ed.* **2016**, *55*, 6771–6775.
- (163) Balendhran, S.; Walia, S.; Nili, H.; Ou, J. Z.; Zhuyikov, S.; Kaner, R. B.; Sriram, S.; Bhaskaran, M.; Kalantar-zadeh, K. Two-Dimensional Molybdenum Trioxide and Dichalcogenides. *Adv. Funct. Mater.* **2013**, *23*, 3952–3970.
- (164) Kalantar-zadeh, K.; Ou, J. Z.; Daenke, T.; Mitchell, A.; Sasaki, T.; Fuhrer, M. S. Two Dimensional and Layered Transition Metal Oxides. *Appl. Mater. Today* **2016**, *5*, 73–89.
- (165) Cheng, H.; Kamegawa, T.; Mori, K.; Yamashita, H. Surfactant-Free Nonaqueous Synthesis of Plasmonic Molybdenum Oxide Nanosheets with Enhanced Catalytic Activity for Hydrogen Generation from Ammonia Borane under Visible Light. *Angew. Chem., Int. Ed.* **2014**, *53*, 2910–2914.
- (166) Xiao, X.; Song, H.; Lin, S.; Zhou, Y.; Zhan, X.; Hu, Z.; Zhang, Q.; Sun, J.; Yang, B.; Li, T.; et al. Scalable Salt-Templated Synthesis of Two-Dimensional Transition Metal Oxides. *Nat. Commun.* **2016**, *7*, 11296.
- (167) Xu, L.; Jiang, Q.; Xiao, Z.; Li, X.; Huo, J.; Wang, S.; Dai, L. Plasma-Engraved Co₃O₄ Nanosheets with Oxygen Vacancies and High Surface Area for the Oxygen Evolution Reaction. *Angew. Chem., Int. Ed.* **2016**, *55*, 5277–5281.
- (168) Sun, Y.; Liu, Q.; Gao, S.; Cheng, H.; Lei, F.; Sun, Z.; Jiang, Y.; Su, H.; Wei, S.; Xie, Y. Pits Confined in Ultrathin Cerium(IV) Oxide for Studying Catalytic Centers in Carbon Monoxide Oxidation. *Nat. Commun.* **2013**, *4*, 2899.
- (169) Yin, H.; Tang, Z. Ultrathin Two-Dimensional Layered Metal Hydroxides: An Emerging Platform for Advanced Catalysis, Energy Conversion and Storage. *Chem. Soc. Rev.* **2016**, *45*, 4873–4891.
- (170) Qian, L.; Lu, Z.; Xu, T.; Wu, X.; Tian, Y.; Li, Y.; Huo, Z.; Sun, X.; Duan, X. Trinary Layered Double Hydroxides as High-Performance Bifunctional Materials for Oxygen Electrocatalysis. *Adv. Energy Mater.* **2015**, *5*, 1500245.
- (171) Gong, M.; Dai, H. A Mini Review of NiFe-Based Materials as Highly Active Oxygen Evolution Reaction Electrocatalysts. *Nano Res.* **2015**, *8*, 23–39.
- (172) Tang, C.; Zhang, Q. Nanocarbon for Oxygen Reduction Electrocatalysis: Dopants, Edges, and Defects. *Adv. Mater.* **2017**, *29*, 1604103.
- (173) Jiang, J.; Zhang, A.; Li, L.; Ai, L. Nickel–Cobalt Layered Double Hydroxide Nanosheets as High-Performance Electrocatalyst for Oxygen Evolution Reaction. *J. Power Sources* **2015**, *278*, 445–451.
- (174) Song, F.; Hu, X. Exfoliation of Layered Double Hydroxides for Enhanced Oxygen Evolution Catalysis. *Nat. Commun.* **2014**, *5*, 4477.

- (175) Subbaraman, R.; Tripkovic, D.; Strmcnik, D.; Chang, K. C.; Uchimura, M.; Paulikas, A. P.; Stamenkovic, V.; Markovic, N. M. Enhancing Hydrogen Evolution Activity in Water Splitting by Tailoring $\text{Li}^+\text{-Ni(OH)}_2\text{-Pt}$ Interfaces. *Science* **2011**, *334*, 1256–1260.
- (176) Subbaraman, R.; Tripkovic, D.; Chang, K. C.; Strmcnik, D.; Paulikas, A. P.; Hirunsit, P.; Chan, M.; Greeley, J.; Stamenkovic, V.; Markovic, N. M. Trends in Activity for the Water Electrolyser Reactions on 3d M(Ni,Co,Fe,Mn) Hydr(oxy)Oxide Catalysts. *Nat. Mater.* **2012**, *11*, 550–557.
- (177) Teramura, K.; Iguchi, S.; Mizuno, Y.; Shishido, T.; Tanaka, T. Photocatalytic Conversion of CO_2 in Water over Layered Double Hydroxides. *Angew. Chem., Int. Ed.* **2012**, *51*, 8008–8011.
- (178) Hong Ng, V. M.; Huang, H.; Zhou, K.; Lee, P. S.; Que, W.; Xu, J. Z.; Kong, L. B. Recent Progress in Layered Transition Metal Carbides and/or Nitrides (MXenes) and Their Composites: Synthesis and Applications. *J. Mater. Chem. A* **2017**, *5*, 3039–3068.
- (179) Naguib, M.; Kurtoglu, M.; Presser, V.; Lu, J.; Niu, J.; Heon, M.; Hultman, L.; Gogotsi, Y.; Barsoum, M. W. Two-Dimensional Nanocrystals Produced by Exfoliation of Ti_3AlC_2 . *Adv. Mater.* **2011**, *23*, 4248–4253.
- (180) Anasori, B.; Lukatskaya, M. R.; Gogotsi, Y. 2D Metal Carbides and Nitrides (MXenes) for Energy Storage. *Nat. Rev. Mater.* **2017**, *2*, 16098.
- (181) Naguib, M.; Mashtalir, O.; Carle, J.; Presser, V.; Lu, J.; Hultman, L.; Gogotsi, Y.; Barsoum, M. W. Two-Dimensional Transition Metal Carbides. *ACS Nano* **2012**, *6*, 1322–1331.
- (182) Xu, C.; Wang, L.; Liu, Z.; Chen, L.; Guo, J.; Kang, N.; Ma, X. L.; Cheng, H. M.; Ren, W. Large-Area High-Quality 2D Ultrathin Mo_2C Superconducting Crystals. *Nat. Mater.* **2015**, *14*, 1135–1141.
- (183) Xiao, X.; Yu, H.; Jin, H.; Wu, M.; Fang, Y.; Sun, J.; Hu, Z.; Li, T.; Wu, J.; Huang, L.; et al. Salt-Templated Synthesis of 2D Metallic MoN and Other Nitrides. *ACS Nano* **2017**, *11*, 2180–2186.
- (184) Zhao, L.; Dong, B.; Li, S.; Zhou, L.; Lai, L.; Wang, Z.; Zhao, S.; Han, M.; Gao, K.; Lu, M.; et al. Interdiffusion Reaction-Assisted Hybridization of Two-Dimensional Metal–Organic Frameworks and $\text{Ti}_3\text{C}_2\text{T}_x$ Nanosheets for Electrocatalytic Oxygen Evolution. *ACS Nano* **2017**, *11*, 5800–5807.
- (185) Ran, J.; Gao, G.; Li, F.-T.; Ma, T.-Y.; Du, A.; Qiao, S.-Z. Ti_3C_2 MXene Co-Catalyst on Metal Sulfide Photo-Absorbers for Enhanced Visible-Light Photocatalytic Hydrogen Production. *Nat. Commun.* **2017**, *8*, 13907.
- (186) Seh, Z. W.; Fredrickson, K. D.; Anasori, B.; Kibsgaard, J.; Strickler, A. L.; Lukatskaya, M. R.; Gogotsi, Y.; Jaramillo, T. F.; Vojvodic, A. Two-Dimensional Molybdenum Carbide (MXene) as an Efficient Electrocatalyst for Hydrogen Evolution. *ACS Energy Lett.* **2016**, *1*, 589–594.
- (187) Geng, D.; Zhao, X.; Chen, Z.; Sun, W.; Fu, W.; Chen, J.; Liu, W.; Zhou, W.; Loh, K. P. Direct Synthesis of Large-Area 2D Mo_2C on in Situ Grown Graphene. *Adv. Mater.* **2017**, *29*, 1700072.
- (188) Fan, Z.; Huang, X.; Tan, C.; Zhang, H. Thin Metal Nanostructures: Synthesis, Properties and Applications. *Chem. Sci.* **2015**, *6*, 95–111.
- (189) Daniel, M.-C.; Astruc, D. Gold Nanoparticles: Assembly, Supramolecular Chemistry, Quantum-Size-Related Properties, and Applications toward Biology, Catalysis, and Nanotechnology. *Chem. Rev.* **2004**, *104*, 293–346.
- (190) Duan, H.; Yan, N.; Yu, R.; Chang, C.-R.; Zhou, G.; Hu, H.-S.; Rong, H.; Niu, Z.; Mao, J.; Asakura, H.; et al. Ultrathin Rhodium Nanosheets. *Nat. Commun.* **2014**, *5*, 3093.
- (191) Fan, Z.; Bosman, M.; Huang, X.; Huang, D.; Yu, Y.; Ong, K. P.; Akimov, Y. A.; Wu, L.; Li, B.; Wu, J.; et al. Stabilization of 4H Hexagonal Phase in Gold Nanoribbons. *Nat. Commun.* **2015**, *6*, 7684.
- (192) Huang, X.; Li, S.; Huang, Y.; Wu, S.; Zhou, X.; Li, S.; Gan, C. L.; Boey, F.; Mirkin, C. A.; Zhang, H. Synthesis of Hexagonal Close-Packed Gold Nanostructures. *Nat. Commun.* **2011**, *2*, 292.
- (193) Huang, X.; Tang, S.; Mu, X.; Dai, Y.; Chen, G.; Zhou, Z.; Ruan, F.; Yang, Z.; Zheng, N. Freestanding Palladium Nanosheets with Plasmonic and Catalytic Properties. *Nat. Nanotechnol.* **2011**, *6*, 28–32.
- (194) Fan, Z.; Huang, X.; Han, Y.; Bosman, M.; Wang, Q.; Zhu, Y.; Liu, Q.; Li, B.; Zeng, Z.; Wu, J.; et al. Surface Modification-Induced Phase Transformation of Hexagonal Close-Packed Gold Square Sheets. *Nat. Commun.* **2015**, *6*, 6571.
- (195) Saleem, F.; Xu, B.; Ni, B.; Liu, H.; Nosheen, F.; Li, H.; Wang, X. Atomically Thick Pt-Cu Nanosheets: Self-Assembled Sandwich and Nanoring-Like Structures. *Adv. Mater.* **2015**, *27*, 2013–2018.
- (196) James, S. L. Metal-Organic Frameworks. *Chem. Soc. Rev.* **2003**, *32*, 276–288.
- (197) Trickett, C. A.; Helal, A.; Al-Maythaly, B. A.; Yamani, Z. H.; Cordova, K. E.; Yaghi, O. M. The Chemistry of Metal–Organic Frameworks for CO_2 Capture, Regeneration and Conversion. *Nat. Rev. Mater.* **2017**, *2*, 17045.
- (198) Wang, W.; Xu, X.; Zhou, W.; Shao, Z. Recent Progress in Metal-Organic Frameworks for Applications in Electrocatalytic and Photocatalytic Water Splitting. *Adv. Sci.* **2017**, *4*, 1600371.
- (199) Zhu, L.; Liu, X. Q.; Jiang, H. L.; Sun, L. B. Metal-Organic Frameworks for Heterogeneous Basic Catalysis. *Chem. Rev.* **2017**, *117*, 8129–8176.
- (200) Zheng, Y.; Qiao, S.-Z. Direct Growth of Well-Aligned MOF Arrays onto Various Substrates. *Chem.* **2017**, *2*, 751–752.
- (201) Zhao, S.; Wang, Y.; Dong, J.; He, C.-T.; Yin, H.; An, P.; Zhao, K.; Zhang, X.; Gao, C.; Zhang, L.; et al. Ultrathin Metal–Organic Framework Nanosheets for Electrocatalytic Oxygen Evolution. *Nat. Energy* **2016**, *1*, 16184.
- (202) Kornienko, N.; Zhao, Y.; Kley, C. S.; Zhu, C.; Kim, D.; Lin, S.; Chang, C. J.; Yaghi, O. M.; Yang, P. Metal–Organic Frameworks for Electrocatalytic Reduction of Carbon Dioxide. *J. Am. Chem. Soc.* **2015**, *137*, 14129–14135.
- (203) Rodenas, T.; Luz, I.; Prieto, G.; Seoane, B.; Miro, H.; Corma, A.; Kapteijn, F.; Llabrés i Xamena, F. X.; Gascon, J. Metal–Organic Framework Nanosheets in Polymer Composite Materials for Gas Separation. *Nat. Mater.* **2015**, *14*, 48–55.
- (204) Duan, J.; Chen, S.; Zhao, C. Ultrathin Metal–Organic Framework Array for Efficient Electrocatalytic Water Splitting. *Nat. Commun.* **2017**, *8*, 15341.
- (205) Chen, Y.; Ji, S.; Wang, Y.; Dong, J.; Chen, W.; Li, Z.; Shen, R.; Zheng, L.; Zhuang, Z.; Wang, D.; et al. Isolated Single Iron Atoms Anchored on N-Doped Porous Carbon as an Efficient Electrocatalyst for the Oxygen Reduction Reaction. *Angew. Chem., Int. Ed.* **2017**, *56*, 6937–6941.
- (206) Yin, P.; Yao, T.; Wu, Y.; Zheng, L.; Lin, Y.; Liu, W.; Ju, H.; Zhu, J.; Hong, X.; Deng, Z.; et al. Single Cobalt Atoms with Precise N-Coordination as Superior Oxygen Reduction Reaction Catalysts. *Angew. Chem., Int. Ed.* **2016**, *55*, 10800–10805.
- (207) Zhao, C.; Dai, X.; Yao, T.; Chen, W.; Wang, X.; Wang, J.; Yang, J.; Wei, S.; Wu, Y.; Li, Y. Ionic Exchange of Metal–Organic Frameworks to Access Single Nickel Sites for Efficient Electroreduction of CO_2 . *J. Am. Chem. Soc.* **2017**, *139*, 8078–8081.
- (208) Diercks, C. S.; Yaghi, O. M. The Atom, the Molecule, and the Covalent Organic Framework. *Science* **2017**, *355*, eaal1585.
- (209) Côté, A. P.; Benin, A. I.; Ockwig, N. W.; Keffe, M.; Matzger, A. J.; Yaghi, O. M. Porous, Crystalline, Covalent Organic Frameworks. *Science* **2005**, *310*, 1166–1170.
- (210) Segura, J. L.; Mancheno, M. J.; Zamora, F. Covalent Organic Frameworks Based on Schiff-Base Chemistry: Synthesis, Properties and Potential Applications. *Chem. Soc. Rev.* **2016**, *45*, 5635–5671.
- (211) Rogge, S. M. J.; Bavykina, A.; Hajek, J.; Garcia, H.; Olivos-Suarez, A. I.; Sepulveda-Escribano, A.; Vimont, A.; Clet, G.; Bazin, P.; Kapteijn, F.; et al. Metal-Organic and Covalent Organic Frameworks as Single-Site Catalysts. *Chem. Soc. Rev.* **2017**, *46*, 3134–3184.
- (212) Peng, P.; Zhou, Z.; Guo, J.; Xiang, Z. Well-Defined 2D Covalent Organic Polymers for Energy Electrocatalysis. *ACS Energy Lett.* **2017**, *2*, 1308–1314.
- (213) Bisbey, R. P.; DeBlase, C. R.; Smith, B. J.; Dichtel, W. R. Two-Dimensional Covalent Organic Framework Thin Films Grown in Flow. *J. Am. Chem. Soc.* **2016**, *138*, 11433–11436.
- (214) Cai, S.-L.; Zhang, K.; Tan, J.-B.; Wang, S.; Zheng, S.-R.; Fan, J.; Yu, Y.; Zhang, W.-G.; Liu, Y. Rationally Designed 2d Covalent Organic

Framework with a Brick-Wall Topology. *ACS Macro Lett.* **2016**, *5*, 1348–1352.

(215) Colson, J. W.; Woll, A. R.; Mukherjee, A.; Levendorf, M. P.; Spittler, E. L.; Shields, V. B.; Spencer, M. G.; Park, J.; Dichtel, W. R. Oriented 2D Covalent Organic Framework Thin Films on Single-Layer Graphene. *Science* **2011**, *332*, 228–231.

(216) Baldwin, L. A.; Crowe, J. W.; Shannon, M. D.; Jaroniec, C. P.; McGrier, P. L. 2D Covalent Organic Frameworks with Alternating Triangular and Hexagonal Pores. *Chem. Mater.* **2015**, *27*, 6169–6172.

(217) Lin, C.-Y.; Zhang, L.; Zhao, Z.; Xia, Z. Design Principles for Covalent Organic Frameworks as Efficient Electrocatalysts in Clean Energy Conversion and Green Oxidizer Production. *Adv. Mater.* **2017**, *29*, 1606635.

(218) Xiang, Z.; Xue, Y.; Cao, D.; Huang, L.; Chen, J.-F.; Dai, L. Highly Efficient Electrocatalysts for Oxygen Reduction Based on 2D Covalent Organic Polymers Complexed with Non-Precious Metals. *Angew. Chem., Int. Ed.* **2014**, *53*, 2433–2437.

(219) Lin, S.; Diercks, C. S.; Zhang, Y.-B.; Kornienko, N.; Nichols, E. M.; Zhao, Y.; Paris, A. R.; Kim, D.; Yang, P.; Yaghi, O. M.; et al. Covalent Organic Frameworks Comprising Cobalt Porphyrins for Catalytic CO₂ Reduction in Water. *Science* **2015**, *349*, 1208–1213.

(220) Gao, G.; Waclawik, E. R.; Du, A. Computational Screening of Two-Dimensional Coordination Polymers as Efficient Catalysts for Oxygen Evolution and Reduction Reaction. *J. Catal.* **2017**, *352*, 579–585.

(221) Dong, R.; Pfeiffermann, M.; Liang, H.; Zheng, Z.; Zhu, X.; Zhang, J.; Feng, X. Large-Area, Free-Standing, Two-Dimensional Supramolecular Polymer Single-Layer Sheets for Highly Efficient Electrocatalytic Hydrogen Evolution. *Angew. Chem., Int. Ed.* **2015**, *54*, 12058–12063.

(222) Bayatsarmadi, B.; Zheng, Y.; Vasileff, A.; Qiao, S.-Z. Recent Advances in Atomic Metal Doping of Carbon-Based Nanomaterials for Energy Conversion. *Small* **2017**, *13*, 1700191.

(223) Deng, D.; Pan, X.; Yu, L.; Cui, Y.; Jiang, Y.; Qi, J.; Li, W.-X.; Fu, Q.; Ma, X.; Xue, Q.; et al. Toward N-Doped Graphene Via Solvothermal Synthesis. *Chem. Mater.* **2011**, *23*, 1188–1193.

(224) Li, Y.; Zhou, Z.; Shen, P.; Chen, Z. Spin Gapless Semiconductor–Metal–Half-Metal Properties in Nitrogen-Doped Zigzag Graphene Nanoribbons. *ACS Nano* **2009**, *3*, 1952–1958.

(225) Zhang, L.; Xia, Z. Mechanisms of Oxygen Reduction Reaction on Nitrogen-Doped Graphene for Fuel Cells. *J. Phys. Chem. C* **2011**, *115*, 11170–11176.

(226) Jiao, Y.; Zheng, Y.; Jaroniec, M.; Qiao, S. Z. Origin of the Electrocatalytic Oxygen Reduction Activity of Graphene-Based Catalysts: A Roadmap to Achieve the Best Performance. *J. Am. Chem. Soc.* **2014**, *136*, 4394–4403.

(227) Chen, S.; Duan, J.; Jaroniec, M.; Qiao, S.-Z. Nitrogen and Oxygen Dual-Doped Carbon Hydrogel Film as a Substrate-Free Electrode for Highly Efficient Oxygen Evolution Reaction. *Adv. Mater.* **2014**, *26*, 2925–2930.

(228) Herzing, A. A.; Kiely, C. J.; Carley, A. F.; Landon, P.; Hutchings, G. J. Identification of Active Gold Nanoclusters on Iron Oxide Supports for CO Oxidation. *Science* **2008**, *321*, 1331–1335.

(229) Heiz, U.; Sanchez, A.; Abbet, S.; Schneider, W. D. Catalytic Oxidation of Carbon Monoxide on Monodispersed Platinum Clusters: Each Atom Counts. *J. Am. Chem. Soc.* **1999**, *121*, 3214–3217.

(230) Lei, Y.; Mehmood, F.; Lee, S.; Greeley, J.; Lee, B.; Seifert, S.; Winans, R. E.; Elam, J. W.; Meyer, R. J.; Redfern, P. C.; et al. Increased Silver Activity for Direct Propylene Epoxidation Via Subnanometer Size Effects. *Science* **2010**, *328*, 224–228.

(231) Liu, J. Catalysis by Supported Single Metal Atoms. *ACS Catal.* **2017**, *7*, 34–59.

(232) Fei, H.; Dong, J.; Arellano-Jiménez, M. J.; Ye, G.; Dong Kim, N.; Samuel, E. L. G.; Peng, Z.; Zhu, Z.; Qin, F.; Bao, J.; et al. Atomic Cobalt on Nitrogen-Doped Graphene for Hydrogen Generation. *Nat. Commun.* **2015**, *6*, 8668.

(233) Lu, Y.-H.; Zhou, M.; Zhang, C.; Feng, Y.-P. Metal-Embedded Graphene: A Possible Catalyst with High Activity. *J. Phys. Chem. C* **2009**, *113*, 20156–20160.

(234) Zheng, Y.; Jiao, Y.; Zhu, Y.; Cai, Q.; Vasileff, A.; Li, L. H.; Han, Y.; Chen, Y.; Qiao, S.-Z. Molecule-Level g-C₃N₄ Coordinated Transition Metals as a New Class of Electrocatalysts for Oxygen Electrode Reactions. *J. Am. Chem. Soc.* **2017**, *139*, 3336–3339.

(235) Lauritsen, J. V.; Kibsgaard, J.; Olesen, G. H.; Moses, P. G.; Hinnemann, B.; Helveg, S.; Nørskov, J. K.; Clausen, B. S.; Topsøe, H.; Lægsgaard, E.; et al. Location and Coordination of Promoter Atoms in Co- and Ni-Promoted MoS₂-Based Hydrotreating Catalysts. *J. Catal.* **2007**, *249*, 220–233.

(236) Besenbacher, F.; Brorson, M.; Clausen, B. S.; Helveg, S.; Hinnemann, B.; Kibsgaard, J.; Lauritsen, J. V.; Moses, P. G.; Nørskov, J. K.; Topsøe, H. Recent Stm, DFT and HAADF-STEM Studies of Sulfide-Based Hydrotreating Catalysts: Insight into Mechanistic, Structural and Particle Size Effects. *Catal. Today* **2008**, *130*, 86–96.

(237) Lauritsen, J. V.; Helveg, S.; Lægsgaard, E.; Stensgaard, I.; Clausen, B. S.; Topsøe, H.; Besenbacher, F. Atomic-Scale Structure of Co–Mo–S Nanoclusters in Hydrotreating Catalysts. *J. Catal.* **2001**, *197*, 1–5.

(238) Byskov, L. S.; Nørskov, J. K.; Clausen, B. S.; Topsøe, H. Dft Calculations of Unpromoted and Promoted MoS₂-Based Hydrodesulfurization Catalysts. *J. Catal.* **1999**, *187*, 109–122.

(239) Bonde, J.; Moses, P. G.; Jaramillo, T. F.; Nørskov, J. K.; Chorkendorff, I. Hydrogen Evolution on Nano-Particulate Transition Metal Sulfides. *Faraday Discuss.* **2009**, *140*, 219–231.

(240) Jiang, D.-e.; Sumpter, B. G.; Dai, S. Unique Chemical Reactivity of a Graphene Nanoribbon's Zigzag Edge. *J. Chem. Phys.* **2007**, *126*, 134701.

(241) Hong, J.; Jin, C.; Yuan, J.; Zhang, Z. Atomic Defects in Two-Dimensional Materials: From Single-Atom Spectroscopy to Functionalities in Opto-/Electronics, Nanomagnetism, and Catalysis. *Adv. Mater.* **2017**, *29*, 1606434.

(242) Jia, Y.; Zhang, L.; Du, A.; Gao, G.; Chen, J.; Yan, X.; Brown, C. L.; Yao, X. Defect Graphene as a Trifunctional Catalyst for Electrochemical Reactions. *Adv. Mater.* **2016**, *28*, 9532–9538.

(243) Tao, L.; Wang, Q.; Dou, S.; Ma, Z.; Huo, J.; Wang, S.; Dai, L. Edge-Rich and Dopant-Free Graphene as a Highly Efficient Metal-Free Electrocatalyst for the Oxygen Reduction Reaction. *Chem. Commun.* **2016**, *52*, 2764–2767.

(244) Li, X.; Cai, W.; An, J.; Kim, S.; Nah, J.; Yang, D.; Piner, R.; Velamakanni, A.; Jung, L.; Tutuc, E.; et al. Large-Area Synthesis of High-Quality and Uniform Graphene Films on Copper Foils. *Science* **2009**, *324*, 1312–1314.

(245) Xie, J.; Zhang, H.; Li, S.; Wang, R.; Sun, X.; Zhou, M.; Zhou, J.; Lou, X. W.; Xie, Y. Defect-Rich MoS₂ Ultrathin Nanosheets with Additional Active Edge Sites for Enhanced Electrocatalytic Hydrogen Evolution. *Adv. Mater.* **2013**, *25*, 5807–5813.

(246) Xu, K.; Chen, P.; Li, X.; Tong, Y.; Ding, H.; Wu, X.; Chu, W.; Peng, Z.; Wu, C.; Xie, Y. Metallic Nickel Nitride Nanosheets Realizing Enhanced Electrochemical Water Oxidation. *J. Am. Chem. Soc.* **2015**, *137*, 4119–4125.

(247) Gao, S.; Gu, B.; Jiao, X.; Sun, Y.; Zu, X.; Yang, F.; Zhu, W.; Wang, C.; Feng, Z.; Ye, B.; et al. Highly Efficient and Exceptionally Durable CO₂ Photoreduction to Methanol over Freestanding Defective Single-Unit-Cell Bismuth Vanadate Layers. *J. Am. Chem. Soc.* **2017**, *139*, 3438–3445.

(248) Gao, S.; Jiao, X.; Sun, Z.; Zhang, W.; Sun, Y.; Wang, C.; Hu, Q.; Zu, X.; Yang, F.; Yang, S.; et al. Ultrathin Co₃O₄ Layers Realizing Optimized CO₂ Electroreduction to Formate. *Angew. Chem., Int. Ed.* **2016**, *55*, 698–702.

(249) Kibsgaard, J.; Chen, Z.; Reinecke, B. N.; Jaramillo, T. F. Engineering the Surface Structure of MoS₂ To preferentially Expose Active Edge Sites For electrocatalysis. *Nat. Mater.* **2012**, *11*, 963–969.

(250) Li, H.; Tsai, C.; Koh, A. L.; Cai, L.; Contryman, A. W.; Fragapane, A. H.; Zhao, J.; Han, H. S.; Manoharan, H. C.; Abild-Pedersen, F.; et al. Activating and Optimizing MoS₂ Basal Planes for Hydrogen Evolution through the Formation of Strained Sulphur Vacancies. *Nat. Mater.* **2016**, *15*, 48–53.

(251) Strasser, P.; Koh, S.; Anniyev, T.; Greeley, J.; More, K.; Yu, C.; Liu, Z.; Kaya, S.; Nordlund, D.; Ogasawara, H.; et al. Lattice-Strain

Control of the Activity in Dealloyed Core–Shell Fuel Cell Catalysts. *Nat. Chem.* **2010**, *2*, 454–460.

(252) Mavrikakis, M.; Hammer, B.; Nørskov, J. K. Effect of Strain on the Reactivity of Metal Surfaces. *Phys. Rev. Lett.* **1998**, *81*, 2819–2822.

(253) Voiry, D.; Yang, J.; Chhowalla, M. Recent Strategies for Improving the Catalytic Activity of 2d Tmd Nanosheets toward the Hydrogen Evolution Reaction. *Adv. Mater.* **2016**, *28*, 6197–6206.

(254) Voiry, D.; Salehi, M.; Silva, R.; Fujita, T.; Chen, M.; Asefa, T.; Shenoy, V. B.; Eda, G.; Chhowalla, M. Conducting MoS₂ Nanosheets as Catalysts for Hydrogen Evolution Reaction. *Nano Lett.* **2013**, *13*, 6222–6227.

(255) Wang, H.; Lu, Z.; Xu, S.; Kong, D.; Cha, J. J.; Zheng, G.; Hsu, P.-C.; Yan, K.; Bradshaw, D.; Prinz, F. B.; et al. Electrochemical Tuning of Vertically Aligned MoS₂ Nanofilms and Its Application in Improving Hydrogen Evolution Reaction. *Proc. Natl. Acad. Sci. U. S. A.* **2013**, *110*, 19701–19706.

(256) Novoselov, K. S.; Mishchenko, A.; Carvalho, A.; Castro Neto, A. H. 2D Materials and Van Der Waals Heterostructures. *Science* **2016**, *353*, aac9439.

(257) Gong, M.; Zhou, W.; Tsai, M. C.; Zhou, J.; Guan, M.; Lin, M. C.; Zhang, B.; Hu, Y.; Wang, D. Y.; Yang, J.; et al. Nanoscale Nickel Oxide/Nickel Heterostructures for Active Hydrogen Evolution Electrocatalysis. *Nat. Commun.* **2014**, *5*, 4695.

(258) Duan, J.; Chen, S.; Jaroniec, M.; Qiao, S. Z. Porous C₃N₄ Nanolayers@N-Graphene Films as Catalyst Electrodes for Highly Efficient Hydrogen Evolution. *ACS Nano* **2015**, *9*, 931–940.

(259) Duan, J.; Chen, S.; Chambers, B. A.; Andersson, G. G.; Qiao, S. Z. 3D WS₂ Nanolayers@Heteroatom-Doped Graphene Films as Hydrogen Evolution Catalyst Electrodes. *Adv. Mater.* **2015**, *27*, 4234–4241.

(260) Chen, S.; Duan, J.; Tang, Y.; Jin, B.; Zhang Qiao, S. Molybdenum Sulfide Clusters-Nitrogen-Doped Graphene Hybrid Hydrogel Film as an Efficient Three-Dimensional Hydrogen Evolution Electrocatalyst. *Nano Energy* **2015**, *11*, 11–18.

(261) Gao, M.-R.; Liang, J.-X.; Zheng, Y.-R.; Xu, Y.-F.; Jiang, J.; Gao, Q.; Li, J.; Yu, S.-H. An Efficient Molybdenum Disulfide/Cobalt Diselenide Hybrid Catalyst for Electrochemical Hydrogen Generation. *Nat. Commun.* **2015**, *6*, 5982.

(262) Staszak-Jirkovsky, J.; Malliakas, C. D.; Lopes, P. P.; Danilovic, N.; Kota, S. S.; Chang, K.-C.; Genorio, B.; Strmcnik, D.; Stamenkovic, V. R.; Kanatzidis, M. G.; et al. Design of Active and Stable Co-Mo-S_x Chalcogenides as pH-Universal Catalysts for the Hydrogen Evolution Reaction. *Nat. Mater.* **2016**, *15*, 197–203.

(263) Yang, J.; Voiry, D.; Ahn, S. J.; Kang, D.; Kim, A. Y.; Chhowalla, M.; Shin, H. S. Two-Dimensional Hybrid Nanosheets of Tungsten Disulfide and Reduced Graphene Oxide as Catalysts for Enhanced Hydrogen Evolution. *Angew. Chem., Int. Ed.* **2013**, *52*, 13751–13754.

(264) Huang, X.; Zeng, Z.; Bao, S.; Wang, M.; Qi, X.; Fan, Z.; Zhang, H. Solution-Phase Epitaxial Growth of Noble Metal Nanostructures on Dispersible Single-Layer Molybdenum Disulfide Nanosheets. *Nat. Commun.* **2013**, *4*, 1444.

(265) Wang, Z. L. Transmission Electron Microscopy of Shape-Controlled Nanocrystals and Their Assemblies. *J. Phys. Chem. B* **2000**, *104*, 1153–1175.

(266) Liu, G.; Robertson, A. W.; Li, M. M.-J.; Kuo, W. C. H.; Darby, M. T.; Muhieddine, M. H.; Lin, Y.-C.; Suenaga, K.; Stamatakis, M.; Warner, J. H.; et al. MoS₂ Monolayer Catalyst Doped with Isolated Co Atoms for the Hydrodeoxygenation Reaction. *Nat. Chem.* **2017**, *9*, 810–816.

(267) Voiry, D.; Fullon, R.; Yang, J.; de Carvalho Castro e Silva, C.; Kapper, R.; Bozkurt, I.; Kaplan, D.; Lagos, M. J.; Batson, P. E.; Gupta, G.; et al. The Role of Electronic Coupling between Substrate and 2D MoS₂ Nanosheets in Electrocatalytic Production of Hydrogen. *Nat. Mater.* **2016**, *15*, 1003–1009.

(268) Gong, Y.; Lin, J.; Wang, X.; Shi, G.; Lei, S.; Lin, Z.; Zou, X.; Ye, G.; Vajtai, R.; Yakobson, B. I.; et al. Vertical and in-Plane Heterostructures from WS₂/ MoS₂ Monolayers. *Nat. Mater.* **2014**, *13*, 1135–1142.

(269) Frenkel, A. I. Applications of Extended X-Ray Absorption Fine-Structure Spectroscopy to Studies of Bimetallic Nanoparticle Catalysts. *Chem. Soc. Rev.* **2012**, *41*, 8163–8178.

(270) van Oversteeg, C. H. M.; Doan, H. Q.; de Groot, F. M. F.; Cuk, T. In Situ X-Ray Absorption Spectroscopy of Transition Metal Based Water Oxidation Catalysts. *Chem. Soc. Rev.* **2017**, *46*, 102–125.

(271) Pacilé, D.; Papagno, M.; Rodríguez, A. F.; Grioni, M.; Papagno, L.; Girit, Ç. Ö.; Meyer, J. C.; Begtrup, G. E.; Zettl, A. Near-Edge X-Ray Absorption Fine-Structure Investigation of Graphene. *Phys. Rev. Lett.* **2008**, *101*, 066806.

(272) Sun, Z.; Liu, Q.; Yao, T.; Yan, W.; Wei, S. X-Ray Absorption Fine Structure Spectroscopy in Nanomaterials. *Sci. China Mater.* **2015**, *58*, 313–341.

(273) Hemraj-Benny, T.; Banerjee, S.; Sambasivan, S.; Balasubramanian, M.; Fischer, D. A.; Eres, G.; Puzos, A. A.; Geohegan, D. B.; Lowndes, D. H.; Han, W.; et al. Near-Edge X-Ray Absorption Fine Structure Spectroscopy as a Tool for Investigating Nanomaterials. *Small* **2006**, *2*, 26–35.

(274) Pasquarello, A.; Petri, I.; Salmon, P. S.; Parisel, O.; Car, R.; Tóth, É.; Powell, D. H.; Fischer, H. E.; Helm, L.; Merbach, A. E. First Solvation Shell of the Cu(II) Aqua Ion: Evidence for Fivefold Coordination. *Science* **2001**, *291*, 856–859.

(275) Zhang, X.-W.; Yan, X.-J.; Zhou, Z.-R.; Yang, F.-F.; Wu, Z.-Y.; Sun, H.-B.; Liang, W.-X.; Song, A.-X.; Lallemand-Breitenbach, V.; Jeanne, M.; et al. Arsenic Trioxide Controls the Fate of the PML-RAR α Oncoprotein by Directly Binding PML. *Science* **2010**, *328*, 240–243.

(276) Chen, L. X.; Jäger, W. J. H.; Jennings, G.; Gosztoła, D. J.; Munkholm, A.; Hessler, J. P. Capturing a Photoexcited Molecular Structure Through Time-Domain X-Ray Absorption Fine Structure. *Science* **2001**, *292*, 262–264.

(277) de Groot, F. High-Resolution X-Ray Emission and X-Ray Absorption Spectroscopy. *Chem. Rev.* **2001**, *101*, 1779–1808.

(278) Hammer, B.; Nørskov, J. K. Theoretical Surface Science and Catalysis—Calculations and Concepts. In *Advances in Catalysis*; Bruce, C., Gates, H. K., Eds.; Academic Press: San Diego, 2000; Vol. 45, pp 71–129.

(279) Nørskov, J. K.; Studt, F.; Abild-Pedersen, F.; Bligaard, T. Relation of Activity to Surface Electronic Structure. *Fundamental Concepts in Heterogeneous Catalysis*; John Wiley & Sons, Inc.: New York, 2014; pp 175–194.

(280) Marković, N. M.; Ross, P. N. Surface Science Studies of Model Fuel Cell Electrocatalysts. *Surf. Sci. Rep.* **2002**, *45*, 117–229.

(281) Kaya, S.; Friebel, D.; Ogasawara, H.; Anniyev, T.; Nilsson, A. Electronic Structure Effects in Catalysis Probed by X-Ray and Electron Spectroscopy. *J. Electron Spectrosc. Relat. Phenom.* **2013**, *190*, 113–124.

(282) Stamenkovic, V. R.; Fowler, B.; Mun, B. S.; Wang, G.; Ross, P. N.; Lucas, C. A.; Marković, N. M. Improved Oxygen Reduction Activity on Pt₃Ni(111) Via Increased Surface Site Availability. *Science* **2007**, *315*, 493–497.

(283) Stamenkovic, V. R.; Mun, B. S.; Arenz, M.; Mayrhofer, K. J. J.; Lucas, C. A.; Wang, G.; Ross, P. N.; Markovic, N. M. Trends in Electrocatalysis on Extended and Nanoscale Pt-Bimetallic Alloy Surfaces. *Nat. Mater.* **2007**, *6*, 241–247.

(284) Stamenkovic, V.; Mun, B. S.; Mayrhofer, K. J. J.; Ross, P. N.; Markovic, N. M.; Rossmeisl, J.; Greeley, J.; Nørskov, J. K. Changing the Activity of Electrocatalysts for Oxygen Reduction by Tuning the Surface Electronic Structure. *Angew. Chem.* **2006**, *118*, 2963–2967.

(285) Montoya, J. H.; Seitz, L. C.; Chakhranont, P.; Vojvodic, A.; Jaramillo, T. F.; Nørskov, J. K. Materials for Solar Fuels and Chemicals. *Nat. Mater.* **2017**, *16*, 70–81.

(286) Sabatier, P. Hydrogénations Et Déshydrogénations Par Catalyse. *Ber. Dtsch. Chem. Ges.* **1911**, *44*, 1984–2001.

(287) Cheng, F.; Chen, J. Metal-Air Batteries: From Oxygen Reduction Electrochemistry to Cathode Catalysts. *Chem. Soc. Rev.* **2012**, *41*, 2172–2192.

(288) Ge, X.; Sumboja, A.; Wu, D.; An, T.; Li, B.; Goh, F. W. T.; Hor, T. S. A.; Zong, Y.; Liu, Z. Oxygen Reduction in Alkaline Media: From Mechanisms to Recent Advances of Catalysts. *ACS Catal.* **2015**, *5*, 4643–4667.

- (289) Hansen, H. A.; Viswanathan, V.; Nørskov, J. K. Unifying Kinetic and Thermodynamic Analysis of $2 e^-$ and $4 e^-$ Reduction of Oxygen on Metal Surfaces. *J. Phys. Chem. C* **2014**, *118*, 6706–6718.
- (290) Stephens, I. E. L.; Bondarenko, A. S.; Gronbjerg, U.; Rossmeisl, J.; Chorkendorff, I. Understanding the Electrocatalysis of Oxygen Reduction on Platinum and its Alloys. *Energy Environ. Sci.* **2012**, *5*, 6744–6762.
- (291) Wu, J.; Yang, H. Platinum-Based Oxygen Reduction Electrocatalysts. *Acc. Chem. Res.* **2013**, *46*, 1848–1857.
- (292) Wang, Y.-J.; Zhao, N.; Fang, B.; Li, H.; Bi, X. T.; Wang, H. Carbon-Supported Pt-Based Alloy Electrocatalysts for the Oxygen Reduction Reaction in Polymer Electrolyte Membrane Fuel Cells: Particle Size, Shape, and Composition Manipulation and Their Impact to Activity. *Chem. Rev.* **2015**, *115*, 3433–3467.
- (293) Qian, Y.; Khan, I. A.; Zhao, D. Electrocatalysts Derived from Metal–Organic Frameworks for Oxygen Reduction and Evolution Reactions in Aqueous Media. *Small* **2017**, *13*, 1701143.
- (294) Rao, C. N. R.; Waghmare, U. V.: *2D Inorganic Materials Beyond Graphene*; World Scientific Publishing Company Pte Limited: Singapore, 2017.
- (295) Yu, L.; Pan, X.; Cao, X.; Hu, P.; Bao, X. Oxygen Reduction Reaction Mechanism on Nitrogen-Doped Graphene: A Density Functional Theory Study. *J. Catal.* **2011**, *282*, 183–190.
- (296) Song, C.; Zhang, J.: *Electrocatalytic Oxygen Reduction Reaction*. In *Pem Fuel Cell Electrocatalysts and Catalyst Layers*; Zhang, J., Ed.; Springer: London, 2008; pp 89–134.
- (297) Yan, H. J.; Xu, B.; Shi, S. Q.; Ouyang, C. Y. First-Principles Study of the Oxygen Adsorption and Dissociation on Graphene and Nitrogen Doped Graphene for Li-Air Batteries. *J. Appl. Phys.* **2012**, *112*, 104316.
- (298) Chai, G.-L.; Hou, Z.; Ikeda, T.; Terakura, K. Two-Electron Oxygen Reduction on Carbon Materials Catalysts: Mechanisms and Active Sites. *J. Phys. Chem. C* **2017**, *121*, 14524–14533.
- (299) Park, J.; Nabae, Y.; Hayakawa, T.; Kakimoto, M.-a. Highly Selective Two-Electron Oxygen Reduction Catalyzed by Mesoporous Nitrogen-Doped Carbon. *ACS Catal.* **2014**, *4*, 3749–3754.
- (300) Nørskov, J. K.; Rossmeisl, J.; Logadottir, A.; Lindqvist, L.; Kitchin, J. R.; Bligaard, T.; Jónsson, H. Origin of the Overpotential for Oxygen Reduction at a Fuel-Cell Cathode. *J. Phys. Chem. B* **2004**, *108*, 17886–17892.
- (301) Huang, J.; Chen, J.; Yao, T.; He, J.; Jiang, S.; Sun, Z.; Liu, Q.; Cheng, W.; Hu, F.; Jiang, Y.; et al. CoOOH Nanosheets with High Mass Activity for Water Oxidation. *Angew. Chem., Int. Ed.* **2015**, *54*, 8722–8727.
- (302) Zhou, R.; Zheng, Y.; Jaroniec, M.; Qiao, S.-Z. Determination of the Electron Transfer Number for the Oxygen Reduction Reaction: From Theory to Experiment. *ACS Catal.* **2016**, *6*, 4720–4728.
- (303) Wang, D.-W.; Su, D. Heterogeneous Nanocarbon Materials for Oxygen Reduction Reaction. *Energy Environ. Sci.* **2014**, *7*, 576–591.
- (304) Wang, H.; Maiyalagan, T.; Wang, X. Review on Recent Progress in Nitrogen-Doped Graphene: Synthesis, Characterization, and Its Potential Applications. *ACS Catal.* **2012**, *2*, 781–794.
- (305) Higgins, D.; Zamani, P.; Yu, A.; Chen, Z. The Application of Graphene and Its Composites in Oxygen Reduction Electrocatalysis: A Perspective and Review of Recent Progress. *Energy Environ. Sci.* **2016**, *9*, 357–390.
- (306) Zheng, Y.; Jiao, Y.; Jaroniec, M.; Jin, Y.; Qiao, S. Z. Nanostructured Metal-Free Electrochemical Catalysts for Highly Efficient Oxygen Reduction. *Small* **2012**, *8*, 3550–3566.
- (307) Zhang, J.; Dai, L. Heteroatom-Doped Graphitic Carbon Catalysts for Efficient Electrocatalysis of Oxygen Reduction Reaction. *ACS Catal.* **2015**, *5*, 7244–7253.
- (308) Paraknowitsch, J. P.; Thomas, A. Doping Carbons Beyond Nitrogen: An Overview of Advanced Heteroatom Doped Carbons with Boron, Sulphur and Phosphorus for Energy Applications. *Energy Environ. Sci.* **2013**, *6*, 2839–2855.
- (309) Biddinger, E. J.; von Deak, D.; Ozkan, U. S. Nitrogen-Containing Carbon Nanostructures as Oxygen-Reduction Catalysts. *Top. Catal.* **2009**, *52*, 1566–1574.
- (310) Wei, D.; Liu, Y.; Wang, Y.; Zhang, H.; Huang, L.; Yu, G. Synthesis of N-Doped Graphene by Chemical Vapor Deposition and Its Electrical Properties. *Nano Lett.* **2009**, *9*, 1752–1758.
- (311) Luo, Z.; Lim, S.; Tian, Z.; Shang, J.; Lai, L.; MacDonald, B.; Fu, C.; Shen, Z.; Yu, T.; Lin, J. Pyridinic N Doped Graphene: Synthesis, Electronic Structure, and Electrocatalytic Property. *J. Mater. Chem.* **2011**, *21*, 8038–8044.
- (312) Jin, Z.; Yao, J.; Kittrell, C.; Tour, J. M. Large-Scale Growth and Characterizations of Nitrogen-Doped Monolayer Graphene Sheets. *ACS Nano* **2011**, *5*, 4112–4117.
- (313) Reddy, A. L. M.; Srivastava, A.; Gowda, S. R.; Gullapalli, H.; Dubey, M.; Ajayan, P. M. Synthesis of Nitrogen-Doped Graphene Films for Lithium Battery Application. *ACS Nano* **2010**, *4*, 6337–6342.
- (314) Sheng, Z.-H.; Shao, L.; Chen, J.-J.; Bao, W.-J.; Wang, F.-B.; Xia, X.-H. Catalyst-Free Synthesis of Nitrogen-Doped Graphene Via Thermal Annealing Graphite Oxide with Melamine and Its Excellent Electrocatalysis. *ACS Nano* **2011**, *5*, 4350–4358.
- (315) Li, X.; Wang, H.; Robinson, J. T.; Sanchez, H.; Diankov, G.; Dai, H. Simultaneous Nitrogen Doping and Reduction of Graphene Oxide. *J. Am. Chem. Soc.* **2009**, *131*, 15939–15944.
- (316) Guo, D.; Shibuya, R.; Akiba, C.; Saji, S.; Kondo, T.; Nakamura, J. Active Sites of Nitrogen-Doped Carbon Materials for Oxygen Reduction Reaction Clarified Using Model Catalysts. *Science* **2016**, *351*, 361–365.
- (317) Xing, T.; Zheng, Y.; Li, L. H.; Cowie, B. C. C.; Gunzelmann, D.; Qiao, S. Z.; Huang, S.; Chen, Y. Observation of Active Sites for Oxygen Reduction Reaction on Nitrogen-Doped Multilayer Graphene. *ACS Nano* **2014**, *8*, 6856–6862.
- (318) Lai, L.; Potts, J. R.; Zhan, D.; Wang, L.; Poh, C. K.; Tang, C.; Gong, H.; Shen, Z.; Lin, J.; Ruoff, R. S. Exploration of the Active Center Structure of Nitrogen-Doped Graphene-Based Catalysts for Oxygen Reduction Reaction. *Energy Environ. Sci.* **2012**, *5*, 7936–7942.
- (319) Liu, Z.; Li, D.; Li, Z.; Liu, Z.; Zhang, Z. Nitrogen-Doped 3D Reduced Graphene Oxide/Polyaniline Composite as Active Material for Supercapacitor Electrodes. *Appl. Surf. Sci.* **2017**, *422*, 339–347.
- (320) Lin, X.; Waller, G. H.; Liu, Y.; Liu, M.; Wong, C.-p. 3D Nitrogen-Doped Graphene Prepared by Pyrolysis of Graphene Oxide with Polypyrrole for Electrocatalysis of Oxygen Reduction Reaction. *Nano Energy* **2013**, *2*, 241–248.
- (321) Sidik, R. A.; Anderson, A. B.; Subramanian, N. P.; Kumaraguru, S. P.; Popov, B. N. O_2 Reduction on Graphite and Nitrogen-Doped Graphite: Experiment and Theory. *J. Phys. Chem. B* **2006**, *110*, 1787–1793.
- (322) Huang, S.-F.; Terakura, K.; Ozaki, T.; Ikeda, T.; Boero, M.; Oshima, M.; Ozaki, J.-i.; Miyata, S. First-Principles Calculation of the Electronic Properties of Graphene Clusters Doped with Nitrogen and Boron: Analysis of Catalytic Activity for the Oxygen Reduction Reaction. *Phys. Rev. B: Condens. Matter Phys.* **2009**, *80*, 235410.
- (323) Ni, S.; Li, Z.; Yang, J. Oxygen Molecule Dissociation on Carbon Nanostructures with Different Types of Nitrogen Doping. *Nanoscale* **2012**, *4*, 1184–1189.
- (324) Sheng, Z.-H.; Gao, H.-L.; Bao, W.-J.; Wang, F.-B.; Xia, X.-H. Synthesis of Boron Doped Graphene for Oxygen Reduction Reaction in Fuel Cells. *J. Mater. Chem.* **2012**, *22*, 390–395.
- (325) Agnoli, S.; Favaro, M. Doping Graphene with Boron: A Review of Synthesis Methods, Physicochemical Characterization, and Emerging Applications. *J. Mater. Chem. A* **2016**, *4*, 5002–5025.
- (326) Rao, C. N. R.; Gopalakrishnan, K.; Govindaraj, A. Synthesis, Properties and Applications of Graphene Doped with Boron, Nitrogen and Other Elements. *Nano Today* **2014**, *9*, 324–343.
- (327) Yang, Z.; Yao, Z.; Li, G.; Fang, G.; Nie, H.; Liu, Z.; Zhou, X.; Chen, X. a.; Huang, S. Sulfur-Doped Graphene as an Efficient Metal-Free Cathode Catalyst for Oxygen Reduction. *ACS Nano* **2012**, *6*, 205–211.
- (328) Hoque, M. A.; Hassan, F. M.; Seo, M.-H.; Choi, J.-Y.; Pritzker, M.; Knights, S.; Ye, S.; Chen, Z. Optimization of Sulfur-Doped Graphene as an Emerging Platinum Nanowires Support for Oxygen Reduction Reaction. *Nano Energy* **2016**, *19*, 27–38.

- (329) Park, J.-e.; Jang, Y. J.; Kim, Y. J.; Song, M.-s.; Yoon, S.; Kim, D. H.; Kim, S.-J. Sulfur-Doped Graphene as a Potential Alternative Metal-Free Electrocatalyst and Pt-Catalyst Supporting Material for Oxygen Reduction Reaction. *Phys. Chem. Chem. Phys.* **2014**, *16*, 103–109.
- (330) Zhang, L.; Niu, J.; Li, M.; Xia, Z. Catalytic Mechanisms of Sulfur-Doped Graphene as Efficient Oxygen Reduction Reaction Catalysts for Fuel Cells. *J. Phys. Chem. C* **2014**, *118*, 3545–3553.
- (331) Jeon, I.-Y.; Zhang, S.; Zhang, L.; Choi, H.-J.; Seo, J.-M.; Xia, Z.; Dai, L.; Baek, J.-B. Edge-Selectively Sulfurized Graphene Nanoplatelets as Efficient Metal-Free Electrocatalysts for Oxygen Reduction Reaction: The Electron Spin Effect. *Adv. Mater.* **2013**, *25*, 6138–6145.
- (332) Zhao, Z.; Li, M.; Zhang, L.; Dai, L.; Xia, Z. Design Principles for Heteroatom-Doped Carbon Nanomaterials as Highly Efficient Catalysts for Fuel Cells and Metal–Air Batteries. *Adv. Mater.* **2015**, *27*, 6834–6840.
- (333) Kattel, S.; Atanassov, P.; Kiefer, B. Density Functional Theory Study of the Oxygen Reduction Reaction Mechanism in a BN Co-Doped Graphene Electrocatalyst. *J. Mater. Chem. A* **2014**, *2*, 10273–10279.
- (334) Wang, S.; Zhang, L.; Xia, Z.; Roy, A.; Chang, D. W.; Baek, J.-B.; Dai, L. BCN Graphene as Efficient Metal-Free Electrocatalyst for the Oxygen Reduction Reaction. *Angew. Chem., Int. Ed.* **2012**, *51*, 4209–4212.
- (335) Xue, Y.; Yu, D.; Dai, L.; Wang, R.; Li, D.; Roy, A.; Lu, F.; Chen, H.; Liu, Y.; Qu, J. Three-Dimensional B,N-Doped Graphene Foam as a Metal-Free Catalyst for Oxygen Reduction Reaction. *Phys. Chem. Chem. Phys.* **2013**, *15*, 12220–12226.
- (336) Liang, J.; Jiao, Y.; Jaroniec, M.; Qiao, S. Z. Sulfur and Nitrogen Dual-Doped Mesoporous Graphene Electrocatalyst for Oxygen Reduction with Synergistically Enhanced Performance. *Angew. Chem., Int. Ed.* **2012**, *51*, 11496–11500.
- (337) Qu, K.; Zheng, Y.; Dai, S.; Qiao, S. Z. Graphene Oxide-Polydopamine Derived N, S-Co-doped Carbon Nanosheets as Superior Bifunctional Electrocatalysts for Oxygen Reduction and Evolution. *Nano Energy* **2016**, *19*, 373–381.
- (338) Wang, X.; Wang, J.; Wang, D.; Dou, S.; Ma, Z.; Wu, J.; Tao, L.; Shen, A.; Ouyang, C.; Liu, Q.; et al. One-Pot Synthesis of Nitrogen and Sulfur Co-Doped Graphene as Efficient Metal-Free Electrocatalysts for the Oxygen Reduction Reaction. *Chem. Commun.* **2014**, *50*, 4839–4842.
- (339) You, J.-M.; Ahmed, M. S.; Han, H. S.; Choe, J. e.; Üstündağ, Z.; Jeon, S. New Approach of Nitrogen and Sulfur-Doped Graphene Synthesis Using Dipyrrolemethane and Their Electrocatalytic Activity for Oxygen Reduction in Alkaline Media. *J. Power Sources* **2015**, *275*, 73–79.
- (340) Bag, S.; Mondal, B.; Das, A. K.; Raj, C. R. Nitrogen and Sulfur Dual-Doped Reduced Graphene Oxide: Synergistic Effect of Dopants Towards Oxygen Reduction Reaction. *Electrochim. Acta* **2015**, *163*, 16–23.
- (341) Yu, D.; Xue, Y.; Dai, L. Vertically Aligned Carbon Nanotube Arrays Co-Doped with Phosphorus and Nitrogen as Efficient Metal-Free Electrocatalysts for Oxygen Reduction. *J. Phys. Chem. Lett.* **2012**, *3*, 2863–2870.
- (342) Zhang, J.; Zhao, Z.; Xia, Z.; Dai, L. A Metal-Free Bifunctional Electrocatalyst for Oxygen Reduction and Oxygen Evolution Reactions. *Nat. Nanotechnol.* **2015**, *10*, 444–452.
- (343) Choi, C. H.; Park, S. H.; Woo, S. I. Phosphorus-Nitrogen Dual Doped Carbon as an Effective Catalyst for Oxygen Reduction Reaction in Acidic Media: Effects of the Amount of P-Doping on the Physical and Electrochemical Properties of Carbon. *J. Mater. Chem.* **2012**, *22*, 12107–12115.
- (344) Razmjooei, F.; Singh, K. P.; Song, M. Y.; Yu, J.-S. Enhanced Electrocatalytic Activity Due to Additional Phosphorous Doping in Nitrogen and Sulfur-Doped Graphene: A Comprehensive Study. *Carbon* **2014**, *78*, 257–267.
- (345) Wang, S.; Iyyamperumal, E.; Roy, A.; Xue, Y.; Yu, D.; Dai, L. Vertically Aligned BCN Nanotubes as Efficient Metal-Free Electrocatalysts for the Oxygen Reduction Reaction: A Synergetic Effect by Co-Doping with Boron and Nitrogen. *Angew. Chem., Int. Ed.* **2011**, *50*, 11756–11760.
- (346) Qu, K.; Zheng, Y.; Zhang, X.; Davey, K.; Dai, S.; Qiao, S. Z. Promotion of Electrocatalytic Hydrogen Evolution Reaction on Nitrogen-Doped Carbon Nanosheets with Secondary Heteroatoms. *ACS Nano* **2017**, *11*, 7293–7300.
- (347) Tang, C.; Wang, H.-F.; Chen, X.; Li, B.-Q.; Hou, T.-Z.; Zhang, B.; Zhang, Q.; Titirici, M.-M.; Wei, F. Topological Defects in Metal-Free Nanocarbon for Oxygen Electrocatalysis. *Adv. Mater.* **2016**, *28*, 6845–6851.
- (348) Jiang, Y.; Yang, L.; Sun, T.; Zhao, J.; Lyu, Z.; Zhuo, O.; Wang, X.; Wu, Q.; Ma, J.; Hu, Z. Significant Contribution of Intrinsic Carbon Defects to Oxygen Reduction Activity. *ACS Catal.* **2015**, *5*, 6707–6712.
- (349) Wang, X.; Li, X.; Ouyang, C.; Li, Z.; Dou, S.; Ma, Z.; Tao, L.; Huo, J.; Wang, S. Nonporous MOF-Derived Dopant-Free Mesoporous Carbon as an Efficient Metal-Free Electrocatalyst for the Oxygen Reduction Reaction. *J. Mater. Chem. A* **2016**, *4*, 9370–9374.
- (350) Shen, A.; Zou, Y.; Wang, Q.; Dryfe, R. A. W.; Huang, X.; Dou, S.; Dai, L.; Wang, S. Oxygen Reduction Reaction in a Droplet on Graphite: Direct Evidence That the Edge Is More Active Than the Basal Plane. *Angew. Chem., Int. Ed.* **2014**, *53*, 10804–10808.
- (351) Zhang, Z.; Zhang, J.; Chen, N.; Qu, L. Graphene Quantum Dots: An Emerging Material for Energy-Related Applications and Beyond. *Energy Environ. Sci.* **2012**, *5*, 8869–8890.
- (352) Tong, X.; Wei, Q.; Zhan, X.; Zhang, G.; Sun, S. The New Graphene Family Materials: Synthesis and Applications in Oxygen Reduction Reaction. *Catalysts* **2017**, *7*, 1–26.
- (353) Shen, J.; Zhu, Y.; Chen, C.; Yang, X.; Li, C. Facile Preparation and Upconversion Luminescence of Graphene Quantum Dots. *Chem. Commun.* **2011**, *47*, 2580–2582.
- (354) Pan, D.; Zhang, J.; Li, Z.; Wu, M. Hydrothermal Route for Cutting Graphene Sheets into Blue-Luminescent Graphene Quantum Dots. *Adv. Mater.* **2010**, *22*, 734–738.
- (355) Dong, Y.; Shao, J.; Chen, C.; Li, H.; Wang, R.; Chi, Y.; Lin, X.; Chen, G. Blue Luminescent Graphene Quantum Dots and Graphene Oxide Prepared by Tuning the Carbonization Degree of Citric Acid. *Carbon* **2012**, *50*, 4738–4743.
- (356) Kosynkin, D. V.; Higginbotham, A. L.; Sinitskii, A.; Lomeda, J. R.; Dimiev, A.; Price, B. K.; Tour, J. M. Longitudinal Unzipping of Carbon Nanotubes to Form Graphene Nanoribbons. *Nature* **2009**, *458*, 872–876.
- (357) Jiao, L.; Zhang, L.; Wang, X.; Diankov, G.; Dai, H. Narrow Graphene Nanoribbons from Carbon Nanotubes. *Nature* **2009**, *458*, 877–880.
- (358) Cataldo, F.; Compagnini, G.; Patané, G.; Ursini, O.; Angelini, G.; Ribic, P. R.; Margaritondo, G.; Cricenti, A.; Palleschi, G.; Valentini, F. Graphene Nanoribbons Produced by the Oxidative Unzipping of Single-Wall Carbon Nanotubes. *Carbon* **2010**, *48*, 2596–2602.
- (359) Talirz, L.; Söde, H.; Cai, J.; Ruffieux, P.; Blankenburg, S.; Jafaar, R.; Berger, R.; Feng, X.; Müllen, K.; Passerone, D.; et al. Termini of Bottom-up Fabricated Graphene Nanoribbons. *J. Am. Chem. Soc.* **2013**, *135*, 2060–2063.
- (360) Vo, T. H.; Shekhirev, M.; Kunkel, D. A.; Morton, M. D.; Berglund, E.; Kong, L.; Wilson, P. M.; Dowben, P. A.; Enders, A.; Sinitskii, A. Large-Scale Solution Synthesis of Narrow Graphene Nanoribbons. *Nat. Commun.* **2014**, *5*, 3189.
- (361) Li, Y.; Zhao, Y.; Cheng, H.; Hu, Y.; Shi, G.; Dai, L.; Qu, L. Nitrogen-Doped Graphene Quantum Dots with Oxygen-Rich Functional Groups. *J. Am. Chem. Soc.* **2012**, *134*, 15–18.
- (362) Liu, Y.; Wu, P. Graphene Quantum Dot Hybrids as Efficient Metal-Free Electrocatalyst for the Oxygen Reduction Reaction. *ACS Appl. Mater. Interfaces* **2013**, *5*, 3362–3369.
- (363) Fei, H.; Ye, R.; Ye, G.; Gong, Y.; Peng, Z.; Fan, X.; Samuel, E. L. G.; Ajayan, P. M.; Tour, J. M. Boron- and Nitrogen-Doped Graphene Quantum Dots/Graphene Hybrid Nanoplatelets as Efficient Electrocatalysts for Oxygen Reduction. *ACS Nano* **2014**, *8*, 10837–10843.
- (364) Favaro, M.; Ferrighi, L.; Fazio, G.; Colazzo, L.; Di Valentin, C.; Durante, C.; Sedona, F.; Gennaro, A.; Agnoli, S.; Granozzi, G. Single and Multiple Doping in Graphene Quantum Dots: Unraveling the Origin of Selectivity in the Oxygen Reduction Reaction. *ACS Catal.* **2015**, *5*, 129–144.

- (365) Fan, M.; Zhu, C.; Yang, J.; Sun, D. Facile Self-Assembly N-Doped Graphene Quantum Dots/Graphene for Oxygen Reduction Reaction. *Electrochim. Acta* **2016**, *216*, 102–109.
- (366) Saidi, W. A. Oxygen Reduction Electrocatalysis Using N-Doped Graphene Quantum-Dots. *J. Phys. Chem. Lett.* **2013**, *4*, 4160–4165.
- (367) Kim, H.; Lee, K.; Woo, S. I.; Jung, Y. On the Mechanism of Enhanced Oxygen Reduction Reaction in Nitrogen-Doped Graphene Nanoribbons. *Phys. Chem. Chem. Phys.* **2011**, *13*, 17505–17510.
- (368) Jin, H.; Huang, H.; He, Y.; Feng, X.; Wang, S.; Dai, L.; Wang, J. Graphene Quantum Dots Supported by Graphene Nanoribbons with Ultrahigh Electrocatalytic Performance for Oxygen Reduction. *J. Am. Chem. Soc.* **2015**, *137*, 7588–7591.
- (369) Banhart, F.; Kotakoski, J.; Krasheninnikov, A. V. Structural Defects in Graphene. *ACS Nano* **2011**, *5*, 26–41.
- (370) Lyth, S. M.; Nabaie, Y.; Moriya, S.; Kuroki, S.; Kakimoto, M.-a.; Ozaki, J.-i.; Miyata, S. Carbon Nitride as a Nonprecious Catalyst for Electrochemical Oxygen Reduction. *J. Phys. Chem. C* **2009**, *113*, 20148–20151.
- (371) Liang, J.; Zheng, Y.; Chen, J.; Liu, J.; Hulicova-Jurcakova, D.; Jaroniec, M.; Qiao, S. Z. Facile Oxygen Reduction on a Three-Dimensionally Ordered Macroporous Graphitic C₃N₄/Carbon Composite Electrocatalyst. *Angew. Chem.* **2012**, *124*, 3958–3962.
- (372) Sun, Y.; Li, C.; Xu, Y.; Bai, H.; Yao, Z.; Shi, G. Chemically Converted Graphene as Substrate for Immobilizing and Enhancing the Activity of a Polymeric Catalyst. *Chem. Commun.* **2010**, *46*, 4740–4742.
- (373) Yang, S.; Feng, X.; Wang, X.; Müllen, K. Graphene-Based Carbon Nitride Nanosheets as Efficient Metal-Free Electrocatalysts for Oxygen Reduction Reactions. *Angew. Chem., Int. Ed.* **2011**, *50*, 5339–5343.
- (374) Zhang, H.; Shen, P. K. Recent Development of Polymer Electrolyte Membranes for Fuel Cells. *Chem. Rev.* **2012**, *112*, 2780–2832.
- (375) Yu, D.; Zhang, Q.; Dai, L. Highly Efficient Metal-Free Growth of Nitrogen-Doped Single-Walled Carbon Nanotubes on Plasma-Etched Substrates for Oxygen Reduction. *J. Am. Chem. Soc.* **2010**, *132*, 15127–15129.
- (376) Li, Y.; Zhou, W.; Wang, H.; Xie, L.; Liang, Y.; Wei, F.; Idrobo, J.-C.; Pennycook, S. J.; Dai, H. An Oxygen Reduction Electrocatalyst Based on Carbon Nanotube-Graphene Complexes. *Nat. Nanotechnol.* **2012**, *7*, 394–400.
- (377) Kundu, S.; Nagaiah, T. C.; Xia, W.; Wang, Y.; Dommele, S. V.; Bitter, J. H.; Santa, M.; Grundmeier, G.; Bron, M.; Schuhmann, W.; et al. Electrocatalytic Activity and Stability of Nitrogen-Containing Carbon Nanotubes in the Oxygen Reduction Reaction. *J. Phys. Chem. C* **2009**, *113*, 14302–14310.
- (378) Shui, J.; Wang, M.; Du, F.; Dai, L. N-Doped Carbon Nanomaterials Are Durable Catalysts for Oxygen Reduction Reaction in Acidic Fuel Cells. *Sci. Adv.* **2015**, *1*, e1400129.
- (379) Shi, Q.; Peng, F.; Liao, S.; Wang, H.; Yu, H.; Liu, Z.; Zhang, B.; Su, D. Sulfur and Nitrogen Co-Doped Carbon Nanotubes for Enhancing Electrochemical Oxygen Reduction Activity in Acidic and Alkaline Media. *J. Mater. Chem. A* **2013**, *1*, 14853–14857.
- (380) Zitolo, A.; Goellner, V.; Armel, V.; Sougrati, M.-T.; Mineva, T.; Stievano, L.; Fonda, E.; Jaouen, F. Identification of Catalytic Sites for Oxygen Reduction in Iron- and Nitrogen-Doped Graphene Materials. *Nat. Mater.* **2015**, *14*, 937–942.
- (381) Appleby, A. J.; Marie, J. Kinetics of Oxygen Reduction on Carbon Materials in Alkaline Solution. *Electrochim. Acta* **1979**, *24*, 195–202.
- (382) Kattel, S.; Atanassov, P.; Kiefer, B. Catalytic Activity of Co-N_x/C Electrocatalysts for Oxygen Reduction Reaction: A Density Functional Theory Study. *Phys. Chem. Chem. Phys.* **2013**, *15*, 148–153.
- (383) Katsounaros, I.; Schneider, W. B.; Meier, J. C.; Benedikt, U.; Biedermann, P. U.; Auer, A. A.; Mayrhofer, K. J. J. Hydrogen Peroxide Electrochemistry on Platinum: Towards Understanding the Oxygen Reduction Reaction Mechanism. *Phys. Chem. Chem. Phys.* **2012**, *14*, 7384–7391.
- (384) Katsounaros, I.; Mayrhofer, K. J. J. The Influence of Non-Covalent Interactions on the Hydrogen Peroxide Electrochemistry on Platinum in Alkaline Electrolytes. *Chem. Commun.* **2012**, *48*, 6660–6662.
- (385) Yan, J.-A.; Chou, M. Y. Oxidation Functional Groups on Graphene: Structural and Electronic Properties. *Phys. Rev. B: Condens. Matter Mater. Phys.* **2010**, *82*, 125403.
- (386) Katsounaros, I.; Schneider, W. B.; Meier, J. C.; Benedikt, U.; Biedermann, P. U.; Cuesta, A.; Auer, A. A.; Mayrhofer, K. J. J. The Impact of Spectator Species on the Interaction of H₂O₂ with Platinum - Implications for the Oxygen Reduction Reaction Pathways. *Phys. Chem. Chem. Phys.* **2013**, *15*, 8058–8068.
- (387) Morales-Guio, C. G.; Liardet, L.; Hu, X. Oxidatively Electrodeposited Thin-Film Transition Metal (Oxy)Hydroxides as Oxygen Evolution Catalysts. *J. Am. Chem. Soc.* **2016**, *138*, 8946–8957.
- (388) Zou, X.; Zhang, Y. Noble Metal-Free Hydrogen Evolution Catalysts for Water Splitting. *Chem. Soc. Rev.* **2015**, *44*, 5148–5180.
- (389) Trotochaud, L.; Young, S. L.; Ranney, J. K.; Boettcher, S. W. Nickel-Iron Oxyhydroxide Oxygen-Evolution Electrocatalysts: The Role of Intentional and Incidental Iron Incorporation. *J. Am. Chem. Soc.* **2014**, *136*, 6744–6753.
- (390) Lu, Z.; Wang, H.; Kong, D.; Yan, K.; Hsu, P.-C.; Zheng, G.; Yao, H.; Liang, Z.; Sun, X.; Cui, Y. Electrochemical Tuning of Layered Lithium Transition Metal Oxides for Improvement of Oxygen Evolution Reaction. *Nat. Commun.* **2014**, *5*, 4345.
- (391) Wu, Y.; Liu, Y.; Li, G.-D.; Zou, X.; Lian, X.; Wang, D.; Sun, L.; Asefa, T.; Zou, X. Efficient Electrocatalysis of Overall Water Splitting by Ultrasmall Ni_xCo_{3-x}S₄ Coupled Ni₃S₂ Nanosheet Arrays. *Nano Energy* **2017**, *35*, 161–170.
- (392) Zhao, Q.; Yan, Z.; Chen, C.; Chen, J. Spinels: Controlled Preparation, Oxygen Reduction/Evolution Reaction Application, and Beyond. *Chem. Rev.* **2017**, *117*, 10121–10211.
- (393) Pi, Y.; Shao, Q.; Wang, P.; Lv, F.; Guo, S.; Guo, J.; Huang, X. Trimetallic Oxyhydroxide Coralloids for Efficient Oxygen Evolution Electrocatalysis. *Angew. Chem., Int. Ed.* **2017**, *56*, 4502–4506.
- (394) Sun, Y.; Gao, S.; Lei, F.; Liu, J.; Liang, L.; Xie, Y. Atomically-Thin Non-Layered Cobalt Oxide Porous Sheets for Highly Efficient Oxygen-Evolving Electrocatalysts. *Chem. Sci.* **2014**, *5*, 3976–3982.
- (395) Zhao, Y.; Jia, X.; Chen, G.; Shang, L.; Waterhouse, G. I. N.; Wu, L.-Z.; Tung, C.-H.; O'Hare, D.; Zhang, T. Ultrafine NiO Nanosheets Stabilized by TiO₂ from Monolayer NiTi-LDH Precursors: An Active Water Oxidation Electrocatalyst. *J. Am. Chem. Soc.* **2016**, *138*, 6517–6524.
- (396) Long, X.; Ma, Z.; Yu, H.; Gao, X.; Pan, X.; Chen, X.; Yang, S.; Yi, Z. Porous FeNi Oxide Nanosheets as Advanced Electrochemical Catalysts for Sustained Water Oxidation. *J. Mater. Chem. A* **2016**, *4*, 14939–14943.
- (397) Song, F.; Hu, X. Ultrathin Cobalt-Manganese Layered Double Hydroxide is an Efficient Oxygen Evolution Catalyst. *J. Am. Chem. Soc.* **2014**, *136*, 16481–16484.
- (398) Fan, K.; Chen, H.; Ji, Y.; Huang, H.; Claesson, P. M.; Daniel, Q.; Philippe, B.; Rensmo, H.; Li, F.; Luo, Y.; et al. Nickel-Vanadium Monolayer Double Hydroxide for Efficient Electrochemical Water Oxidation. *Nat. Commun.* **2016**, *7*, 11981.
- (399) Long, X.; Xiao, S.; Wang, Z.; Zheng, X.; Yang, S. Co Intake Mediated Formation of Ultrathin Nanosheets of Transition Metal LDH-an Advanced Electrocatalyst for Oxygen Evolution Reaction. *Chem. Commun.* **2015**, *51*, 1120–1123.
- (400) Zhang, J.; Hu, Y.; Liu, D.; Yu, Y.; Zhang, B. Enhancing Oxygen Evolution Reaction at High Current Densities on Amorphous-Like Ni-Fe-S Ultrathin Nanosheets Via Oxygen Incorporation and Electrochemical Tuning. *Adv. Sci.* **2017**, *4*, 1600343.
- (401) Chen, S.; Kang, Z.; Hu, X.; Zhang, X.; Wang, H.; Xie, J.; Zheng, X.; Yan, W.; Pan, B.; Xie, Y. Delocalized Spin States in 2D Atomic Layers Realizing Enhanced Electrocatalytic Oxygen Evolution. *Adv. Mater.* **2017**, *29*, 1701687.
- (402) Fang, Z.; Peng, L.; Lv, H.; Zhu, Y.; Yan, C.; Wang, S.; Kalyani, P.; Wu, X.; Yu, G. Metallic Transition Metal Selenide Holey Nanosheets for Efficient Oxygen Evolution Electrocatalysis. *ACS Nano* **2017**, *11*, 9550–9557.

- (403) Zhang, J.-Y.; Lv, L.; Tian, Y.; Li, Z.; Ao, X.; Lan, Y.; Jiang, J.; Wang, C. Rational Design of Cobalt–Iron Selenides for Highly Efficient Electrochemical Water Oxidation. *ACS Appl. Mater. Interfaces* **2017**, *9*, 33833–33840.
- (404) Liu, Y.; Xiao, C.; Lyu, M.; Lin, Y.; Cai, W.; Huang, P.; Tong, W.; Zou, Y.; Xie, Y. Ultrathin Co_3S_4 Nanosheets That Synergistically Engineer Spin States and Exposed Polyhedra that Promote Water Oxidation under Neutral Conditions. *Angew. Chem., Int. Ed.* **2015**, *54*, 11231–11235.
- (405) Tang, T.; Jiang, W.-J.; Niu, S.; Liu, N.; Luo, H.; Chen, Y.-Y.; Jin, S.-F.; Gao, F.; Wan, L.-J.; Hu, J.-S. Electronic and Morphological Dual Modulation of Cobalt Carbonate Hydroxides by Mn Doping toward Highly Efficient and Stable Bifunctional Electrocatalysts for Overall Water Splitting. *J. Am. Chem. Soc.* **2017**, *139*, 8320–8328.
- (406) Wang, P. Y.; Pu, Z. H.; Li, Y. H.; Wu, L.; Tu, Z. K.; Jiang, M.; Kou, Z. K.; Amiin, I. S.; Mu, S. C. Iron-Doped Nickel Phosphide Nanosheet Arrays: An Efficient Bifunctional Electrocatalyst for Water Splitting. *ACS Appl. Mater. Interfaces* **2017**, *9*, 26001–26007.
- (407) Li, Y.; Zhang, H.; Jiang, M.; Kuang, Y.; Sun, X.; Duan, X. Ternary NiCoP Nanosheet Arrays: An Excellent Bifunctional Catalyst for Alkaline Overall Water Splitting. *Nano Res.* **2016**, *9*, 2251–2259.
- (408) Chen, P. Z.; Xu, K.; Zhou, T. P.; Tong, Y.; Wu, J. C.; Cheng, H.; Lu, X. L.; Ding, H.; Wu, C. Z.; Xie, Y. Strong-Coupled Cobalt Borate Nanosheets/Graphene Hybrid as Electrocatalyst for Water Oxidation under Both Alkaline and Neutral Conditions. *Angew. Chem., Int. Ed.* **2016**, *55*, 2488–2492.
- (409) Hu, C.; Dai, L. Multifunctional Carbon-Based Metal-Free Electrocatalysts for Simultaneous Oxygen Reduction, Oxygen Evolution, and Hydrogen Evolution. *Adv. Mater.* **2017**, *29*, 1604942.
- (410) Trotochaud, L.; Ranney, J. K.; Williams, K. N.; Boettcher, S. W. Solution-Cast Metal Oxide Thin Film Electrocatalysts for Oxygen Evolution. *J. Am. Chem. Soc.* **2012**, *134*, 17253–17261.
- (411) Yan, X.; Li, L.-s. Solution-Chemistry Approach to Graphene Nanostructures. *J. Mater. Chem.* **2011**, *21*, 3295–3300.
- (412) Deng, X.; Tüysüz, H. Cobalt-Oxide-Based Materials as Water Oxidation Catalyst: Recent Progress and Challenges. *ACS Catal.* **2014**, *4*, 3701–3714.
- (413) Suntivich, J.; May, K. J.; Gasteiger, H. A.; Goodenough, J. B.; Shao-Horn, Y. A Perovskite Oxide Optimized for Oxygen Evolution Catalysis from Molecular Orbital Principles. *Science* **2011**, *334*, 1383–1385.
- (414) Hong, W. T.; Stoerzinger, K. A.; Lee, Y.-L.; Giordano, L.; Grimaud, A.; Johnson, A. M.; Hwang, J.; Crumlin, E. J.; Yang, W.; Shao-Horn, Y. Charge-Transfer-Energy-Dependent Oxygen Evolution Reaction Mechanisms for Perovskite Oxides. *Energy Environ. Sci.* **2017**, *10*, 2190–2200.
- (415) Friebe, D.; Louie, M. W.; Bajdich, M.; Sanwald, K. E.; Cai, Y.; Wise, A. M.; Cheng, M.-J.; Sokaras, D.; Weng, T.-C.; Alonso-Mori, R.; et al. Identification of Highly Active Fe Sites in $(\text{Ni,Fe})\text{OOH}$ for Electrocatalytic Water Splitting. *J. Am. Chem. Soc.* **2015**, *137*, 1305–1313.
- (416) Gerken, J. B.; Shaner, S. E.; Masse, R. C.; Porubsky, N. J.; Stahl, S. S. A Survey of Diverse Earth Abundant Oxygen Evolution Electrocatalysts Showing Enhanced Activity from Ni-Fe Oxides Containing a Third Metal. *Energy Environ. Sci.* **2014**, *7*, 2376–2382.
- (417) Steimecke, M.; Seiffarth, G.; Bron, M. In Situ Characterization of Ni and Ni/Fe Thin Film Electrodes for Oxygen Evolution in Alkaline Media by a Raman-Coupled Scanning Electrochemical Microscope Setup. *Anal. Chem.* **2017**, *89*, 10679–10686.
- (418) Zhao, Z.; Wu, H.; He, H.; Xu, X.; Jin, Y. Self-Standing Non-Noble Metal (Ni-Fe) Oxide Nanotube Array Anode Catalysts with Synergistic Reactivity for High-Performance Water Oxidation. *J. Mater. Chem. A* **2015**, *3*, 7179–7186.
- (419) Tang, C.; Titirici, M.-M.; Zhang, Q. A Review of Nanocarbons in Energy Electrocatalysis: Multifunctional Substrates and Highly Active Sites. *J. Energy Chem.* **2017**, *26*, 1077–1093.
- (420) Tang, C.; Wang, H.-F.; Zhu, X.-L.; Li, B.-Q.; Zhang, Q. Advances in Hybrid Electrocatalysts for Oxygen Evolution Reactions: Rational Integration of NiFe Layered Double Hydroxides and Nanocarbon. *Part. Part. Syst. Charact.* **2016**, *33*, 473–486.
- (421) Sun, Y.; Gao, S.; Lei, F.; Xiao, C.; Xie, Y. Ultrathin Two-Dimensional Inorganic Materials: New Opportunities for Solid State Nanochemistry. *Acc. Chem. Res.* **2015**, *48*, 3–12.
- (422) Liang, L.; Cheng, H.; Lei, F.; Han, J.; Gao, S.; Wang, C.; Sun, Y.; Qamar, S.; Wei, S.; Xie, Y. Metallic Single-Unit-Cell Orthorhombic Cobalt Diselenide Atomic Layers: Robust Water-Electrolysis Catalysts. *Angew. Chem., Int. Ed.* **2015**, *54*, 12004–12008.
- (423) Wu, J.; Liu, M.; Chatterjee, K.; Hackenberg, K. P.; Shen, J.; Zou, X.; Yan, Y.; Gu, J.; Yang, Y.; Lou, J.; et al. Exfoliated 2D Transition Metal Disulfides for Enhanced Electrocatalysis of Oxygen Evolution Reaction in Acidic Medium. *Adv. Mater. Interfaces* **2016**, *3*, 1500669.
- (424) Dutta, A.; Pradhan, N. Developments of Metal Phosphides as Efficient OER Precatalysts. *J. Phys. Chem. Lett.* **2017**, *8*, 144–152.
- (425) Zhang, B.; Xiao, C.; Xie, S.; Liang, J.; Chen, X.; Tang, Y. Iron–Nickel Nitride Nanostructures in Situ Grown on Surface-Redox-Etching Nickel Foam: Efficient and Ultrasustainable Electrocatalysts for Overall Water Splitting. *Chem. Mater.* **2016**, *28*, 6934–6941.
- (426) Yu, F.; Zhou, H.; Zhu, Z.; Sun, J.; He, R.; Bao, J.; Chen, S.; Ren, Z. Three-Dimensional Nanoporous Iron Nitride Film as an Efficient Electrocatalyst for Water Oxidation. *ACS Catal.* **2017**, *7*, 2052–2057.
- (427) Chen, P. Z.; Xu, K.; Fang, Z. W.; Tong, Y.; Wu, J. C.; Lu, X. L.; Peng, X.; Ding, H.; Wu, C. Z.; Xie, Y. Metallic Co_4N Porous Nanowire Arrays Activated by Surface Oxidation as Electrocatalysts for the Oxygen Evolution Reaction. *Angew. Chem., Int. Ed.* **2015**, *54*, 14710–14714.
- (428) Wang, J. M.; Ma, X.; Qu, F. L.; Asiri, A. M.; Sun, X. P. Fe-Doped Ni_2P Nanosheet Array for High-Efficiency Electrochemical Water Oxidation. *Inorg. Chem.* **2017**, *56*, 1041–1044.
- (429) Jin, S. Are Metal Chalcogenides, Nitrides, and Phosphides Oxygen Evolution Catalysts or Bifunctional Catalysts? *ACS Energy Lett.* **2017**, *2*, 1937–1938.
- (430) Miner, E. M.; Fukushima, T.; Sheberla, D.; Sun, L.; Surendranath, Y.; Dinca, M. Electrochemical Oxygen Reduction Catalysed by $\text{Ni}_3(\text{Hexaminotriphenylene})_2$. *Nat. Commun.* **2016**, *7*, 10942.
- (431) Zhao, M. T.; Wang, Y. X.; Ma, Q. L.; Huang, Y.; Zhang, X.; Ping, J. F.; Zhang, Z. C.; Lu, Q. P.; Yu, Y. F.; Xu, H.; et al. Ultrathin 2d Metal-Organic Framework Nanosheets. *Adv. Mater.* **2015**, *27*, 7372–7378.
- (432) Balogun, M.-S.; Qiu, W.; Yang, H.; Fan, W.; Huang, Y.; Fang, P.; Li, G.; Ji, H.; Tong, Y. A Monolithic Metal-Free Electrocatalyst for Oxygen Evolution Reaction and Overall Water Splitting. *Energy Environ. Sci.* **2016**, *9*, 3411–3416.
- (433) Kong, X.; Huang, Y.; Liu, Q. Two-Dimensional Boron-Doped Graphyne Nanosheet: A New Metal-Free Catalyst for Oxygen Evolution Reaction. *Carbon* **2017**, *123*, 558–564.
- (434) Zhu, J.; Xiao, P.; Li, H.; Carabineiro, S. A. C. Graphitic Carbon Nitride: Synthesis, Properties, and Applications in Catalysis. *ACS Appl. Mater. Interfaces* **2014**, *6*, 16449–16465.
- (435) Ma, T. Y.; Dai, S.; Jaroniec, M.; Qiao, S. Z. Graphitic Carbon Nitride Nanosheet-Carbon Nanotube Three-Dimensional Porous Composites as High-Performance Oxygen Evolution Electrocatalysts. *Angew. Chem., Int. Ed.* **2014**, *53*, 7281–7285.
- (436) Zeng, K.; Zhang, D. Recent Progress in Alkaline Water Electrolysis for Hydrogen Production and Applications. *Prog. Energy Combust. Sci.* **2010**, *36*, 307–326.
- (437) Carmo, M.; Fritz, D. L.; Mergel, J.; Stolten, D. A Comprehensive Review on Pmem Water Electrolysis. *Int. J. Hydrogen Energy* **2013**, *38*, 4901–4934.
- (438) Wang, M.; Wang, Z.; Gong, X.; Guo, Z. The Intensification Technologies to Water Electrolysis for Hydrogen Production – a Review. *Renewable Sustainable Energy Rev.* **2014**, *29*, 573–588.
- (439) Danilovic, N.; Subbaraman, R.; Chang, K.-C.; Chang, S. H.; Kang, Y. J.; Snyder, J.; Paulikas, A. P.; Strmcnik, D.; Kim, Y.-T.; Myers, D.; et al. Activity–Stability Trends for the Oxygen Evolution Reaction on Monometallic Oxides in Acidic Environments. *J. Phys. Chem. Lett.* **2014**, *5*, 2474–2478.
- (440) Spöri, C.; Kwan, J. T. H.; Bonakdarpour, A.; Wilkinson, D. P.; Strasser, P. The Stability Challenges of Oxygen Evolving Catalysts:

Towards a Common Fundamental Understanding and Mitigation of Catalyst Degradation. *Angew. Chem., Int. Ed.* **2017**, *56*, 5994–6021.

(441) Baumann, N.; Cremers, C.; Pinkwart, K.; Tübke, J. Supported Ir_{1-x}Ru_xO₂ Anode Catalysts for PEM-Water Electrolysis. *Fuel Cells* **2017**, *17*, 259–267.

(442) Lee, Y.; Suntivich, J.; May, K. J.; Perry, E. E.; Shao-Horn, Y. Synthesis and Activities of Rutile IrO₂ and RuO₂ Nanoparticles for Oxygen Evolution in Acid and Alkaline Solutions. *J. Phys. Chem. Lett.* **2012**, *3*, 399–404.

(443) Danilovic, N.; Subbaraman, R.; Chang, K. C.; Chang, S. H.; Kang, Y.; Snyder, J.; Paulikas, A. P.; Strmcnik, D.; Kim, Y. T.; Myers, D.; et al. Using Surface Segregation to Design Stable Ru-Ir Oxides for the Oxygen Evolution Reaction in Acidic Environments. *Angew. Chem.* **2014**, *126*, 14240–14245.

(444) Seitz, L. C.; Dickens, C. F.; Nishio, K.; Hikita, Y.; Montoya, J.; Doyle, A.; Kirk, C.; Vojvodic, A.; Hwang, H. Y.; Nørskov, J. K.; et al. A Highly Active and Stable IrO₂/SrIrO₃ Catalyst for the Oxygen Evolution Reaction. *Science* **2016**, *353*, 1011–1014.

(445) Chen, Y.; Yang, K.; Jiang, B.; Li, J.; Zeng, M.; Fu, L. Emerging Two-Dimensional Nanomaterials for Electrochemical Hydrogen Evolution. *J. Mater. Chem. A* **2017**, *5*, 8187–8208.

(446) Wang, H.; Gao, L. Recent Developments in Electrochemical Hydrogen Evolution Reaction. *Curr. Opin. Electrochem.* **2018**, *7*, 7–14.

(447) Vielstich, W.; Lamm, A.; Yokokawa, H.; Gasteiger, H. A. *Handbook of Fuel Cells: Fundamentals Technology and Applications*; John Wiley & Sons: New York, 2009; Vol. 2.

(448) Strmcnik, D.; Lopes, P. P.; Genorio, B.; Stamenkovic, V. R.; Markovic, N. M. Design Principles for Hydrogen Evolution Reaction Catalyst Materials. *Nano Energy* **2016**, *29*, 29–36.

(449) Parsons, R. The Rate of Electrolytic Hydrogen Evolution and the Heat of Adsorption of Hydrogen. *Trans. Faraday Soc.* **1958**, *54*, 1053–1063.

(450) Nørskov, J. K.; Bligaard, T.; Logadottir, A.; Kitchin, J. R.; Chen, J. G.; Pandelov, S.; Stimming, U. Trends in the Exchange Current for Hydrogen Evolution. *J. Electrochem. Soc.* **2005**, *152*, J23–J26.

(451) Skúlason, E.; Tripkovic, V.; Björketun, M. E.; Gudmundsdóttir, S.; Karlberg, G.; Rossmeisl, J.; Bligaard, T.; Jónsson, H.; Nørskov, J. K. Modeling the Electrochemical Hydrogen Oxidation and Evolution Reactions on the Basis of Density Functional Theory Calculations. *J. Phys. Chem. C* **2010**, *114*, 18182–18197.

(452) Danilovic, N.; Subbaraman, R.; Strmcnik, D.; Stamenkovic, V. R.; Markovic, N. M. Electrocatalysis of the HER in Acid and Alkaline Media. *J. Serb. Chem. Soc.* **2013**, *78*, 2007–2015.

(453) Zeng, Z. H.; Chang, K. C.; Kubal, J.; Markovic, N. M.; Greeley, J. Stabilization of Ultrathin (Hydroxy) Oxide Films on Transition Metal Substrates for Electrochemical Energy Conversion. *Nat. Energy* **2017**, *2*, 17070.

(454) Sheng, W.; Myint, M.; Chen, J. G.; Yan, Y. Correlating the Hydrogen Evolution Reaction Activity in Alkaline Electrolytes with the Hydrogen Binding Energy on Monometallic Surfaces. *Energy Environ. Sci.* **2013**, *6*, 1509–1512.

(455) Sheng, W. C.; Zhuang, Z. B.; Gao, M. R.; Zheng, J.; Chen, J. G.; Yan, Y. S. Correlating Hydrogen Oxidation and Evolution Activity on Platinum at Different Ph with Measured Hydrogen Binding Energy. *Nat. Commun.* **2015**, *6*, 5848.

(456) Zheng, J.; Sheng, W. C.; Zhuang, Z. B.; Xu, B. J.; Yan, Y. S. Universal Dependence of Hydrogen Oxidation and Evolution Reaction Activity of Platinum-Group Metals on Ph and Hydrogen Binding Energy. *Sci. Adv.* **2016**, *2*, e1501602.

(457) Ledezma-Yanez, I.; Wallace, W. D. Z.; Sebastián-Pascual, P.; Climent, V.; Feliu, J. M.; Koper, M. T. Interfacial Water Reorganization as a pH-Dependent Descriptor of the Hydrogen Evolution Rate on Platinum Electrodes. *Nat. Energy* **2017**, *2*, 17031.

(458) Skúlason, E.; Karlberg, G. S.; Rossmeisl, J.; Bligaard, T.; Greeley, J.; Jónsson, H.; Nørskov, J. K. Density Functional Theory Calculations for the Hydrogen Evolution Reaction in an Electrochemical Double Layer on the Pt(111) Electrode. *Phys. Chem. Chem. Phys.* **2007**, *9*, 3241–3250.

(459) Rossmeisl, J.; Skúlason, E.; Björketun, M. E.; Tripkovic, V.; Nørskov, J. K. Modeling the Electrified Solid–Liquid Interface. *Chem. Phys. Lett.* **2008**, *466*, 68–71.

(460) Jiang, H.; Zhu, Y.; Su, Y.; Yao, Y.; Liu, Y.; Yang, X.; Li, C. Highly Dual-Doped Multilayer Nanoporous Graphene: Efficient Metal-Free Electrocatalysts for the Hydrogen Evolution Reaction. *J. Mater. Chem. A* **2015**, *3*, 12642–12645.

(461) Qiu, H. J.; Ito, Y.; Cong, W.; Tan, Y.; Liu, P.; Hirata, A.; Fujita, T.; Tang, Z.; Chen, M. Nanoporous Graphene with Single-Atom Nickel Dopants: An Efficient and Stable Catalyst for Electrochemical Hydrogen Production. *Angew. Chem., Int. Ed.* **2015**, *54*, 14031–14035.

(462) Zhou, Y.; Leng, Y.; Zhou, W.; Huang, J.; Zhao, M.; Zhan, J.; Feng, C.; Tang, Z.; Chen, S.; Liu, H. Sulfur and Nitrogen Self-Doped Carbon Nanosheets Derived from Peanut Root Nodules as High-Efficiency Non-Metal Electrocatalyst for Hydrogen Evolution Reaction. *Nano Energy* **2015**, *16*, 357–366.

(463) Ito, Y.; Cong, W.; Fujita, T.; Tang, Z.; Chen, M. High Catalytic Activity of Nitrogen and Sulfur Co-Doped Nanoporous Graphene in the Hydrogen Evolution Reaction. *Angew. Chem., Int. Ed.* **2015**, *54*, 2131–2136.

(464) Wan, J.; Wu, J.; Gao, X.; Li, T.; Hu, Z.; Yu, H.; Huang, L. Structure Confined Porous Mo₂C for Efficient Hydrogen Evolution. *Adv. Funct. Mater.* **2017**, *27*, 1703933.

(465) Liu, Y.; Wu, J.; Hackenberg, K. P.; Zhang, J.; Wang, Y. M.; Yang, Y.; Keyshar, K.; Gu, J.; Ogitsu, T.; Vajtai, R.; et al. Self-Optimizing, Highly Surface-Active Layered Metal Dichalcogenide Catalysts for Hydrogen Evolution. *Nat. Energy* **2017**, *2*, 17127.

(466) Chen, Z.; Cummins, D.; Reinecke, B. N.; Clark, E.; Sunkara, M. K.; Jaramillo, T. F. Core–Shell MoO₃–MoS₂ Nanowires for Hydrogen Evolution: A Functional Design for Electrocatalytic Materials. *Nano Lett.* **2011**, *11*, 4168–4175.

(467) Lu, Z.; Zhang, H.; Zhu, W.; Yu, X.; Kuang, Y.; Chang, Z.; Lei, X.; Sun, X. In Situ Fabrication of Porous MoS₂ Thin-Films as High-Performance Catalysts for Electrochemical Hydrogen Evolution. *Chem. Commun.* **2013**, *49*, 7516–7518.

(468) Ge, X.; Chen, L.; Zhang, L.; Wen, Y.; Hirata, A.; Chen, M. Nanoporous Metal Enhanced Catalytic Activities of Amorphous Molybdenum Sulfide for High-Efficiency Hydrogen Production. *Adv. Mater.* **2014**, *26*, 3100–3104.

(469) Zheng, X.; Xu, J.; Yan, K.; Wang, H.; Wang, Z.; Yang, S. Space-Confined Growth of MoS₂ Nanosheets within Graphite: The Layered Hybrid of MoS₂ and Graphene as an Active Catalyst for Hydrogen Evolution Reaction. *Chem. Mater.* **2014**, *26*, 2344–2353.

(470) Vrabel, H.; Merki, D.; Hu, X. Hydrogen Evolution Catalyzed by MoS₃ and MoS₂ Particles. *Energy Environ. Sci.* **2012**, *5*, 6136–6144.

(471) Wang, H.; Lu, Z.; Kong, D.; Sun, J.; Hymel, T. M.; Cui, Y. Electrochemical Tuning of MoS₂ Nanoparticles on Three-Dimensional Substrate for Efficient Hydrogen Evolution. *ACS Nano* **2014**, *8*, 4940–4947.

(472) Benck, J. D.; Chen, Z.; Kuritzky, L. Y.; Forman, A. J.; Jaramillo, T. F. Amorphous Molybdenum Sulfide Catalysts for Electrochemical Hydrogen Production: Insights into the Origin of Their Catalytic Activity. *ACS Catal.* **2012**, *2*, 1916–1923.

(473) Kong, D.; Wang, H.; Cha, J. J.; Pasta, M.; Koski, K. J.; Yao, J.; Cui, Y. Synthesis of MoS₂ and MoSe₂ Films with Vertically Aligned Layers. *Nano Lett.* **2013**, *13*, 1341–1347.

(474) Wang, H.; Kong, D.; Johanes, P.; Cha, J. J.; Zheng, G.; Yan, K.; Liu, N.; Cui, Y. MoSe₂ and WSe₂ Nanofilms with Vertically Aligned Molecular Layers on Curved and Rough Surfaces. *Nano Lett.* **2013**, *13*, 3426–3433.

(475) Kibsgaard, J.; Tuxen, A.; Knudsen, K. G.; Brorson, M.; Topsoe, H.; Laegsgaard, E.; Lauritsen, J. V.; Besenbacher, F. Comparative Atomic-Scale Analysis of Promotional Effects by Late 3D-Transition Metals in MoS₂ Hydrotreating Catalysts. *J. Catal.* **2010**, *272*, 195–203.

(476) Merki, D.; Vrabel, H.; Rovelli, L.; Fierro, S.; Hu, X. L. Fe, Co, and Ni Ions Promote the Catalytic Activity of Amorphous Molybdenum Sulfide Films for Hydrogen Evolution. *Chem. Sci.* **2012**, *3*, 2515–2525.

(477) Wang, H.; Tsai, C.; Kong, D.; Chan, K.; Abild-Pedersen, F.; Nørskov, J. K.; Cui, Y. Transition-Metal Doped Edge Sites in Vertically

Aligned MoS₂ Catalysts for Enhanced Hydrogen Evolution. *Nano Res.* **2015**, *8*, 566–575.

(478) Sun, X.; Dai, J.; Guo, Y. Q.; Wu, C. Z.; Hu, F. T.; Zhao, J. Y.; Zeng, X. C.; Xie, Y. Semimetallic Molybdenum Disulfide Ultrathin Nanosheets as an Efficient Electrocatalyst for Hydrogen Evolution. *Nanoscale* **2014**, *6*, 8359–8367.

(479) Xu, C.; Peng, S. J.; Tan, C. L.; Ang, H. X.; Tan, H. T.; Zhang, H.; Yan, Q. Y. Ultrathin S-Doped MoSe₂ Nanosheets for Efficient Hydrogen Evolution. *J. Mater. Chem. A* **2014**, *2*, 5597–5601.

(480) Tang, H.; Dou, K.; Kaun, C.-C.; Kuang, Q.; Yang, S. MoSe₂ Nanosheets and Their Graphene Hybrids: Synthesis, Characterization and Hydrogen Evolution Reaction Studies. *J. Mater. Chem. A* **2014**, *2*, 360–364.

(481) Fu, Q.; Yang, L.; Wang, W.; Han, A.; Huang, J.; Du, P.; Fan, Z.; Zhang, J.; Xiang, B. Synthesis and Enhanced Electrochemical Catalytic Performance of Monolayer WS₂(1-x)Se_{2x} with a Tunable Band Gap. *Adv. Mater.* **2015**, *27*, 4732–4738.

(482) Kiran, V.; Mukherjee, D.; Jenjeti, R. N.; Sampath, S. Active Guests in the MoS₂/MoSe₂ Host Lattice: Efficient Hydrogen Evolution Using Few-Layer Alloys of MoS₂(1-x)Se_{2x}. *Nanoscale* **2014**, *6*, 12856–12863.

(483) Gong, Q.; Cheng, L.; Liu, C.; Zhang, M.; Feng, Q.; Ye, H.; Zeng, M.; Xie, L.; Liu, Z.; Li, Y. Ultrathin MoS₂(1-x)Se_{2x} Alloy Nanoflakes for Electrocatalytic Hydrogen Evolution Reaction. *ACS Catal.* **2015**, *5*, 2213–2219.

(484) Yang, L.; Fu, Q.; Wang, W.; Huang, J.; Huang, J.; Zhang, J.; Xiang, B. Large-Area Synthesis of Monolayered MoS₂(1-x)Se_{2x} with a Tunable Band Gap and Its Enhanced Electrochemical Catalytic Activity. *Nanoscale* **2015**, *7*, 10490–10497.

(485) Wang, L.; Sofer, Z.; Luxa, J.; Pumera, M. Mo₃W_{1-x}S₂ Solid Solutions as 3D Electrodes for Hydrogen Evolution Reaction. *Adv. Mater. Interfaces* **2015**, *2*, 1500041.

(486) Yang, K.; Wang, X.; Li, H.; Chen, B.; Zhang, X.; Li, S.; Wang, N.; Zhang, H.; Huang, X.; Huang, W. Composition- and Phase-Controlled Synthesis and Applications of Alloyed Phase Heterostructures of Transition Metal Disulphides. *Nanoscale* **2017**, *9*, 5102–5109.

(487) Ye, G.; Gong, Y.; Lin, J.; Li, B.; He, Y.; Pantelides, S. T.; Zhou, W.; Vajtai, R.; Ajayan, P. M. Defects Engineered Monolayer MoS₂ for Improved Hydrogen Evolution Reaction. *Nano Lett.* **2016**, *16*, 1097–1103.

(488) Tsai, C.; Li, H.; Park, S.; Park, J.; Han, H. S.; Nørskov, J. K.; Zheng, X. L.; Abild-Pedersen, F. Electrochemical Generation of Sulfur Vacancies in the Basal Plane of MoS₂ for Hydrogen Evolution. *Nat. Commun.* **2017**, *8*, 15113.

(489) Tsai, C.; Abild-Pedersen, F.; Nørskov, J. K. Tuning the MoS₂ Edge-Site Activity for Hydrogen Evolution Via Support Interactions. *Nano Lett.* **2014**, *14*, 1381–1387.

(490) Chang, Y. H.; Lin, C. T.; Chen, T. Y.; Hsu, C. L.; Lee, Y. H.; Zhang, W.; Wei, K. H.; Li, L. J. Highly Efficient Electrocatalytic Hydrogen Production by Moss Grown on Graphene-Protected 3D Ni Foams. *Adv. Mater.* **2013**, *25*, 756–760.

(491) Tan, Y.; Liu, P.; Chen, L.; Cong, W.; Ito, Y.; Han, J.; Guo, X.; Tang, Z.; Fujita, T.; Hirata, A.; Chen, M. W. Monolayer MoS₂ Films Supported by 3D Nanoporous Metals for High-Efficiency Electrocatalytic Hydrogen Production. *Adv. Mater.* **2014**, *26*, 8023–8028.

(492) Li, H.; Du, M.; Mleczko, M. J.; Koh, A. L.; Nishi, Y.; Pop, E.; Bard, A. J.; Zheng, X. Kinetic Study of Hydrogen Evolution Reaction over Strained MoS₂ with Sulfur Vacancies Using Scanning Electrochemical Microscopy. *J. Am. Chem. Soc.* **2016**, *138*, 5123–5129.

(493) Lin, Y.-C.; Dumcenco, D. O.; Huang, Y.-S.; Suenaga, K. Atomic Mechanism of the Semiconducting-to-Metallic Phase Transition in Single-Layered MoS₂. *Nat. Nanotechnol.* **2014**, *9*, 391–396.

(494) Gao, G.; Jiao, Y.; Ma, F.; Jiao, Y.; Waclawik, E.; Du, A. Charge Mediated Semiconducting-to-Metallic Phase Transition in Molybdenum Disulfide Monolayer and Hydrogen Evolution Reaction in New 1t' Phase. *J. Phys. Chem. C* **2015**, *119*, 13124–13128.

(495) Tsai, C.; Chan, K.; Nørskov, J. K.; Abild-Pedersen, F. Theoretical Insights into the Hydrogen Evolution Activity of Layered Transition Metal Dichalcogenides. *Surf. Sci.* **2015**, *640*, 133–140.

(496) Tang, Q.; Jiang, D.-e. Mechanism of Hydrogen Evolution Reaction on 1T-MoS₂ from First Principles. *ACS Catal.* **2016**, *6*, 4953–4961.

(497) Putungan, D. B.; Lin, S.-H.; Kuo, J.-L. A First-Principles Examination of Conducting Monolayer 1T'-MX₂ (M= Mo, W; X= S, Se, Te): Promising Catalysts for Hydrogen Evolution Reaction and Its Enhancement by Strain. *Phys. Chem. Chem. Phys.* **2015**, *17*, 21702–21708.

(498) Lukowski, M. A.; Daniel, A. S.; Meng, F.; Forticaux, A.; Li, L.; Jin, S. Enhanced Hydrogen Evolution Catalysis from Chemically Exfoliated Metallic MoS₂ Nanosheets. *J. Am. Chem. Soc.* **2013**, *135*, 10274–10277.

(499) Yin, Y.; Han, J.; Zhang, Y.; Zhang, X.; Xu, P.; Yuan, Q.; Samad, L.; Wang, X.; Wang, Y.; Zhang, Z.; et al. Contributions of Phase, Sulfur Vacancies, and Edges to the Hydrogen Evolution Reaction Catalytic Activity of Porous Molybdenum Disulfide Nanosheets. *J. Am. Chem. Soc.* **2016**, *138*, 7965–7972.

(500) Lukowski, M. A.; Daniel, A. S.; English, C. R.; Meng, F.; Forticaux, A.; Hamers, R. J.; Jin, S. Highly Active Hydrogen Evolution Catalysis from Metallic WS₂ Nanosheets. *Energy Environ. Sci.* **2014**, *7*, 2608–2613.

(501) Yin, Y.; Zhang, Y.; Gao, T.; Yao, T.; Zhang, X.; Han, J.; Wang, X.; Zhang, Z.; Xu, P.; Zhang, P.; et al. Synergistic Phase and Disorder Engineering in 1T-MoSe₂ Nanosheets for Enhanced Hydrogen-Evolution Reaction. *Adv. Mater.* **2017**, *29*, 1700311.

(502) Ambrosi, A.; Sofer, Z.; Pumera, M. 2H→1T Phase Transition and Hydrogen Evolution Activity of MoS₂, MoSe₂, WS₂ and WSe₂ Strongly Depends on the MX₂ Composition. *Chem. Commun.* **2015**, *51*, 8450–8453.

(503) Fan, X.-L.; Yang, Y.; Xiao, P.; Lau, W.-M. Site-Specific Catalytic Activity in Exfoliated MoS₂ Single-Layer Polytypes for Hydrogen Evolution: Basal Plane and Edges. *J. Mater. Chem. A* **2014**, *2*, 20545–20551.

(504) Ding, Q.; Song, B.; Xu, P.; Jin, S. Efficient Electrocatalytic and Photoelectrochemical Hydrogen Generation Using MoS₂ and Related Compounds. *Chem.* **2016**, *1*, 699–726.

(505) Najmaei, S.; Liu, Z.; Zhou, W.; Zou, X.; Shi, G.; Lei, S.; Yakobson, B. I.; Idrobo, J.-C.; Ajayan, P. M.; Lou, J. Vapour Phase Growth and Grain Boundary Structure of Molybdenum Disulphide Atomic Layers. *Nat. Mater.* **2013**, *12*, 754–759.

(506) Liu, J.; Zheng, Y.; Zhu, D.; Vasileff, A.; Ling, T.; Qiao, S. Identification of pH-Dependent Synergy on Ru/MoS₂ Interface: A Comparison of Alkaline and Acidic Hydrogen Evolution. *Nanoscale* **2017**, *9*, 16616–16621.

(507) Zhang, B.; Liu, J.; Wang, J. S.; Ruan, Y. J.; Ji, X.; Xu, K.; Chen, C.; Wan, H. Z.; Miao, L.; Jiang, J. J. Interface Engineering: The Ni(OH)₂/MoS₂ Heterostructure for Highly Efficient Alkaline Hydrogen Evolution. *Nano Energy* **2017**, *37*, 74–80.

(508) Lu, C. B.; Tranca, D.; Zhang, J.; Hernandez, F. R.; Su, Y. Z.; Zhuang, X. D.; Zhang, F.; Seifert, G.; Feng, X. L. Molybdenum Carbide-Embedded Nitrogen-Doped Porous Carbon Nanosheets as Electrocatalysts for Water Splitting in Alkaline Media. *ACS Nano* **2017**, *11*, 3933–3942.

(509) Sheng, W.; Gasteiger, H. A.; Yang, S.-H. Hydrogen Oxidation and Evolution Reaction Kinetics on Platinum: Acid vs Alkaline Electrolytes. *J. Electrochem. Soc.* **2010**, *157*, B1529–B1536.

(510) Durst, J.; Siebel, A.; Simon, C.; Hasche, F.; Herranz, J.; Gasteiger, H. A. New Insights into the Electrochemical Hydrogen Oxidation and Evolution Reaction Mechanism. *Energy Environ. Sci.* **2014**, *7*, 2255–2260.

(511) Rheinländer, P. J.; Herranz, J.; Durst, J.; Gasteiger, H. A. Kinetics of the Hydrogen Oxidation/Evolution Reaction on Polycrystalline Platinum in Alkaline Electrolyte Reaction Order with Respect to Hydrogen Pressure. *J. Electrochem. Soc.* **2014**, *161*, F1448–F1457.

(512) Zheng, Y.; Jiao, Y.; Qiao, S.; Vasileff, A. Hydrogen Evolution Reaction in Alkaline Solution: From Theory, Single Crystal Models, to Practical Electrocatalysts. *Angew. Chem., Int. Ed.* **2017**, XXXX DOI: 10.1002/anie.201710556.

- (513) Whipple, D. T.; Kenis, P. J. A. Prospects of CO₂ Utilization Via Direct Heterogeneous Electrochemical Reduction. *J. Phys. Chem. Lett.* **2010**, *1*, 3451–3458.
- (514) Jones, J.-P.; Prakash, G. K. S.; Olah, G. A. Electrochemical CO₂ Reduction: Recent Advances and Current Trends. *Isr. J. Chem.* **2014**, *54*, 1451–1466.
- (515) Hori, Y.; Wakebe, H.; Tsukamoto, T.; Koga, O. Electrochemical Process of Co Selectivity in Electrochemical Reduction of CO₂ at Metal Electrodes in Aqueous Media. *Electrochim. Acta* **1994**, *39*, 1833–1839.
- (516) Hori, Y. Electrochemical CO₂ Reduction on Metal Electrodes. In *Modern Aspects of Electrochemistry*; Vayenas, C. G., White, R. E., Gamboa-Aldeco, M. E., Eds.; Springer: New York, 2008; pp 89–189.
- (517) Chen, Y.; Li, C. W.; Kanan, M. W. Aqueous CO₂ Reduction at Very Low Overpotential on Oxide-Derived Au Nanoparticles. *J. Am. Chem. Soc.* **2012**, *134*, 19969–19972.
- (518) Li, C. W.; Kanan, M. W. CO₂ Reduction at Low Overpotential on Cu Electrodes Resulting from the Reduction of Thick Cu₂O Films. *J. Am. Chem. Soc.* **2012**, *134*, 7231–7234.
- (519) Rosen, J.; Hutchings, G. S.; Lu, Q.; Forest, R. V.; Moore, A.; Jiao, F. Electrodeposited Zn Dendrites with Enhanced CO Selectivity for Electrocatalytic CO₂ Reduction. *ACS Catal.* **2015**, *5*, 4586–4591.
- (520) Guo, S.; Zhao, S.; Gao, J.; Zhu, C.; Wu, X.; Fu, Y.; Huang, H.; Liu, Y.; Kang, Z. Cu-CDots Nanocorals as Electrocatalyst for Highly Efficient CO₂ Reduction to Formate. *Nanoscale* **2017**, *9*, 298–304.
- (521) Raciti, D.; Livi, K. J.; Wang, C. Highly Dense Cu Nanowires for Low-Overpotential CO₂ Reduction. *Nano Lett.* **2015**, *15*, 6829–6835.
- (522) Zhang, S.; Kang, P.; Meyer, T. J. Nanostructured Tin Catalysts for Selective Electrochemical Reduction of Carbon Dioxide to Formate. *J. Am. Chem. Soc.* **2014**, *136*, 1734–1737.
- (523) Ding, C.; Li, A.; Lu, S.-M.; Zhang, H.; Li, C. In Situ Electrodeposited Indium Nanocrystals for Efficient CO₂ Reduction to Co with Low Overpotential. *ACS Catal.* **2016**, *6*, 6438–6443.
- (524) Loiudice, A.; Lobaccaro, P.; Kamali, E. A.; Thao, T.; Huang, B. H.; Ager, J. W.; Buonsanti, R. Tailoring Copper Nanocrystals Towards C₂ Products in Electrochemical CO₂ Reduction. *Angew. Chem., Int. Ed.* **2016**, *55*, 5789–5792.
- (525) Dai, L.; Qin, Q.; Wang, P.; Zhao, X.; Hu, C.; Liu, P.; Qin, R.; Chen, M.; Ou, D.; Xu, C.; et al. Ultrastable Atomic Copper Nanosheets for Selective Electrochemical Reduction of Carbon Dioxide. *Sci. Adv.* **2017**, *3*, e1701069.
- (526) Gao, S.; Sun, Z.; Liu, W.; Jiao, X.; Zu, X.; Hu, Q.; Sun, Y.; Yao, T.; Zhang, W.; Wei, S.; et al. Atomic Layer Confined Vacancies for Atomic-Level Insights into Carbon Dioxide Electrorreduction. *Nat. Commun.* **2017**, *8*, 14503.
- (527) Schlögl, R. Heterogeneous Catalysis. *Angew. Chem., Int. Ed.* **2015**, *54*, 3465–3520.
- (528) Zhang, L.; Zhao, Z.-J.; Gong, J. Nanostructured Materials for Heterogeneous Electrocatalytic CO₂ Reduction and Their Related Reaction Mechanisms. *Angew. Chem., Int. Ed.* **2017**, *56*, 11326–11353.
- (529) Tang, Q.; Lee, Y.; Li, D.-Y.; Choi, W.; Liu, C. W.; Lee, D.; Jiang, D.-e. Lattice-Hydride Mechanism in Electrocatalytic CO₂ Reduction by Structurally Precise Copper-Hydride Nanoclusters. *J. Am. Chem. Soc.* **2017**, *139*, 9728–9736.
- (530) Huang, P.; Ci, S.; Wang, G.; Jia, J.; Xu, J.; Wen, Z. High-Activity Cu Nanowires Electrocatalysts for CO₂ Reduction. *J. CO₂ Util.* **2017**, *20*, 27–33.
- (531) Alvarez-Guerra, M.; Albo, J.; Alvarez-Guerra, E.; Irabien, A. Ionic Liquids in the Electrochemical Valorisation of CO₂. *Energy Environ. Sci.* **2015**, *8*, 2574–2599.
- (532) Rosen, B. A.; Salehi-Khojin, A.; Thorson, M. R.; Zhu, W.; Whipple, D. T.; Kenis, P. J. A.; Masel, R. I. Ionic Liquid-Mediated Selective Conversion of CO₂ to CO at Low Overpotentials. *Science* **2011**, *334*, 643–644.
- (533) Mizuno, T.; Naitoh, A.; Ohta, K. Electrochemical Reduction of CO₂ in Methanol at –30°C. *J. Electroanal. Chem.* **1995**, *391*, 199–201.
- (534) Kauffman, D. R.; Thakkar, J.; Siva, R.; Matranga, C.; Ohodnicki, P. R.; Zeng, C.; Jin, R. Efficient Electrochemical CO₂ Conversion Powered by Renewable Energy. *ACS Appl. Mater. Interfaces* **2015**, *7*, 15626–15632.
- (535) Kim, D.; Resasco, J.; Yu, Y.; Asiri, A. M.; Yang, P. Synergistic Geometric and Electronic Effects for Electrochemical Reduction of Carbon Dioxide Using Gold–Copper Bimetallic Nanoparticles. *Nat. Commun.* **2014**, *5*, 4948.
- (536) Kim, S.; Dong, W. J.; Gim, S.; Sohn, W.; Park, J. Y.; Yoo, C. J.; Jang, H. W.; Lee, J.-L. Shape-Controlled Bismuth Nanoflakes as Highly Selective Catalysts for Electrochemical Carbon Dioxide Reduction to Formate. *Nano Energy* **2017**, *39*, 44–52.
- (537) Li, F.; Chen, L.; Knowles, G. P.; MacFarlane, D. R.; Zhang, J. Hierarchical Mesoporous SnO₂ Nanosheets on Carbon Cloth: A Robust and Flexible Electrocatalyst for CO₂ Reduction with High Efficiency and Selectivity. *Angew. Chem., Int. Ed.* **2017**, *56*, 505–509.
- (538) Lum, Y.; Yue, B.; Lobaccaro, P.; Bell, A. T.; Ager, J. W. Optimizing C–C Coupling on Oxide-Derived Copper Catalysts for Electrochemical CO₂ Reduction. *J. Phys. Chem. C* **2017**, *121*, 14191–14203.
- (539) Chan, K.; Tsai, C.; Hansen, H. A.; Nørskov, J. K. Molybdenum Sulfides and Selenides as Possible Electrocatalysts for CO₂ Reduction. *ChemCatChem* **2014**, *6*, 1899–1905.
- (540) Hong, X.; Chan, K.; Tsai, C.; Nørskov, J. K. How Doped MoS₂ Breaks Transition-Metal Scaling Relations for CO₂ Electrochemical Reduction. *ACS Catal.* **2016**, *6*, 4428–4437.
- (541) Sharma, P. P.; Wu, J.; Yadav, R. M.; Liu, M.; Wright, C. J.; Tiwary, C. S.; Jakobson, B. I.; Lou, J.; Ajayan, P. M.; Zhou, X.-D. Nitrogen-Doped Carbon Nanotube Arrays for High-Efficiency Electrochemical Reduction of CO₂: On the Understanding of Defects, Defect Density, and Selectivity. *Angew. Chem., Int. Ed.* **2015**, *54*, 13701–13705.
- (542) Lu, X.; Tan, T. H.; Ng, Y. H.; Amal, R. Highly Selective and Stable Reduction of CO₂ to CO by a Graphitic Carbon Nitride/Carbon Nanotube Composite Electrocatalyst. *Chem. - Eur. J.* **2016**, *22*, 11991–11996.
- (543) Zhang, S.; Kang, P.; Ubnoske, S.; Brennaman, M. K.; Song, N.; House, R. L.; Glass, J. T.; Meyer, T. J. Polyethylenimine-Enhanced Electrocatalytic Reduction of CO₂ to Formate at Nitrogen-Doped Carbon Nanomaterials. *J. Am. Chem. Soc.* **2014**, *136*, 7845–7848.
- (544) Kumar, B.; Asadi, M.; Pisasale, D.; Sinha-Ray, S.; Rosen, B. A.; Haasch, R.; Abiade, J.; Yarin, A. L.; Salehi-Khojin, A. Renewable and Metal-Free Carbon Nanofibre Catalysts for Carbon Dioxide Reduction. *Nat. Commun.* **2013**, *4*, 2819.
- (545) Wu, J.; Ma, S.; Sun, J.; Gold, J. I.; Tiwary, C.; Kim, B.; Zhu, L.; Chopra, N.; Odeh, I. N.; Vajtai, R.; et al. A Metal-Free Electrocatalyst for Carbon Dioxide Reduction to Multi-Carbon Hydrocarbons and Oxygenates. *Nat. Commun.* **2016**, *7*, 13869.
- (546) Wu, J.; Yadav, R. M.; Liu, M.; Sharma, P. P.; Tiwary, C. S.; Ma, L.; Zou, X.; Zhou, X.-D.; Jakobson, B. I.; Lou, J.; et al. Achieving Highly Efficient, Selective, and Stable CO₂ Reduction on Nitrogen-Doped Carbon Nanotubes. *ACS Nano* **2015**, *9*, 5364–5371.
- (547) Cui, X.; Pan, Z.; Zhang, L.; Peng, H.; Zheng, G. Selective Etching of Nitrogen-Doped Carbon by Steam for Enhanced Electrochemical CO₂ Reduction. *Adv. Energy Mater.* **2017**, *7*, 1701456.
- (548) Jiao, Y.; Zheng, Y.; Chen, P.; Jaroniec, M.; Qiao, S.-Z. Molecular Scaffolding Strategy with Synergistic Active Centers to Facilitate Electrocatalytic CO₂ Reduction to Hydrocarbon/Alcohol. *J. Am. Chem. Soc.* **2017**, *139*, 18093–18100.
- (549) Jiao, Y.; Zheng, Y.; Smith, S. C.; Du, A.; Zhu, Z. Electrocatalytically Switchable CO₂ Capture: First Principle Computational Exploration of Carbon Nanotubes with Pyridinic Nitrogen. *ChemSusChem* **2014**, *7*, 435–441.
- (550) Tan, X.; Tahini, H. A.; Smith, S. C. Charge-Modulated CO₂ Capture. *Curr. Opin. Electrochem.* **2017**, *4*, 118–123.
- (551) Lv, W.; Bei, J.; Zhang, R.; Wang, W.; Kong, F.; Wang, L.; Wang, W. Bi₂O₂CO₃ Nanosheets as Electrocatalysts for Selective Reduction of CO₂ to Formate at Low Overpotential. *ACS Omega* **2017**, *2*, 2561–2567.
- (552) Varela, A. S.; Ranjbar Sahraie, N.; Steinberg, J.; Ju, W.; Oh, H.-S.; Strasser, P. Metal-Doped Nitrogenated Carbon as an Efficient Catalyst for Direct CO₂ Electroreduction to CO and Hydrocarbons. *Angew. Chem.* **2015**, *127*, 10908–10912.

- (553) Cheng, M.-J.; Kwon, Y.; Head-Gordon, M.; Bell, A. T. Tailoring Metal-Porphyrin-Like Active Sites on Graphene to Improve the Efficiency and Selectivity of Electrochemical CO₂ Reduction. *J. Phys. Chem. C* **2015**, *119*, 21345–21352.
- (554) Li, N.; Chen, X.; Ong, W.-J.; MacFarlane, D. R.; Zhao, X.; Cheetham, A. K.; Sun, C. Understanding of Electrochemical Mechanisms for CO₂ Capture and Conversion into Hydrocarbon Fuels in Transition-Metal Carbides (MXenes). *ACS Nano* **2017**, *11*, 10825–10833.
- (555) Chen, Y.; Bellini, M.; Bevilacqua, M.; Fornasiero, P.; Lavacchi, A.; Miller, H. A.; Wang, L.; Vizza, F. Direct Alcohol Fuel Cells: Toward the Power Densities of Hydrogen-Fed Proton Exchange Membrane Fuel Cells. *ChemSusChem* **2015**, *8*, 524–533.
- (556) Uhm, S.; Kwon, Y.; Chung, S. T.; Lee, J. Highly Effective Anode Structure in a Direct Formic Acid Fuel Cell. *Electrochim. Acta* **2008**, *53*, 5162–5168.
- (557) Xu, W.; Wu, Z.; Tao, S. Urea-Based Fuel Cells and Electrocatalysts for Urea Oxidation. *Energy Technology* **2016**, *4*, 1329–1337.
- (558) Chen, G.-F.; Cao, X.; Wu, S.; Zeng, X.; Ding, L.-X.; Zhu, M.; Wang, H. Ammonia Electrosynthesis with High Selectivity under Ambient Conditions Via a Li⁺ Incorporation Strategy. *J. Am. Chem. Soc.* **2017**, *139*, 9771–9774.
- (559) Rittle, J.; Peters, J. C. An Fe-N₂ Complex That Generates Hydrazine and Ammonia Via Fe = NNH₂: Demonstrating a Hybrid Distal-to-Alternating Pathway for N₂ Reduction. *J. Am. Chem. Soc.* **2016**, *138*, 4243–4248.
- (560) Li, H.; Shang, J.; Ai, Z.; Zhang, L. Efficient Visible Light Nitrogen Fixation with Biobr Nanosheets of Oxygen Vacancies on the Exposed {001} Facets. *J. Am. Chem. Soc.* **2015**, *137*, 6393–6399.
- (561) van der Ham, C. J. M.; Koper, M. T. M.; Hetterscheid, D. G. H. Challenges in Reduction of Dinitrogen by Proton and Electron Transfer. *Chem. Soc. Rev.* **2014**, *43*, 5183–5191.
- (562) Rosca, V.; Duca, M.; de Groot, M. T.; Koper, M. T. M. Nitrogen Cycle Electrocatalysis. *Chem. Rev.* **2009**, *109*, 2209–2244.
- (563) Lan, R.; Tao, S.; Irvine, J. T. S. A Direct Urea Fuel Cell - Power from Fertiliser and Waste. *Energy Environ. Sci.* **2010**, *3*, 438–441.
- (564) Forslund, R. P.; Mefford, J. T.; Hardin, W. G.; Alexander, C. T.; Johnston, K. P.; Stevenson, K. J. Nanostructured LaNiO₃ Perovskite Electrocatalyst for Enhanced Urea Oxidation. *ACS Catal.* **2016**, *6*, 5044–5051.
- (565) Ding, R.; Qi, L.; Jia, M.; Wang, H. Facile Synthesis of Mesoporous Spinel NiCo₂O₄ Nanostructures as Highly Efficient Electrocatalysts for Urea Electro-Oxidation. *Nanoscale* **2014**, *6*, 1369–1376.
- (566) Wang, D.; Yan, W.; Vijapur, S. H.; Botte, G. G. Enhanced Electrocatalytic Oxidation of Urea Based on Nickel Hydroxide Nanoribbons. *J. Power Sources* **2012**, *217*, 498–502.
- (567) Wang, D.; Yan, W.; Botte, G. G. Exfoliated Nickel Hydroxide Nanosheets for Urea Electrolysis. *Electrochem. Commun.* **2011**, *13*, 1135–1138.
- (568) Zhu, X.; Dou, X.; Dai, J.; An, X.; Guo, Y.; Zhang, L.; Tao, S.; Zhao, J.; Chu, W.; Zeng, X. C.; et al. Metallic Nickel Hydroxide Nanosheets Give Superior Electrocatalytic Oxidation of Urea for Fuel Cells. *Angew. Chem., Int. Ed.* **2016**, *55*, 12465–12469.
- (569) Xiao, C.; Li, S.; Zhang, X.; MacFarlane, D. R. MnO₂/MnCo₂O₄/Ni Heterostructure with Quadruple Hierarchy: A Bifunctional Electrode Architecture for Overall Urea Oxidation. *J. Mater. Chem. A* **2017**, *5*, 7825–7832.
- (570) Goldsmith, Z. K.; Harshan, A. K.; Gerken, J. B.; Vörös, M.; Galli, G.; Stahl, S. S.; Hammes-Schiffer, S. Characterization of NiFe Oxyhydroxide Electrocatalysts by Integrated Electronic Structure Calculations and Spectroelectrochemistry. *Proc. Natl. Acad. Sci. U. S. A.* **2017**, *114*, 3050–3055.
- (571) Chen, G.; Zhou, W.; Guan, D.; Sunarso, J.; Zhu, Y.; Hu, X.; Zhang, W.; Shao, Z. Two Orders of Magnitude Enhancement in Oxygen Evolution Reactivity on Amorphous Ba_{0.5}Sr_{0.5}Co_{0.8}Fe_{0.2}O_{3-δ} Nanofilms with Tunable Oxidation State. *Sci. Adv.* **2017**, *3*, e1603206.
- (572) Canfield, D. E.; Glazer, A. N.; Falkowski, P. G. The Evolution and Future of Earth's Nitrogen Cycle. *Science* **2010**, *330*, 192–196.
- (573) Jia, H.-P.; Quadrelli, E. A. Mechanistic Aspects of Dinitrogen Cleavage and Hydrogenation to Produce Ammonia in Catalysis and Organometallic Chemistry: Relevance of Metal Hydride Bonds and Dihydrogen. *Chem. Soc. Rev.* **2014**, *43*, 547–564.
- (574) Pickett, C. J.; Talarmin, J. Electrosynthesis of Ammonia. *Nature* **1985**, *317*, 652–653.
- (575) Brown, K. A.; Harris, D. F.; Wilker, M. B.; Rasmussen, A.; Khadka, N.; Hamby, H.; Keable, S.; Dukovic, G.; Peters, J. W.; Seefeldt, L. C.; et al. Light-Driven Dinitrogen Reduction Catalyzed by a CdS:Nitrogenase MoFe Protein Biohybrid. *Science* **2016**, *352*, 448–450.
- (576) Kitano, M.; Inoue, Y.; Yamazaki, Y.; Hayashi, F.; Kanbara, S.; Matsuishi, S.; Yokoyama, T.; Kim, S.-W.; Hara, M.; Hosono, H. Ammonia Synthesis Using a Stable Electride as an Electron Donor and Reversible Hydrogen Store. *Nat. Chem.* **2012**, *4*, 934–940.
- (577) Marnellos, G.; Stoukides, M. Ammonia Synthesis at Atmospheric Pressure. *Science* **1998**, *282*, 98–100.
- (578) Bao, D.; Zhang, Q.; Meng, F.-L.; Zhong, H.-X.; Shi, M.-M.; Zhang, Y.; Yan, J.-M.; Jiang, Q.; Zhang, X.-B. Electrochemical Reduction of N₂ under Ambient Conditions for Artificial N₂ Fixation and Renewable Energy Storage Using N₂/NH₃ Cycle. *Adv. Mater.* **2017**, *29*, 1604799.
- (579) Shipman, M. A.; Symes, M. D. Recent Progress Towards the Electrosynthesis of Ammonia from Sustainable Resources. *Catal. Today* **2017**, *286*, 57–68.
- (580) Zhao, J.; Chen, Z. Single Mo Atom Supported on Defective Boron Nitride Monolayer as an Efficient Electrocatalyst for Nitrogen Fixation: A Computational Study. *J. Am. Chem. Soc.* **2017**, *139*, 12480–12487.
- (581) McEnaney, J. M.; Singh, A. R.; Schwabe, J. A.; Kibsgaard, J.; Lin, J. C.; Cargnello, M.; Jaramillo, T. F.; Nørskov, J. K. Ammonia Synthesis from N₂ and H₂O Using a Lithium Cycling Electrification Strategy at Atmospheric Pressure. *Energy Environ. Sci.* **2017**, *10*, 1621–1630.
- (582) Bauer, N. Theoretical Pathways for the Recution of N₂ Molecules in Aqueous Media: Thermodynamics of N₂H_n¹. *J. Phys. Chem.* **1960**, *64*, 833–837.
- (583) Shilov, A. E. Catalytic Reduction of Molecular Nitrogen in Solutions. *Russ. Chem. Bull.* **2003**, *52*, 2555–2562.
- (584) Skulason, E.; Bligaard, T.; Gudmundsdottir, S.; Studt, F.; Rossmeisl, J.; Abild-Pedersen, F.; Vegge, T.; Jonsson, H.; Nørskov, J. K. A Theoretical Evaluation of Possible Transition Metal Electro-Catalysts for N₂ Reduction. *Phys. Chem. Chem. Phys.* **2012**, *14*, 1235–1245.
- (585) Abghoui, Y.; Garden, A. L.; Hlynsson, V. F.; Bjorgvinsdottir, S.; Olafsdottir, H.; Skulason, E. Enabling Electrochemical Reduction of Nitrogen to Ammonia at Ambient Conditions through Rational Catalyst Design. *Phys. Chem. Chem. Phys.* **2015**, *17*, 4909–4918.
- (586) Li, S.-J.; Bao, D.; Shi, M.-M.; Wulan, B.-R.; Yan, J.-M.; Jiang, Q. Amorphizing of Au Nanoparticles by CeO_x-RGO Hybrid Support Towards Highly Efficient Electrocatalyst for N₂ Reduction under Ambient Conditions. *Adv. Mater.* **2017**, *29*, 1700001.
- (587) Licht, S.; Cui, B.; Wang, B.; Li, F.-F.; Lau, J.; Liu, S. Ammonia Synthesis by N₂ and Steam Electrolysis in Molten Hydroxide Suspensions of Nanoscale Fe₂O₃. *Science* **2014**, *345*, 637–640.
- (588) Lu, Y.; Li, J.; Tada, T.; Toda, Y.; Ueda, S.; Yokoyama, T.; Kitano, M.; Hosono, H. Water Durable Electride Y₃Si₃; Electronic Structure and Catalytic Activity for Ammonia Synthesis. *J. Am. Chem. Soc.* **2016**, *138*, 3970–3973.
- (589) Huang, W.; Wang, H.; Zhou, J.; Wang, J.; Duchesne, P. N.; Muir, D.; Zhang, P.; Han, N.; Zhao, F.; Zeng, M.; et al. Highly Active and Durable Methanol Oxidation Electrocatalyst Based on the Synergy of Platinum–Nickel Hydroxide–Graphene. *Nat. Commun.* **2015**, *6*, 10035.
- (590) Zhao, Y.; Zhao, Y.; Waterhouse, G. I. N.; Zheng, L.; Cao, X.; Teng, F.; Wu, L.-Z.; Tung, C.-H.; O'Hare, D.; Zhang, T. Layered-Double-Hydroxide Nanosheets as Efficient Visible-Light-Driven Photocatalysts for Dinitrogen Fixation. *Adv. Mater.* **2017**, *29*, 1703828.
- (591) Yu, X.; Pickup, P. G. Recent Advances in Direct Formic Acid Fuel Cells (DFAFC). *J. Power Sources* **2008**, *182*, 124–132.

(592) Feng, L.; Chang, J.; Jiang, K.; Xue, H.; Liu, C.; Cai, W.-B.; Xing, W.; Zhang, J. Nanostructured Palladium Catalyst Poisoning Depressed by Cobalt Phosphide in the Electro-Oxidation of Formic Acid for Fuel Cells. *Nano Energy* **2016**, *30*, 355–361.

(593) Winter, M.; Brodd, R. J. What Are Batteries, Fuel Cells, and Supercapacitors? *Chem. Rev.* **2004**, *104*, 4245–4270.

(594) Zhao, X.; Yin, M.; Ma, L.; Liang, L.; Liu, C.; Liao, J.; Lu, T.; Xing, W. Recent Advances in Catalysts for Direct Methanol Fuel Cells. *Energy Environ. Sci.* **2011**, *4*, 2736–2753.

(595) Liu, J.; Huang, Z.; Cai, K.; Zhang, H.; Lu, Z.; Li, T.; Zuo, Y.; Han, H. Clean Synthesis of an Economical 3D Nanochain Network of PdCu Alloy with Enhanced Electrocatalytic Performance Towards Ethanol Oxidation. *Chem. - Eur. J.* **2015**, *21*, 17779–17785.

(596) Huang, H.; Wang, X. Recent Progress on Carbon-Based Support Materials for Electrocatalysts of Direct Methanol Fuel Cells. *J. Mater. Chem. A* **2014**, *2*, 6266–6291.

(597) Lv, R.; Cui, T.; Jun, M.-S.; Zhang, Q.; Cao, A.; Su, D. S.; Zhang, Z.; Yoon, S.-H.; Miyawaki, J.; Mochida, I.; et al. Open-Ended, N-Doped Carbon Nanotube–Graphene Hybrid Nanostructures as High-Performance Catalyst Support. *Adv. Funct. Mater.* **2011**, *21*, 999–1006.

(598) Li, Y.-H.; Hung, T.-H.; Chen, C.-W. A First-Principles Study of Nitrogen- and Boron-Assisted Platinum Adsorption on Carbon Nanotubes. *Carbon* **2009**, *47*, 850–855.

(599) Jiang, Y.; Yan, Y.; Chen, W.; Khan, Y.; Wu, J.; Zhang, H.; Yang, D. Single-Crystalline Pd Square Nanoplates Enclosed by {100} Facets on Reduced Graphene Oxide for Formic Acid Electro-Oxidation. *Chem. Commun.* **2016**, *52*, 14204–14207.

Chapter 3: Constructing Tunable Dual Active Sites on Two-Dimensional C₃N₄@MoN Hybrid for Electrocatalytic Hydrogen Evolution

3.1 Introduction and Significance

Recently, 2D materials have shown great potential in various energy related electrocatalytic processes. However, their performance is inadequate for some kinetically sluggish electrocatalytic processes (e.g. the hydrogen evolution reaction, HER, in alkaline media). On the other hand, the reaction pathway and mechanism of alkaline HER are still under debate due to their complexity. To address this, a well-defined 2D C₃N₄@MoN hybrid electrocatalyst was developed to expand its electrocatalytic application. By combining electrochemical measurements with density functional theory (DFT) calculations, the possibility of quantitatively and qualitatively adjusting the multiple active sites of 2D heterostructure was demonstrated. The highlights of this Chapter include:

- A new 2D electrocatalyst with dual active sites was synthesized which exhibited highly efficient alkaline HER performance.
- Through the combination of electrochemical characterizations and theoretical computation, the activity origin of the C₃N₄@MoN hybrid was identified to be its newly formed heterostructure, which provided unique electronic properties and favourable adsorption energies of reaction intermediates.
- By using C₃N₄@MoN as a model, the contribution of hydrogen and hydroxyl adsorption properties to the electrocatalytic activity was defined, which is instructive in settling the contested alkaline HER mechanism.
- It is demonstrated that the binding abilities of multiple intermediates can be tuned through the construction of a well-designed 2D heterostructure, which provides new insights into developing more 2D electrocatalysts for alkaline HER.


3.2 Constructing Tunable Dual Active Sites on Two-Dimensional C₃N₄@MoN Hybrid for Electrocatalytic Hydrogen Evolution

This Chapter is included as it appears as a journal paper published by **Huanyu Jin** , Xin Liu, Yan Jiao, Anthony Vasileff, Yao Zheng,* Shi-Zhang Qiao* Constructing Tunable Dual Active Sites on Two-Dimensional C₃N₄@MoN Hybrid for Electrocatalytic Hydrogen Evolution. *Nano Energy* 2018, 53, 690–697.

Statement of Authorship

Title of Paper	Constructing Tunable Dual Active Sites on Two-Dimensional C ₃ N ₄ @MoN Hybrid for Electrocatalytic Hydrogen Evolution
Publication Status	<input checked="" type="checkbox"/> Published <input type="checkbox"/> Accepted for Publication <input type="checkbox"/> Submitted for Publication <input type="checkbox"/> Unpublished and Unsubmitted work written in manuscript style
Publication Details	Huanyu Jin, Xin Liu, Yan Jiao, Anthony Vasileff, Yao Zheng,* Shi-Zhang Qiao* Constructing Tunable Dual Active Sites on Two-Dimensional C ₃ N ₄ @MoN Hybrid for Electrocatalytic Hydrogen Evolution. Nano Energy 2018, 53, 690–697.


Principal Author


Name of Principal Author (Candidate)	Huanyu Jin		
Contribution to the Paper	Research plan, material synthesis, most of the characterizations and data analysis, electrochemical characterization, and manuscript draft.		
Overall percentage (%)	80		
Certification:	This paper reports on original research I conducted during the period of my Higher Degree by Research candidature and is not subject to any obligations or contractual agreements with a third party that would constrain its inclusion in this thesis. I am the primary author of this paper.		
Signature		Date	22/June/2020

Co-Author Contributions

By signing the Statement of Authorship, each author certifies that:

- the candidate's stated contribution to the publication is accurate (as detailed above);
- permission is granted for the candidate to include the publication in the thesis; and
- the sum of all co-author contributions is equal to 100% less the candidate's stated contribution.

Name of Co-Author	Xin Liu		
Contribution to the Paper	Computational calculations.		
Signature		Date	22/June/2020

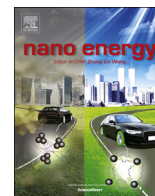
Name of Co-Author	Yan Jiao		
Contribution to the Paper	Discussion of computational calculations and manuscript.		
Signature		Date	22/June/2020

Name of Co-Author	Anthony Vasileff		
Contribution to the Paper	Editing process and manuscript revision.		
Signature		Date	22/June/2020

Name of Co-Author	Yao Zheng		
Contribution to the Paper	Supervision of the work, discussion of this manuscript and manuscript evaluation.		
Signature		Date	22/June/2020

Name of Co-Author	Shi-Zhang Qiao		
Contribution to the Paper	Supervision of the work, discussion of this manuscript and manuscript evaluation.		
Signature		Date	22/June/2020

Please cut and paste additional co-author panels here as required.



Full paper

Constructing tunable dual active sites on two-dimensional $C_3N_4@MoN$ hybrid for electrocatalytic hydrogen evolution

Huanyu Jin, Xin Liu, Yan Jiao, Anthony Vasileff, Yao Zheng*, Shi-Zhang Qiao*

School of Chemical Engineering, The University of Adelaide, Adelaide SA5005, Australia



ARTICLE INFO

Keywords:

Carbon nitride
2D materials
Heterostructure
Hydrogen evolution
Dual active sites
DFT calculation

ABSTRACT

Electrocatalysts are increasingly being used for the production of clean energy. In the past few decades, a wide range of two-dimensional (2D) materials have shown great potential in replacing noble metal catalysts for various electrocatalytic reactions. However, development of alkaline hydrogen evolution technology (a kinetically sluggish process for the conversion of electricity to hydrogen fuel in water electrolyzes) is greatly hindered due to the lack of active candidate materials and mechanistic understanding. In this work, we prepared a hybrid material of 2D graphitic carbon nitride and 2D molybdenum nitride ($C_3N_4@MoN$) using an interface engineering strategy. The resultant material had a well-designed heterostructure and unique electronic structure. The intimate interaction of both inert graphitic carbon nitride (g- C_3N_4) and MoN surfaces induced a highly active interface with tunable dual active sites for alkaline HER. Thus, the 2D $C_3N_4@MoN$ hybrid exhibited highly efficient electrocatalytic performance which is better than most of the recently reported non-noble metal catalysts. The combination of experimental characterization with density functional theory calculations shows that the enhanced activity originates from the synergy between the optimized hydrogen adsorption energy on the g- C_3N_4 sites and enhanced hydroxyl adsorption energy on the MoN sites.

1. Introduction

The rate of a surface electrocatalytic reaction occurring on a solid electrocatalyst is governed by the adsorption dynamics of multiple reaction intermediates [1]. Therefore, the adjustment of each state to an appropriate level is key to achieving optimized apparent performance [2]. However, due to the inherent scaling relationship of adsorption energies among different intermediates, it is difficult to optimize these energies simultaneously on electrocatalysts with a single kind of active site, inevitably leading to poor electrocatalytic performance. For the hydrogen evolution reaction (HER) in alkaline media (fundamental in water electrolysis for high-purity hydrogen fuel), current electrocatalysts (even precious metal Pt) exhibit inadequate activity, generally two to three orders of magnitude lower than that in the acidic media [3–7]. More importantly, the alkaline HER mechanism is yet to be settled due to the existence of an additional water dissociation process [7–9]. Consequently, balance of the multiple intermediates in alkaline HER is the key factor in the pursuit of efficient electrocatalysts.

For both practical applications and mechanistic studies, 2D materials are some of the most promising candidates for a wide range of electrocatalytic processes due to their uniformly exposed lattice plane and tunable electronic structures [5,10–17]. Furthermore, 2D materials

are more molecularly defined than nanoparticles or nanowires. As a result, the structure-activity studies at the molecular level are simplified. Unfortunately, most 2D materials are inert for alkaline HER even though in principle some of them have appropriate hydrogen adsorption abilities [7,8,18,19]. One of the main reasons is that the overall HER rate in alkaline media is governed by the thermodynamics and/or kinetics of multiple steps, and optimizing the hydrogen adsorption behavior on one crystal surface only is insufficient [8]. The hydrogen adsorption (H_{ad}) energy is commonly used as the sole activity descriptor for the HER in acidic media. However, for the HER in alkaline media, the water dissociation ability of one certain surface or interface may also influence the overall HER activity [7,9,20]. Therefore, from a microscopic view, optimal alkaline HER activity is governed by three factors: appropriate (not too strong nor too weak) H-binding and/or OH-binding energies, and a low barrier to water dissociation [8,21]. However, the design of a material with adjustable active sites which accounts for these factors is highly challenging.

To date, many strategies have demonstrated that the binding ability of some key reaction intermediates on an electrocatalyst surface can be tuned to a desired level by controlling their electronic states [15,22–27]. 2D material serves as an ideal platform to extend this principle to the field of alkaline HER [28]. More specifically, the

* Corresponding authors.

E-mail addresses: yao.zheng01@adelaide.edu.au (Y. Zheng), s.qiao@adelaide.edu.au (S.-Z. Qiao).

<https://doi.org/10.1016/j.nanoen.2018.09.046>

Received 16 July 2018; Received in revised form 3 September 2018; Accepted 18 September 2018

Available online 19 September 2018

2211-2855/ © 2018 Elsevier Ltd. All rights reserved.

construction of easily exposed heterostructures is one of the most suitable ways to promote alkaline HER because it can realize dual active sites (one for H_{ad} and the other for OH_{ad}) for facilitating hydrogen adsorption/desorption and water dissociation at the well-designed interface(s). Previously, we demonstrated that the electronic structure of 2D graphitic carbon nitride ($g-C_3N_4$) could be easily tuned to an appropriate level for H_{ad} by hybridizing with N-doped graphene; therefore, the hybrids showed an excellent acidic HER activity [27]. However, due to the poor water dissociation ability of both $g-C_3N_4$ and N-doped graphene, its performance in alkaline HER is inadequate. Given the abundant active sites of $g-C_3N_4$ for hydrogen adsorption, coupling $g-C_3N_4$ with a suitable 2D material with water dissociation ability is a possible solution to this problem. However, the current available 2D candidates for water dissociation are all limited to nickel-based materials with poor electrical conductivity and stability [4,29–31]. Recently, 2D MoN was successfully synthesized and found to have good corrosion resistance and metallic conductivity [32]. The Mo(III) atoms in MoN can be tuned to possess higher or lower oxidation state, and based on this, adjustable water dissociation ability can be achieved [32].

In this work, by rationally constructing a heterostructure composed of 2D MoN and 2D $g-C_3N_4$ ($C_3N_4@MoN$), dual active sites were formed and were able to promote the reaction kinetics of the alkaline HER at the interfaces. With well-designed electronic properties and adsorption abilities, the hybrid exhibits efficient electrocatalysis which is better than most non-noble metal catalysts. A combination of theoretical calculations and electrochemical measurements confirmed that the high activity of $C_3N_4@MoN$ originates from the synergy between favorable OH adsorption on MoN and optimized H adsorption on $g-C_3N_4$. Moreover, the contribution of each active site to the overall alkaline HER activity can be easily tuned, which demonstrates the ability to tailor functional 2D materials for specific catalytic applications.

2. Results and discussion

2.1. Preparation and characterizations of 2D $C_3N_4@MoN$

A MoN substrate was prepared by a salt-templated method, which comprised a 2D morphology and good hydrophilicity in aqueous solutions (Figs. S1 and S2) [32,33]. Subsequently, the $g-C_3N_4$ precursor (Dicyandiamide, DCDA) was dispersed in the MoN solution where DCDA was deposited on the MoN surface by the electrostatic interactions between negatively charged MoN and positively charged DCDA. The $C_3N_4@MoN$ was then obtained after this solution was lyophilized and annealed in an argon atmosphere. The lateral size of the as prepared $C_3N_4@MoN$ nanosheet was $\sim 1 \mu m$, and the presence of wrinkles on the surface demonstrates the materials flexibility (Fig. 1A). Scanning electron microscopy (SEM) images show that the morphology of the 2D MoN is consistent throughout and that no bulk $g-C_3N_4$ was formed (Fig. S2E). This indicates that the $g-C_3N_4$ grew uniformly on the MoN surface, which was further confirmed by high-angle annular dark-field imaging transmission electron microscopy (TEM) and corresponding elemental mapping (Figs. S3A and S3B). The thickness of one $C_3N_4@MoN$ sheet is $\sim 2.58 \text{ nm}$ (Fig. 1B) which is thicker than that of pristine MoN ($\sim 1.14 \text{ nm}$ as shown in Fig. S3C), indicating that the C_3N_4 on MoN is mono-layered or few-layered.

The 2D morphologies of individual $C_3N_4@MoN$ sheets can also be distinguished under low-resolution TEM imaging due to their graphene-like morphology and high transparency (Fig. 1C, D). To confirm the distribution of $g-C_3N_4$ on MoN at the molecular level, we conducted HRTEM imaging of $C_3N_4@MoN$. During TEM imaging, $g-C_3N_4$ is less stable than 2D MoN due to the decomposition of polymeric melon units under the electron beam. Therefore, the $g-C_3N_4$ regions can be identified based on time-lapse TEM images.²⁷ As shown in Fig. 1E, the initial TEM image of $C_3N_4@MoN$ displays many amorphous areas (highlighted in yellow). However, after 30 s of electron beam irradiation (Fig. 1F), the amorphous areas were significantly smaller, and the MoN crystal

lattice was ubiquitous within the frame (Fig. S3D). Given the assignment of the yellow region in Fig. 1E to $g-C_3N_4$, and the other region to MoN, this evidence demonstrates the successful formation of a $C_3N_4@MoN$ heterostructure. X-Ray diffraction (XRD) profiles (Fig. 2A) show that changes in the crystal structure of the MoN are negligible after hybridization, and no (001) peak of $g-C_3N_4$ on $C_3N_4@MoN$ is detected. This indicates that the crystal structure of MoN was retained after hybridization and that no bulk $g-C_3N_4$ was formed. From this evidence, we can confirm that the 2D MoN is partially covered by $g-C_3N_4$ nanodomains on its surface, and that the nanosheets stack parallel to each other [27].

2.2. Interfacial interaction and electronic structure of $C_3N_4@MoN$

Fourier-transform infrared spectroscopy (FT-IR), thermo-gravimetric analysis (TGA), and X-ray photoelectron spectroscopy (XPS) survey scans also confirm the existence of a $g-C_3N_4$ phase in the $C_3N_4@MoN$ hybrid (Figs. 2B, S3E, S3F, and S4) [34]. Compared to pure MoN, the N 1s peak of MoN in the $C_3N_4@MoN$ hybrid positively shifts by 0.8 eV (Fig. 2C), indicating that the strong interaction between Mo atom and C_3N_4 could indirectly weaken the Mo and nitrogen bonds by decreasing the electron density around N atoms in MoN. The molecular level interaction of $g-C_3N_4$ and MoN was further revealed by high resolution Mo 3d spectra. As shown in Fig. 2E, the spectrum of physically mixed $g-C_3N_4$ and MoN components (C_3N_4/MoN) displays no obvious difference compared to the spectrum for pristine MoN, indicating that there is no chemical interaction between them. Conversely, in the spectrum for $C_3N_4@MoN$, the concentration of Mo^{3+} (at $\sim 228.5 \text{ eV}$) is lower than Mo^{4+} (at $\sim 229.2 \text{ eV}$). This indicates that the valence state of Mo atoms in the $C_3N_4@MoN$ hybrid is higher than in C_3N_4/MoN and pristine MoN. Consequently, the $C_3N_4@MoN$ hybrid may have stronger adsorption energy for certain intermediates (e.g. OH_{ad}) and hence higher water dissociation ability [19,32].

The charge transfer induced by hybridization between $g-C_3N_4$ and MoN was revealed at the atomic level by density functional theory (DFT) calculations (Fig. 2E). As indicated by the projected density of states (PDOS), pure $g-C_3N_4$ and 2D MoN shows semi-conductive and the metallic character, respectively (Fig. 2F). After hybridization, a charge redistribution occurs at the interlayer of the hybrid in the form of electron accumulation at the interface, and overall electrons transfer from the MoN to the $g-C_3N_4$ layer (Fig. 2E). This is consistent with the experimental XPS results (Fig. 2D). This electron redistribution confirms the strong interaction between the $g-C_3N_4$ layer and MoN layer, which can provide a pathway for electron transfer during electrochemical reactions, and, more importantly, can modify the electronic structure and adsorption abilities of the hybrid materials. As shown in Fig. 2F, different from both individual materials, the hybrid has more states near the Fermi level.

2.3. Electrochemical activity of $C_3N_4@MoN$

The electrocatalytic HER performance of the as-prepared catalysts in 1M KOH electrolyte was first studied by linear sweep voltammetry (LSV). As shown in Fig. 3A, the $C_3N_4@MoN$ hybrid shows an overpotential of 110 mV at a current density of 10 mA cm^{-2} , which is significantly lower than that for the C_3N_4/MoN mixture and for $g-C_3N_4$ and MoN individually. This activity enhancement can be attributed to the highly active interface and modified electronic state in the hybrid catalyst. Interestingly, because the 2D nanostructure is favorable for mass transport, the apparent HER performance of $C_3N_4@MoN$ is even better than commercial Pt/C under large overpotentials (Fig. S5A) and displays good stability (Fig. S5B). Additionally, $C_3N_4@MoN$ shows a Tafel slope of 57.8 mV dec^{-1} , indicating the Volmer step is no longer the rate determining step due to the optimized water dissociation ability (Fig. 3B). As shown in the electrochemical impedance spectra (Fig. S6), $C_3N_4@MoN$ also has a lower Faradaic resistance than the $C_3N_4/$

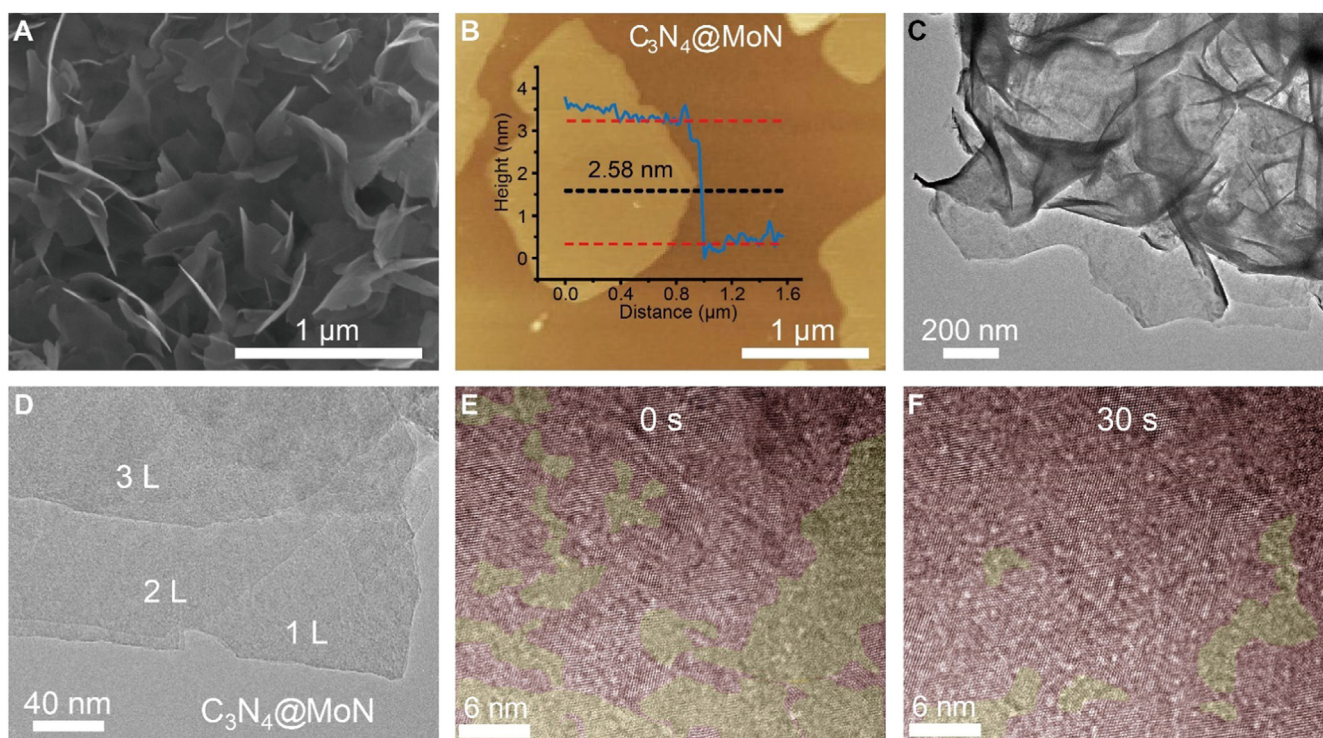


Fig. 1. (A) SEM image of $C_3N_4@MoN$. (B) AFM image of $C_3N_4@MoN$. (C and D) Low-resolution TEM image of $C_3N_4@MoN$ nanosheet. (E and F) HRTEM image of $C_3N_4@MoN$ before and after electron beam irradiation. The red region belongs to MoN, yellow region belongs to g- C_3N_4 . (For interpretation of the references to color in this figure legend, the reader is referred to the web version of this article.)

MoN mixture, indicating a faster charge-transfer kinetics [27].

To achieve a comprehensive assessment of the newly developed electrocatalyst, we compared the Tafel slope and overpotential of $C_3N_4@MoN$ with other recently reported alkaline HER electrocatalysts (Fig. 3C and Table S1) [30,35–46]. Evidently, the value of Tafel slope on $C_3N_4@MoN$ is lower than most of the reported non-noble metal electrocatalysts for alkaline HER. Regarding stability, Fig. 3D depicts the LSV curves collected from $C_3N_4@MoN$ at the first cycle and 1000th cycle. Negligible change in the current response is observed after 1000 cycles. Additionally, chronoamperometry (Fig. 3D inset) was carried out for 10 h at a constant overpotential of 110 mV. The stable current response ($\sim 10 \text{ mA cm}^{-2}$) further indicates that the hybrid material is stable under operating conditions.

2.4. Activity origin

According to experimental observations, the alkaline HER performance of an electrocatalyst is related to its adsorption abilities of both H^* and OH^* [47]. Here, we conducted DFT calculation to quantify these two properties in our newly developed $C_3N_4@MoN$ hybrid material. We first calculated the hydrogen adsorption free energy (ΔG_{H^*}) of g- C_3N_4 , MoN, and $C_3N_4@MoN$ to study their hydrogen adsorption ability. As shown in Figs. 4A and S7, both pure g- C_3N_4 and MoN exhibit strong hydrogen adsorption, indicated by their large negative values of ΔG_{H^*} (-0.34 eV and -0.96 eV , respectively). This is one of the main reasons for their poor HER performance, as confirmed in acidic media where ΔG_{H^*} can be used as the sole activity descriptor (Fig. S8). However, the calculated ΔG_{H^*} for $C_3N_4@MoN$ at the N (g- C_3N_4) site is -0.23 eV , which indicates that the hybrid structure has more favorable desorption thermodynamics of the H_{ad} intermediate (Fig. 4A, C). This optimization can also be shown by HER measurement in acidic media where the $C_3N_4@MoN$ demonstrated better performance than pure g- C_3N_4 and MoN samples (Fig. S8).

The OH_{ad} adsorption free energies (ΔG_{OH^*}) of g- C_3N_4 , MoN, and $C_3N_4@MoN$ were calculated to determine their water dissociation

abilities via a proportional relationship [2,7,48,49]. As shown in Fig. 4B, C, the ΔG_{OH^*} of $C_3N_4@MoN$ at the Mo site is -4.6 eV , which is more negative (i.e. stronger adsorption) than that of pristine MoN and g- C_3N_4 individually (Fig. S9). This indicates that $C_3N_4@MoN$ is more favorable for water dissociation. The enhanced OH^* adsorption in the hybrid material may be due to its higher valence state Mo atoms. Based on these observations, we propose a qualitative description of the dual active sites for alkaline HER in the $C_3N_4@MoN$ heterostructure: water dissociation proceeds at the boundary of 2D MoN and g- C_3N_4 , whereby Mo atoms on MoN expedite OH_{ad} adsorption and N atoms on g- C_3N_4 expedite H_{ad} adsorption (Fig. 4D). Subsequently, H_{ad} evolves H_2 and OH^- desorbs from the 2D MoN, followed by adsorption of another water molecule on the same dual active sites (Fig. S10).

2.5. Balance of dual active sites

Beyond DFT calculations, the ability to quantitatively define the contribution of adsorption ability for different intermediates is crucial in evaluating the activity of an electrocatalyst. First, we conducted electrochemical cyclic voltammetry (CV) to estimate the relative electrochemical active surface areas (ECSA) of the different electrocatalysts (Fig. S11). The $C_3N_4@MoN$ shows the lowest electrochemical double-layer capacitance (C_{dl}) but best performance, revealing that the performance enhancement does not originate from surface area variation but from the optimized adsorption energy of key intermediates on the surface of $C_3N_4@MoN$ (Fig. S12). Then, we balance the effects of H_{ad} and OH_{ad} adsorption by tuning the ratio of g- C_3N_4 /MoN in the hybrid (Fig. S13). It is demonstrated that the ratio of MoN and g- C_3N_4 plays an important role on the alkaline HER performance (Fig. 5A). From this, a volcano-shaped plot is obtained (Fig. 5B) which indicates that the performance of electrocatalysts for the alkaline HER is highly related to the balance of hydrogen adsorption with water dissociation ability. In addition, to isolate the impact of a certain intermediate adsorption on alkaline HER activity, we designed and synthesized two groups of control samples: i) $C_3N_4@MoN$ with the g- C_3N_4 phase removed in order

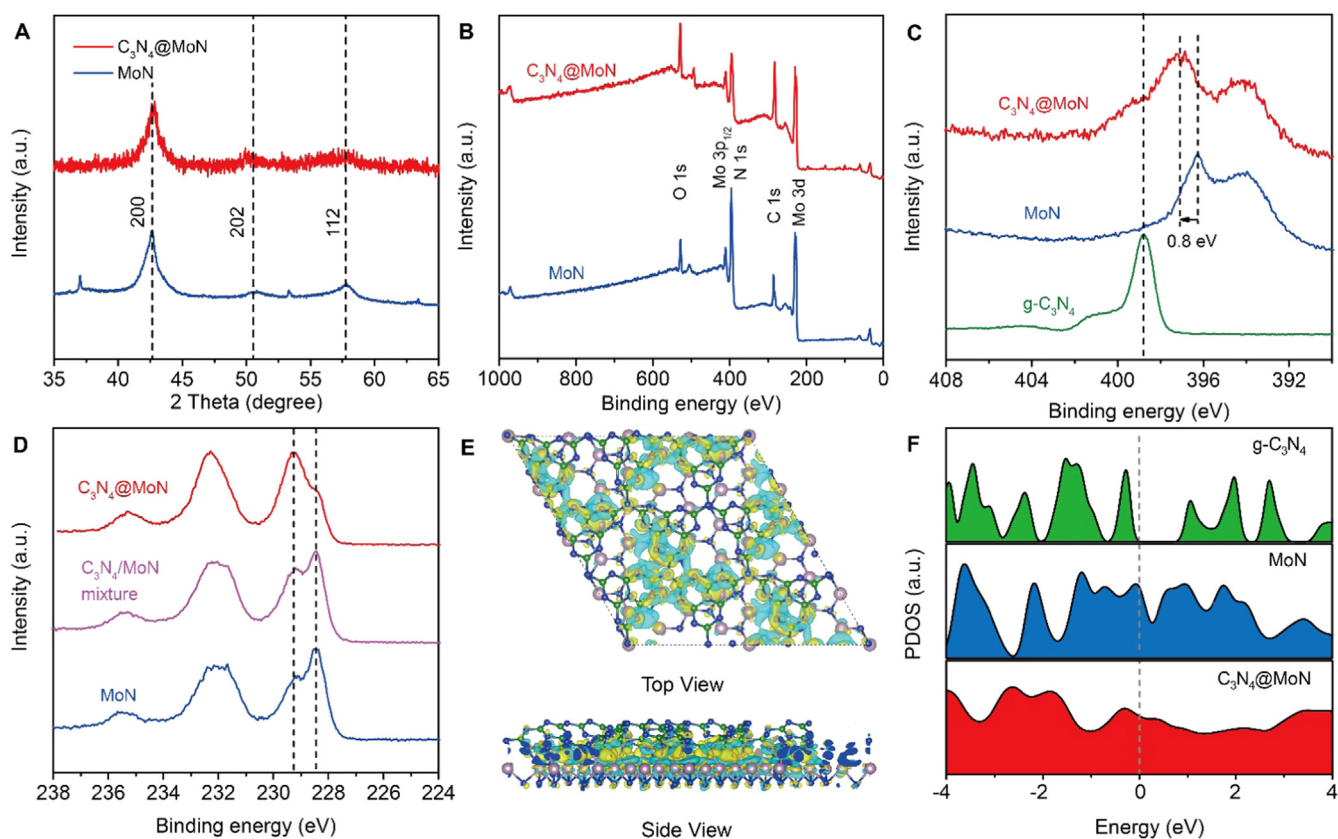


Fig. 2. (A) XRD spectra of pristine MoN and $C_3N_4@MoN$. The JCPDS code is 00-025-1367 for MoN. (B) XPS survey scans of pristine MoN and $C_3N_4@MoN$. (C) N 1s spectra of various catalysts. The peak at 398.8 eV is attributable to the sp^2 N involved in triazine rings of g- C_3N_4 . The N 1s peak of MoN in $C_3N_4@MoN$ shifted from 396.3 eV to 397.1 eV. (D) Mo 3d XPS spectra of MoN, C_3N_4/MoN mixture, and $C_3N_4@MoN$. The Mo $3d_{5/2}$ peaks at 228.5 eV and 229.2 eV represent Mo^{3+} and Mo^{4+} . (E) Interfacial electron transfer in $C_3N_4@MoN$. Yellow and cyan iso-surface represents electron accumulation and electron depletion. Pink, blue, and green spheres represent Mo, N, and C atoms, respectively. The isosurface value is $0.005 e \text{ \AA}^{-3}$. (F) The density of states on g- C_3N_4 , MoN, and $C_3N_4@MoN$. (For interpretation of the references to color in this figure legend, the reader is referred to the web version of this article.)

to prevent favorable hydrogen adsorption; ii) $C_3N_4@MoN$ with the MoN phase replaced by a poor OH_{ad} adsorbing material (N-doped graphene; denoted $C_3N_4@NG$) in order to prevent favorable water dissociation ability. As shown in Fig. 5C, after removing the H_{ad} adsorption site (g- C_3N_4), the performance of the electrocatalyst declined dramatically in both acidic and alkaline conditions, indicating that the optimized H_{ad} site is essential for alkaline HER. Additionally, it can be seen from Fig. 5C that hybridization of g- C_3N_4 with N-graphene can significantly improve its HER performance in acidic conditions, due to its optimized ΔG_{H^+} [27]. However, according to DFT calculations (Fig. S14), both g- C_3N_4 and N-graphene have poor affinity for OH_{ad} adsorption due to their more positive ΔG_{OH^*} of 1.02 and -0.17 eV, respectively. This suggests that they possess poor water dissociation abilities in alkaline conditions and explains the poor HER activity of $C_3N_4@NG$ in alkaline despite its appropriate ΔG_{H^+} . By comparing these two control samples, it can be seen that the optimization of water dissociation barriers contributed more to the activity enhancement for the alkaline HER than optimization of the H_{ad} adsorption energy. Therefore, we can conclude that an ideal catalyst for the alkaline HER should have both favorable hydroxyl affinity and appropriate hydrogen adsorption. In this case, we could achieve these parameters by constructing 2D heterostructures with tunable properties.

3. Conclusion

In summary, using the 2D $C_3N_4@MoN$ hybrid as a model catalyst, we demonstrated the possibility of activating 2D materials as efficient electrocatalysts for the alkaline HER. The construction of highly active

C_3N_4 and MoN interfaces facilitated the formation of dual active sites, which realized the balance of H_{ad} and OH_{ad} intermediates. It was also found that the contribution of H_{ad} and water dissociation in this electrocatalyst could be balanced by regulating the proportion of g- C_3N_4 to MoN. As expected, the 2D $C_3N_4@MoN$ hybrid exhibited significant enhancement in alkaline HER, requiring a low overpotential of 110 mV to produce 10 mA cm^{-2} , which is much better than pristine g- C_3N_4 or MoN. By merging electrochemical measurements and DFT calculations, we have shown that the activity enhancement originates from the optimized hydrogen adsorption energy on the N sites of g- C_3N_4 and the stronger OH adsorption energy of Mo atoms on MoN. This work demonstrates the feasibility of tuning the binding energies of multiple active sites through the construction of 2D heterostructures for alkaline HER.

4. Experimental procedures

4.1. Synthesis of 2D MoN

The 2D MoN nanosheets were synthesized according to a previous report with modifications [32]. Typically, 0.37 g of Mo powder was dispersed in 40 mL ethanol with magnetic stirring for 10 min. Then, 1.2 mL of H_2O_2 (30%) solution was injected dropwise into the suspension. After stirring for 12 h at room temperature, the solution turned into a dark blue color. The precursor solution was then mixed with 640 g of NaCl powder and dried at 50°C with continuous hand stirring. The mixture was then annealed at 650°C for 5 h at the heating rate of 1°C min^{-1} and under a 5% NH_3/Ar atmosphere. Finally, the product

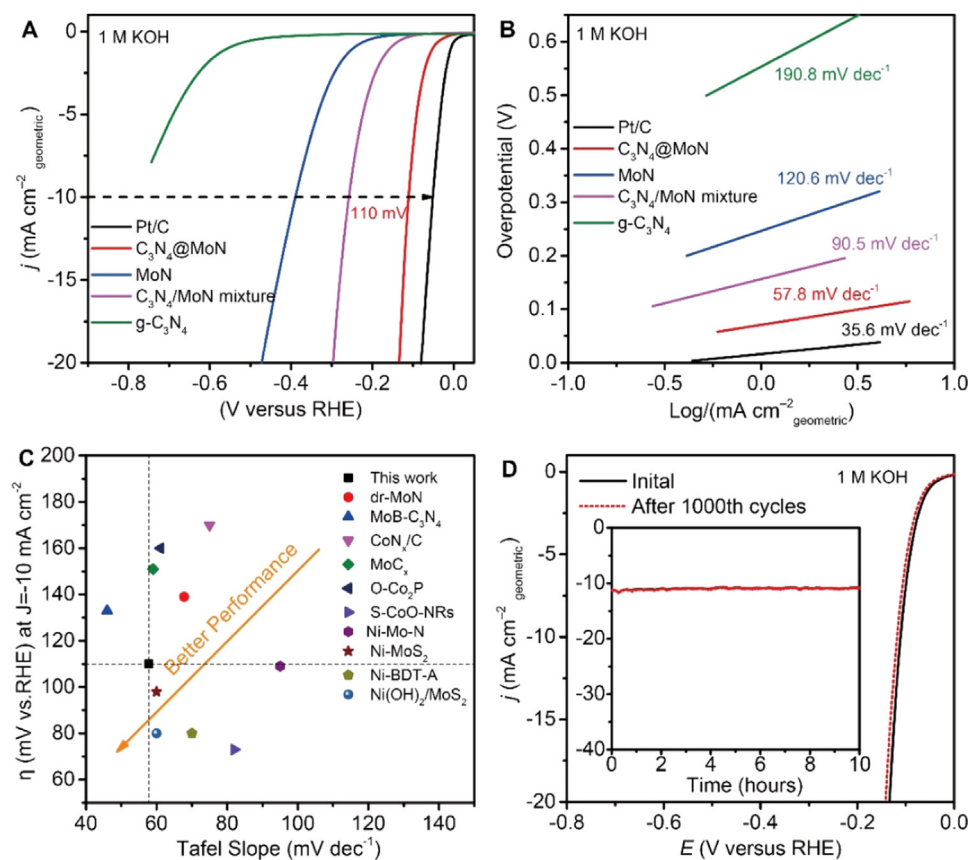


Fig. 3. (A) LSV curves of the different catalysts measured in Ar-saturated 1M KOH. (B) Tafel slope of the different catalysts obtained from Fig. 3A. (C) Comparison of Tafel values and overpotentials of $C_3N_4@MoN$ with other recently reported HER electrocatalysts in 1M KOH. (D) LSV curves of $C_3N_4@MoN$ at the 1st and 1000th cycles. Inset: Chronoamperometric curve of $C_3N_4@MoN$ at an overpotential of 110 mV.

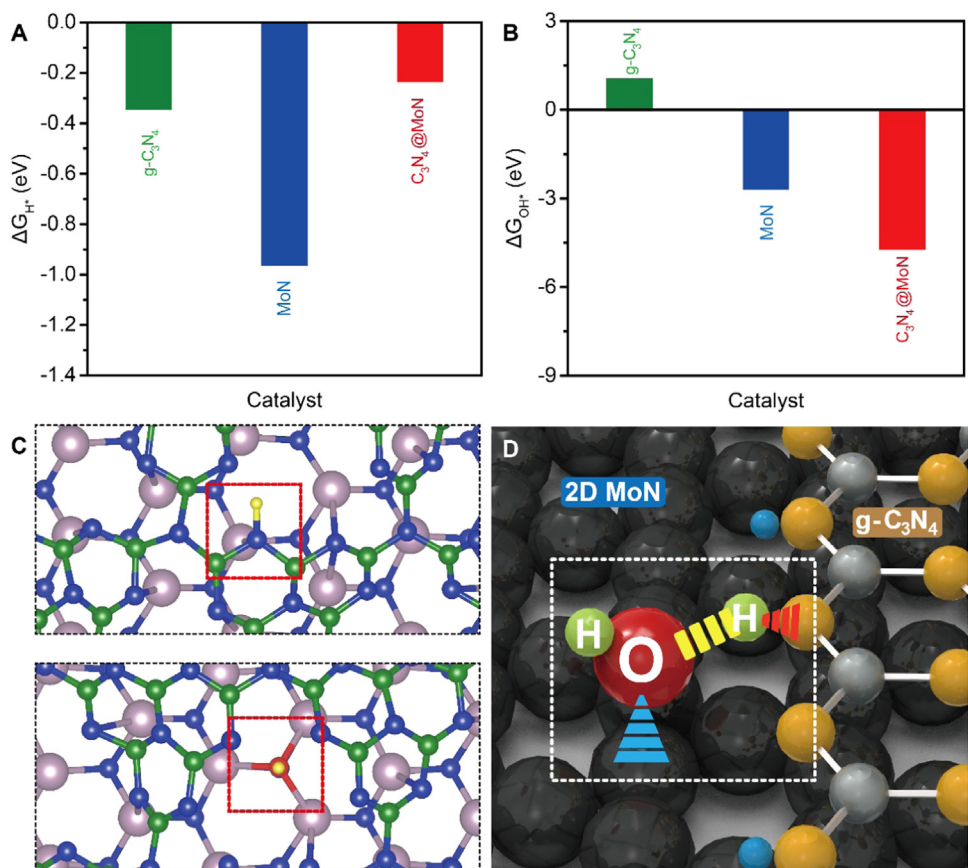


Fig. 4. (A and B) The calculated H_{ad} and OH_{ad} free energy diagram of MoN, $g-C_3N_4$, and $C_3N_4@MoN$. (C) The atomic configurations of H_{ad} (top) and OH_{ad} (bottom) on $C_3N_4@MoN$. Color codes: blue, pink and green represent Mo, N and C atoms of $C_3N_4@MoN$. Red and yellow represent oxygen and hydrogen atoms in a single water molecule. (D) Schematic representation of water dissociation step of $C_3N_4@MoN$. Color codes: black represents Mo atoms. Yellow and silver represent the N atoms and C atoms of $g-C_3N_4$, respectively. Red and green represent oxygen and hydrogen atoms in a single water molecule. (For interpretation of the references to color in this figure legend, the reader is referred to the web version of this article.)

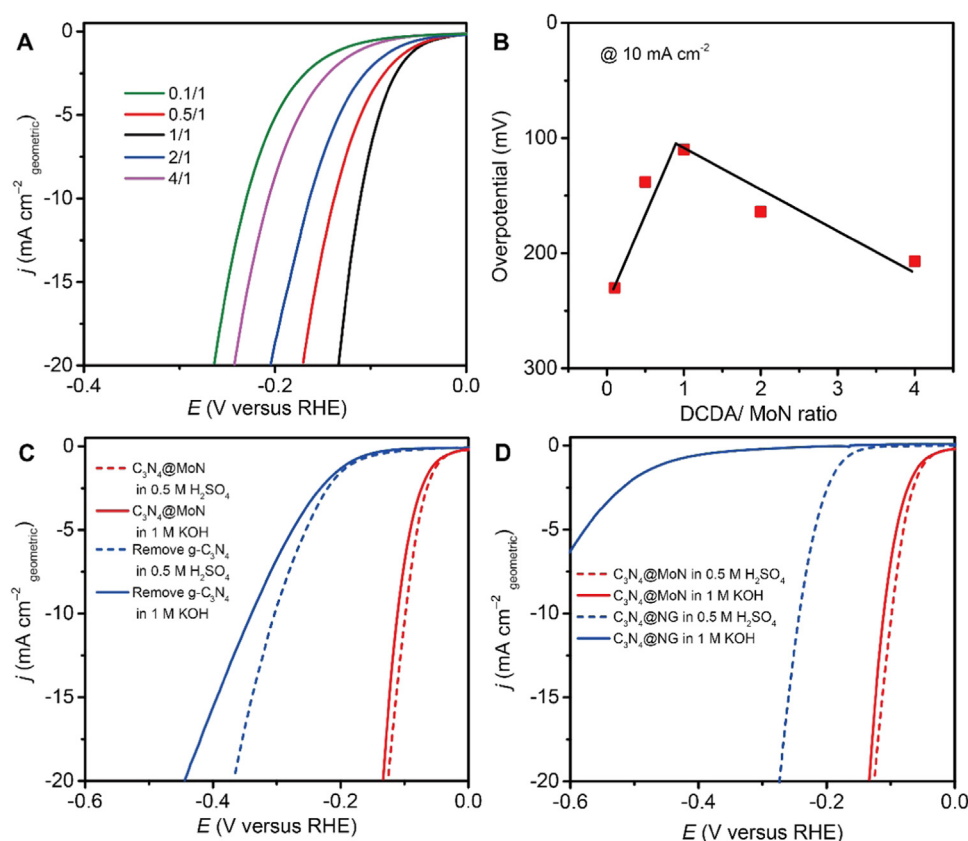


Fig. 5. (A) LSV curves of $C_3N_4@MoN$ with different DCDA/MoN ratio. Sample with a DCDA/MoN of 1:1 shows the best performance. (B) Overpotential of $C_3N_4@MoN$ catalysts with different DCDA/MoN ratios at a current density of 10 mA cm^{-2} . (C) LSV curves in different electrolytes for $C_3N_4@MoN$ and MoN after removing C_3N_4 . (D) LSV curves in different electrolytes for $C_3N_4@MoN$ and $C_3N_4@NG$.

was washed with deionized water several times to remove the NaCl template and dried using vacuum filtration.

4.2. Synthesis of 2D $C_3N_4@MoN$

The $C_3N_4@MoN$ hybrid was synthesized by mixing a given amount (1, 5, 10, 20 and 40 mg) of DCDA with 20 mL of 0.5 mg mL^{-1} MoN dispersion. The mixture was stirred for 12 h and then lyophilized for further use. DCDA was deposited on the MoN surface by the electrostatic interactions between the negatively charged MoN and positively charged DCDA during the drying process. The black sponge-like mixture was collected and put into a crucible with a cap to avoid melamine sublimation during heating and then annealed under an argon atmosphere at 550°C for 4 h at a heating rate of 4°C min^{-1} .

4.3. Synthesis of 2D C_3N_4/MoN mixture

Pure g- C_3N_4 nanosheets were synthesized by heating DCDA at 550°C for 4 h in muffle furnace with a heating rate of $2.3^\circ\text{C min}^{-1}$ and a cooling rate of 1°C min^{-1} . The resultant yellow agglomerates were milled into powder by an agate mortar. The powder was annealed in a muffle furnace at 500°C for 2 h with a ramp rate of 5°C min^{-1} . Then, the light-yellow g- C_3N_4 nanosheets were ultrasonicated for 30 min and then centrifuged at 2500 rpm for 20 min. The collected supernatant liquid was mixed with the MoN solution and freeze-dried for two days to obtain the C_3N_4/MoN mixture.

4.4. Electrochemical characterization

Typically, 4 mg of catalyst (e.g. $C_3N_4@MoN$) was dispersed in $700 \mu\text{L}$ of deionized water. Then $100 \mu\text{L}$ 1 wt% of Nafion/water and $200 \mu\text{L}$ carbon black (2 mg mL^{-1}) were added to the catalyst dispersion. Next, $20 \mu\text{L}$ of catalyst dispersion (4 mg mL^{-1}) were transferred onto a glassy carbon rotating disk electrode (0.196 cm^2) serving as a working

electrode. The reference electrode was an Ag/AgCl in 4M AgCl-KCl solution and the counter electrode was a graphite rod. All potentials were referenced to the reversible hydrogen electrode by adding a value of $(0.205 + 0.059 \times \text{pH})$ and all polarization curves were corrected for the iR contribution within the cell. A flow of Ar was maintained over the electrolyte during the experiment to eliminate dissolved oxygen. The working electrode was rotated at 1600 rpm to remove the hydrogen gas which formed on the catalyst surface.

4.5. Imaging and spectroscopic characterization

Field-emission SEM imaging and EDS mapping were conducted on a FEI QUANTA 450 electron microscope. Aberration-corrected HRTEM imaging was carried out on a FEI Titan G2 electron microscope equipped with image-corrector operated at 120 kV. HAADF imaging and EDS data were taken on a FEI Titan G2 transmission electron microscope operated at 200 kV. Atomic force microscopy (AFM, Shimadzu) was used to explore the morphology and thickness of the samples. XRD patterns were obtained using a D4 endeavor (Bruker) X-ray diffraction system with $\text{Co K}\alpha$ radiation. XPS data were collected under ultrahigh vacuum ($< 10^{-8}$ Torr) using a monochromatic Al $\text{K}\alpha$ X-ray source.

4.6. Computational details

DFT calculations were performed using the Vienna Ab Initio Simulation Package (VASP) [50–53]. The exchange–correlation interactions were treated within the generalized gradient approximation (GGA) in the form of the Perdew–Burke–Ernzerhof (PBE) functional [54]. The van der Waals interactions were described using the empirical correction in Grimme's scheme [55]. The electron wave functions were expanded using plane waves with a cutoff energy of 400 eV, and the convergence criteria of energy change during all calculations were set to 10^{-4} eV. The k-points for single cells of g- C_3N_4 and MoN (002) was

set to be $5 \times 5 \times 1$, and $1 \times 1 \times 1$. A k-points grid was applied to the $C_3N_4@MoN$ hybrid, which contained a $(2\sqrt{3} \times 2\sqrt{3})$ supercell of MoN (002) with a (3×3) g- C_3N_4 lattice ($a = b = 7.09 \text{ \AA}$). The convergence tolerance of force on each atom during full structure relaxation of g- C_3N_4 and MoN was set to be 0.01 eV/\AA . For the large hybrids configuration, the convergence tolerance of force on each atom during the relaxation with MoN fixed was set to be 0.05 eV/\AA . In order to avoid interactions between periodic images, a vacuum space of 20 \AA was applied to all calculations. For density of state calculations, the k-points was set to be $10 \times 10 \times 1$ for g- C_3N_4 and MoN and $1 \times 1 \times 1$ for $C_3N_4@MoN$. The adsorption free energy of intermediates on the catalyst surface is defined as:

$$\Delta G = \Delta E_{\text{ad}} + \Delta E_{\text{ZPE}} - T\Delta S + \Delta G_{\text{sol}}$$

where ΔE_{ad} is the adsorption energy defined as the electronic energy difference between the initial and the corresponding final states. ΔE_{ZPE} is the change in zero-point energies, T is the temperature ($T = 298.15 \text{ K}$), and ΔS is the entropy change, ΔE_{ZPE} and ΔS can be obtained by frequency calculations. ΔG_{sol} represents the correction terms for solvent effect, 0 eV for H^+ , [56] and -0.5 eV for OH^+ [57].

Acknowledgements

H. Jin and X. Liu contributed equally to this work. We acknowledge financial support by the Australian Research Council (DP170104464, DP160104866, DE160101163 and FL170100154). DFT computations within this research was undertaken with the assistance of resources and services from the National Computational Infrastructure (NCI), which is supported by the Australian Government.

Declaration of interests

The authors declare no competing financial interests.

Appendix A. Supporting information

Supplementary data associated with this article can be found in the online version at [doi:10.1016/j.nanoen.2018.09.046](https://doi.org/10.1016/j.nanoen.2018.09.046).

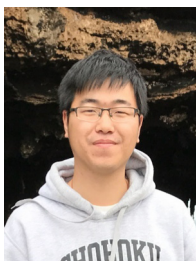
References

- [1] Z.W. Seh, J. Kibsgaard, C.F. Dickens, I. Chorkendorff, J.K. Nørskov, T.F. Jaramillo, *Science* 355 (2017) (eaad4998).
- [2] Y. Kang, P. Yang, N.M. Markovic, V.R. Stamenkovic, *Nano Today* 11 (2016) 587–600.
- [3] N.M. Markovic, *Science* 334 (2011) 1256–1260.
- [4] V.R. Stamenkovic, D. Strmcnik, P.P. Lopes, N.M. Markovic, *Nat. Mater.* 16 (2016) 57–69.
- [5] Y. Jiao, Y. Zheng, K. Davey, S.-Z. Qiao, *Nat. Energy* 1 (2016) 16130.
- [6] Z. Zeng, K.-C. Chang, J. Kubal, N.M. Markovic, J. Greeley, *Nat. Energy* 2 (2017) 17070.
- [7] R. Subbaraman, D. Tripkovic, K.C. Chang, D. Strmcnik, A.P. Paulikas, P. Hirunsit, M. Chan, J. Greeley, V. Stamenkovic, N.M. Markovic, *Nat. Mater.* 11 (2012) 550–557.
- [8] Y. Zheng, Y. Jiao, S. Qiao, A. Vasileff, *Angew. Chem. Int. Ed.* 57 (2017) 7568–7579, <https://doi.org/10.1002/anie.201710556>.
- [9] I. Ledezma-Yanez, W.D.Z. Wallace, P. Sebastián-Pascual, V. Climent, J.M. Feliu, M.T.M. Koper, *Nat. Energy* 2 (2017) 17031.
- [10] M. Chhowalla, H.S. Shin, G. Eda, L.J. Li, K.P. Loh, H. Zhang, *Nat. Chem.* 5 (2013) 263–275.
- [11] J. Kibsgaard, Z. Chen, B.N. Reinecke, T.F. Jaramillo, *Nat. Mater.* 11 (2012) 963–969.
- [12] D. Deng, K.S. Novoselov, Q. Fu, N. Zheng, Z. Tian, X. Bao, *Nat. Nanotech.* 11 (2016) 218–230.
- [13] C. Tan, X. Cao, X.J. Wu, Q. He, J. Yang, X. Zhang, J. Chen, W. Zhao, S. Han, G.H. Nam, et al., *Chem. Rev.* 117 (2017) 6225–6331.
- [14] J. Zhao, Z. Chen, *J. Am. Chem. Soc.* 139 (2017) 12480–12487.
- [15] Y. Zheng, Y. Jiao, Y. Zhu, Q. Cai, A. Vasileff, L.H. Li, Y. Han, Y. Chen, S.-Z. Qiao, *J. Am. Chem. Soc.* 139 (2017) 3336–3339.
- [16] K. Xu, P. Chen, X. Li, Y. Tong, H. Ding, X. Wu, W. Chu, Z. Peng, C. Wu, Y. Xie, *J. Am. Chem. Soc.* 137 (2015) 4119–4125.
- [17] M. Asadi, K. Kim, C. Liu, A.V. Addepalli, P. Abbasi, P. Yasaei, P. Phillips, A. Behranginia, J.M. Cerrato, R. Haasch, et al., *Science* 353 (2016) 467–470.
- [18] M. Gong, W. Zhou, M.C. Tsai, J. Zhou, M. Guan, M.C. Lin, B. Zhang, Y. Hu,

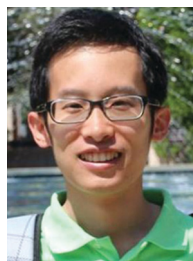
- [19] D.Y. Wang, J. Yang, et al., *Nat. Commun.* 5 (2014) 4695.
- [20] J. Staszak-Jirkovsky, C.D. Malliakas, P.P. Lopes, N. Danilovic, S.S. Kota, K.C. Chang, B. Genorio, D. Strmcnik, V.R. Stamenkovic, M.G. Kanatzidis, et al., *Nat. Mater.* 15 (2016) 197–203.
- [21] Y. Zheng, Y. Jiao, Y. Zhu, L.H. Li, Y. Han, Y. Chen, M. Jaroniec, S.Z. Qiao, *J. Am. Chem. Soc.* 138 (2016) 16174–16181.
- [22] J. Liu, Y. Zheng, D. Zhu, A. Vasileff, T. Ling, S.-Z. Qiao, *Nanoscale* 9 (2017) 16616–16621.
- [23] Y. Zheng, Y. Jiao, S.Z. Qiao, *Adv. Mater.* 27 (2015) 5372–5378.
- [24] Y. Jiao, Y. Zheng, P. Chen, M. Jaroniec, S.-Z. Qiao, *J. Am. Chem. Soc.* 139 (2017) 18093–18100.
- [25] W. Fu, H. He, Z. Zhang, C. Wu, X. Wang, H. Wang, Q. Zeng, L. Sun, X. Wang, J. Zhou, et al., *Nano Energy* 27 (2016) 44–50.
- [26] M.-R. Gao, J.-X. Liang, Y.-R. Zheng, Y.-F. Xu, J. Jiang, Q. Gao, J. Li, S.-H. Yu, *Nat. Commun.* 6 (2015) 5982.
- [27] J. Xie, H. Zhang, S. Li, R. Wang, X. Sun, M. Zhou, J. Zhou, X.W. Lou, Y. Xie, *Adv. Mater.* 25 (2013) 5807–5813.
- [28] Y. Zheng, Y. Jiao, Y. Zhu, L.H. Li, Y. Han, Y. Chen, A. Du, M. Jaroniec, S.Z. Qiao, *Nat. Commun.* 5 (2014) 3783.
- [29] H. Jin, C. Guo, X. Liu, J. Liu, A. Vasileff, Y. Jiao, Y. Zheng, S.-Z. Qiao, *Chem. Rev.* 118 (2018) 6337–6408.
- [30] Y. Wang, L. Chen, X. Yu, Y. Wang, G. Zheng, *Adv. Energy Mater.* 7 (2017) 1601390.
- [31] B. Zhang, J. Liu, J. Wang, Y. Ruan, X. Ji, K. Xu, C. Chen, H. Wan, L. Miao, J. Jiang, *Nano Energy* 37 (2017) 74–80.
- [32] H. Yin, S. Zhao, K. Zhao, A. Muqsit, H. Tang, L. Chang, H. Zhao, Y. Gao, Z. Tang, *Nat. Commun.* 6 (2015) 6430.
- [33] X. Xiao, H. Yu, H. Jin, M. Wu, Y. Fang, J. Sun, Z. Hu, T. Li, J. Wu, L. Huang, et al., *ACS Nano* 11 (2017) 2180–2186.
- [34] X. Xiao, H. Song, S. Lin, Y. Zhou, X. Zhan, Z. Hu, Q. Zhang, J. Sun, B. Yang, T. Li, et al., *Nat. Commun.* 7 (2016) 11296.
- [35] Q. Han, Z. Cheng, J. Gao, Y. Zhao, Z. Zhang, L. Dai, L. Qu, *Adv. Funct. Mater.* 27 (2017) 1606352.
- [36] J.-X. Feng, J.-Q. Wu, Y.-X. Tong, G.-R. Li, *J. Am. Chem. Soc.* 140 (2018) 610–617.
- [37] J. Zhang, T. Wang, P. Liu, S. Liu, R. Dong, X. Zhuang, M. Chen, X. Feng, *Energy Environ. Sci.* 9 (2016) 2789–2793.
- [38] T. Zhang, M.-Y. Wu, D.-Y. Yan, J. Mao, H. Liu, W.-B. Hu, X.-W. Du, T. Ling, S.-Z. Qiao, *Nano Energy* 43 (2018) 103–109.
- [39] J. Tian, Q. Liu, A.M. Asiri, X. Sun, *J. Am. Chem. Soc.* 136 (2014) 7587–7590.
- [40] C. Hu, Q. Ma, S.-F. Hung, Z.-N. Chen, D. Ou, B. Ren, H.M. Chen, G. Fu, N. Zheng, *Chem* 3 (2017) 122–133.
- [41] H.B. Wu, B.Y. Xia, L. Yu, X.Y. Yu, X.W. Lou, *Nat. Commun.* 6 (2015) 6512.
- [42] H.-W. Liang, S. Brüller, R. Dong, J. Zhang, X. Feng, K. Müllen, *Nat. Commun.* 6 (2015) 7992.
- [43] T. Ling, D.-Y. Yan, H. Wang, Y. Jiao, Z. Hu, Y. Zheng, L. Zheng, J. Mao, H. Liu, X.-W. Du, et al., *Nat. Commun.* 8 (2017) 1509.
- [44] J. Xiong, W. Cai, W. Shi, X. Zhang, J. Li, Z. Yang, L. Feng, H. Cheng, *J. Mater. Chem. A* 5 (2017) 24193–24198.
- [45] Z. Zhuang, Y. Li, Z. Li, F. Lv, Z. Lang, K. Zhao; L. Zhou, L. Moskalova, S. Guo, L. Mai, *Angew. Chem. Int. Ed.*, 57, 496–500.
- [46] Q. Ma, C. Hu, K. Liu, S.-F. Hung, D. Ou, H.M. Chen, G. Fu, N. Zheng, *Nano Energy* 41 (2017) 148–153.
- [47] K. Xu, H. Ding, M. Zhang, M. Chen, Z. Hao, L. Zhang, C. Wu, Y. Xie, *Adv. Mater.* 29 (2017) 1606980.
- [48] J.K. Nørskov, T. Bligaard, J. Rossmeisl, C.H. Christensen, *Nat. Chem.* 1 (2009) 37–46.
- [49] J. Zhang, T. Wang, D. Pohl, B. Rellinghaus, R. Dong, S. Liu, X. Zhuang, X. Feng, *Angew. Chem. Int. Ed.* 128 (2016) 6814–6819.
- [50] J. Zhang, T. Wang, P. Liu, Z. Liao, S. Liu, X. Zhuang, M. Chen, E. Zschech, X. Feng, *Nat. Commun.* 8 (2017) 15437.
- [51] G. Kresse, J. Furthmüller, *Comput. Mater. Sci.* 6 (1996) 15–50.
- [52] G. Kresse, J. Furthmüller, *Phys. Rev. B* 54 (1996) 11169–11186.
- [53] G. Kresse, J. Hafner, *Phys. Rev. B* 47 (1993) 558–561.
- [54] G. Kresse, J. Hafner, *Phys. Rev. B* 49 (1994) 14251–14269.
- [55] J.P. Perdew, K. Burke, M. Ernzerhof, *Phys. Rev. Lett.* 77 (1996) 3865–3868.
- [56] S. Grimme, *J. Comput. Chem.* 27 (2006) 1787–1799.
- [57] J.K. Nørskov, T. Bligaard, A. Logadottir, J.R. Kitchin, J.G. Chen, S. Pandalov, J.K. Nørskov, *J. Electrochem. Soc.* 152 (2005) J23–J26.
- [58] Y.W. Li, H.B. Su, S.H. Chan, Q. Sun, *ACS Catal.* 5 (2015) 6658–6664.



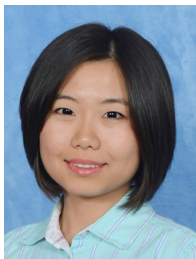
Huanyu Jin received his B.S. in Optical Information Science and Technology from Huazhong University of Science and Technology (China) in 2013, and then completed his M.Phil. in Applied Physics from The Hong Kong Polytechnic University in 2015. Currently, he is a Ph.D. candidate in Chemical Engineering under the supervision of Prof. Shi-Zhang Qiao at The University of Adelaide. His research interest focuses on the development of novel nanomaterials for energy related applications.



Xin Liu received his B.E. and M.E. degrees in Thermal Engineering at the Harbin Institute of Technology (China) in 2014 and 2016, respectively. He is currently a Ph.D. student under the supervision of Prof. Shi-Zhang Qiao in the School of Chemical Engineering at The University of Adelaide. His current research focuses on revealing the electronic structure origin of electrocatalytic activity in some key electrocatalysis processes like hydrogen evolution and nitrogen reduction reactions.



Yao Zheng received his Ph.D. degree in Chemical Engineering from the University of Queensland in 2014. Currently he is a DECRA research fellow working with Prof. Shi-Zhang Qiao in The University of Adelaide. His research focuses on fundamental studies of some key electrocatalysis processes such as oxygen reduction, hydrogen evolution, and CO₂ reduction reactions. He has co-authored more than 60 papers in refereed journals with over 9000 citations.



Yan Jiao received her Ph.D. in 2012 from the University of Queensland. She is currently a University of Adelaide fellow working with Prof. Shi-Zhang Qiao. Her current research area is computational electrochemistry, which involves investigating the nature and origin of electrocatalytic activity on nanostructured materials and developing novel catalysts for clean energy conversion reactions using Density Functional Theory computations.



Shi-Zhang Qiao is currently a Chair Professor at the School of Chemical Engineering of the University of Adelaide, Australia. His research expertise is in nanomaterials for new energy technologies (electrocatalysis, photocatalysis, batteries, fuel cell, supercapacitors). He has co-authored more than 330 papers in refereed journals with over 33,500 citations and h-index ~94. He is also an ESI highly cited researcher in categories of chemistry and materials.



Anthony Vasileff is a Ph.D. candidate in the School of Chemical Engineering at The University of Adelaide. Anthony received his Bachelor's degree in Chemical Engineering at The University of Adelaide. His graduate research is focused on developing novel non-metal electrocatalysts and supports, particularly nanostructured carbon, for electrochemical processes. Currently, he is working on developing new nanomaterials for carbon dioxide reduction in order to advance clean energy storage technologies.

Supporting Information

Constructing Tunable Dual Active Sites on Two-Dimensional C₃N₄@MoN Hybrid for Electrocatalytic Hydrogen Evolution

Huanyu Jin, Xin Liu, Yan Jiao, Anthony Vasileff, Yao Zheng, Shi-Zhang Qiao

School of Chemical Engineering, The University of Adelaide, Adelaide, SA5005, Australia

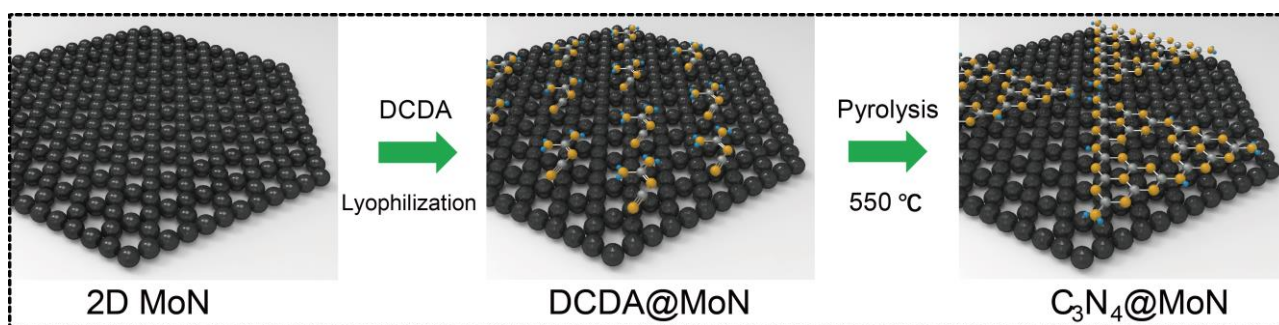


Fig. S1. Schematics of the preparation of C₃N₄@MoN.

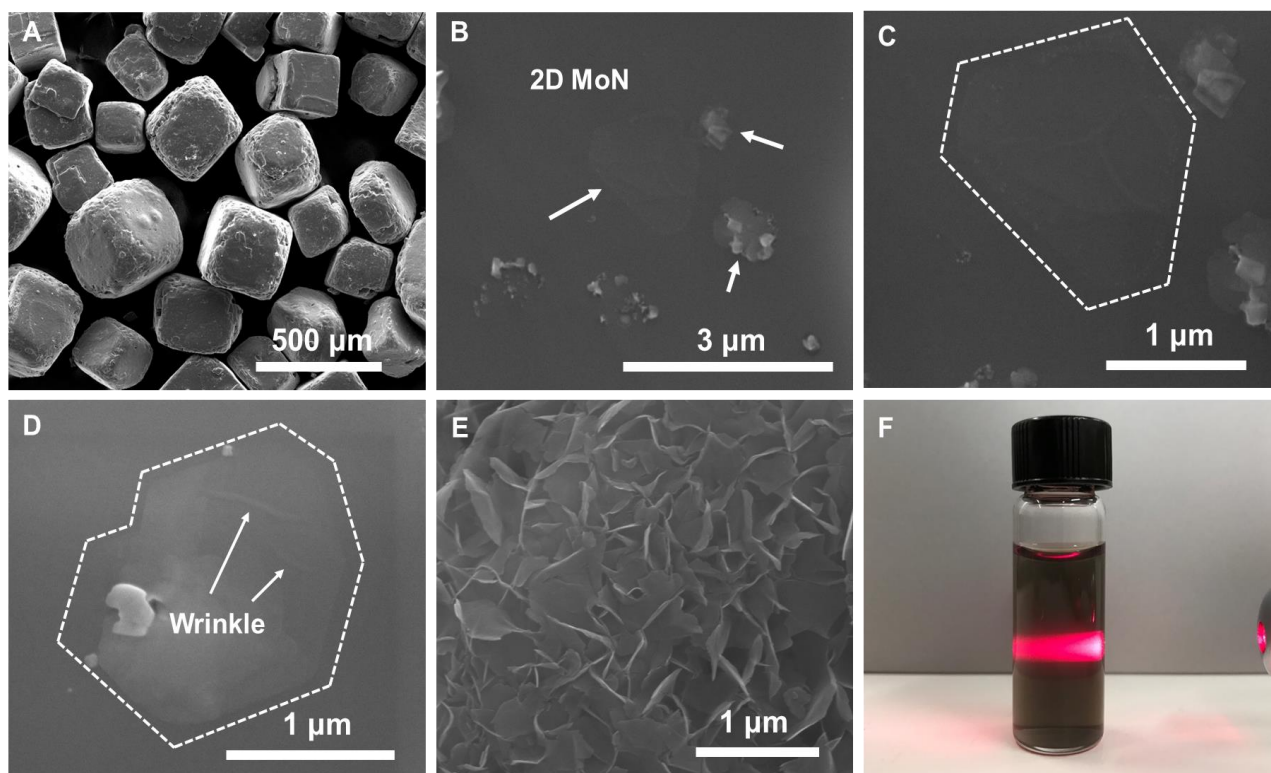


Fig. S2. (A) SEM images of 2D MoN on NaCl crystal. (B), (C) and (D) show the epitaxial growth of MoN on NaCl surface with the lateral size of 1 μm . (E) SEM image of 2D MoN powder. (F) Photo of Tyndall effect of 2D MoN in water. The Tyndall effect can be clearly seen, demonstrating its good dispersability in water.

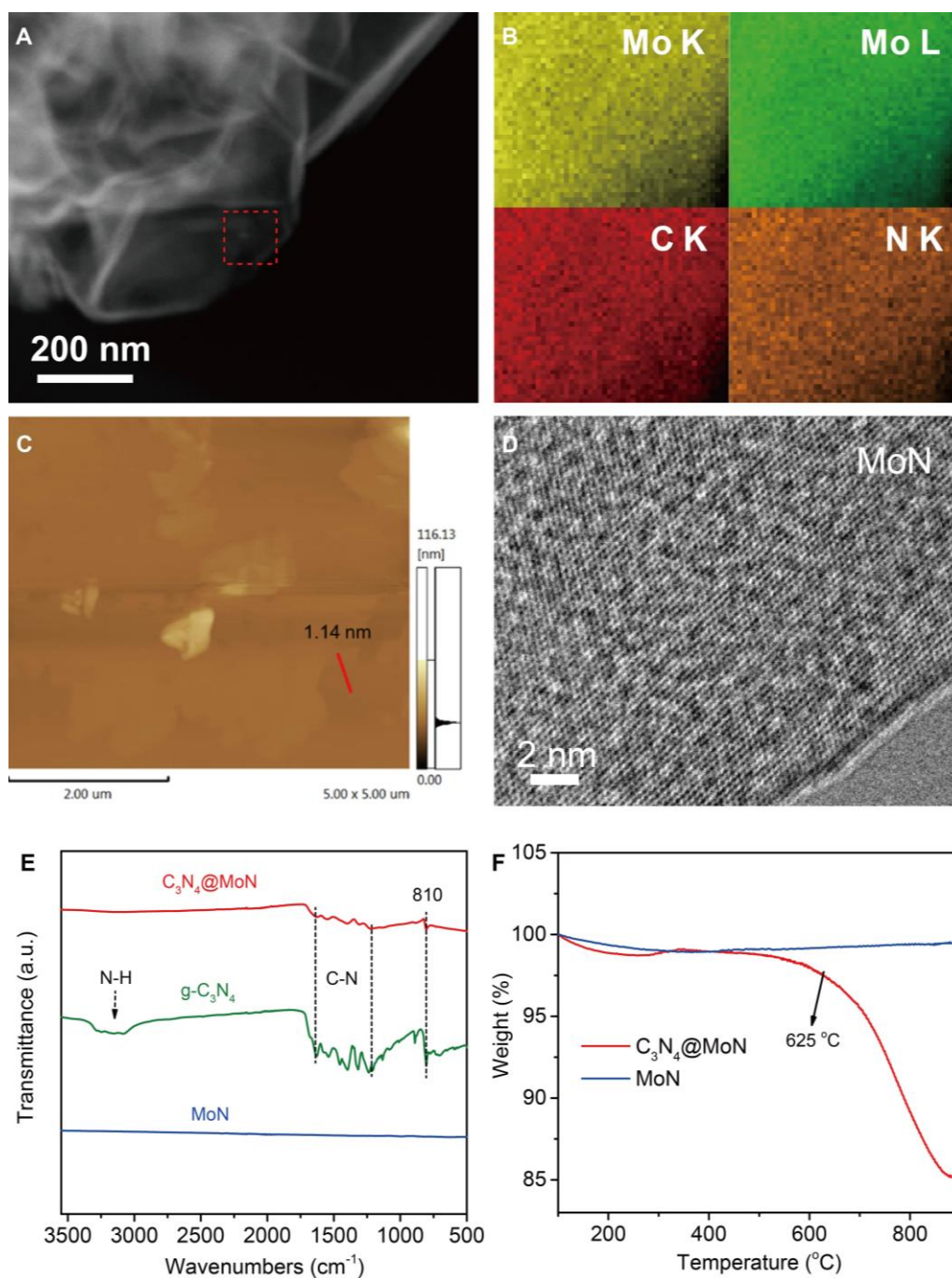


Fig. S3. (A) HADDF-TEM and elemental mapping of $C_3N_4@MoN$. The Mo K, Mo L, C K and N K mappings are shown in (B). (C and D) AFM and HRTEM images of pristine MoN. (E) FT-IR spectra of $C_3N_4@MoN$, $g-C_3N_4$ and MoN, respectively. The peak at 810 cm^{-1} is assigned to the breathing mode of triazine units. Several peaks from 1238 to 1640 cm^{-1} correspond to the characteristic stretching modes of C–N heterocycles. The broad peak around 3000 – 3700 cm^{-1} , which belongs to N–H stretching at the edge of $g-C_3N_4$, disappeared in $C_3N_4@MoN$, indicating that the $g-C_3N_4$ is covered on MoN without suspended edge. (F) TGA curve of $C_3N_4@MoN$ and MoN. The endothermic peak appeared at 625 °C in Figure S3F is belong to the decomposition of $g-C_3N_4$, which also proves the existence of $g-C_3N_4$

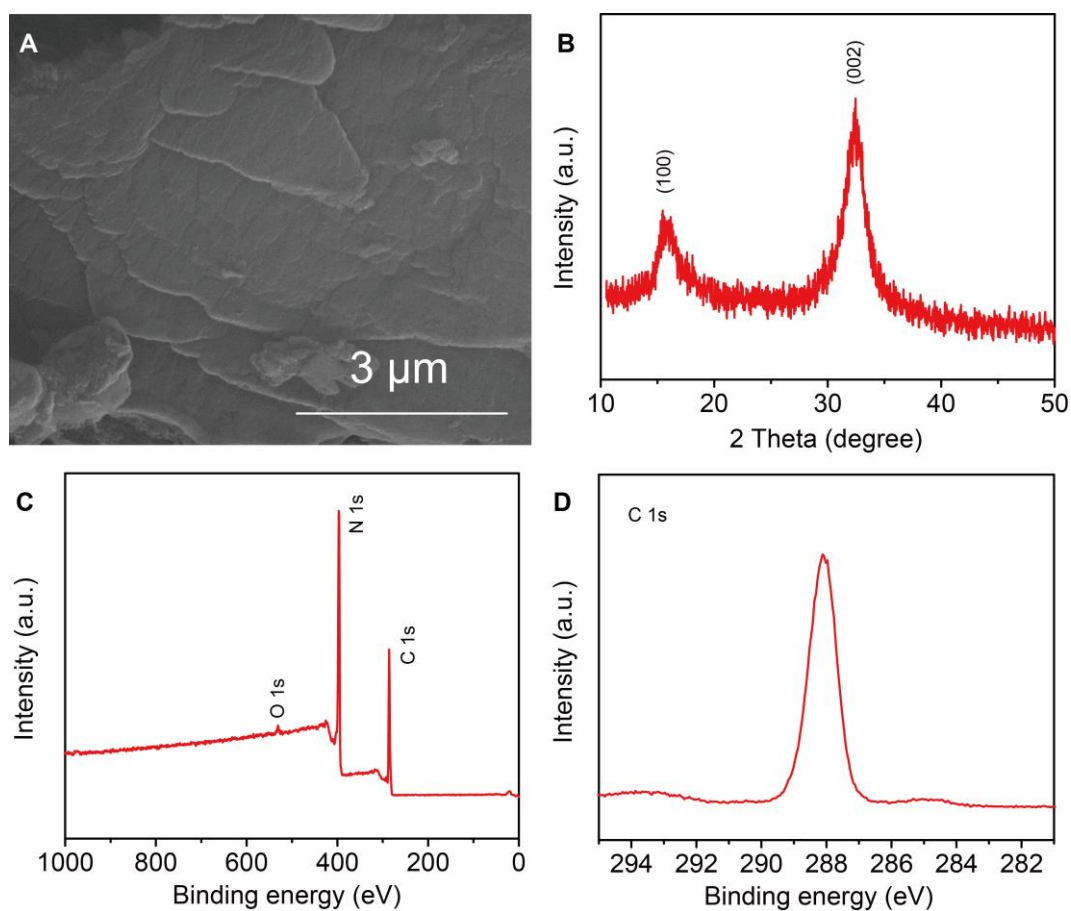


Fig. S4. (A) SEM image. (B) XRD. (C) XPS survey scan. (D) High resolution C1s peak.

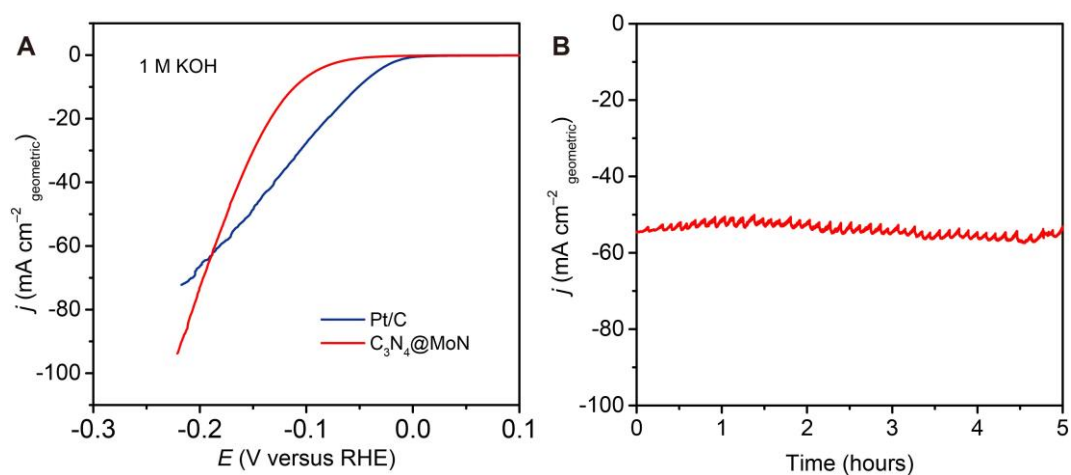


Fig. S5. (A) LSV curves of $C_3N_4@MoN$ and commercial 20% Pt/C. At large current density, the HER performance of $C_3N_4@MoN$ exceeds commercial Pt based catalysts, demonstrating the potential for practical applications. (B) Stability test of $C_3N_4@MoN$ at large current density.

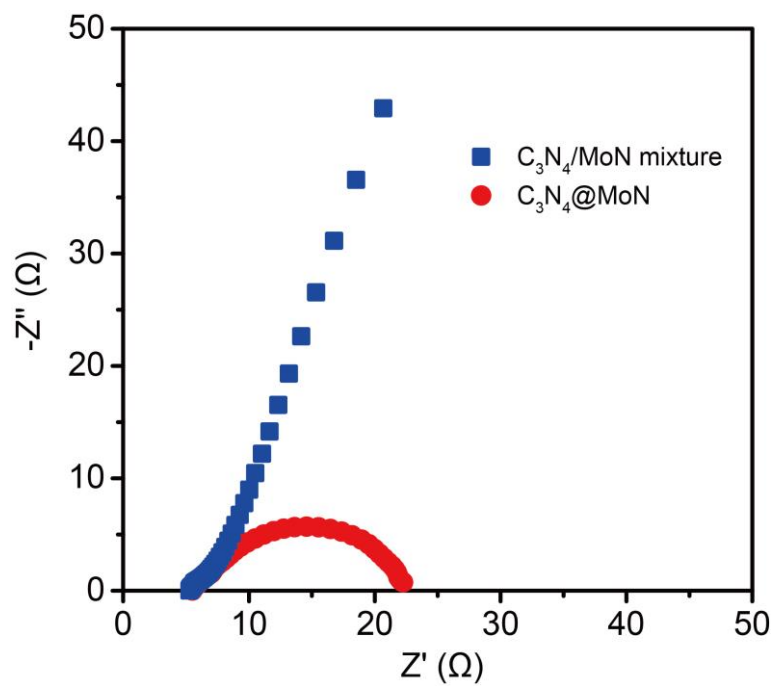


Fig. S6. EIS spectra of C₃N₄@MoN and C₃N₄/MoN mixture at an overpotential of 200 mV.

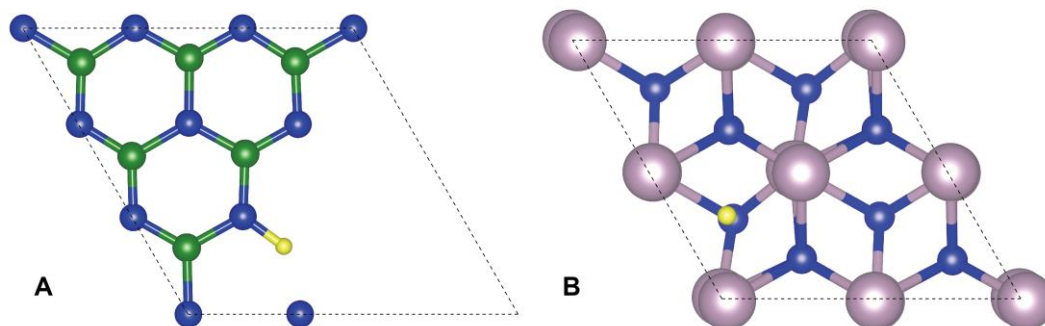


Fig. S7. The molecular configurations of H_{ad} on (A) g-C₃N₄ and (B) MoN.

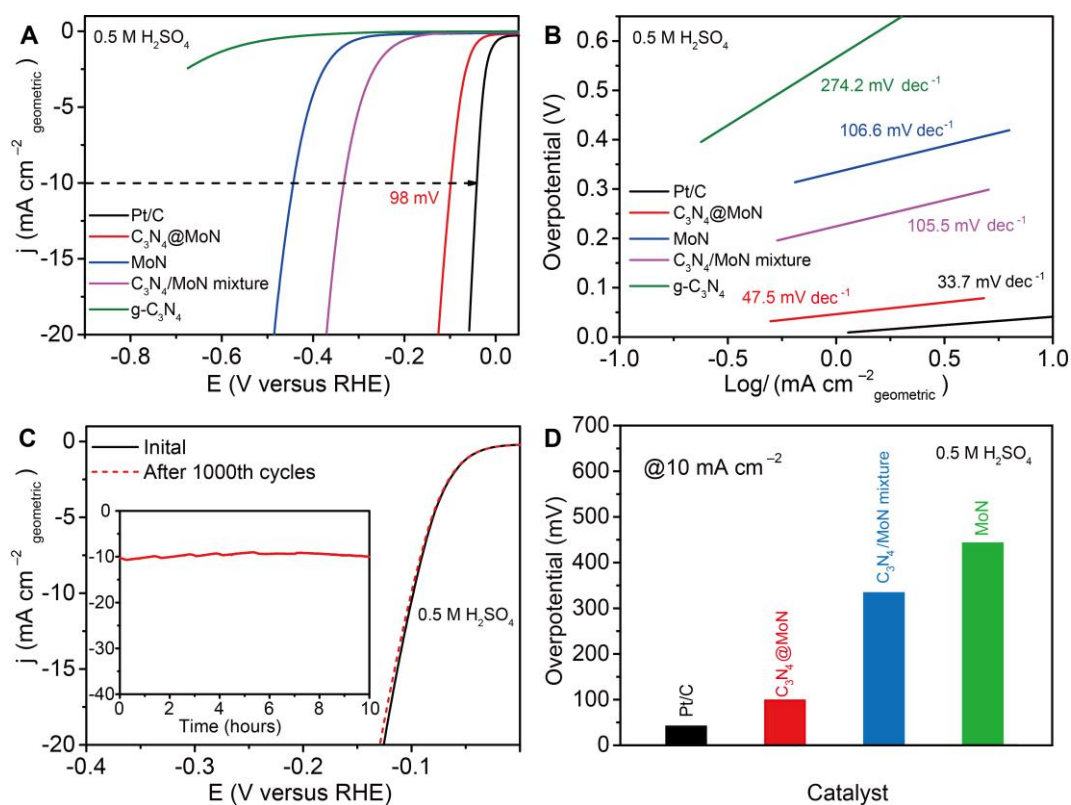


Fig. S8. (A) LSV curves of different catalysts. (B) Tafel plot calculated from (A). (C) Stability test of $C_3N_4@MoN$. (D) Overpotential of different catalysts at the current density of 10 mA cm^{-2} .

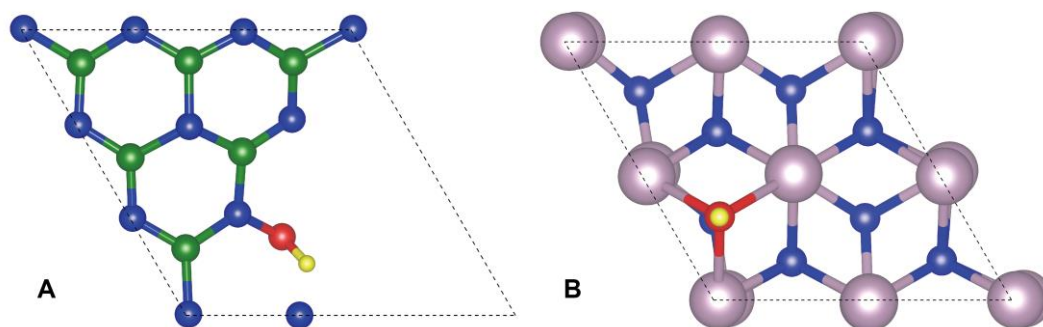


Fig. S9. The molecular configurations of OH_{ad} on (A) $g-C_3N_4$ and (B) MoN .

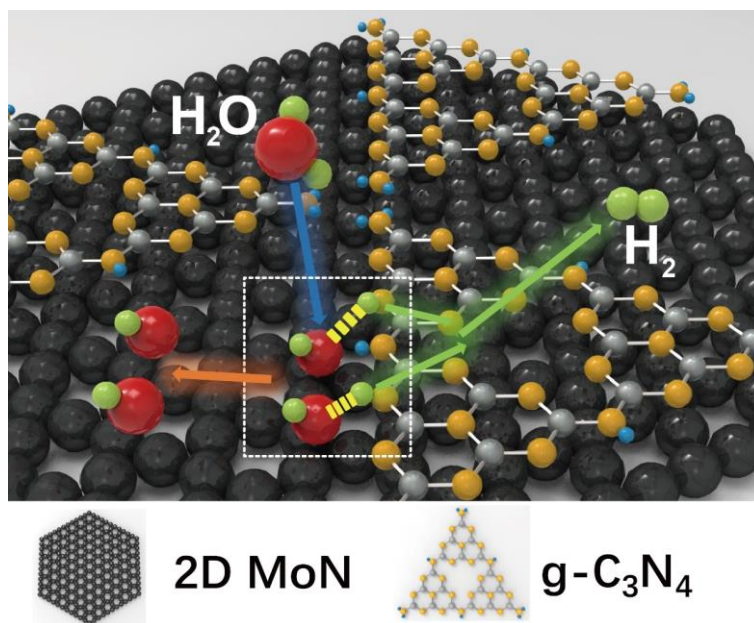


Fig. S10. Schematic diagram of the reaction route of C₃N₄@MoN.

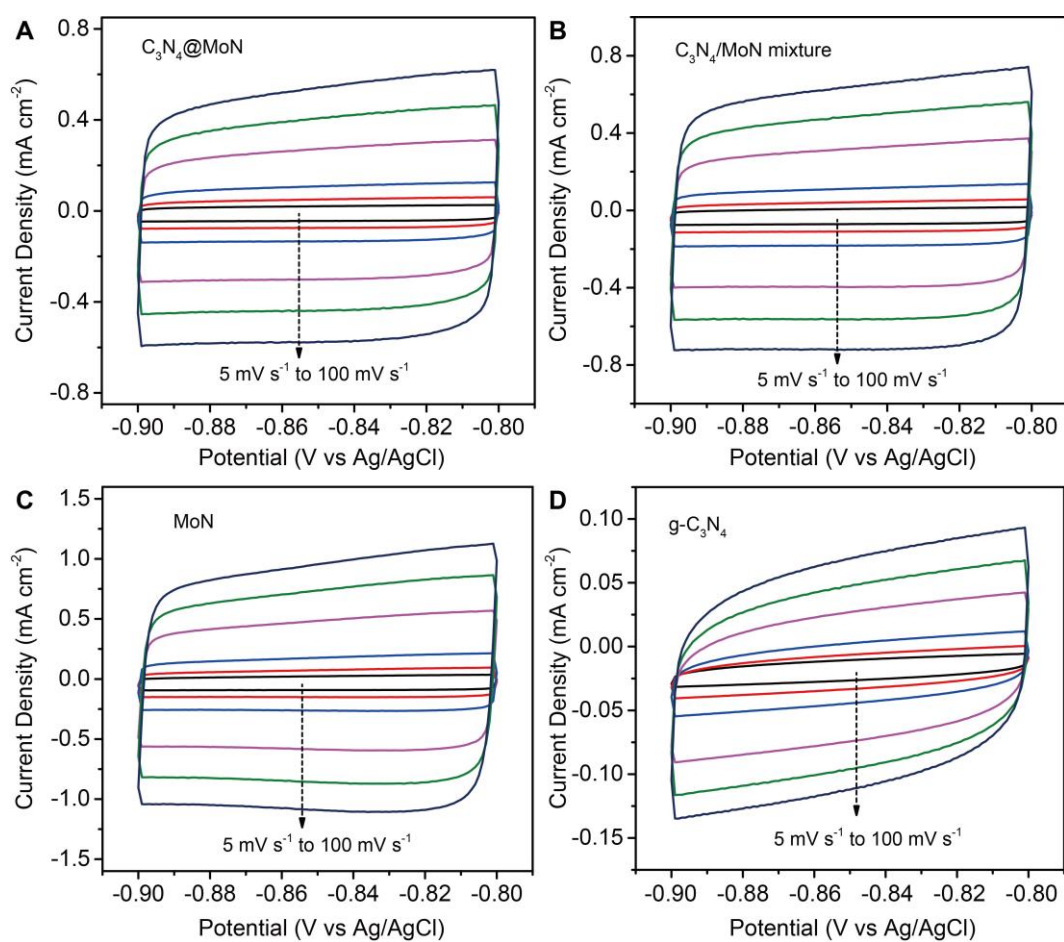


Fig. S11. CV curves of different catalysts with scan rates from 5 mV s⁻¹ to 100 mV s⁻¹.

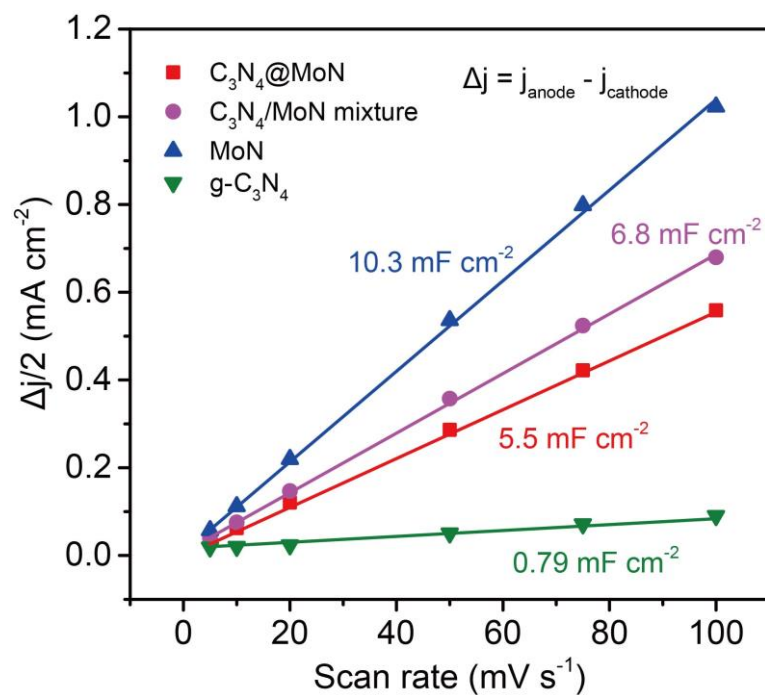


Fig. S12. Current density difference at -0.85 V plotted against scan rate to give the double-layer capacitance for C₃N₄@MoN, C₃N₄/MoN mixture, MoN and g-C₃N₄, respectively.

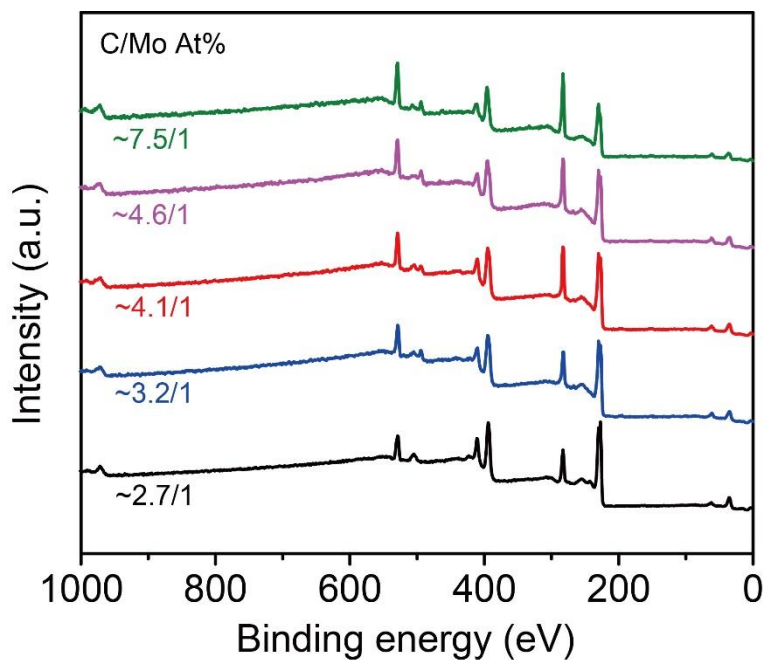


Fig. S13. XPS survey scan of C₃N₄@MoN with different MoN/DCDA ratio.

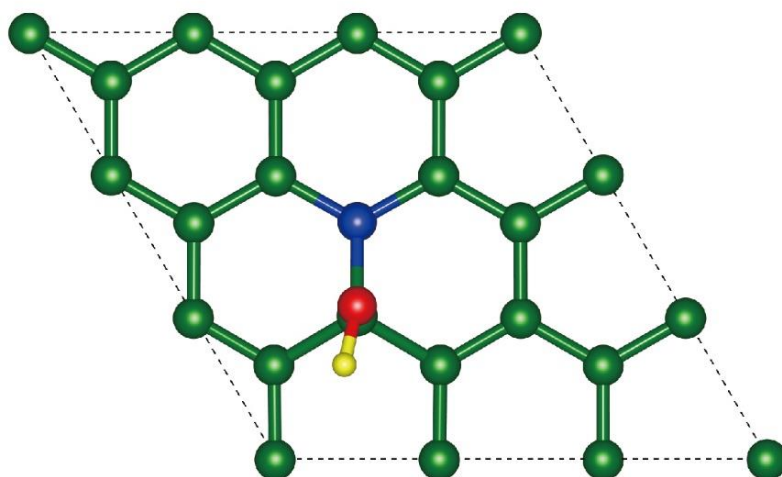


Fig. S14. The molecular configurations of OH_{ad} on nitrogen doped graphene.

Table S1. Summary of some recently reported representative HER electrocatalysts in alkaline electrolytes.

Catalyst	η (mV vs. RHE) @ $J = -10 \text{ mA cm}^{-2}$	Tafel slope (mA decade^{-1})	Ref.
$\text{C}_3\text{N}_4@\text{MoN}$	110	57.8	This work
$\text{C}_3\text{N}_4@\text{N-graphene}$	610	N/A	1
dr-MoN	139	67.82	2
MoB- C_3N_4	133	46	3
Co/CoP	135	64	4
CoN_x/C	170	75	5
MoC _x nano-octahedrons	151	59	6
O-Co ₂ P	160	61.1	7
NiO NRs	110	100	8
S-CoO NRs	73	82	9
Ni-Mo-N	109	95	10
CoP	209	129	11
Ni-MoS ₂	98	60	12
Ni-BDT-A	80	70	13
Ni(OH) ₂ /MoS ₂	80	60	14
NF-NiS ₂ -A	67	63	15

SUPPLEMENTARY REFERENCES

- (1) Zheng, Y.; Jiao, Y.; Zhu, Y.; Li, L. H.; Han, Y.; Chen, Y.; Du, A.; Jaroniec, M.; Qiao, S. Z. *Nat. Commun.* **2014**, *5*, 3783.
- (2) Xiong, J.; Cai, W.; Shi, W.; Zhang, X.; Li, J.; Yang, Z.; Feng, L.; Cheng, H. *J. Mater. Chem. A* **2017**, *5*, 24193-24198.
- (3) Zhuang, Z.; Li, Y.; Li, Z.; Lv, F.; Lang, Z.; Zhao, K.; Zhou, L.; Moskaleva, L.; Guo, S.; Mai, L. *Angew. Chem. Int. Ed.* **2018**, *57*, 496-500.
- (4) Wang, H.; Min, S.; Wang, Q.; Li, D.; Casillas, G.; Ma, C.; Li, Y.; Liu, Z.; Li, L. J.; Yuan, J.; Antonietti, M.; Wu, T. *ACS Nano* **2017**, *11*, 4358-4364.
- (5) Liang, H.-W.; Brüller, S.; Dong, R.; Zhang, J.; Feng, X.; Müllen, K. *Nat. Commun.* **2015**, *6*, 7992.
- (6) Wu, H. B.; Xia, B. Y.; Yu, L.; Yu, X. Y.; Lou, X. W. *Nat Commun* **2015**, *6*, 6512.
- (7) Xu, K.; Ding, H.; Zhang, M.; Chen, M.; Hao, Z.; Zhang, L.; Wu, C.; Xie, Y. *Adv. Mater.* **2017**, *29*, 1606980.
- (8) Zhang, T.; Wu, M.-Y.; Yan, D.-Y.; Mao, J.; Liu, H.; Hu, W.-B.; Du, X.-W.; Ling, T.; Qiao, S.-Z. *Nano Energy* **2018**, *43*, 103-109.
- (9) Ling, T.; Yan, D.-Y.; Wang, H.; Jiao, Y.; Hu, Z.; Zheng, Y.; Zheng, L.; Mao, J.; Liu, H.; Du, X.-W.; Jaroniec, M.; Qiao, S.-Z. *Nat. Commun.* **2017**, *8*, 1509.
- (10) Zhang, Y.; Ouyang, B.; Xu, J.; Chen, S.; Rawat, R. S.; Fan, H. J. *Adv. Energy Mater.* **2016**, *6*, 1600221.
- (11) Tian, J.; Liu, Q.; Asiri, A. M.; Sun, X. *J. Am. Chem. Soc.* **2014**, *136*, 7587-7590.
- (12) Zhang, J.; Wang, T.; Liu, P.; Liu, S.; Dong, R.; Zhuang, X.; Chen, M.; Feng, X. *Energy Environ. Sci.* **2016**, *9*, 2789-2793.
- (13) Hu, C.; Ma, Q.; Hung, S.-F.; Chen, Z.-N.; Ou, D.; Ren, B.; Chen, H. M.; Fu, G.; Zheng, N. *Chem* **2017**, *3*, 122-133.
- (14) Zhang, B.; Liu, J.; Wang, J.; Ruan, Y.; Ji, X.; Xu, K.; Chen, C.; Wan, H.; Miao, L.; Jiang, J. *Nano Energy* **2017**, *37*, 74-80.
- (15) Ma, Q.; Hu, C.; Liu, K.; Hung, S.-F.; Ou, D.; Chen, H. M.; Fu, G.; Zheng, N. *Nano Energy* **2017**, *41*, 148-153.

Chapter 4: Single-Crystal Nitrogen-Rich Two-Dimensional Mo_5N_6 Nanosheets for Efficient and Stable Seawater Splitting

4.1 Introduction and Significance

Transition metal nitrides (TMNs) have great potential for energy-related electrocatalytic processes because of their unique properties. However, it is difficult for TMN materials to achieve both high activity and stability under practical electrocatalytic conditions as they are susceptible to oxidative attack. To address this, a single-crystal nitrogen-rich 2D Mo_5N_6 nanosheet with Pt-like electronic structure and good corrosion resistance was developed. Such 2D nanosheets exhibit both better activity and stability for the hydrogen evolution reaction (HER) in various electrolytes compared to other nitrogen-deficient TMNs. Significantly, the 2D Mo_5N_6 can be directly used as a HER catalyst in seawater, and its performance in seawater is superior to commercial Pt/C. Confirmed by synchrotron-based spectroscopy and theoretical calculations, the excellent properties of 2D Mo_5N_6 originate from its appropriate electronic structure and the high valence state of its Mo atoms. The highlights of this Chapter include:

- Nitrogen-rich 2D Mo_5N_6 single crystal nanosheets are synthesized using a simple synthetic scheme.
- Synchrotron-based spectroscopy and density of state calculations are used to comprehensively understand the unique electronic structure and activity origin of the nitrogen-rich 2D Mo_5N_6 nanosheets.
- The nitrogen-rich 2D Mo_5N_6 shows enhanced HER performance compared to other nitrogen deficient TMNs in a wide range of electrolytes because its d band centre position is close to that of Pt.
- Nitrogen-rich 2D Mo_5N_6 shows superior HER performance in seawater, which is higher than the Pt benchmark due to its resistance to corrosion and active site poisoning.

- The 2D Mo₅N₆ nanosheets combine good activity and stability simultaneously, demonstrating the successful application of 2D nitrogen-rich TMNs for electrocatalytic processes in harsh electrocatalytic environments.

4.2 Single-Crystal Nitrogen-Rich Two-Dimensional Mo₅N₆ Nanosheets for Efficient and Stable Seawater Splitting

This Chapter is included as it appears as a journal paper published by **Huanyu Jin**, Xin Liu, Anthony Vasileff, Yan Jiao , Yongqiang Zhao, Yao Zheng, Shi-Zhang Qiao Single-Crystal Nitrogen-Rich Two-Dimensional Mo₅N₆ Nanosheets for Efficient and Stable Seawater Splitting. *ACS Nano* 2018, 12, 12761–12769.

Statement of Authorship

Title of Paper	Single-Crystal Nitrogen-Rich Two-Dimensional Mo ₅ N ₆ Nanosheets for Efficient and Stable Seawater Splitting
Publication Status	<input checked="" type="checkbox"/> Published <input type="checkbox"/> Accepted for Publication <input type="checkbox"/> Submitted for Publication <input type="checkbox"/> Unpublished and Unsubmitted work written in manuscript style
Publication Details	Huanyu Jin, Xin Liu, Anthony Vasileff, Yan Jiao, Yongqiang Zhao, Yao Zheng,* Shi-Zhang Qiao* Single-Crystal Nitrogen-Rich Two-Dimensional Mo ₅ N ₆ Nanosheets for Efficient and Stable Seawater Splitting. ACS Nano 2018, 12, 12761–12769.

Principal Author

Name of Principal Author (Candidate)	Huanyu Jin		
Contribution to the Paper	Research plan, material synthesis, most of the characterizations and data analysis, electrochemical characterization, and manuscript draft.		
Overall percentage (%)	90		
Certification:	This paper reports on original research I conducted during the period of my Higher Degree by Research candidature and is not subject to any obligations or contractual agreements with a third party that would constrain its inclusion in this thesis. I am the primary author of this paper.		
Signature		Date	22/June/2020

Co-Author Contributions

By signing the Statement of Authorship, each author certifies that:

- the candidate's stated contribution to the publication is accurate (as detailed above);
- permission is granted for the candidate to include the publication in the thesis; and
- the sum of all co-author contributions is equal to 100% less the candidate's stated contribution.

Name of Co-Author	Xin Liu		
Contribution to the Paper	Computational calculations.		
Signature		Date	22/June/2020

Name of Co-Author	Anthony Vasileff		
Contribution to the Paper	Editing process and manuscript revision.		
Signature		Date	22/June/2020

Name of Co-Author	Yan Jiao		
Contribution to the Paper	Discussion of computational calculations.		
Signature		Date	22/June/2020

Name of Co-Author	Yongqiang Zhao		
Contribution to the Paper	Assistance with electrochemical tests and data analysis.		
Signature		Date	22/June/2020

Name of Co-Author	Yao Zheng		
Contribution to the Paper	Supervision of the work, discussion of this manuscript and manuscript evaluation.		
Signature		Date	22/June/2020

Name of Co-Author	Shi-Zhang Qiao		
Contribution to the Paper	Supervision of the work, discussion of this manuscript and manuscript evaluation.		
Signature		Date	22/June/2020

Please cut and paste additional co-author panels here as required.

Single-Crystal Nitrogen-Rich Two-Dimensional Mo_5N_6 Nanosheets for Efficient and Stable Seawater Splitting

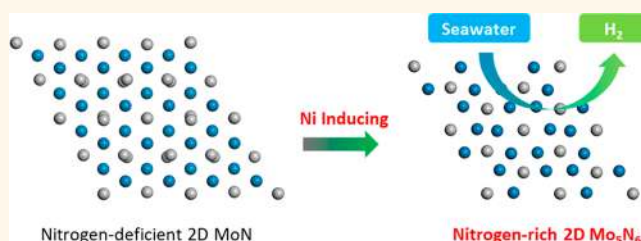
Huanyu Jin, Xin Liu, Anthony Vasileff, Yan Jiao,^{1b} Yongqiang Zhao, Yao Zheng,^{1b} and Shi-Zhang Qiao^{1b}

School of Chemical Engineering, The University of Adelaide, Adelaide, SA 5005, Australia

S Supporting Information

ABSTRACT: Transition metal nitrides (TMNs) have great potential for energy-related electrocatalysis because of their inherent electronic properties. However, incorporating nitrogen into a transition metal lattice is thermodynamically unfavorable, and therefore most of the developed TMNs are deficient in nitrogen. Consequently, these TMNs exhibit poor structural stability and unsatisfactory performance for electrocatalytic applications. In this work, we design and synthesize an atomically thin nitrogen-rich nanosheets, Mo_5N_6 , with the help of a Ni-inducing growth method. The as-prepared single-crystal electrocatalyst with abundant metal–nitrogen electroactive sites displays outstanding activity for the hydrogen evolution reaction (HER) in a wide range of electrolytes (pH 0–14). Further, the two-dimensional Mo_5N_6 nanosheets exhibit high HER activity and stability in natural seawater that are superior to other TMNs and even the Pt benchmark. By combining synchrotron-based spectroscopy and the calculations of electron density of state, we find that the enhanced properties of these nitrogen-rich Mo_5N_6 nanosheets originates from its Pt-like electronic structure and the high valence state of its Mo atoms.

KEYWORDS: 2D materials, nitrogen-rich, metal nitrides, hydrogen evolution, seawater splitting



Hydrogen is a promising energy carrier for clean energy systems because it has a high energy density and can be produced using renewable energy.^{1–3} To produce high-purity hydrogen, water electrolysis is superior to current methods, such as natural gas reforming or coal gasification, which require extensive processing and energy.^{4–6} Seawater is the most abundant water source and natural electrolyte on the earth, which makes it very suitable for low-cost and large-scale hydrogen production.⁷ However, compared to the hydrogen evolution reaction (HER) in acid or alkaline media, electrocatalytic HER in natural seawater is extremely challenging due to its intrinsic low conductivity, ion poisoning, and high corrosivity.^{7–9} For example, Pt exhibits outstanding HER performance in conventional water electrolysis systems but poor performance in seawater conditions due to the poisoning effects from a range of undesirable anions.

Recently, transition metal nitrides (TMNs) have emerged as promising electrocatalyst materials for various electrocatalytic processes (e.g., HER, oxygen evolution reaction, oxygen reduction reaction, and so forth).^{5,10–14} Because of their inherent electronic structure and good electrical conductivity, TMNs could potentially replace noble metal catalysts for water splitting.^{13,15–17} However, most TMNs are vulnerable to oxidation during electrocatalytic processes due to the low

valence state of the metal atoms.¹⁷ This causes them to be relatively unstable. Given this, nitrogen-rich TMNs (N/metal >1) are preferable for electrocatalysis because of the higher valence state of the metal atoms leading to their better corrosion resistance.^{17–19} However, incorporating nitrogen atoms into the crystalline lattices of transition metals is thermodynamically unfavorable, and they tend to diffuse out of the metal lattice.^{16–18} Therefore, most of the TMNs reported have low nitrogen content with molar ratios of N/metal less than unity (e.g., Ni_3N , Cu_3N , Co_4N , Mo_2N , and so forth).^{17,20}

For various energy related applications, two-dimensional (2D) TMNs have superior performance to their bulk counterpart due to their uniform crystal lattice and tunable electronic structure.^{21–25} Hence, synthesis of nitrogen-rich 2D TMNs with uniform exposure of specific facets would be key to optimizing these electrocatalysts for high performance applications.^{17,26,27} However, the development of nitrogen-rich 2D TMNs is limited by the harsh synthetic conditions required and the inability to control their morphologies well. Recently, Yu et al. realized the synthesis of the nitrogen-rich W_2N_3 under

Received: October 14, 2018

Accepted: November 29, 2018

Published: November 29, 2018

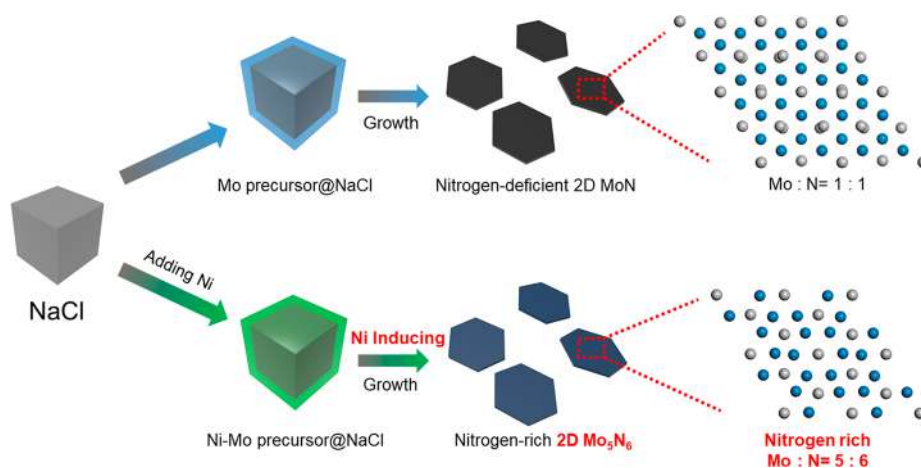


Figure 1. Schematic illustration of the synthesis of MoN and Mo₅N₆ nanosheets through an ammonization synthesis with and without the addition of Ni in the precursor.

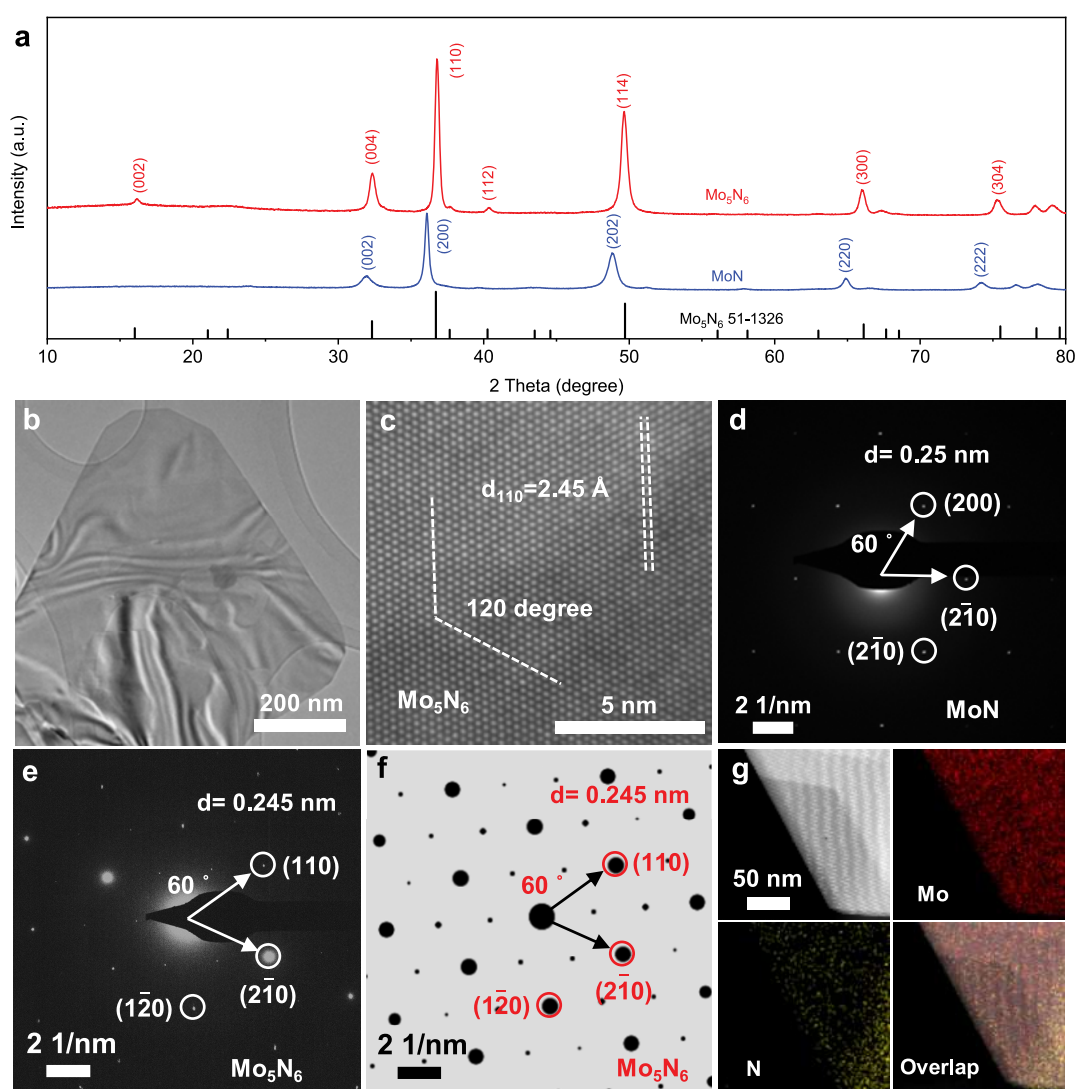


Figure 2. Characterization of Mo₅N₆ and MoN. (a) XRD pattern, (b) low-resolution TEM image, (c) high-resolution STEM image of Mo₅N₆, (d) SAED pattern of MoN, (e,f) SAED patterns and (g) elemental mapping of Mo₅N₆.

atmospheric pressure using salt template method, which would otherwise require higher pressures.²⁸ In the meantime, researchers found that the first row transition metals (e.g.,

Fe, Co and Ni) can induce the transformation of β -WN to anomalous δ -WN under atmospheric pressure.¹¹ In these cases, the transition metal component and salt crystal serve as

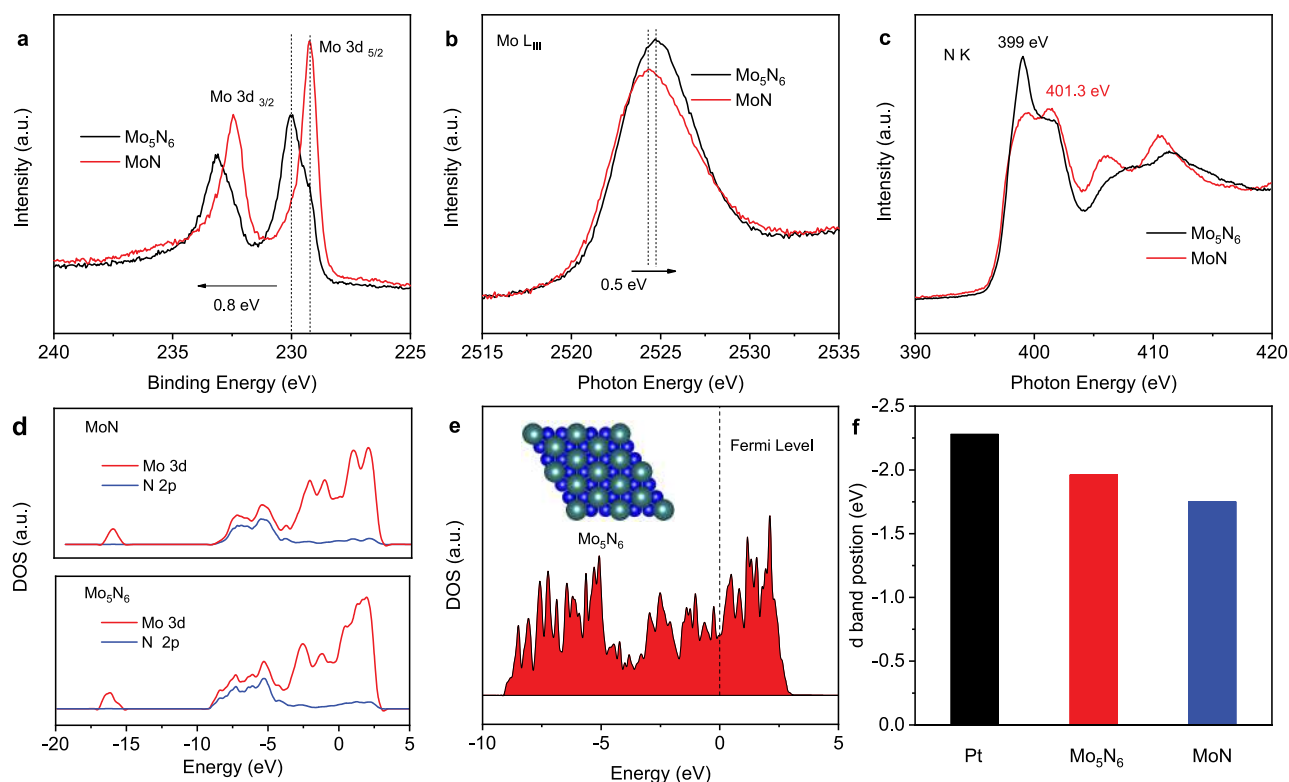


Figure 3. (a) Mo 3d XPS spectra of MoN and Mo₅N₆. (b) Mo L_{III} edge of MoN and Mo₅N₆. (c) N K edge of MoN and Mo₅N₆. (d) DOS of Mo 3d and N 2p orbitals for MoN and Mo₅N₆. (e) DOS of Mo₅N₆. (f) d band center position of Pt (111), Mo₅N₆ and MoN, respectively.

the catalyst and template which induce the formation of anomalous metal nitrides. We speculate the same concept is likely suitable for the synthesis of nitrogen-rich TMNs under mild conditions.

In this work, we apply this transition metal-catalyzed phase transformation method with 2D lateral growth methods to synthesize the atomically thin Mo₅N₆ nanosheets. With rich metal-nitrogen bonding, the as-prepared 2D Mo₅N₆ nanosheets show enhanced HER activity compared to conventional nitrogen-deficient TMNs in various electrolytes (pH 0–14). More significantly, Mo₅N₆ exhibits an outstanding HER performance in natural seawater with a highly stable catalytic current over 100 h, which is much better than Pt/C benchmark and other TMNs counterparts. Synchrotron-based X-ray absorption near edge structure (XANES) and the calculations of electron DOS confirm that the high activity of Mo₅N₆ originates from its Pt-like electronic structure, and its stability derives from the high valence state of its Mo atoms which make it relatively unsusceptible to active site poisoning from deleterious seawater ions.

RESULTS AND DISCUSSION

The 2D Mo₅N₆ nanosheets were prepared by a Ni-induced salt-templated method, which is schematically shown in Figure 1.^{21,28–30} First, nickel acetate and MoO(OH)_x were used as precursors, and the former was reduced to Ni metal by ammonia gas at high temperature (Figure S1a). The Ni metal was then removed by an acid wash which yielded pure phase Mo₅N₆ (Figure S1). It should be noted that without the addition of Ni salt, the final product obtained was regular MoN. From Figure S1b, the O 1s peak is observed which we attributed to oxygen termination on the Mo₅N₆ surface.

Through a comparison of the X-ray diffraction (XRD) patterns, the synthesized Mo₅N₆ possesses the different peak position with that of MoN (Figure 2a), indicating that the extra (20%) nitrogen-incorporation can greatly change the crystal structure of conventional MoN. The 2D morphology of the Mo₅N₆ nanosheets were observed under scanning electron microscope (SEM) and transmission electron microscopy (TEM) imaging, which showed that the nanosheets are transparent and wrinkled (Figure 2b, Figure S2). Furthermore, the Mo₅N₆ nanosheet is only 3 nm thick, demonstrating its atomically thin 2D structure with uniformly exposed lattice and large surface area (Figure S3).

The crystal structure parameters of Mo₅N₆ were determined using aberration-corrected scanning TEM imaging and corresponding selected area electron diffraction (SAED). The scanning TEM image (Figure 2c) shows the hexagonal structure of Mo₅N₆ with an interplanar distance of 2.45 Å for (110) facets, which is smaller than that of 2.5 Å for the (200) facets of MoN (Figure S4). This demonstrates the more compact hexagonal structure of Mo₅N₆ compared to MoN. Moreover, one set of diffraction spots in the SAED image of Mo₅N₆ reveals its single crystalline nature (Figure 2e). We also determine the (110) lattice plane spacing of Mo₅N₆ to be 0.245 nm, consisting with the result of XRD and high-resolution TEM. For MoN, the (200) lattice plane spacing is 0.25 nm, which is larger than that of Mo₅N₆ (Figure 2d), further indicating the different crystal structure of MoN and Mo₅N₆ (Figure 2f). The interplanar angle and distance of the experimental and simulated SAED patterns of Mo₅N₆ (Figure 2f) also match well with one another, demonstrating the pure phase of the Mo₅N₆. Energy dispersive spectroscopy (EDS) mapping clearly shows the spatial distribution of Mo and N

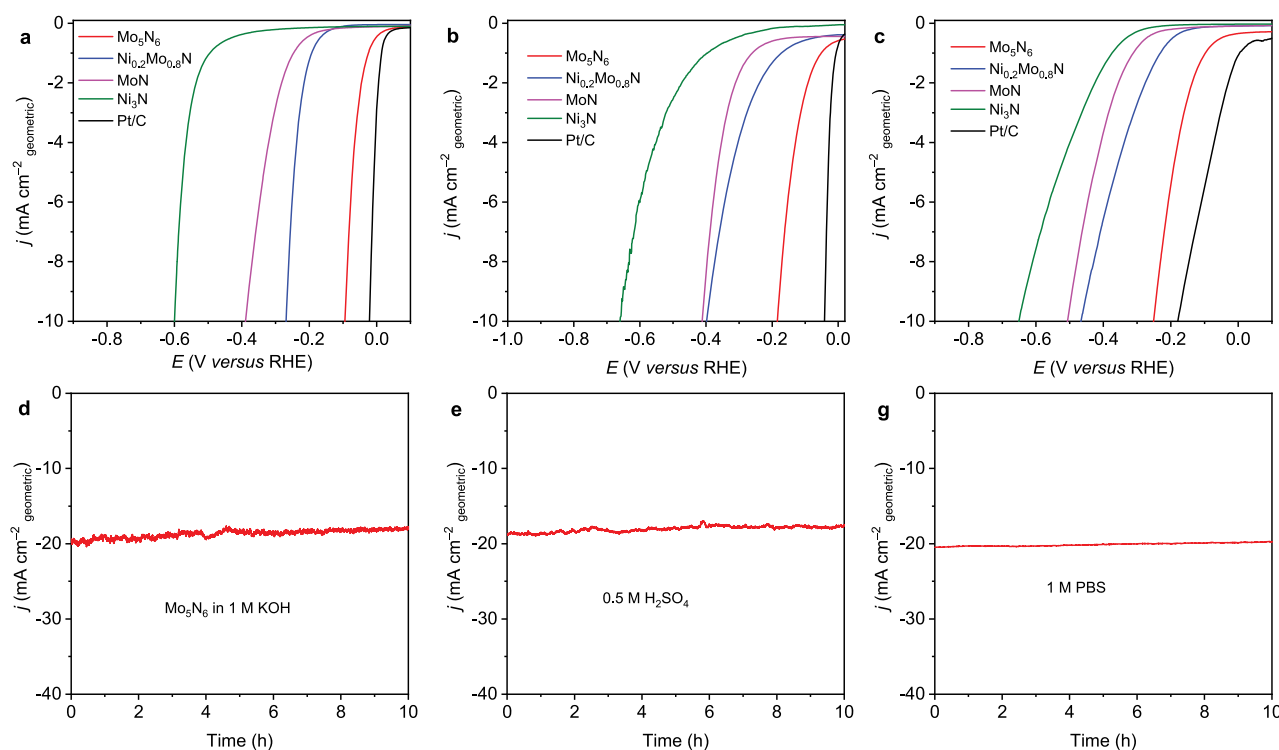


Figure 4. Electrochemical performance of Mo₅N₆ and other catalysts in different electrolytes: (a–c) LSV curves of Mo₅N₆, MoN, Ni_{0.2}Mo_{0.8}N, Ni₃N, and commercial Pt/C electrodes measured in Ar-saturated 1 M KOH, 0.5 M H₂SO₄, and 1 M PBS, respectively. (d–f) Chronoamperometric results of Mo₅N₆ in different electrolytes. The applied potentials for d–f are 130, 230, and 330 mV, respectively.

atoms on the hexagonal corner area and the uniform composition of the synthesized Mo₅N₆ nanosheets (Figure 2g).

We conducted a range of spectroscopic measurements and theoretical calculations to evaluate the electronic structure of Mo₅N₆ at the atomic level, and more importantly, its difference with conventional MoN. As shown in the high-resolution Mo 3d XPS spectra (Figure 3a), the dominant valence state of Mo in Mo₅N₆ is 4+ (binding energy of 230.0 eV), which is higher than that of MoN (+3, binding energy of 229.3 eV). The higher valence state of Mo in Mo₅N₆ is likely due to the greater number of nitrogen atoms in the crystal lattice leading to an increased electron redistribution from Mo to N atoms. The Mo L_{III}-edge XANES spectrum also confirms the higher oxidation state of the Mo cation in Mo₅N₆ than that of MoN (Figure 3b), by identifying a positive energy shift of 0.5 eV. Importantly, according to previous study, Mo (4+) species can facilitate OH* intermediate adsorption during water dissociation, which is critical for HER performance in alkaline media.^{30,31} Other than valence state, periodic Mo vacancies are observed in the molecular structure of Mo₅N₆ (Figure S5), which inevitably changes the metal-nitrogen bonding in the supercell and consequently leads to a different electronic structure. Experimentally, the N K-edge XANES of MoN and Mo₅N₆ are characterized by two sharp resonances at lower energy (399.0 and 401.3 eV) and two broad features at higher energy (405–415 eV). The former two peaks can be assigned to the transitions of N 1s electrons to the p–d(t_{2g}) and p–d(e_g) hybridized orbitals, respectively. The latter two peaks can be assigned to the transition of N 1s electrons to an orbital that involves contributions from 2p and 3p orbitals of nitrogen and the d and s states of Mo.^{32,33} As shown in Figure 3c, the relative peak intensity of Mo₅N₆ at 399.0 eV is stronger than

the peak at 401.3 eV, indicating that more N 1s electrons transfer to the p–d(t_{2g}) orbital compared to in MoN, and further confirming that there are extra N atoms in the Mo metal lattice.

In order to obtain an in-depth understanding of the changes at the atomic level, the electronic structures of MoN and Mo₅N₆ for Mo 3d and N 2p orbitals were analyzed by DOS calculations (Figure 3d). It can be seen that the different N content greatly affects the electronic environment of Mo–N bonding with more complicated electron orbital hybridization in Mo₅N₆, which is in accordance with the experimental XANES data shown in Figure 3c. Figure 3e shows the total DOS of Mo₅N₆ with a continuous distribution near the Fermi level, indicating its metallic character. It should be noted that the electron hybridization of MoN and Mo₅N₆ are quite different, which may change their d band positions and catalytic performances. For example, the calculated d band center position for Mo₅N₆ is located at –1.96 eV, which is closer to the d band center of Pt (–2.28 eV) compared to MoN (–1.75 eV), indicating an electronic structure more like Pt (Figure S6). It should be noted that the d band center and hydrogen binding energy of electrocatalysts exhibit a linear relationship.³⁴ Consequently, the inherent electronic structure of Mo₅N₆ and the high valence state of its Mo atoms is potentially favorable for high catalytic activity and good stability, respectively.

The electrocatalytic HER performance of Mo₅N₆ was studied in a range of electrolytes (pH 0–14). Figure 4a shows the linear sweep voltammetry (LSV) curves of different catalysts in 1 M KOH. The Mo₅N₆ shows an overpotential of 94 mV at a current density of 10 mA cm⁻², which is significantly lower than that for MoN (389 mV) and close to commercial Pt/C catalysts (21 mV; Figure S7). Furthermore,

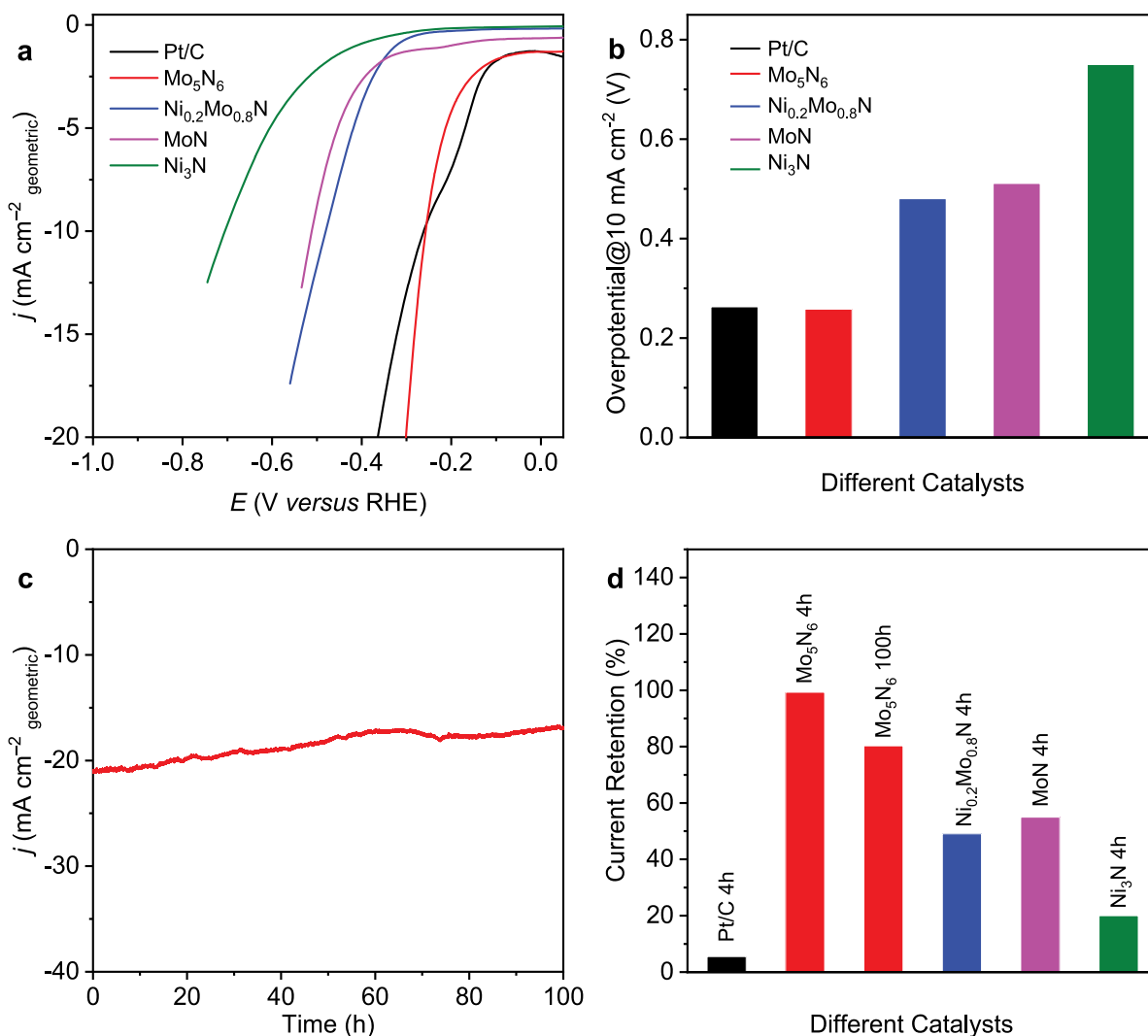


Figure 5. (a) LSV curves of different catalysts measured in Ar-saturated natural seawater. (b) Comparison of overpotentials of Mo₃N₆ with other catalysts at a current density of 10 mA cm⁻². (c) Chronoamperometric curve of Mo₃N₆ over 100 h operation. The applied potential is 310 mV. (d) Comparison of catalytic current retention of Mo₃N₆ with other TMNs and Pt/C in seawater conditions.

we also compared the performance of Mo₃N₆ with other TMN catalysts which are relatively deficient in nitrogen contents. Clearly, the HER performance of Mo₃N₆ is superior than Ni_{0.2}Mo_{0.8}N and Ni₃N individually (Figure S8). Also, Mo₃N₆ shows a Tafel slope of 66 mV dec⁻¹, indicating the sluggish water dissociation is not the rate-determining step in overall HER process. This is also different from other TMNs that have Tafel slopes of ~120 mV dec⁻¹.

Other than in alkaline media, the HER performance of these catalysts was also evaluated in acidic and neutral electrolytes (Figure 4b,c). Similarly, Mo₃N₆ showed the best performance compared to the other TMN catalysts, exhibiting the lowest overpotential in these electrolytes. This pH universal activity enhancement can be attributed to the nitrogen enrichment which altered the d band center position closer to that of Pt and increased the valence state of Mo for optimized water dissociation kinetics. Importantly, Mo₃N₆ shows a smaller electrochemical double-layer capacitance (C_{dl}) than MoN, indicating that the enhanced performance of Mo₃N₆ does not derive from the surface area but from the optimized adsorption energy of key intermediates on the surface (Figures S9 and

S10). Regarding stability, chronoamperometry was carried out for 10 h at a constant overpotential in different electrolytes (Figure 4d–f). Over 10 h, the current response of Mo₃N₆ remained almost unchanged under each operating condition, indicating its very stable performance over a wide range of pH.

On the basis of the above observations, Mo₃N₆ is a highly efficient Pt-like electrocatalyst in alkaline, acid, and neutral electrolytes. Additionally, the nitrogen-rich Mo₃N₆ has high corrosion resistance due to the high valence state of its Mo atoms, making it a promising candidate for natural seawater electrolysis. As expected, Mo₃N₆ exhibited good HER performance in natural seawater, requiring an overpotential of 257 mV to produce 10 mA cm⁻² of catalytic current density. This was lower than that of Pt/C and other nitrogen-deficient TMNs (Figure 5a,b). Further, the j_{10} overpotential (overpotential at current density of 10 mA cm⁻²) on Mo₃N₆ was also lower than most of the non-noble metal catalysts reported for natural seawater HER in the literature (Table S1).^{7,35,36} More importantly, the hydrogen production of Mo₃N₆ in natural seawater was extremely stable for 100 h at an overpotential of 300 mV (Figure 5c). In comparison, the

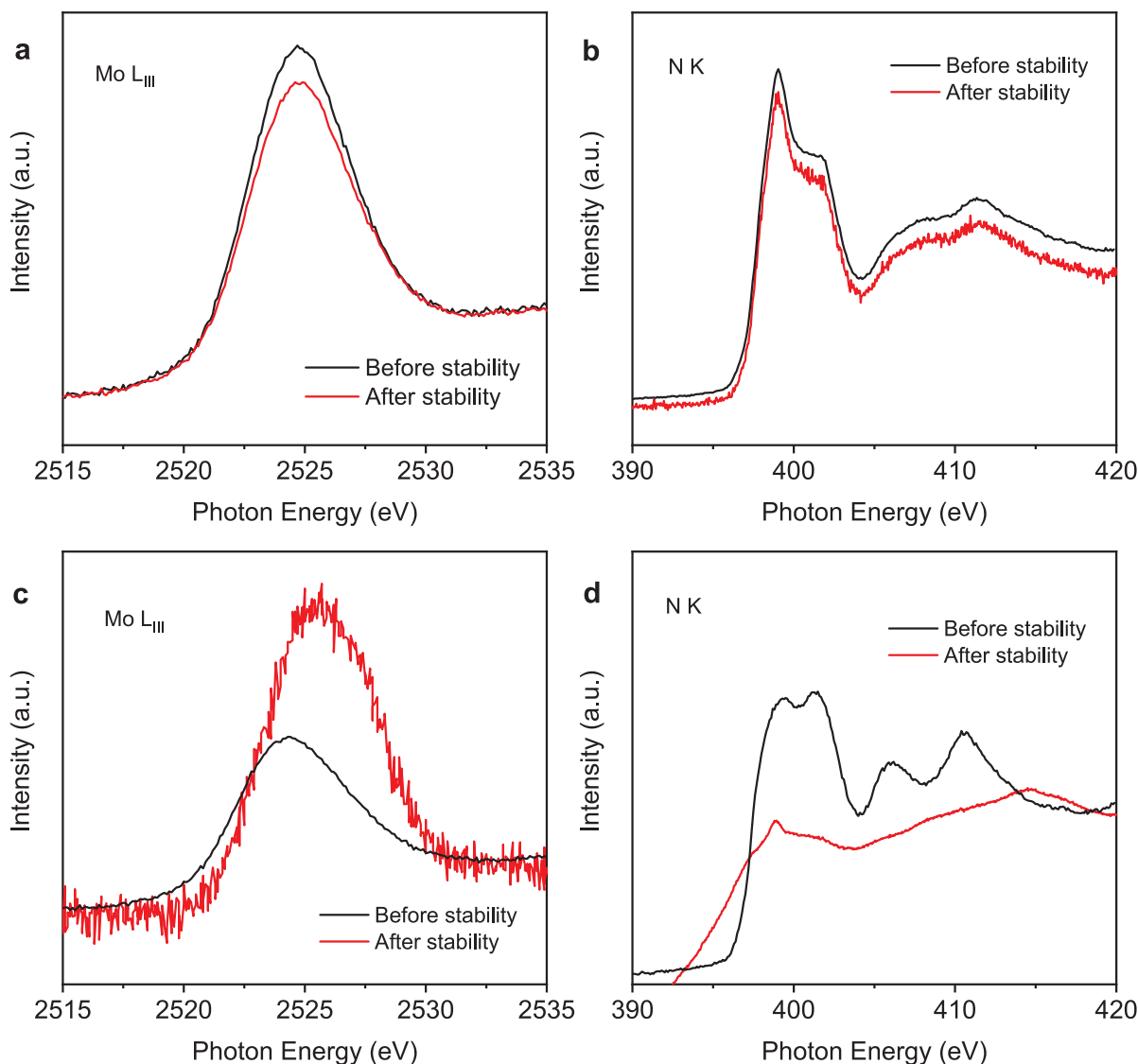


Figure 6. (a,c) Mo L_{III} edge of Mo₅N₆ and MoN before and after stability testing in natural seawater. (b,d) N K edge of Mo₅N₆ and MoN before and after stability testing in natural seawater.

stability of Pt/C was very poor, retaining only 5.5% of its catalytic current density after only 4 h of continuous operation (Figure 5d). This poor stability is likely attributed to the poisoning from ions in seawater which block the active sites for hydrogen evolution, as has been detailed in other works.^{36,37} In addition, Figures 5d and S11 also compare the stability of Mo₅N₆ with other related TMNs. As expected, Mo₅N₆ exhibited high stability with a catalytic current retention of 99.3% after 4 h, which was higher than MoN (55.0% for 4 h), Ni_{0.2}Mo_{0.8}N (49.1% for 4 h), and Ni₃N (20.0% for 4 h), respectively.

To probe the origin of the high stability of Mo₅N₆ in seawater, XRD and XANES of the samples before and after stability testing were carried out. As shown in Figure 6a,b, there was negligible shift for the Mo L_{III} and N K edge of Mo₅N₆ before and after the 100 h stability test in natural seawater, confirming its good resistance to corrosion and poisoning of active sites. From the XRD spectra (Figure S12), it is clear that the crystal structure of Mo₅N₆ was also stable throughout stability testing. In comparison, the structures of

MoN, Ni_{0.2}Mo_{0.8}N, and Ni₃N were significantly less stable as evidenced from Figures 6c,d and S13. A positive shift in their XANES spectra indicates that the Mo and Ni valence states of the other TMNs increased. This was likely due to the low valence state of the metal atoms and poor metal–nitrogen bonding making them susceptible to corrosion from the seawater. Furthermore, the significantly different N K-edge XANES spectra of the nitrogen-deficient TMNs indicates disrupted metal–nitrogen bonding. As a result, Mo₅N₆ nanosheets combines the advantages of Pt-like electronic structure and excellent corrosion resistance, resulting ultra-stable performance for hydrogen evolution from seawater.

CONCLUSION

In summary, synthesis of 2D nitrogen-rich Mo₅N₆ nanosheets was successfully achieved using a simple Ni-induced salt-template method. The additional nitrogen atoms incorporated in the Mo₅N₆ lattice greatly changed its inherent properties, leading to a higher Mo valence state and Pt-like electronic structure. As expected, the Mo₅N₆ nanosheet exhibited

excellent HER performance in various electrolytes, especially in seawater. For seawater HER, its performance was significantly better than other nitrogen-deficient TMNs and the Pt/C benchmark. The Mo₃N₆ catalyst combines high activity and good stability simultaneously, demonstrating the possibility of using 2D nitrogen-rich TMNs for electrocatalytic processes in harsh electrocatalytic environments.

METHODS

Synthesis of 2D Mo₃N₆ Nanosheets. The 2D Mo₃N₆ nanosheets were synthesized through a Ni-induced salt-templated method: 0.4 g of Mo powder was dispersed in 40 mL of ethanol with magnetic stirring for 10 min. Then, 1.2 mL of H₂O₂ (30%) solution was injected dropwise into the suspension. After stirring for 12 h at room temperature, the solution turned into a dark blue color. Separately, 10 mg of Ni(OCOCH₃)₂·4H₂O was dissolved in 10 mL of ethanol and mixed with the dark blue suspension to form the precursor. The precursor solution was then mixed with 640 g of NaCl powder and dried at 50 °C with continuous hand stirring. After that, the mixture was annealed at 750 °C for 5 h at a heating rate of 1 °C min⁻¹ under a 5% NH₃/Ar atmosphere. Finally, the product was washed with deionized water and dilute hydrochloric acid several times to remove the NaCl template and Ni nanoparticles before being dried using vacuum filtration.

Synthesis of 2D MoN Nanosheets. The 2D MoN nanosheets were synthesized without the addition of Ni. The Mo precursor was mixed with 640 g of NaCl and annealed at 750 °C for 5 h. The final product was obtained by removing NaCl using deionized water and vacuum filtration.

Synthesis of Ni_{0.2}Mo_{0.8}N. Ni_{0.2}Mo_{0.8}N was synthesized by adding 0.26 g of Ni(OCOCH₃)₂·4H₂O into the Mo precursor and directly annealing the mixture without the salt-template at 550 °C at a heating rate of 3 °C min⁻¹ for 2 h.

Synthesis of Ni₃N. First, Ni(OH)₂ nanosheets were synthesized using a reported method.¹⁴ In a typical procedure, 630 mg of hexamethylenetetramine was dissolved in 100 mL of deionized water and purged with N₂ gas. Then, 120 mg of NiCl₂·6H₂O was added to the solution. The reactants were heated under reflux temperature for 12 h with continuous N₂ flow. Light green products were collected from the flask, washed with water and ethanol several times, and freeze-dried for the following steps. Ni₃N was then prepared by annealing Ni(OH)₂ at 390 °C for 2 h at a heating rate of 3 °C min⁻¹ under a 5% NH₃/Ar atmosphere.

Characterization. XRD data was collected on a Rigaku MiniFlex 600 X-ray diffractometer. The field-emission scanning electron microscope images were acquired on a FEI Quanta 450 FEG scanning electron microscope. The transmission electron microscope images, aberration-corrected TEM images, high-angle annular dark-field imaging, and EDS data were taken on a FEI Titan Themis 80-200 operating at 200 kV. Atomic force microscopy (AFM, Shimadzu) was used to explore the morphology and thickness of the samples.

The synchrotron-based XPS and XANES measurements were carried out on the soft X-ray spectroscopy beamline at the Australian Synchrotron, which is equipped with a hemispherical electron analyzer and a microchannel plate detector that enables simultaneous recording of the total electron yield and partial electron yield. The raw XANES and XPS data were normalized to the photoelectron current of the photon beam, measured on an Au grid.

Computational Details. Density functional theory calculations were performed using the Vienna *Ab Initio* Simulation Package (VASP).^{38–41} The exchange-correlation interactions were treated within the generalized gradient approximation (GGA) in the form of the Perdew–Burke–Ernzerhof functional.⁴² The van der Waals interactions were described using the empirical correction in Grimme's scheme.⁴³ The electron wave functions were expanded using plane waves with a cutoff energy of 400 eV, and the convergence criteria of energy change during all calculations were set to 10⁻⁵ eV. The *k*-points were set to be 11 × 11 × 1 for single cells of Mo₃N₆, MoN, and Pt(111) in density of states calculations. The convergence

tolerance of force on each atom during full structure relaxation was set to be 0.01 eV/Å. To avoid interactions between periodic images, a vacuum space of 20 Å was applied to all calculations.

Electrochemical Measurements. Typically, 4 mg of catalyst (e.g., 2D Mo₃N₆) was dispersed in 800 μL of deionized water. Then 200 μL of 1 wt % of Nafion/water were added to the catalyst dispersion. Because all of the catalysts are electrically conductive, carbon black was not added. Next, 20 μL of catalyst dispersion (4 mg mL⁻¹) was transferred onto a 5 mm glassy carbon rotating disk electrode (0.4 mg cm⁻²) serving as the working electrode. The reference electrode was Ag/AgCl in 4 M AgCl–KCl solution and the counter electrode was a graphite rod. All potentials were referenced to the reversible hydrogen electrode by adding (0.205 + 0.059 × pH) and all polarization curves were corrected for the *i*R compensation within the cell. A flow of Ar was maintained over the electrolyte during the experiment to eliminate dissolved oxygen. The working electrode was rotated at 1,600 rpm to remove the hydrogen gas which formed on the catalyst surface. The seawater used in this study was collected from Henley Beach (Adelaide, Australia) with a pH value of ~8.4.

ASSOCIATED CONTENT

Supporting Information

The Supporting Information is available free of charge on the ACS Publications website at DOI: 10.1021/acsnano.8b07841.

Additional figures, table, and references (PDF)

AUTHOR INFORMATION

Corresponding Authors

*E-mail: yao.zheng01@adelaide.edu.au

*E-mail: s.qiao@adelaide.edu.au

ORCID

Yan Jiao: 0000-0003-1329-4290

Yao Zheng: 0000-0002-2411-8041

Shi-Zhang Qiao: 0000-0002-4568-8422

Notes

The authors declare no competing financial interest.

ACKNOWLEDGMENTS

This work is financially supported by the Australian Research Council (DP170104464, DP160104866, DE160101163, and FL170100154). We acknowledge Adelaide Microscopy at The University of Adelaide, an AMMRF facility for the microscopy and microanalysis services. We acknowledge the support of ANSTO in providing the XANES and XRD data, which were undertaken on the Soft X-ray Spectroscopy beamline and Powder Diffraction beamline.

REFERENCES

- (1) Seh, Z. W.; Kibsgaard, J.; Dickens, C. F.; Chorkendorff, I.; Nørskov, J. K.; Jaramillo, T. F. Combining Theory and Experiment in Electrocatalysis: Insights into Materials Design. *Science* **2017**, *355*, No. eaad4998.
- (2) Gasteiger, H. A.; Marković, N. M. Just a Dream—or Future Reality? *Science* **2009**, *324*, 48–49.
- (3) Jin, H.; Guo, C.; Liu, X.; Liu, J.; Vasileff, A.; Jiao, Y.; Zheng, Y.; Qiao, S.-Z. Emerging Two-Dimensional Nanomaterials for Electrocatalysis. *Chem. Rev.* **2018**, *118*, 6337–6408.
- (4) Hu, C.; Ma, Q.; Hung, S.-F.; Chen, Z.-N.; Ou, D.; Ren, B.; Chen, H. M.; Fu, G.; Zheng, N. *In Situ* Electrochemical Production of Ultrathin Nickel Nanosheets for Hydrogen Evolution Electrocatalysis. *Chem.* **2017**, *3*, 122–133.
- (5) Chen, Z.; Song, Y.; Cai, J.; Zheng, X.; Han, D.; Wu, Y.; Zang, Y.; Niu, S.; Liu, Y.; Zhu, J.; Liu, X.; Wang, G. Tailoring the d-Band

Centers Enables Co₄N Nanosheets to Be Highly Active for Hydrogen Evolution Catalysis. *Angew. Chem.* **2018**, *130*, 5170–5174.

(6) Zhang, J.; Wang, T.; Pohl, D.; Rellinghaus, B.; Dong, R.; Liu, S.; Zhuang, X.; Feng, X. Interface Engineering of MoS₂/Ni₃S₂ Heterostructures for Highly Enhanced Electrochemical Overall-Water-Splitting Activity. *Angew. Chem.* **2016**, *128*, 6814–6819.

(7) Lu, X.; Pan, J.; Lovell, E.; Tan, T. H.; Ng, Y. H.; Amal, R. A Sea-Change: Manganese Doped Nickel/Nickel Oxide Electrocatalysts for Hydrogen Generation from Seawater. *Energy Environ. Sci.* **2018**, *11*, 1898.

(8) Zhao, Y.; Jin, B.; Zheng, Y.; Jin, H.; Jiao, Y.; Qiao, S.-Z. Charge State Manipulation of Cobalt Selenide Catalyst for Overall Seawater Electrolysis. *Adv. Energy Mater.* **2018**, *8*, 1801926.

(9) Bennett, J. E. Electrodes for Generation of Hydrogen and Oxygen from Seawater. *Int. J. Hydrogen Energy* **1980**, *5*, 401–408.

(10) Wang, Y.; Chen, L.; Yu, X.; Wang, Y.; Zheng, G. Superb Alkaline Hydrogen Evolution and Simultaneous Electricity Generation by Pt-Decorated Ni₃N Nanosheets. *Adv. Energy Mater.* **2017**, *7*, 1601390.

(11) Jin, H.; Zhang, H.; Chen, J.; Mao, S.; Jiang, Z.; Wang, Y. A General Synthetic Approach for Hexagonal Phase Tungsten Nitride Composites and Their Application in the Hydrogen Evolution Reaction. *J. Mater. Chem. A* **2018**, *6*, 10967–10975.

(12) Xiong, J.; Cai, W.; Shi, W.; Zhang, X.; Li, J.; Yang, Z.; Feng, L.; Cheng, H. Salt-Templated Synthesis of Defect-Rich MoN Nanosheets for Boosted Hydrogen Evolution Reaction. *J. Mater. Chem. A* **2017**, *5*, 24193–24198.

(13) Xie, J.; Li, S.; Zhang, X.; Zhang, J.; Wang, R.; Zhang, H.; Pan, B.; Xie, Y. Atomically-Thin Molybdenum Nitride Nanosheets with Exposed Active Surface Sites for Efficient Hydrogen Evolution. *Chem. Sci.* **2014**, *5*, 4615–4620.

(14) Xu, K.; Chen, P.; Li, X.; Tong, Y.; Ding, H.; Wu, X.; Chu, W.; Peng, Z.; Wu, C.; Xie, Y. Metallic Nickel Nitride Nanosheets Realizing Enhanced Electrochemical Water Oxidation. *J. Am. Chem. Soc.* **2015**, *137*, 4119–4125.

(15) Xie, J.; Xie, Y. Transition Metal Nitrides for Electrocatalytic Energy Conversion: Opportunities and Challenges. *Chem. - Eur. J.* **2016**, *22*, 3588–3598.

(16) Chen, J. G. Carbide and Nitride Overlayers on Early Transition Metal Surfaces: Preparation, Characterization, and Reactivities. *Chem. Rev.* **1996**, *96*, 1477–1498.

(17) Wang, S.; Ge, H.; Sun, S.; Zhang, J.; Liu, F.; Wen, X.; Yu, X.; Wang, L.; Zhang, Y.; Xu, H.; Neufeind, J. C.; Qin, Z.; Chen, C.; Jin, C.; Li, Y.; He, D.; Zhao, Y. A New Molybdenum Nitride Catalyst with Rhombohedral MoS₂ Structure for Hydrogenation Applications. *J. Am. Chem. Soc.* **2015**, *137*, 4815–4822.

(18) Salamat, A.; Hector, A. L.; Kroll, P.; McMillan, P. F. Nitrogen-Rich Transition Metal Nitrides. *Coord. Chem. Rev.* **2013**, *257*, 2063–2072.

(19) Wang, S.; Yu, X.; Lin, Z.; Zhang, R.; He, D.; Qin, J.; Zhu, J.; Han, J.; Wang, L.; Mao, H.-k.; Zhang, J.; Zhao, Y. Synthesis, Crystal Structure, and Elastic Properties of Novel Tungsten Nitrides. *Chem. Mater.* **2012**, *24*, 3023–3028.

(20) Bykov, M.; Bykova, E.; Aprilis, G.; Glazyrin, K.; Koemets, E.; Chuvashova, I.; Kupenko, I.; McCammon, C.; Mezouar, M.; Prakupenka, V.; Liermann, H. P.; Tasnádi, F.; Ponomareva, A. V.; Abrikosov, I. A.; Dubrovinskaya, N.; Dubrovinsky, L. Fe-N System at High Pressure Reveals a Compound Featuring Polymeric Nitrogen Chains. *Nat. Commun.* **2018**, *9*, 2756.

(21) Xiao, X.; Yu, H.; Jin, H.; Wu, M.; Fang, Y.; Sun, J.; Hu, Z.; Li, T.; Wu, J.; Huang, L.; Gogotsi, Y.; Zhou, J. Salt-Templated Synthesis of 2D Metallic MoN and Other Nitrides. *ACS Nano* **2017**, *11*, 2180–2186.

(22) Anasori, B.; Lukatskaya, M. R.; Gogotsi, Y. 2D Metal Carbides and Nitrides (MXenes) for Energy Storage. *Nat. Rev. Mater.* **2017**, *2*, 16098.

(23) Jaramillo, T. F.; Jørgensen, K. P.; Bonde, J.; Nielsen, J. H.; Hørch, S.; Chorkendorff, I. Identification of Active Edge Sites for

Electrochemical H₂ Evolution from MoS₂ Nanocatalysts. *Science* **2007**, *317*, 100.

(24) Voiry, D.; Yamaguchi, H.; Li, J.; Silva, R.; Alves, D. C. B.; Fujita, T.; Chen, M.; Asefa, T.; Shenoy, V. B.; Eda, G.; Chhowalla, M. Enhanced Catalytic Activity in Strained Chemically Exfoliated WS₂ Nanosheets for Hydrogen Evolution. *Nat. Mater.* **2013**, *12*, 850–855.

(25) Yang, W.; Zhang, X.; Xie, Y. Advances and Challenges in Chemistry of Two-Dimensional Nanosheets. *Nano Today* **2016**, *11*, 793–816.

(26) Ganin, A. Y.; Kienle, L.; Vajenine, G. V. Synthesis and Characterisation of Hexagonal Molybdenum Nitrides. *J. Solid State Chem.* **2006**, *179*, 2339–2348.

(27) Sun, G.-D.; Zhang, G.-H.; Chou, K.-C. Synthesis of Molybdenum Nitrides Nanosheets by Nitriding 2H-MoS₂ with Ammonia. *J. Am. Ceram. Soc.* **2018**, *101*, 2796–2808.

(28) Yu, H.; Yang, X.; Xiao, X.; Chen, M.; Zhang, Q.; Huang, L.; Wu, J.; Li, T.; Chen, S.; Song, L.; Gu, L.; Xia, B. Y.; Feng, G.; Li, J.; Zhou, J. Atmospheric-Pressure Synthesis of 2D Nitrogen-Rich Tungsten Nitride. *Adv. Mater.* **2018**, 1805655.

(29) Xiao, X.; Song, H.; Lin, S.; Zhou, Y.; Zhan, X.; Hu, Z.; Zhang, Q.; Sun, J.; Yang, B.; Li, T.; Jiao, L.; Zhou, J.; Tang, J.; Gogotsi, Y. Scalable Salt-Templated Synthesis of Two-Dimensional Transition Metal Oxides. *Nat. Commun.* **2016**, *7*, 11296.

(30) Jin, H.; Liu, X.; Jiao, Y.; Vasileff, A.; Zheng, Y.; Qiao, S.-Z. Constructing Tunable Dual Active Sites on Two-Dimensional C₃N₄@MoN Hybrid for Electrocatalytic Hydrogen Evolution. *Nano Energy* **2018**, *53*, 690–697.

(31) Staszak-Jirkovsky, J.; Malliakas, C. D.; Lopes, P. P.; Danilovic, N.; Kota, S. S.; Chang, K. C.; Genorio, B.; Strmcnik, D.; Stamenkovic, V. R.; Kanatzidis, M. G.; Markovic, N. M. Design of Active and Stable Co-Mo-S_x Chalcogenides as pH-Universal Catalysts for the Hydrogen Evolution Reaction. *Nat. Mater.* **2016**, *15*, 197–203.

(32) Bennett, L. H.; Cuthill, J. R.; McAlister, A. J.; Erickson, N. E.; Watson, R. E. Electronic Structure and Catalytic Behavior of Tungsten Carbide. *Science* **1974**, *184*, 563.

(33) Kapoor, R.; Oyama, S. T.; Friihberger, B.; DeVries, B. D.; Chen, J. G. Characterization of Early Transition Metal Carbides and Nitrides by NEXAFS. *Catal. Lett.* **1995**, *34*, 179–189.

(34) Jiao, Y.; Zheng, Y.; Jaroniec, M.; Qiao, S. Z. Design of Electrocatalysts for Oxygen- and Hydrogen-Involving Energy Conversion Reactions. *Chem. Soc. Rev.* **2015**, *44*, 2060–2086.

(35) Gao, S.; Li, G.-D.; Liu, Y.; Chen, H.; Feng, L.-L.; Wang, Y.; Yang, M.; Wang, D.; Wang, S.; Zou, X. Electrocatalytic H₂ Production from Seawater Over Co, N-Codoped Nanocarbons. *Nanoscale* **2015**, *7*, 2306–2316.

(36) Ma, Y.-Y.; Wu, C.-X.; Feng, X.-J.; Tan, H.-Q.; Yan, L.-K.; Liu, Y.; Kang, Z.-H.; Wang, E.-B.; Li, Y.-G. Highly Efficient Hydrogen Evolution from Seawater by a Low-Cost and Stable CoMoP@C Electrocatalyst Superior to Pt/C. *Energy Environ. Sci.* **2017**, *10*, 788–798.

(37) Hsu, S. H.; Miao, J.; Zhang, L.; Gao, J.; Wang, H.; Tao, H.; Hung, S. F.; Vasileff, A.; Qiao Shi, Z.; Liu, B. An Earth-Abundant Catalyst-Based Seawater Photoelectrolysis System with 17.9% Solar-to-Hydrogen Efficiency. *Adv. Mater.* **2018**, *30*, 1707261.

(38) Kresse, G.; Furthmüller, J. Efficiency of *ab-initio* Total Energy Calculations for Metals and Semiconductors using a Plane-Wave Basis Set. *Comput. Mater. Sci.* **1996**, *6*, 15–50.

(39) Kresse, G.; Furthmüller, J. Efficient Iterative Schemes for *ab initio* Total-Energy Calculations Using a Plane-Wave Basis Set. *Phys. Rev. B: Condens. Matter Mater. Phys.* **1996**, *54*, 11169–11186.

(40) Kresse, G.; Hafner, J. *Ab initio* Molecular Dynamics for Liquid Metals. *Phys. Rev. B: Condens. Matter Mater. Phys.* **1993**, *47*, 558–561.

(41) Kresse, G.; Hafner, J. *Ab initio* Molecular-Dynamics Simulation of the Liquid-Metal–Amorphous-Semiconductor Transition in Germanium. *Phys. Rev. B: Condens. Matter Mater. Phys.* **1994**, *49*, 14251–14269.

(42) Perdew, J. P.; Burke, K.; Ernzerhof, M. Generalized Gradient Approximation Made Simple. *Phys. Rev. Lett.* **1996**, *77*, 3865–3868.

(43) Grimme, S. Semiempirical GGA-Type Density Functional Constructed with a Long-Range Dispersion Correction. *J. Comput. Chem.* **2006**, *27*, 1787–1799.

Supporting Information

Single-Crystal Nitrogen-Rich 2D Mo₅N₆ Nanosheets for Efficient and Stable Seawater Splitting

Huanyu Jin,[†] Xin Liu,[†] Anthony Vasileff,[†] Yan Jiao,[†] Yongqiang Zhao,[†] Yao Zheng,^{†*} and Shi-
Zhang Qiao^{†*}

[†]School of Chemical Engineering, The University of Adelaide, Adelaide, SA 5005, Australia

E-mail: yao.zheng01@adelaide.edu.au, s.qiao@adelaide.edu.au

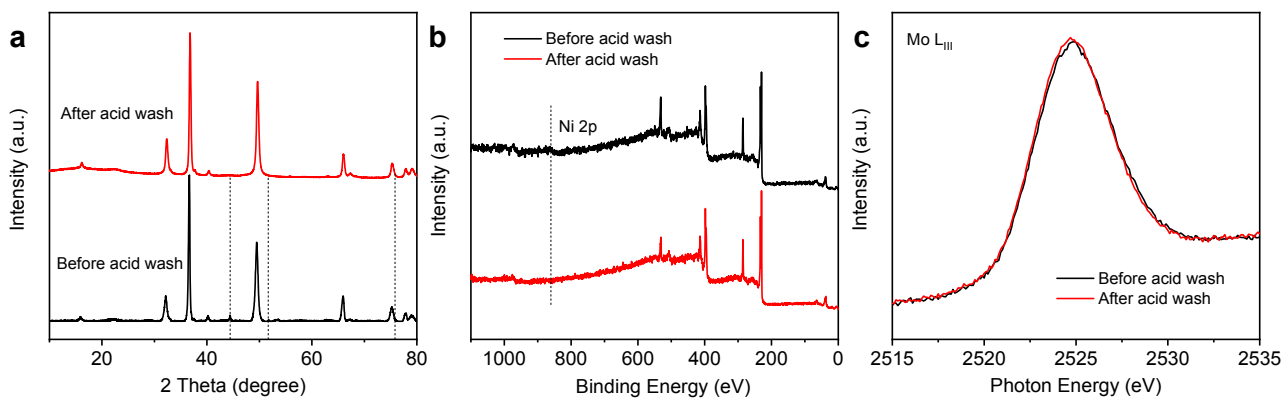


Figure S1. XRD (a), XPS survey scan (b) and Mo L_{III} edge (c) of Mo₅N₆ nanosheets before and after the acid wash.

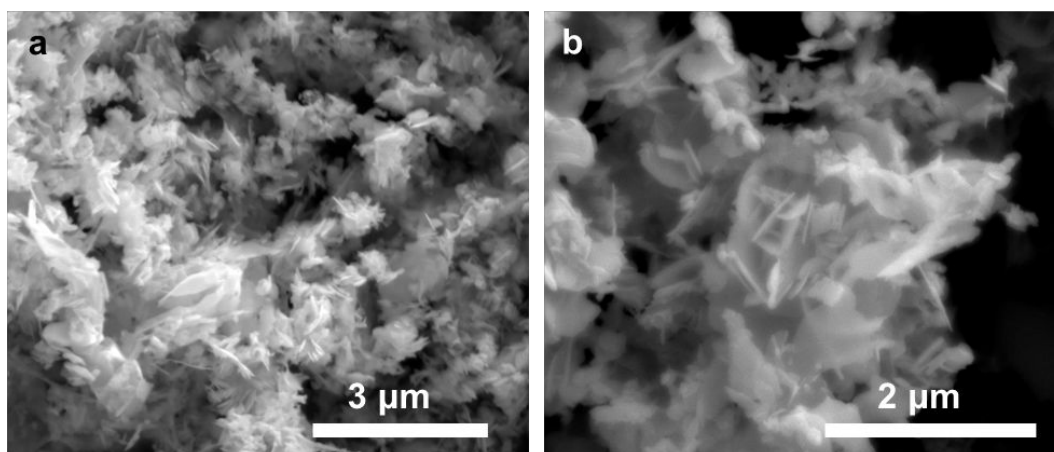


Figure S2. SEM images of Mo₅N₆ nanosheets.

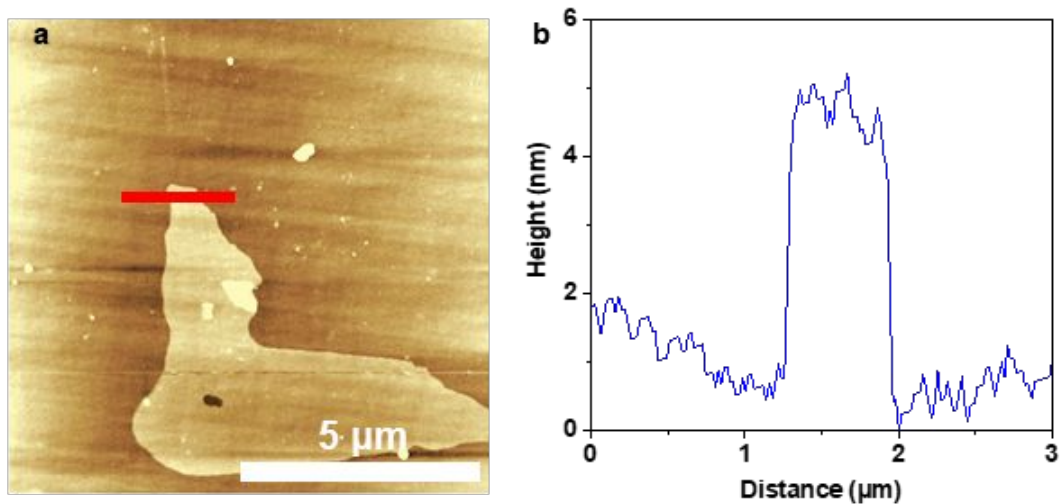


Figure S3. AFM measurement of a Mo_5N_6 nanosheet.

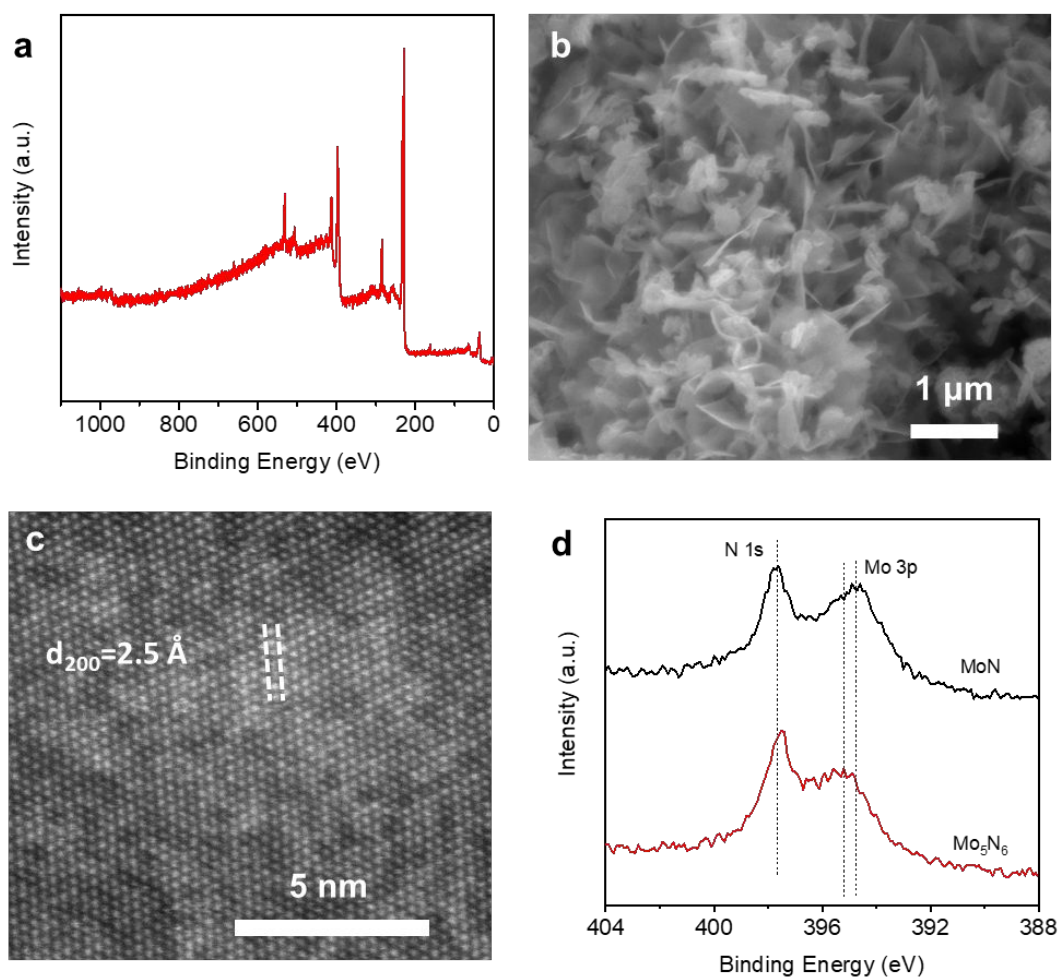


Figure S4. (a) Survey scan of MoN. (b) SEM image of 2D MoN nanosheets. (c) High resolution STEM image of MoN. (d) N 1s and Mo 3p spectra of Mo_5N_6 and MoN.

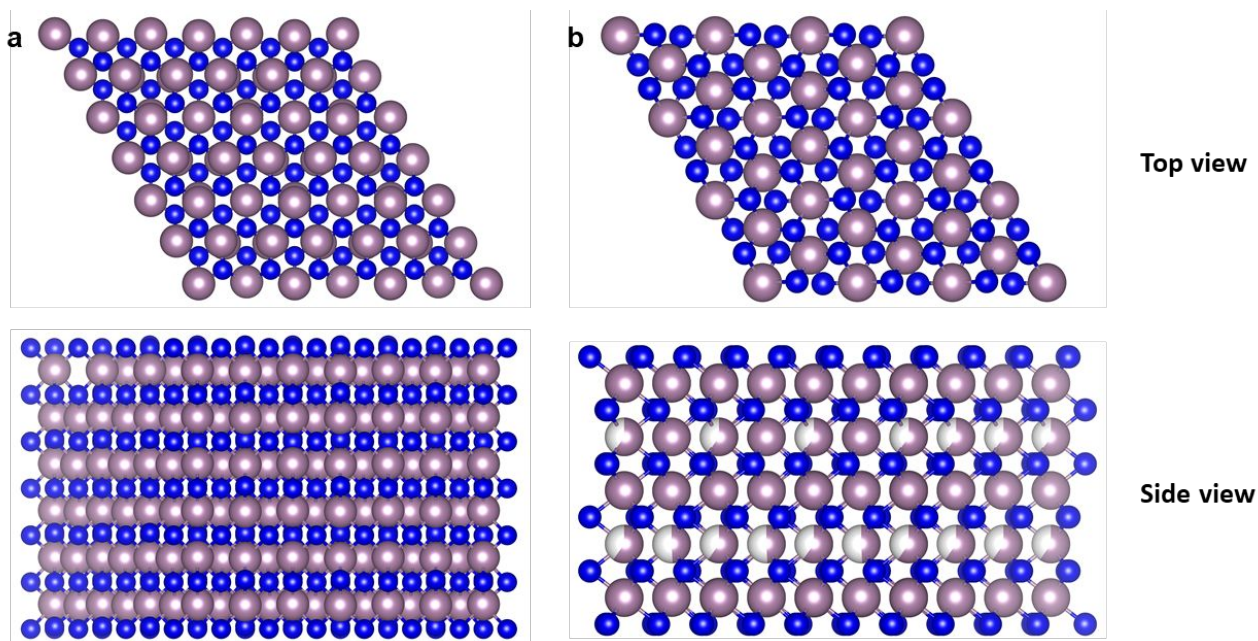


Figure S5. Atomic structure of MoN (a) and Mo₅N₆ (b).

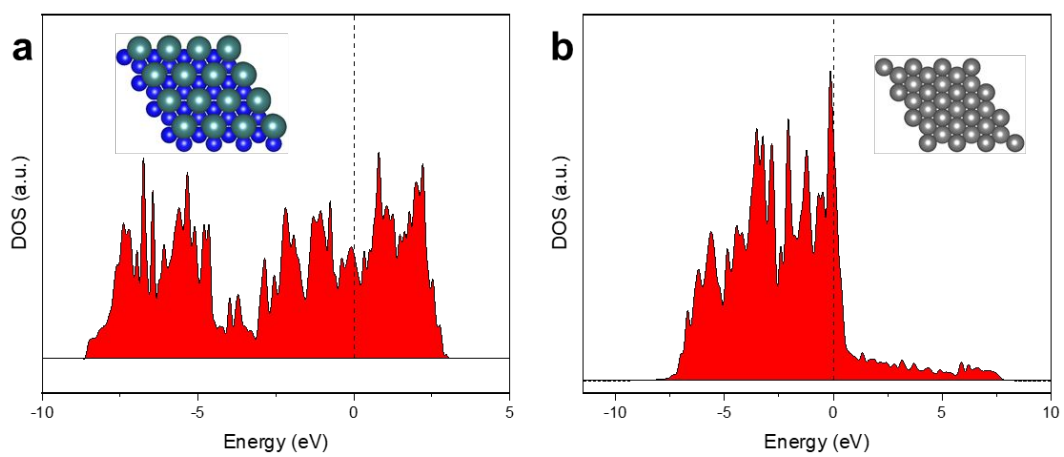


Figure S6. DOS of MoN (a) and Pt (111) (b).

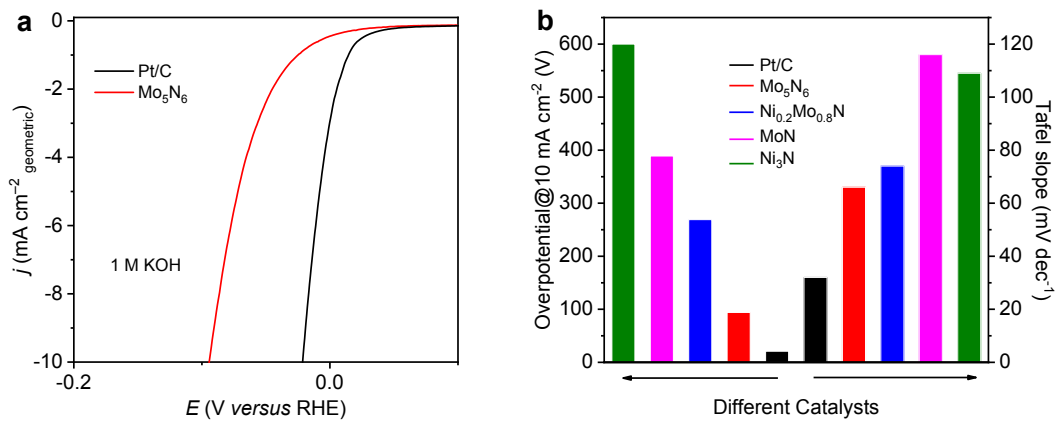


Figure S7. (a) LSV curves of Pt/C and Mo₅N₆. (b) Comparison of overpotential and Tafel slope of different catalysts.

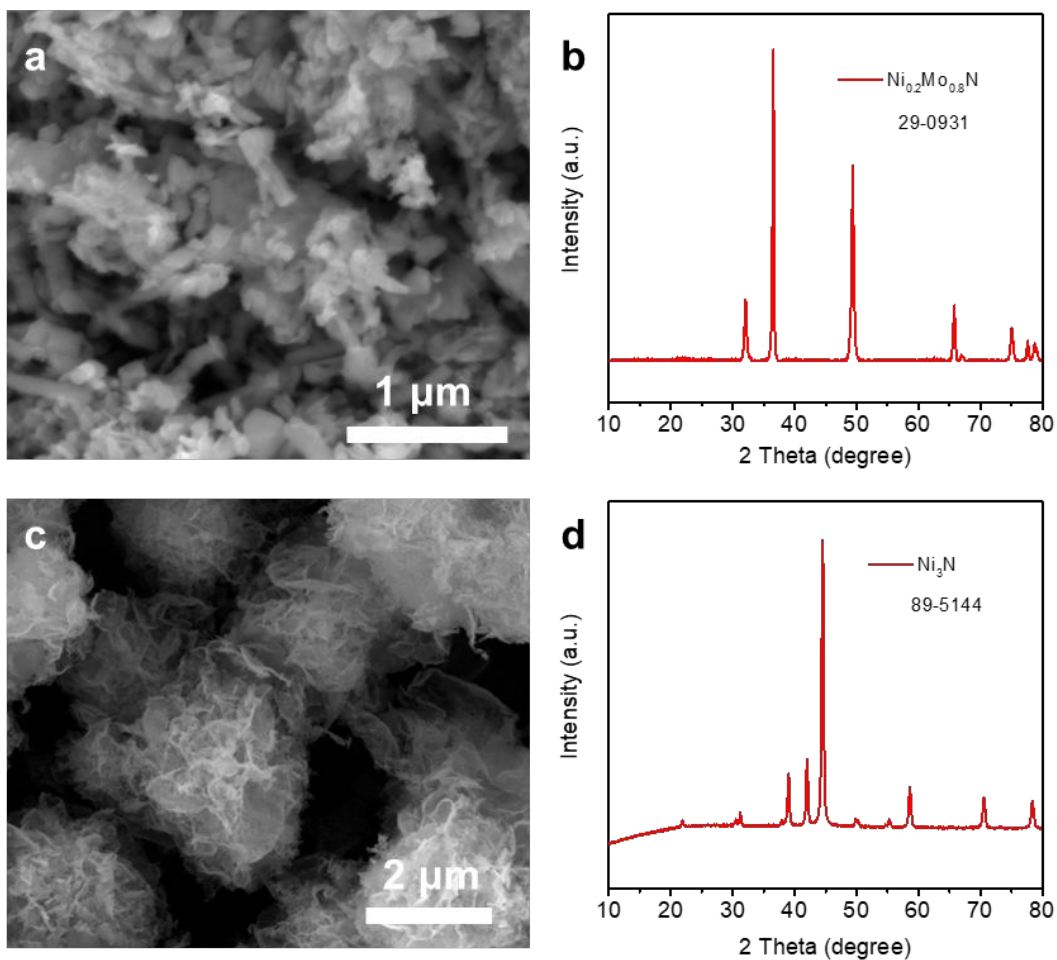


Figure S8. (a) SEM image and (b) XRD pattern of Ni_{0.2}Mo_{0.8}N. (c) SEM image and (d) XRD pattern of Ni₃N.

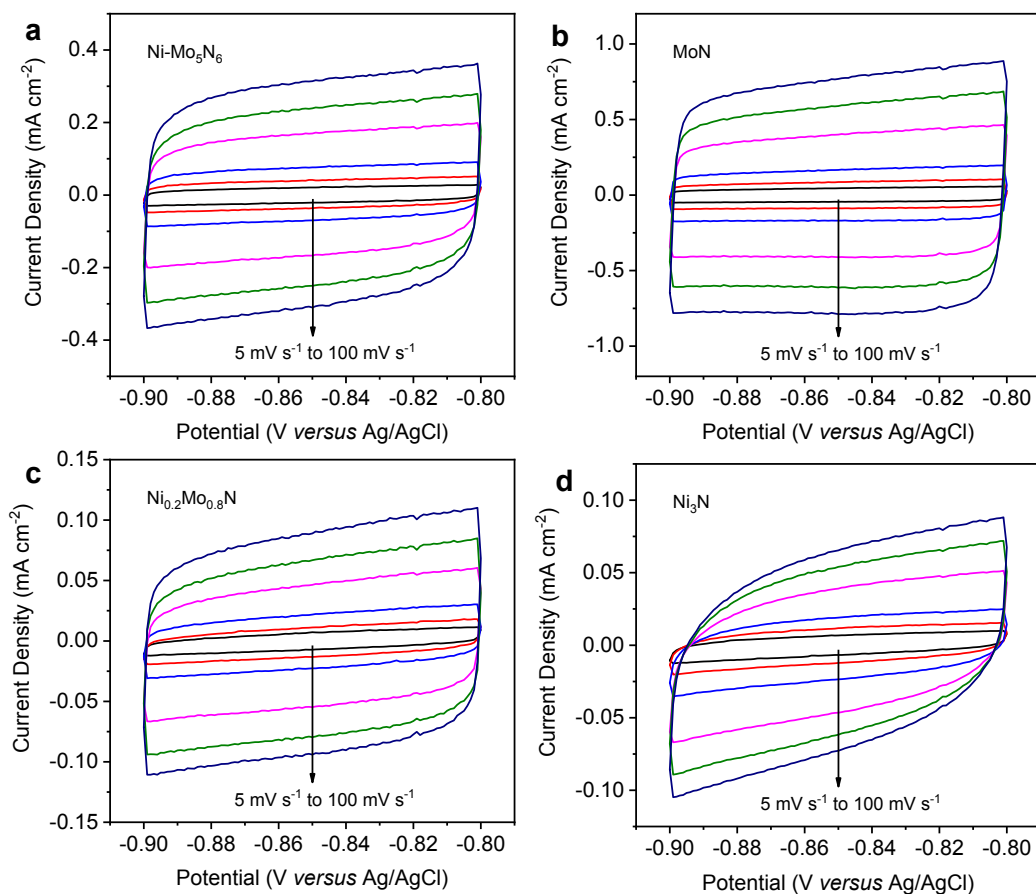


Figure S9. CV curves of different catalysts with scan rates from 5 mV s⁻¹ to 100 mV s⁻¹.

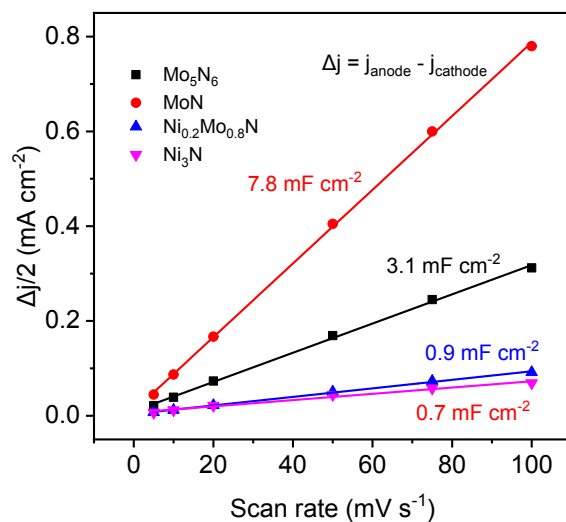


Figure S10. Current density difference at -0.85 V plotted against scan rate to give the double-layer capacitance for Mo₅N₆, MoN, Ni_{0.2}Mo_{0.8}N, and Ni₃N.

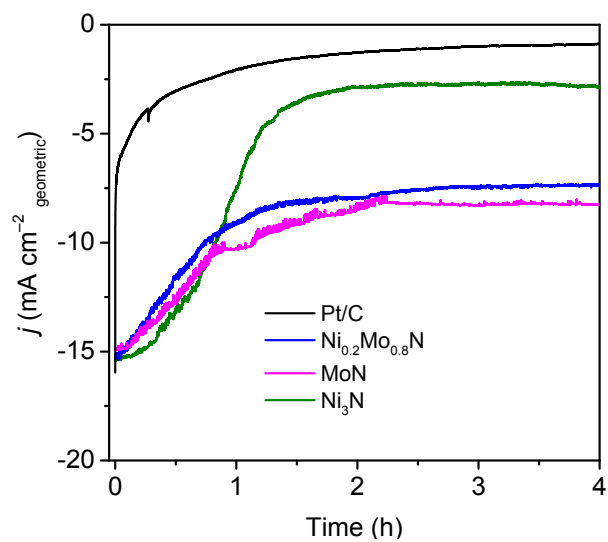


Figure S11. Chronoamperometric results of different catalysts for 4 h in seawater.

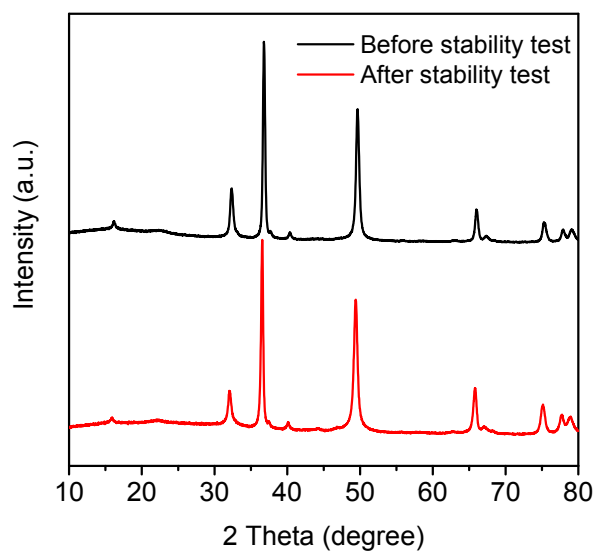


Figure S12. XRD patterns of Mo_5N_6 before and after stability testing.

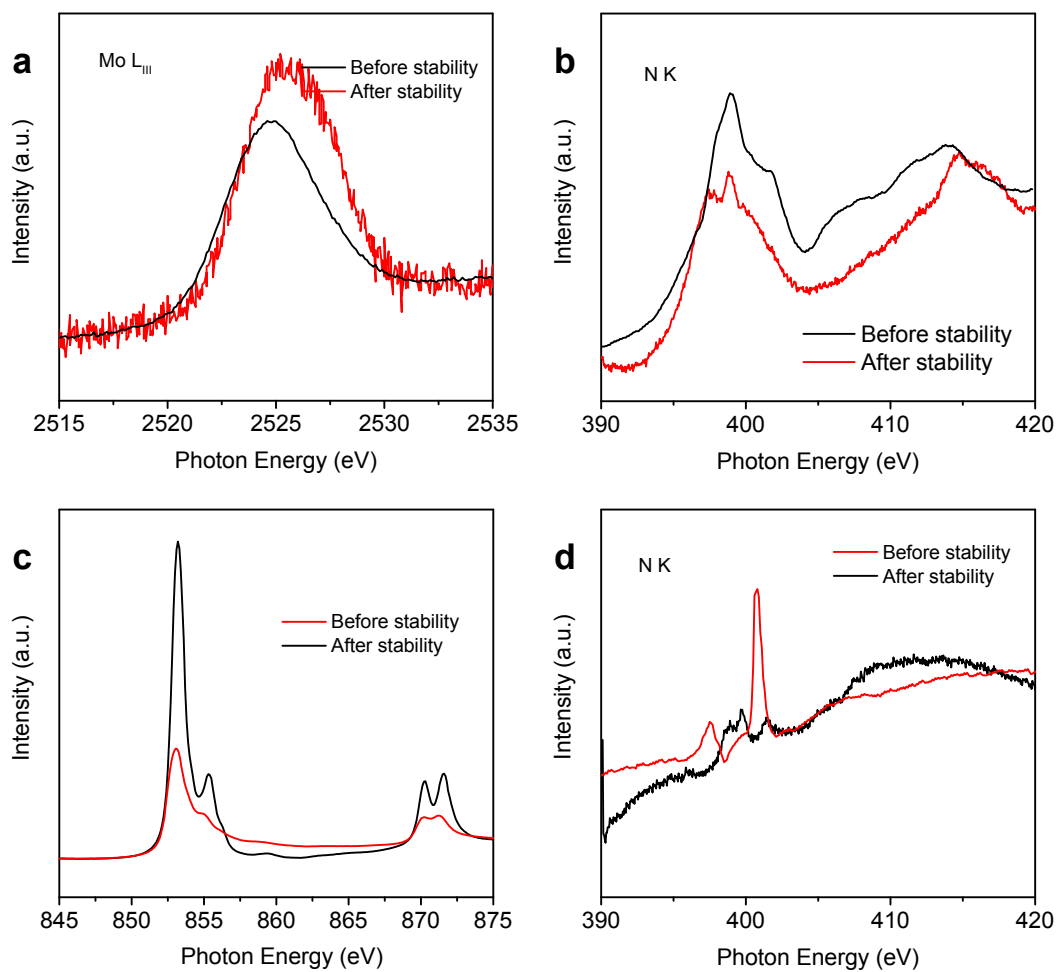


Figure S13. (a) Mo L_{III} and (b) N K of Ni_{0.2}Mo_{0.8}N before and after stability testing. (c) Ni L and (d) N K of Ni₃N before and after stability testing.

Table S1. Summary of some recently reported representative HER electrocatalysts in natural seawater.

Catalyst	η (mV vs. RHE) @ $J = -10 \text{ mA cm}^{-2}$	η (mV vs. RHE) @ $J = -20 \text{ mA cm}^{-2}$	Ref.
Mo_5N_6	258	300	This work
20 % Pt/C	263	363	This work
U-CNT-900	~680	~810	1
Mn-NiO-Ni/Ni-F	~185	~300	2
CoMoP@C	~450	~530	3
CoSe	330		4

References

- (1) Gao, S.; Li, G.-D.; Liu, Y.; Chen, H.; Feng, L.-L.; Wang, Y.; Yang, M.; Wang, D.; Wang, S.; Zou, X., Electrocatalytic H_2 Production From Seawater Over Co, N-Codoped Nanocarbons. *Nanoscale* **2015**, *7*, 2306–2316.
- (2) Lu, X.; Pan, J.; Lovell, E.; Tan, T. H.; Ng, Y. H.; Amal, R., A Sea-Change: Manganese Doped Nickel/Nickel Oxide Electrocatalysts for Hydrogen Generation From Seawater. *Energy Environ. Sci.* **2018**, *11*, 1898–1910.
- (3) Ma, Y.-Y.; Wu, C.-X.; Feng, X.-J.; Tan, H.-Q.; Yan, L.-K.; Liu, Y.; Kang, Z.-H.; Wang, E.-B.; Li, Y.-G., Highly Efficient Hydrogen Evolution From Seawater by a Low-Cost and Stable CoMoP@C Electrocatalyst Superior to Pt/C. *Energy Environ. Sci.* **2017**, *10*, 788–798.
- (4) Zhao, Y.; Jin, B.; Zheng, Y.; Jin, H.; Jiao, Y.; Qiao, S.-Z., Charge State Manipulation of Cobalt Selenide Catalyst for Overall Seawater Electrolysis. *Adv. Energy Mater.* **2018**, 1801926.

Chapter 5: Heteroatom-Doped Transition Metal Electrocatalysts for Hydrogen Evolution Reaction

5.1 Introduction and Significance

Transition metals (TMs) are a class of very important catalysts for the hydrogen evolution reaction (HER). An ideal way to optimize their HER performance is to tune their electronic structures. However, it is difficult to control the inherent properties of TMs alone using conventional approaches (alloying, compounding, nanostructuring *etc.*). To address this, a multifaceted heteroatom-doping method was developed to tune the electronic properties and subsequent HER activity of TMs controllably and continuously without changing their main chemical composition. By switching doping modes (e.g. single or dual doping), transition metals such as Ni and Co can be tuned with optimum electronic and adsorption characteristics. For example, nitrogen and phosphorus co-doped Ni exhibits the best HER performance among other doped Ni catalysts due to appropriate optimization, which is even better than many noble metal catalysts. The highlights of this Chapter include:

- Direct and continuous tuning of the HER activity of TMs is achieved through controllable non-metallic heteroatom doping.
- A series of comprehensive synchrotron-based X-ray absorption measurements are adopted to study the local coordination of doped-TM samples at the atomic level.
- The doping-induced charge redistribution in the transition metals is found to have a significant influence on their catalytic performance for alkaline HER with a volcano relationship.
- The N, P co-doped Ni shows the best HER performance which is even superior to noble metal catalysts.
- This is a universal method for optimizing the HER performance of TMs. It also provides insight into activating unconventional materials for clean energy storage and conversion systems.

5.2 Heteroatom-Doped Transition Metal Electrocatalysts for Hydrogen Evolution Reaction

This Chapter is included as it appears as a journal paper published by **Huanyu Jin**, Xin Liu, Shuangming Chen,[#] Anthony Vasileff, Laiquan Li, Yan Jiao, Li Song, Yao Zheng,* Shi-Zhang Qiao* Heteroatom-Doped Transition Metal Electrocatalysts for Hydrogen Evolution Reaction. *ACS Energy Lett.* 2019, 4, 805–810.

Statement of Authorship

Title of Paper	Heteroatom-Doped Transition Metal Electrocatalysts for Hydrogen Evolution Reaction
Publication Status	<input checked="" type="checkbox"/> Published <input type="checkbox"/> Accepted for Publication <input type="checkbox"/> Submitted for Publication <input type="checkbox"/> Unpublished and Unsubmitted work written in manuscript style
Publication Details	Huanyu Jin, Xin Liu, Shuangming Chen, Anthony Vasileff, Laiquan Li, Yan Jiao, Li Song, Yao Zheng,* Shi-Zhang Qiao* Heteroatom-Doped Transition Metal Electrocatalysts for Hydrogen Evolution Reaction. ACS Energy Lett. 2019, 4, 805–810.

Principal Author

Name of Principal Author (Candidate)	Huanyu Jin		
Contribution to the Paper	Research plan, material synthesis, most of the characterizations and data analysis, electrochemical characterization, and manuscript draft.		
Overall percentage (%)	80		
Certification:	This paper reports on original research I conducted during the period of my Higher Degree by Research candidature and is not subject to any obligations or contractual agreements with a third party that would constrain its inclusion in this thesis. I am the primary author of this paper.		
Signature	_____	Date	22/June/2020

Co-Author Contributions

By signing the Statement of Authorship, each author certifies that:

- the candidate's stated contribution to the publication is accurate (as detailed above);
- permission is granted for the candidate to include the publication in the thesis; and
- the sum of all co-author contributions is equal to 100% less the candidate's stated contribution.

Name of Co-Author	Xin Liu		
Contribution to the Paper	Computational calculations.		
Signature	_____	Date	22/June/2020

Name of Co-Author	Shuangming Chen		
Contribution to the Paper	Data analysis.		
Signature	_____	Date	22/June/2020

Name of Co-Author	Anthony Vasileff		
Contribution to the Paper	Editing process and manuscript revision.		
Signature		Date	22/June/2020

Name of Co-Author	Laiquan Li		
Contribution to the Paper	Assistance with electrochemical tests and data analysis.		
Signature		Date	22/June/2020

Name of Co-Author	Yan Jiao		
Contribution to the Paper	Discussion of manuscript and computational calculations.		
Signature		Date	22/June/2020

Name of Co-Author	Li Song		
Contribution to the Paper	Data analysis.		
Signature		Date	22/June/2020

Name of Co-Author	Yao Zheng		
Contribution to the Paper	Supervision of the work, discussion of this manuscript and manuscript evaluation.		
Signature		Date	22/June/2020

Name of Co-Author	Shi-Zhang Qiao		
Contribution to the Paper	Supervision of the work, discussion of this manuscript and manuscript evaluation.		
Signature		Date	22/June/2020

Please cut and paste additional co-author panels here as required.

Heteroatom-Doped Transition Metal Electrocatalysts for Hydrogen Evolution Reaction

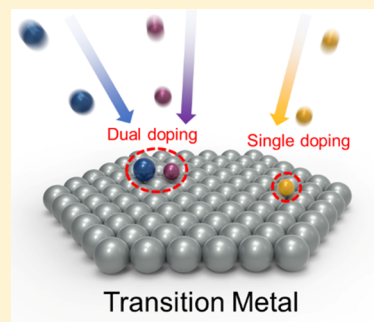
Huanyu Jin,^{†,§} Xin Liu,^{†,§} Shuangming Chen,^{‡,§} Anthony Vasileff,[†] Laiquan Li,[†] Yan Jiao,[†] Li Song,[‡] Yao Zheng,^{*,†} and Shi-Zhang Qiao^{*,†}

[†]School of Chemical Engineering, The University of Adelaide, Adelaide, South Australia 5005, Australia

[‡]National Synchrotron Radiation Laboratory, CAS Center for School of Chemical Engineering, Excellence in Nanoscience, University of Science and Technology of China, Hefei 230029, Anhui, People's Republic of China

S Supporting Information

ABSTRACT: Developing efficient and low-cost electrocatalysts for the hydrogen evolution reaction (HER) is important for clean energy systems. Non-noble transition metals are the most promising candidates for replacement of conventional Pt group catalysts for the HER. However, most non-noble metals show poor HER activity due to their intrinsic electronic structures. Herein, we use a multifaceted heteroatom doping method (nitrogen, sulfur, and phosphorus) to directly and continuously fine-tune the electronic structure and HER activity of non-noble metals without changing their chemical composition. As a proof-of-concept, a nitrogen and phosphorus dual-doped Ni catalyst is explored by precisely manipulating doping modes, revealing the best HER performance among all doped Ni catalysts tested. The doping-induced charge redistribution in the Ni metal significantly influences its catalytic performance for the HER in alkaline media, which is confirmed by merging theoretical calculation with synchrotron-based spectroscopy. The principle that can bridge the doping modes and HER activity of the doped catalysts is built with a volcano relationship.



Hydrogen is considered a sustainable and clean energy carrier for future energy systems. The hydrogen evolution reaction (HER) is core to producing high-purity hydrogen in water electrolysis systems. To date, transition metal electrocatalysts (TMEs) are the most commonly utilized catalysts for hydrogen-related clean energy conversion processes.^{1–5} However, the most efficient TMEs for HER are noble metals such as Pt and Ru. These metals are expensive and scarce, which hinders their large-scale application. Consequently, activating and optimizing non-noble TMEs for HER is an alternative way for low-cost hydrogen production. One strategy for optimizing the catalytic activity of known non-noble metal TMEs is to modify their electronic structures.^{6–8} However, strategies such as alloying, lattice strain, and single-atom synthesis face difficulty in achieving continuous control over their electronic structures and usually introduce additional variables such as ligand effect or composition change,^{9,10} leading to obstacles in identifying and optimizing the electronic structure of the TMEs alone.^{11–13} Thus, new methods that can flexibly and effectively control the electronic structure of non-noble TMEs for HER are needed.

Heteroatom doping is a promising method that can tune the electronic structure of host materials by introducing charge

redistribution.^{14–18} By doping heteroatoms (e.g. boron, nitrogen, sulfur, phosphorus) with different electronegativity, the resultant charge redistribution can change the electronic, catalytic, and optical properties of the materials for energy-related applications.^{19–21} Furthermore, one of the advantages of heteroatom doping is that it does not change the composition of the host materials (which can retain their desired intrinsic features).²² To date, heteroatom doping has been widely used in modifying the electronic structure of carbon materials and metal compounds, demonstrating great potential for tuning the electrocatalytic performance of the matrix.^{23–26} However, it is difficult to apply this method to TMEs due to the formation of corresponding compounds like metal nitrides, sulfides, etc. Only a few works have reported the synthesis of single-doped TMEs that showed significant HER activity enhancement in comparison to their nondoped counterparts and relevant metal compounds.^{5,27–29} The heteroatom site on a metal surface can promote the water dissociation step of HER by decreasing the free-energy barrier. However, these works did not realize multifaceted regulation in

Received: February 14, 2019

Accepted: February 26, 2019

Published: February 26, 2019

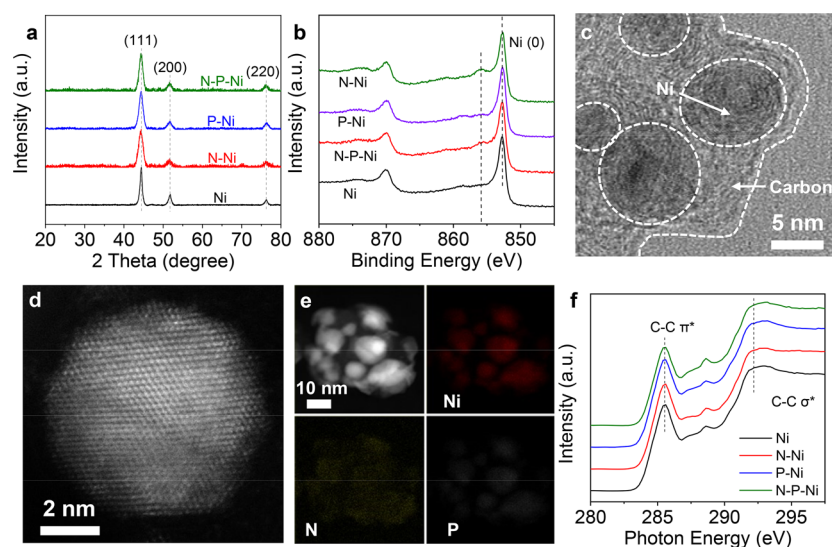


Figure 1. (a) XRD patterns of single- and dual-doped Ni nanoparticles. (b) Ni 2p XPS spectra of single- and dual-doped catalysts. (c) TEM image of N–P–Ni. (d) HAADF-STEM of a N–P–Ni nanoparticle. (e) Elemental mapping of N–P–Ni. (f) Synchrotron-based C K edge XANES spectra of different catalysts.

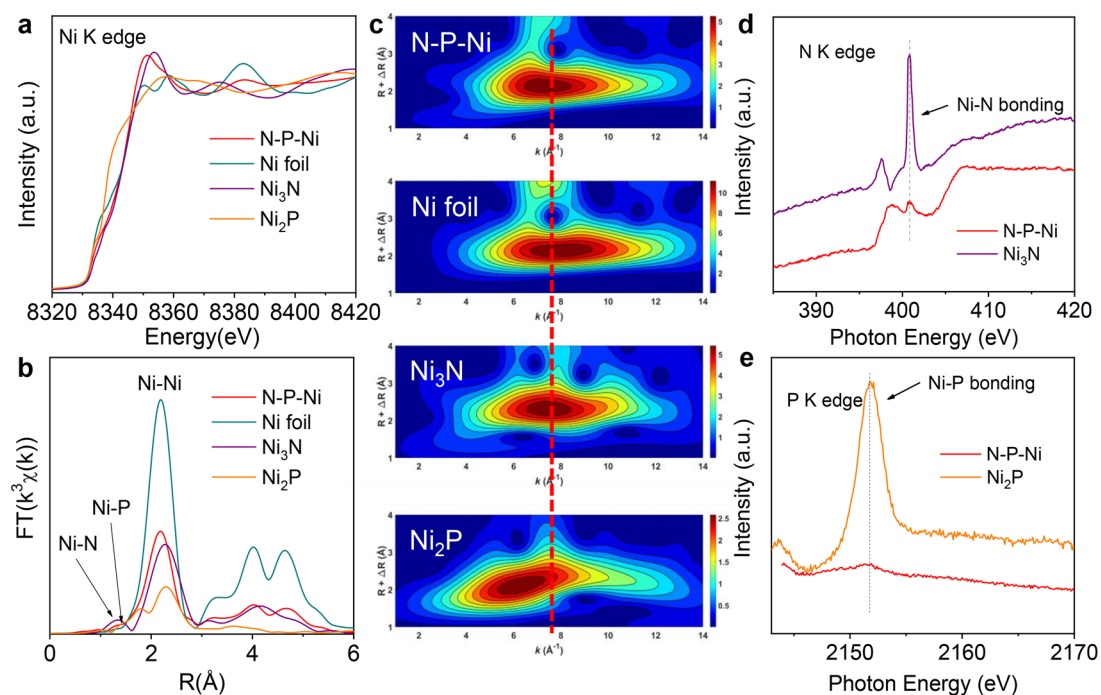


Figure 2. Synchrotron-based (a) XAS spectra, (b) FT curves, and (c) WT-EXFAS plots of the as-prepared N–P–Ni and other relevant materials. (d) N K edge XANES of Ni_3N and N–P–Ni. (e) P K edge XANES of Ni_2P and N–P–Ni.

the electronic state due to the simple doping strategies used. Consequently, it is necessary to introduce multiple doping modes that can continuously control the electronic state of TMEs in order to precisely optimize HER catalysts.

Recently, design principles for heteroatom-doped graphene materials for the HER in acidic media were established by continuously tuning their electronic structures through multiple heteroatom doping.¹⁴ The electrons from different dopants can be transferred directionally, leading to the formation of desired active sites for the HER. For example, in boron and nitrogen co-doping, the boron atom acts as an electron donor while nitrogen is the electron acceptor due to differences in electronegativity. Thus, the adsorption energy of intermediates

on the active sites can be continuously tuned to either a strong or weak state by changing the doping mode. By extension, continuous control of the electronic structure of TMEs could possibly be realized using different doping modes, which could also unveil their activity mechanism. However, multifaceted heteroatom doping on pure transition metals has not been achieved.

In this work, for the first time, multifaceted heteroatom doping on TMEs was realized, and in turn, the optimization of multiple intermediates for the HER was achieved. Using Ni metal as the example, the *d* band center of the TME was tuned by switching between single- and dual-doping modes (N, P, S). The effects of the doping mechanism on HER activity (for

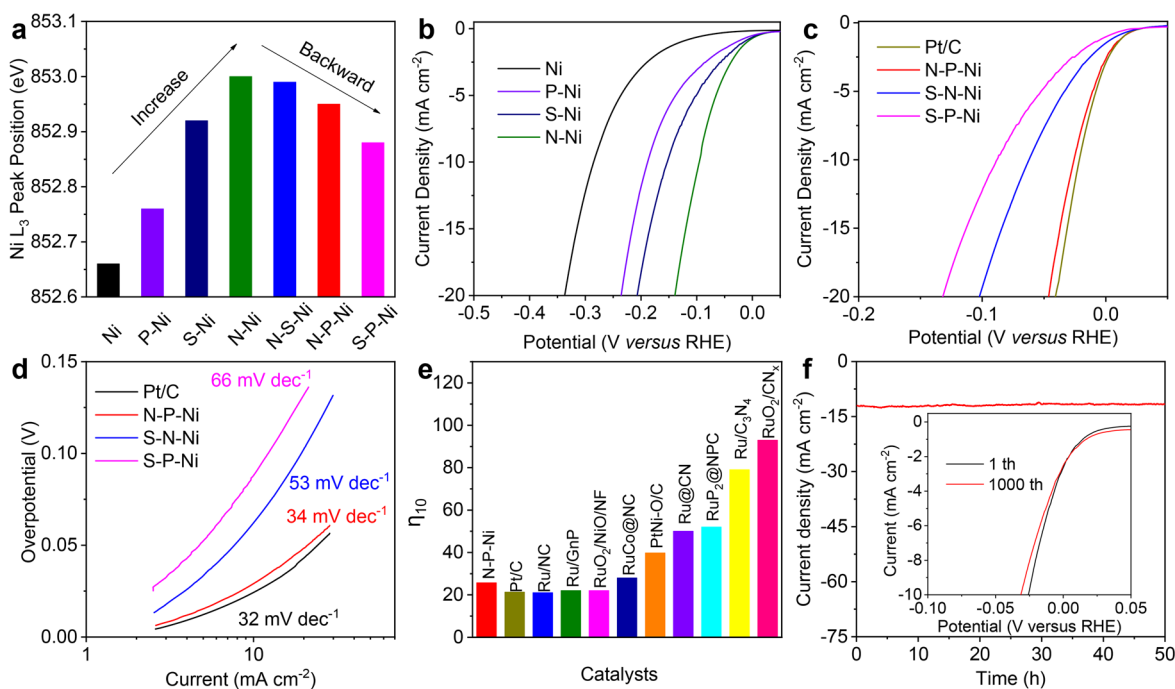


Figure 3. (a) Synchrotron-based Ni L₃ edge peak position of single-doped and dual-doped Ni catalysts. (b) LSV curves of the single-doped Ni catalysts. (c,d) LSV curves and Tafel plot of the dual-doped N–P–Ni, S–P–Ni, S–N–Ni, and Pt/C. (e) Comparison of N–P–Ni (η_{10}) with other noble metal-based catalysts. (f) Chronoamperometric curves and LSV (inset) of N–P–Ni in a long-term stability test.

both single and dual doping) was explained by mutually corroborating experiments and theoretical computation. Significantly, the N, P co-doped Ni exhibited the best HER performance with an overpotential of 25.8 mV at a current density of 10 mA cm⁻², which is even better than that of many noble metal catalysts. Importantly, a volcano plot between different doping modes on Ni catalysts and their HER performance were built, which demonstrates the possibility of using heteroatom doping methods to optimize the HER activity of TMEs. At last, we also observed similar enhancement for doped Co metal catalysts, manifesting the general applicability of this method.

A series of single and dual heteroatom-doped (N, P, S) Ni nanoparticles (N–Ni, P–Ni, S–Ni, N–P–Ni, S–N–Ni, and S–P–Ni) were synthesized (Figure S1). The X-ray diffraction (XRD) patterns (Figures 1a and S2a,b) indicate that the doped Ni catalysts are isostructural to metallic Ni (JCPDS Card No. 04-0850). Therefore, the doping method did not significantly change the crystal structure of the metal host, and no detectable Ni-based compounds were formed. As shown in the Ni 2p X-ray photoelectron spectroscopy (XPS) spectra (Figures 1b and S2c), the valence state of Ni is dominated by Ni(0) after heteroatom doping, indicating that the majority of the catalytic surface is metallic Ni and no metal compound is formed (e.g., Ni₃N, Ni₂P). The shoulder peak at 855.8 eV increased slightly after doping, indicating that the heteroatoms were successfully doped on the Ni. As confirmed by synchrotron-based XPS, the doping level of each element was about 0.5 atom % (Table S1), which is likely to be the saturation level. It was also found that formation of the corresponding metal compound (such as Ni₂P) was favored upon increasing the amount of heteroatom precursor (Figure S3). Taking N–P–Ni as an example, the highly crystalline nanoparticles were distributed on the carbon support uniformly and had an average particle diameter of about 7

nm (Figures 1c and S4). The exposed (111) plane of N–P–Ni nanoparticles is shown in the aberration-corrected high-angle annular dark field scanning transmission electron microscopy (HAADF-STEM) image (Figure 1d). Energy dispersive spectroscopy (EDS) mapping of N–P–Ni shows the spatial distribution of N and P on the Ni particles (Figure 1e). The consistent O 1s XPS, C 1s XPS, and C K edge X-ray absorption near edge structure (XANES) spectra between the different catalysts indicate that the heteroatoms were doped on Ni instead of the carbon or oxygen (Figures 1f and S5).

A series of synchrotron-based X-ray adsorption (XAS) measurements were then performed to characterize the local coordination of doped Ni samples at the atomic level (Figure 2a). The spectrum of N–P–Ni is similar to that of Ni foil and different from that of the Ni₃N and Ni₂P, further indicating that no bulk Ni compound was formed. The absorption edge of N–P–Ni shifts to higher energy than that of Ni foil, indicating the formation of positively charged Ni sites after heteroatom doping. Figure 2b shows the Ni K edge extended X-ray adsorption fine structure (EXAFS) spectra of the different catalysts. N–P–Ni shows a main coordination peak at 2.18 Å, which is assigned to Ni–Ni bonding. The small peak at around 1.3 Å can be assigned to Ni–N and Ni–P coordination,³⁰ which indicates the successful doping of N and P on the Ni surface. The fitting results show that the coordination number of Ni–N and Ni–P increases after heteroatom doping (Figure S6 and Table S2). Wavelet transform (WT) was adopted to further analyze the Ni K edge EXFAS oscillations (Figures 2c and S7). The WT contour plots of N–P–Ni exhibit one intensity maximum at 7.6 Å, which is closer to that of Ni foil (8 Å). The negative shift indicates that N and P were successfully doped on the Ni particle. However, the patterns for N–P–Ni are totally different from that of Ni₂P and Ni₃N, indicating that no nitride or phosphide was formed. As confirmed by N and P K edge

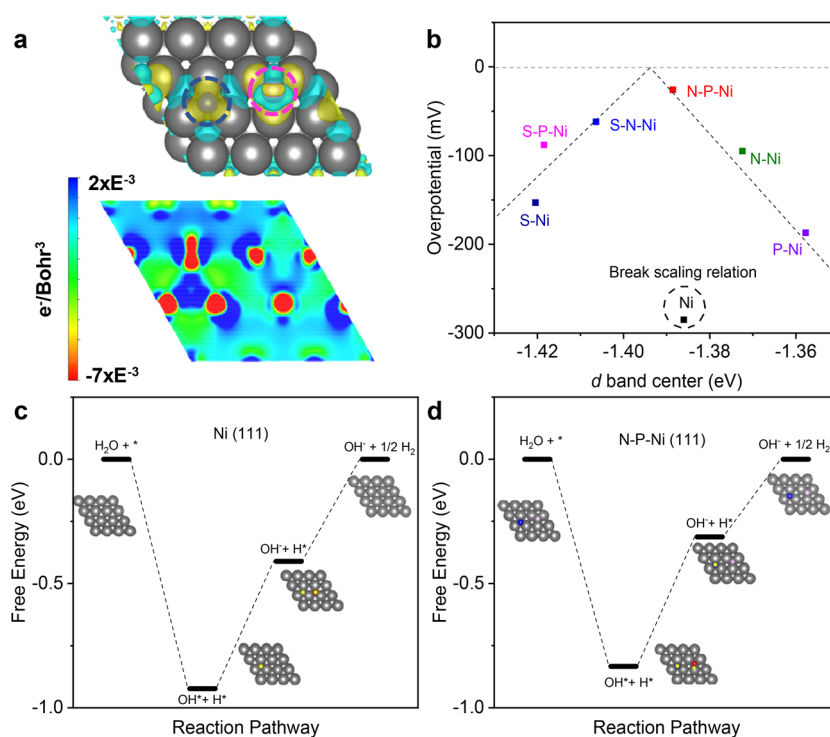


Figure 4. (a) Top: Interfacial electron transfer in N–P–Ni. Color: gray, Ni; blue circle, N; pink circle, P. Yellow and cyan isosurfaces represent electron accumulation and electron depletion at an isosurface cutoff of $0.003 \text{ e}^-/\text{Bohr}^3$. Bottom: Electron density change plots of N–P–Ni. (b) Volcano plot of η_{10} as a function of the d band position for various heteroatom-doped Ni catalysts. (c,d) Reaction pathways of Ni and N–P–Ni for alkaline HER.

XANES (Figure 2d,e), the peaks at 400.8 and 2151.8 eV correspond to the newly formed Ni–N and Ni–P species in N–P–Ni. The XANES spectra of the other samples also show characteristic peaks (Ni–N, Ni–S, and Ni–P) at relevant positions (Figure S8), indicating that heteroatom doping occurred on Ni instead of the carbon.

The electronic interaction and HER activity between N, P, and S dopants and Ni atoms was then investigated. As confirmed by the Ni L_3 edge XANES of different samples, the valence state of Ni slightly increased after single doping (Figures 3a and S9). More interestingly, the magnitude of the shift for the Ni L_3 edge peak is positively correlated to the electronegativity of the heteroatoms. Consequently, as N has the largest electronegativity, N–Ni demonstrated the biggest shift of 0.34 eV. The valence state of Ni increased after single doping, which can be explained by the electronic interaction between Ni and the different heteroatom dopants. In single doping, an electron is transferred from Ni to the more electronegative heteroatom (N, P, or S). Therefore, the interaction between the fully occupied π -symmetry (t_{2g}) d orbitals of Ni and the bridging heteroatom is strong in the single-doping mode, leading to an increase in the valence state of the metal atoms.³¹ We then measured the electrocatalytic HER performance of single-doped Ni catalysts to evaluate the relationship between the charge redistribution of single-doped Ni and their electrocatalytic activity. Figure 3b shows the linear sweep voltammetry (LSV) curves of different single-doped catalysts. N–Ni exhibited an overpotential of 95 mV at a current density of 10 mA cm^{-2} (η_{10}), which is much better than that of pristine Ni (285 mV). Further, S- and P-doped Ni also exhibited enhanced HER activity compared to Ni (Figures 3b and S10a,b). The activity enhancement of single-doped Ni

nanoparticles is likely attributed to the changes in electron structure of the metal and heteroatom sites.

For finer control of the electronic state, we produced dual-doped structures to counter some of the effects of the electronegative dopant. As shown in Figure 3a, the valence state of Ni after co-doping (judged by the peak position of Ni L_3 edge XANES) still increased in comparison to that of pristine Ni. However, the overall valence state decreased compared to that of N–Ni (the material with the highest valence state). The reduction of the Ni valence state indicates that there is an interesting interaction between Ni and the two heteroatoms. Taking N–P–Ni as an example, the dopant atoms are bonded with Ni in a co-doping mode. Because the electronegativity of N (3.04) is larger than that of P (2.19), electrons from P transfer to N and weaken the interaction between N and Ni. As the P provides extra electrons to the whole system, this leads to the overall valence state of Ni being lower than that of N–Ni, which is in accordance with the XANES and XPS data. As expected, all of the dual-doped catalysts exhibited enhanced HER performance compared to their single-doped counterparts and the pristine Ni catalyst. This demonstrates the superiority of dual-heteroatom doping. Significantly, the N–P-doped Ni exhibited excellent performance with a small η_{10} of 25.8 mV, which is better than those of other catalysts including Ni_3N and Ni_2P (Figures 3c and S11). The i_0 of N–P–Ni (1.22 mA cm^{-2}) is very close to that of commercial Pt/C (1.3 mA cm^{-2}) and 8-fold higher than that of pristine Ni (0.154 mA cm^{-2} ; Figure S10b). N–P–Ni also shows a small Tafel slope of 34 mV dec^{-1} , indicating that the Volmer step is no longer rate-determining as water dissociation kinetics on this material are significantly improved. Significantly, the overall performance of N–P–Ni is even better than those of many reported noble metal and other catalysts, as

shown in Figure 3e and Table S3.^{32–36} Regarding stability, chronoamperometry (Figure 3f) was carried out for 50 h at a constant overpotential of 30 mV. The stable current response further indicates that the catalyst is stable under operating conditions. The Figure 3f inset depicts the LSV curves collected from N–P–Ni at the 1st and 1000th cycles. Negligible change in the current response is observed after 1000 cycles. By spectroscopic and TEM measurements (Figure S12), N–P–Ni was also found to be very stable during operation. Furthermore, several control experiments were conducted to highlight the importance of the heteroatoms in TMEs (Figures S13 and S14). In order to explore the versatility of this method, cobalt metal-based catalysts were prepared and subjected to the same doping treatment (Figure S15). Similar enhancement is observed in N–P–Co, which demonstrates the effectiveness of this method for improving the HER activities of inexpensive TMEs.

DFT calculations studying the different catalysts were conducted to probe the electronic structure of Ni after heteroatom doping. The electron density difference in Figure 4a demonstrates the charge transfer induced by N–P dual doping: electrons transfer from the surrounding Ni atoms to the Ni–N bonding area, suggesting a strong interaction between the N and Ni, as indicated by the large isosurface; however, P donates electrons to surrounding Ni atoms, displayed as a blue electron depletion isosurface. From the two-dimensional electron density difference plot, we clearly see that electron density accumulates at N and the surrounding Ni near the P dopant. For the N–P doping mode, electrons transfer from Ni to N (Figure 4a, top view). After P doping, the electrons transfer from P to Ni due to its unsaturated electron orbital. Consequently, the average valence state of Ni can be incrementally increased or decreased. Further, we calculated electronic structures of all of the samples to reveal the underlying activity origin trend. As shown in Figure S16, the *d* band center position of different catalysts referenced to the Fermi level and slightly shifted is plotted against an experimental descriptor (η_{10}). Interestingly, the η_{10} as a function of *d* band position (Figure 4b) shows a volcano plot, which indicates that there is an optimal value of *d* band position. This is a quantitative illustration of the Sabatier principle: an active catalyst binds reaction intermediate(s) neither too strongly nor too weakly.³⁷ It is thus of great importance to continuously tune the electronic structure to reach the summit of the volcano rather than overoptimizing the electronic structure and missing the peak. Furthermore, the Gibbs free energy and theoretical HER overpotentials for each reaction step of Ni and N–P–Ni are shown in Figure 4c,d. The hydroxide desorption and hydrogen evolution steps are endergonic, while the water adsorption and dissociation are exergonic. Therefore, the potential-determining step should be either hydroxide desorption or hydrogen evolution, of which the free-energy difference should be the theoretical overpotential to drive the reaction at an appropriate rate. After N, P doping, both hydroxide desorption and hydrogen evolution on Ni(111) are optimized, which therefore boosts HER performance significantly.

In summary, a multifaceted heteroatom doping method was developed to optimize the HER activity of non-noble metal catalysts. Out of all of the doped Ni catalysts tested, N,P co-doped Ni exhibited the best HER performance with a very small overpotential of 25.8 mV at a current density of 10 mA cm⁻². As confirmed by experiments and DFT calculations,

doping-induced charge redistribution on the Ni surface can change the electronic structure of the Ni metal, resulting in catalytic properties similar to those of noble metal catalysts. Similar enhancement was also observed for Co metal catalysts, elucidating the versatility of this method. This study demonstrates the possibility of activating TMEs via heteroatom doping and provides new insight for activating unconventional materials for applications in other energy storage and conversion systems.

■ ASSOCIATED CONTENT

📄 Supporting Information

The Supporting Information is available free of charge on the ACS Publications website at DOI: 10.1021/acseenergylett.9b00348.

Experimental section, TEM figures, spectroscopic characterization, and electrocatalytic data (PDF)

■ AUTHOR INFORMATION

Corresponding Authors

*E-mail: s.qiao@adelaide.edu.au.

*E-mail: yao.zheng01@adelaide.edu.au.

ORCID

Huanyu Jin: 0000-0002-1950-2364

Laiquan Li: 0000-0002-3301-9029

Yan Jiao: 0000-0003-1329-4290

Li Song: 0000-0003-0585-8519

Yao Zheng: 0000-0002-2411-8041

Shi-Zhang Qiao: 0000-0002-4568-8422

Author Contributions

[§]H.J., X.L., and S.C. contributed equally.

Notes

The authors declare no competing financial interest.

■ ACKNOWLEDGMENTS

This work is financially supported by the Australian Research Council (DP160104866, DE160101163, and FL170100154). XANES measurements were undertaken on the soft X-ray beamline at the Australian Synchrotron.

■ REFERENCES

- (1) Seh, Z. W.; Kibsgaard, J.; Dickens, C. F.; Chorkendorff, I.; Nørskov, J. K.; Jaramillo, T. F. Combining Theory and Experiment in Electrocatalysis: Insights into Materials Design. *Science* **2017**, *355*, No. eaad4998.
- (2) Stamenkovic, V. R.; Fowler, B.; Mun, B. S.; Wang, G.; Ross, P. N.; Lucas, C. A.; Marković, N. M. Improved Oxygen Reduction Activity on Pt₃Ni (111) via Increased Surface Site Availability. *Science* **2007**, *315*, 493–497.
- (3) Wang, H.; Xu, S.; Tsai, C.; Li, Y.; Liu, C.; Zhao, J.; Liu, Y.; Yuan, H.; Abild-Pedersen, F.; Prinz, F. B.; et al. Direct and Continuous Strain Control of Catalysts with Tunable Battery Electrode Materials. *Science* **2016**, *354*, 1031–1036.
- (4) Liu, M.; Pang, Y.; Zhang, B.; De Luna, P.; Voznyy, O.; Xu, J.; Zheng, X.; Dinh, C. T.; Fan, F.; Cao, C.; et al. Enhanced Electrocatalytic CO₂ Reduction via Field-induced Reagent Concentration. *Nature* **2016**, *537*, 382–386.
- (5) Zhou, Y.; Che, F.; Liu, M.; Zou, C.; Liang, Z.; De Luna, P.; Yuan, H.; Li, J.; Wang, Z.; Xie, H.; et al. Dopant-induced Electron Localization Drives CO₂ Reduction to C₂ Hydrocarbons. *Nat. Chem.* **2018**, *10*, 974–980.
- (6) Strasser, P.; Koh, S.; Anniyev, T.; Greeley, J.; More, K.; Yu, C.; Liu, Z.; Kaya, S.; Nordlund, D.; Ogasawara, H.; et al. Lattice-Strain

Control of the Activity in Dealloyed Core-shell Fuel Cell Catalysts. *Nat. Chem.* **2010**, *2*, 454–460.

(7) Khorshidi, A.; Violet, J.; Hashemi, J.; Peterson, A. A. How Strain Can Break the Scaling Relations of Catalysis. *Nat. Catal.* **2018**, *1*, 263–268.

(8) Wang, L.; Zhang, W.; Zheng, X.; Chen, Y.; Wu, W.; Qiu, J.; Zhao, X.; Zhao, X.; Dai, Y.; Zeng, J. Incorporating Nitrogen Atoms into Cobalt Nanosheets as A Strategy to Boost Catalytic Activity Toward CO₂ Hydrogenation. *Nat. Energy* **2017**, *2*, 869–876.

(9) Wang, X.; Zhu, Y.; Vasileff, A.; Jiao, Y.; Chen, S.; Song, L.; Zheng, B.; Zheng, Y.; Qiao, S.-Z. Strain Effect in Bimetallic Electrocatalysts in the Hydrogen Evolution Reaction. *ACS Energy Lett.* **2018**, *3*, 1198–1204.

(10) Ling, T.; Yan, D.-Y.; Wang, H.; Jiao, Y.; Hu, Z.; Zheng, Y.; Zheng, L.; Mao, J.; Liu, H.; Du, X.-W.; et al. Activating Cobalt(II) Oxide Nanorods for Efficient Electrocatalysis by Strain Engineering. *Nat. Commun.* **2017**, *8*, 1509.

(11) Stamenkovic, V. R.; Strmcnik, D.; Lopes, P. P.; Markovic, N. M. Energy and Fuels from Electrochemical Interfaces. *Nat. Mater.* **2017**, *16*, 57–69.

(12) Subbaraman, R.; Tripkovic, D.; Chang, K. C.; Strmcnik, D.; Paulikas, A. P.; Hirunsit, P.; Chan, M.; Greeley, J.; Stamenkovic, V.; Markovic, N. M. Trends in Activity for the Water Electrolyser Reactions on 3d M(Ni,Co,Fe,Mn) Hydr(Oxy)Oxide Catalysts. *Nat. Mater.* **2012**, *11*, 550–557.

(13) Bayatsarmadi, B.; Zheng, Y.; Tang, Y.; Jaroniec, M.; Qiao, S.-Z. Significant Enhancement of Water Splitting Activity of N-Carbon Electrocatalyst by Trace Level Co Doping. *Small* **2016**, *12*, 3703–3711.

(14) Jiao, Y.; Zheng, Y.; Davey, K.; Qiao, S.-Z. Activity Origin and Catalyst Design Principles for Electrocatalytic Hydrogen Evolution on Heteroatom-Doped Graphene. *Nat. Energy* **2016**, *1*, 16130.

(15) Dang, L.; Liang, H.; Zhuo, J.; Lamb, B. K.; Sheng, H.; Yang, Y.; Jin, S. Direct Synthesis and Anion Exchange of Noncarbonate-Intercalated NiFe-Layered Double Hydroxides and the Influence on Electrocatalysis. *Chem. Mater.* **2018**, *30*, 4321–4330.

(16) Zhu, X.; Dou, X.; Dai, J.; An, X.; Guo, Y.; Zhang, L.; Tao, S.; Zhao, J.; Chu, W.; Zeng, X. C.; et al. Metallic Nickel Hydroxide Nanosheets Give Superior Electrocatalytic Oxidation of Urea for Fuel Cells. *Angew. Chem., Int. Ed.* **2016**, *55*, 12465–12469.

(17) Lei, C.; Wang, Y.; Hou, Y.; Liu, P.; Yang, J.; Zhang, T.; Zhuang, X.; Chen, M.; Yang, B.; Lei, L.; et al. Efficient Alkaline Hydrogen Evolution on Atomically Dispersed Ni–N_x Species Anchored Porous Carbon with Embedded Ni Nanoparticles by Accelerating Water Dissociation Kinetics. *Energy Environ. Sci.* **2019**, *12*, 149–156.

(18) Zheng, X.; De Luna, P.; García de Arquer, F. P.; Zhang, B.; Becknell, N.; Ross, M. B.; Li, Y.; Banis, M. N.; Li, Y.; Liu, M.; et al. Sulfur-Modulated Tin Sites Enable Highly Selective Electrochemical Reduction of CO₂ to Formate. *Joule* **2017**, *1*, 794–805.

(19) Liu, X.; Dai, L. Carbon-Based Metal-Free Catalysts. *Nat. Rev. Mater.* **2016**, *1*, 16064.

(20) Jin, H.; Guo, C.; Liu, X.; Liu, J.; Vasileff, A.; Jiao, Y.; Zheng, Y.; Qiao, S.-Z. Emerging Two-Dimensional Nanomaterials for Electrocatalysis. *Chem. Rev.* **2018**, *118*, 6337–6408.

(21) Jin, H.; Liu, X.; Jiao, Y.; Vasileff, A.; Zheng, Y.; Qiao, S.-Z. Constructing Tunable Dual Active Sites on Two-Dimensional C₃N₄@MoN Hybrid for Electrocatalytic Hydrogen Evolution. *Nano Energy* **2018**, *53*, 690–697.

(22) Zhang, J.; Zhao, Z.; Xia, Z.; Dai, L. A Metal-Free Bifunctional Electrocatalyst for Oxygen Reduction and Oxygen Evolution Reactions. *Nat. Nanotechnol.* **2015**, *10*, 444–452.

(23) Zheng, Y.; Jiao, Y.; Ge, L.; Jaroniec, M.; Qiao, S. Z. Two-Step Boron and Nitrogen Doping in Graphene for Enhanced Synergistic Catalysis. *Angew. Chem.* **2013**, *125*, 3192–3198.

(24) Wu, Y.; Liu, X.; Han, D.; Song, X.; Shi, L.; Song, Y.; Niu, S.; Xie, Y.; Cai, J.; Wu, S.; et al. Electron Density Modulation of NiCo₂S₄ Nanowires by Nitrogen Incorporation for Highly Efficient Hydrogen Evolution Catalysis. *Nat. Commun.* **2018**, *9*, 1425.

(25) Jiao, Y.; Zheng, Y.; Jaroniec, M.; Qiao, S. Z. Design of Electrocatalysts for Oxygen- and Hydrogen-Involving Energy Conversion Reactions. *Chem. Soc. Rev.* **2015**, *44*, 2060–2086.

(26) Voiry, D.; Yamaguchi, H.; Li, J.; Silva, R.; Alves, D. C. B.; Fujita, T.; Chen, M.; Asefa, T.; Shenoy, V. B.; Eda, G.; Chhowalla, M. Enhanced Catalytic Activity in Strained Chemically Exfoliated WS₂ Nanosheets for Hydrogen Evolution. *Nat. Mater.* **2013**, *12*, 850–855.

(27) You, B.; Liu, X.; Hu, G.; Gul, S.; Yano, J.; Jiang, D.-e.; Sun, Y. Universal Surface Engineering of Transition Metals for Superior Electrocatalytic Hydrogen Evolution in Neutral Water. *J. Am. Chem. Soc.* **2017**, *139*, 12283–12290.

(28) Hu, C.; Ma, Q.; Hung, S.-F.; Chen, Z.-N.; Ou, D.; Ren, B.; Chen, H. M.; Fu, G.; Zheng, N. In Situ Electrochemical Production of Ultrathin Nickel Nanosheets for Hydrogen Evolution Electrocatalysis. *Chem.* **2017**, *3*, 122–133.

(29) Li, Y.; Tan, X.; Chen, S.; Bo, X.; Ren, H.; Smith, S. C.; Zhao, C. Processable Surface Modification of Nickel-Heteroatom (N, S) Bridge Sites for Promoted Alkaline Hydrogen Evolution. *Angew. Chem.* **2018**, *131*, 471–476.

(30) Yang, J.; Qiu, Z.; Zhao, C.; Wei, W.; Chen, W.; Li, Z.; Qu, Y.; Dong, J.; Luo, J.; Li, Z.; et al. In Situ Thermal Atomization to Convert Supported Nickel Nanoparticles into Surface-Bound Nickel Single-Atom Catalysts. *Angew. Chem.* **2018**, *130*, 14291–14296.

(31) Jiang, J.; Sun, F.; Zhou, S.; Hu, W.; Zhang, H.; Dong, J.; Jiang, Z.; Zhao, J.; Li, J.; Yan, W.; et al. Atomic-Level Insight into Super-Efficient Electrocatalytic Oxygen Evolution on Iron and Vanadium Co-Doped Nickel (Oxy)Hydroxide. *Nat. Commun.* **2018**, *9*, 2885.

(32) Caban-Acevedo, M.; Stone, M. L.; Schmidt, J. R.; Thomas, J. G.; Ding, Q.; Chang, H. C.; Tsai, M. L.; He, J. H.; Jin, S. Efficient Hydrogen Evolution Catalysis using Ternary Pyrite-Type Cobalt Phosphosulphide. *Nat. Mater.* **2015**, *14*, 1245–1251.

(33) Mahmood, J.; Li, F.; Jung, S. M.; Okyay, M. S.; Ahmad, I.; Kim, S. J.; Park, N.; Jeong, H. Y.; Baek, J. B. An Efficient and pH-Universal Ruthenium-Based Catalyst for the Hydrogen Evolution Reaction. *Nat. Nanotechnol.* **2017**, *12*, 441–446.

(34) Li, F.; Han, G.-F.; Noh, H.-J.; Ahmad, I.; Jeon, I.-Y.; Baek, J.-B. Mechanochemically Assisted Synthesis of a Ru Catalyst for Hydrogen Evolution with Performance Superior to Pt in Both Acidic and Alkaline Media. *Adv. Mater.* **2018**, *30*, 1803676.

(35) Mahmood, J.; Anjum, M. A. R.; Shin, S.-H.; Ahmad, I.; Noh, H.-J.; Kim, S.-J.; Jeong, H. Y.; Lee, J. S.; Baek, J.-B. Encapsulating Iridium Nanoparticles Inside a 3D Cage-Like Organic Network as an Efficient and Durable Catalyst for the Hydrogen Evolution Reaction. *Adv. Mater.* **2018**, *30*, 1805606.

(36) Chen, G.; Wang, T.; Zhang, J.; Liu, P.; Sun, H.; Zhuang, X.; Chen, M.; Feng, X. Accelerated Hydrogen Evolution Kinetics on NiFe-Layered Double Hydroxide Electrocatalysts by Tailoring Water Dissociation Active Sites. *Adv. Mater.* **2018**, *30*, 1706279.

(37) Greeley, J.; Mavrikakis, M. Alloy Catalysts Designed from First Principles. *Nat. Mater.* **2004**, *3*, 810–815.

Supporting Information

Heteroatom-Doped Transition Metal Electrocatalysts for Hydrogen Evolution Reaction

*Huanyu Jin,^a Xin Liu,^a Shuangming Chen,^b Anthony Vasileff,^a Laiquan Li,^a Yan Jiao,^a Li Song,^b
Yao Zheng,^{*a} and Shi-Zhang Qiao^{*a}*

^a School of Chemical Engineering, The University of Adelaide, Adelaide, SA 5005, Australia

^b National Synchrotron Radiation Laboratory, CAS Center for School of Chemical Engineering,
Excellence in Nanoscience, University of Science and Technology of China, Hefei 230029,
Anhui, P. R. China.

Corresponding Authors

*E-mail: s.qiao@adelaide.edu.au

*E-mail: yao.zheng01@adelaide.edu.au

This PDF file includes:

Experimental Methods

Figures S1 to S18

Tables S1 to S3

References 1-23

Experimental Methods

Synthesis of Ni and Co Nanoparticle. Carbon supported Ni nanoparticles were synthesized by a pyrolysis method.¹ First, 0.59 g ethylenediaminetetraacetic acid (EDTA) and 1.0 mL triethylamine were added to 30 mL DMF at 80 °C. Then, 1.16316 g $\text{Ni}(\text{NO}_3)_2 \cdot 6\text{H}_2\text{O}$ / 1.1642 g $\text{Co}(\text{NO}_3)_2 \cdot 6\text{H}_2\text{O}$ was dissolved in 20 mL N,N-dimethylformamide (DMF) solution and mixed with EDTA solution with continuous stirring. After reacting for 30 min, $\text{Ni}_2(\text{EDTA})/\text{Co}_2(\text{EDTA})$ was formed by a complexation reaction and collected by centrifugation, subsequently washed with DMF, and dried in an oven at 80 °C. The precursor was then placed into a tube furnace and heated to 500 °C under Ar atmosphere at a rate of 5 °C min⁻¹. After maintaining a temperature of 500 °C for 2h, the sample was cooled to room temperature and the carbon supported Ni nanoparticles were obtained.

Process of Nitrogen Doping. Nitrogen doping was realized using NH_3 gas as the nitrogen source. In detail, 100 mg $\text{Ni}_2(\text{EDTA})/\text{Co}_2(\text{EDTA})$ was placed in the center of a tube furnace. Then the precursor was heated under Ar atmosphere at a rate of 5 °C min⁻¹. When the temperature reached 390 °C, the gas was changed to 5% NH_3/Ar and kept for 2 min with a flow rate of 15 sccm. The gas was then changed back to Ar (150 sccm) and the temperature was ramped to 500 °C with at a rate of 5 °C min⁻¹. After maintaining a temperature of 500°C for 2h, the tube furnace was cooled to room temperature at a rate of 10 °C min⁻¹.

Process of Phosphorus Doping. Sodium dihydrogen phosphate (NaH_2PO_4) was chosen as the phosphorus source. In detail, 100 mg $\text{Ni}_2(\text{EDTA})/\text{Co}_2(\text{EDTA})$ was placed in the center of a tube furnace. 20 mg NaH_2PO_4 was place at the upstream side and near to $\text{Ni}_2(\text{EDTA})/\text{Co}_2(\text{EDTA})$. The precursor was then heated to 500 °C under Ar atmosphere (150 sccm) at a heating rate of 5 °C min⁻¹. After maintaining a temperature of 500°C for 2h, the tube furnace was cooled to room temperature at a rate of 10 °C min⁻¹.

Process of Sulfur Doping. Sulfur powder was used as the sulfur source. Typically, 2 mg of sulfur and 100 mg $\text{Ni}_2(\text{EDTA})$ were placed at opposite sides of a porcelain boat with sulfur at the upstream side of the tube furnace. Subsequently, the sample was heated to 500 °C with the heating rate of 5 °C min⁻¹ under an Ar flow rate of 150 sccm. After maintaining a temperature of 500°C for 2h, the product was cooled to ambient temperature under Ar.

Process of N-P doping. N-P doping was realized using NH_3 gas and NaH_2PO_4 as the nitrogen and phosphorus source. In detail, 100 mg $\text{Ni}_2(\text{EDTA})/\text{Co}_2(\text{EDTA})$ was placed in the center of a tube furnace. 20 mg NaH_2PO_4 was placed at the upstream side and near to $\text{Ni}_2(\text{EDTA})/\text{Co}_2(\text{EDTA})$. Then the tube furnace was heated under Ar atmosphere at a rate of $5\text{ }^\circ\text{C min}^{-1}$. When the temperature reached $390\text{ }^\circ\text{C}$, the gas was changed to 5% NH_3/Ar and kept for 2 min with a flow rate of 15 sccm. The gas was then changed back to Ar (150 sccm) and the temperature was ramped to $500\text{ }^\circ\text{C}$ with at a rate of $5\text{ }^\circ\text{C min}^{-1}$. After maintaining a temperature of 500°C for 2h, the tube furnace was cooled to room temperature at a rate of $10\text{ }^\circ\text{C min}^{-1}$.

Process of N-S doping. N-S doping was realized using NH_3 gas and sulfur powder as the nitrogen and sulfur source. In detail, 100 mg $\text{Ni}_2(\text{EDTA})$ was placed in the center of a tube furnace. 2 mg sulfur was placed at the upstream side and near to $\text{Ni}_2(\text{EDTA})$. Then the tube furnace was heated under Ar atmosphere at a rate of $5\text{ }^\circ\text{C min}^{-1}$. When the temperature reached $390\text{ }^\circ\text{C}$, the gas was changed to 5% NH_3/Ar and kept for 2 min with a flow rate of 15 sccm. The gas was then changed back to Ar (150 sccm) and the temperature was ramped to $500\text{ }^\circ\text{C}$ with at a rate of $5\text{ }^\circ\text{C min}^{-1}$. After maintaining a temperature of 500°C for 2h, the tube furnace was cooled to room temperature at a rate of $10\text{ }^\circ\text{C min}^{-1}$.

Process of S-P doping. S-P doping was realized using NaH_2PO_4 and sulfur powder as the phosphorus and sulfur source. In detail, 100 mg $\text{Ni}_2(\text{EDTA})$ was placed in the center of a tube furnace. 2 mg sulfur and 20 mg NaH_2PO_4 was placed at the upstream side and near to $\text{Ni}_2(\text{EDTA})$. Subsequently, the sample was heated to $500\text{ }^\circ\text{C}$ with the heating rate of $5\text{ }^\circ\text{C min}^{-1}$ under an Ar flow rate of 150 sccm. After maintaining a temperature of 500°C for 2h, the product was cooled to ambient temperature under Ar.

Synthesis of Ni_3N and Ni_2P . $\text{Ni}(\text{OH})_2$ was purchased from Sigma-Aldrich. In a typical procedure, Ni_3N was prepared by annealing $\text{Ni}(\text{OH})_2$ at $390\text{ }^\circ\text{C}$ for 2 hours at a heating rate of $3\text{ }^\circ\text{C min}^{-1}$ under 5% NH_3/Ar atmosphere (flow rate of 50 sccm). Ni_2P was prepared by adding 50 mg of $\text{Ni}(\text{OH})_2$ to the center of a tube furnace with 1.0 g of NaH_2PO_2 being placed upstream of it. After it was flushed with Ar gas, the center of the furnace was quickly elevated to the reaction temperature of $400\text{ }^\circ\text{C}$ at a ramp rate of $10\text{ }^\circ\text{C min}^{-1}$ and kept at $400\text{ }^\circ\text{C}$ for 2 h to obtain the nickel phosphides.

Characterization. X-Ray Powder Diffraction (XRD) data was collected on a Rigaku MiniFlex 600 X-Ray Diffractometer. The transmission electron microscope images, aberration-corrected TEM images, high-angle annular dark-field imaging and EDS data were taken on a FEI Titan Themis 80-200 operating at 200 kV.

The synchrotron-based XPS and XANES measurements were carried out on the soft X-ray spectroscopy beamline at the Australian Synchrotron, which is equipped with a hemispherical electron analyzer and a microchannel plate detector that enables simultaneous recording of the total electron yield and partial electron yield. The raw XANES and XPS data were normalized to the photoelectron current of the photon beam, measured on an Au grid.

The Ni K edge XAS spectra were collected in transmission mode (Si 111) at the 1W1B Endstation of Beijing Synchrotron Radiation Facility (BSRF) in China. The data was normalized and analyzed using WinXAS3.1 software.² Theoretical amplitudes and phase-shift functions of Ni-N, Ni-P and Ni-Ni were calculated with the FEFF8.2 code³ using the crystal structural parameters of the Ni₃N, Ni₂P and Ni foil, respectively. A Cauchy wavelet was used to wavelet transform the k^3 -weighted EXAFS signals (Funke, H., Chukalina, M., Wavelet Transform for EXAFS: <http://www.esrf.eu/UsersAndScience/Experiments/CRG/BM20/Software/Wavelets.>).

Computational Details. Spin-polarized density functional theory (DFT) calculations were performed using the Vienna *ab initio* simulation package (VASP).⁴⁻⁷ The exchange–correlation interactions were treated within the generalized gradient approximation (GGA) in the form of the Perdew–Burke–Ernzerhof (PBE) function.⁸ The van der Waals interactions were described using the empirical correction in Grimme’s scheme.⁹ The electron wave functions were expanded using plane waves with a cutoff energy of 500 eV, and the convergence criteria of energy change during all calculations were set to 10^{-4} eV. The Brillouin zone was sampled by $(3 \times 3 \times 1)$ Monkhorst–Pack k-point mesh. The top two layers of the slab were allowed to relax together with the adsorbates and the convergence threshold for structural optimization was set to be 0.01 eV/Å. In order to avoid interactions between periodic images, a vacuum space of 20 Å was applied to all calculations. For density of state calculations, the k-points was set to be $7 \times 7 \times 1$. The free energy diagram along the reaction pathway was calculated as follows:

$$\Delta G = \Delta E_{\text{ad}} + \Delta E_{\text{ZPE}} - T\Delta S + \Delta G_{\text{sol}}$$

where ΔE_{ad} is the adsorption energy defined as the electronic energy difference ; ΔE_{ZPE} is the change in zero-point energies, T is the temperature ($T = 298.15\text{K}$), and ΔS is the entropy changes. ΔG_{sol} represents the correction terms for solvent effect, 0 eV for H^* ,¹⁰ and -0.5 eV for OH^* ¹¹.

Electrochemical Measurements. The electrochemical measurements were undertaken in a standard three-electrode cell (PINE research, USA) in 1 M KOH. Typically, 5 mg of catalyst (e.g. N-P-Ni) was dispersed in 1 mL of deionized water which contains 0.1 wt% of Nafion. Next, 20 μL of catalyst dispersion (5 mg mL^{-1}) was transferred onto a glassy carbon rotating disk electrode (diameter 5 mm, loading mass: 0.5 mg cm^{-2}) serving as the working electrode. The Ag/AgCl in 4 M AgCl-KCl solution and graphite rod were chosen as the reference electrode and counter electrode, respectively. The working electrodes were scanned several times until the current response stabilized. All potentials were referenced to the reversible hydrogen electrode according to Nernst equation ($E_{\text{RHE}} = E_{\text{Ag/AgCl}} + 0.059 \times \text{pH} + 0.205$), and all polarization curves were corrected for the iR compensation within the cell. A flow of Ar (30 sccm) was maintained over the electrolyte during the experiment to eliminate dissolved oxygen and nitrogen. The working electrode was rotated at 1,600 rpm to remove the hydrogen gas which was formed on the catalyst surface.

Figures

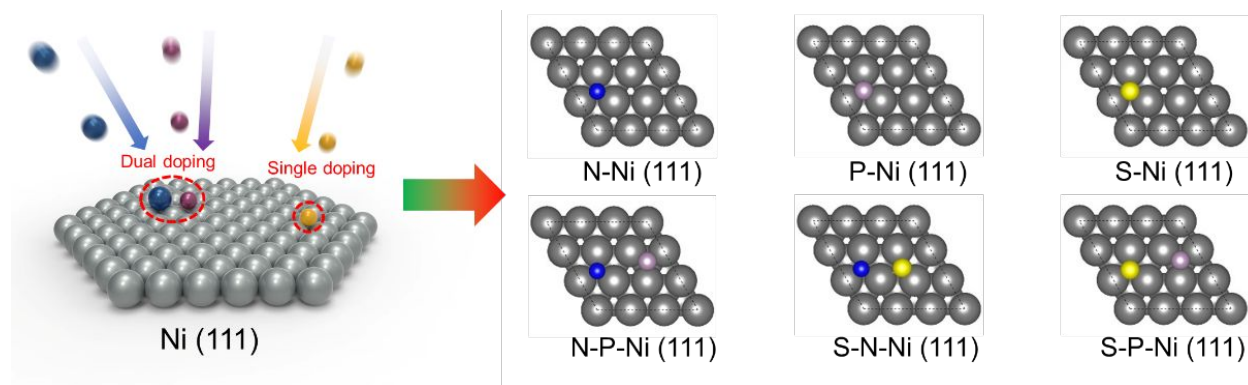


Figure S1. Schematic diagram of heteroatom doped Ni catalysts.

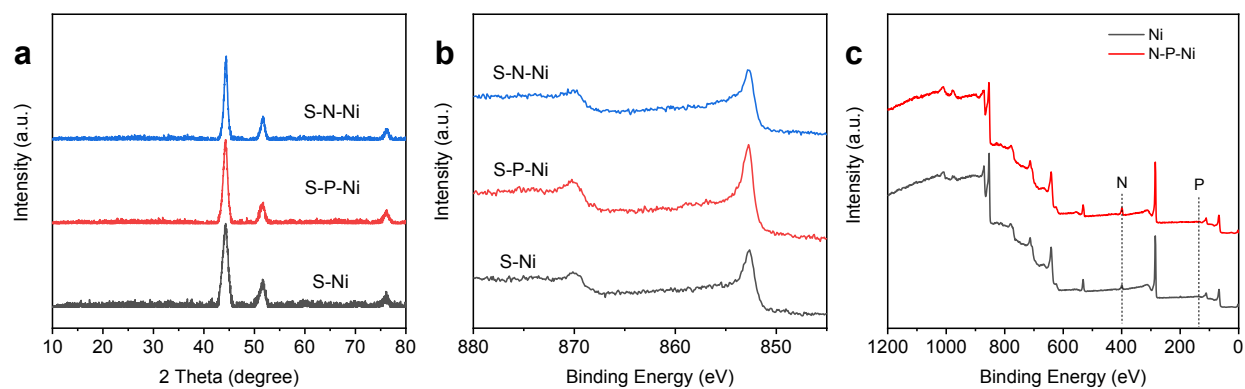


Figure S2. XRD patterns (a) and Ni 2p XPS spectra (b) of S-Ni, S-P-Ni and S-N-Ni, (c) XPS survey scan of Ni and N-P-Ni.

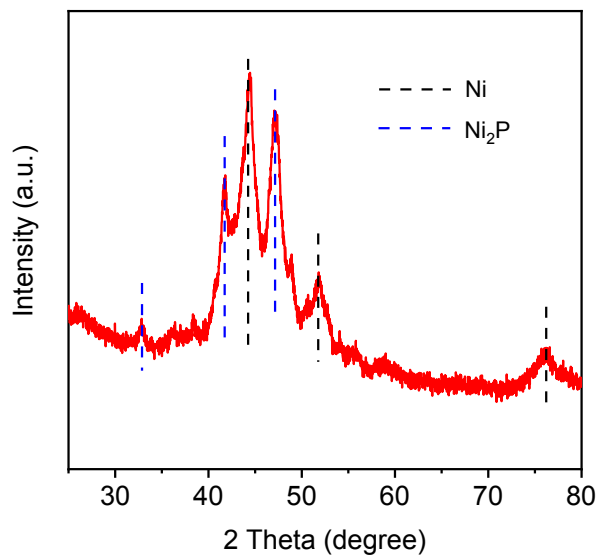


Figure S3. XRD pattern of the P doped Ni when the amount of NaH_2PO_4 is added up to 25 mg.

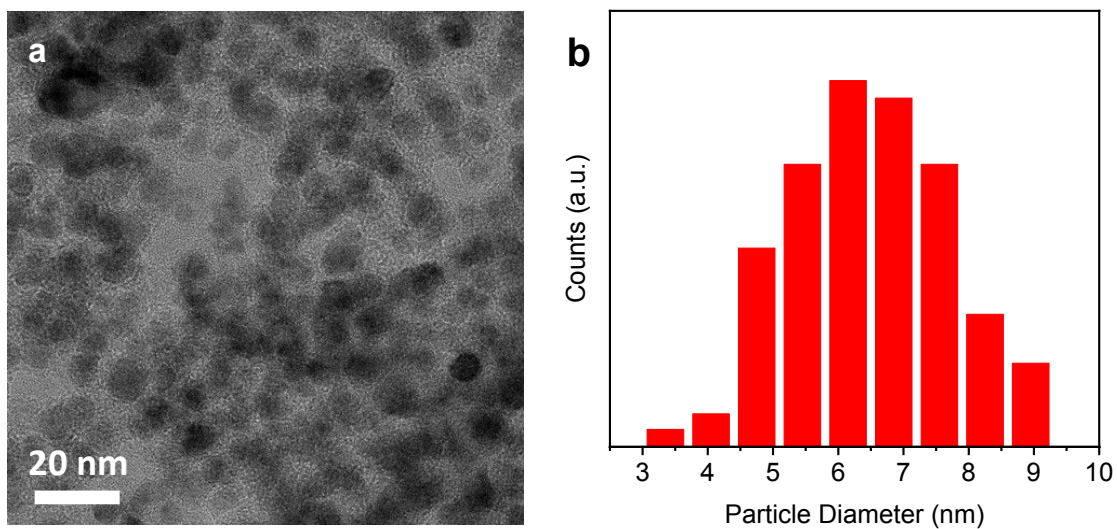


Figure S4. (a) TEM image and (b) Average particle size of N-P-Ni.

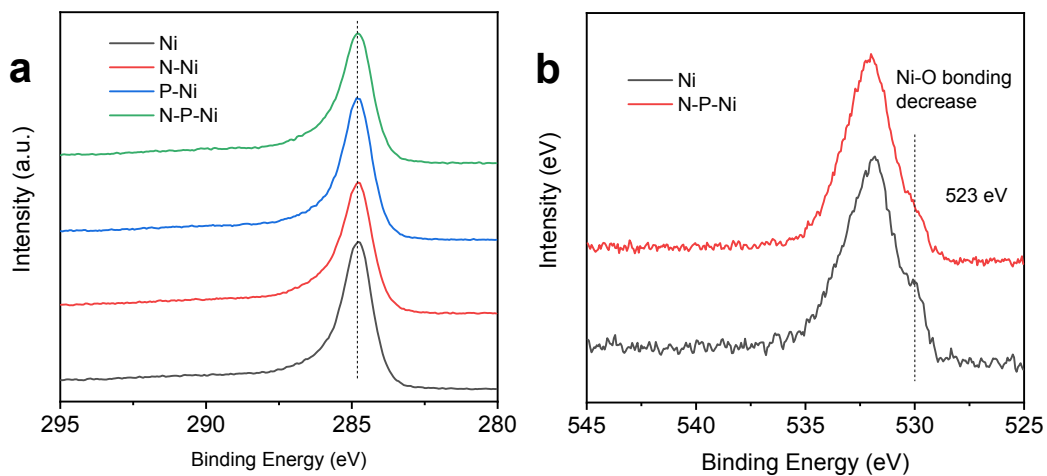


Figure S5. (a) C 1s XPS spectra of Ni, N-Ni, P-Ni and N-P-Ni. (b) O 1s XPS spectra of Ni and N-P-Ni.

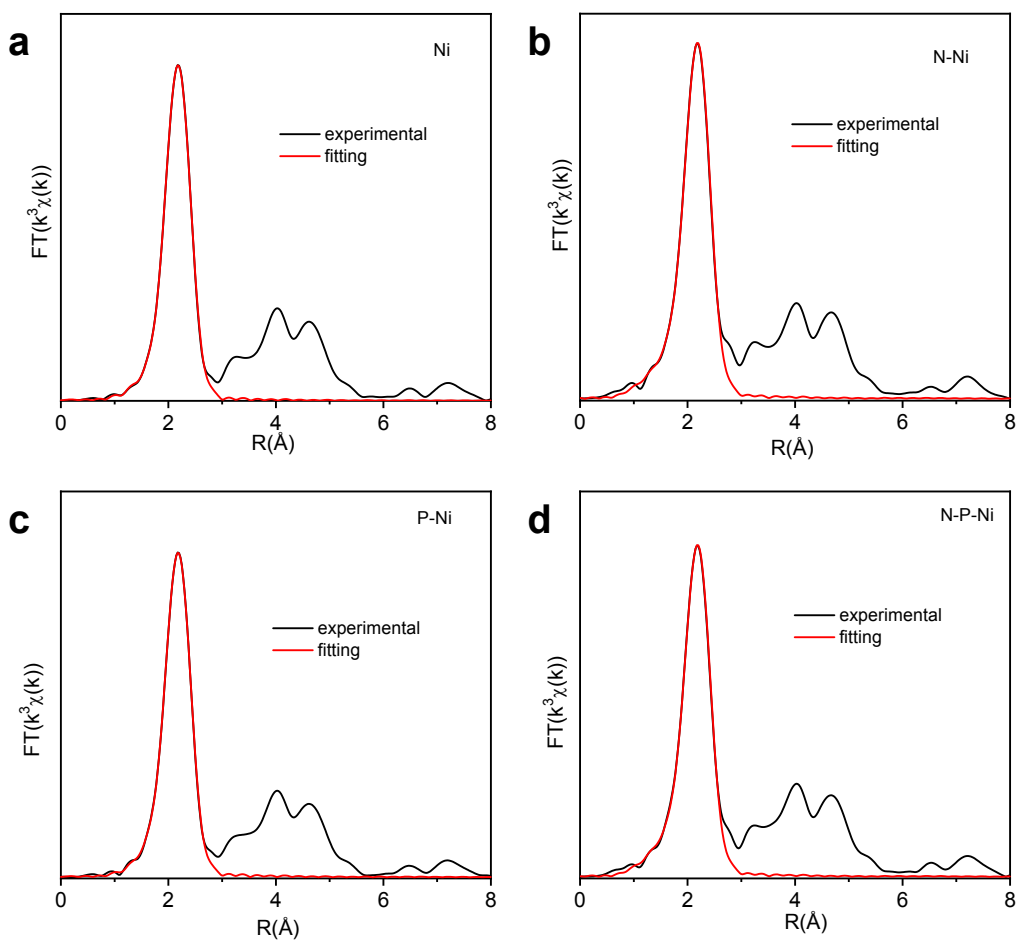


Figure S6. Synchrotron-based XAS fitting results of (a) Ni, (b) N-Ni, (c) P-Ni, and (d) N-P-Ni.

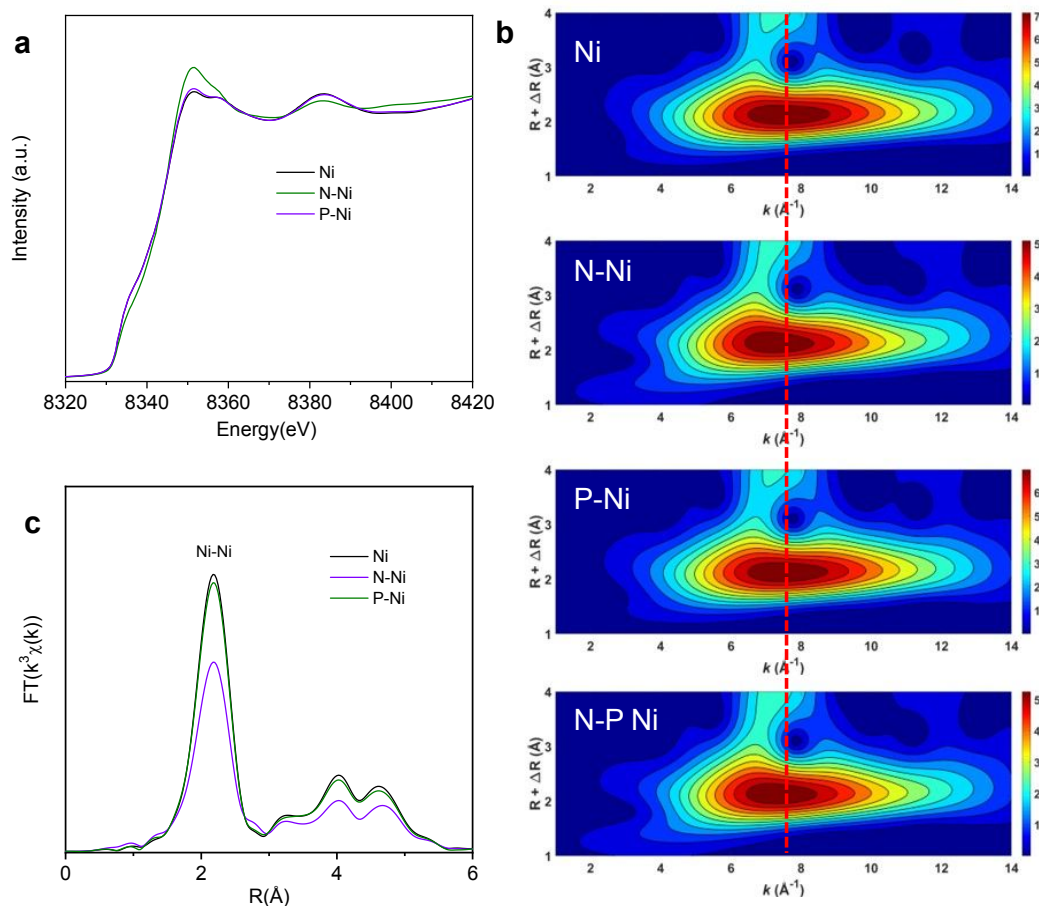


Figure S7. (a) Synchrotron-based XAS spectra of Ni, P-Ni and N-Ni. (b) WT-EXFAS plot of Ni, P-Ni, N-Ni and N-P-Ni. (c) EXAFS of Ni, P-Ni and N-Ni.

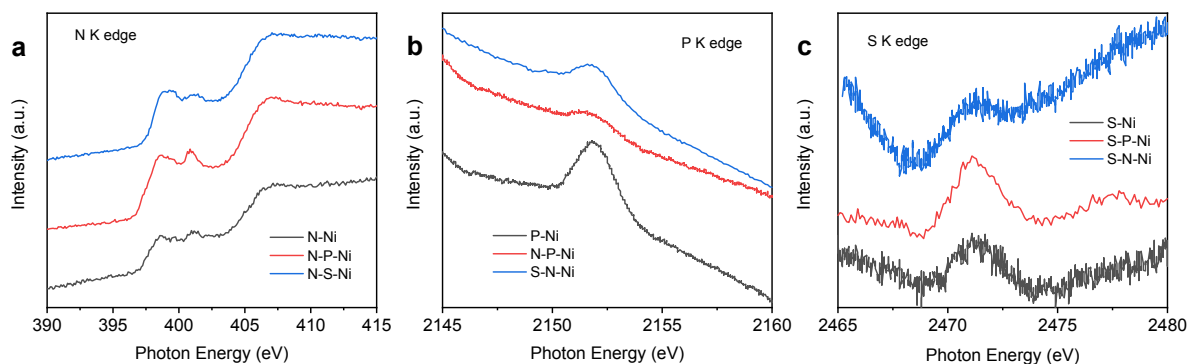


Figure S8. (a) Synchrotron-based N K edge XANES spectra of N-Ni, N-P-Ni and S-N-Ni. (b) P K edge of P-Ni, N-P-Ni and S-P-Ni. (c) S K edge of S-Ni, S-P-Ni and S-N-Ni.

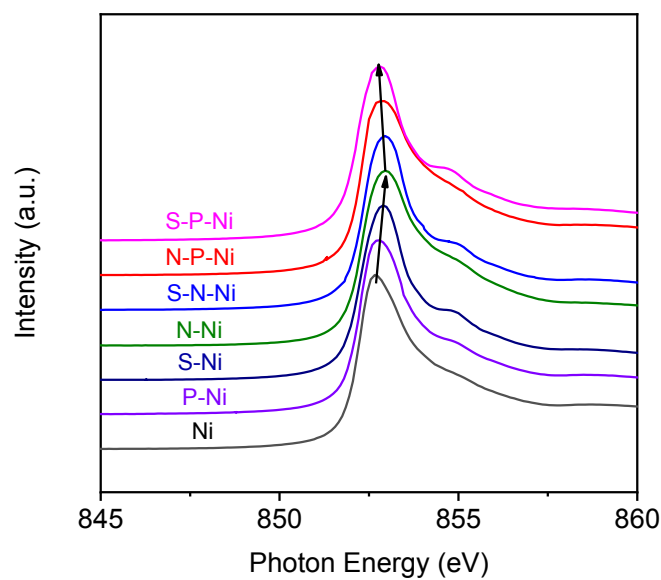


Figure S9. Synchrotron-based Ni L_3 edge XANES spectra of different catalysts.

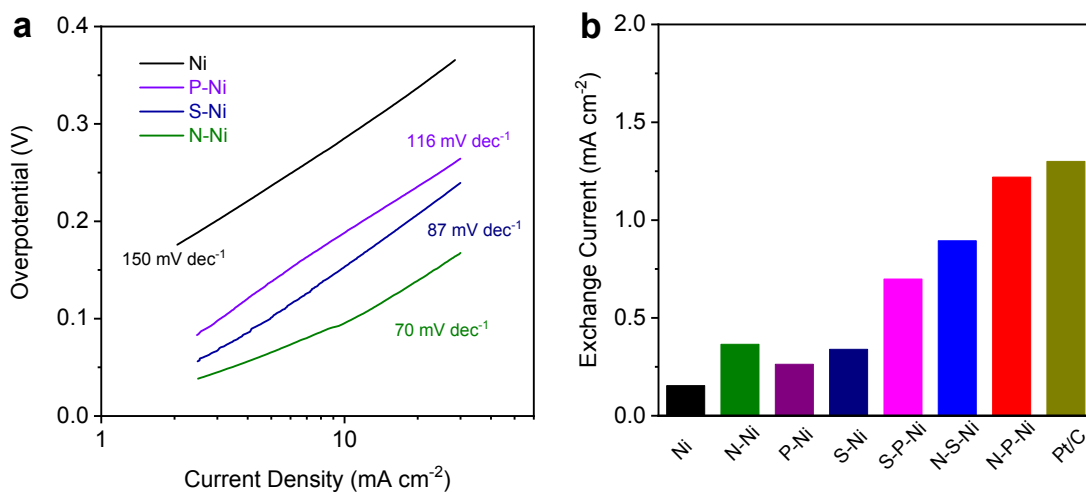


Figure S10. (a) Tafel plot of single and dual-doped Ni catalysts. (b) Exchange current density of different catalysts.

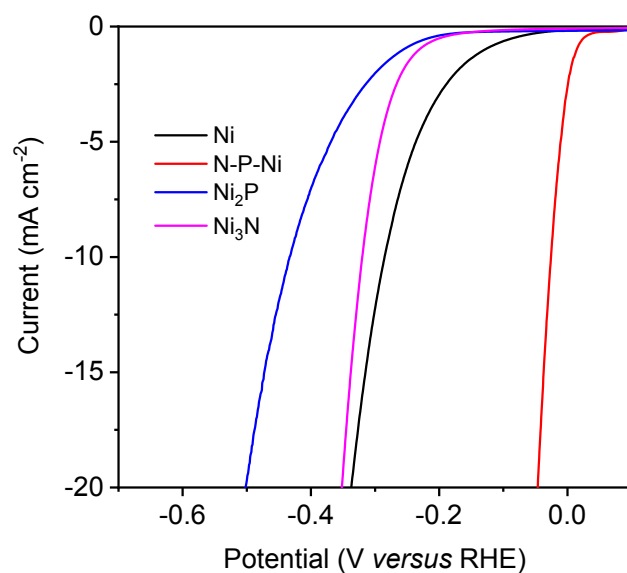


Figure S11. LSV curves of Ni, N-P-Ni, Ni₂P and Ni₃N.

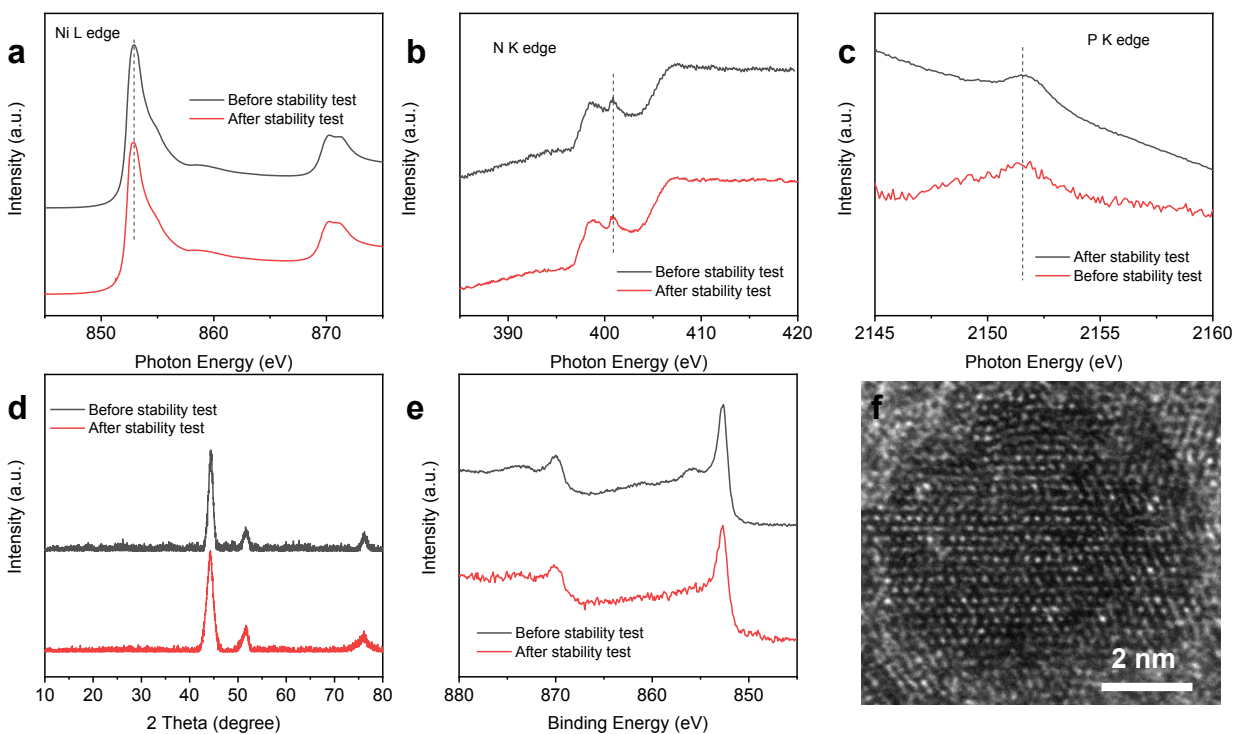


Figure S12. Synchrotron-based (a) Ni L edge (b) N K edge and (c) P K edge of N-P-Ni before and after stability test. (d) XRD patterns and (e) Ni 2p spectra of N-P-Ni before and after stability test. (f) HRTEM image of N-P-Ni after stability test.

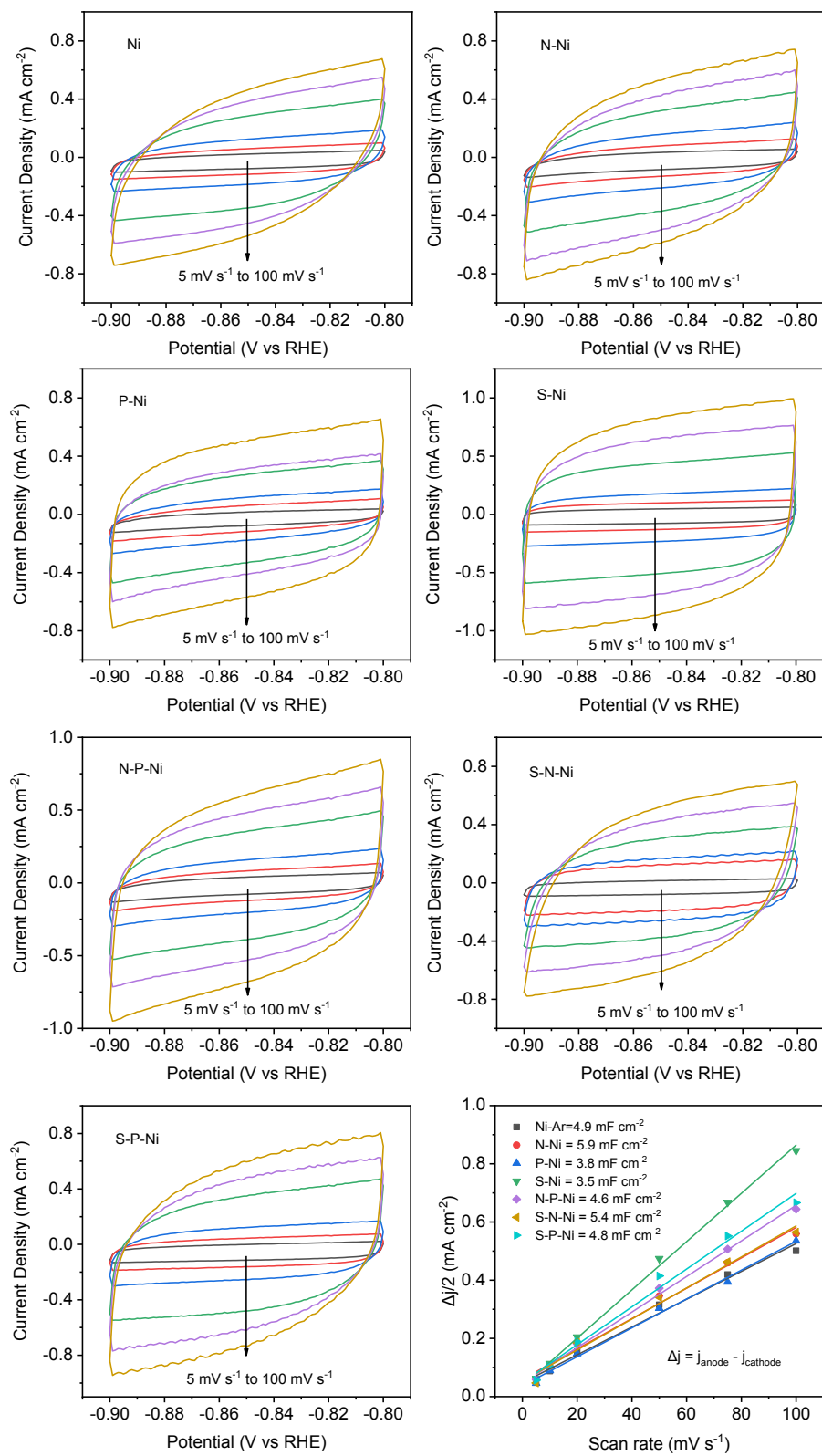


Figure S13. CV measurements for testing the ECSA of different catalysts.

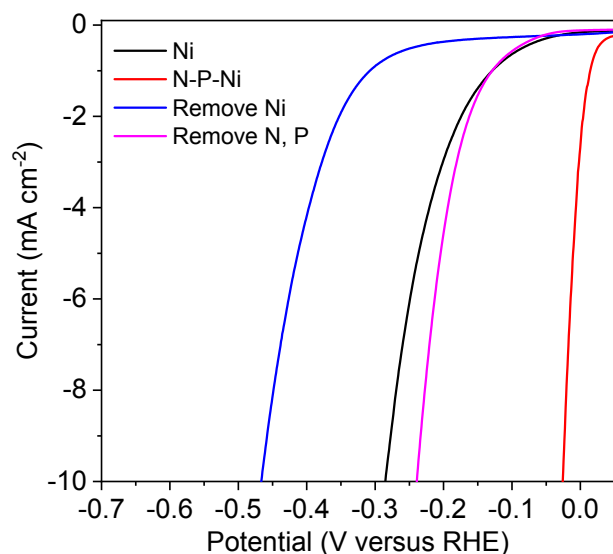


Figure S14. LSV curves of Ni, N-P-Ni, N-P-Ni (removing Ni using acid wash) and N-P-Ni (removing N, P by hydrogen annealing). After removing Ni or heteroatoms using acid wash or annealing in hydrogen, the HER activity enhancement is vanished. Consequently, the enhanced activity originates from the heteroatom doping.

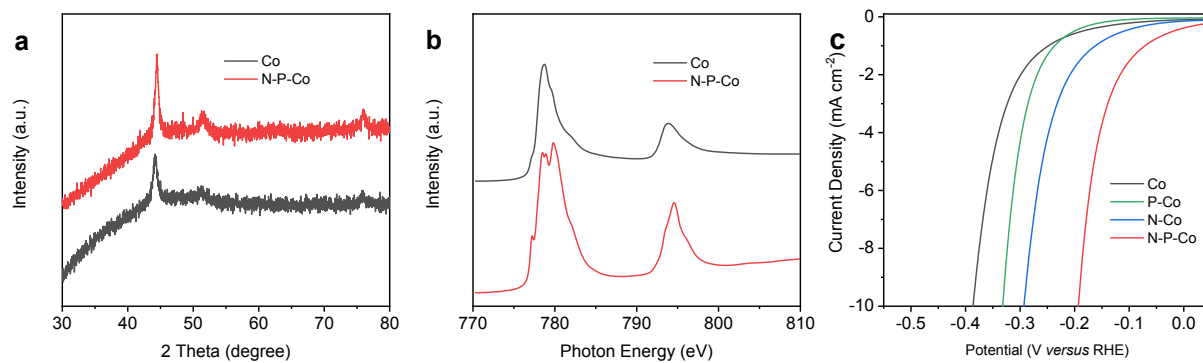


Figure S15. (a) XRD patterns, (b) Synchrotron-based Co L edge, (c) LSV curves of Co, P-Co, N-Co and N-P-Co.

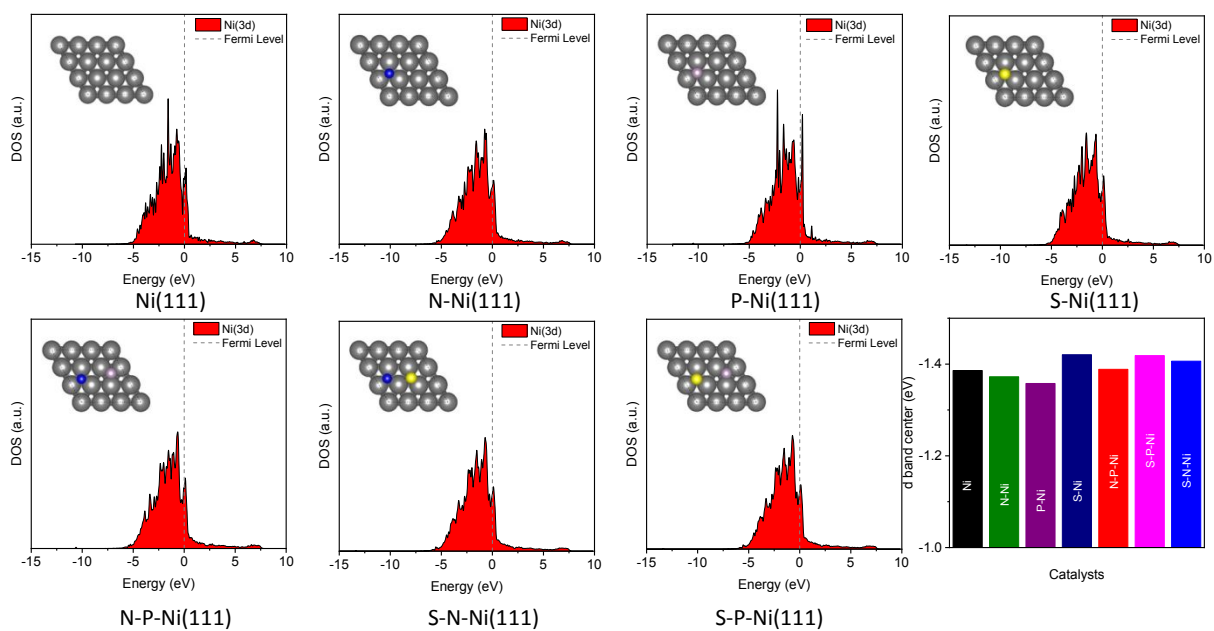


Figure S16. DOS of different samples and their *d* band center positions.

Tables

Table S1. Elemental contents of different catalysts obtained from XPS measurement.

Sample	C %	N %	O %	Ni %	S %	P %
Ni	77.53	5.23	6.6	10.64		
N-Ni	76.43	7.33	5.2	11.04		
P-Ni	77.23	4.78	5.8	11.63		0.56
S-Ni	77.2	5.04	5.96	11.24	0.56	
N-P-Ni	76.46	6.9	5.2	10.89		0.55
S-P-Ni	76.67	5.16	6.1	11.03	0.53	0.51
N-S-Ni	76.15	7.06	5.3	10.94	0.55	

Table S2. EXAFS curve-fitting results.

Sample	Path	N	R [Å]	$\sigma^2(10^{-3} \text{ \AA}^2)$
Ni	Ni-C	1.7	1.97	22.3
	Ni-Ni	9.0	2.48	7.6
N-Ni	Ni-C/N	2.9	1.99	23.8
	Ni-Ni	7.6	2.49	9.0
P-Ni	Ni-C/P	2.0	2.02	22.8
	Ni-Ni	8.9	2.48	7.7
N-P-Ni	Ni-C/N/P	3.2	2.00	24.3
	Ni-Ni	7.6	2.49	8.7
Ni ₃ N	Ni-N	2*	1.88	5.1
	Ni-Ni	12*	2.65	9.1
Ni ₂ P	N-P	4*	2.23	8.1
	Ni-Ni	8*	2.61	8.9
Ni foil	Ni-Ni	12*	2.48	6.2

N , coordination number; R , bond length; σ^2 , Debye-Waller factor; Error bounds (accuracies) were estimated as N , $\pm 10\%$; R , $\pm 1\%$; σ^2 , $\pm 10\%$. * is fixed coordination number according to the standard crystal structure.

Table S3. Summary of HER performances of different catalysts in alkaline media.

Sample	Loading amount (mg cm ⁻²)	η_{10} (mV)	Tafel (mV dec ⁻¹)	i_0 (mA cm ⁻²)	Electrolyte	Reference
N-P-Ni	0.51	-25.8	34	1.22	1 M KOH	This work
Pt/C (commerical)	0.51	-21.3	32	1.3	1 M KOH	This work
Ni	0.51	-285	150	0.154	1 M KOH	This work
N-Ni	0.51	-95	70	0.37	1 M KOH	This work
P-Ni	0.51	-187	116	0.26	1 M KOH	This work
S-Ni	0.51	-153	87	0.34	1 M KOH	This work
S-N-Ni	0.51	-62	53	0.89	1 M KOH	This work
S-P-Ni	0.51	-88	66	0.70	1 M KOH	This work
Pt/C (commerical)	0.5	-23	37	1.29	1 M KOH	Ref. ¹²
Ir/C (commerical)	0.5	-28.3	32	0.66	1 M KOH	Ref. ¹²
Ir@CON	0.5	-12.9	29	1.4	1 M KOH	Ref. ¹²
Ru/NC	0.013	-21	31	2.43	1 M KOH	Ref. ¹³
Ru/GnP	0.25	-22	28	-	1 M KOH	Ref. ¹⁴
RuO₂/NiO/NF	0.2	-22	31.7	-	1 M KOH	Ref. ¹⁵
RuCo@NC	0.275	-28	31	~0.56	1 M KOH	Ref. ¹⁶
PtNi-O/C	0.0051	-39.8	-	-	1 M KOH	Ref. ¹⁷
Ru@CN	0.25	-32	53	-	1 M KOH	Ref. ¹⁸
Ru@C₃N₄	-	-79	-	-	0.1 M KOH	Ref. ¹⁹
RuO₂-CN_x	-	-95	70	0.28	0.5 M KOH	Ref. ²⁰
NiCoP@Ru	0.28	-52	42	-	1 M KOH	Ref. ²¹
Co(OH)₂/Pt(111)	-	-248	-	-	0.1 M KOH	Ref. ²²
RuP₂@NPC	1	-52	69	1.99	1 M KOH	Ref. ²³

References

- (1) Lee, K. J.; Sa, Y. J.; Jeong, H. Y.; Bielawski, C. W.; Joo, S. H.; Moon, H. R. Simple Coordination Complex-Derived Three-Dimensional Mesoporous Graphene as an Efficient Bifunctional Oxygen Electrocatalyst. *Chem. Commun.* **2015**, *51*, 6773-6776.
- (2) Ressler, T. WinXAS: a Program for X-ray Absorption Spectroscopy Data Analysis under MS-Windows. *Journal of Synchrotron Radiation* **1998**, *5*, 118-122.
- (3) Ankudinov, A. L.; Ravel, B.; Rehr, J. J.; Conradson, S. D. Real-Space Multiple-Scattering Calculation and Interpretation of X-Ray-Absorption Near-Edge Structure. *Phys. Rev. B* **1998**, *58*, 7565-7576.
- (4) Kresse, G.; Furthmüller, J. Efficiency of *Ab-Initio* Total Energy Calculations for Metals and Semiconductors Using a Plane-Wave Basis Set. *Computational Materials Science* **1996**, *6*, 15-50.
- (5) Kresse, G.; Furthmüller, J. Efficient Iterative Schemes for *Ab Initio* Total-Energy Calculations Using a Plane-Wave Basis Set. *Phys. Rev. B* **1996**, *54*, 11169-11186.
- (6) Kresse, G.; Hafner, J. *Ab Initio* Molecular Dynamics for Liquid Metals. *Phys. Rev. B* **1993**, *47*, 558-561.
- (7) Kresse, G.; Hafner, J. *Ab Initio* Molecular-Dynamics Simulation of the Liquid-Metal–Amorphous-Semiconductor Transition in Germanium. *Phys. Rev. B* **1994**, *49*, 14251-14269.
- (8) Perdew, J. P.; Burke, K.; Ernzerhof, M. Generalized Gradient Approximation Made Simple. *Phys. Rev. Lett.* **1996**, *77*, 3865-3868.
- (9) Grimme, S. Semiempirical GGA-Type Density Functional Constructed with a Long-Range Dispersion Correction. *J. Comput. Chem.* **2006**, *27*, 1787-1799.
- (10) Norskov, J. K.; Bligaard, T.; Logadottir, A.; Kitchin, J. R.; Chen, J. G.; Pandelov, S.; Norskov, J. K. Trends in the Exchange Current for Hydrogen Evolution. *J Electrochem Soc* **2005**, *152*, J23-J26.
- (11) Li, Y. W.; Su, H. B.; Chan, S. H.; Sun, Q. CO₂ Electroreduction Performance of Transition Metal Dimers Supported on Graphene: A Theoretical Study. *ACS Catal.* **2015**, *5*, 6658-6664.

- (12) Mahmood, J.; Anjum, M. A. R.; Shin, S.-H.; Ahmad, I.; Noh, H.-J.; Kim, S.-J.; Jeong, H. Y.; Lee, J. S.; Baek, J.-B. Encapsulating Iridium Nanoparticles Inside a 3D Cage-Like Organic Network as an Efficient and Durable Catalyst for the Hydrogen Evolution Reaction. *Adv. Mater.* **2018**, *30*, 1805606.
- (13) Zhang, J.; Liu, P.; Wang, G.; Zhang, P. P.; Zhuang, X. D.; Chen, M. W.; Weidinger, I. M.; Feng, X. L. Ruthenium/Nitrogen-Doped Carbon as an Electrocatalyst for Efficient Hydrogen Evolution in Alkaline Solution. *J. Mater. Chem. A* **2017**, *5*, 25314-25318.
- (14) Li, F.; Han, G.-F.; Noh, H.-J.; Ahmad, I.; Jeon, I.-Y.; Baek, J.-B. Mechanochemically Assisted Synthesis of a Ru Catalyst for Hydrogen Evolution with Performance Superior to Pt in Both Acidic and Alkaline Media. *Adv. Mater.* **2018**, *30*, 1803676.
- (15) Liu, J.; Zheng, Y.; Jiao, Y.; Wang, Z.; Lu, Z.; Vasileff, A.; Qiao, S.-Z. NiO as a Bifunctional Promoter for RuO₂ toward Superior Overall Water Splitting. *Small* **2018**, *14*, 1704073.
- (16) Su, J.; Yang, Y.; Xia, G.; Chen, J.; Jiang, P.; Chen, Q. Ruthenium-Cobalt Nanoalloys Encapsulated in Nitrogen-Doped Graphene as Active Electrocatalysts for Producing Hydrogen in Alkaline Media. *Nat. Commun.* **2017**, *8*, 14969.
- (17) Zhao, Z.; Liu, H.; Gao, W.; Xue, W.; Liu, Z.; Huang, J.; Pan, X.; Huang, Y. Surface-Engineered PtNi-O Nanostructure with Record-High Performance for Electrocatalytic Hydrogen Evolution Reaction. *J. Am. Chem. Soc.* **2018**, *140*, 9046-9050.
- (18) Yao, Y.; Huang, Z.; Xie, P.; Lacey, S. D.; Jacob, R. J.; Xie, H.; Chen, F.; Nie, A.; Pu, T.; Rehwoldt, M. *et al.* Carbothermal Shock Synthesis Of High-Entropy-Alloy Nanoparticles. *Science* **2018**, *359*, 1489.
- (19) Zheng, Y.; Jiao, Y.; Zhu, Y.; Li, L. H.; Han, Y.; Chen, Y.; Jaroniec, M.; Qiao, S.-Z. High Electrocatalytic Hydrogen Evolution Activity of an Anomalous Ruthenium Catalyst. *J. Am. Chem. Soc.* **2016**, *138*, 16174-16181.
- (20) Bhowmik, T.; Kundu, M. K.; Barman, S. Growth of One-Dimensional RuO₂ Nanowires on g-Carbon Nitride: An Active and Stable Bifunctional Electrocatalyst for Hydrogen and Oxygen Evolution Reactions at All pH Values. *ACS Appl. Mater. Interfaces* **2016**, *8*, 28678-28688.

(21) Liu, S.; Liu, Q.; Lv, Y.; Chen, B.; Zhou, Q.; Wang, L.; Zheng, Q.; Che, C.; Chen, C. Ru Decorated with NiCoP: an Efficient and Durable Hydrogen Evolution Reaction Electrocatalyst in Both Acidic and Alkaline Conditions. *Chem. Commun.* **2017**, *53*, 13153-13156.

(22) Subbaraman, R.; Tripkovic, D.; Chang, K. C.; Strmcnik, D.; Paulikas, A. P.; Hirunsit, P.; Chan, M.; Greeley, J.; Stamenkovic, V.; Markovic, N. M. Trends in Activity for The Water Electrolyser Reactions on 3d M(Ni,Co,Fe,Mn) Hydr(Oxy)Oxide Catalysts. *Nat. Mater.* **2012**, *11*, 550-557.

(23) Pu, Z.; Amiin, I. S.; Kou, Z.; Li, W.; Mu, S. RuP₂-Based Catalysts with Platinum-like Activity and Higher Durability for the Hydrogen Evolution Reaction at All pH Values. *Angew. Chem. Int. Ed.* **2017**, *56*, 11559-11564.

Chapter 6: Nitrogen Vacancies on 2D Layered W_2N_3 : A Stable and Efficient Active Site for Nitrogen Reduction Reaction

6.1 Introduction and Significance

Electrochemical nitrogen reduction to ammonia provides an alternative route to produce carbon-free energy carriers for clean energy systems. However, the selectivity and activity of the nitrogen reduction reaction (NRR) is hindered by the competitive hydrogen evolution reaction and sluggish reaction kinetics. In this regard, vacancy-engineered two-dimensional (2D) tungsten nitride (W_2N_3), a novel layered Van der Waals 2D transition metal nitride, was used as a catalyst for high performance NRR under ambient conditions. By vacancy and morphology engineering, the as-prepared W_2N_3 nanosheets exhibit high ammonia production rate ($11.66 \pm 0.98 \mu\text{g h}^{-1} \text{mg}_{\text{cat}}^{-1}$) and Faradaic efficiency ($11.67 \pm 0.93\%$) under ambient conditions. The NRR on vacancy-rich 2D W_2N_3 occurs via a distal mechanism without nitrogen atoms detaching from the crystal lattice, confirmed by $^{15}\text{N}_2$ isotopic labelling experiments and theoretical calculations. The density of state calculation also shows that the nitrogen vacancies on 2D W_2N_3 have an electron-deficient environment which can promote dinitrogen adsorption and activation. The highlights of this Chapter include:

- A new layered van der Waals 2D W_2N_3 nanosheet is prepared and utilized as a NRR catalyst.
- Nitrogen vacancies on 2D layered W_2N_3 is a selective and stable active site for NRR.
- A series of ex situ synchrotron-based X-ray absorption measurements are adopted to study the local coordination of nitrogen vacancies during the NRR.
- The enhanced NRR performance of 2D W_2N_3 was determined by density function theory calculations.
- This study provides insight into vacancy-engineered 2D materials for clean energy storage and conversion systems.


6.2 Nitrogen Vacancies on 2D Layered W_2N_3 : A Stable and Efficient Active Site for Nitrogen Reduction Reaction

This Chapter is included as it appears as a journal paper published by **Huanyu Jin**, Laiquan Li, Xin Liu, Cheng Tang, Wenjie Xu, Shuangming Chen, Li Song, Yao Zheng, Shi-Zhang Qiao, Nitrogen Vacancies on 2D Layered W_2N_3 : A Stable and Efficient Active Site for Nitrogen Reduction Reaction. *Adv. Mater.* 2019, 31, 1902709.

Statement of Authorship

Title of Paper	Nitrogen Vacancies on 2D Layered W_2N_3 : A Stable and Efficient Active Site for Nitrogen Reduction Reaction
Publication Status	<input checked="" type="checkbox"/> Published <input type="checkbox"/> Accepted for Publication <input type="checkbox"/> Submitted for Publication <input type="checkbox"/> Unpublished and Unsubmitted work written in manuscript style
Publication Details	Huanyu Jin, Laiquan Li, Xin Liu, Cheng Tang, Wenjie Xu, Shuangming Chen, Li Song, Yao Zheng, Shi-Zhang Qiao* Nitrogen Vacancies on 2D Layered W_2N_3 : A Stable and Efficient Active Site for Nitrogen Reduction Reaction. Adv. Mater. 2019, 31, 1902709.


Principal Author


Name of Principal Author (Candidate)	Huanyu Jin		
Contribution to the Paper	Research plan, material synthesis, most of the characterizations and data analysis, electrochemical characterization, and manuscript draft.		
Overall percentage (%)	70		
Certification:	This paper reports on original research I conducted during the period of my Higher Degree by Research candidature and is not subject to any obligations or contractual agreements with a third party that would constrain its inclusion in this thesis. I am the primary author of this paper.		
Signature		Date	22/June/2020

Co-Author Contributions

By signing the Statement of Authorship, each author certifies that:

- the candidate's stated contribution to the publication is accurate (as detailed above);
- permission is granted for the candidate to include the publication in the thesis; and
- the sum of all co-author contributions is equal to 100% less the candidate's stated contribution.

Name of Co-Author	Laiquan Li		
Contribution to the Paper	Assistance with electrochemical tests and data analysis.		
Signature		Date	22/June/2020

Name of Co-Author	Xin Liu		
Contribution to the Paper	Computational calculations.		
Signature		Date	22/June/2020

Name of Co-Author	Cheng Tang		
Contribution to the Paper	Discussion, evaluation, and revision of this manuscript.		
Signature		Date	22/June/2020

Name of Co-Author	Wenjie Xu		
Contribution to the Paper	Data analysis.		
Signature		Date	22/June/2020

Name of Co-Author	Shuangming Chen		
Contribution to the Paper	Data analysis.		
Signature		Date	22/June/2020

Name of Co-Author	Li Song		
Contribution to the Paper	Data analysis.		
Signature		Date	22/June/2020

Name of Co-Author	Yao Zheng		
Contribution to the Paper	Discussion of this manuscript.		
Signature		Date	22/June/2020

Name of Co-Author	Shi-Zhang Qiao		
Contribution to the Paper	Supervision of the work, discussion of this manuscript and manuscript evaluation.		
Signature		Date	22/June/2020

Please cut and paste additional co-author panels here as required.

Nitrogen Vacancies on 2D Layered W_2N_3 : A Stable and Efficient Active Site for Nitrogen Reduction Reaction

Huanyu Jin, Laiquan Li, Xin Liu, Cheng Tang, Wenjie Xu, Shuangming Chen, Li Song, Yao Zheng, and Shi-Zhang Qiao*

Electrochemical nitrogen reduction reaction (NRR) under ambient conditions provides an avenue to produce carbon-free hydrogen carriers. However, the selectivity and activity of NRR are still hindered by the sluggish reaction kinetics. Nitrogen Vacancies on transition metal nitrides are considered as one of the most ideal active sites for NRR by virtue of their unique vacancy properties such as appropriate adsorption energy to dinitrogen molecule. However, their catalytic performance is usually limited by the unstable feature. Herein, a new 2D layered W_2N_3 nanosheet is prepared and the nitrogen vacancies are demonstrated to be active for electrochemical NRR with a steady ammonia production rate of $11.66 \pm 0.98 \mu\text{g h}^{-1} \text{mg}_{\text{cata}}^{-1}$ ($3.80 \pm 0.32 \times 10^{-11} \text{ mol cm}^{-2} \text{ s}^{-1}$) and Faradaic efficiency of $11.67 \pm 0.93\%$ at -0.2 V versus reversible hydrogen electrode for 12 cycles (24 h). A series of ex situ synchrotron-based characterizations prove that the nitrogen vacancies on 2D W_2N_3 are stable by virtue of the high valence state of tungsten atoms and 2D confinement effect. Density function theory calculations suggest that nitrogen vacancies on W_2N_3 can provide an electron-deficient environment which not only facilitates nitrogen adsorption, but also lowers the thermodynamic limiting potential of NRR.

Artificial nitrogen fixation offers an appealing route to traditional agriculture and clean energy fields that can facilitate the food production and carbon-free energy generation in a sustainable way.^[1–3] However, due to the strong triple-bond in dinitrogen molecule (bond energy of $940.95 \text{ kJ mol}^{-1}$), it is very difficult to reduce N_2 to NH_3 mildly.^[4–6] In industry, the main route to produce NH_3 is through the Haber–Bosch process under harsh synthetic conditions, which costs $\approx 2\%$ of the annual energy consumption of the world.^[1,7–9] Meanwhile, the hydrogen used in Haber–Bosch process is mainly obtained from steam reforming of natural gas, which could

also aggravate the greenhouse effect.^[8] Considering the huge energy consumption of this process and the great potential of NH_3 in future energy systems, proton-assisted electrocatalytic nitrogen reduction reaction (NRR) under ambient conditions is becoming increasingly important in realizing low-cost artificial nitrogen fixation.^[10–12] More importantly, the NRR system can be easily integrated with renewable solar and wind energy into an environmentally benign process for NH_3 production.^[2,7] Even though various materials have shown NRR activity in aqueous system, their performance are still hindered by the sluggish reaction kinetics and competitive hydrogen evolution reaction (HER) resulting in poor activity and unsatisfactory selectivity.^[13–15]


The active site for electrochemical NRR needs twofold properties: for one thing, it can accept the lone-pair electrons for effective N_2 adsorption and for the other thing

it can donate electrons to antibonding orbitals of dinitrogen molecules for the $N \equiv N$ triple-bond activation.^[9,13,16–20] From this perspective, vacancy-engineering materials are ideal for practical applications.^[9,16,20] By virtue of the electron redistribution and special chemical properties, the vacancies can provide unique active sites for nitrogen adsorption and activation.^[9,21–24] Up to now, the most common vacancy that has been studied for NRR is oxygen vacancy. For example, oxygen vacancies on transition metal oxides are active for NRR by enhancing the dinitrogen molecule adsorption.^[9,25] However, oxygen vacancy can also improve the HER performance of the host matrix, which may result in poor NRR selectivity.^[26–28]

Alternatively, nitrogen vacancies on transition metal nitride (TMN) are considered as an ideal active site for NRR because of its unique vacancy properties for dinitrogen molecule adsorption and poor HER activity.^[29,30] However, the nitrogen vacancy on TMN would be deactivated during NRR process thus results in poor stability.^[29] In addition, researchers claim that some TMNs are inactive toward NRR in aqueous system, which is in contrary to theoretical calculations.^[31] To gain insightful understanding of NRR mechanism, it is necessary to design TMNs with simplex structure and stable surface vacancies for the linkage of theoretical models and real-world catalysts. 2D material has onefold and fully exposed crystal surface, which is widely used as platform for both theoretical calculations and

H. Jin, L. Li, X. Liu, Dr. C. Tang, Dr. Y. Zheng, Prof. S.-Z. Qiao
School of Chemical Engineering
The University of Adelaide
Adelaide, South Australia 5005, Australia
E-mail: s.qiao@adelaide.edu.au

W. Xu, Dr. S. Chen, Prof. L. Song
National Synchrotron Radiation Laboratory
CAS Center for Excellence in Nanoscience
University of Science and Technology of China
Hefei 230029, Anhui, P. R. China

 The ORCID identification number(s) for the author(s) of this article can be found under <https://doi.org/10.1002/adma.201902709>.

DOI: 10.1002/adma.201902709

practical applications in electrocatalysis.^[7,32–36] In the meantime, many works have shown that 2D materials have surface distortion, which can endow 2D materials and their vacancies with excellent structural stability.^[37–43] Thus, the use of vacancy-engineered 2D TMNs with single exposed crystal facet and stable vacancy-site is a feasible way to construct high-performance NRR catalysts.

Herein, we successfully synthesized a new ultrathin 2D layered W_2N_3 with surface nitrogen vacancies for electrochemical NRR. The NRR activity and stability of nitrogen vacancies on W_2N_3 nanosheets are investigated by mutually corroborating electrochemical experiments and theoretical computation. Significantly, the as-prepared catalysts exhibited an average NH_3 formation rate as high as $11.66 \pm 0.98 \mu g h^{-1} mg_{cata}^{-1}$ ($3.80 \pm 0.32 \times 10^{-11} mol cm^{-2} s^{-1}$) with a high Faradaic efficiency (FE) of $11.67 \pm 0.93\%$ at $-0.2 V$ versus reversible hydrogen electrode (RHE) under ambient conditions. Density functional theory (DFT) calculations suggest that the electron deficient environment induced by nitrogen vacancies on W_2N_3 can effectively facilitate the acceptance of the lone-pair electrons of N_2 and promote the subsequent reduction steps. More importantly, the nitrogen vacancies on 2D W_2N_3 are stable as a result of the high valence state of tungsten atoms and 2D confinement effect,

which have been proved by a series of ex situ characterizations. This new catalyst demonstrates a potential strategy to optimize 2D materials toward high-performance electrochemical NRR under ambient conditions.

The 2D W_2N_3 nanosheets were prepared by annealing $Na_2W_4O_{13}$ under ammonia atmosphere (Figure S1, Supporting Information). The synthesis of W_2N_3 usually needs harsh synthetic conditions (5 GPa and 1480 K) due to the large formation energy of W–N bonding. Inspired by Zhou and co-workers who firstly realized the atmospheric-pressure synthesis of nitrogen-rich transition metal nitride by domain matching epitaxy, the sodium ion in $Na_2W_4O_{13}$ can lead to a facile synthesis of W_2N_3 with lower formation energy.^[35,40] The as-prepared 2D W_2N_3 was then annealed under 5% H_2/Ar at 500 °C for 3 h to generate nitrogen vacancies on W_2N_3 surface (the sample is denoted as NV- W_2N_3). Scanning electron microscopy (SEM) images and transmission electron microscopy (TEM) images (Figure 1a and Figure S2, Supporting Information) show the 2D morphology of W_2N_3 and NV- W_2N_3 with an average lateral size of 500 nm. The X-ray diffraction (XRD) patterns of W_2N_3 and NV- W_2N_3 with almost the same peak positions are shown Figure 1b, in accordance with the standard pattern.^[44] These results indicate

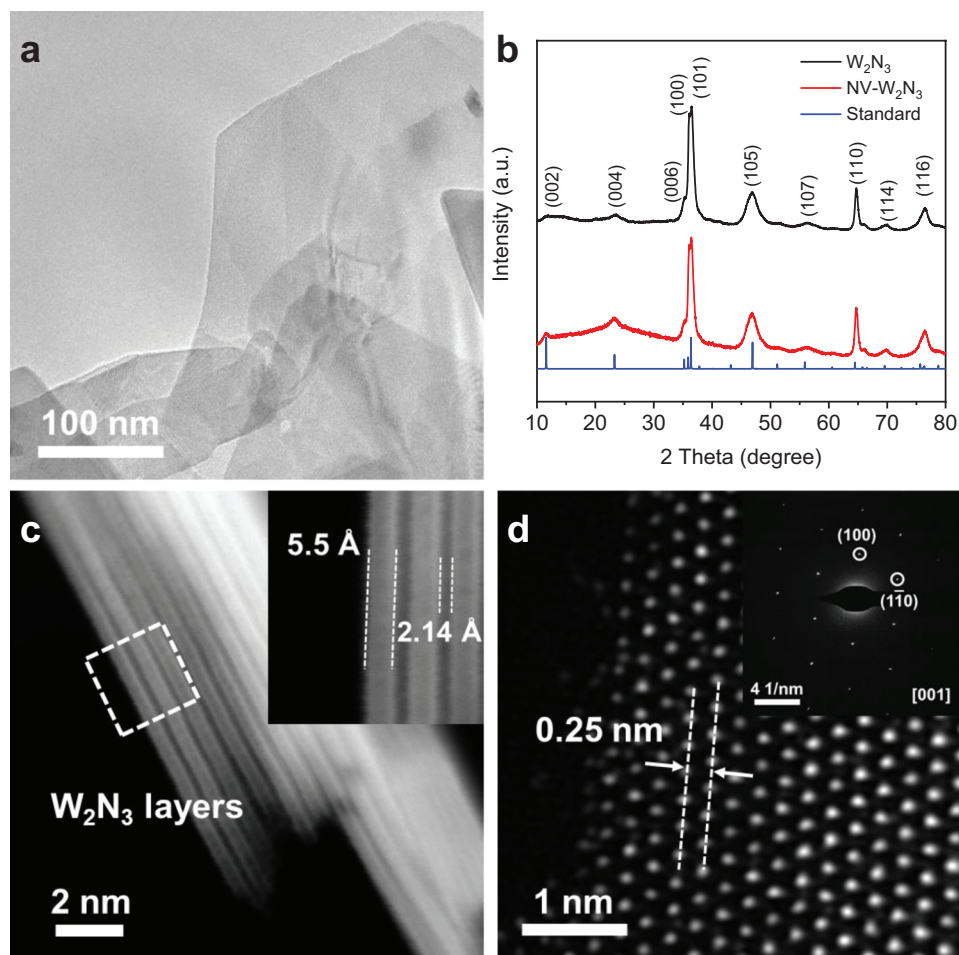


Figure 1. a) TEM image of NV- W_2N_3 . b) XRD patterns of W_2N_3 and NV- W_2N_3 . c) HAADF-STEM images of NV- W_2N_3 that show the single-layered thickness and interlayer spacing of NV- W_2N_3 . d) HAADF-STEM image and corresponding SAED pattern (inset) of NV- W_2N_3 .

that the morphology and crystal structure of W_2N_3 remain unchanged during hydrogen annealing. Aberration-corrected high-angle annular dark-field scanning transmission electron microscopy (HAADF-STEM) image in Figure 1c shows a vertical NV- W_2N_3 nanosheet with the thickness about 6 nm. The layered structure of NV- W_2N_3 can be clearly seen in this image with single-layer thickness of 5.5 Å and interlayer spacing about 2.14 Å, which match well with theoretical values (Figure S3, Supporting Information).^[45] The in-plane crystal parameters of NV- W_2N_3 were determined using aberration-corrected STEM imaging and corresponding selected area electron diffraction (SAED). The STEM image in Figure 1d shows the hexagonal structure of W_2N_3 with an interplanar distance of 0.25 nm for (100) facets. The only one set of diffraction spots in SAED pattern of NV- W_2N_3 reveals its single crystalline nature. The (100) lattice plane spacing of W_2N_3 calculated from SAED results is also 0.25 nm, which is in accordance with aberration-corrected HAADF-STEM images and XRD data.

A range of spectroscopic measurements were conducted to evaluate the electronic structure, and more importantly, the nitrogen vacancies of NV- W_2N_3 at atomic level. As shown in the synchrotron-based X-ray photoelectron spectroscopy (XPS) survey scan in Figure 2a, no chemical composition changes of W_2N_3 is observed before and after hydrogen annealing. However, the W 4f peaks in NV- W_2N_3 are negatively shifted by 0.1 eV

compared to pristine W_2N_3 , which indicates the decreased valence state of W after H_2 annealing (Figure 2b). Furthermore, in N 1s XPS spectra, the intensity of the peak for NV- W_2N_3 around 400.2 eV, which can be assigned to be nitrogen vacancy, increases compared to that of the pristine W_2N_3 , demonstrating a higher amount of nitrogen vacancies on NV- W_2N_3 than that on the pristine W_2N_3 (Figure 2c). By comparing W/N atom ratio through XPS data, the concentration of nitrogen vacancies in NV- W_2N_3 is about 6.6% (% = percentage of nitrogen atoms removed), which is higher than that of pristine W_2N_3 (4.3%). We further conducted elemental sensitive synchrotron-based X-ray adsorption (XAS) measurements to investigate the local coordination of nitrogen vacancies at atomic level. Figure 2d shows the Fourier transform (FT) extended X-ray adsorption fine structure (EXAFS) spectra of the W_2N_3 and NV- W_2N_3 , which are obtained from normalized W L_3 -edge curves (Figure S4, Supporting Information). Both samples show a main coordination peak at 2.8 Å which is assigned to W–W bonding.^[40] However, the intensity of the peak for NV- W_2N_3 at 1.8 Å (W–N bonding) becomes weaker compared to that of the pristine W_2N_3 , indicating the decreased W–N bonding number. Quantitative EXAFS analysis (Table 1 and Figure S5, Supporting Information) also shows that the coordination number of W–N decreases from 4.3 to 4.0 after hydrogen annealing, giving powerful evidence for the formation of nitrogen vacancies. Thus,

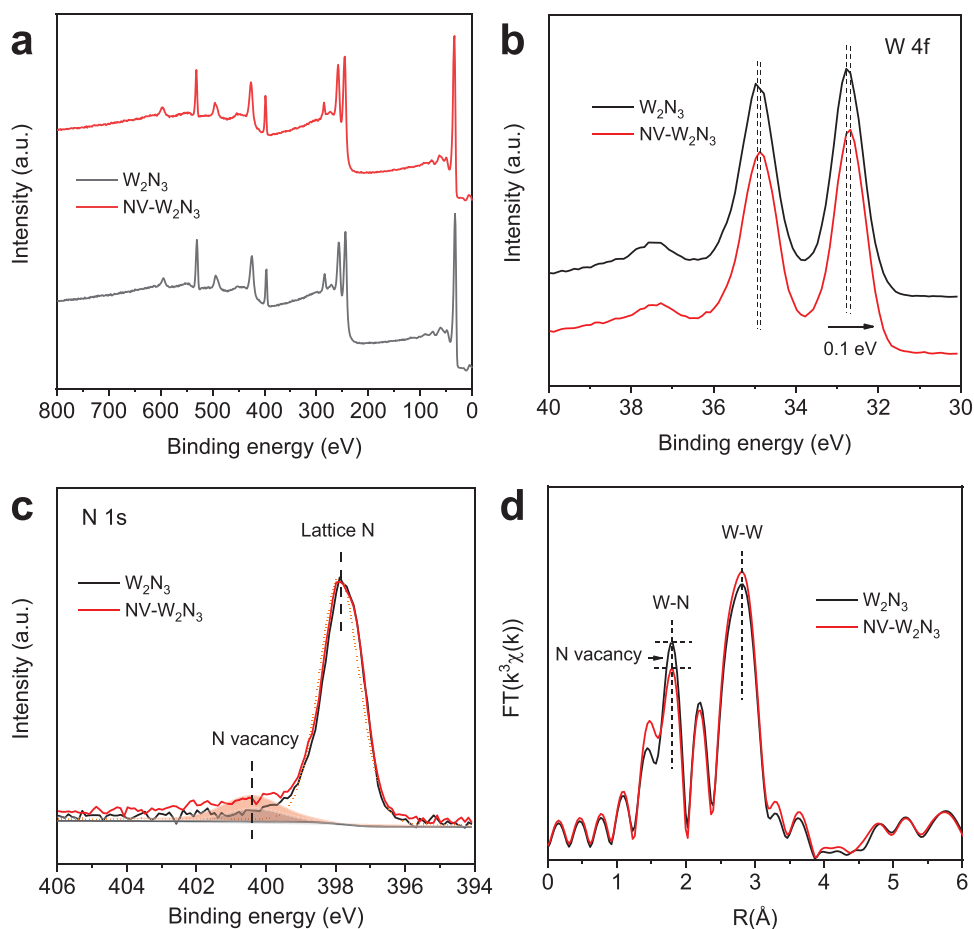


Figure 2. a–d) Synchrotron-based XPS survey scan (a), W 4f spectra (b), N 1s spectra (c), and FT-EXFAS plots (d) of the as-prepared NV- W_2N_3 and W_2N_3 .

Table 1. EXAFS curve-fitting results (Error bounds (accuracies) were estimated as N , $\pm 10\%$; R , $\pm 1\%$; σ^2 , $\pm 10\%$).

Sample	Path	N^a	R [\AA] ^b	σ^2 [10^{-3}\AA^2] ^c
W_2N_3	W–N	4.3	2.11	4.7
	W–W	0.8	2.68	3.9
	W–W	5.4	2.88	4.1
NV- W_2N_3	W–N	4.0	2.09	4.7
	W–W	0.8	2.72	3.2
	W–W	5.4	2.87	3.5
NV- W_2N_3 after stability test	W–N	4.0	2.11	4.9
	W–W	0.8	2.67	3.6
	W–W	5.3	2.88	4.5

^a) N , coordination number; ^b) R , bond length; ^c) σ^2 , Debye–Waller factor.

the synchrotron-based EXAFS results clearly demonstrate the distinct nitrogen vacancy concentrations in the as-obtained two samples, fairly agreeing with the N 1s XPS results.

We then explored the NRR performance of NV- W_2N_3 in 0.10 M KOH using a gas-tight H-cell separated by a proton-exchanged membrane (Nafion 211) at room temperature and atmospheric pressure. Ultrahigh purity N_2 gas (99.999%) was first purged into the cathodic chamber at least for 30 min and then bubbled with a constant flow rate of 20 sccm throughout the electrolysis process. The UV–vis absorption spectra of the electrolytes stained with indophenol indicator after electrolysis

for 2 h were collected to quantify the produced ammonia (Figures S6 and S7, Supporting Information). Ammonia production rates of NV- W_2N_3 at different potentials (Figure S8, Supporting Information) were shown in Figure 3a. The highest ammonia production rate of $11.66 \pm 0.98 \mu\text{g h}^{-1} \text{mg}_{\text{cata}}^{-1}$ ($3.80 \pm 0.32 \times 10^{-11} \text{mol cm}^{-2} \text{s}^{-1}$) was obtained at -0.2 V versus RHE with the Faradaic efficiency of $11.67 \pm 0.93\%$ (Figure 3b and Table S1, Supporting Information), which are comparable to most of the catalysts in aqueous electrolytes under ambient conditions (Table S2, Supporting Information).^[10,20,46–49] In addition, no N_2H_4 by-product was detected under all applied potentials (Figure S9, Supporting Information). To elucidate the importance of nitrogen vacancies on W_2N_3 for NRR, samples that annealed under different temperatures were prepared. As shown in Figure 3c, the NV- W_2N_3 reveals higher ammonia production rate than that of pristine W_2N_3 and the samples obtained from lower annealing temperatures (Figure S10, Supporting Information), which manifests that the NRR activity originates from the nitrogen vacancies. However, the sample with the highest annealing temperature (600°C) exhibits inferior NRR activity, which is attributed to the re-stack of 2D layered materials (smaller electrochemical active surface area) at higher temperature (Figure S11, Supporting Information).

Since the catalysts used in this work contain nitrogen species which may cause false positive results, plenty of control experiments were conducted to exclude possible interference from any contaminants. As shown in Figure 3d, no ammonia could be detected in electrolytes at open-circuit potential (OCP) under

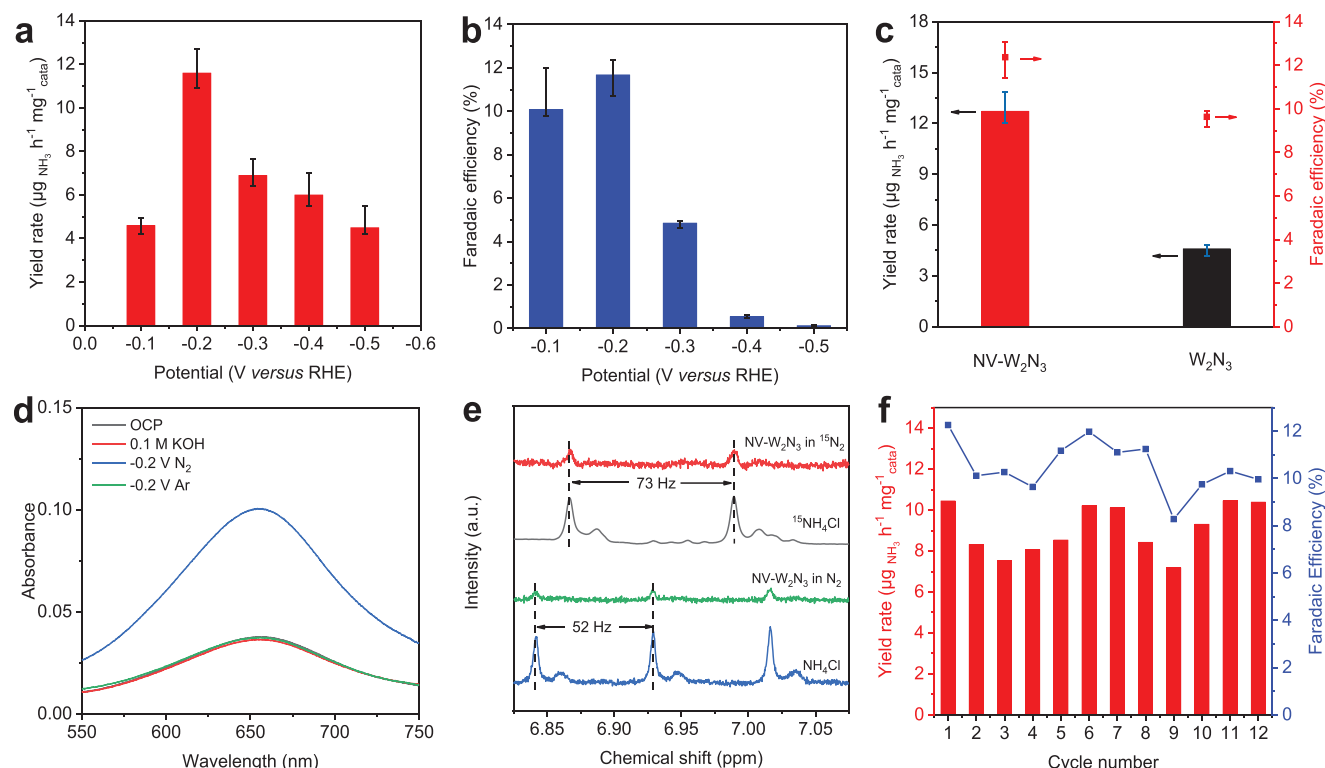


Figure 3. a) NH_3 yield and b) Faradaic efficiency of NV- W_2N_3 at different overpotentials. c) NH_3 yield of NV- W_2N_3 and W_2N_3 at -0.2 V versus RHE. d) UV–vis spectra of electrolytes stained with indophenol indicator for NV- W_2N_3 at different conditions. e) Isotopic labeling results of both $^{14}NH_4^+$ and $^{15}NH_4^+$ obtained from the NRR reaction (at -0.2 V vs RHE) using $^{14}N_2$ or $^{15}N_2$ as the nitrogen source, respectively. f) Cycling stability of NV- W_2N_3 for 12 cycles.

N_2 atmosphere or Ar-saturated solution electrolyzed for 2 h (Figure S12, Supporting Information). In addition, only $^{15}NH_4^+$ is detected in NMR test using $^{15}N_2$ as the feed gas (Figure 3e), indicating the ammonia is produced by electrochemical NRR instead of decomposition of catalysts or other contaminations. Furthermore, we evaluated the catalytic stability of NV- W_2N_3 by testing the ammonia production every 2 h for 12 cycles and 10 h chronoamperometry test (Figures S13 and S14, Supporting Information). As shown in Figure 3f, no obvious change in the ammonia production rate and FE and no current density loss are observed during the long-term electrolysis process for 10 h at -0.2 V versus RHE (Figures S13 and S14, Supporting Information), demonstrating the good stability of NV- W_2N_3 for NRR. It is worth noting that the total amount of nitrogen in the ammonia produced within 24 h ($36.7 \mu g$) is ≈ 2 times the nitrogen content in the NV- W_2N_3 loaded on the carbon paper ($19.2 \mu g$). Thus, we can convincingly confirm that the ammonia originates from NRR instead of catalysts.

We further evaluated the stability of nitrogen vacancies by conducting a series of ex situ characterizations on NV- W_2N_3 before and after NRR reaction. First, the XRD patterns (Figure S15, Supporting Information) of NV- W_2N_3 before and after stability test (10 h) barely show any change, revealing the stable feature of W_2N_3 crystal during NRR.

At atomic level, HAADF-STEM images, energy-dispersive spectroscopy (EDS) mapping and electron energy loss spectrum (EELS) for N K edge of NV- W_2N_3 before and after NRR test are all invariant, demonstrating the morphology and atom arrangement are completely maintained (Figure 4a and Figures S16–S18, Supporting Information). Furthermore, Synchrotron-based N 1s XPS spectra and N K edge X-ray absorption near edge structure (XANES) spectra of NV- W_2N_3 before and after stability test (Figure 4b and Figure S19, Supporting Information) show that the lattice nitrogen and nitrogen vacancies don't change during NRR electrolysis. The nitrogen coordination environment of NV- W_2N_3 is also stable and remains unchanged during NRR test, which is confirmed by synchrotron-based XAS and EXFAS (Figure 4c,d and Figure S20 (Supporting Information) and Table 1). At last, elemental analysis of NV- W_2N_3 before and after NRR test and inductively coupled plasma mass spectrometry (ICP-MS) detection of the electrolyte after NRR test were conducted to evaluate the nitrogen and tungsten loss during NRR process. No cation or anion detached from the matrix is observed, indicating the high stability of the catalyst (Tables S3 and S4, Supporting Information). As aforementioned, vacancies in 2D materials are stable by virtue of the surface distortion induced excellent structural stability.^[43] Furthermore, our previous work elucidates that

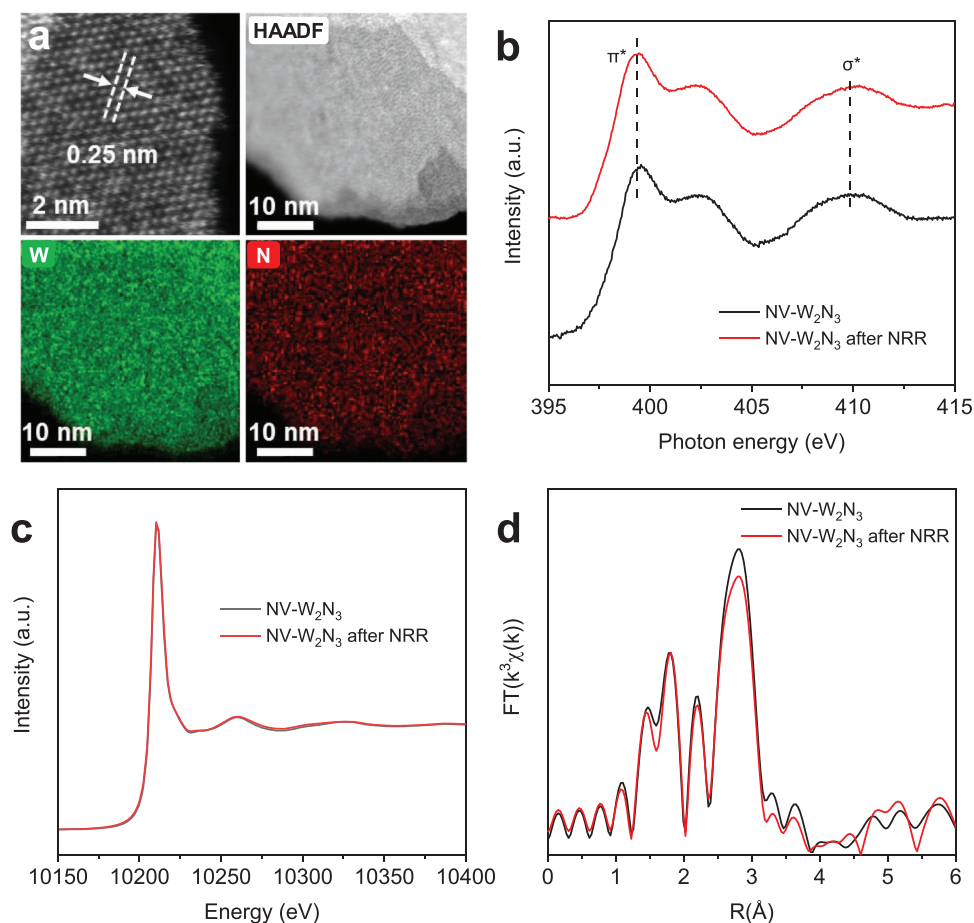


Figure 4. a) HAADF-STEM images and EDS mapping of NV- W_2N_3 after NRR test. b) Synchrotron-based N K edge XANES spectra of NV- W_2N_3 before and after NRR test for 10 h. c) W L_3 edge XANES spectra of NV- W_2N_3 before and after NRR test for 10 h and d) corresponding FT-EXFAS results.

nitrogen-rich transition metal nitrides (metal/N ratio <1) are very stable for electrocatalysis due to the high valence state of metal atoms.^[50] Thus, the good stability of NV-W₂N₃ can be attributed to the 2D morphology induced surface distortion as well as the high valence state of tungsten atoms.

To gain further insight of the reaction mechanisms of NRR on W₂N₃ at atomic level, we then employed DFT calculations. The slab model was constructed based on the theoretical structure of W₂N₃, and a nitrogen vacancy was induced to investigate its role in capturing and reducing dinitrogen molecule.^[45] As seen in Figure S21 (Supporting Information), the perfect W₂N₃ cannot effectively stabilize and activate N₂, since there is little charge transferred between perfect W₂N₃ and the adsorbed N₂ molecule. However, when a nitrogen vacancy is involved, significant charge transfer is observed (Figure S21b, Supporting Information). The full NRR reaction pathway on NV-W₂N₃ via a distal mechanism was then calculated (Figure 5a), and the results indicate that the free energy change of the first protonation step (N₂ + H⁺ + e⁻ + * → *NNH) on is only 0.55 eV. This is in accordance with previous analysis of charge transfer process that the nitrogen vacancies effectively activate the triple bond and make it easy to be attacked by protons in the solution (Figure S21b, Supporting Information). The free energy change of the following two protonation steps are -1.42 and 0.14 eV to form the first ammonia. Meanwhile, the last step to release the second ammonia is thermodynamically uphill with a free

energy change of 0.97 eV, indicating that this is the potential determining step. However, the corresponding free energy change on perfect W₂N₃ is over 2 eV which is much larger than that of NV-W₂N₃ (Figure 5b) and hard to occur under ambient conditions. The results in Figure 5b are in accordance with our experimental data that the nitrogen vacancy could facilitate NRR compared with perfect W₂N₃. We then conducted charge density difference calculations to reveal the electronic structures of the vacancy site. An electron deficient area (shown in cyan) compared with perfect W₂N₃ is produced due to the existence of a nitrogen vacancy (Figure 5c). Consequently, the lone-pair of electrons in N₂ molecule could be accommodated at the electron-deficient area and this explains the origins of activating N₂ on the vacancy site. Furthermore, as shown in Figure S21b (Supporting Information), the tungsten will donate electrons into empty antibonding orbitals of N₂ and thus activate the adsorbed dinitrogen.

In summary, we have presented that nitrogen vacancies confined on 2D W₂N₃ nanosheets are stable and active for the electrocatalytic reduction of N₂ to NH₃ under ambient conditions. The activity and stability of nitrogen vacancies are evaluated by electrochemical measurements and various ex situ characterizations. Significantly, the nitrogen-vacancy-engineered 2D W₂N₃ exhibits superior NRR performance with average NH₃ formation rate of 11.66 ± 0.98 μg h⁻¹ mg_{cata}⁻¹ (3.80 ± 0.32 × 10⁻¹¹ mol cm⁻² s⁻¹) and Faradaic efficiency of 11.67 ± 0.93% at

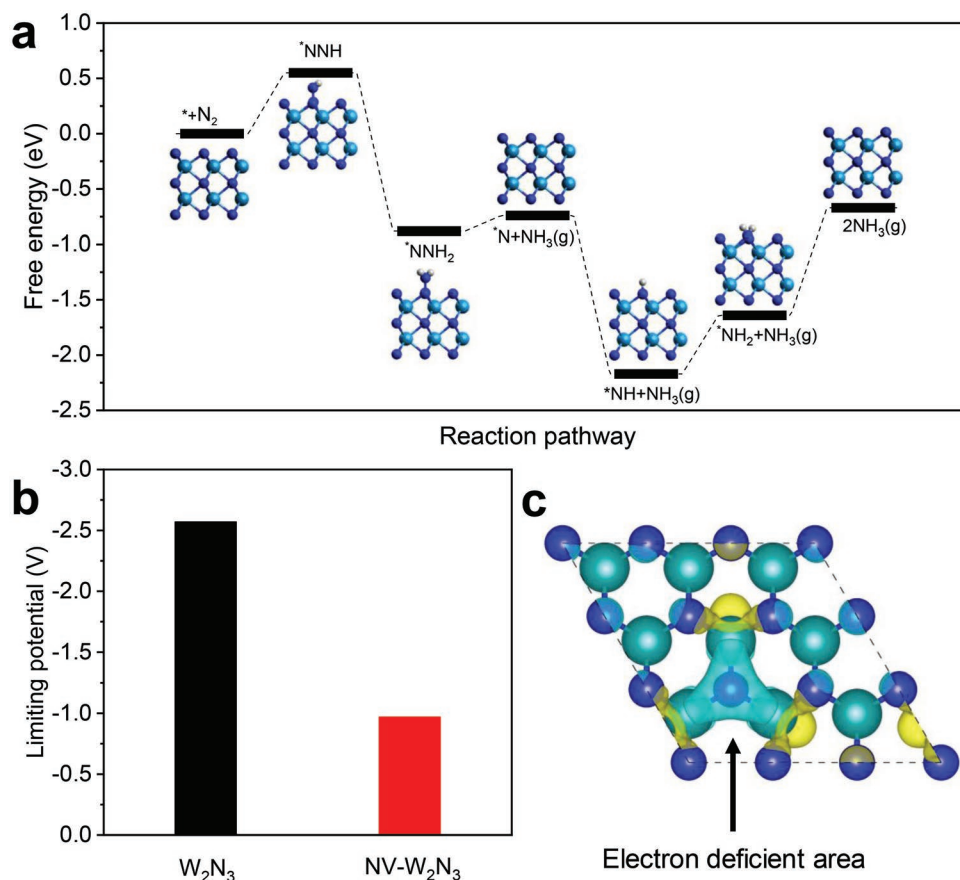


Figure 5. a) Reaction path way of NV-W₂N₃ for NRR. b) Magnitudes of the theoretical limiting potentials of NH₃ production on W₂N₃ and NV-W₂N₃. c) Charge density difference induced by nitrogen vacancy on NV-W₂N₃. The value of iso-surface is 0.005 e Bohr⁻³.

−0.2 V versus RHE in 0.10 M KOH. Electrochemical and isotopic labeling experiments reveal that the NV-W₂N₃ follows a distal mechanism that is different from conventional TMNs. The theoretical calculations demonstrate that the electron loss induced by the nitrogen vacancies can lower the thermodynamic limiting potential and thus facilitate the overall NRR. This work highlights the potential of vacancy engineering on 2D materials for catalytic NRR and provides new insight for preparing novel materials for applications in energy storage and conversion systems.

Supporting Information

Supporting Information is available from the Wiley Online Library or from the author.

Acknowledgements

H.J., L.L., X.L., and C.T. contributed equally to this work. This work is financially supported by the Australian Research Council (DP170104464, DP160104866, LP160100927, DE160101163, and FL170100154). XANES and XAS measurements were undertaken on the soft X-ray beamline and the X-ray absorption spectroscopy beamline respectively at Australian Synchrotron. The authors thank Dr. Bruce Cowie at the Australian Synchrotron for his help in XANES. SEM, ICP-MS, and TEM measurements were undertaken at Adelaide Microscopy, the Centre for Advanced Microscopy and Microanalysis. DFT computations within this research was undertaken with the assistance of resources and services from the National Computational Infrastructure (NCI), which is supported by the Australian Government.

Conflict of Interest

The authors declare no conflict of interest.

Keywords

2D materials, ammonia, electrocatalysis, nitrogen reduction, nitrogen vacancy

Received: April 28, 2019

Revised: May 27, 2019

Published online:

- [1] J. G. Chen, R. M. Crooks, L. C. Seefeldt, K. L. Bren, R. M. Bullock, M. Y. Darensbourg, P. L. Holland, B. Hoffman, M. J. Janik, A. K. Jones, M. G. Kanatzidis, P. King, K. M. Lancaster, S. V. Lymar, P. Pfromm, W. F. Schneider, R. R. Schrock, *Science* **2018**, *360*, eaar6611.
- [2] S. Chu, A. Majumdar, *Nature* **2012**, *488*, 294.
- [3] V. Smil, *Nature* **1999**, *400*, 415.
- [4] S. L. Foster, S. I. P. Bakovic, R. D. Duda, S. Maheshwari, R. D. Milton, S. D. Minteer, M. J. Janik, J. N. Renner, L. F. Greenlee, *Nat. Catal.* **2018**, *1*, 490.
- [5] B. H. R. Suryanto, H.-L. Du, D. Wang, J. Chen, A. N. Simonov, D. R. MacFarlane, *Nat. Catal.* **2019**, *2*, 290.

- [6] Y. Luo, G.-F. Chen, L. Ding, X. Chen, L.-X. Ding, H. Wang, *Joule* **2019**, *3*, 279.
- [7] H. Jin, C. Guo, X. Liu, J. Liu, A. Vasileff, Y. Jiao, Y. Zheng, S.-Z. Qiao, *Chem. Rev.* **2018**, *118*, 6337.
- [8] C. Guo, J. Ran, A. Vasileff, S.-Z. Qiao, *Energy Environ. Sci.* **2018**, *11*, 45.
- [9] Y. Zhao, Y. Zhao, R. Shi, B. Wang, G. I. N. Waterhouse, L.-Z. Wu, C.-H. Tung, T. Zhang, *Adv. Mater.* **2019**, *31*, 1806482.
- [10] L. Zhang, X. Ji, X. Ren, Y. Ma, X. Shi, Z. Tian, A. M. Asiri, L. Chen, B. Tang, X. Sun, *Adv. Mater.* **2018**, *30*, 1800191.
- [11] M. M. Shi, D. Bao, B. R. Wulan, Y. H. Li, Y. F. Zhang, J. M. Yan, Q. Jiang, *Adv. Mater.* **2017**, *29*, 1606550.
- [12] S. J. Li, D. Bao, M. M. Shi, B. R. Wulan, J. M. Yan, Q. Jiang, *Adv. Mater.* **2017**, *29*, 1700001.
- [13] H. Tao, C. Choi, L.-X. Ding, Z. Jiang, Z. Han, M. Jia, Q. Fan, Y. Gao, H. Wang, A. W. Robertson, S. Hong, Y. Jung, S. Liu, Z. Sun, *Chem* **2019**, *5*, 204.
- [14] S. Chen, S. Perathoner, C. Ampelli, C. Mebrahtu, D. Su, G. Centi, *Angew. Chem., Int. Ed.* **2017**, *56*, 2699.
- [15] X. Ren, J. Zhao, Q. Wei, Y. Ma, H. Guo, Q. Liu, Y. Wang, G. Cui, A. M. Asiri, B. Li, B. Tang, X. Sun, *ACS Cent. Sci.* **2019**, *5*, 116.
- [16] C. Lv, Y. Qian, C. Yan, Y. Ding, Y. Liu, G. Chen, G. Yu, *Angew. Chem., Int. Ed.* **2018**, *57*, 10246.
- [17] Z. Geng, Y. Liu, X. Kong, P. Li, K. Li, Z. Liu, J. Du, M. Shu, R. Si, J. Zeng, *Adv. Mater.* **2018**, *30*, 1803498.
- [18] X. Yu, P. Han, Z. Wei, L. Huang, Z. Gu, S. Peng, J. Ma, G. Zheng, *Joule* **2018**, *2*, 1610.
- [19] C. Liu, Q. Li, C. Wu, J. Zhang, Y. Jin, D. R. MacFarlane, C. Sun, *J. Am. Chem. Soc.* **2019**, *141*, 2884.
- [20] C. Ling, X. Niu, Q. Li, A. Du, J. Wang, *J. Am. Chem. Soc.* **2018**, *140*, 14161.
- [21] Y. Fang, Z. Liu, J. Han, Z. Jin, Y. Han, F. Wang, Y. Niu, Y. Wu, Y. Xu, *Adv. Energy Mater.* **2019**, *9*, 1803406.
- [22] J.-X. Yao, D. Bao, Q. Zhang, M.-M. Shi, Y. Wang, R. Gao, J.-M. Yan, Q. Jiang, *Small Methods* **2018**, *3*, 1800333.
- [23] X. Li, T. Li, Y. Ma, Q. Wei, W. Qiu, H. Guo, X. Shi, P. Zhang, A. M. Asiri, L. Chen, B. Tang, X. Sun, *Adv. Energy Mater.* **2018**, *8*, 1801357.
- [24] Y. Zhang, W. Qiu, Y. Ma, Y. Luo, Z. Tian, G. Cui, F. Xie, L. Chen, T. Li, X. Sun, *ACS Catal.* **2018**, *8*, 8540.
- [25] L. Zhang, L.-X. Ding, G.-F. Chen, X. Yang, H. Wang, *Angew. Chem., Int. Ed.* **2019**, *58*, 2612.
- [26] T. Zhang, M.-Y. Wu, D.-Y. Yan, J. Mao, H. Liu, W.-B. Hu, X.-W. Du, T. Ling, S.-Z. Qiao, *Nano Energy* **2018**, *43*, 103.
- [27] R. Wu, J. Zhang, Y. Shi, D. Liu, B. Zhang, *J. Am. Chem. Soc.* **2015**, *137*, 6983.
- [28] F. Lei, Y. Sun, K. Liu, S. Gao, L. Liang, B. Pan, Y. Xie, *J. Am. Chem. Soc.* **2014**, *136*, 6826.
- [29] X. Yang, J. Nash, J. Anibal, M. Dunwell, S. Kattel, E. Stavitski, K. Attenkofer, J. G. Chen, Y. Yan, B. Xu, *J. Am. Chem. Soc.* **2018**, *140*, 13387.
- [30] Y. Abghoui, E. Skúlason, *Catal. Today* **2017**, *286*, 69.
- [31] H.-L. Du, T. R. Gengenbach, R. Hodgetts, D. R. MacFarlane, A. N. Simonov, *ACS Sustainable Chem. Eng.* **2019**, *7*, 6839.
- [32] Y. Zheng, Y. Jiao, Y. Zhu, Q. Cai, A. Vasileff, L. H. Li, Y. Han, Y. Chen, S.-Z. Qiao, *J. Am. Chem. Soc.* **2017**, *139*, 3336.
- [33] H. Jin, X. Liu, Y. Jiao, A. Vasileff, Y. Zheng, S.-Z. Qiao, *Nano Energy* **2018**, *53*, 690.
- [34] Y. Yao, Z. Huang, P. Xie, S. D. Lacey, R. J. Jacob, H. Xie, F. Chen, A. Nie, T. Pu, M. Rehwoldt, D. Yu, M. R. Zachariah, C. Wang, R. Shahbazian-Yassar, J. Li, L. Hu, *Science* **2018**, *359*, 1489.
- [35] Z. Hu, X. Xiao, H. Jin, T. Li, M. Chen, Z. Liang, Z. Guo, J. Li, J. Wan, L. Huang, Y. Zhang, G. Feng, J. Zhou, *Nat. Commun.* **2017**, *8*, 15630.

- [36] W. Qiu, X.-Y. Xie, J. Qiu, W.-H. Fang, R. Liang, X. Ren, X. Ji, G. Cui, A. M. Asiri, G. Cui, B. Tang, X. Sun, *Nat. Commun.* **2018**, *9*, 3485.
- [37] Y. Liu, H. Cheng, M. Lyu, S. Fan, Q. Liu, W. Zhang, Y. Zhi, C. Wang, C. Xiao, S. Wei, B. Ye, Y. Xie, *J. Am. Chem. Soc.* **2014**, *136*, 15670.
- [38] H. Tao, Y. Gao, N. Talreja, F. Guo, J. Texter, C. Yan, Z. Sun, *J. Mater. Chem. A* **2017**, *5*, 7257.
- [39] Y. Sun, S. Gao, F. Lei, Y. Xie, *Chem. Soc. Rev.* **2015**, *44*, 623.
- [40] H. Yu, X. Yang, X. Xiao, M. Chen, Q. Zhang, L. Huang, J. Wu, T. Li, S. Chen, L. Song, L. Gu, B. Y. Xia, G. Feng, J. Li, J. Zhou, *Adv. Mater.* **2018**, *30*, 1805655.
- [41] W. Yang, X. Zhang, Y. Xie, *Nano Today* **2016**, *11*, 793.
- [42] Y. Sun, Q. Liu, S. Gao, H. Cheng, F. Lei, Z. Sun, Y. Jiang, H. Su, S. Wei, Y. Xie, *Nat. Commun.* **2013**, *4*, 2899.
- [43] S. Gao, Z. Sun, W. Liu, X. Jiao, X. Zu, Q. Hu, Y. Sun, T. Yao, W. Zhang, S. Wei, Y. Xie, *Nat. Commun.* **2017**, *8*, 14503.
- [44] S. Wang, X. Yu, Z. Lin, R. Zhang, D. He, J. Qin, J. Zhu, J. Han, L. Wang, H.-k. Mao, J. Zhang, Y. Zhao, *Chem. Mater.* **2012**, *24*, 3023.
- [45] N. Mounet, M. Gibertini, P. Schwaller, D. Campi, A. Merkys, A. Marrazzo, T. Sohier, I. E. Castelli, A. Cepellotti, G. Pizzi, N. Marzari, *Nat. Nanotechnol.* **2018**, *13*, 246.
- [46] H. Cheng, L.-X. Ding, G.-F. Chen, L. Zhang, J. Xue, H. Wang, *Adv. Mater.* **2018**, *30*, 1803694.
- [47] D. Bao, Q. Zhang, F. L. Meng, H. X. Zhong, M. M. Shi, Y. Zhang, J. M. Yan, Q. Jiang, X. B. Zhang, *Adv. Mater.* **2017**, *29*, 1604799.
- [48] J. Wang, L. Yu, L. Hu, G. Chen, H. Xin, X. Feng, *Nat. Commun.* **2018**, *9*, 1795.
- [49] F. Pang, Z. Wang, K. Zhang, J. He, W. Zhang, C. Guo, Y. Ding, *Nano Energy* **2019**, *58*, 834.
- [50] H. Jin, X. Liu, A. Vasileff, Y. Jiao, Y. Zhao, Y. Zheng, S.-Z. Qiao, *ACS Nano* **2018**, *12*, 12761.

ADVANCED MATERIALS

Supporting Information

for *Adv. Mater.*, DOI: 10.1002/adma.201902709

Nitrogen Vacancies on 2D Layered W_2N_3 : A Stable and Efficient Active Site for Nitrogen Reduction Reaction

*Huanyu Jin, Laiquan Li, Xin Liu, Cheng Tang, Wenjie Xu, Shuangming Chen, Li Song, Yao Zheng, and Shi-Zhang Qiao**

Copyright WILEY-VCH Verlag GmbH & Co. KGaA, 69469 Weinheim, Germany, 2019.

Supporting Information

Nitrogen Vacancies on 2D Layered W_2N_3 : A Stable and Efficient Active Site for Nitrogen Reduction Reaction

Huanyu Jin^{+, [a]}, Laiquan Li^{+, [a]}, Xin Liu^{+, [a]}, Cheng Tang^{+, [a]}, Wenjie Xu,^[b] Shuangming Chen,^[b] Li Song,^[b] Yao Zheng,^[a] and Shi-Zhang Qiao^{, [a]}*

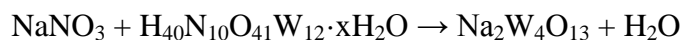
[+] These authors contributed equally to this work.

H. Jin, L. Li, X. Liu, Dr. C. Tang, Dr. Y. Zheng, Prof. S. Z. Qiao
School of Chemical Engineering
The University of Adelaide
Adelaide, South Australia 5005, Australia.
Corresponding author: S. Z. Q. (s.qiao@adelaide.edu.au)

W. Xu, Dr. S. Chen, Prof. L. Song
National Synchrotron Radiation Laboratory, CAS Center for Excellence in Nanoscience,
University of Science and Technology of China, Hefei 230029, Anhui, P. R. China.

Experimental Methods

Synthesis of 2D Na₂W₄O₁₃ nanosheets. 2D Na₂W₄O₁₃ nanosheets were synthesized by a molten salt method.^[1]



Typically, 5.0 g of sodium nitrate was added into a crucible and transferred to the pre-heated muffle furnace (350°C) for at least 20 min. When the sodium nitrate turned to molten state, 0.2 g of ammonium tungstate hydrate was added into the molten sodium nitrate quickly and reacted for 60 s. Then, the product was removed from the muffle furnace and cooled down to room temperature. Finally, the product was washed by Milli-Q water several times to remove the extra sodium nitrate followed by lyophilization for two days to obtain the precursor materials (white powder).

Synthesis of W₂N₃ nanosheet. Atmospheric-pressure synthesis of 2D W₂N₃ nanosheet was realized using NH₃ gas as the nitrogen source and Na₂W₄O₁₃ nanosheets as the W precursor.



In detail, 100 mg of Na₂W₄O₁₃ nanosheets were placed in the center of a tube furnace. Then the tube furnace was heated to 750°C under 5% NH₃/Ar atmosphere at a rate of 5°C min⁻¹. The flow rate of the 5% NH₃/Ar gas is 15 sccm. After maintaining the temperature of 750°C for 5h, the tube furnace was cooled to room temperature at a rate of 10°C min⁻¹. The final product was the mixture of W₂N₃ nanosheet and Na₂WO₄. Then the mixture was washed by ultrasonic probe dispersion equipment for 10 min to remove the Na₂WO₄. The W₂N₃ nanosheets (black powder) were finally collected by centrifugation at 9000 rpm for 10 min and freeze-dried for two days.

Construction of nitrogen vacancies. The vacancies were produced by annealing 2D W₂N₃ nanosheet under hydrogen atmosphere. In detail, 100 mg of W₂N₃ nanosheets were placed in the center of a tube furnace. Then the tube furnace was heated to 500°C under 5% H₂/Ar atmosphere at a rate of 3°C min⁻¹. The flow rate of the 5% H₂/Ar gas was 50 sccm. After maintaining the temperature of 500°C for 3 h, the tube furnace was cooled to room temperature at a rate of 10°C min⁻¹.

Computational Details. Spin-polarized density functional theory (DFT) calculations were performed using the Vienna *ab initio* simulation package (VASP).^[2-5] The exchange–correlation interactions were treated within the generalized gradient approximation (GGA) in the form of the Perdew–Burke–Ernzerhof (PBE) functional.^[6] The van der Waals interactions were described using the empirical correction in Grimme’s scheme.^[7] The electron wave functions were expanded using plane waves with a cutoff energy of 500 eV, and the convergence criteria of energy change during all calculations were set to 10⁻⁴ eV. The Brillouin zone was sampled by 3 × 3 × 1 Monkhorst–Pack

k-point mesh. The top two layers of the slab were allowed to relax together with the adsorbates and the convergence threshold for structural optimization was set to be 0.01 eV/Å. In order to avoid interactions between periodic images, a vacuum space of 20 Å was applied to all calculations. The free energy diagram along the reaction pathway was calculated as follows:

$$\Delta G = \Delta E_{\text{ad}} + \Delta E_{\text{ZPE}} - T\Delta S$$

where ΔE_{ad} is the adsorption energy defined as the electronic energy difference, ΔE_{ZPE} is the change of zero-point energies, T is the temperature (T = 298.15K), and ΔS is the entropy changes. The entropy of gas molecules are taken from standard values.^[8]

Characterization. X-Ray Powder Diffraction (XRD) data was collected on a Rigaku MiniFlex 600 X-Ray Diffractometer. Field-emission SEM imaging was conducted on a FEI QUANTA 450 electron microscope. The transmission electron microscope images, aberration-corrected TEM images, high-angle annular dark-field imaging and EDS mapping were taken on a FEI Titan Themis 80-200 operating at 200 kV. The UV absorbance data of spectrophotometer were collected on SHIMADZU UV2600 ultraviolet-visible (UV-Vis) spectrophotometer. ICP-MS analysis was conducted by an Agilent 7500cx instrument.

Elemental analysis (EA) was conducted using a Perkin Elmer 2400 series II CHNS/O Elemental Analyzer in CHN configuration. The combustion tube was packed using Perkin Elmer EA-1000, Silver Vanadate & Silver Tungstate/Magnesium Oxide. The reduction tube was packed with Perkin Elmer High-Purity copper with a combustion temperature of 925°C and reduction temperature of 640°C. Results were calibrated to 4 mg of Perkin Elmer Organic Analytical Standard of Acetanilide with known abundances of carbon (71.09%), hydrogen (6.71%) and nitrogen (10.36%). The accepted error range between standards was $\pm 0.3\%$ for carbon, hydrogen and nitrogen and calculated against 12 replicates.

The synchrotron-based XPS and XANES measurements were carried out on the soft X-ray spectroscopy beamline at the Australian Synchrotron, which is equipped with a hemispherical electron analyzer and a microchannel plate detector that enables simultaneous recording of the total electron yield and partial electron yield. The calibration of XPS data were normalized to the photoelectron current of the photon beam, measured on an Au grid. The raw XANES data were normalized using software Igor Pro 8.

The W L₃ edge XAS spectra were normalized and analyzed using WinXAS3.1 software.^[9] Theoretical amplitudes and phase-shift functions were calculated with the FEFF6 code.

Electrochemical Measurements. Carbon paper (Toray Paper 090) was used as the current collector. In detail, carbon paper was first treated in O₂ plasma environment at a pressure of 500 mTorr for 20 min. After soaking in H₂SO₄ for 12 h, the carbon paper was then washed with ethanol

and deionized water several times and dried at 60°C for 2 days. The Nafion 211 membrane was chosen as the separator. The pretreatment procedures are as follows. The membrane was first preconditioned by boiling in 5% H₂O₂ solution and ultrapure deionized water at 80°C each for 1 h. Then the as-treated Nafion 211 was soaked in 0.05 M H₂SO₄ for 3 h and Milli-Q water for another 1 h.

The electrochemical measurements were undertaken in a standard H-cell in 0.10 M KOH. The volume of the electrolyte in the anode and cathode chamber was 30 mL for each. For working electrode preparation, 2 mg of catalyst was dispersed in 1 mL of deionized water which contained 0.1 wt% of Nafion. Next, 100 µL of catalyst dispersion (2 mg mL⁻¹) was dipped onto a carbon fiber paper as the working electrode (1 × 1 cm⁻², loading mass: 0.2 mg cm⁻²). The working electrode was soaked in 10 mL of 0.10 M KOH for 2 h to eliminate the contamination before NRR. An acid trap is connected with the cathode chamber with two 10 mL clean PP tubes with 5 mL of 0.05 M H₂SO₄ in each tube. The saturated calomel electrode (SCE) and graphite rod were chosen as the reference electrode and counter electrode, respectively. The working electrode was scanned several times until the current response stabilized. Then all electrolytes in H-cell was replaced by fresh 0.10 M KOH. All potentials were referenced to the reversible hydrogen electrode according to Nernst equation ($E_{\text{RHE}} = E_{\text{SCE}} + 0.059 \times \text{pH} + 0.241$). The SCE electrode was also calibrated in H₂-saturated 0.10 M KOH using a CV method (a Pt wire was used as the working electrode). The scan rate is 0.1 mV s⁻¹. The electrolyte was purged with ultra-high purity N₂ (99.999%) for 30 min before nitrogen reduction measurement (~50 sccm). A flow of ultra-high purity N₂ or Ar (20 sccm) was maintained over the electrolyte during the experiment. The stability test was performed by replacing the electrolyte every 2 hour without changing the working electrode and Nafion membrane.

Quantification of Ammonia. The ammonia detection was detected by a reported indophenol blue method.

Chromogenic reagent (A): 5 g of sodium salicylate and 5 g of potassium sodium tartrate were dissolved in 100 mL of 1 M NaOH.

Oxidizing solution (B): 3.5 mL of sodium hypochlorite (available chlorine 10-15 %) was added into 100 mL of deionized water.

Catalyzing reagent (C): 0.2 g of sodium nitroferricyanide was dissolved in 20 mL of deionized water.

Standard solutions preparation:

1000 ppm NH₃ (1 ppm: 1 µg_{NH₃} mL⁻¹): 0.3146 g of pre-dried NH₄Cl (105 °C for 4 h) was added in 100 mL of 0.10 M KOH (or 0.05 M H₂SO₄) solution. 10 ppm NH₃: 1 mL of 1000 ppm NH₃ solution

was added in a 100 mL volumetric flask and add 0.10 M KOH (or 0.05 M H₂SO₄) solution to the scale mark. 0.2, 0.4, 0.8, 1.2, 1.6 and 2.0 mL of 10 ppm NH₃ solution were separately added into a 20 mL volumetric flask and added 0.10 M KOH (or 0.05 M H₂SO₄) solution to the scale mark to obtain 0.1, 0.2, 0.4, 0.6, 0.8 and 1.0 ppm NH₃ standard solutions.

UV-vis measurement. 2 mL of standard solutions or sample electrolyte was added to test tubes, to which 2 mL of reagent (A), 1 mL of reagent (B) and 0.2 mL of reagent (C) were then successively added. After keeping for 1 h, the concentration of the produced indophenol blue was measured using UV-vis spectrophotometer. The standard curve was plotted with the absorbance values at wavelength of 655 nm as y axis and the concentration of NH₃ as x axis.

Hydrazine Detection. The possible hydrazine product in the electrolytes was estimated by the method of Watt and Chrisp. The sensitive chromogenic reagent was prepared by dissolving 5.99 g para-(dimethylamino) benzaldehyde in a mixture of 30 mL concentrated HCl and 300 mL ethanol. The absorbance of hydrazine after mixing with the chromogenic reagent in the resulting electrolyte was estimated at 460 nm.

Calculation of NH₃ yield and Faradaic efficiency. The NH₃ formation rate was determined using the following equation:

$$r(\text{NH}_3) = (c \times V) / (t \times A)$$

where *c* is the measured NH₃ concentration, *V* is the volume of the electrolyte or acid trap, *t* is the reduction reaction time, and *A* is the effective area of the electrode (geometric area).

The Faradaic efficiency was calculated as follows:

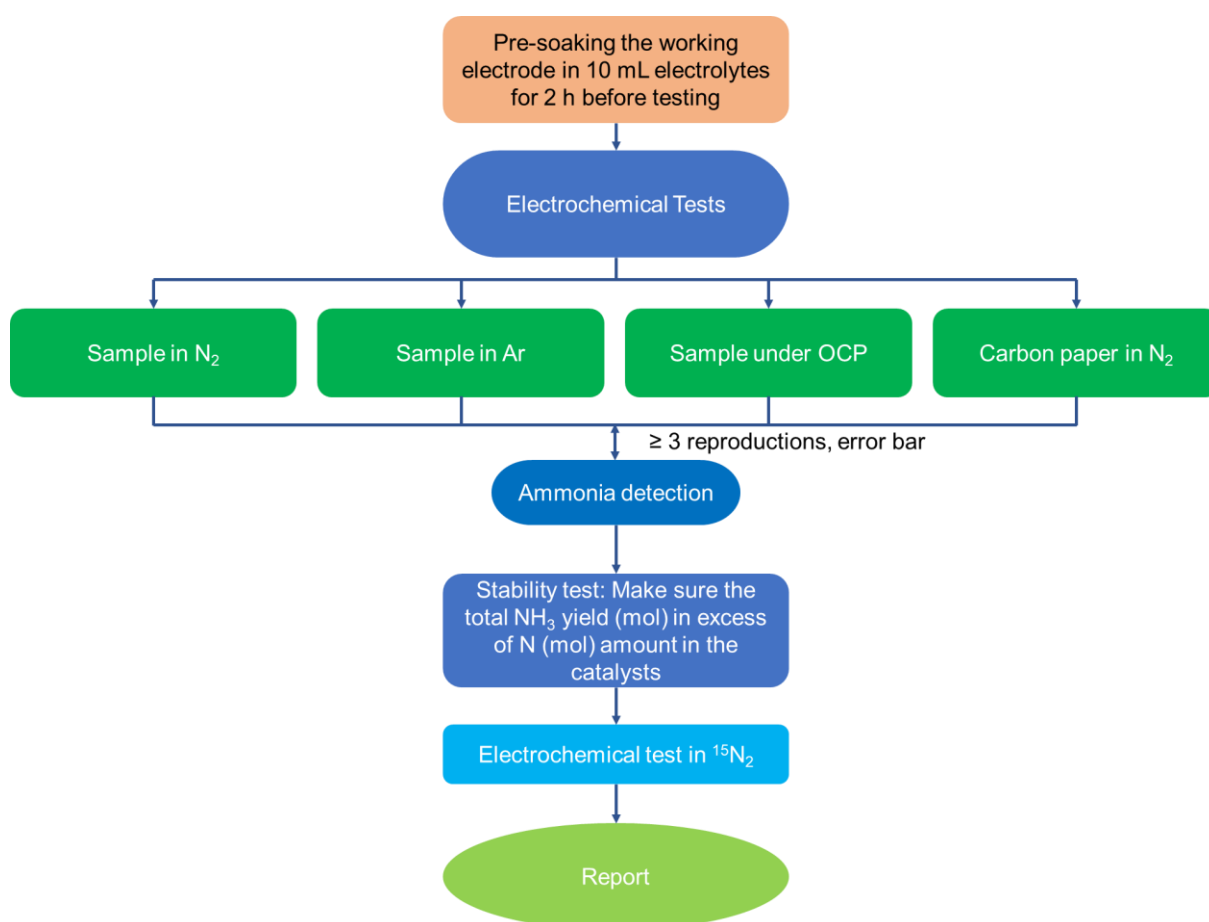
$$\text{FE} = 3F \times c \times V / (17 \times Q)$$

where *F* is the Faraday constant, *c* is the measured NH₃ concentration, *V* is the volume of the electrolyte or acid trap, and *Q* is the quantity of electric charge for one electron of NRR testing. The total ammonia production is calculated as the summary of the ammonia products in cathodic electrolytes and acid traps.

¹⁵N₂ Isotope Labeling Experiments. An isotopic labeling experiment used ¹⁵N₂ (98 atom % ¹⁵N purchased from Sigma-Aldrich Chemical Reagent Co. CAS Number 29817-79-6) as the feed gas was conducted to elucidate the activity origin of NV-W₂N₃. The volume of the electrolyte was changed to 10 mL to obtain the electrolyte with higher ammonia concentration. The ¹⁵N₂ gas was purified by passing through an acid trap (0.05 M H₂SO₄) before entering the electrochemical chamber. After ¹⁵NRR for 2 h at -0.2 V *versus* RHE in 0.10 M KOH solution with the flow rate of 5 sccm, the obtained ¹⁵NH₄⁺ electrolyte was determined by 1H nuclear magnetic resonance (NMR, 600 MHz).

To prepare the NMR sample, 4 mL of electrolyte after NRR was concentrated to ~1 mL. Then 600 μL of the concentrated solution were acidified with 3 M H_2SO_4 to achieve pH ~1-2. Then 30 μL of 100 ppm dimethyl sulfoxide (DMSO) and 70 μL deuterium oxide (D_2O) was added in the solution. Similarly, the amount of $^{14}\text{NH}_4^+$ was determined by this method when $^{14}\text{N}_2$ (99.999%) was used as the feed gas. All NMR measurements were carried out with water suppression and 4000 scans.

NRR Experimental Protocols. As the samples contain nitrogen which may cause false positive results, standard and control experiments were conducted as following flow chat to exclude possible interference from any contaminants.



Figures

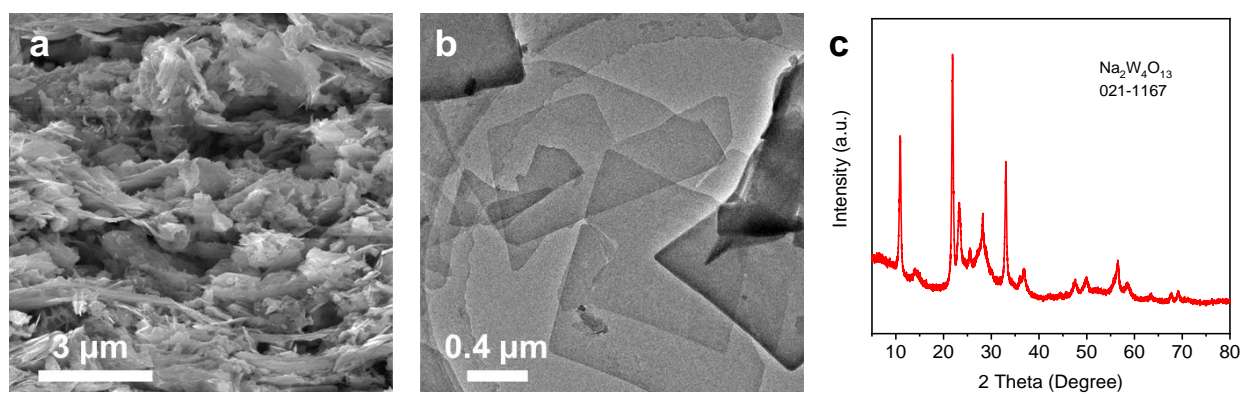


Figure S1. (a) SEM image, (b) TEM image and (c) XRD pattern of 2D Na₂W₄O₁₃ nanosheets.

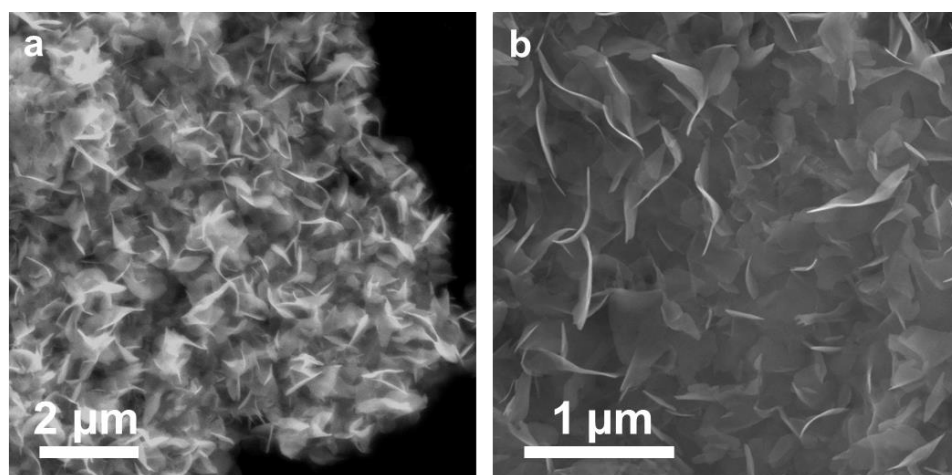


Figure S2. SEM images of (a) W₂N₃ and (b) NV-W₂N₃.

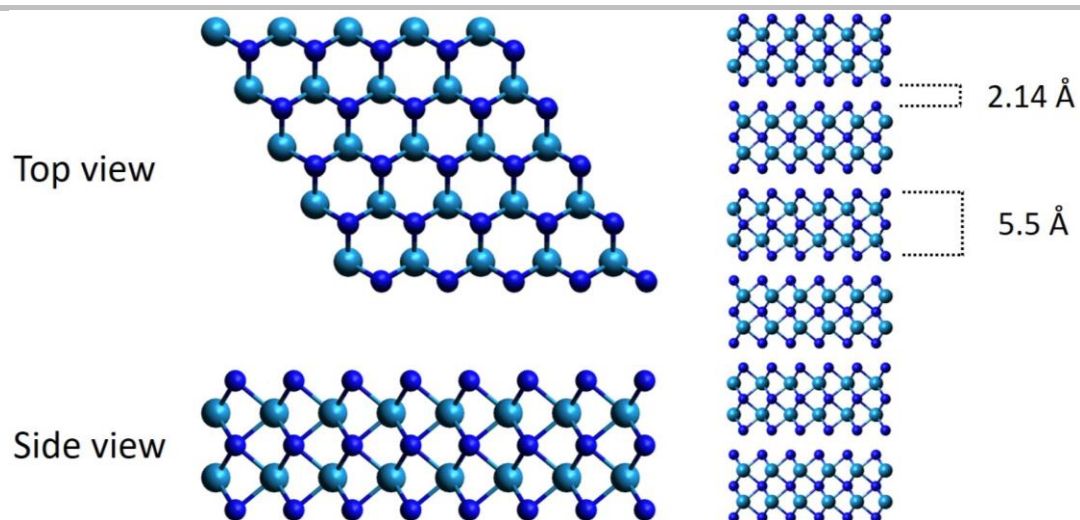


Figure S3. Theoretical model of 2D layered W_2N_3 that shows its crystal parameter.

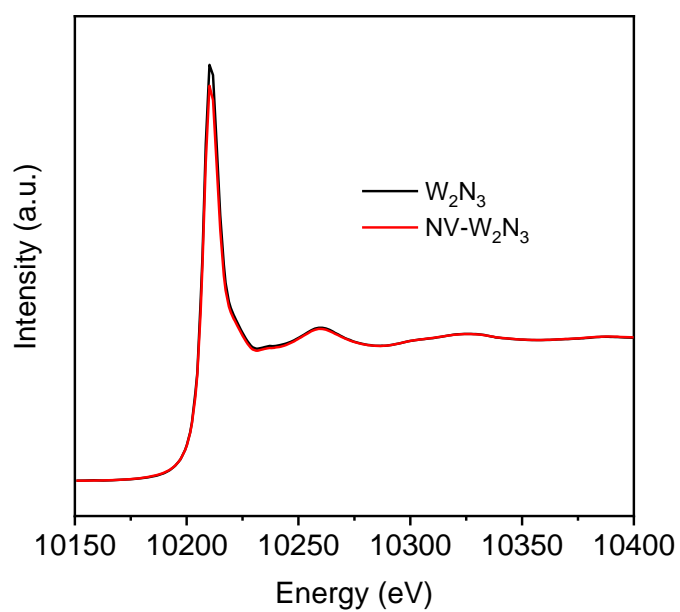


Figure S4. Synchrotron-based W L_3 edge XAS spectra of W_2N_3 and NV- W_2N_3 .

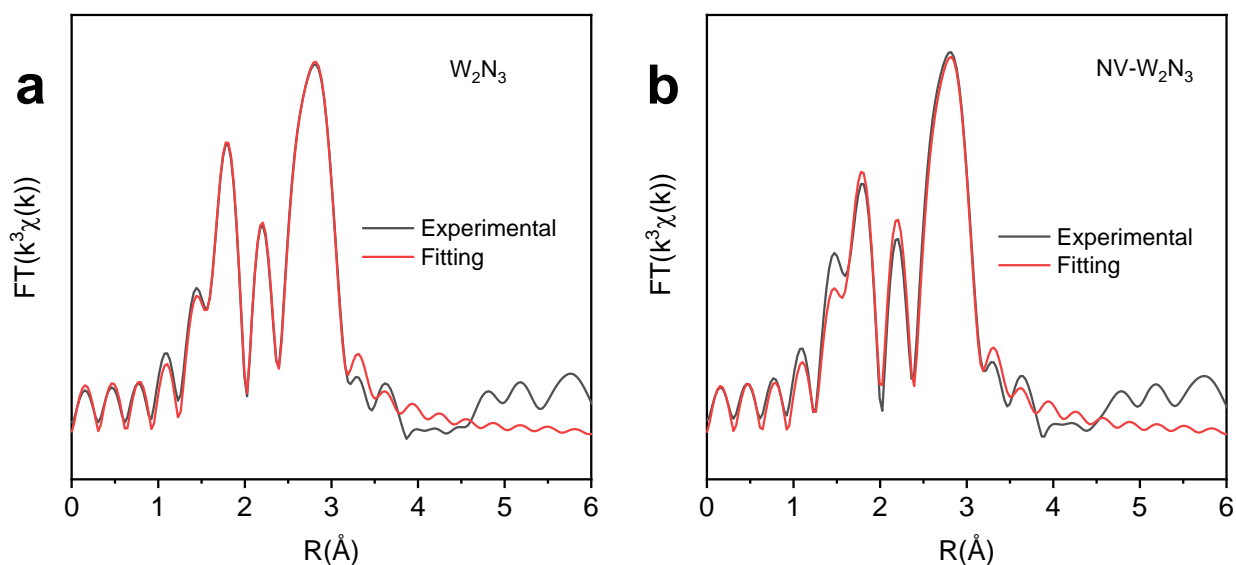


Figure S5. (a) XAS fitting results of W_2N_3 and (b) $NV-W_2N_3$.

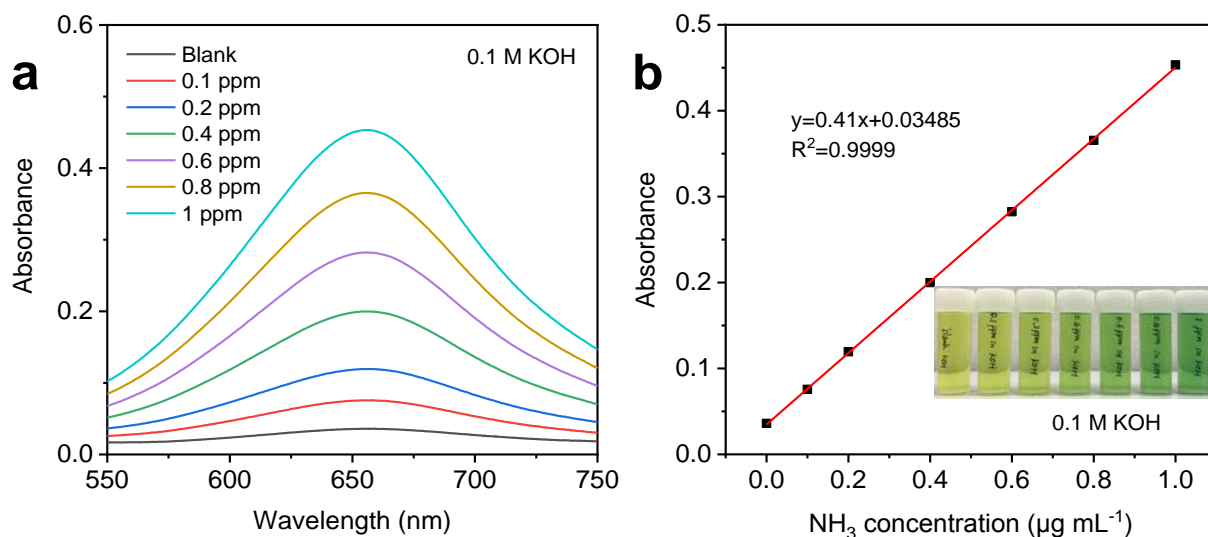


Figure S6. Calibration curve in 0.10 M KOH using ammonium chloride solutions of known concentration as standards (1 ppm: $1 \mu\text{g}_{NH_3} \text{ mL}^{-1}$). (a) UV-vis curves of indophenol assays after incubated for 1 hour and (b) calibration curve used for estimation of NH_3 concentration.

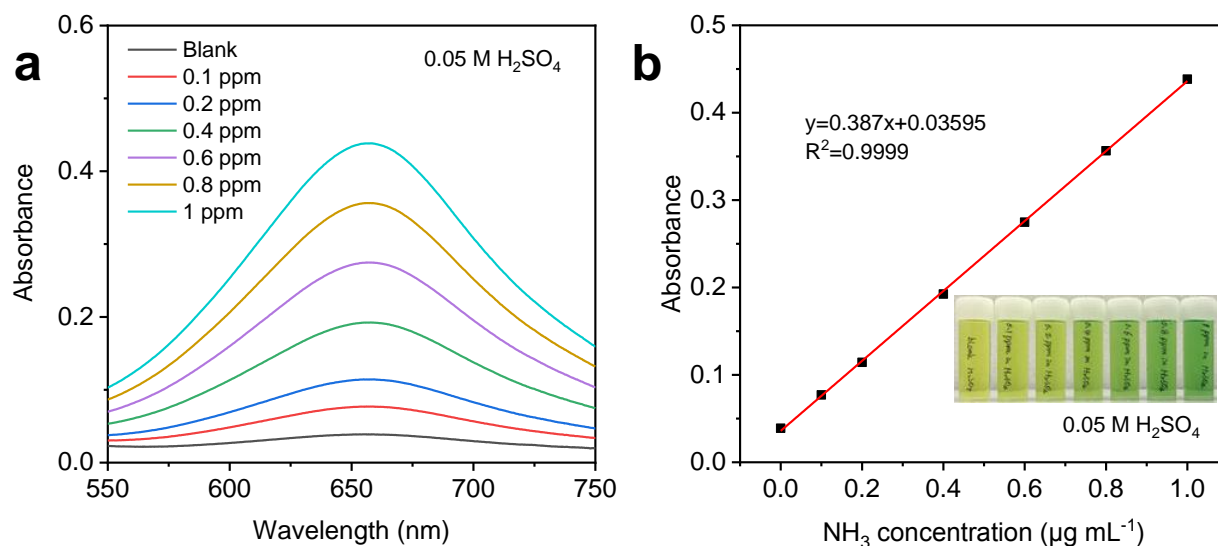


Figure S7. Calibration curve in 0.05 M H₂SO₄ using ammonium chloride solutions of known concentration as standards. (a) UV-vis curves of indophenol assays after incubated for 1 hour and (b) calibration curve used for estimation of NH₃ concentration.

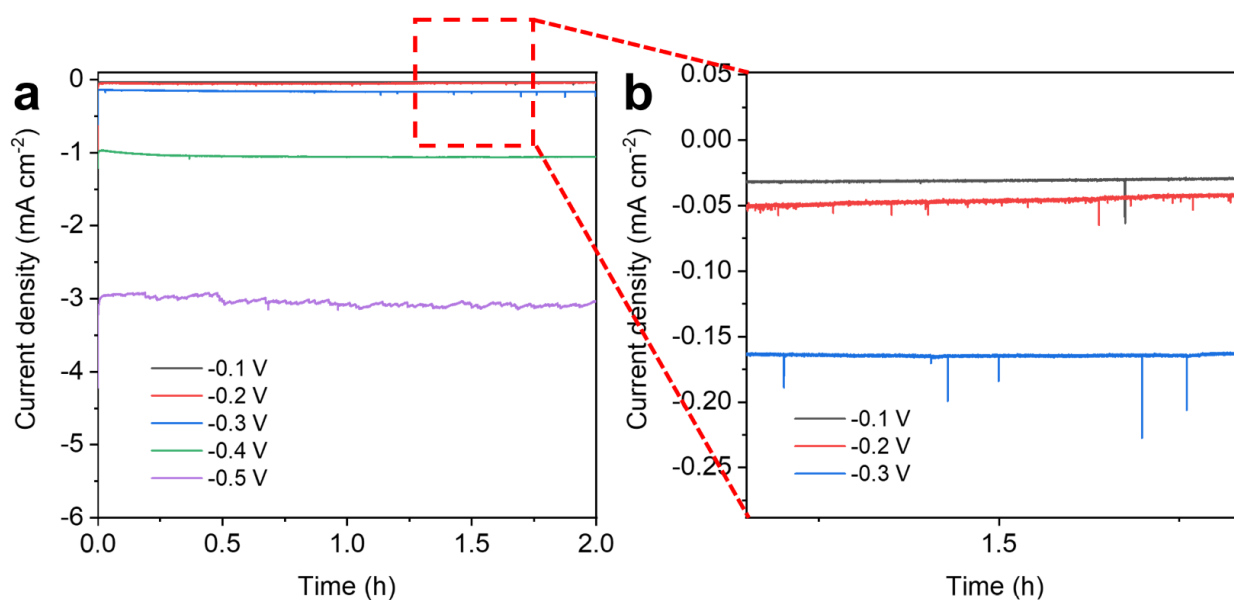


Figure S8. Chronoamperometry results of NV-W₂N₃ at different applied potentials.

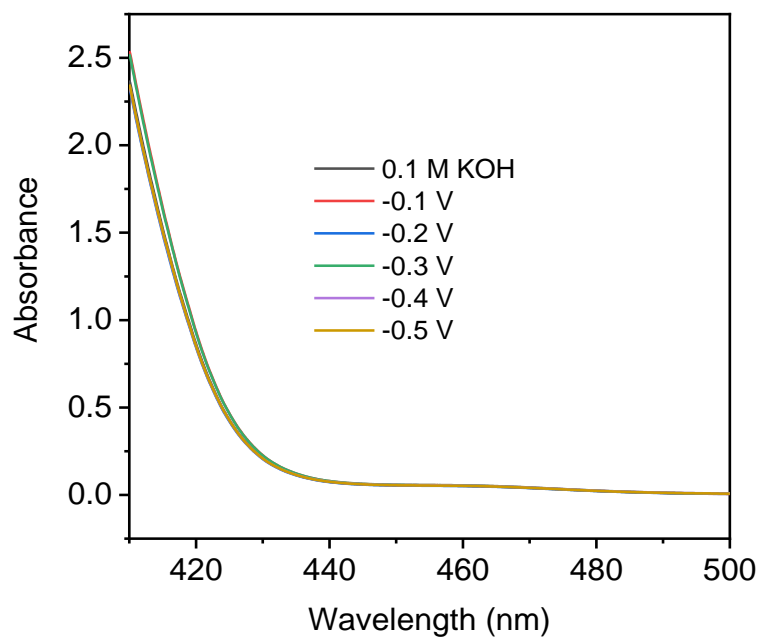


Figure S9. UV-Vis absorption spectra of the electrolytes stained with p-C₉H₁₁NO indicator after NRR electrolysis at a series of potentials.

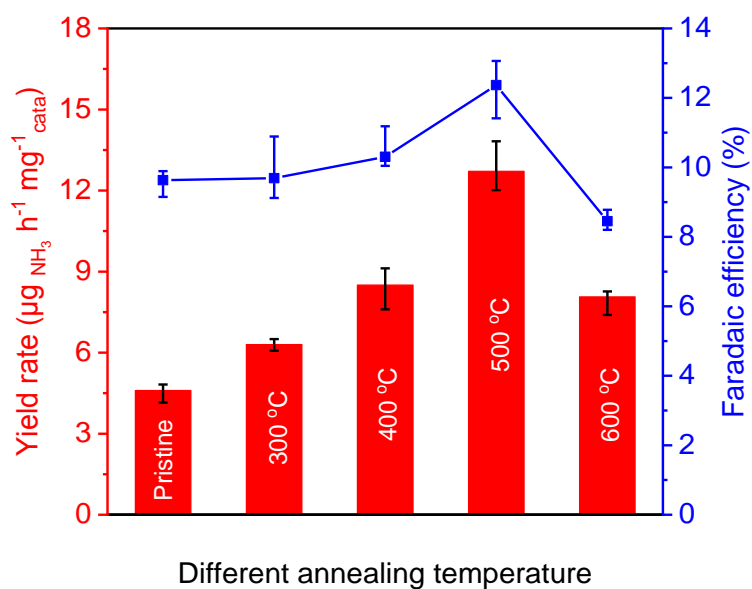


Figure S10. NRR performance of W₂N₃ obtained under different annealing temperature.

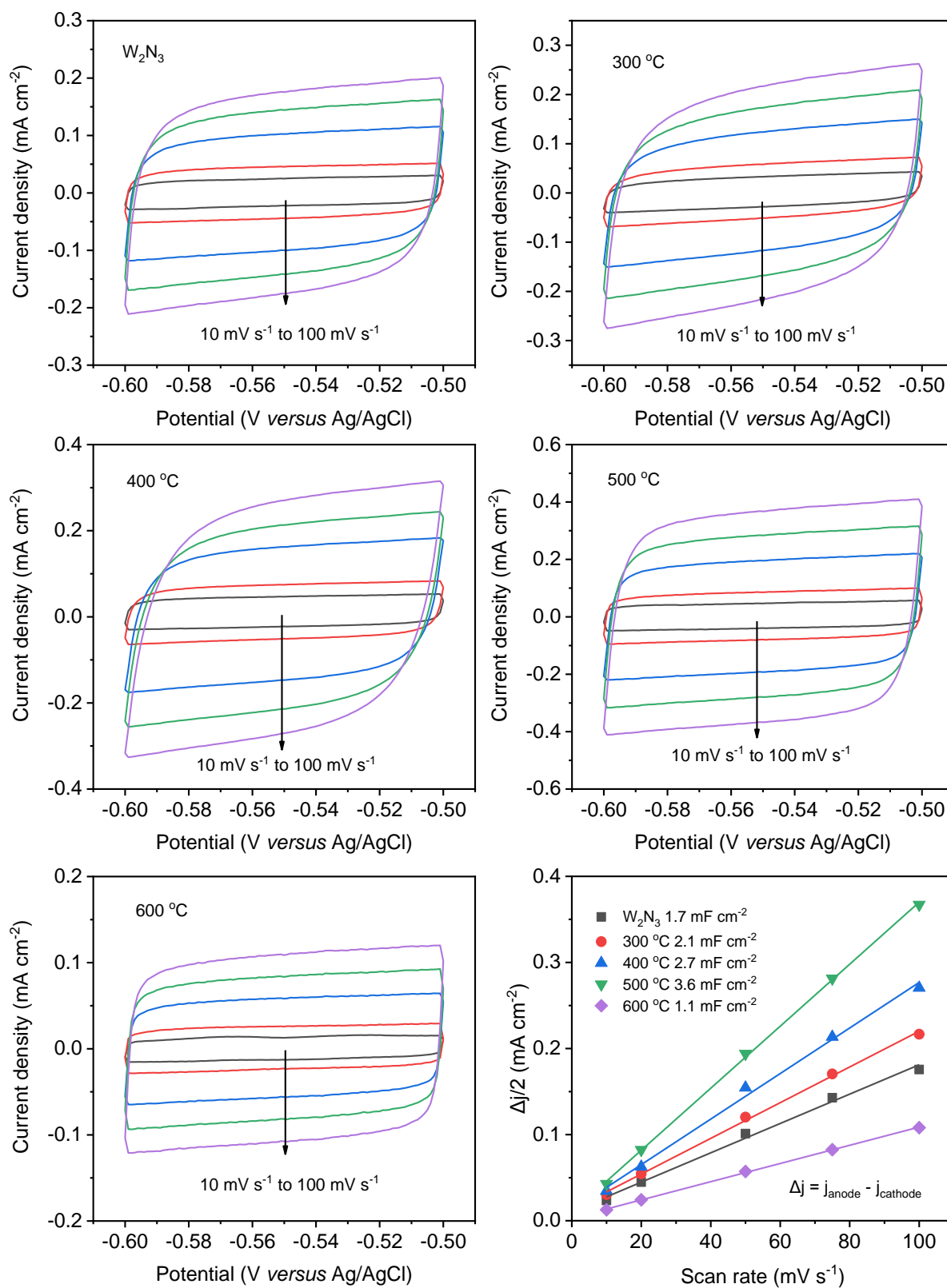


Figure S11. CV measurements for testing the ECSA of different catalysts.

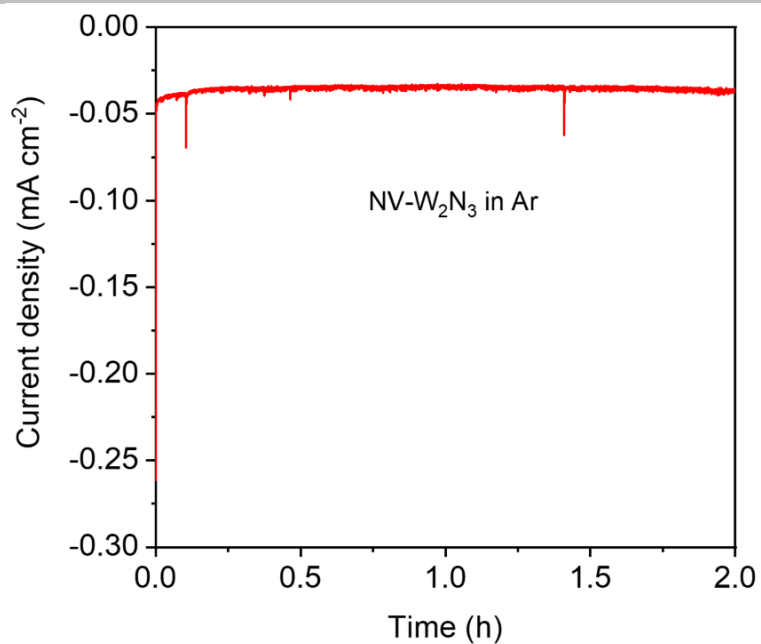


Figure S12. Chronoamperometry curves for NV-W₂N₃ at -0.2 V *versus* RHE in argon-saturated electrolyte for 2 h.

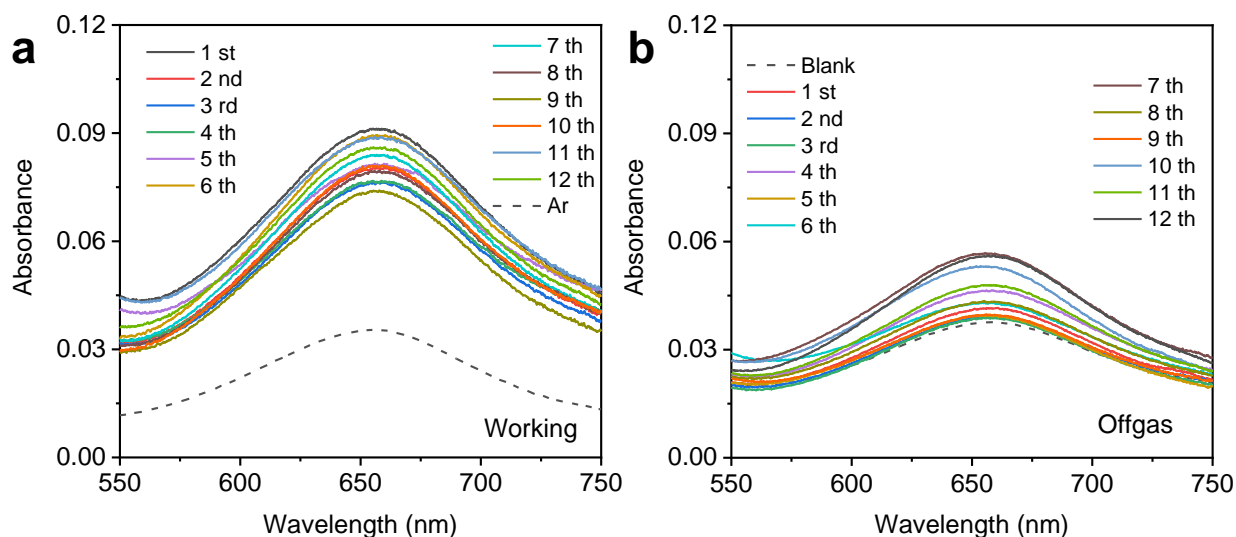


Figure S13. UV-Vis absorption spectra of (a) working electrolytes and (b) acid traps (5mL \times 2) for 12 cycles.

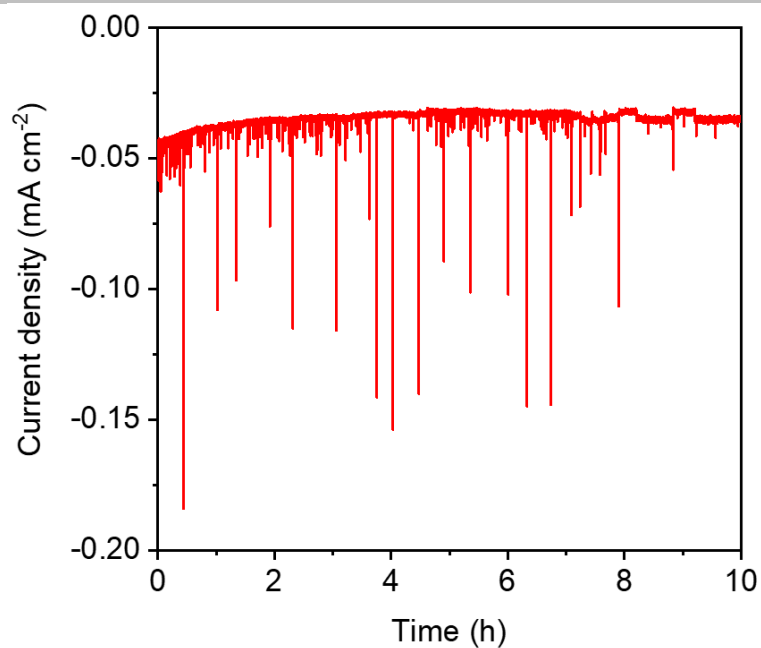


Figure S14. Long-term chronoamperometry curve of NV-W₂N₃ electrode at -0.2 V *versus* RHE in N₂-saturated electrolyte showing good stability.

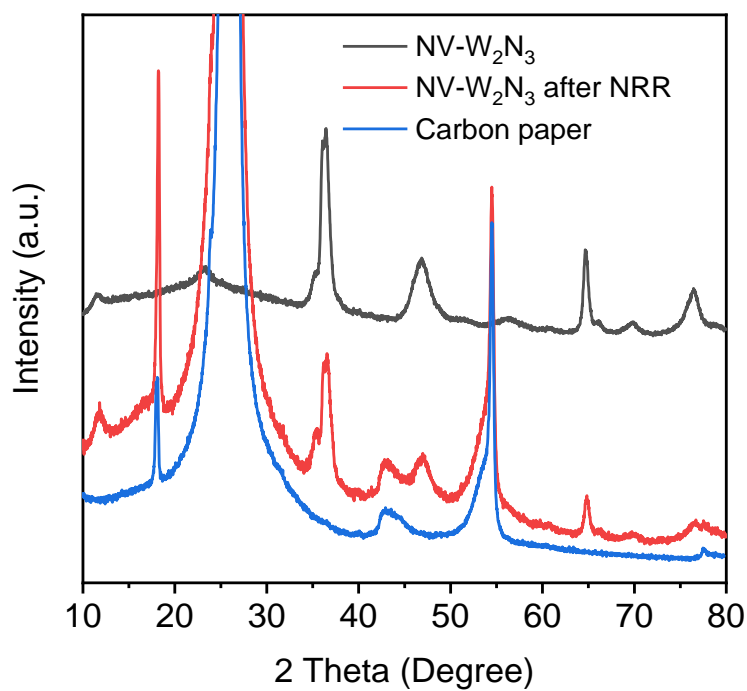


Figure S15. XRD patterns of NV-W₂N₃ before and after stability test.

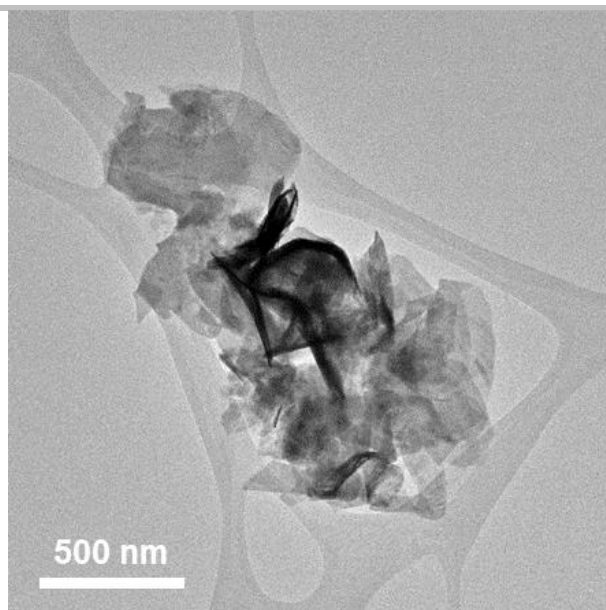


Figure S16. TEM image of NV- W_2N_3 after NRR test.

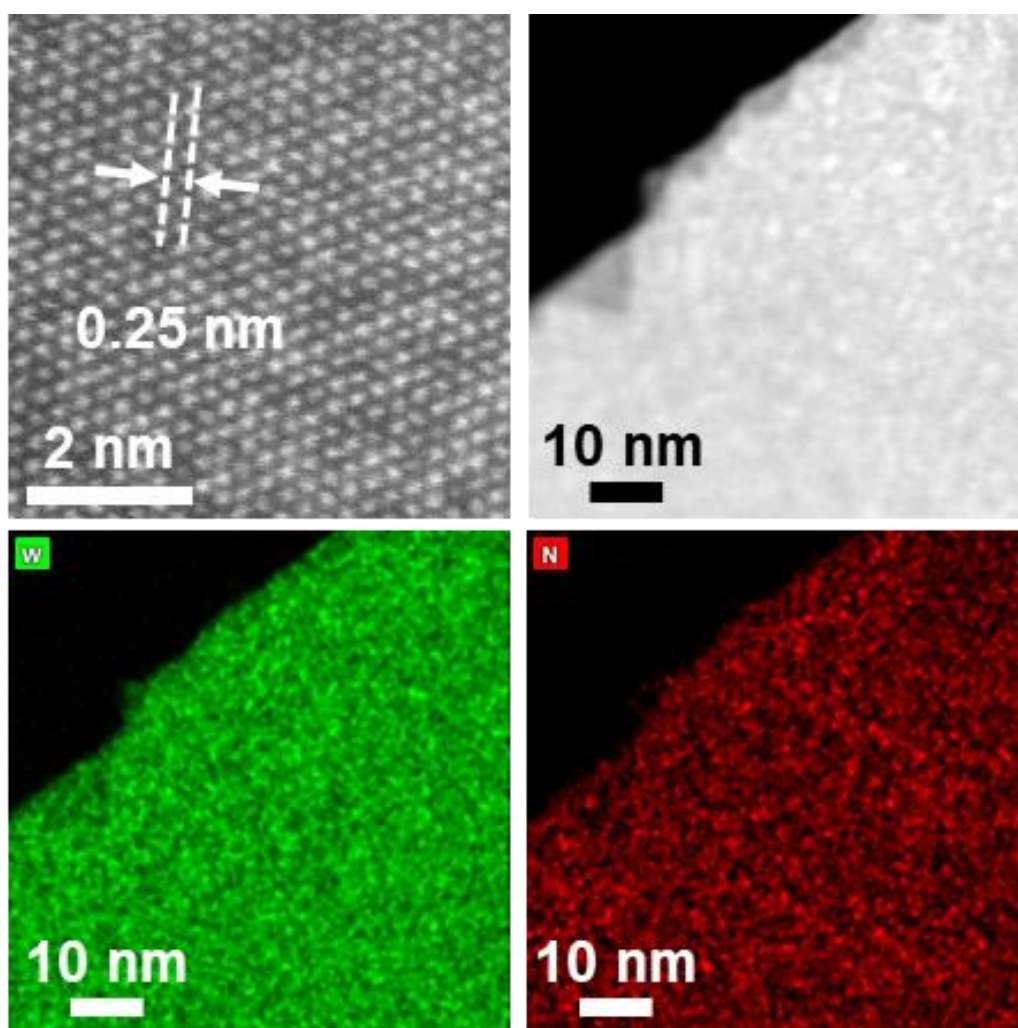


Figure S17. HAADF-STEM images and EDS mapping of NV- W_2N_3 before NRR test.

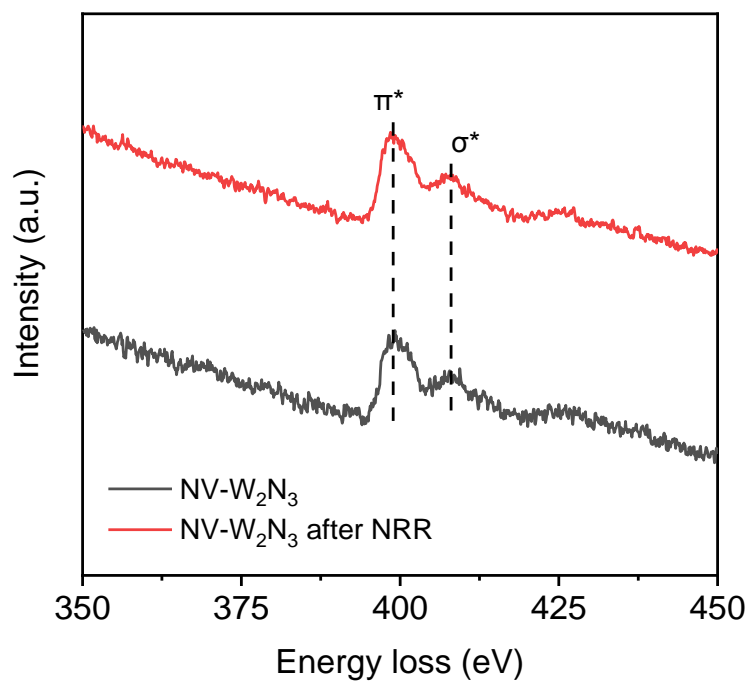


Figure S18. EELS spectra of NV-W₂N₃ before and after NRR test for 10 h.

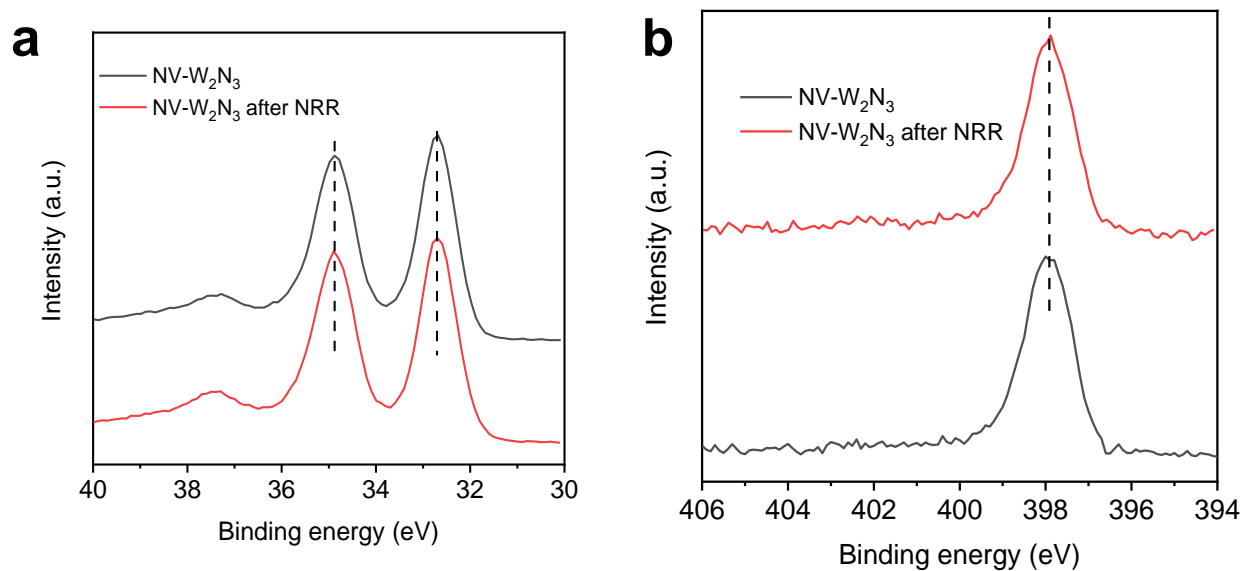


Figure S19. (a) W 4f and (b) N 1s XPS spectra of NV-W₂N₃ before and after NRR for 10 h.

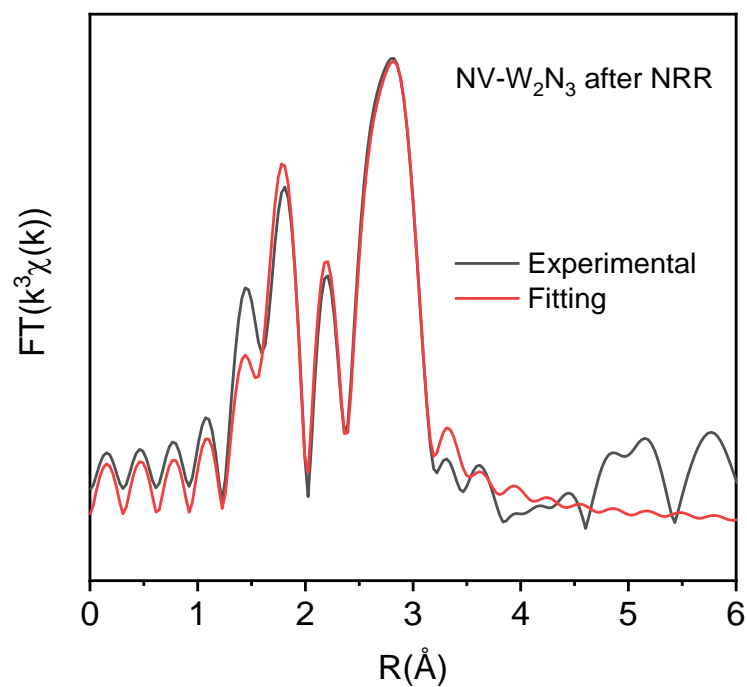


Figure S20. XAS Fitting results of NV-W₂N₃ after NRR test obtained from Synchrotron-based W L₃ edge XANES.

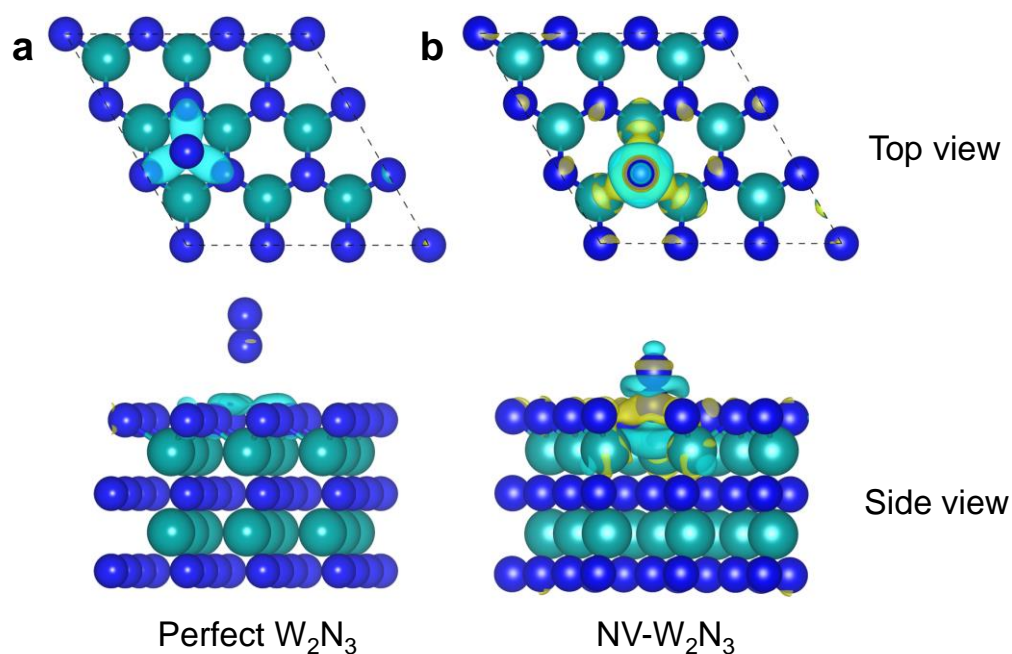


Figure S21. Interfacial electron transfer of dinitrogen molecule on (a) perfect W₂N₃ and (b) NV-W₂N₃.

Tables

Table S1. Ammonia yield and corresponding Faradaic efficiency of NV-W₂N₃ and controls.

Sample	Potential (vs. RHE)	Peak _{WE}	Peak _{KOH}	Peak _{offgas}	Peak _{H2SO4}	NH ₃ Yield* ($\mu\text{g h}^{-1} \text{mg}_{\text{cata}}^{-1}$)	Q (C)	FE %
NV- W ₂ N ₃	-0.1 1 st	0.0628	0.0366	0.0399	0.0385	4.88	0.28	11.88
	-0.1 2 nd	0.0608	0.0366	0.041	0.0385	4.59	0.31	10.08
	-0.1 3 rd	0.0581	0.0366	0.0426	0.0385	4.20	0.29	9.86
	-0.2 1 st	0.1008	0.0366	0.0523	0.0385	12.64	0.7	12.29
	-0.2 2 nd	0.1000	0.0366	0.0394	0.0385	11.66	0.68	11.67
	-0.2 3 rd	0.0937	0.0366	0.0452	0.0385	10.88	0.69	10.74
	-0.3 1 st	0.077	0.0366	0.0436	0.0385	7.72	1.06	4.96
	-0.3 2 nd	0.0736	0.0366	0.0404	0.0385	6.89	0.97	4.84
	-0.3 3 rd	0.0695	0.0366	0.0442	0.0385	6.39	0.94	4.63
	-0.4 1 st	0.0739	0.0366	0.0416	0.0385	7.02	7.53	0.64
	-0.4 2 nd	0.0682	0.0366	0.0441	0.0385	6.14	7.61	0.55
	-0.4 3 rd	0.0623	0.0366	0.0499	0.0385	5.44	7.49	0.49
	-0.5 1 st	0.0624	0.0366	0.0502	0.0385	5.48	21.94	0.17
	-0.5 2 nd	0.0588	0.0366	0.0452	0.0385	4.49	23.57	0.13
	-0.5 3 rd	0.055	0.0366	0.0512	0.0385	4.19	24.68	0.12
W ₂ N ₃	-0.2 1 st	0.0607	0.0345	0.0362	0.0357	4.82	0.33	9.96
	-0.2 2 nd	0.0596	0.0345	0.0359	0.0357	4.60	0.33	9.50
	-0.2 3 rd	0.0559	0.0345	0.0392	0.0357	4.14	0.31	9.10
300 °C	-0.2 1 st	0.0687	0.0345	0.0396	0.0357	6.51	0.41	10.81
	-0.2 2 nd	0.0688	0.0345	0.0363	0.0357	6.31	0.44	9.77
	-0.2 3 rd	0.0645	0.0345	0.0449	0.0357	6.08	0.45	9.21
400 °C	-0.2 1 st	0.0805	0.0345	0.0468	0.0357	9.13	0.56	11.11
	-0.2 2 nd	0.0766	0.0345	0.0481	0.0357	8.50	0.56	10.34

	-0.2 3 rd	0.0734	0.0345	0.0445	0.0357	7.68	0.52	10.06
	-0.2 1 st	0.0767	0.0345	0.0443	0.0357	8.28	0.64	8.81
600 °C	-0.2 2 nd	0.0734	0.0345	0.0503	0.0357	8.06	0.65	8.44
	-0.2 3 rd	0.0744	0.0345	0.0372	0.0357	7.40	0.62	8.12
Cycle								
No.								
1	-0.2	0.0912	0.0355	0.0416	0.0377	10.44	0.58	12.26
2	-0.2	0.0804	0.0355	0.0394	0.0377	8.32	0.56	10.12
3	-0.2	0.0763	0.0355	0.0389	0.0377	7.54	0.5	10.27
4	-0.2	0.0765	0.0355	0.0465	0.0377	8.07	0.57	9.64
5	-0.2	0.0815	0.0355	0.0396	0.0377	8.53	0.52	11.18
6	-0.2	0.0894	0.0355	0.043	0.0377	10.2	0.58	11.98
7	-0.2	0.0840	0.0355	0.0568	0.0377	10.11	0.62	11.1
8	-0.2	0.0795	0.0355	0.0435	0.0377	8.42	0.51	11.25
9	-0.2	0.0740	0.0355	0.0398	0.0377	7.18	0.59	8.28
10	-0.2	0.0809	0.0355	0.0531	0.0377	9.3	0.65	9.74
11	-0.2	0.0890	0.0355	0.0479	0.0377	10.45	0.69	10.31
12	-0.2	0.0858	0.0355	0.0561	0.0377	10.39	0.71	9.97

* The NH₃ yield is calculated based on the total NH₃ products in cathodic electrolyte (30 mL) and the acid traps (5mL × 2).

Table S2. Summary of NRR performances of different catalysts.

Sample	Loading mass (mg cm ⁻²)	NH ₃ yield	FE (%)	Detection method	Electrolyte	Over-potential (vs. RHE)	Ref.
NV-W ₂ N ₃	0.2	11.66 μg h ⁻¹ mg _{cata} ⁻¹ 2.23 μg h ⁻¹ cm ⁻²	11.67	Indophenol blue	0.10 M KOH	-0.2 V	This work
Bi NS	0.192	13.23 μg h ⁻¹ mg _{cata} ⁻¹	10.49	Indophenol blue	0.10 M Na ₂ SO ₄	-0.8 V	[10]
B ₄ C	0.1	2.657 μg h ⁻¹ cm ⁻²	15.95	Indophenol blue	0.10 M HCl	-0.75 V	[11]
Ti ₃ C ₂ T _x MXene	1.76	4.72 μg h ⁻¹ cm ⁻²	4.62	Nessler's reagent	0.50 M Li ₂ SO ₄	-0.1 V	[12]
Black phosphorus	0.2	31.37 μg h ⁻¹ mg _{cata} ⁻¹	3.09	Indophenol blue	0.01 M HCl	-0.7 V	[13]
Fe-N-C	1	7.48 μg h ⁻¹ mg _{cata} ⁻¹	56.55	Indophenol blue	1.0 M KOH	0 V	[14]
BiNCs	1	3400 μg h ⁻¹ mg _{cata} ⁻¹	66	Nessler's reagent	0.50 M K ₂ SO ₄	-0.6 V	[15]
Amorphous Au/CeO _x	2.62	8.3 μg h ⁻¹ mg _{cata} ⁻¹	10.1	Indophenol blue	0.10 M HCl	-0.2 V	[16]
Ru single-atom	2	3.665 μg h ⁻¹ mg _{cata} ⁻¹	7.5	Indophenol blue	0.10 M HCl	-0.21 V	[17]
Pd/C	0.3	4.5 μg h ⁻¹ mg _{cata} ⁻¹	8.2	Indophenol blue	0.10 M PBS	0.1 V	[18]
Au Nanorod	0.3	6.042 μg h ⁻¹ mg _{cata} ⁻¹	3.879	Nessler's reagent	0.10 M KOH	-0.2 V	[19]
Mo ₂ C	0.1	11.3 μg h ⁻¹ mg _{cata} ⁻¹	1.1	Nessler's reagent	0.50 M Li ₂ SO ₄	-0.3 V	[20]
Defect-rich MoS ₂	0.4	29.28 μg h ⁻¹ mg _{cata} ⁻¹	8.34	Indophenol blue	0.10 M Na ₂ SO ₄	-0.4 V	[21]
Ru/MoS ₂	1	6.98 μg h ⁻¹ mg _{cata} ⁻¹	17.6	Indophenol blue	0.01 M HCl	-0.15 V	[22]
Ru nanoparticles	1.7	0.55 μg h ⁻¹ cm ⁻²	5.4	Indophenol blue	0.01 M HCl	0.01 V	[23]
MoS ₂	N/A	5.38 μg h ⁻¹ cm ⁻²	1.17	Indophenol blue	0.10 M HCl	-0.5 V	[24]
C ₃ N ₄ -NV _x	2	8.09 μg h ⁻¹ cm ⁻²	11.59	Indophenol blue	0.10 M HCl	-0.2 V	[25]
VN _x nanoparticles	0.5	20.6 μg h ⁻¹ cm ⁻²	6	Nessler's reagent	0.05 M H ₂ SO ₄	-0.1 V	[26]
BiVO ₄	1	8.6 μg h ⁻¹ mg _{cata} ⁻¹	10.04	Indophenol Blue	0.20 M Na ₂ SO ₄	-0.5 V	[27]
PEBCD	1.28	2.01 μg h ⁻¹ cm ⁻²	1.71	Nessler's reagent	0.50 M Li ₂ SO ₄	-0.7 V	[28]

Table S3. Elemental analysis of NV-W₂N₃ before and after NRR test. The two electrodes have the same loading mass of NV-W₂N₃.

Sample	Mass (Carbon paper + NV-W₂N₃ + Nafion binder)	N %
NV-W₂N₃	12.29 mg	0.53
NV-W₂N₃ after NRR	12.10 mg	0.55

Table S4. ICP-MS of electrolytes after NRR test.

Sample	Conc. [ppb] W⁺
0.10 M KOH	<0.993
10 ppb W⁺	3.737169277
20 ppb W⁺	15.05726579
50 ppb W⁺	28.12337586
100 ppb W⁺	75.29028278
200 ppb W⁺	218.6314296
Electrolyte after NRR	<0.993

References

- [1] Z. Hu, X. Xiao, H. Jin, T. Li, M. Chen, Z. Liang, Z. Guo, J. Li, J. Wan, L. Huang, Y. Zhang, G. Feng, J. Zhou, *Nat. Commun.* **2017**, *8*, 15630.
- [2] G. Kresse, J. Furthmüller, *Comput. Mater. Sci.* **1996**, *6*, 15.
- [3] G. Kresse, J. Furthmüller, *Phys. Rev. B* **1996**, *54*, 11169.
- [4] G. Kresse, J. Hafner, *Phys. Rev. B* **1993**, *47*, 558.
- [5] G. Kresse, J. Hafner, *Phys. Rev. B* **1994**, *49*, 14251.
- [6] J. P. Perdew, K. Burke, M. Ernzerhof, *Phys. Rev. Lett.* **1996**, *77*, 3865.
- [7] S. Grimme, *J. Comput. Chem.* **2006**, *27*, 1787.
- [8] W. M. Haynes, *CRC Handbook of Chemistry and Physics*, CRC press, 2014.
- [9] T. Ressler, *Journal of Synchrotron Radiation* **1998**, *5*, 118.
- [10] L. Li, C. Tang, B. Xia, H. Jin, Y. Zheng, S.-Z. Qiao, *ACS Catal.* **2019**, *9*, 2902.
- [11] W. Qiu, X.-Y. Xie, J. Qiu, W.-H. Fang, R. Liang, X. Ren, X. Ji, G. Cui, A. M. Asiri, G. Cui, B. Tang, X. Sun, *Nat. Commun.* **2018**, *9*, 3485.
- [12] Y. Luo, G.-F. Chen, L. Ding, X. Chen, L.-X. Ding, H. Wang, *Joule* **2019**, *3*, 279.
- [13] G. Zhang, Q. Ji, K. Zhang, Y. Chen, Z. Li, H. Liu, J. Li, J. Qu, *Nano Energy* **2019**, *59*, 10.
- [14] M. Wang, S. Liu, T. Qian, J. Liu, J. Zhou, H. Ji, J. Xiong, J. Zhong, C. Yan, *Nat. Commun.* **2019**, *10*, 341.
- [15] Y.-C. Hao, Y. Guo, L.-W. Chen, M. Shu, X.-Y. Wang, T.-A. Bu, W.-Y. Gao, N. Zhang, X. Su, X. Feng, J.-W. Zhou, B. Wang, C.-W. Hu, A.-X. Yin, R. Si, Y.-W. Zhang, C.-H. Yan, *Nat. Catal.* **2019**, *2*, 448.
- [16] S. J. Li, D. Bao, M. M. Shi, B. R. Wulan, J. M. Yan, Q. Jiang, *Adv. Mater.* **2017**, *29*, 1700001.
- [17] H. Tao, C. Choi, L.-X. Ding, Z. Jiang, Z. Han, M. Jia, Q. Fan, Y. Gao, H. Wang, A. W. Robertson, S. Hong, Y. Jung, S. Liu, Z. Sun, *Chem* **2019**, *5*, 204.
- [18] J. Wang, L. Yu, L. Hu, G. Chen, H. Xin, X. Feng, *Nat. Commun.* **2018**, *9*, 1795.
- [19] D. Bao, Q. Zhang, F. L. Meng, H. X. Zhong, M. M. Shi, Y. Zhang, J. M. Yan, Q. Jiang, X. B. Zhang, *Adv. Mater.* **2017**, *29*, 1604799.

- [20] H. Cheng, L.-X. Ding, G.-F. Chen, L. Zhang, J. Xue, H. Wang, *Adv. Mater.* **2018**, *30*, 1803694.
- [21] X. Li, T. Li, Y. Ma, Q. Wei, W. Qiu, H. Guo, X. Shi, P. Zhang, A. M. Asiri, L. Chen, B. Tang, X. Sun, *Adv. Energy Mater.* **2018**, *8*, 1801357.
- [22] B. H. R. Suryanto, D. Wang, L. M. Azofra, M. Harb, L. Cavallo, R. Jalili, D. R. G. Mitchell, M. Chatti, D. R. MacFarlane, *ACS Energy Lett.* **2019**, *4*, 430.
- [23] D. Wang, L. M. Azofra, M. Harb, L. Cavallo, X. Zhang, B. H. R. Suryanto, D. R. MacFarlane, *ChemSusChem* **2018**, *11*, 3416.
- [24] L. Zhang, X. Ji, X. Ren, Y. Ma, X. Shi, Z. Tian, A. M. Asiri, L. Chen, B. Tang, X. Sun, *Adv. Mater.* **2018**, *30*, 1800191.
- [25] C. Lv, Y. Qian, C. Yan, Y. Ding, Y. Liu, G. Chen, G. Yu, *Angew. Chem. Int. Ed.* **2018**, *57*, 10246.
- [26] X. Yang, J. Nash, J. Anibal, M. Dunwell, S. Kattel, E. Stavitski, K. Attenkofer, J. G. Chen, Y. Yan, B. Xu, *J. Am. Chem. Soc.* **2018**, *140*, 13387.
- [27] J.-X. Yao, D. Bao, Q. Zhang, M.-M. Shi, Y. Wang, R. Gao, J.-M. Yan, Q. Jiang, *Small Methods* **2018**, *3*, 1800333.
- [28] G. F. Chen, X. Cao, S. Wu, X. Zeng, L. X. Ding, M. Zhu, H. Wang, *J. Am. Chem. Soc.* **2017**, *139*, 9771.

Chapter 7: Molten Salt-Directed Catalytic Synthesis of 2D Layered Transition Metal Nitrides for Efficient Hydrogen Evolution

7.1 Introduction and Significance

Exploratory synthesis of new 2D layered transition metal nitrides (TMNs) is very important in various research fields. However, stringent synthesis constraints have limited the exploration and preparation of this important class of functional materials. In this work, molten salts were used as catalysts to synthesize 2D layered TMNs under mild conditions. A new family of atomically thin 2D layered TMNs ($\text{MoN}_{1.2}$, $\text{WN}_{1.5}$ and MoWN_x alloy) was synthesized without further exfoliation and exhibited significant potential for the hydrogen evolution reaction. The salts in our method are not consumed or changed during the reaction but can facilitate the growth of 2D layered TMNs by providing a liquid-gas environment and forming a unique TMN-salt-TMN superstructure as an intermediate. The catalytic molten salt method is simple and universal, which creates new opportunities for the exploration and preparation of 2D layered materials with high formation energy for various applications. The highlights of this Chapter include:

- A new family of 2D TMNs was successfully synthesized for the first time.
- Molten salt can act as a catalyst for the synthesis of high-energy 2D layered TMNs.
- A series of ex-situ experiments reveal the growth mechanism and a unique TMN-salt-TMN superstructure is determined as an intermediate in the reaction.
- Both binary and ternary 2D TMNs nanosheets can be synthesized by simply changing the alkali metal salts.
- The 2D TMNs reveal low overpotentials for hydrogen evolution reaction with η_{10} of 129 mV in acidic media and 122 mV in alkaline media, which are much better than the corresponding values reported for most 2D layered electrocatalysts.

7.2 Molten Salt-Directed Catalytic Synthesis of 2D Layered Transition Metal Nitrides for Efficient Hydrogen Evolution

This Chapter is included as it appears as a journal paper published by **Huanyu Jin**, Qinfen Gu, Bo Chen, Cheng Tang, Yao Zheng, Hua Zhang, Mietek Jaroniec, Shi-Zhang Qiao Molten Salt-Directed Catalytic Synthesis of 2D Layered Transition Metal Nitrides for Efficient Hydrogen Evolution. *Chem* 2020, <https://doi.org/10.1016/j.chempr.2020.06.037>.

Statement of Authorship

Title of Paper	Molten Salt-Directed Catalytic Synthesis of 2D Layered Transition Metal Nitrides for Efficient Hydrogen Evolution
Publication Status	<input checked="" type="checkbox"/> Published <input type="checkbox"/> Accepted for Publication <input type="checkbox"/> Submitted for Publication <input type="checkbox"/> Unpublished and Unsubmitted work written in manuscript style
Publication Details	Huanyu Jin, Qinfen Gu, Bo Chen, Cheng Tang, Yao Zheng, Hua Zhang, Mietek Jaroniec, Shi-Zhang Qiao* Molten Salt-Directed Catalytic Synthesis of 2D Layered Transition Metal Nitrides for Efficient Hydrogen Evolution. <i>Chem</i> 2020, https://doi.org/10.1016/j.chempr.2020.06.037 .

Principal Author

Name of Principal Author (Candidate)	Huanyu Jin		
Contribution to the Paper	Research plan, material synthesis, most of the characterizations and data analysis, electrochemical characterization, and manuscript draft.		
Overall percentage (%)	90		
Certification:	This paper reports on original research I conducted during the period of my Higher Degree by Research candidature and is not subject to any obligations or contractual agreements with a third party that would constrain its inclusion in this thesis. I am the primary author of this paper.		
Signature	_____	Date	29/July/2020

Co-Author Contributions

By signing the Statement of Authorship, each author certifies that:

- the candidate's stated contribution to the publication is accurate (as detailed above);
- permission is granted for the candidate to include the publication in the thesis; and
- the sum of all co-author contributions is equal to 100% less the candidate's stated contribution.

Name of Co-Author	Qinfen Gu		
Contribution to the Paper	X-ray diffraction analysis and discussion.		
Signature	_____	Date	29/July/2020

Name of Co-Author	Bo Chen		
Contribution to the Paper	Transmission electron microscopy analysis.		
Signature	_____	Date	29/July/2020

Name of Co-Author	Cheng Tang		
Contribution to the Paper	Editing process and manuscript revision.		
Signature		Date	29/July/2020

Name of Co-Author	Yao Zheng		
Contribution to the Paper	Discussion of this manuscript.		
Signature		Date	29/July/2020

Name of Co-Author	Hua Zhang		
Contribution to the Paper	Transmission electron microscopy analysis and discussion of this manuscript.		
Signature		Date	29/July/2020

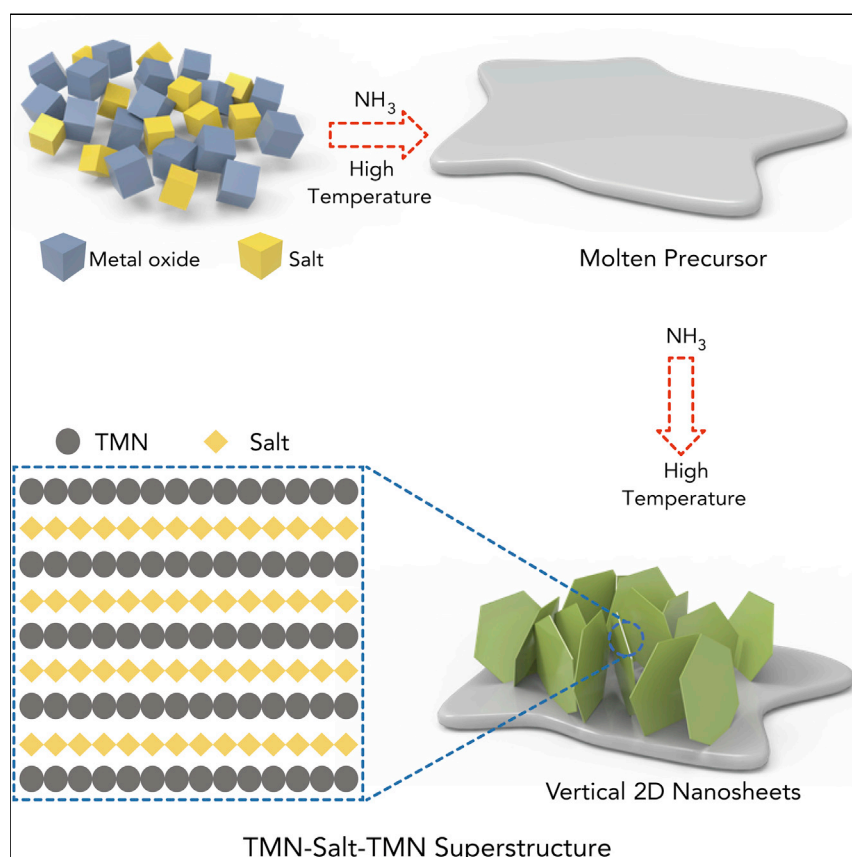
Name of Co-Author	Mietek Jaroniec		
Contribution to the Paper	Editing process and manuscript revision.		
Signature		Date	29/July/2020

Name of Co-Author	Shi-Zhang Qiao		
Contribution to the Paper	Supervision of the work, discussion of this manuscript and manuscript evaluation.		
Signature		Date	29/July/2020

Please cut and paste additional co-author panels here as required.

Article

Molten Salt-Directed Catalytic Synthesis of 2D Layered Transition-Metal Nitrides for Efficient Hydrogen Evolution



Exploratory synthesis of novel 2D layered materials is of vital importance for energy-related applications. In this work, 2D layered transition-metal nitrides were facilely synthesized *via* a catalytic molten salt method. Both binary and ternary 2D TMN nanosheets can be obtained by simply changing the salts with different alkali ions. The catalytic molten salt method is facile and universal, which opens new opportunities for the exploration and preparation of 2D layered materials for clean energy conversion and storage.

Huanyu Jin, Qinfen Gu, Bo Chen, ..., Hua Zhang, Mietek Jaroniec, Shi-Zhang Qiao

s.qiao@adelaide.edu.au

HIGHLIGHTS

Facile synthesis of 2D layered transition-metal nitrides is realized

Molten salt can act as a catalyst for the synthesis of high-energy 2D materials

2D layered transition-metal nitrides exhibit excellent activity for electrocatalysis



Article

Molten Salt-Directed Catalytic Synthesis of 2D Layered Transition-Metal Nitrides for Efficient Hydrogen Evolution

Huanyu Jin,¹ Qinfen Gu,² Bo Chen,³ Cheng Tang,¹ Yao Zheng,¹ Hua Zhang,^{4,5} Mietek Jaroniec,⁶ and Shi-Zhang Qiao^{1,7,*}

SUMMARY

Facile synthesis of single-crystal 2D layered transition-metal nitrides (TMNs) is of crucial importance for the development of forthcoming technologies, such as superconducting, electromagnetic interference shielding, and energy-related applications. However, the fabrication of TMNs with natural 2D layered structure is thermodynamically difficult, in which stringent synthesis constraints have limited the exploration of this important class of functional materials. Here, we employed alkali molten salts as catalysts to achieve facile and large-scale (over decagram) synthesis of a family of 2D layered TMNs, such as MoN_{1.2}, WN_{1.5}, and Mo_{0.7}W_{0.3}N_{1.2}, under atmospheric pressure. Ex-situ experiments reveal that the molten salt can lower the formation energy of 2D layered TMNs by assuring a liquid-gas synthesis and forming a TMN-salt-TMN superstructure as an intermediate. The resultant 2D layered TMNs show superior performance in hydrogen evolution reaction, demonstrating the immense potential of 2D layered TMNs for energy-related applications and beyond.

INTRODUCTION

Layered two-dimensional (2D) materials, which have unique electronic structure and large surface-to-volume ratios, are of great interest for electronics, physics, and chemistry.^{1–6} Over the past decades, a variety of 2D layered materials has been synthesized through many advanced methods, and have shown immense potential in various applications.^{7–12} The most extensively used classes of transition-metal-based 2D layered compounds are transition-metal oxides, hydroxides, and chalcogenides,^{10,13–19} but these do not always meet forthcoming technological requirements, such as superconducting, electromagnetic interference shielding, and energy-related applications.^{20–23} In sharp contrast, transition-metal nitrides (TMNs) are an exciting class of materials for superconductors, catalysis, energy storage, and so on.^{24–27} The nitride anion (N^{3–}) imparts unique electronic and bonding characteristics that are difficult to achieve in other compounds, leading to useful physical and chemical properties.²⁸ However, TMNs, especially 2D layered TMNs are rare due to the thermodynamic constraints for their synthesis.^{29,30} For instance, high-throughput computation predicted 1,036 exfoliable layered materials but only one is van der Waals layered 2D TMN.^{31,32} This is because TMNs are less thermodynamically stable compared with oxides under ambient conditions, and this, in turn, is driven by the high thermodynamic stability of N₂ compared with O₂.^{33,34} Consequently, conventional methods for the synthesis of 2D materials (e.g., chemical vapor deposition, liquid, and mechanical exfoliation) are limited for the preparation

The Bigger Picture

Exploratory synthesis of 2D layered materials is important in various research fields, such as electronics, physics, and chemistry. However, the preparation of 2D layered materials with a high formation energy is hindered by sluggish growth thermodynamics. 2D layered transition-metal nitrides (TMNs) represent an important class of materials, the synthesis of which is challenging. Here, we report a molten salt method that permits catalytic synthesis of a family of single-crystal 2D layered TMNs under relatively mild conditions. With the assistance of molten salt, the atomically thin 2D layered TMN nanosheets can be synthesized directly without further exfoliation process. We also investigated the effect of different alkali metal ions (Li⁺, Na⁺, and K⁺) on the growth of 2D TMNs, and both binary and ternary 2D layered TMNs were obtained. The catalytic molten salt method is a generic synthesis strategy, which opens opportunities for the exploration and preparation of 2D materials.

of 2D layered TMNs. Previously, we obtained 2D layered W_2N_3 nanosheets by ammoniation of 2D $Na_2W_4O_{13}$ templates under atmospheric pressure. However, the limited choice of suitable templates constrains the exploration of 2D layered TMNs.³⁵ Recently, researchers realized the synthesis of 2D layered TMN (MXene) by chemical exfoliation of $M_{n+1}AN_n$ matrix (M refers to an early transition metal, A usually refers to an element of 13 and 14 groups, and N is nitrogen atom).^{36,37} However, due to the poor stability of $M_{n+1}N_n$ layers during etching (e.g., HF), the synthesis of high-quality 2D layered TMNs is still challenging, and the only known 2D layered MXene nitrides are limited to Ti-based MXenes.^{8,36,37}

To explore 2D layered TMNs, the most effective way is the use of high pressure to prevent the out-diffusion of N atom from the metal lattice at high temperatures.^{35,38–40} However, such method is very expensive from the industrial perspective. Consequently, exploration and synthesis of 2D layered TMNs under atmospheric pressure is urgently needed. Notably, alkali metal ion plays a key role in lowering the formation energy of high-energy phased 2D materials. For example, the presence of K^+ ion can significantly reduce the formation energy of high-energy 2D transition-metal chalcogenides (e.g., $1T'-MoS_2$).⁴¹ Li^+ ions are pre-intercalated into the interlayers of $2H-MoS_2$, facilitating the formation of the high-energy $1T-MoS_2$.^{42,43} In the meantime, Hu et al., for the first time, found that the molten salt-assisted method can provide “naked” ions, which can further lower the growth energy of 2D materials by eliminating the ion desolvation and then increase the overall reaction rate.^{44,45} However, conventional molten salt methods use salts as reactants,^{10,44–46} and the lack of a stable ammoniate molten salt at high temperatures limits the synthesis of 2D layered TMNs.

In this work, we use molten alkali salts as catalysts to synthesize 2D layered TMNs under atmospheric pressure. Different from previous reports, the salts in our method act as catalysts instead of reactants, which are not consumed or changed in the reaction but can facilitate the growth of 2D layered TMNs. *Ex-situ* experiments revealed that the molten salt can lead to a liquid-gas growth of 2D TMNs by lowering the melting point of metal oxide precursors. Furthermore, it can intercalate into the interlayer space of 2D TMNs during the reaction to form a TMN-salt-TMN superstructure, which can lower the formation energy and stabilize the 2D layered structure. We also investigated the effect of different alkali metal ions (Li^+ , Na^+ and K^+) in the synthesis of 2D TMNs, and both 2D layered ternary and binary TMN nanosheets were obtained. In this work, we successfully synthesized binary 2D layered $MoN_{1.2}$, $WN_{1.5}$, and $Mo_{0.7}W_{0.3}N_{1.2}$ nanosheets for the first time. These 2D layered TMNs demonstrated superior electrocatalytic performance in hydrogen evolution reaction. Notably, the 2D layered $Mo_{0.7}W_{0.3}N_{1.2}$ exhibits small overpotentials of 129 and 122 mV at a current density of 10 mA cm^{-2} in 0.5 M H_2SO_4 and 1 M KOH, respectively, surpassing most of the 2D layered electrocatalysts. They also exhibit excellent oxidation resistance and film-forming property for practical applications.

RESULTS

Catalytic Molten Salt Method

Most metals or metal oxides have high melting points, so their direct ammoniation under NH_3 atmosphere is a solid-gas reaction. Such process is limited by the thermodynamically sluggish stuffing of N atoms into metal lattice.²⁸ Consequently, most of metal nitrides are nitrogen deficient (nitrogen over metal ratio < 1) with simple chemical compositions and crystal structures (e.g., Mo_2N , W_2N , and Ni_3N). On the contrary, mixed salts can significantly reduce the melting point of the metal and metal oxide precursors, and lead to a liquid-gas synthesis.^{10,47} Under molten state,

¹School of Chemical Engineering and Advanced Materials, The University of Adelaide, Adelaide, SA 5005, Australia

²Australian Synchrotron (ANSTO), 800 Blackburn Road, Clayton, VIC 3168, Australia

³Center for Programmable Materials, School of Materials Science and Engineering, Nanyang Technological University, 50 Nanyang Avenue, Singapore 639798, Singapore

⁴Department of Chemistry, City University of Hong Kong, Tat Chee Avenue, Kowloon, Hong Kong, China

⁵Hong Kong Branch of National Precious Metals Material Engineering Research Center (NPMM), City University of Hong Kong, Hong Kong, China

⁶Department of Chemistry and Biochemistry & Advanced Materials and Liquid Crystal Institute, Kent State University, Kent, OH 44242, USA

⁷Lead Contact

*Correspondence: s.qiao@adelaide.edu.au
<https://doi.org/10.1016/j.chempr.2020.06.037>

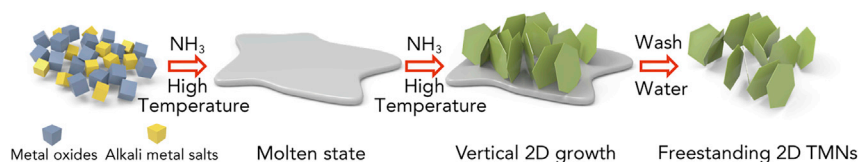


Figure 1. Synthesis of Materials via the Catalytic Molten Salt Method

A schematic illustration of the synthesis of 2D layered TMNs.

the metal precursors melt into monomers, which have higher reaction activity and faster reaction rate.⁴⁴ Using this method, we have synthesized a family of 2D layered materials, such as $\text{MoN}_{1.2}$, $\text{WN}_{1.5}$, and $\text{Mo}_{0.7}\text{W}_{0.3}\text{N}_{1.2}$. The composition of $\text{Mo}_{0.7}\text{W}_{0.3}\text{N}_{1.2}$ was confirmed using inductively coupled plasma mass spectrometry (ICP-MS). Figure 1 shows the flow chart for the synthesis of 2D layered TMNs using the molten salt method. Typically, metal oxide powders (e.g., MoO_3) were mixed with their alkali metal salts (e.g., Na_2MoO_4) via ball milling. Then the precursor was annealed under 5% NH_3 in Ar. Before ammoniation, the mixed precursor melted first, and then a bottom-up 2D vertical growth on the molten mixture surface took place. After water washing to remove the salts, the freestanding 2D layered TMN nanosheets were obtained. Since the final products were atomically thin nanosheets, no further exfoliation process was required. It should be noted that, without adding the salts, the final products are conventional 3D non-van der Waals MoN_x and W_2N nanoparticles (Figure S1). The resulting 2D layered TMNs nanosheets exhibited a good dispersity and stability in water, which is shown in Figure S2. After 60 days, no oxidation was observed, demonstrating good oxidation resistance of the produced 2D layered TMNs in water. We further investigated the stability of the 2D layered TMNs using X-ray photoelectron spectroscopy (XPS). After exposing $\text{MoN}_{1.2}$ to air for 8 months, this sample was shown to be stable without any obvious compositional change (Figures S2C and S2D). The observed good stability originates from the surface O terminations (Figure S2C), which can prevent further oxidation of 2D layered TMN. It should be noted that over a decagram of 2D layered TMNs powder can be obtained (Figure S3A) by one-time synthesis, which reveals the immense potential of this approach for large-scale production. In the meantime, the lyophilized 2D TMN powder can be directly rolled into a freestanding film with good hydrophilicity (Figures S3B and S4). The film is flat and thin, which is suitable for energy conversion and storage application.⁴⁸

Characterization of 2D Layered TMNs

The morphology and atomic structure of the 2D crystals are revealed by scanning electron microscopy (SEM) and spherical-aberration-corrected scanning transmission electron microscopy (STEM). Figures 2A, 2E, and 2I show the SEM images of $\text{MoN}_{1.2}$, $\text{WN}_{1.5}$, and $\text{Mo}_{0.7}\text{W}_{0.3}\text{N}_{1.2}$ after washing with water. Compared with the samples before washing (Figures S5 and S6), the 2D morphology was successfully preserved, demonstrating the structure stability of these 2D TMNs. Notably, the samples before washing were atomically thin 2D nanosheets instead of bulk particles. The atomic structure of the as-prepared 2D crystals exhibited a hexagonal molecular phase with similar in-plane crystal lattice of 0.25 nm (Figures 2B, 2F, and 2J). The selected area electron diffraction (SAED) in Figure S7 shows only one hexagonal pattern, indicating the single-crystal phase of 2D TMNs. The layered structure of the 2D crystals can be clearly seen in high-angle annular dark-field (HAADF) STEM images (Figures 2C, 2G, and 2K). The $\text{MoN}_{1.2}$ and $\text{Mo}_{0.7}\text{W}_{0.3}\text{N}_{1.2}$ materials show similar layered structure with single-layer thickness of about 0.6 nm (consisting 3 layers of Mo atoms per unit) and an interlayer distance of about 0.5 nm. Whereas a single

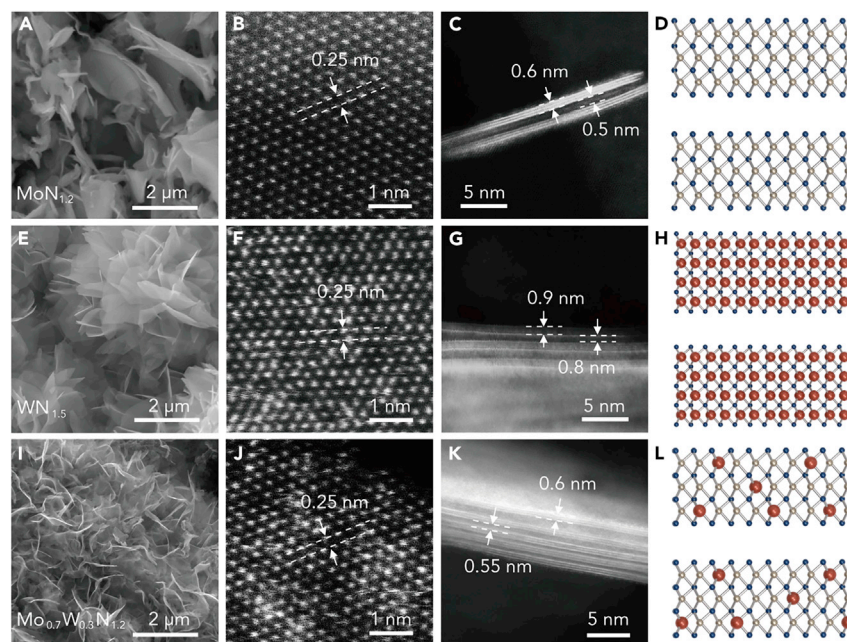


Figure 2. Structure Analysis of 2D Layered TMN Nanosheets by Electron Microscopy

(A, E, and I) SEM images of MoN_{1.2} (A), WN_{1.5} (E), and Mo_{0.7}W_{0.3}N_{1.2} (I). (B, F, and J) High resolution HAADF-STEM images of 2D layered MoN_{1.2} (B), WN_{1.5} (F), and Mo_{0.7}W_{0.3}N_{1.2} (J) nanosheets. (C, G, and K) Cross-sectional HAADF-STEM images of MoN_{1.2} (C), WN_{1.5} (G), and Mo_{0.7}W_{0.3}N_{1.2} (K), which show the thickness of the monolayer nanosheets and the distance of the interlayer space. (D, H, and L) Schematic illustration of the corresponding atomic arrangements of MoN_{1.2} (D), WN_{1.5} (H), and Mo_{0.7}W_{0.3}N_{1.2} (L). Blue, golden, and red spheres represent N, Mo, and W atoms, respectively.

layered WN_{1.5} consists of 4 layers of W atoms with single-layer thickness of 0.9 nm and interlayer space of 0.8 nm, which is different from MoN_{1.2} and the known W₂N₃.³⁵ Due to the large contrast of Mo or W atoms to N atoms under STEM mode, the N atom cannot be observed. The schematic illustration of the expected atomic arrangements is shown in Figures 2D, 2H, and 2L. Furthermore, Figure S8 shows the in-plane structure of Mo_{0.7}W_{0.3}N_{1.2}, in which W atoms are uniformly distributed on the MoN_{1.2} substrate, demonstrating a doped structure similar to MoWS_x chalcogenides.⁴⁹ We also compared the sample before and after washing with water (Figures 2C, 2G, 2K, and S9). The layered atomic structure remain unchanged, which was in accordance with the SEM images.

The crystal structure of the prepared 2D TMNs was further analyzed by X-ray diffraction (XRD). MoN_{1.2} and Mo_{0.7}W_{0.3}N_{1.2} have the similar XRD patterns as that of Mo₅N₆.⁵⁰ WN_{1.5} has the similar crystal structure as W₂N₃ (Figures 3A, 3B, and S10).³⁵ However, according to the TEM images perpendicular to the layers, the atom arrangement of MoN_{1.2} and WN_{1.5} at [001] facet clearly shows the unique layered structure, which is totally different from that of Mo₅N₆ (non-layered material) and W₂N₃ (2 layers of W atoms per unit) (Figure S11), indicating that our TMNs are newfound 2D materials. The broad peak before 10 degree for MoN_{1.2} and WN_{1.5} reflects the layered structure of 2D TMNs. To elucidate the chemical composition of 2D TMNs, we conducted XRD and XPS analysis for the samples before and after washing with water. As shown in Figure S12, the products before washing are only 2D TMNs and alkali metal salts (e.g., Na₂MoO₄). Apparently, in the reaction, the composition and content of the salt remains the same, demonstrating the catalytic

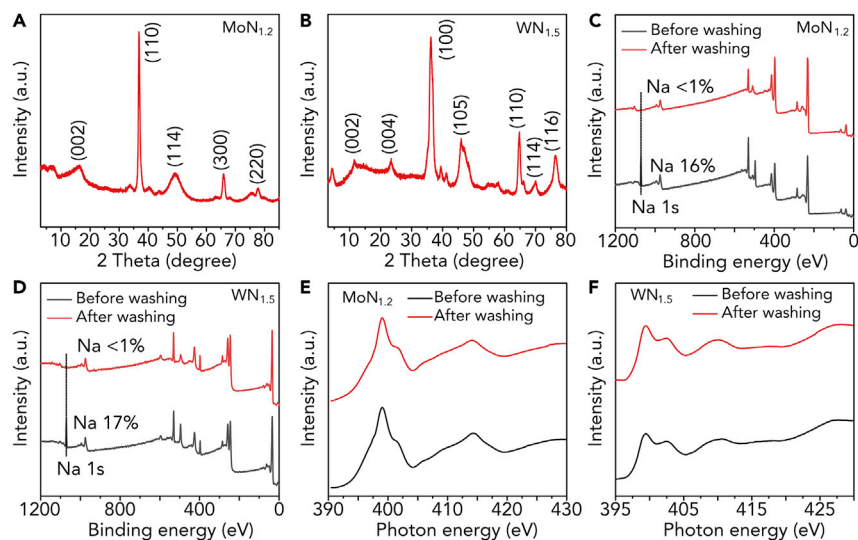


Figure 3. Characterization of 2D Layered TMNs

(A and B) XRD patterns of $\text{MoN}_{1.2}$ (A) and $\text{WN}_{1.5}$ (B).

(C and D) XPS surveys of $\text{MoN}_{1.2}$ (C) and $\text{WN}_{1.5}$ (D) before and after washing by water. The salt can be washed off easily due to the high solubility of Na_2MoO_4 and Na_2WO_4 in water.

(E and F) N K edge XANES spectra of $\text{MoN}_{1.2}$ (E) and $\text{WN}_{1.5}$ (F) before and after washing by water. The unchanged N K edge spectra elucidate the stable feature of 2D TMNs during desalination.

synthesis (Table S1). As shown in Figures 3C and 3D, the sodium content is significantly reduced to an undetectable level (Figure S13), indicating that the alkali metal salts are washed-out completely. In the meantime, the energy-dispersive X-ray spectroscopy (EDS) mapping under STEM mode also reveals that the sodium salts have been washed-out (Figures S14–S16). The high-resolution XPS spectra of Mo, W, and N indicate that the washing process only removes the salt, the nitrides remain stable (Figures S17–S19). By comparing the composition of the samples before and after reaction, the chemical content of 2D TMNs is determined (N over Mo ratio ~ 1.2 , N over W ratio ~ 1.5). Since the only invariable element during the washing process is nitrogen, we further conducted synchrotron-based X-ray absorption near edge structure (XANES) to observe the N K edge of 2D TMNs before and after washing. As expected, the N K edge spectra remain unchanged (Figures 3E and 3F), demonstrating the stable structure of 2D TMNs even after removal of salts.

DISCUSSION

Growth Mechanism

We further investigated the growth mechanism by a series of experiments and theoretical calculations. In this method, the key variables are the temperature and alkali metal salts. Consequently, we identified the growth mechanism by controlling these two factors. First, differential scanning calorimetry (DSC) and thermogravimetric analysis (TGA) were performed on different specimens to corroborate the temperature zone. As shown in Figure 4A, the melting point of $\text{MoO}_3\text{-Na}_2\text{MoO}_4$ mixture (608°C) is lower than that of MoO_3 (787°C) and Na_2MoO_4 (682°C), individually. Thus, we can conclude that before reaction, all the reactants are turned into molten state (Figures S20 and S21). The 2D growth zone is determined at 650°C – 700°C for $\text{MoN}_{1.2}$ and 700°C – 800°C for $\text{WN}_{1.5}$ by *ex-situ* measurement of the products obtained at different temperatures (Figures S22–S25). When the temperature is higher or lower, 2D nanosheets are not observed (Figure 4B). For example, when the

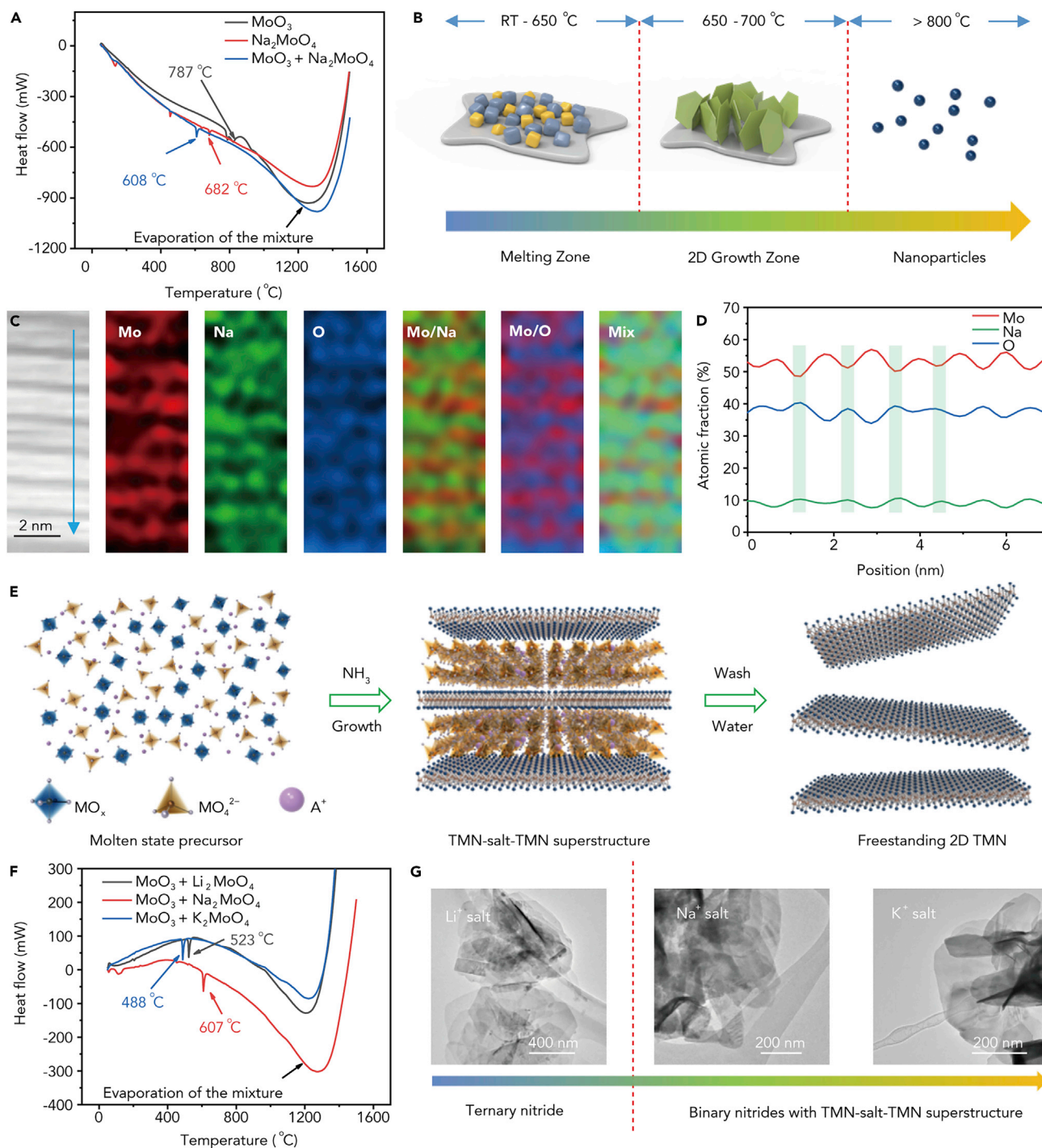


Figure 4. Growth Mechanism of 2D Layered TMN via the Catalytic Molten Salt Method

(A) DSC of different samples.

(B) Schematic illustration of the morphology evolution at different temperatures.

(C) Cross-sectional elemental mapping of a $\text{MoN}_{1.2}$ nanosheet before washing.

(D) Intensity line profile perpendicular to the layers of $\text{MoN}_{1.2}$, which shows the atomic fraction of different elements.

(E) Growth process of 2D layered TMN. When the precursor becomes molten state, $[\text{MO}_x]_{\text{octahedron}}$ monomer and ions are formed. Then, $[\text{MO}_x]_{\text{octahedron}}$ reacts with NH_3 first and the ions guide the self-assembly of the 2D structure.

(F) DSC profiles of MoO_3 mixed with different salts.

(G) TEM images of 2D TMN nanosheets obtained using different salts.

temperature rises to 900°C, the 2D WN_{1.5} structure collapses into conventional TMNs nanoparticles (Mo₂N and W₂N) (Figures S22 and S24).

Second, we explored the role of salts during synthesis. For molybdenum nitride, the final product without the salt is a mixture of MoN and MoO₂. Thus, we calculated the formation enthalpy of MoN and MoN_{1.2} to evaluate their thermodynamic stability. As expected, the formation enthalpy of MoN_{1.2} is -0.378 eV, which is higher than that for MoN (-0.395 eV). Consequently, it is more difficult to synthesize MoN_{1.2} under mild conditions. After adding salt, MoN_{1.2} is obtained instead of MoN, which indicates that the molten salt can lower the formation energy of 2D layered TMNs.

Now, we explain why the 2D morphology, rather than the three-dimensional (bulk) morphology, was obtained in this study. For 2D structured materials, such as MoN_{1.2}, the reaction rate constant (*k*) in different growth directions determines the thickness (*k_a* for the [001] direction) and lateral size (*k_b* for the [110] direction). Thus, we need to confirm the relationship between *k* and activation energy (*E*) in the molten salt system, which is shown in Equation 1:⁴⁴

$$\frac{k_b}{k_a} = e^{\frac{E_a - E_b}{RT}} \quad (\text{Equation 1})$$

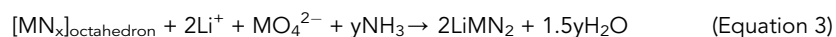
where, *E_a* and *E_b* are the activation energies in different growth directions, *R* is the molar gas constant (8.314 J mol⁻¹ K⁻¹) and *T* is the reaction temperature. Interestingly, the cross-sectional elemental mapping of the MoN_{1.2} nanosheets before washing (Figures 4C and 4D) clearly shows that the salt is distributed in the interlayer space of 2D TMNs, demonstrating the formation of a TMN-salt-TMN superstructure (Figure S26). This is similar to the exfoliation of 2H-MoS₂ in which Li⁺ ions tend to intercalate into the interlayer space rather than into the in-plane crystal lattice of the matrix.^{51,52} Consequently, the salt interacts with (110) facet directly and lowers its activation energy (*E_b*). With the lower values of *E_b*, the *k_b* over *k_a* increases. As a result, the growth of 2D layered TMNs along the [110] direction is favorable and leads to a 2D morphology.

Based on these investigations, we can conclude that the formation of 2D layered TMNs consists of three steps. The first step is the formation of [MO_{*x*}]_{octahedron} seeds from the melted metal oxides (*M* represents metal ion; *x* is the number of oxygen atoms), followed by ammoniation of [MO_{*x*}]_{octahedron} seeds. Finally, the growth of TMN crystals is based on the assembly of the ammonized [MoN_{*x*}]_{octahedron} seeds induced by the ions from the molten salts (Figures 4E and S27). Taking MoN_{1.2} as an example, MoO₃ is transformed to MoO₂ due to the reducibility of NH₃ (Figure S23), and then [MoO₆]_{octahedron} is formed by melting MoO₂ during the reaction. When the temperature reaches 650°C, [MoO₆]_{octahedron} is transformed to [MoN_{*x*}]_{octahedron} first (Equation 2) and then assembled into a 2D plane with the cation and anion intercalated into the interlayer to stabilize the layered structure and form the 2D TMN-salt-TMN superstructure (Equation 3).



In order to examine the universality of this method, we further investigated the effect of other alkali metal salts on the synthesis of 2D layered TMNs. Here, we use Mo-based nitrides as examples. Molybdates with different alkali metal ions (Li₂MoO₄

and K_2MoO_4) were chosen for the synthesis of TMNs under the same conditions. As expected, both lithium salt and potassium salt led to the growth of 2D layered TMNs via the molten salt method (Figures 4F and S28–S30). However, due to the small ionic radius of Li^+ ion, lithium salt becomes a reactant other than a catalyst, which leads to the growth of ternary nitrides nanosheets, such as LiMoN_2 or LiWN_2 , as shown in Equation 4 (Figure S29).



However, for sodium and potassium salts, 2D binary nitrides with TMN-salt-TMN superstructure are formed (Figures 4G, S30, and S31). Based on these results, we can conclude that the molten salt method is a facile and general approach, which can be applied to the growth of $\text{MoN}_{1.2}$, $\text{WN}_{1.5}$, and $\text{Mo}_{0.7}\text{W}_{0.3}\text{N}_{1.2}$ by forming a unique TMN-salt-TMN superstructure as an intermediate. Three factors were considered for choosing salts in the synthesis of binary 2D layered TMNs: (1) the salt should contain alkali metal ion (e.g., Na^+) to guarantee an ion-induced 2D growth, (2) the salt should not react with the metal oxide precursor or NH_3 at growth temperature to ensure the catalytic synthesis of 2D layered TMNs, and (3) the melting point of the salts should be appropriate to ensure a molten state growth at certain temperature.

Electrochemical Properties of 2D Layered TMNs

We further investigated the performance of these 2D layered TMNs in energy-related applications, such as hydrogen evolution reaction (HER). Since TMNs have excellent electron conductivity and noble metal-like electronic structure,^{50,53} 2D TMNs are expected to exhibit good catalytic performance in HER. Figures 5A and 5D show the linear sweep voltammetry (LSV) curves for different 2D layered TMNs in 0.5 M H_2SO_4 and 1 M KOH, respectively. At the current density of 10 mA cm^{-2} , the 2D $\text{Mo}_{0.7}\text{W}_{0.3}\text{N}_{1.2}$ exhibits the lowest overpotential (η_{10}) of 129 mV in acidic electrolyte and 122 mV in alkaline electrolyte, which are significantly lower than those for $\text{MoN}_{1.2}$ and $\text{WN}_{1.5}$, individually. This activity enhancement can be attributed to the optimized W sites induced by the doping process. Additionally, $\text{Mo}_{0.7}\text{W}_{0.3}\text{N}_{1.2}$ shows the Tafel slope of 59 and 47 mV dec^{-1} (Figures 5B and 5E) under acidic and alkaline conditions, indicating that the Volmer step is no longer the rate-determining step due to the optimization of hydrogen adsorption ability. Importantly, the unique metal-nitrogen bonds can guarantee a noble-metal-like electronic structure of transition-metal nitrides.⁵⁰ Therefore, the 2D layered $\text{Mo}_{0.7}\text{W}_{0.3}\text{N}_{1.2}$ features a robust stability in both acidic and alkaline solutions, which is required for a sustainable hydrogen production (Figures 5C and 5F). XRD and SEM measurements for the samples after HER were conducted (Figure S32) and demonstrated high stability of $\text{Mo}_{0.7}\text{W}_{0.3}\text{N}_{1.2}$ during HER. To achieve a comprehensive assessment of the 2D layered electrocatalysts, the η_{10} values of $\text{Mo}_{0.7}\text{W}_{0.3}\text{N}_{1.2}$ in acidic (Figure 5G; Table S2) and alkaline media (Figure 5H; Table S3) were compared with other 2D layered HER catalysts reported in recent studies. Evidently, the value of η_{10} and Tafel slope for $\text{Mo}_{0.7}\text{W}_{0.3}\text{N}_{1.2}$ are lower than the corresponding values for most of the reported 2D electrocatalysts for HER, by virtue of the rich metal-nitrogen bonding and higher valence state of the metal atoms.^{6,13,54–57}

In addition, our 2D layered TMNs can also serve as the promising electrode materials for capacitive energy storage owing to the unique 2D layered structure, rapid ion transport, and film-forming ability. The highest volumetric capacitance of $\text{MoN}_{1.2}$ is 842 F cm^{-3} , which is comparable to the MXene materials (Figures S33–S37).^{48,58}

This work demonstrates that the catalytic molten salt method is well suited for scalable synthesis of a family of 2D layered TMNs under mild conditions. The

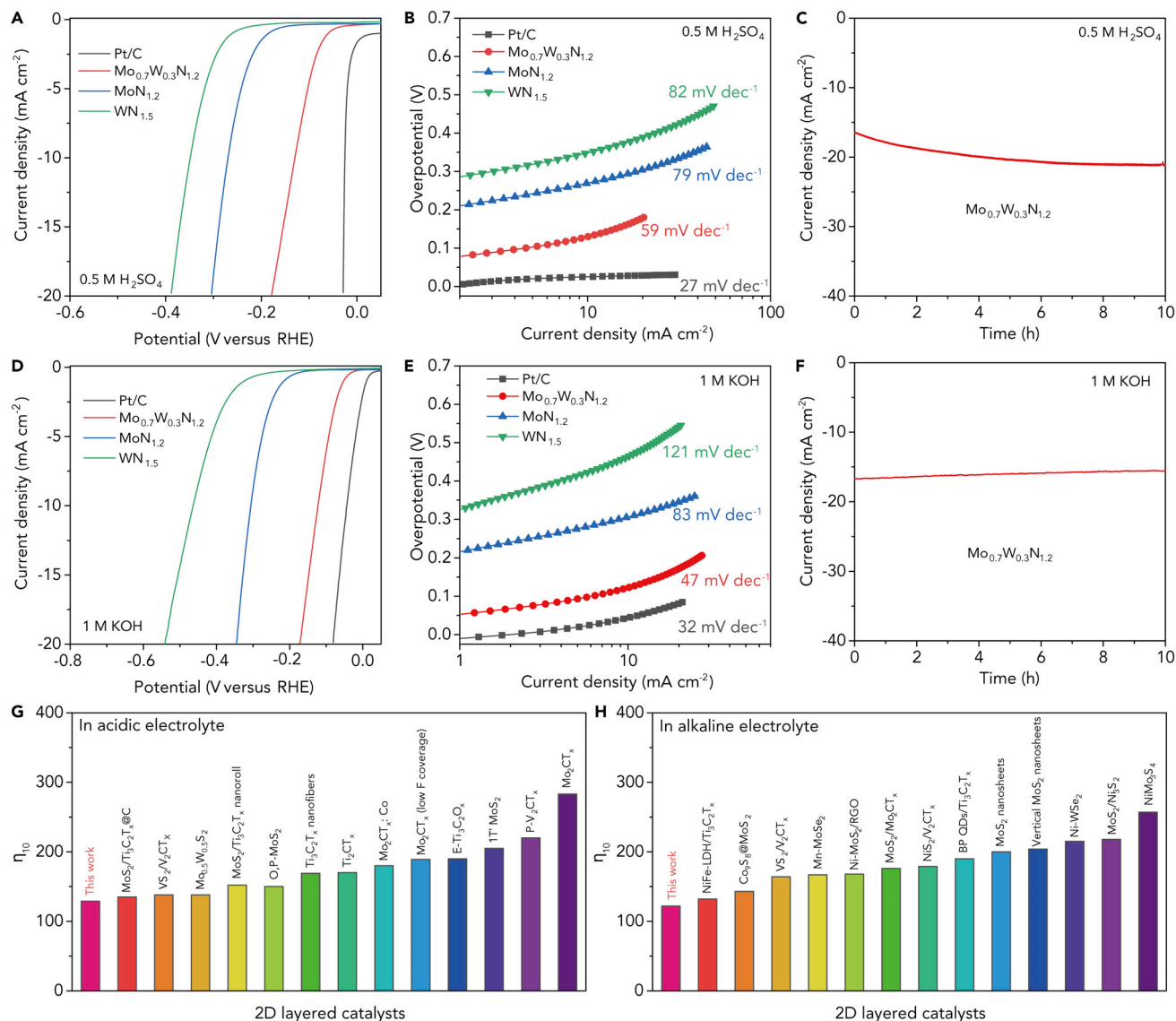


Figure 5. HER Performance of 2D Layered TMNs

(A and B) LSV curves (A) and corresponding Tafel plots (B) of the 2D layered TMNs in Ar-saturated 0.5 M H₂SO₄ solution. Scan rate: 5 mV s⁻¹. RHE, reversible hydrogen electrode.

(C) Long-term stability of Mo_{0.7}W_{0.3}N_{1.2} for HER under acidic conditions.

(D and E) LSV curves (D) and corresponding Tafel plots (E) of the 2D layered TMNs in Ar-saturated 1 M KOH solution. Scan rate: 5 mV s⁻¹.

(F) Long-term stability of Mo_{0.7}W_{0.3}N_{1.2} for HER under alkaline conditions.

(G and H) Comparison of η_{10} with recently reported 2D layered HER catalysts in both acidic (G) and alkaline (H) conditions. η_{10} , overpotential at the current density of 10 mA cm⁻².

molten salts act as catalysts during the synthesis and enable the formation of a unique TMN-salt-TMN superstructure. The control experiments reveal the critical role of alkali metal ion and reaction temperature in the synthesis, which provides the unique ion-induced growth environment and lower formation energy. The resulting 2D TMNs show excellent HER performance as the HER electrocatalysts and high volumetric capacitance as the capacitive electrode materials, which are better than most of the conventional 2D layered materials. The catalytic molten salt method is facile and scalable for synthesizing a series of 2D layered TMNs and

represents a promising route for manufacturing 2D layered materials for various applications.

EXPERIMENTAL PROCEDURES

Resource Availability

Lead Contact

Further information and requests for resources and reagents should be directed to and will be fulfilled by the Lead Contact, Shi-Zhang Qiao (s.qiao@adelaide.edu.au).

Materials Availability

This study did not generate new unique reagents.

Data and Code Availability

The data supporting the findings of this study are available for the article and [Supplemental Information](#) or from the corresponding authors upon request.

Synthesis of 2D Layered MoN_{1.2} Nanosheets

The 2D MoN_{1.2} nanosheets were synthesized via a three-step method. First, 1.44 g of MoO₃ powder and 2.42 g of Na₂MoO₄·2H₂O (or 2.38 g of K₂MoO₄) powders (mole ratio of 1:1) were mixed via ball milling. Ball milling was carried out in a planetary micro mill system (Fritsch PULVERISSETTE 7 premium line) with a rotation speed of 400 rpm for 20 min (two cycles). Then, 100 mg of this mixture was put flatly into a porcelain boat. It should be noted that if the thickness of the accumulation was too large, the reaction would have been incomplete due to the formation of molten salt shield. The 2D MoN_{1.2} material was produced by annealing the as-prepared precursor at 650°C for 5 h at the ramp rate of 1°C min⁻¹ under 5% NH₃ in Ar atmosphere. Finally, the product was washed by ultrasonication in deionized water to remove the salt.

Synthesis of 2D Layered WN_{1.5} Nanosheets

The 2D layered WN_{1.5} nanosheets were synthesized via a three-step method like that used for the preparation of MoN_{1.2}. First, 2.31 g of WO₃ powder and 3.3 g of Na₂WO₄·2H₂O (or 3.26 g of K₂WO₄) powder (mole ratio of 1:1) were mixed via ball milling. Then, 100 mg of this mixture was put into a porcelain boat uniformly. The 2D WN_{1.5} material was produced by annealing the as-prepared precursor at 750°C for 5 h at the ramp rate of 1°C min⁻¹ under 5% NH₃ in Ar atmosphere. Finally, the product was washed by ultrasonication in deionized water to remove the salt.

Synthesis of 2D Layered Mo_{0.7}W_{0.3}N_{1.2} Nanosheets

First, 50 mg of MoO₃-Na₂MoO₄·2H₂O mixture and 50 mg of WO₃-Na₂WO₄·2H₂O were mixed. Then, the mixture was put into a porcelain boat uniformly. The 2D Mo_{0.7}W_{0.3}N_{1.2} material was produced by annealing the as-prepared precursor at 650°C for 5 h at the ramp rate of 1°C min⁻¹ under 5% NH₃ in Ar atmosphere. Finally, the product was washed by ultrasonication in deionized water.

Synthesis of 2D Ternary TMN Nanosheets

Li₂MoO₄ (Li₂WO₄) was mixed with MoO₃ (WO₃) with the mole ratio of 1:1 using ball milling. Then, the mixture was annealed at 650°C (750°C for W) for 5 h at the ramp rate of 1°C min⁻¹ under 5% NH₃ in Ar atmosphere. Finally, the product was washed by ultrasonication in deionized water.

Electrochemical Test for HER

Typically, 4 mg of catalyst was dispersed in 800 μL of deionized water. Then 200 μL of 1 wt % Nafion in water was added to the catalyst dispersion. Since all the catalysts are

electrically conductive, carbon black was not added. Next, 20 μL of the catalyst dispersion (4 mg mL^{-1}) was transferred onto a 5 mm glassy carbon rotating disk electrode (0.4 mg cm^{-2}) serving as the working electrode. The reference electrode was Ag–AgCl in 3.5 M KCl solution and the counter electrode was a graphite rod. All potentials were referenced to the reversible hydrogen electrode by adding $(0.205 + 0.059 \times \text{pH})$ and all polarization curves were corrected for the iR compensation within the cell. A flow of Ar was maintained over the electrolyte during the experiment to eliminate dissolved oxygen. The working electrode was rotated at 1,600 rpm to remove hydrogen gas formed on the catalyst surface.

SUPPLEMENTAL INFORMATION

Supplemental Information can be found online at <https://doi.org/10.1016/j.chempr.2020.06.037>.

ACKNOWLEDGMENTS

This work is financially supported by the Australian Research Council (DP170104464, DP160104866, LP160100927, DE160101163, and FL170100154). XANES measurements were undertaken on the soft X-ray beamline at Australian Synchrotron. SEM and TEM measurements were undertaken at Adelaide Microscopy, the Centre for Advanced Microscopy and Microanalysis. We thank Dr. Xiaobo Zheng from the Institute for Superconducting & Electronic Materials, University of Wollongong for performing DFT calculations. H.Z. thanks the financial support from ITC via Hong Kong Branch of National Precious Metals Material Engineering Research Center (NPMM), and the start-up grant (project no. 9380100) and grants (project no. 9610478 and 1886921) in City University of Hong Kong.

AUTHOR CONTRIBUTIONS

H.J. and S.-Z.Q. conceived the project and designed the experiments. H.J. carried out experiments. H.J., Q.G., B.C., C.T., Y.Z., H.Z., M.J., and S.-Z.Q. analyzed the data; B.C. assisted in TEM measurements, Q.G. assisted in analysis of XRD, H.J., M.J., and S.-Z.Q. wrote the paper. All authors have given approval to the final version of the manuscript.

DECLARATION OF INTERESTS

The authors declare no competing interests.

Received: April 7, 2020

Revised: May 11, 2020

Accepted: June 28, 2020

Published: July 24, 2020

REFERENCES

1. Novoselov, K.S., Mishchenko, A., Carvalho, A., and Castro Neto, A.H. (2016). 2D materials and van der Waals heterostructures. *Science* 353, aac9439.
2. Novoselov, K.S., Geim, A.K., Morozov, S.V., Jiang, D., Zhang, Y., Dubonos, S.V., Grigorieva, I.V., and Firsov, A.A. (2004). Electric field effect in atomically thin carbon films. *Science* 306, 666–669.
3. Jaramillo, T.F., Jørgensen, K.P., Bonde, J., Nielsen, J.H., Hørch, S., and Chorkendorff, I. (2007). Identification of active edge sites for electrochemical H_2 evolution from MoS_2 nanocatalysts. *Science* 317, 100–102.
4. Lin, Z., Huang, Y., and Duan, X. (2019). Van der Waals thin-film electronics. *Nat. Electron.* 2, 378–388.
5. Wang, M., Ballabio, M., Wang, M., Lin, H.H., Biswal, B.P., Han, X., Paasch, S., Brunner, E., Liu, P., Chen, M., et al. (2019). Unveiling electronic properties in metal–phthalocyanine-based pyrazine-linked conjugated two-dimensional covalent organic frameworks. *J. Am. Chem. Soc.* 141, 16810–16816.
6. Du, Z., Yang, S., Li, S., Lou, J., Zhang, S., Wang, S., Li, B., Gong, Y., Song, L., Zou, X., and Ajayan, P.M. (2020). Conversion of non-van der Waals solids to 2D transition-metal chalcogenides. *Nature* 577, 492–496.
7. Nicolosi, V., Chhowalla, M., Kanatzidis, M.G., Strano, M.S., and Coleman, J.N. (2013). Liquid exfoliation of layered materials. *Science* 340, 1226419.
8. Anasori, B., Lukatskaya, M.R., and Gogotsi, Y. (2017). 2D metal carbides and nitrides

- (MXenes) for energy storage. *Nat. Rev. Mater.* **2**, 16098.
9. Chhowalla, M., Shin, H.S., Eda, G., Li, L.J., Loh, K.P., and Zhang, H. (2013). The chemistry of two-dimensional layered transition metal dichalcogenide nanosheets. *Nat. Chem.* **5**, 263–275.
 10. Zhou, J., Lin, J., Huang, X., Zhou, Y., Chen, Y., Xia, J., Wang, H., Xie, Y., Yu, H., Lei, J., et al. (2018). A library of atomically thin metal chalcogenides. *Nature* **556**, 355–359.
 11. Xiao, X., Wang, H., Bao, W., Urbankowski, P., Yang, L., Yang, Y., Maleski, K., Cui, L., Billinge, S.J.L., Wang, G., and Gogotsi, Y. (2019). Two-dimensional arrays of transition metal nitride nanocrystals. *Adv. Mater.* **31**, e1902393.
 12. Xiao, X., Wang, H., Urbankowski, P., and Gogotsi, Y. (2018). Topochemical synthesis of 2D materials. *Chem. Soc. Rev.* **47**, 8744–8765.
 13. Yu, Y., Nam, G.-H., He, Q., Wu, X.J., Zhang, K., Yang, Z., Chen, J., Ma, Q., Zhao, M., Liu, Z., et al. (2018). High phase-purity 1T'-MoS₂- and 1T'-MoSe₂-layered crystals. *Nat. Chem.* **10**, 638–643.
 14. McManus, D., Vranic, S., Withers, F., Sanchez-Romaguera, V., Macucci, M., Yang, H., Sorrentino, R., Parvez, K., Son, S.K., Iannaccone, G., et al. (2017). Water-based and biocompatible 2D crystal inks for all-inkjet-printed heterostructures. *Nat. Nanotechnol.* **12**, 343–350.
 15. Xiao, X., Song, H., Lin, S., Zhou, Y., Zhan, X., Hu, Z., Zhang, Q., Sun, J., Yang, B., Li, T., et al. (2016). Scalable salt-templated synthesis of two-dimensional transition metal oxides. *Nat. Commun.* **7**, 11296.
 16. Yang, J., Zeng, Z., Kang, J., Betzler, S., Czarnik, C., Zhang, X., Ophus, C., Yu, C., Bustillo, K., Pan, M., et al. (2019). Formation of two-dimensional transition metal oxide nanosheets with nanoparticles as intermediates. *Nat. Mater.* **18**, 970–976.
 17. Lin, Z., Liu, Y., Halim, U., Ding, M., Liu, Y., Wang, Y., Jia, C., Chen, P., Duan, X., Wang, C., et al. (2018). Solution-processable 2D semiconductors for high-performance large-area electronics. *Nature* **562**, 254–258.
 18. Zheng, Y.-R., Wu, P., Gao, M.-R., Zhang, X.-L., Gao, F.-Y., Ju, H.-X., Wu, R., Gao, Q., You, R., Huang, W.-X., et al. (2018). Doping-induced structural phase transition in cobalt diselenide enables enhanced hydrogen evolution catalysis. *Nat. Commun.* **9**, 2533.
 19. Wang, H., Xiao, X., Liu, S., Chiang, C.-L., Kuai, X., Peng, C.-K., Lin, Y.-C., Meng, X., Zhao, J., Choi, J., et al. (2019). Structural and electronic optimization of MoS₂ edges for hydrogen evolution. *J. Am. Chem. Soc.* **141**, 18578–18584.
 20. Xu, C., Wang, L., Liu, Z., Chen, L., Guo, J., Kang, N., Ma, X.L., Cheng, H.M., and Ren, W. (2015). Large-area high-quality 2D ultrathin Mo₂C superconducting crystals. *Nat. Mater.* **14**, 1135–1141.
 21. Shahzad, F., Alhabeb, M., Hatter, C.B., Anasori, B., Man Hong, S., Koo, C.M., and Gogotsi, Y. (2016). Electromagnetic interference shielding with 2D transition metal carbides (MXenes). *Science* **353**, 1137–1140.
 22. Qi, K., Cui, X., Gu, L., Yu, S., Fan, X., Luo, M., Xu, S., Li, N., Zheng, L., Zhang, Q., et al. (2019). Single-atom cobalt array bound to distorted 1T MoS₂ with ensemble effect for hydrogen evolution catalysis. *Nat. Commun.* **10**, 5231.
 23. Pomerantseva, E., Bonaccorso, F., Feng, X., Cui, Y., and Gogotsi, Y. (2019). Energy storage: the future enabled by nanomaterials. *Science* **366**, eaan8285.
 24. Guo, Y., Peng, J., Qin, W., Zeng, J., Zhao, J., Wu, J., Chu, W., Wang, L., Wu, C., and Xie, Y. (2019). Freestanding cubic ZrN single-crystalline films with two-dimensional superconductivity. *J. Am. Chem. Soc.* **141**, 10183–10187.
 25. Yuan, Y., Wang, J., Adimi, S., Shen, H., Thomas, T., Ma, R., Attfield, J.P., and Yang, M. (2020). Zirconium nitride catalysts surpass platinum for oxygen reduction. *Nat. Mater.* **19**, 282–286.
 26. Song, F., Li, W., Yang, J., Han, G., Liao, P., and Sun, Y. (2018). Interfacing nickel nitride and nickel boosts both electrocatalytic hydrogen evolution and oxidation reactions. *Nat. Commun.* **9**, 4531.
 27. Xi, S., Lin, G., Jin, L., Li, H., and Xie, K. (2019). Metallic porous nitride single crystals at two-centimeter scale delivering enhanced pseudocapacitance. *Nat. Commun.* **10**, 4727.
 28. Chen, J.G. (1996). Carbide and nitride overlayers on early transition metal surfaces: preparation, characterization, and reactivities. *Chem. Rev.* **96**, 1477–1498.
 29. Xie, J., and Xie, Y. (2015). Transition metal nitrides for electrocatalytic energy conversion: opportunities and challenges. *Chemistry* **22**, 3588–3598.
 30. Bykov, M., Chariton, S., Fei, H., Fedotenko, T., Aprilis, G., Ponomareva, A.V., Tasnádi, F., Abrikosov, I.A., Merle, B., Feldner, P., et al. (2019). High-pressure synthesis of ultraincompressible hard rhenium nitride pernitride Re₂(N₂)(N)₂ stable at ambient conditions. *Nat. Commun.* **10**, 2994.
 31. Mounet, N., Gibertini, M., Schwaller, P., Campi, D., Merkys, A., Marrazzo, A., Söhler, T., Castellì, I.E., Cepellotti, A., Pizzi, G., and Marzari, N. (2018). Two-dimensional materials from high-throughput computational exfoliation of experimentally known compounds. *Nat. Nanotechnol.* **13**, 246–252.
 32. Wang, S., Yu, X., Lin, Z., Zhang, R., He, D., Qin, J., Zhu, J., Han, J., Wang, L., Mao, H.-k., et al. (2012). Synthesis, crystal structure, and elastic properties of novel tungsten nitrides. *Chem. Mater.* **24**, 3023–3028.
 33. Sun, W., Bartel, C.J., Arca, E., Bauers, S.R., Matthews, B., Orvañanos, B., Chen, B.R., Toney, M.F., Schelhas, L.T., Tumas, W., et al. (2019). A map of the inorganic ternary metal nitrides. *Nat. Mater.* **18**, 732–739.
 34. Riedel, R., and Yu, Z. (2019). Charting stability space. *Nat. Mater.* **18**, 664–665.
 35. Jin, H., Li, L., Liu, X., Tang, C., Xu, W., Chen, S., Song, L., Zheng, Y., and Qiao, S.-Z. (2019). Nitrogen vacancies on 2D layered W₂N₃: a stable and efficient active site for nitrogen reduction reaction. *Adv. Mater.* **31**, 1902709.
 36. Urbankowski, P., Anasori, B., Makaryan, T., Er, D., Kota, S., Walsh, P.L., Zhao, M., Shenoy, V.B., Barsoum, M.W., and Gogotsi, Y. (2016). Synthesis of two-dimensional titanium nitride Ti₄N₃ (MXene). *Nanoscale* **8**, 11385–11391.
 37. Soundiraraju, B., and George, B.K. (2017). Two-dimensional titanium nitride (Ti₂N) MXene: synthesis, characterization, and potential application as surface-enhanced Raman scattering substrate. *ACS Nano* **11**, 8892–8900.
 38. Salamat, A., Hector, A.L., Kroll, P., and McMillan, P.F. (2013). Nitrogen-rich transition metal nitrides. *Coord. Chem. Rev.* **257**, 2063–2072.
 39. Wang, S., Ge, H., Sun, S., Zhang, J., Liu, F., Wen, X., Yu, X., Wang, L., Zhang, Y., Xu, H., et al. (2015). A new molybdenum nitride catalyst with rhombohedral MoS₂ structure for hydrogenation applications. *J. Am. Chem. Soc.* **137**, 4815–4822.
 40. Yu, H., Yang, X., Xiao, X., Chen, M., Zhang, Q., Huang, L., Wu, J., Li, T., Chen, S., Song, L., et al. (2018). Atmospheric-pressure synthesis of 2D nitrogen-rich tungsten nitride. *Adv. Mater.* **30**, e1805655.
 41. Liu, L., Wu, J., Wu, L., Ye, M., Liu, X., Wang, Q., Hou, S., Lu, P., Sun, L., Zheng, J., et al. (2018). Phase-selective synthesis of 1T' MoS₂ monolayers and heterophase bilayers. *Nat. Mater.* **17**, 1108–1114.
 42. Tan, C., Cao, X., Wu, X.J., He, Q., Yang, J., Zhang, X., Chen, J., Zhao, W., Han, S., Nam, G.-H., et al. (2017). Recent advances in ultrathin two-dimensional nanomaterials. *Chem. Rev.* **117**, 6225–6331.
 43. Zeng, M., Xiao, Y., Liu, J., Yang, K., and Fu, L. (2018). Exploring two-dimensional materials toward the next-generation circuits: from monomer design to assembly control. *Chem. Rev.* **118**, 6236–6296.
 44. Hu, Z., Xiao, X., Jin, H., Li, T., Chen, M., Liang, Z., Guo, Z., Li, J., Wan, J., Huang, L., et al. (2017). Rapid mass production of two-dimensional metal oxides and hydroxides via the molten salts method. *Nat. Commun.* **8**, 15630.
 45. Jin, H., Hu, Z., Li, T., Huang, L., Wan, J., Xue, G., and Zhou, J. (2019). Mass production of high-quality transition metal dichalcogenides nanosheets via a molten salt method. *Adv. Funct. Mater.* **29**, 1900649.
 46. Dash, A., Vaßen, R., Guillon, O., and Gonzalez-Julian, J. (2019). Molten salt shielded synthesis of oxidation prone materials in air. *Nat. Mater.* **18**, 465–470.
 47. Wang, H., Sandoz-Rosado, E.J., Tsang, S.H., Lin, J., Zhu, M., Mallick, G., Liu, Z., and Teo, E.H.T. (2019). Elastic properties of 2D ultrathin tungsten nitride crystals grown by chemical vapor deposition. *Adv. Funct. Mater.* **29**, 1902663.
 48. Tao, Q., Dahlqvist, M., Lu, J., Kota, S., Meshkian, R., Halim, J., Palisaitis, J., Hultman, L., Barsoum, M.W., Persson, P.O.Å., and Rosen, J. (2017). Two-dimensional Mo_{1.33}C MXene with divacancy ordering prepared from parent 3D laminate with in-plane chemical ordering. *Nat. Commun.* **8**, 14949.

49. Lei, Y., Pakhira, S., Fujisawa, K., Wang, X., Iyola, O.O., Perea López, N., Laura Elías, A., Pulickal Rajukumar, L., Zhou, C., Kabius, B., et al. (2017). Low-temperature synthesis of heterostructures of transition metal dichalcogenide alloys ($W_2Mo_{1-x}S_2$) and graphene with superior catalytic performance for hydrogen evolution. *ACS Nano* *11*, 5103–5112.
50. Jin, H., Liu, X., Vasileff, A., Jiao, Y., Zhao, Y., Zheng, Y., and Qiao, S.Z. (2018). Single-crystal Nitrogen-rich two-dimensional Mo_5N_6 nanosheets for efficient and stable seawater splitting. *ACS Nano* *12*, 12761–12769.
51. Wang, H., Yuan, H., Sae Hong, S., Li, Y., and Cui, Y. (2015). Physical and chemical tuning of two-dimensional transition metal dichalcogenides. *Chem. Soc. Rev.* *44*, 2664–2680.
52. Voiry, D., Mohite, A., and Chhowalla, M. (2015). Phase engineering of transition metal dichalcogenides. *Chem. Soc. Rev.* *44*, 2702–2712.
53. Xie, J., Li, S., Zhang, X., Zhang, J., Wang, R., Zhang, H., Pan, B., and Xie, Y. (2014). Atomically-thin molybdenum nitride nanosheets with exposed active surface sites for efficient hydrogen evolution. *Chem. Sci.* *5*, 4615–4620.
54. Kuznetsov, D.A., Chen, Z., Kumar, P.V., Tsoukalou, A., Kierzkowska, A., Abdala, P.M., Safonova, O.V., Fedorov, A., and Müller, C.R. (2019). Single site cobalt substitution in 2D molybdenum carbide (MXene) enhances catalytic activity in the hydrogen evolution reaction. *J. Am. Chem. Soc.* *141*, 17809–17816.
55. Wang, H., Ouyang, L., Zou, G., Sun, C., Hu, J., Xiao, X., and Gao, L. (2018). Optimizing MoS_2 edges by alloying isovalent W for robust hydrogen evolution activity. *ACS Catal.* *8*, 9529–9536.
56. Seh, Z.W., Fredrickson, K.D., Anasori, B., Kibsgaard, J., Strickler, A.L., Lukatskaya, M.R., Gogotsi, Y., Jaramillo, T.F., and Vojvodic, A. (2016). Two-dimensional molybdenum carbide (MXene) as an efficient electrocatalyst for hydrogen evolution. *ACS Energy Lett.* *1*, 589–594.
57. Li, S., Tuo, P., Xie, J., Zhang, X., Xu, J., Bao, J., Pan, B., and Xie, Y. (2018). Ultrathin MXene nanosheets with rich fluorine termination groups realizing efficient electrocatalytic hydrogen evolution. *Nano Energy* *47*, 512–518.
58. Ghidui, M., Lukatskaya, M.R., Zhao, M.Q., Gogotsi, Y., and Barsoum, M.W. (2014). Conductive two-dimensional titanium carbide ‘clay’ with high volumetric capacitance. *Nature* *516*, 78–81.

Chem, Volume 6

Supplemental Information

Molten Salt-Directed Catalytic Synthesis of 2D Layered Transition-Metal Nitrides for Efficient Hydrogen Evolution

Huanyu Jin, Qinfen Gu, Bo Chen, Cheng Tang, Yao Zheng, Hua Zhang, Mietek Jaroniec, and Shi-Zhang Qiao

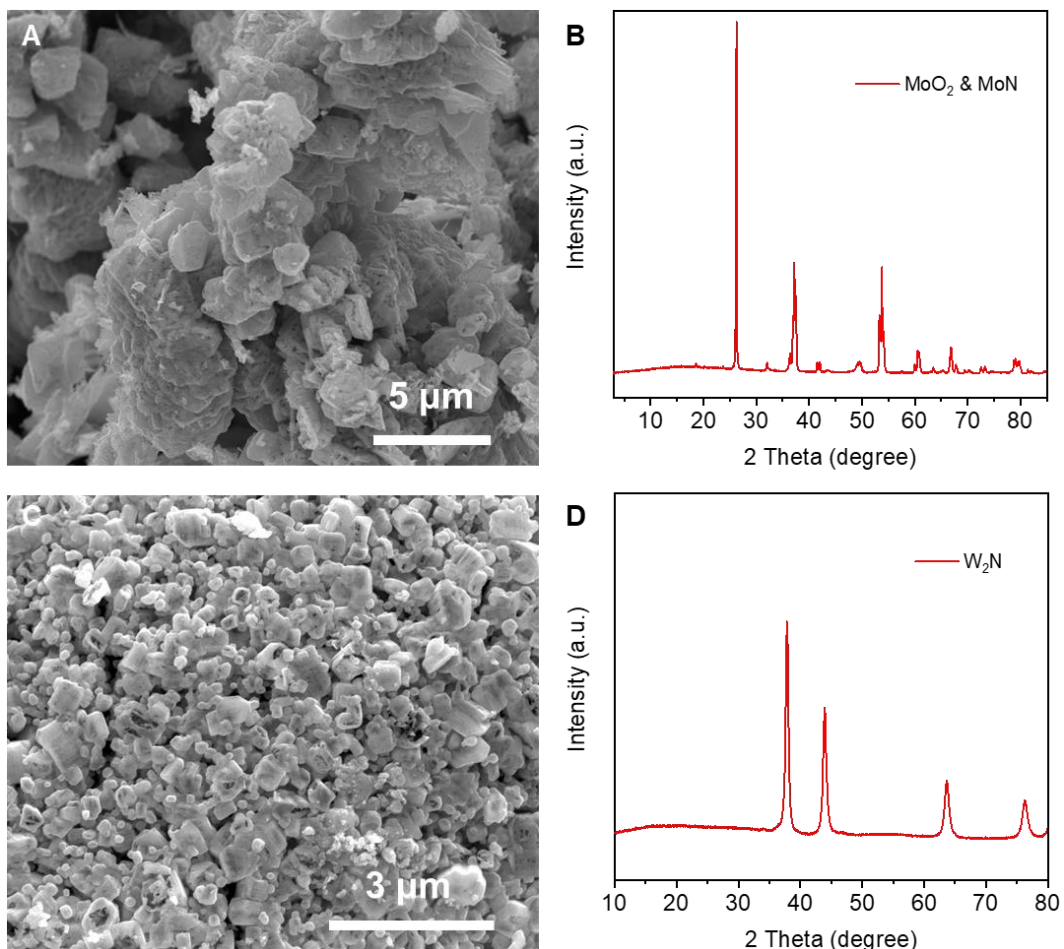


Figure S1. SEM images and XRD patterns of the ammoniated samples from MoO_3 and WO_3 powders without salts.

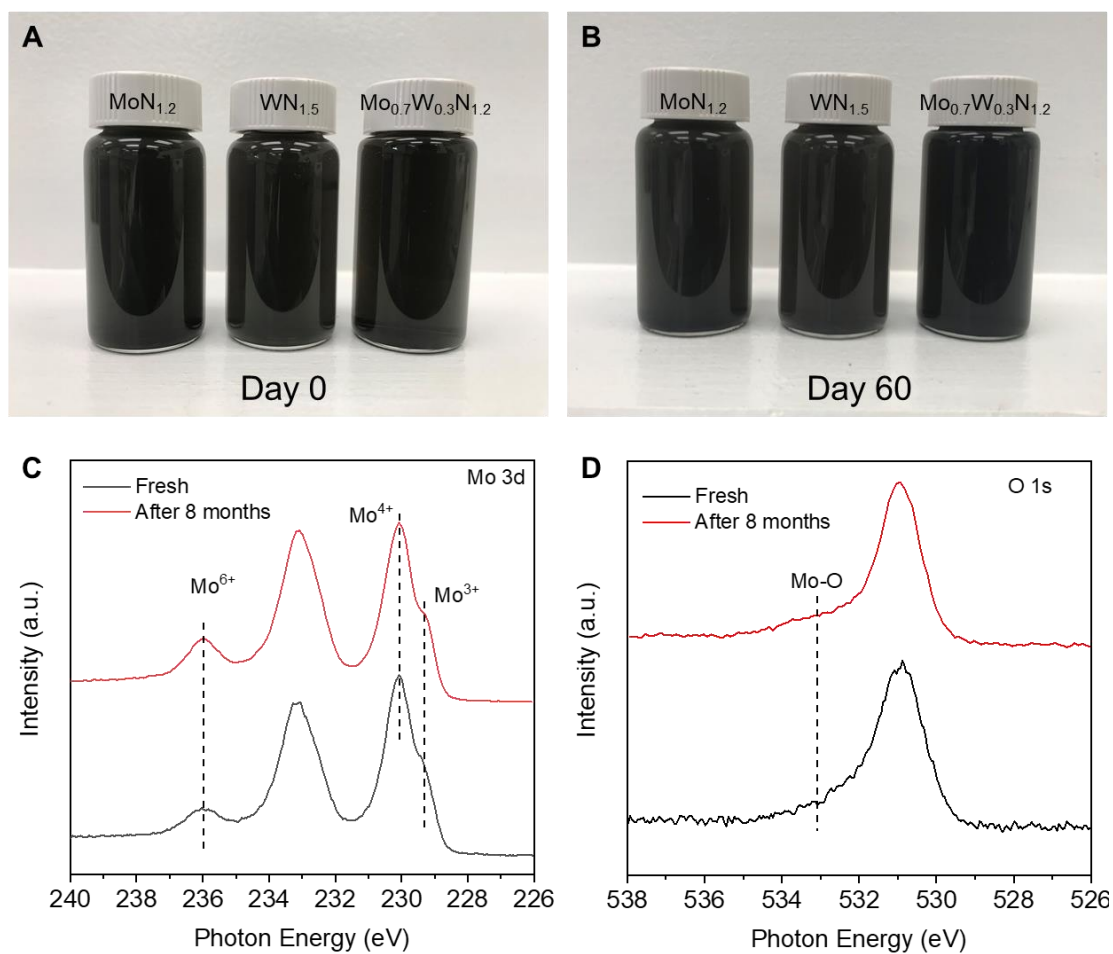


Figure S2. (A) and (B) Images of the 2D TMN fresh dispersion in Milli-Q water (day 0) and dispersion in the 60th day. (C) Mo 3d and (D) O 1s XPS spectra of MoN_{1.2} before and after exposure to air for 8 months. The intensity of the peak at 532 eV (Mo-O bonding) increases slightly after 8 months, indicating the existence of surface O termination.

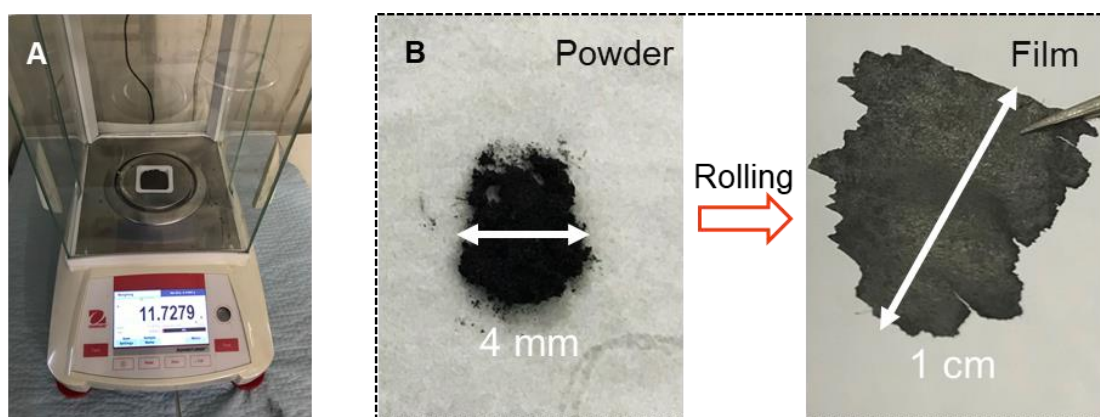


Figure S3. (A) Photograph of 2D MoN_{1.2} powder obtained from one-pot synthesis by increasing the amount of precursors. (B) The freeze-dried 2D TMNs (MoN_{1.2}) powder behaves like a clay, which can be rolled to produce the freestanding films.

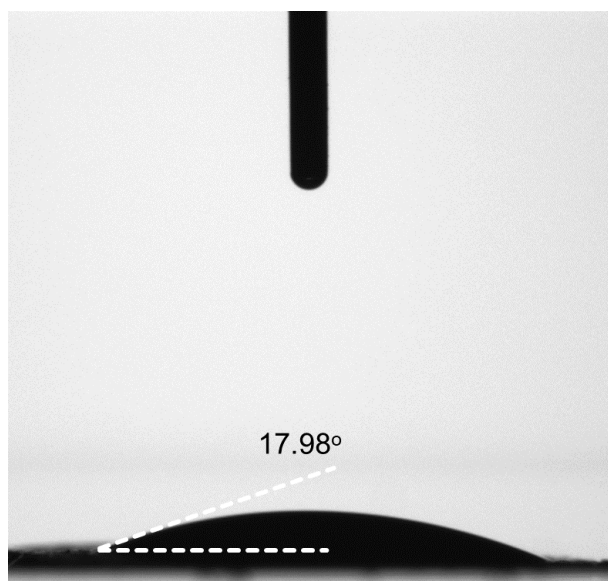


Figure S4. Digital image showing the contact angle of a water droplet on a rolled TMN film.

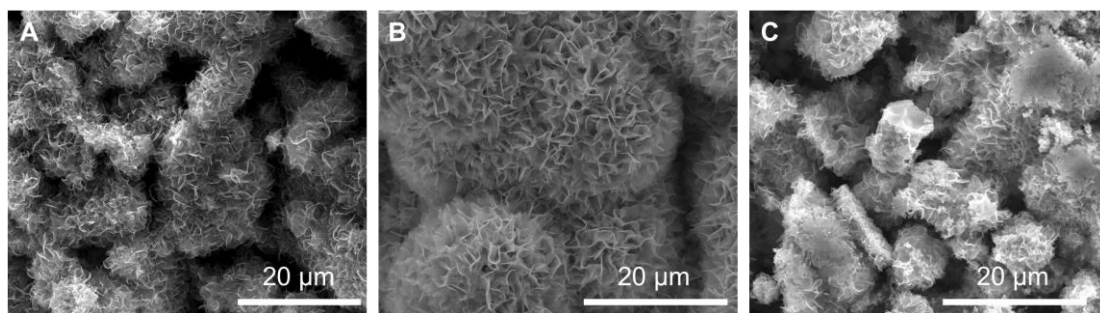


Figure S5. Low resolution SEM images of (A) $\text{MoN}_{1.2}$, (B) $\text{WN}_{1.5}$ and (C) $\text{Mo}_{0.7}\text{W}_{0.3}\text{N}_{1.2}$ before washing.

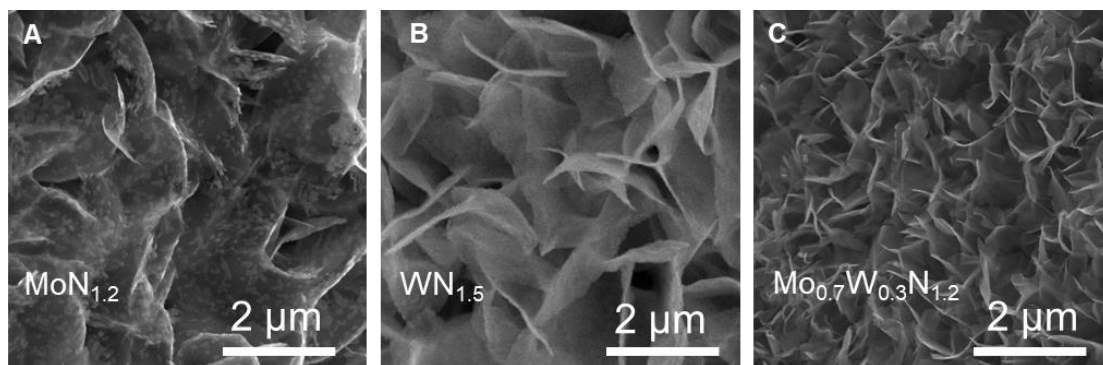


Figure S6. High resolution SEM images of (A) $\text{MoN}_{1.2}$, (B) $\text{WN}_{1.5}$ and (C) $\text{Mo}_{0.7}\text{W}_{0.3}\text{N}_{1.2}$ before washing.

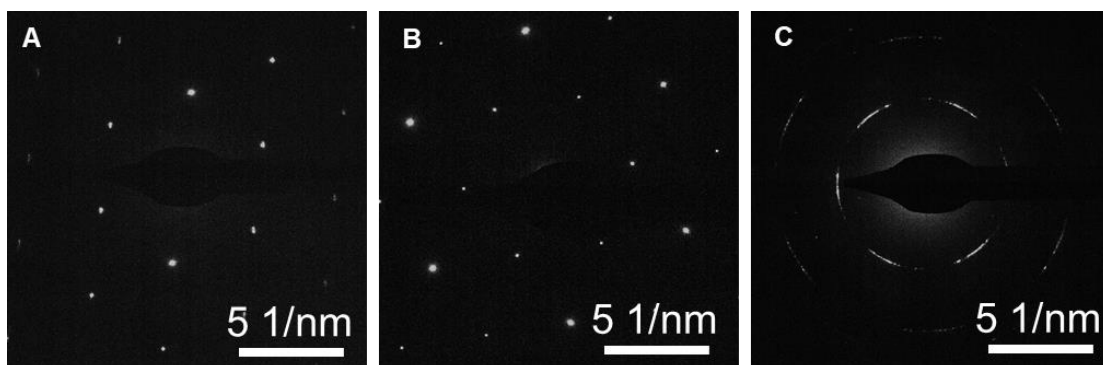


Figure S7. SAED patterns that demonstrate the single-crystal structure of 2D layered TMNs. (A) $\text{MoN}_{1.2}$, (B) $\text{WN}_{1.5}$ and (C) $\text{Mo}_{0.7}\text{W}_{0.3}\text{N}_{1.2}$. The ring-shaped pattern in (C) is due to the overlapping of multiple nanosheets.

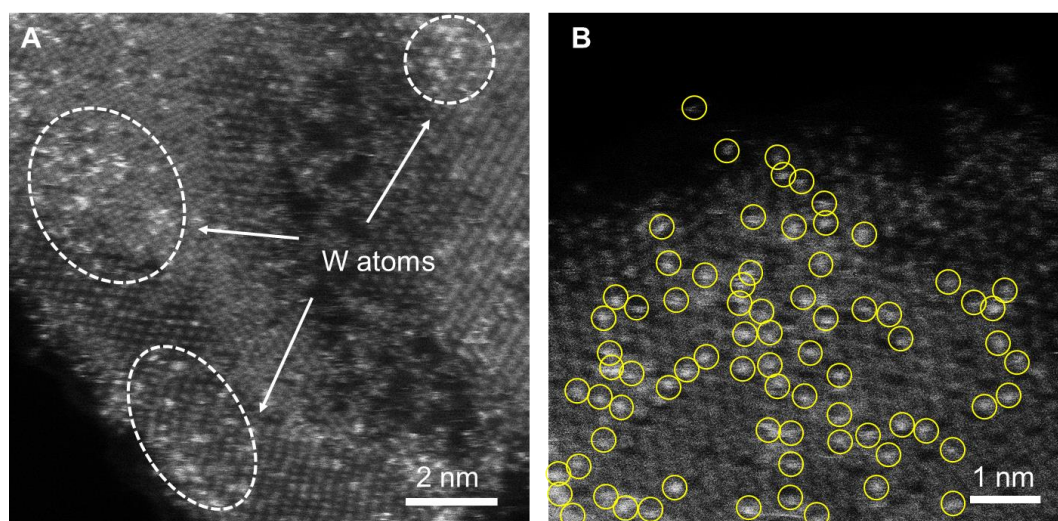


Figure S8. STEM images of $\text{Mo}_{0.7}\text{W}_{0.3}\text{N}_{1.2}$. The bright dots represent W atoms on $\text{MoN}_{1.2}$ nanosheets.

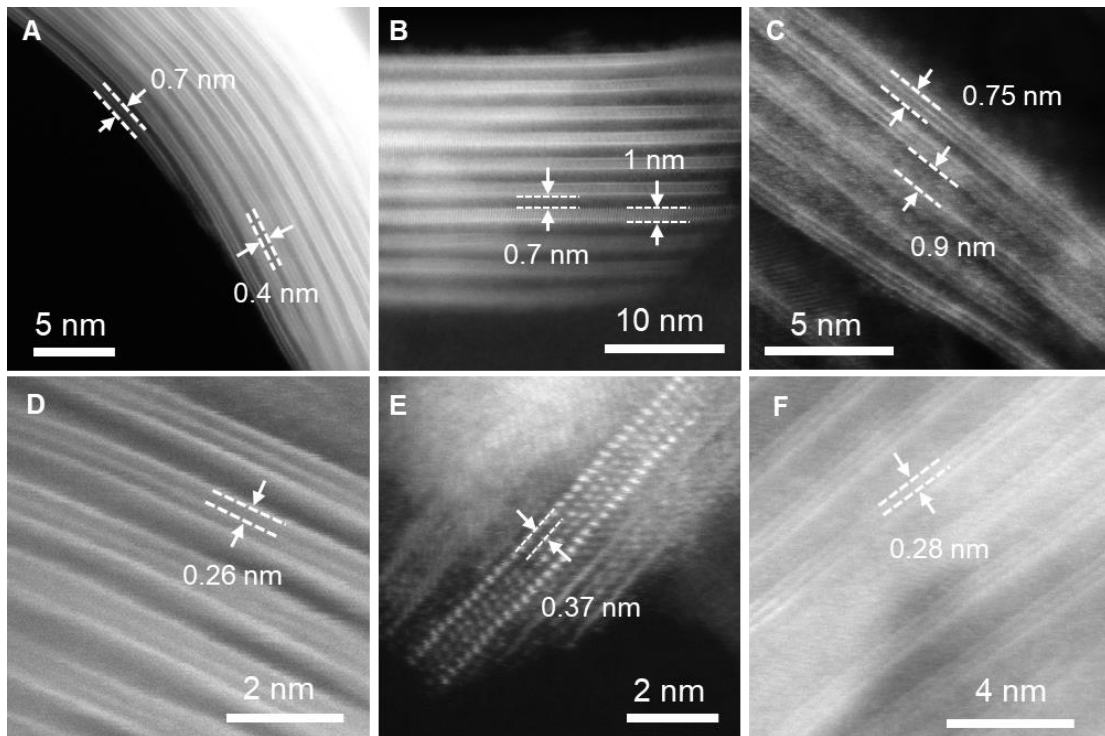


Figure S9. Cross-sectional HAADF-STEM images of (A), (D) MoN_{1.2}, (B), (E) WN_{1.5} and (C), (F) Mo_{0.7}W_{0.3}N_{1.2} before washing.

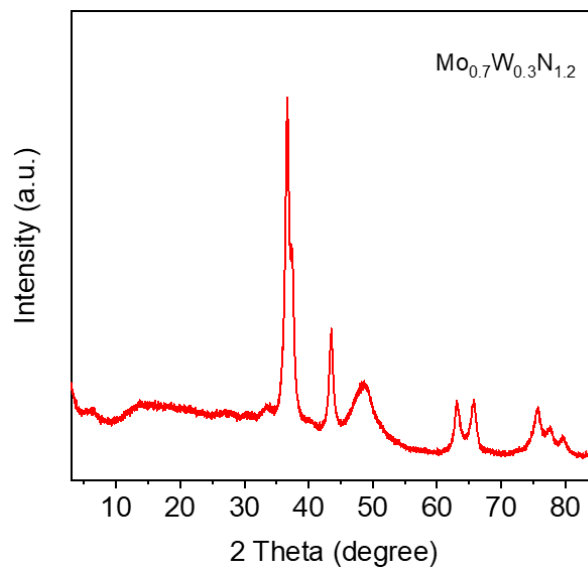


Figure S10. XRD pattern of Mo_{0.7}W_{0.3}N_{1.2} after washing.

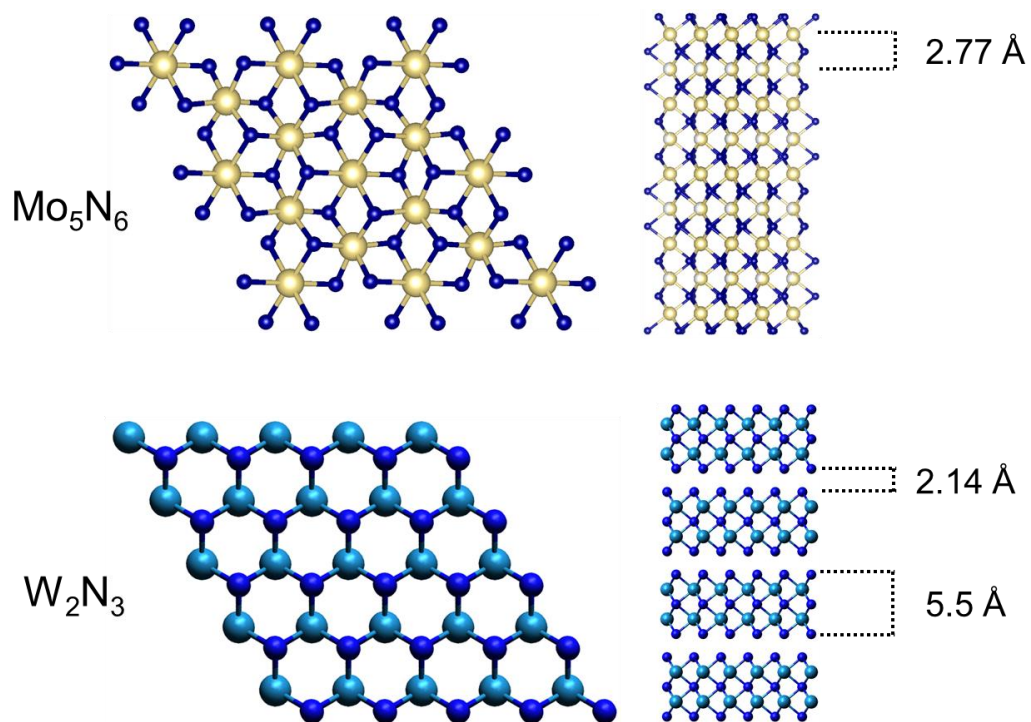


Figure S11. Theoretical models of Mo_5N_6 and W_2N_3 that show their crystal parameters.

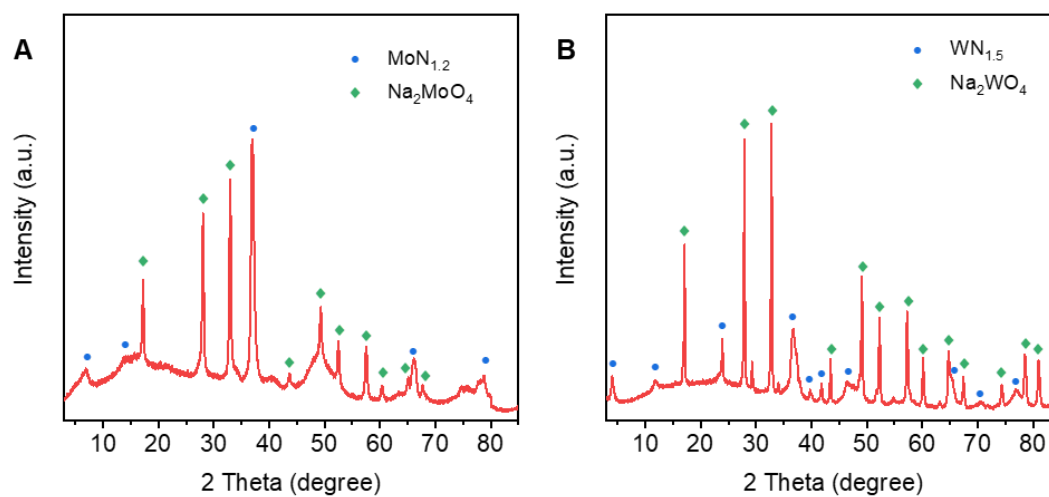


Figure S12. XRD pattern of $\text{MoN}_{1.2}$ and $\text{WN}_{1.5}$ before washing.

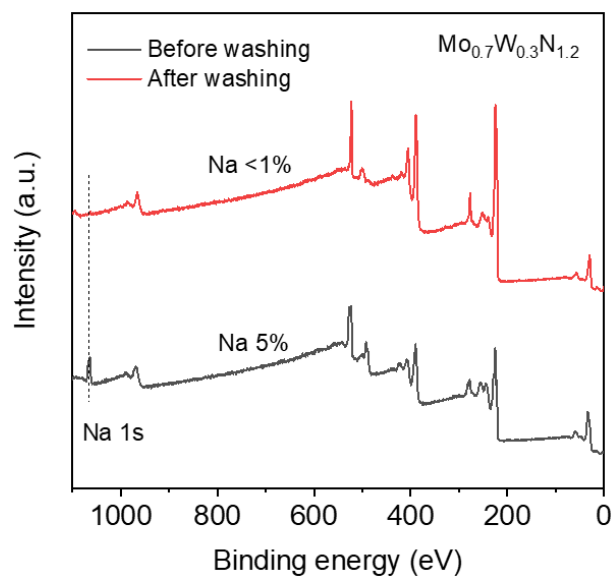


Figure S13. XPS survey scan of $\text{Mo}_{0.7}\text{W}_{0.3}\text{N}_{1.2}$ before and after washing.

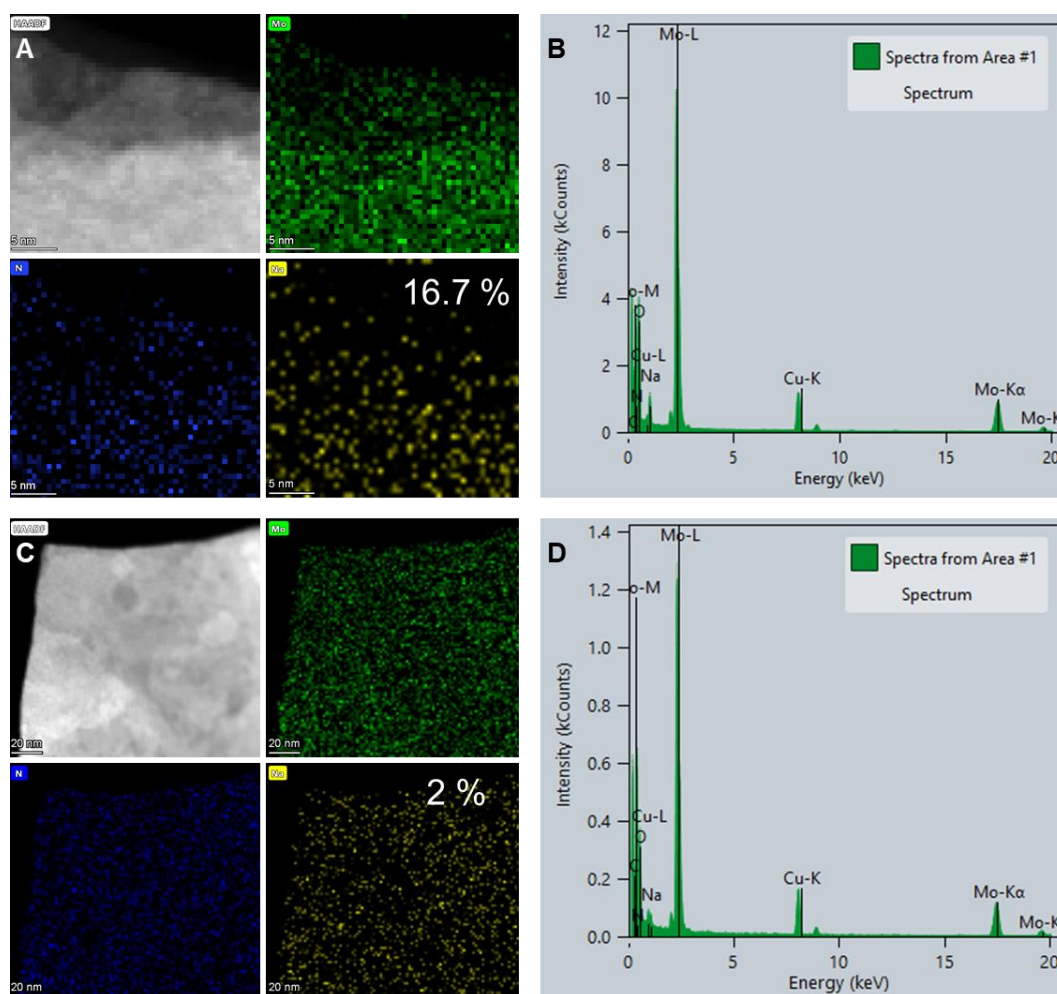


Figure S14. Elemental mapping and EDS of $\text{MoN}_{1.2}$ before and after washing.

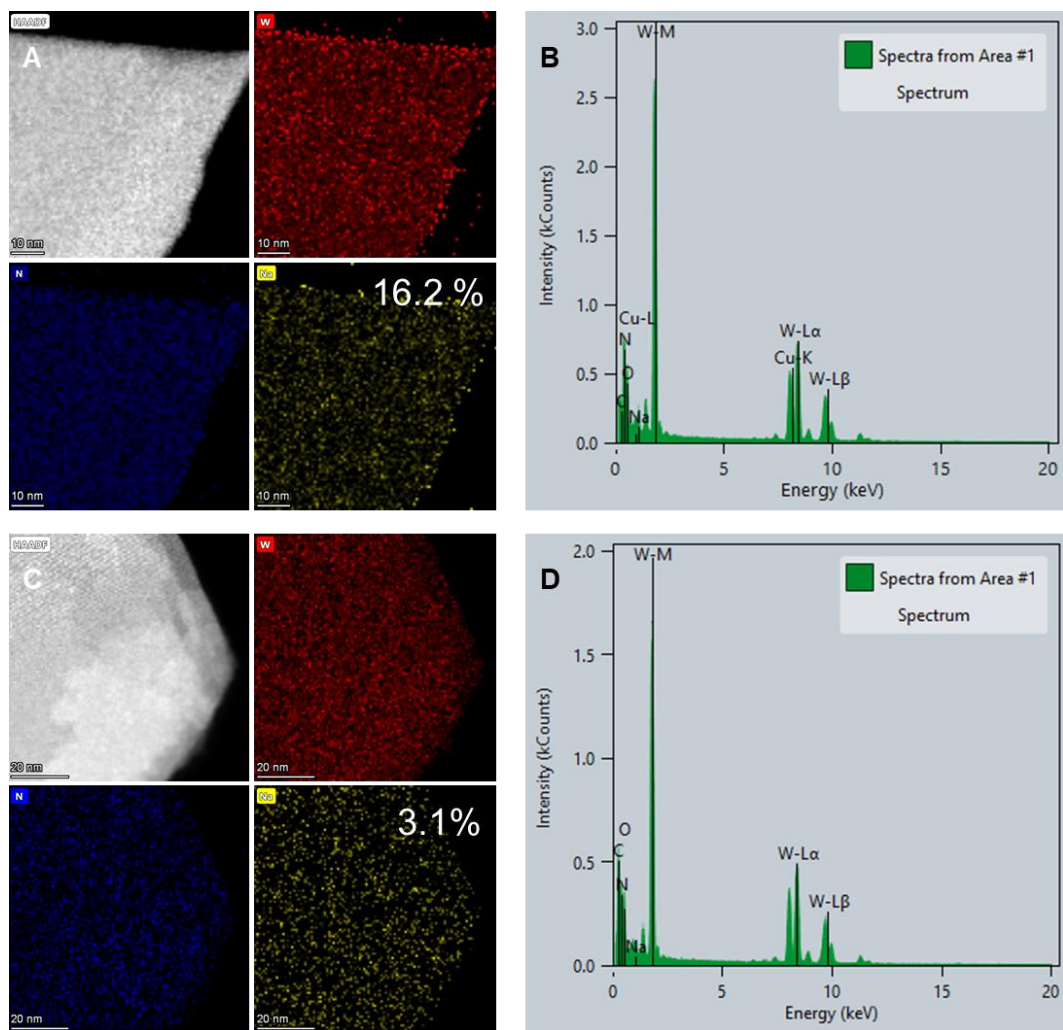


Figure S15. Elemental mapping and EDS of $WN_{1.5}$ before and after washing.

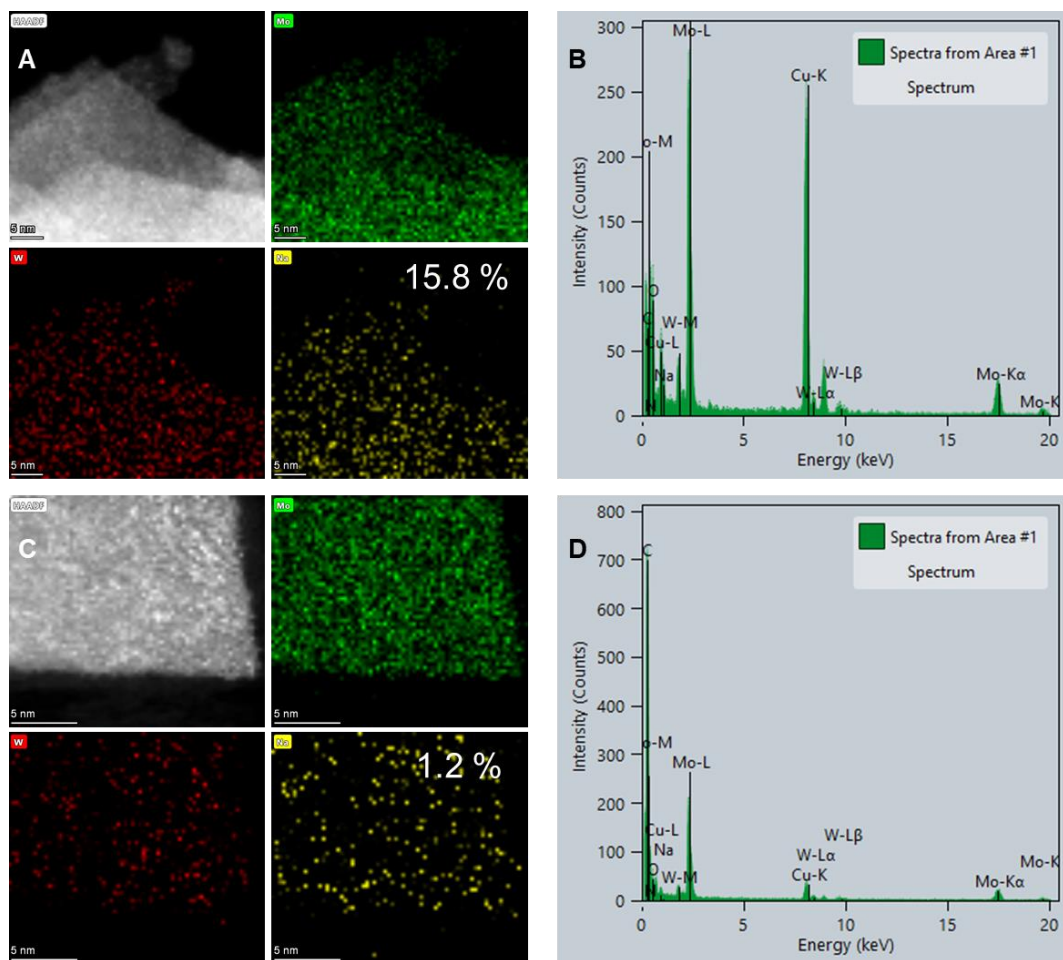


Figure S16. Elemental mapping and EDS of $\text{Mo}_{0.7}\text{W}_{0.3}\text{N}_{1.2}$ before and after washing.

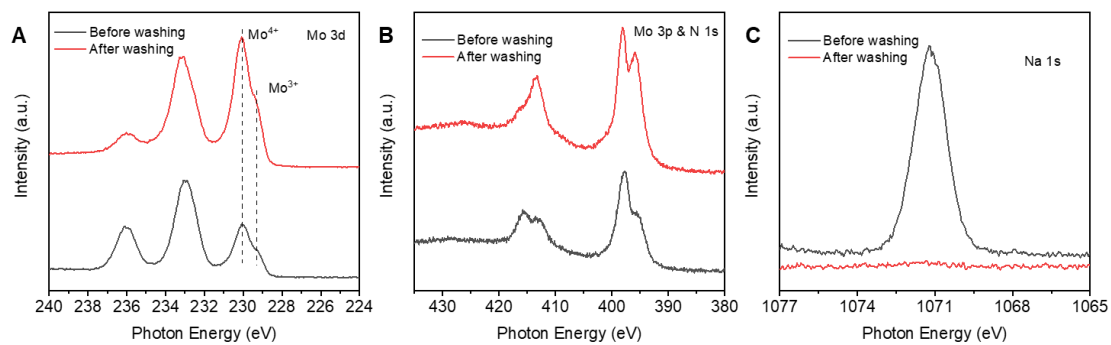


Figure S17. High resolution XPS spectra of (A) Mo 3d, (B) Mo 3p and N 1s and (C) Na 1s of $\text{MoN}_{1.2}$ before and after washing.

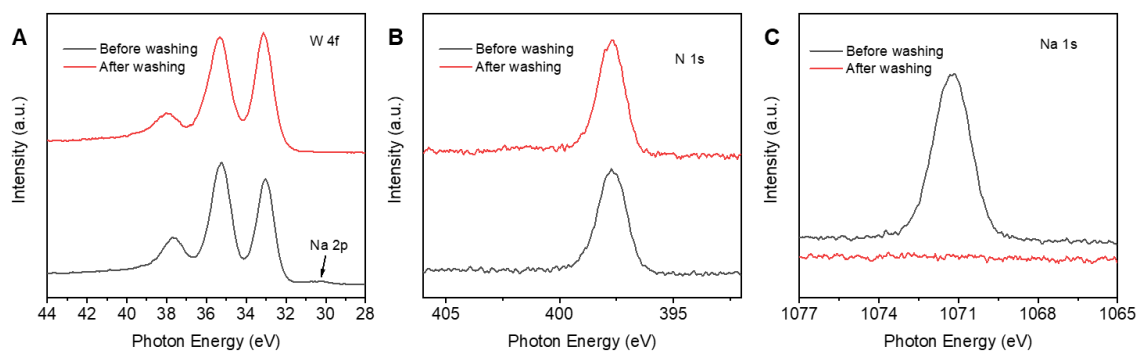


Figure S18. High resolution XPS spectra of (A) W 4f, (B) N 1s and (C) Na 1s of $\text{WN}_{1.5}$ before and after washing.

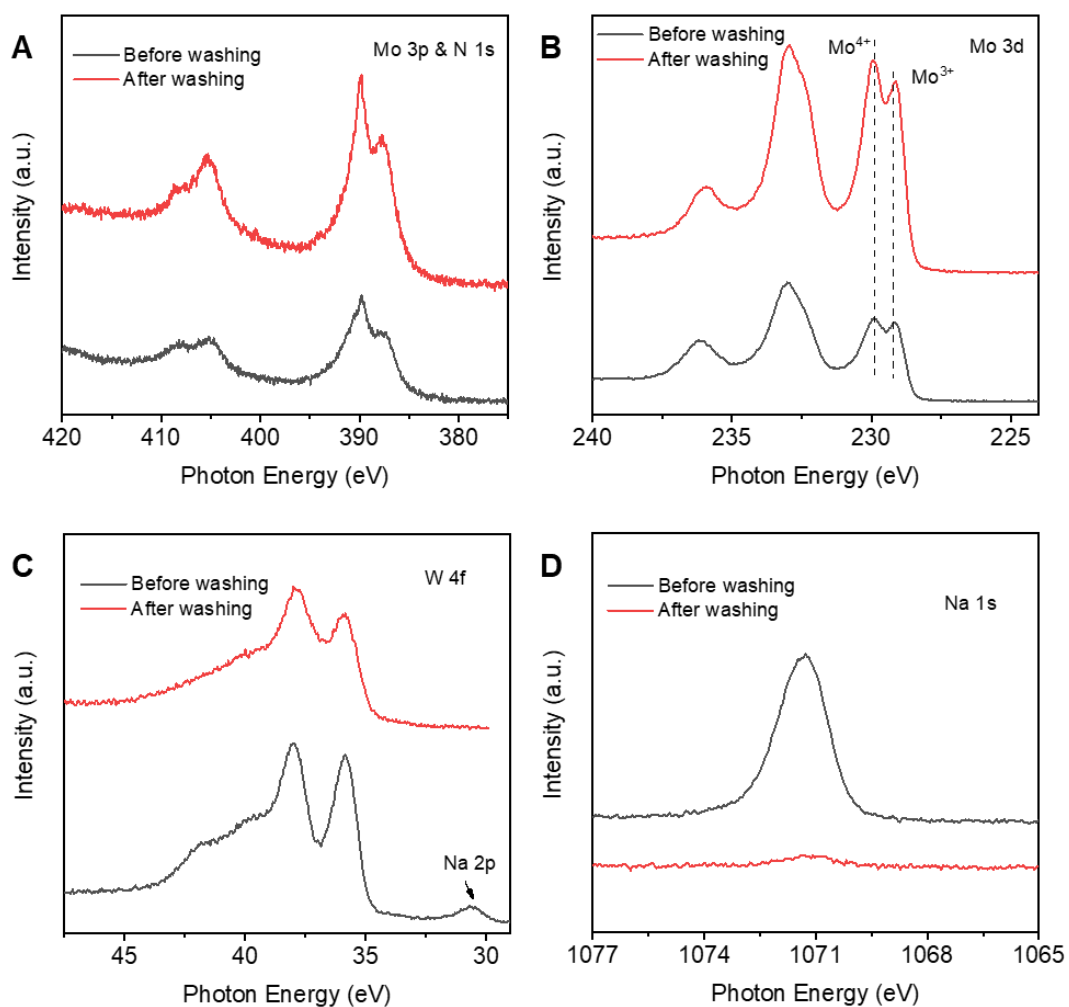


Figure S19. High resolution XPS spectra of (A) Mo 3p and N 1s, (B) Mo 3d, (C) W 4f and (D) Na 1s of $\text{Mo}_{0.7}\text{W}_{0.3}\text{N}_{1.2}$ before and after washing.

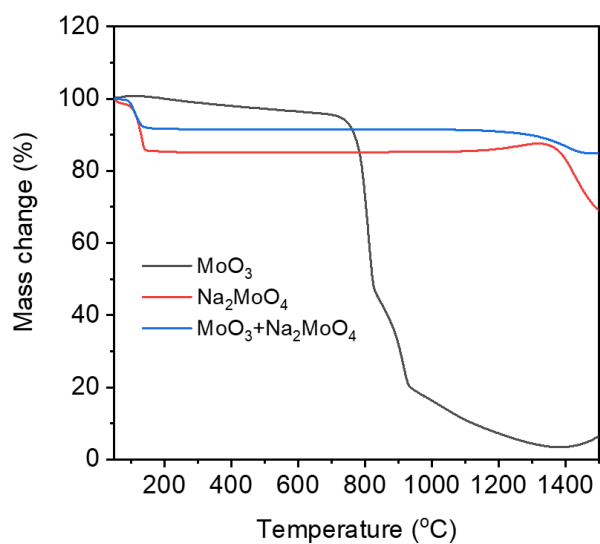


Figure S20. TGA profiles of MoO_3 , Na_2MoO_4 and their mixture. The mixed salts can lower the melting point of MoO_3 , however, increase its evaporating point.

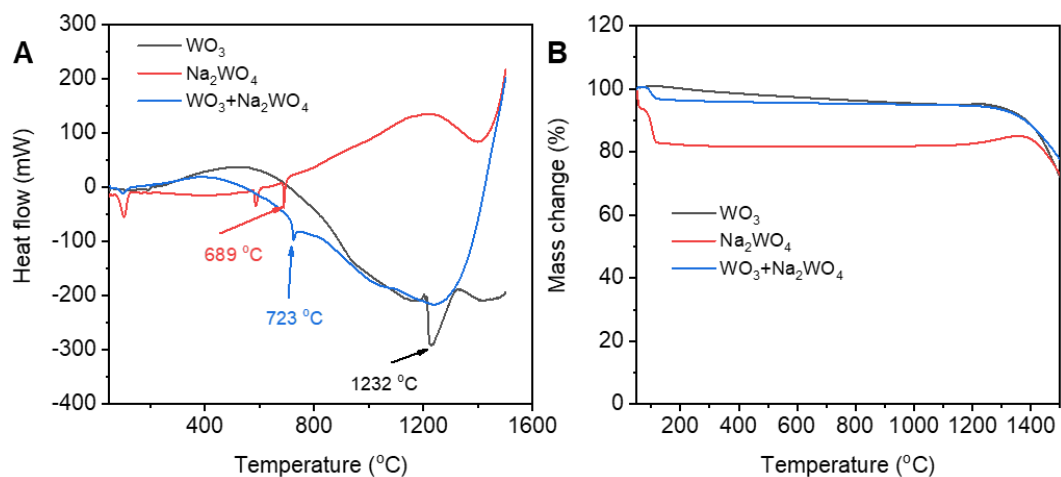


Figure S21. TGA and DSC profiles of WO_3 , Na_2WO_4 and their mixture.

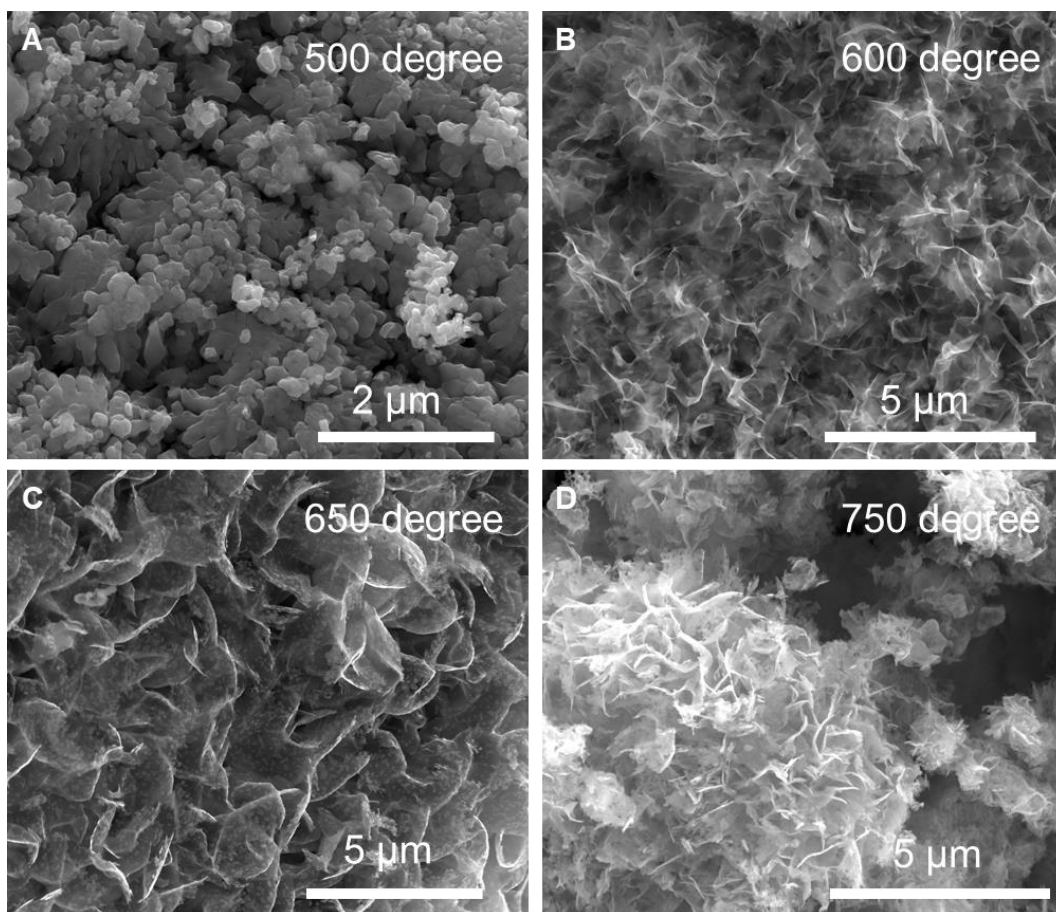


Figure S22. SEM images of the Mo based samples obtained at different temperatures. (A) At 500 °C, the sample is MoO₂ nanoparticles. (B) At 600 °C, small nanosheets start to grow on the surface of molten salt. (C) At 650 °C, the 2D nanosheets can be observed clearly with a flower like morphology. (D) When the temperature reaches 750 °C, the nanosheet is starting to collapse, which is due to the outward diffusion of N atom from Mo lattice at high temperature.

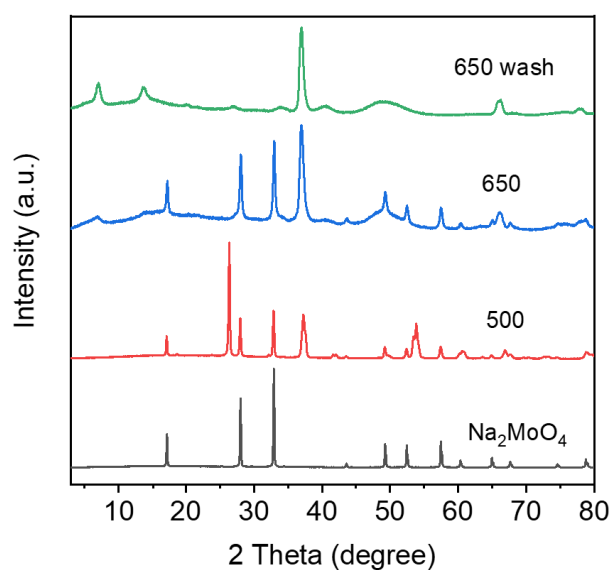


Figure S23. XRD patterns of the Mo based samples obtained at different temperatures. At 500 °C, MoO₃ is turned into MoO₂ due to the reducibility of NH₃. When the temperature increases to 650 °C, MoO₂ is turned into MoN_{1.2}.

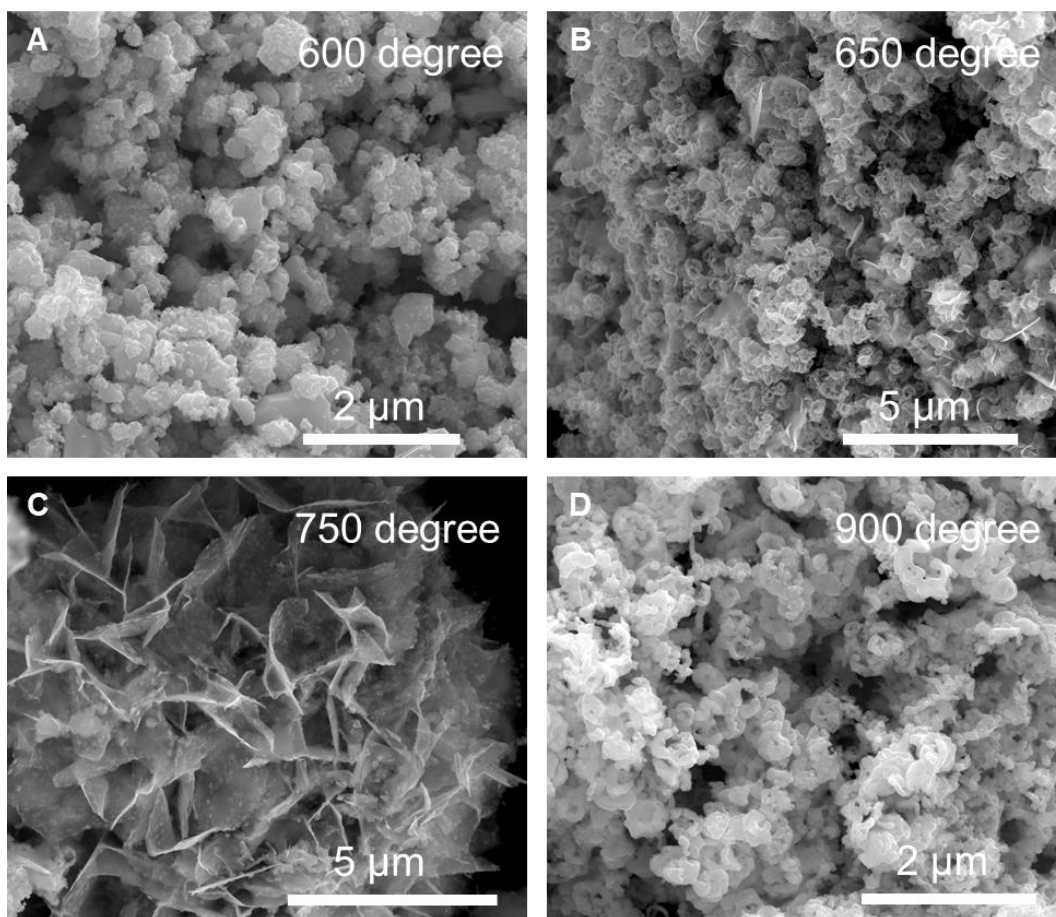


Figure S24. SEM images of the W based samples obtained at different temperatures. (A) At 500 °C, the sample is WO_x nanoparticles. (B) At 650 °C, ultra-small nanosheets start to grow. (C) When the temperature reaches 750 °C, the 2D growth can be observed clearly. (D) When the temperature reaches 900 °C, the outward diffusion of N atom from W lattice occurs, and the 2D $\text{WN}_{1.5}$ nanosheets are turned into W_2N nanoparticles.

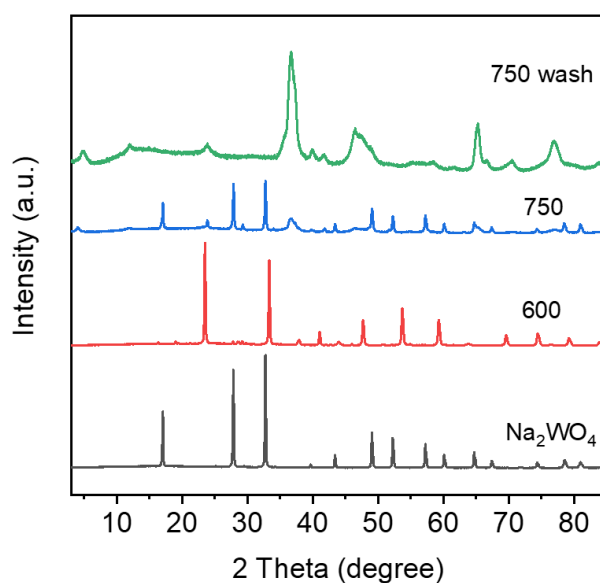


Figure S25. XRD patterns of the W based samples obtained at different temperatures. At 600 °C, WO_{3-x} reacts with Na_2WO_4 and forms NaWO_3 . When the temperature increases to 750 °C, NaWO_3 is turned into Na_2WO_4 and $\text{WN}_{1.5}$.

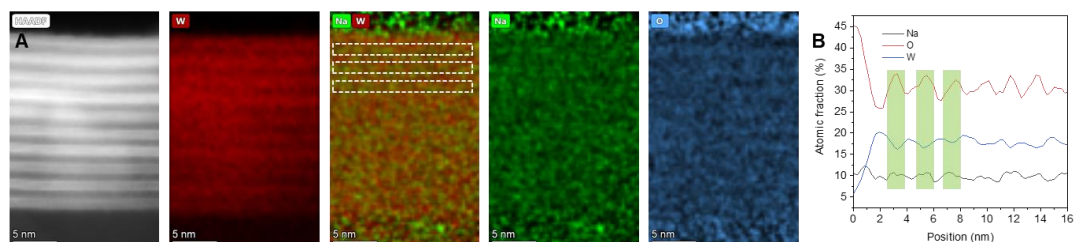


Figure S26. (A) Cross-sectional element mapping of a $WN_{1.5}$ nanosheet before washing. (B) Intensity line profile perpendicular to the layers of $WN_{1.5}$, which shows the atomic fraction of different elements.

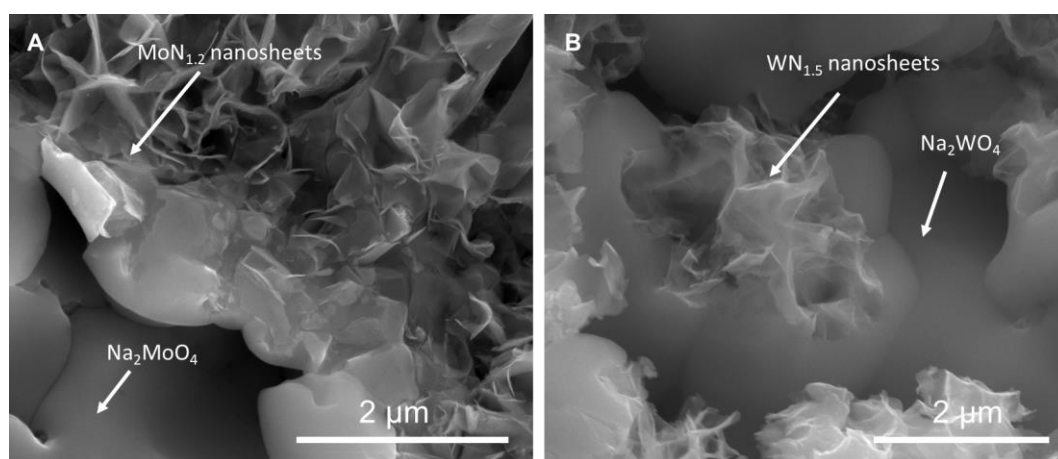


Figure S27. SEM images of $MoN_{1.2}$ and $WN_{1.5}$ obtained from the precursors with the oxide/salt molar ratio of 1:3. An increase in the salt amount does not affect the final product, demonstrating the catalytic property of salt. In these two images, the vertical growth of 2D nanosheets on the salt surface can be observed.

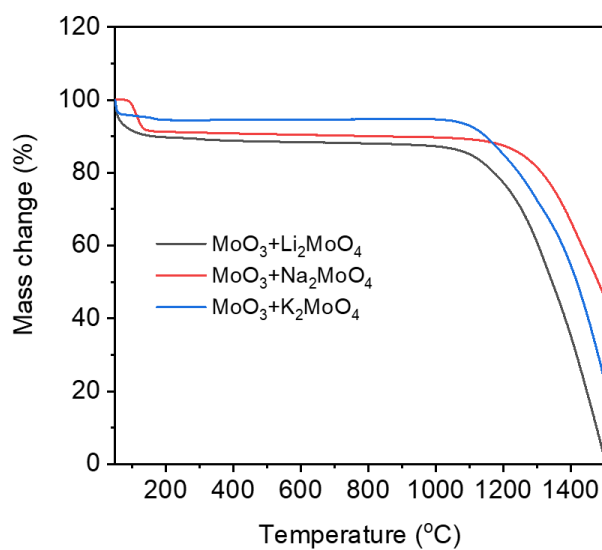


Figure S28. TGA profiles of MoO_3 mixed with different salts.

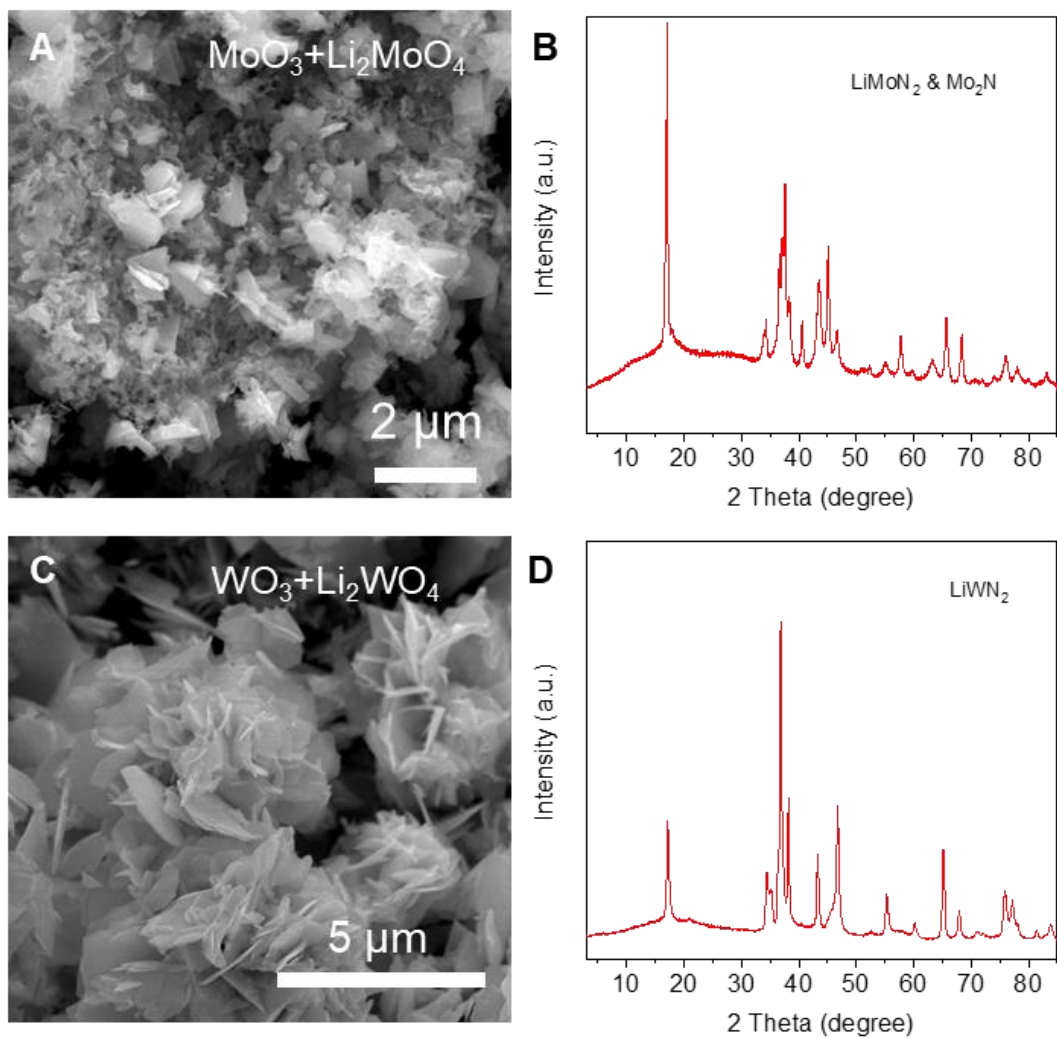


Figure S29. SEM images and XRD patterns of the sample synthesized using Li^+ salts. Ternary 2D TMNs nanosheets are obtained. It should be noted that LiMoN_2 and LiWN_2 also have layered structure with Li^+ ion in the interlayer.

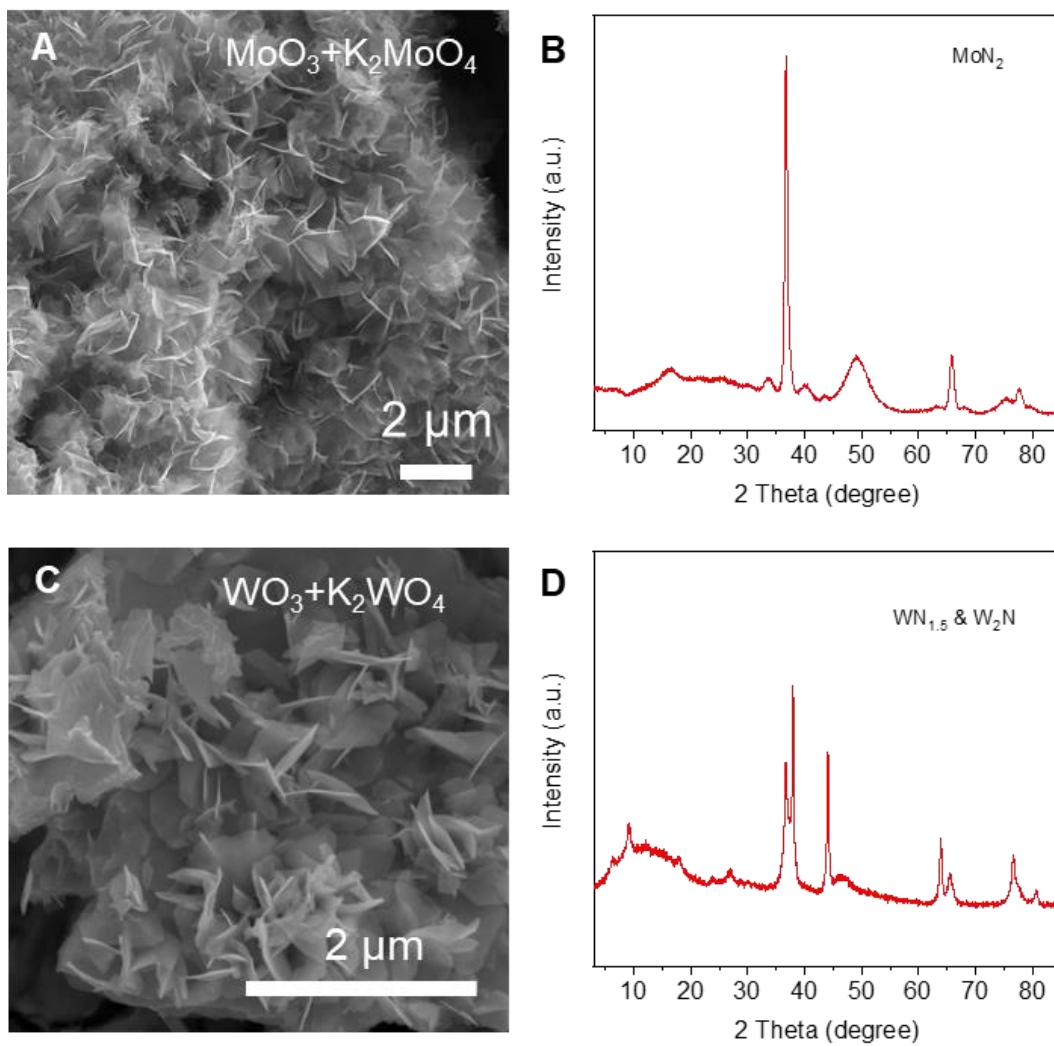


Figure S30. SEM images and XRD patterns of the sample synthesized using K^+ salts. The impurity of W_2N may be due to the high melting point of K_2WO_4 .

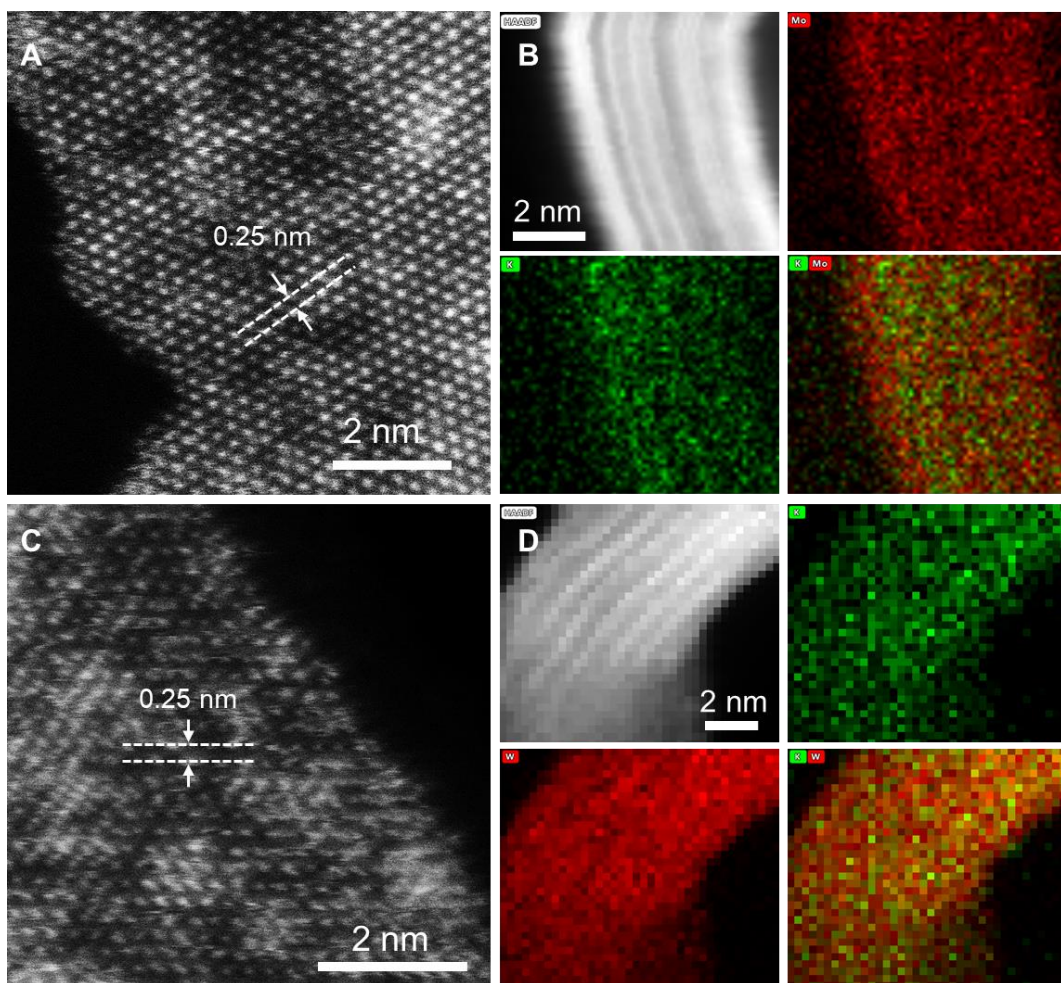


Figure S31. HAADF-STEM images and elemental mapping of (A), (B) MoN_{1.2}, and (C), (D) WN_{1.5} obtained using K⁺ salts.

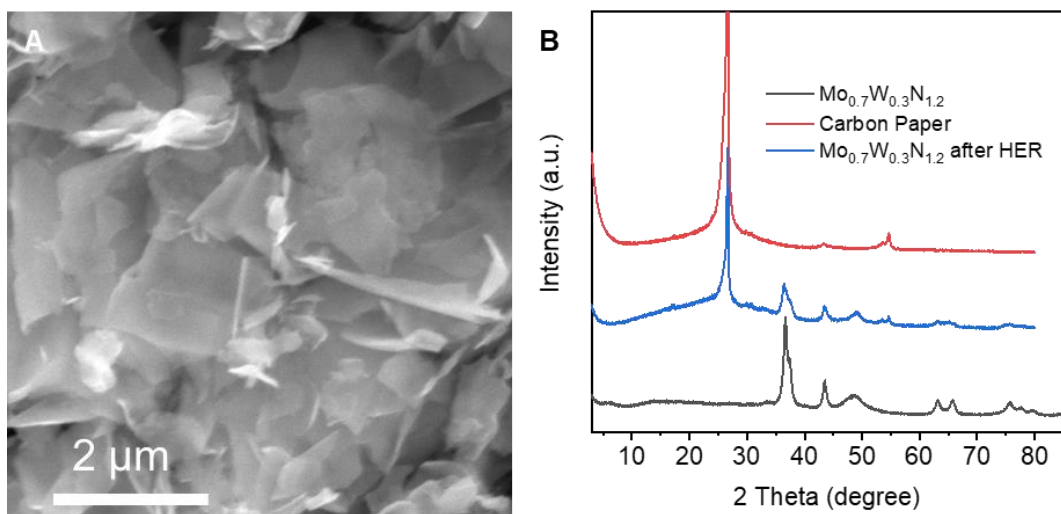


Figure S32. (A) SEM images and (B) XRD spectrum of Mo_{0.7}W_{0.3}N_{1.2} after HER stability test.

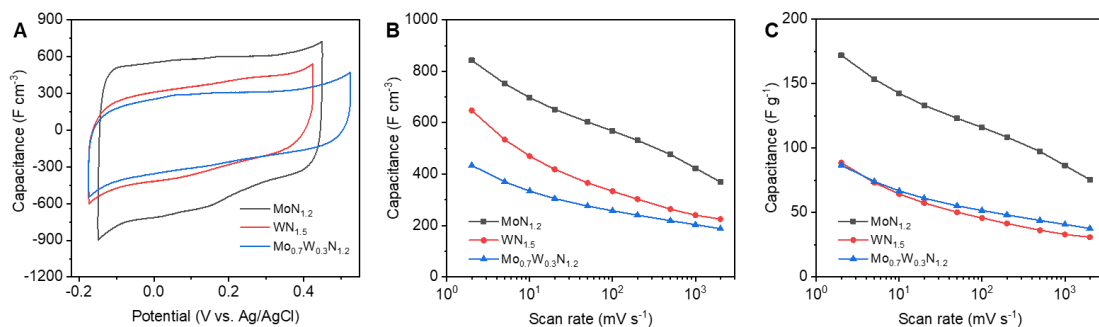


Figure S33. (A) CV curves of 2D layered TMNs at the scan rate of 100 mV s⁻¹. (B) Volumetric capacitance obtained at different scan rates. (C) Gravimetric capacitance obtained at different scan rates.

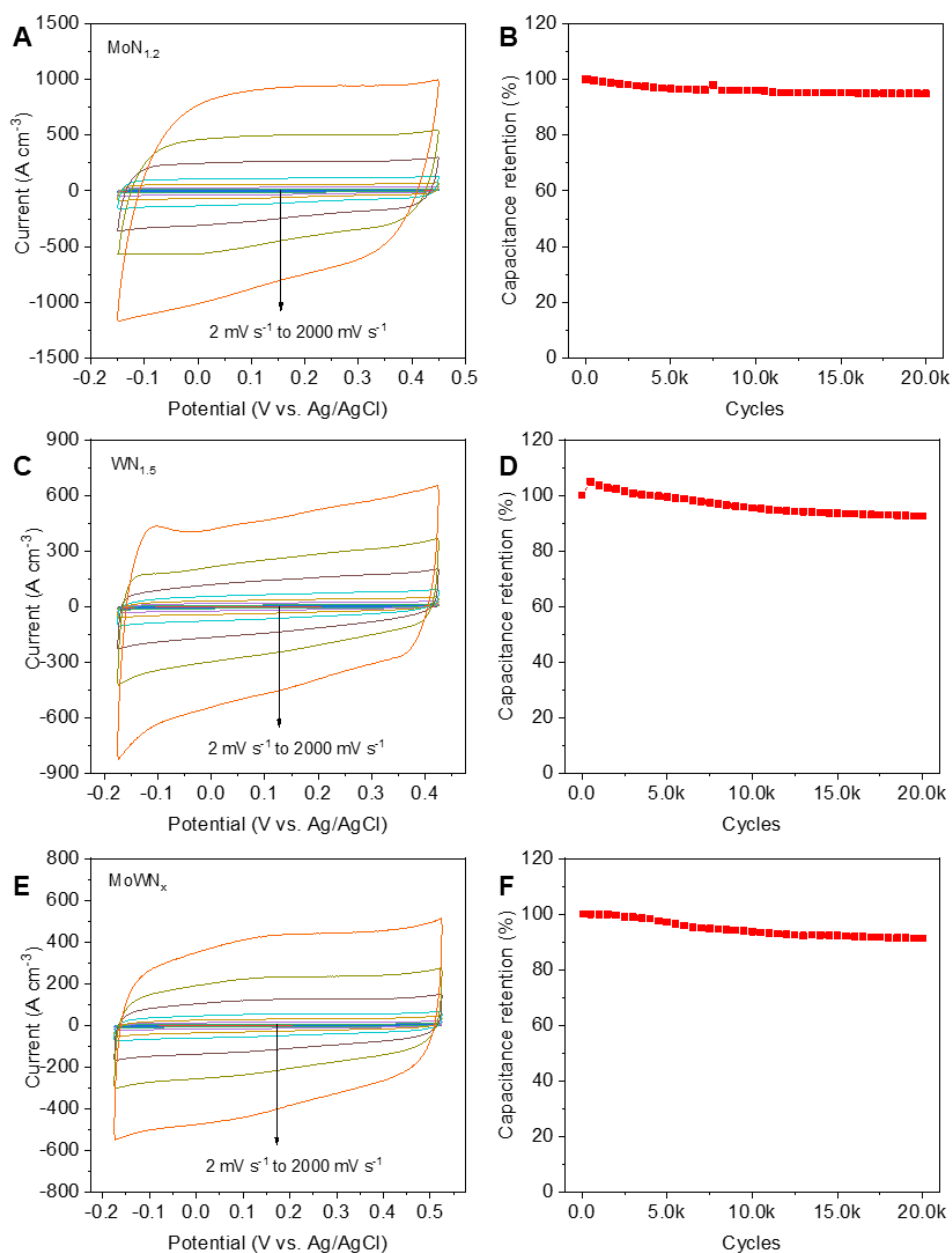


Figure S34. (A), (C), (E) CV curves obtained from 2 mV s⁻¹ to 2000 mV s⁻¹. (B), (D), (F), Long-term stability test of MoN_{1.2} for 20k cycles.

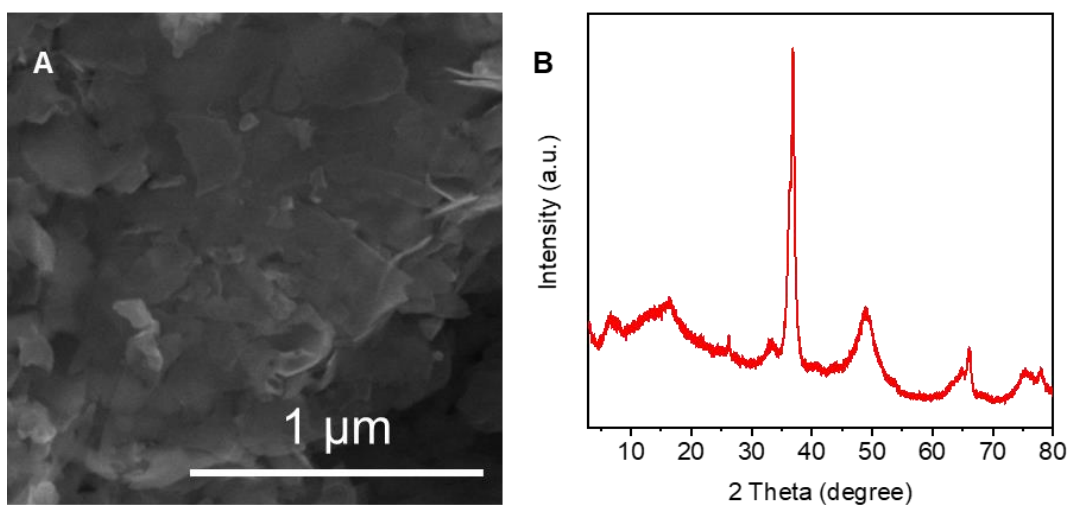


Figure S35. (A) SEM images and (B) XRD spectrum of MoN_{1.2} film after capacitive performance test.

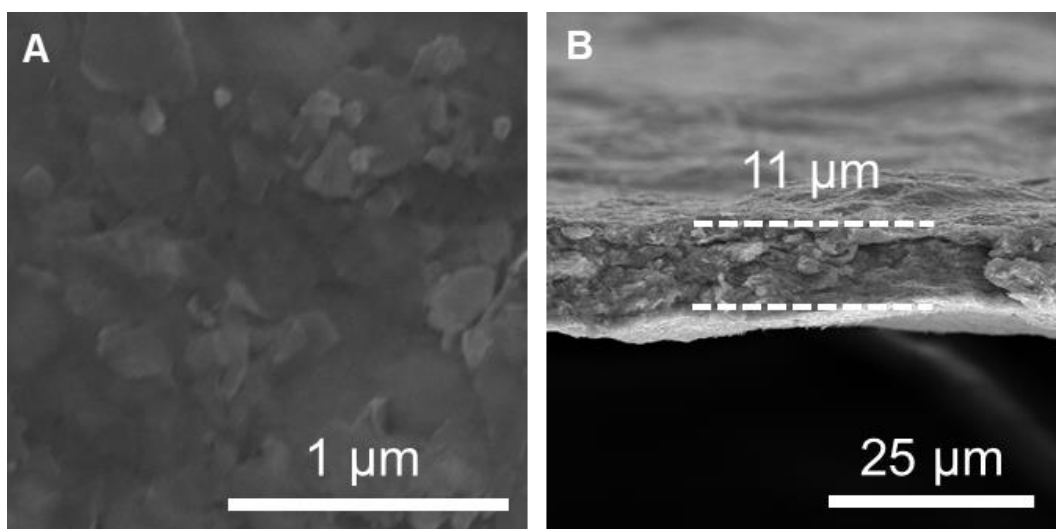


Figure S36. SEM images of the (A) in-plane and (B) fracture surface of the ~11 μm-thick MoN_{1.2} film.

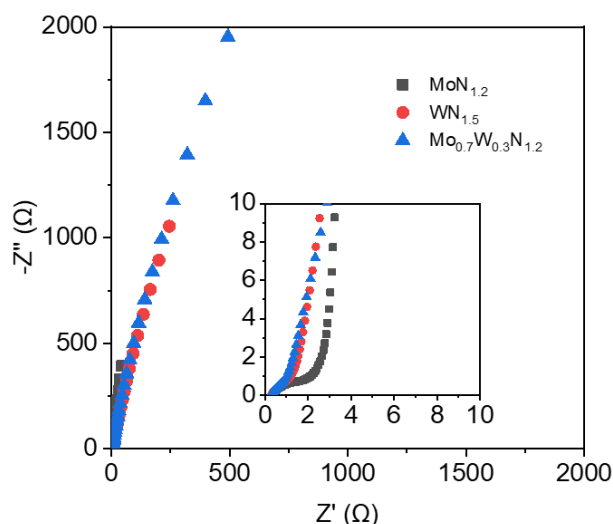


Figure S37. Electrochemical impedance spectroscopy (EIS) measurement of 2D TMNs.

Figure S33A shows the cyclic voltammetry (CV) curves for 2D TMNs obtained at the scan rates of 100 mV s^{-1} . The rectangular voltammograms demonstrate the good double-layer capacitance. The specific capacitances in Figure S33B and S33C are calculated based on the CV curves at the scan rate from 2 mV s^{-1} to 2 V s^{-1} . All these 2D TMNs show excellent cycling stability (Figure S34). After stability test the morphology and chemical composition of 2D TMNs remain the same (Figure S35). At 2 mV s^{-1} , the volumetric capacitance of a $11 \text{ }\mu\text{m}$ thick $\text{MoN}_{1.2}$ electrode (Figure S36) was 842 F cm^{-3} , which is higher than that for $\text{WN}_{1.5}$ (647 F cm^{-3}) and $\text{Mo}_{0.7}\text{W}_{0.3}\text{N}_{1.2}$ (434 F cm^{-3}). This value is among the highest volumetric capacitance values obtained for pristine 2D materials such as $\text{Ti}_3\text{C}_2\text{T}_x$ clay and $\text{Mo}_{1.33}\text{C}$ MXene with the similar film thickness.^{1,2} EIS was also performed to examine the electron/ion transport (Figure S37). The results reveal a typical capacitive behavior with no apparent charge-transfer resistance, which indicates a fast electron transport in the restacked film type electrodes. These practical results demonstrate the superior performance of 2D layered TMNs synthesized by catalytic molten salt method for energy related applications.

Table S1. Elemental composition of 2D TMNs before and after washing.

2D TMNs	W (%)	Mo (%)	N (%)	O (%)	Na (%)
MoN _{1.2} before washing		20.59	26.76	36.82	15.82
MoN _{1.2} after washing		30.09	34.85	33.81	1.25
WN _{1.5} before washing	24.94		25.95	32.28	16.83
WN _{1.5} after washing	25.77		37.39	35.89	0.95
Mo _{0.7} W _{0.3} N _{1.2} before washing	10.69	18.34	39.83	25.80	5.34
Mo _{0.7} W _{0.3} N _{1.2} after washing	10.25	21.73	52.73	15.29	N/A

Table S2. Summary of HER activities of our 2D layered TMNs and other 2D electrocatalysts under acidic conditions.

Catalysts	η_{10} (mV)	Tafel slope (mV dec ⁻¹)	Ref.
Mo _{0.7} W _{0.3} N _{1.2}	129	59	This work
MoN _{1.2}	270	79	This work
WN _{1.5}	348	82	This work
MoS ₂ /Ti ₃ C ₂ T _x @C	135	45	3
VS ₂ /V ₂ CT _x	138	37.9	4
Mo _{0.5} W _{0.5} S ₂	138	55	5
MoS ₂ /Ti ₃ C ₂ T _x nanoroll	152	70	6
O, P-MoS ₂	150	53	7
Ti ₃ C ₂ T _x nanofibers	169	97	8
Ti ₂ CT _x	170	100	9
Mo ₂ CT _x : Co	180	N/A	10
Mo ₂ CT _x (low F coverage)	189	75	11
E-Ti ₃ C ₂ O _x	190	60.7	12
1T' MoS ₂	205	51	13
P-V ₂ CT _x	220	74	14
Mo ₂ CT _x	283	N/A	15

Table S3. Summary of HER activities of our 2D layered TMNs and other 2D electrocatalysts under alkaline conditions.

Catalysts	η_{10} (mV)	Tafel slope (mV dec ⁻¹)	Ref.
Mo _{0.7} W _{0.3} N _{1.2}	122	47	This work
MoN _{1.2}	306	83	This work
WN _{1.5}	463	121	This work
NiFe-LDH/Ti ₃ C ₂ T _x	132	70	16
Co ₉ S ₈ @MoS ₂	143	117	17
VS ₂ /V ₂ CT _x	164	47.6	4
Mn-MoSe ₂	167	60	18
Ni-MoS ₂ /RGO	168	69.5	19
MoS ₂ /Mo ₂ CT _x	176	207	20
NiS ₂ /V ₂ CT _x	179	85	21
BP QDs/Ti ₃ C ₂ T _x	190	83	22
MoS ₂ nanosheets	200	104	17
Vertical MoS ₂ nanosheets	204	76.6	23
Ni-WSe ₂	215	109	24
MoS ₂ /Ni ₃ S ₂	218	83.1	25
NiMo ₃ S ₄	257	98	26

Supplemental Experimental Procedures

Chemicals

MoO₃ (99.97%), WO₃ (99.9%), Na₂MoO₄·2H₂O (≥99.5%), K₂MoO₄ (98%), Li₂WO₄ (98%), Na₂WO₄·2H₂O (≥99%) and K₂WO₄ (94%) were purchased from Sigma-Aldrich without further purification. Li₂MoO₄ (99%) was purchased from Tianjin HEOWNS Biochemical Technology Co., Ltd., China.

Electrochemical Tests for Supercapacitor

We used a typical three-electrode configuration for aqueous electrolyte testing in Swagelok cells (Swagelok, USA). In this setup, carbon black was the counter electrode, Ag/AgCl was the reference electrode, and a Celgard film served as the separator (Celgard, USA). All the electrochemical tests were carried out using CHI760D, and electrochemical impedance was measured with potential amplitude of 10 mV from 1 mHz to 1 MHz.

Characterization

X-Ray Powder Diffraction (XRD) data were collected on a Rigaku MiniFlex 600 X-Ray Diffractometer. Field-emission SEM imaging was conducted on a FEI QUANTA 450 electron microscope. The transmission electron microscope images, aberration-corrected TEM images, high-angle annular dark-field imaging and EDS mapping were taken on a FEI Titan Themis 80-200 operating at 200 kV. Melting point of the samples was determined by thermogravimetric analysis (TGA, METTLER TOLEDO TGA/DSC 2) under Ar with a temperature ramp of 20 °C min⁻¹. Inductively coupled plasma mass spectrometry (ICP-MS) analysis was conducted using an Agilent 7500cx instrument with attached laser ablation system.

The synchrotron based XANES measurements were carried out on the soft X-ray spectroscopy beamline at the Australian Synchrotron, which is equipped with a hemispherical electron analyzer and a microchannel plate detector that enables simultaneous recording of the total electron yield and partial electron yield. The calibration of XPS data was normalized to the photoelectron current of the photon beam, measured on an Au grid. The raw XANES data were normalized using software Igor Pro 8.

DFT calculations

First-principles calculations were performed by CASTEP package code with density-functional theory (DFT).²⁷ The data were collected using generalized gradient approximation with the exchange-correlation function of the Perdew–Burke–Ernzerh.^{28,29} The cutoff energy of plane wave was set at 500 eV. All the structural models were optimized and the energy and force convergence are 10⁻⁵ eV per atom and 0.03 eV Å⁻¹, respectively.

Supplemental References

1. Ghidui, M., Lukatskaya, M.R., Zhao, M.Q., Gogotsi, Y., and Barsoum, M.W. (2014). Conductive two-dimensional titanium carbide 'clay' with high volumetric capacitance. *Nature* 516, 78-81.
2. Tao, Q., Dahlqvist, M., Lu, J., Kota, S., Meshkian, R., Halim, J., Palisaitis, J., Hultman, L., Barsoum, M.W., Persson, P.O.Å., *et al.* (2017). Two-dimensional Mo_{1.33}C MXene with divacancy ordering prepared from parent 3D laminate with in-plane chemical ordering. *Nat. Commun.* 8, 14949.
3. Wu, X., Wang, Z., Yu, M., Xiu, L., and Qiu, J. (2017). Stabilizing the MXenes by carbon nanoplating for developing hierarchical nanohybrids with efficient lithium storage and hydrogen evolution capability. *Adv. Mater.* 29, 1607017.
4. Wang, Z., Xu, W., Yu, K., Feng, Y., and Zhu, Z. (2020). 2D heterogeneous vanadium compound interfacial modulation enhanced synergistic catalytic hydrogen evolution for full pH range seawater splitting. *Nanoscale* 12, 6176-6187.
5. Wang, H., Ouyang, L., Zou, G., Sun, C., Hu, J., Xiao, X., and Gao, L. (2018). Optimizing MoS₂ edges by alloying isovalent W for robust hydrogen evolution activity. *ACS Catal.* 8, 9529-9536.
6. Liu, J., Liu, Y., Xu, D., Zhu, Y., Peng, W., Li, Y., Zhang, F., and Fan, X. (2019). Hierarchical "nanoroll" like MoS₂/Ti₃C₂T_x hybrid with high electrocatalytic hydrogen evolution activity. *Appl. Catal., B* 241, 89-94.
7. Liu, J., Wang, Z., Li, J., Cao, L., Lu, Z., and Zhu, D. (2020). Structure engineering of MoS₂ via simultaneous oxygen and phosphorus incorporation for improved hydrogen evolution. *Small* 16, 1905738.
8. Yuan, W., Cheng, L., An, Y., Wu, H., Yao, N., Fan, X., and Guo, X. (2018). MXene nanofibers as highly active catalysts for hydrogen evolution reaction. *ACS Sustain. Chem. Eng.* 6, 8976-8982.
9. Li, S., Tuo, P., Xie, J., Zhang, X., Xu, J., Bao, J., Pan, B., and Xie, Y. (2018). Ultrathin MXene nanosheets with rich fluorine termination groups realizing efficient electrocatalytic hydrogen evolution. *Nano Energy* 47, 512-518.
10. Kuznetsov, D.A., Chen, Z., Kumar, P.V., Tsoukalou, A., Kierzkowska, A., Abdala, P.M., Safonova, O.V., Fedorov, A., and Müller, C.R. (2019). Single site cobalt substitution in 2D molybdenum carbide (MXene) enhances catalytic activity in the hydrogen evolution reaction. *J. Am. Chem. Soc.* 141, 17809-17816.
11. Handoko, A.D., Fredrickson, K.D., Anasori, B., Convey, K.W., Johnson, L.R., Gogotsi, Y., Vojvodic, A., and Seh, Z.W. (2018). Tuning the basal plane functionalization of two-dimensional metal carbides (MXenes) to control hydrogen evolution activity. *ACS Applied Energy Materials* 1, 173-180.
12. Jiang, Y., Sun, T., Xie, X., Jiang, W., Li, J., Tian, B., and Su, C. (2019). Oxygen-functionalized ultrathin Ti₃C₂T_x MXene for enhanced electrocatalytic hydrogen evolution. *ChemSusChem* 12, 1368-1373.
13. Liu, L., Wu, J., Wu, L., Ye, M., Liu, X., Wang, Q., Hou, S., Lu, P., Sun, L., Zheng, J., *et al.* (2018). Phase-selective synthesis of 1T' MoS₂ monolayers and heterophase bilayers. *Nat. Mater.* 17, 1108-1114.
14. Yoon, Y., Tiwari, A.P., Choi, M., Novak, T.G., Song, W., Chang, H., Zyung, T., Lee, S.S., Jeon, S., and An, K.-S. (2019). Precious-metal-free electrocatalysts for activation of hydrogen evolution with nonmetallic electron donor: chemical composition controllable phosphorous doped vanadium carbide MXene. *Adv. Funct. Mater.* 29, 1903443.
15. Seh, Z.W., Fredrickson, K.D., Anasori, B., Kibsgaard, J., Strickler, A.L., Lukatskaya, M.R., Gogotsi, Y., Jaramillo, T.F., and Vojvodic, A. (2016). Two-dimensional molybdenum carbide (MXene) as an efficient electrocatalyst for hydrogen evolution. *ACS Energy Lett.* 1, 589-594.

16. Yu, M., Wang, Z., Liu, J., Sun, F., Yang, P., and Qiu, J. (2019). A hierarchically porous and hydrophilic 3D nickel–iron/MXene electrode for accelerating oxygen and hydrogen evolution at high current densities. *Nano Energy* 63, 103880.
17. Bai, J., Meng, T., Guo, D., Wang, S., Mao, B., and Cao, M. (2018). Co₉S₈@MoS₂ core–shell heterostructures as trifunctional electrocatalysts for overall water splitting and Zn–air batteries. *ACS Appl. Mater. Interfaces* 10, 1678-1689.
18. Kuraganti, V., Jain, A., Bar-Ziv, R., Ramasubramaniam, A., and Bar-Sadan, M. (2019). Manganese doping of MoSe₂ promotes active defect sites for hydrogen evolution. *ACS Appl. Mater. Interfaces* 11, 25155-25162.
19. Lin, C., Gao, Z., and Jin, J. (2019). Boosting alkaline hydrogen evolution activity with Ni-doped MoS₂/reduced graphene oxide hybrid aerogel. *ChemSusChem* 12, 457-466.
20. Ren, J., Zong, H., Sun, Y., Gong, S., Feng, Y., Wang, Z., Hu, L., Yu, K., and Zhu, Z. (2020). 2D organ-like molybdenum carbide (MXene) coupled with MoS₂ nanoflowers enhances the catalytic activity in the hydrogen evolution reaction. *CrystEngComm* 22, 1395-1403.
21. Kuang, P., He, M., Zhu, B., Yu, J., Fan, K., and Jaroniec, M. (2019). 0D/2D NiS₂/V-MXene composite for electrocatalytic H₂ evolution. *J. Catal.* 375, 8-20.
22. Zhu, X.-D., Xie, Y., and Liu, Y.-T. (2018). Exploring the synergy of 2D MXene-supported black phosphorus quantum dots in hydrogen and oxygen evolution reactions. *J. Mater. Chem. A* 6, 21255-21260.
23. Hu, J., Zhang, C., Jiang, L., Lin, H., An, Y., Zhou, D., Leung, M.K.H., and Yang, S. (2017). Nanohybridization of MoS₂ with layered double hydroxides efficiently synergizes the hydrogen evolution in alkaline media. *Joule* 1, 383-393.
24. Kadam, S.R., Enyashin, A.N., Houben, L., Bar-Ziv, R., and Bar-Sadan, M. (2020). Ni–WSe₂ nanostructures as efficient catalysts for electrochemical hydrogen evolution reaction (HER) in acidic and alkaline media. *J. Mater. Chem. A* 8, 1403-1416.
25. Zhang, J., Wang, T., Pohl, D., Rellinghaus, B., Dong, R., Liu, S., Zhuang, X., and Feng, X. (2016). Interface engineering of MoS₂/Ni₃S₂ heterostructures for highly enhanced electrochemical overall-water-splitting activity. *Angew. Chem. Int. Ed.* 55, 6702-6707.
26. Jiang, J., Gao, M., Sheng, W., and Yan, Y. (2016). Hollow chevrel-phase NiMo₃S₄ for hydrogen evolution in alkaline electrolytes. *Angew. Chem. Int. Ed.* 55, 15240-15245.
27. Clark, S.J., Segall, M.D., Pickard, C.J., Hasnip, P.J., Probert, M.J., Refson, K., and Payne, M.C. (2005). First principles methods using CASTEP. *Zeitschrift Fur Kristallographie* 220, 567-570.
28. Perdew, J.P., Chevary, J.A., Vosko, S.H., Jackson, K.A., Pederson, M.R., Singh, D.J., and Fiolhais, C. (1992). Atoms, molecules, solids, and surfaces: Applications of the generalized gradient approximation for exchange and correlation. *Physical Review B* 46, 6671.
29. Perdew, J.P., Burke, K., and Ernzerhof, M. (1996). Generalized gradient approximation made simple. *Phys. Rev. Lett.* 77, 3865.

Chapter 8: Conclusions and Perspectives

8.1 Conclusions

This Thesis focuses on designing new atomically thin 2D materials and their derivatives for energy-relevant electrocatalysis applications and gaining insights into the reaction mechanisms of these processes. According to the works in this thesis, the following conclusions can be drawn:

1. Using 2D $C_3N_4@MoN$ hybrids as a model catalyst, the possibility of activating 2D materials as efficient electrocatalysts for the alkaline HER was demonstrated. The construction of highly active C_3N_4 and MoN interfaces facilitated the formation of dual active sites, which realized the balance of H_{ad} and OH_{ad} intermediates. It was also found that the contribution of H_{ad} and water dissociation in this electrocatalyst could be balanced by regulating the proportion of g- C_3N_4 to MoN. Confirmed by electrochemical measurements and DFT calculations, the activity enhancement originates from the optimized hydrogen adsorption energy on the N sites of g- C_3N_4 and the stronger OH adsorption energy of the Mo atoms in MoN. This demonstrates the feasibility of tuning the binding energies of multiple active sites through the construction of 2D heterostructures for the alkaline HER.
2. The facile synthesis of 2D nitrogen-rich Mo_5N_6 nanosheets for HER was achieved using a simple Ni induced salt-template method. The additional nitrogen atoms incorporated in the Mo_5N_6 lattice greatly changed its inherent properties, leading to a higher Mo valence state and Pt-like electronic structure. The Mo_5N_6 nanosheets exhibited excellent HER performance in various electrolytes, especially in seawater. For seawater HER, its performance was significantly better than other nitrogen-deficient TMNs and the Pt/C benchmark. The Mo_5N_6 catalyst combines high activity and good stability simultaneously, demonstrating the possibility of using 2D nitrogen-rich TMNs for electrocatalytic processes in harsh electrocatalytic environments.
3. A multifaceted heteroatom-doping method was developed to optimize the HER activity of non-noble metal catalysts on graphene supports. Out of all the doped Ni

catalysts tested, N-P co-doped Ni exhibited the best HER performance with a very small overpotential of 24 mV at a current density of 10 mA cm⁻². As confirmed by experiments and DFT calculations, doping-induced charge redistribution on the Ni surface can change the electronic structure of the Ni metal, resulting in catalytic properties similar to noble metal catalysts. Similar enhancement was also observed for Co metal catalysts, demonstrating the versatility of this method. This study demonstrates the possibility of activating TMEs *via* heteroatom doping and provides new insight for activating unconventional materials for applications in other energy storage and conversion systems.

4. The nitrogen vacancies confined on 2D W₂N₃ nanosheets was confirmed as a stable active site for the electrocatalytic reduction of N₂ to NH₃ under ambient conditions. The activity and stability of nitrogen vacancies is evaluated by electrochemical measurements and various *ex situ* characterization. Significantly, the nitrogen-vacancy-engineered 2D W₂N₃ exhibits significant NRR performance. Electrochemical and isotopic labeling experiments reveal that the NV-W₂N₃ follows a distal mechanism that is different from conventional TMNs. The theoretical calculations demonstrate that the electron loss induced by the nitrogen vacancies can lower the thermodynamic limiting potential and thus facilitate the overall NRR. This work highlights the potential of vacancy engineering on 2D materials for catalytic NRR and provides new insight for preparing novel materials for applications in energy storage and conversion systems.

5. The facile and scalable synthesis of a new family of 2D layered TMNs for the HER is achieved by a catalytic molten salt method. The molten salts act as the catalysts during the synthesis and enable the formation of a unique TMN-salt-TMN superstructure. The control experiments reveal the critical role of the alkali metal ion and reaction temperature in the synthesis, which provides the unique ion-induced growth environment and lower formation energy. The resulting 2D TMNs show excellent HER performance as HER electrocatalysts and high volumetric capacitance as capacitor electrode materials, which are better than most of conventional 2D layered materials. The catalytic molten salt method is simple and scalable for synthesizing a

series of 2D layered TMNs and represents a new route for manufacturing 2D layered materials for various applications.

In summary, novel 2D nanomaterials were demonstrated as efficient electrocatalysts for energy-relevant electrocatalytic processes such as the HER and NRR. By modifying their surface properties and electronic structures at the atomic level, the 2D materials can be extended to other research areas. Moreover, discovering the reaction mechanisms of these electrocatalyst materials can provide a solid foundation for the design and optimization of more efficient 2D electrocatalysts.

8.2 Perspectives

Although great achievements have been made in the research area of 2D materials for electrocatalysis, additional endeavors are still required to accelerate the development of 2D electrocatalysts for clean and renewable energy technologies. These include:

1. The current production yield, quality, and quantity of 2D nanomaterials are still inadequate for industrial and commercial requirements. Consequently, the optimization of current synthesis methods is highly needed.
2. Although there has been significant progress on the development of high performance 2D electrocatalysts, a fundamental understanding of their activity origins in many electrocatalytic processes is still required. It is therefore necessary to increase computing power and calculations to investigate the physicochemical properties of 2D electrocatalysts in more detail.
3. Current characterization of 2D electrocatalysts is usually based on *ex-situ* methods. However, one of the most important factors in electrocatalysis is the adsorption of reaction intermediates which cannot be probed using these methods. This generally leads to a poor understanding of the working mechanism. Consequently, more advanced *in-situ* characterization methods are needed.
4. 2D electrocatalysts at present cannot satisfy current commercial and fundamental requirements. Most electrocatalytic processes lack efficient 2D electrocatalysts, resulting in many development opportunities in these fields. Consequently,

synthesizing new 2D electrocatalysts with suitable compositions and functionalities are highly needed.

5. Advanced synthetic methods should be developed to realize precise control of the physical and chemical properties for modelling 2D nanomaterials, such as size, thickness, edges, doping sites, defects, etc. These model catalysts can therefore bridge the gap between molecular configurations in theoretical calculations and the actual samples used in experiments.

2D electrocatalysts represent a significant contribution in both fundamental studies and practical applications in clean energy systems. First, the development of new types of 2D nanomaterials is very promising because they can be tailored to target specific electrocatalytic process. Second, to fully utilize the unique properties of different 2D nanomaterials, hybridization is a promising solution for specific applications. More intriguingly, hybridization of 2D nanomaterials can also generate new properties and functionalities. Last, further efforts are needed to elucidate many details of the working mechanisms, as they currently remain poorly understood. It is of paramount importance to fill the gap between theory and experiments for 2D electrocatalysts, which requires close collaboration amongst material scientists, computational chemists, and electrochemists.

Appendix: Publications during PhD Candidature

- [1] **Huanyu Jin**, Chunxian Guo, Xin Liu, Jinlong Liu, Anthony Vasileff, Yan Jiao, Yao Zheng,* Shi-Zhang Qiao* Emerging Two-Dimensional Nanomaterials for Electrocatalysis. *Chem. Rev.* 2018, 118, 6337–6408.
- [2] **Huanyu Jin**, Xin Liu, Yan Jiao, Anthony Vasileff, Yao Zheng,* Shi-Zhang Qiao* Constructing Tunable Dual Active Sites on Two-Dimensional C₃N₄@MoN Hybrid for Electrocatalytic Hydrogen Evolution. *Nano Energy* 2018, 53, 690–697.
- [3] **Huanyu Jin**, Xin Liu, Anthony Vasileff, Yan Jiao , Yongqiang Zhao, Yao Zheng,* Shi-Zhang Qiao* Single-Crystal Nitrogen-Rich Two-Dimensional Mo₅N₆ Nanosheets for Efficient and Stable Seawater Splitting. *ACS Nano* 2018, 12, 12761–12769.
- [4] **Huanyu Jin**, Xin Liu, Shuangming Chen, Anthony Vasileff, Laiquan Li, Yan Jiao, Li Song, Yao Zheng,* Shi-Zhang Qiao* Heteroatom-Doped Transition Metal Electrocatalysts for Hydrogen Evolution Reaction. *ACS Energy Lett.* 2019, 4, 805–810.
- [5] **Huanyu Jin**, Laiquan Li, Xin Liu, Cheng Tang, Wenjie Xu, Shuangming Chen, Li Song, Yao Zheng, Shi-Zhang Qiao* Nitrogen Vacancies on 2D Layered W₂N₃: A Stable and Efficient Active Site for Nitrogen Reduction Reaction. *Adv. Mater.* 2019, 31, 1902709.
- [6] **Huanyu Jin**, Qinfen Gu, Bo Chen, Cheng Tang, Yao Zheng, Hua Zhang, Mietek Jaroniec, Shi-Zhang Qiao* Molten Salt-Directed Catalytic Synthesis of 2D Layered Transition Metal Nitrides for Efficient Hydrogen Evolution. *Chem* 2020, <https://doi.org/10.1016/j.chempr.2020.06.037>.
- [7] Chao Ye, Yan Jiao, **Huanyu Jin**, Ashley D. Slattery, Kenneth Davey, Haihui Wang,* Shi-Zhang Qiao* 2D MoN-VN Heterostructure To Regulate Polysulfides for Highly Efficient Lithium-Sulfur Batteries, *Angew. Chem. Int. Ed.* 2018, 57, 16703–16707.

- [8] Laiquan Li, Cheng Tang, Bingquan Xia, **Huanyu Jin**, Yao Zheng, Shi-Zhang Qiao* Two-Dimensional Mosaic Bismuth Nanosheets for Highly Selective Ambient Electrocatalytic Nitrogen Reduction. *ACS Catal.* 2019, 9, 2902–2908.
- [9] Yongqiang Zhao, Bo Jin, Yao Zheng, **Huanyu Jin**, Yan Jiao, Shi-Zhang Qiao* Charge State Manipulation of Cobalt Selenide Catalyst for Overall Seawater Electrolysis. *Adv. Energy Mater.* 2018, 8, 1801926.
- [10] Dazhi Yao, Cheng Tang, Laiquan Li, Bingquan Xia, Anthony Vasileff, **Huanyu Jin**, Yanzhao Zhang, Shi-Zhang Qiao, In situ Fragmented Bismuth Nanoparticles for Electrocatalytic Nitrogen Reduction, *Adv. Energy Mater.* 2020, 10, 2001289.